Matrix Product State Approaches to Non-equilibrium Spectral Quantities of Strongly Correlated Fermions in One Dimension

Dissertation
zur Erlangung des mathematisch-naturwissenschaftlichen Doktorgrades
"Doctor rerum naturalium"
der Georg-August-Universität Göttingen

im Promotionsstudiengang Physik
der Georg-August University School of Science (GAUSS)

vorgelegt von

Constantin Meyer
aus Bochum

Göttingen, 2022

Betreuungsausschuss:

Priv.-Doz. Dr. Salvatore R. Manmana

Institut für Theoretische Physik, Georg-August-Universität Göttingen

Prof. Dr. Fabian Heidrich-Meisner

Institut für Theoretische Physik, Georg-August-Universität Göttingen

Priv.-Doz. Dr. Martin Wenderoth

IV. Physikalisches Institut, Georg-August-Universität Göttingen

Mitglieder der Prüfungskommission:

Referent: Priv.-Doz. Dr. Salvatore R. Manmana

Institut für Theoretische Physik, Georg-August-Universität Göttingen

Korreferent: Prof. Dr. Stefan Kehrein

Institut für Theoretische Physik, Georg-August-Universität Göttingen

Weitere Mitglieder der Prüfungskommission:

Priv.-Doz. Dr. Martin Wenderoth

IV. Physikalisches Institut, Georg-August-Universität Göttingen

apl. Prof. Dr. Michael Seibt

IV. Physikalisches Institut, Georg-August-Universität Göttingen

Prof. Dr. Peter E. Blöchl

Institut für Theoretische Physik, Technische Universität Clausthal

Prof. Dr. Matthias Krüger

Institut für Theoretische Physik, Georg-August-Universität Göttingen

Tag der mündlichen Prüfung: 19. April 2022

Abstract

In this thesis we numerically study non-equilibrium phenomena in one-dimensional quantum many-body systems. We discuss extensions of the concepts of spectral functions and of the optical conductivity to time-dependent non-equilibrium setups and compute these quantities by means of matrix product state (MPS)-based methods.

In a first application we study the effect of a spin-selective particle-hole-like excitation on a Hubbard model with an additional magnetic superstructure. Following the excitation, this model exhibits a stable charge density, as well as a stable spin density pattern mirroring the superstructure. For interacting systems we find an additional in-gap signal in the spectral function in the spin direction opposite to the one we applied the excitation in, which also persists over time. Our results are confirmed by a computation of the corresponding optical conductivity. We interpret our results as a trace of an exciton, which we support by an analysis in the atomic limit, and therefore refer to our findings as a peculiar spinful exciton. In contrast to many other setups, no long-range Coulomb term is needed for this exciton to form.

Second, we apply the same calculus to compute non-equilibrium spectral functions of a Floquet-driven system of interacting spinless fermions in the charge density wave (CDW) Mott insulator phase, where we model the driving through a Peierls substitution ansatz. We find good agreement of our results with computations from an effective model obtained from Floquet theory, as well as Floquet side bands. These, however, do not show at all times as expected. Furthermore, another in-gap signal occurs, that is somewhat reminiscent of free particles, which goes hand in hand with a melting of the CDW pattern.

Author's Note

Parts of this thesis are based on or taken from works published in or submitted to peer-reviewed journals as listed below. The first work is already published, the other ones are submitted and in the review process, preprints being available.

[198] T. Köhler et al. "Formation of spatial patterns by spin-selective excitations of interacting fermions". In: *Phys. Rev. B* 102 (23 Dec. 2020), p. 235166. DOI: 10.1103/PhysRevB.102.235166. URL: https://link.aps.org/doi/10.1103/PhysRevB.102.235166

[243] Constantin Meyer and Salvatore R. Manmana. *Formation of spinful dark excitons in Hubbard systems with magnetic superstructures*. 2021. arXiv: 2109.07037 [cond-mat.str-el]

[278] Alexander Osterkorn, Constantin Meyer, and Salvatore R. Manmana. *In-Gap Band Formation in a Periodically Driven Charge Density Wave Insulator*. 2022. arXiv: 2205.09557 [cond-mat.str-el]

In addition, while working on this thesis, the author contributed to the following paper, which is based on his master thesis.

[417] M. Yarmohammadi et al. "Dynamical properties of a driven dissipative dimerized $S = \frac{1}{2}$ chain". In: *Phys. Rev. B* 103 (4 Jan. 2021), p. 045132. DOI: 10.1103/PhysRevB.103.045132. URL: https://link.aps.org/doi/10.1103/PhysRevB.103.045132

All MPS-data were produced using the SymMPS toolkit implemented by Sebastian Paeckel and Thomas Köhler.

[281] Sebastian Paeckel and Thomas Köhler. *SymMPS*. https://www.symmps.eu. Accessed: 2020-09-23. URL: https://www.symmps.eu

All figures depicting tensor networks or finite state machines were generated using modified LaTeX scripts of Thomas Köhler's and Sebastian Paeckel's, and will, hence, bear similarities to their works [195, 282, 283, 280].

Contents

1 Introduction

Characterizing different (classes of) materials for their properties is one of the major tasks in condensed matter physics, both theoretically and experimentally. While in earlier times research was mainly focused on setups at equilibrium, more recently interest has increased in also investigating out-of-equilibrium situations. For instance, excited states have been investigated for their symmetries [374] and dynamics [119, 267]. The investigation of thermalization processes being also pursued [329], one reason for the shift of focus to out-of-equilibrium situations is the observation that non-equilibrium quantum systems may show an entirely different behavior than their equilibrium counterparts.

An example is the emergence of order in non-equilibrium quantum systems which has inspired a lot of experimental and theoretical research. For instance, so-called time-crystal phases [312, 247] have been predicted by theory to exist in Floquet-driven systems [190, 93] and to be stable [189, 94]. Research went as far as mapping out a phase diagram [415, 416], and, indeed, such systems were realized in experiment through an interacting spin chain of trapped atomic ions [425] or spin impurities in diamond [60]. Other than this also metastable ordered states have been found in experiment following a photoexcitation, including hidden charge density wave (CDW) states [352], light induced magnetic textures [89], or structural order in organic charge transfer crystals [66]. In this context transitional structures have been measured [25] and non-equilibrium phase transitions have been observed [302]. However, not only the creation of CDWs has been observed but also the transformation of already existing ones. Materials to exhibit CDWs are for example cuprate superconductors [115, 137, 411, 88, 7], where they actually compete with superconducting phases [55, 116, 166, 341, 52]. The alteration of CDWs includes the optically driven transition between different CDW states [394, 208], the enhancement of existent order [342], or even its transient melting [317, 376, 351, 142, 344] following an excitation. In a similar experiment non-thermal melting of germanium [340] has been observed as early as in 1999. The melting process can nowadays even be controlled [232] and the stability of transient CDWs can be quantified [299]. Also, the vaporization of CDW structures is possible [306] and, hence, transient CDWs can be classified by their lifetime [147]. Instabilities in CDWs can also be measured [56] as can the effect of doping on electron dynamics be measured [18]. While some of these experiments rely on diffraction methods, the majority is conducted by means of photoemission spectroscopy (PES) [176, 177], a subclass of spectroscopy [19], where the photoexcitation is achieved using ultrashort laser pulses [202] in pump-probe setups. With this type of experiments, phase transitions can be observed [156, 265], but also the lifetimes of photoelectrons have been measured [365]. Another interesting effect is the observation of transient superconducting states in such non-equilibrium setups [157], which can stem from or be influenced by orbital manipulation [308] or a transition from an ordered state [100] but more importantly occurs at elevated temperatures [244]. In this context, the theoretical concept of η-pairing is discussed, c.f. for instance [91]. Also, the effect of dissipation was discussed [264]. Recently, a mechanism for the ultrafast control of magnetic subsystems by means of optically induced spin transfer (OISTR) has been proposed theoretically [92, 78] and was later verified in experiment [366, 348, 150]. Further experimental results in non-equilibrium quantum systems [168] include the investigation of photoinduced magnetic switching [215], quantum interference [397], or

of the dynamics of hot carriers [53], photoinduced strange metal states [74], or photodoped charge transfer insulators [122], as well as the experimental observation of doublon dynamics [220, 219], impact ionization [239, 313], the laser-assisted photoelectric effect [188, 186], or Auger recombination [187].

Identifying theoretical mechanisms predicting the behavior in non-equilibrium setups is also actively pursued in ongoing research. For instance, the enhancement [224] and melting [338] of charge order following a transient laser pulse in strongly correlated systems were explained and similarly has photoinduced enhancement of charge correlations been investigated [418]. In references [401] and [284] light-induced superconductivity was examined, while reference [87] deals with the relaxation times of photo carriers. Also, non-equilibrium steady-states have been found to exist [214]. Further studies are devoted to investigating non-equilibrium dynamics [373, 403] which also includes research on spin liquids [63] and the effects of frustration [34], the formation and relaxation of dressed quasi particles [263], dynamical symmetry breaking [380], light-matter coupling [318], and reflectivity transients [315].

In this work we will focus on the analysis of strongly correlated systems, of which the properties are determined by interactions of particles. The theoretical description of strongly correlated systems is a challenging topic since due to the interactions a treatment in terms of single-particle problems is in general not guaranteed to yield qualitatively correct results. Hence, perturbative or fully numerical approaches need to be applied. A very simple ansatz would be to perform a mean-field decoupling, in which the interaction term is replaced such that single particles are coupled to the average value of their neighbors. This approach, however, can produce incorrect results. Nevertheless have effective single particle pictures been successfully applied in terms of band theory, which states a system to be insulating when its Fermi energy lies between two separated bands and conductive otherwise. That way, a framework to distinguish metals, semiconductors and insulators was found. However, certain systems that are predicted to behave as conductors by band theory, turn out to be insulating. Such systems are referred to as Mott insulators and are subject to intense research, both in theory and in experiment [112].

Strong correlations in such materials are discussed as possible sources for increasing the efficiency of photovoltaic devices [237, 236, 294]. Such an effect could be achieved through the formation of multiple exciton generation, e.g. due to impact ionization. Excitons are bound particle-hole pairs that come into existence in solids due to Coulomb interaction leading to a binding energy between an electron excited to the conduction band and the remaining hole in the valence band [192, 193, 145]. Since they have strong influence on the optical properties of their compounds [23], for instance by causing a bandgap renormalization [222, 58], excitons are subject to intense studies. Important questions are how they are formed and which characteristics they possess in the presence of strong correlations. Excitonic states have been discussed at equilibrium [412, 303], where those excitons that are accessible by light are distinguished from those that are not, the latter of which are usually referred to as dark excitons [330, 231, 13, 309]. In recent years other types of excitons have been found. Among those are so-called interlayer excitons, where its electron and hole are spatially separated into two layers [205, 419, 424] or moiré excitons, which form in moiré (super)lattices consisting of two misaligned lattices [377, 174]. Such van-der-Waals heterostructures are frequently encountered in well-controllable [295] transition metal dichalcogenides [175, 95, 426, 428]. Even and hints for the existence moiré trions, which can in a very simple picture be regarded as excitons with a charge, have been reported [221], as has the observation of biexcitons [246]. By doping, excitons can be charged [44], there are studies concerning their lifetimes [143] and recombination times [211, 210, 245], and, perhaps most importantly, they can also be altered be it by a melting [121] or a

photoinduced enhancement [249, 364] of the band gap. Even more so, can the formation of excitons be induced by optical excitations [172, 300, 301]. In Mott insulators [248, 112], excitons lead to resonances, which may also occur in the gap region of the optical conductivity [170, 96].

More recently, the question has been studied how to identify (dark) excitons in angle resolved PES-type (ARPES) measurements, both experimentally [398, 80, 228] and theoretically [292, 345, 35, 61]. To describe the results of ARPES-type experiments, spectral functions are employed [400]. As for the presence of excitons, in theoretical studies a midgap signature in the corresponding spectral function is shown to occur, where the existence of nearest-neighbor or longer-range Coulomb interactions is common to all the applied model systems.

In this thesis, we investigate the formation of excitons in Hubbard-like systems with only on-site electron-electron interactions and an additional magnetic superstructure, but without longer-range Coulomb interactions [197, 195, 33]. Instead, we investigate the effect of a single, direct particle-hole-like excitation, in which a particle is assumed to be instantly excited over the gap without changing its momentum. We apply this excitation in a single spin direction only, i.e. the electrons of the other spin direction are not affected by the incoming light. Such a spin-selective excitation then leads to the formation of spatially periodic charge-density or spin-density patterns, which are stable on comparably long time scales [198]. This approach is motivated by the realization of spin-selective photoexcitations as in spin-polarized ARPES or time-resolved ARPES (trARPES) experiments, c.f. e.g. [194, 268, 8] for further reading or [427, 32] for applications. Indeed, nowadays trARPES is a frequently and very powerful applied method in experimental physics when it comes to the analysis of materials. Apart from the detection of excitons, for instance, also electron-phonon couplings have been measured [250]. We will not simulate trARPES experiments in total, but rather aspects of them. In doing so, we conduct simulations using time-dependent matrix product states (MPSs) [320, 283] and study the time evolution of single-particle spectral functions, where we find the photoexcitation to lead to additional signals only in the *opposite* spin direction than the one excited, and the time-dependent optical conductivity. Therefore we call the excitonic signals we observe spinful excitons. We study the recombination process of the particle-hole excitation and find its time scale to be much longer than the ones amenable to MPS, which in our simulations corresponds to times of ~ 30fs in pump-probe experiments. Both the definitions for the time-dependent spectral functions, as well as for the time-dependent optical conductivity are derived from their equilibrium counterparts. However, these definitions are not unique, such that different variants may be more suitable for certain problems. This problem becomes especially apparent when we apply our formalism to a Floquet-driven system, which are also intensively studied, c.f. for instance [227, 57]. Here, we consider a so-called tV-chain of interacting spinless fermions and find, as Floquet theory predicts, side bands, however not at all times. We further encounter another peculiar in-gap feature in the spectrum, which we associate to the melting of a CDW.

This thesis is structured as follows: In chapter 2 we give a very brief review of quantum mechanics. In chapter 3 we discuss basic numerical routines amongst other concepts. Chapter 4 will be devoted to introducing the concept of matrix product states and operators including their properties. Based on these insights we will present principal MPS-based algorithms in chapter 5, where we shall restrict ourselves to zero temperature setups. We will introduce the models to be considered in chapter 7 followed by an introduction of our main observables in chapter 6. We will discuss different ways to describe out-of-equilibrium setups with particular respect to the definition of non-equilibrium spectral functions and optical conductivities. A motivation for the respective definitions will be given. Chapters 8 and 9 then contain our main results, the former focusing on equilibrium properties to gain a basic understanding of the models, the latter on the out-of-equilibrium situations. In

chapter 10 we discuss Floquet-driven systems also explaining the pitfalls of our earlier set up scheme, as well as its limits. Finally, a summary and an outlook will be provided in chapter 11.

2 Basic Concepts of Quantum Mechanics

We begin with a very quick overview of quantum mechanics. Most of the concepts introduced here will be applied in later sections of this work. This entire chapter is primarily based on the textbooks [64, 65] and [314]. At first, we shall briefly introduce quantum states and operators. Next, the Hilbert space and the Schrödinger equation are discussed, followed by the time-evolution operator and an overview of the different dynamical pictures. Lastly, we introduce the concept of exact diagonalization, which, in principle, allows to compute all quantum systems exactly, but due to its complexity cannot be applied to arbitrary problems in practice. We will restrict our considerations to $T = 0$ as we will not be dealing with thermal systems in the remainder of this thesis. Note further that this is the only section in this work where the reduced Planck constant $\hbar$ is denoted. Afterwards we shall set $\hbar = 1$.

2.1 States, Operators, and Second Quantization

The description of quantum systems is governed by so-called quantum states, which are obtained from a generalization of representations of a system's wave function ψ. We denote the quantum state corresponding to a wave function ψ by $|\psi\rangle$ in Dirac notation [79]. The state vectors of a physical system constitute a vector space, the so-called Hilbert space $\mathscr{H}$, thus $|\psi\rangle \in \mathscr{H}$. We further denote the scalar product of two states $|\psi\rangle, |\psi'\rangle \in \mathscr{H}$ by

$$o = \langle\psi|\psi'\rangle \in \mathbb{C}, \tag{2.1}$$

which satisfies

$$\langle\psi|\psi'\rangle = \langle\psi'|\psi\rangle^* . \tag{2.2}$$

By $\langle\psi|$ we denote the vector of the dual space $\mathscr{H}^*$ corresponding to $|\psi\rangle$. Commonly $|\psi\rangle$ is called a ket-vector or in short ket, while $\langle\psi|$ is referred to as a bra-vector or simply bra, o is also known as the overlap of $|\psi\rangle$ and $|\psi'\rangle$. A state $|\psi\rangle$ to satisfy

$$\| |\psi\rangle \| \coloneqq \sqrt{\langle\psi|\psi\rangle} = 1 \tag{2.3}$$

is called normalized, $\| |\psi\rangle \|$ is the norm of $|\psi\rangle$.

Quantum mechanical states may be modified by linear maps, so-called operators, $\hat{O} \colon \mathscr{H} \mapsto \mathscr{H}$ such that

$$|\psi'\rangle = \hat{O}\,|\psi\rangle. \tag{2.4}$$

According to the correspondence principle, to every classical quantity there exists an operator in quantum mechanics. Operators to fulfill

$$\hat{O} = \hat{O}^\dagger \tag{2.5}$$

are said to be Hermitian. Such Hermitian operators are observables

$$O_{|\psi\rangle} = \langle\psi|\,\hat{O}\,|\psi\rangle = \left\langle\hat{O}\right\rangle = O \in \mathbb{R}, \tag{2.6}$$

which can be measured in experiment. The average result of multiple measurements of physical quantity described by an observable then corresponds to the expectation value of the operator $\hat{O}$ with respect to the quantum state $|\psi\rangle$. The last two notations in the above equations are frequently encountered short forms used when the state $|\psi\rangle$ with respect to which the measurement is conducted is either clear or irrelevant. In most applications this will then be the so-called ground state of the system we shall properly introduce in section 2.3. Operators in general do not commute, that is for two operators $\hat{O}_1$ and $\hat{O}_2$ the commutator

$$\left[\hat{O}_1, \hat{O}_2\right] = \hat{O}_1\hat{O}_2 - \hat{O}_2\hat{O}_1 \neq 0 \tag{2.7}$$

does not vanish in general. An important concept in terms of operators commonly known as second quantization is the introduction of creation and annihilation operators which each are adjoints of the respective other. The former describes the creation of its corresponding (quasi) particle, the latter its destruction. Creation and annihilation operators, $\hat{b}_n^\dagger$ and $\hat{b}_m$ that fulfill

$$\left[\hat{b}_n, \hat{b}_m\right] = 0 \tag{2.8}$$

$$\left[\hat{b}_n^\dagger, \hat{b}_m^\dagger\right] = 0 \tag{2.9}$$

$$\left[\hat{b}_n, \hat{b}_m^\dagger\right] = \delta_{n,m} \tag{2.10}$$

are called bosonic, their corresponding (quasi) particles are referred to as bosons. If in turn for operators $\hat{f}_n^\dagger$ and $\hat{f}_m$

$$\left\{\hat{f}_n, \hat{f}_m\right\} = 0 \tag{2.11}$$

$$\left\{\hat{f}_n^\dagger, \hat{f}_m^\dagger\right\} = 0 \tag{2.12}$$

$$\left\{\hat{f}_n, \hat{f}_m^\dagger\right\} = \delta_{n,m} \tag{2.13}$$

holds true, we encounter fermionic operators describing fermions. Here we have introduced the anti-commutator $\{\cdot,\cdot\}$ which is defined via

$$\left\{\hat{O}_1, \hat{O}_2\right\} = \hat{O}_1\hat{O}_2 + \hat{O}_2\hat{O}_1. \tag{2.14}$$

The above equations show a fundamental difference between fermions and bosons. While for the former it is impossible for two identical particles to exist at the same instant, for the latter there is no such upper bound. This property of fermions is referred to as the fermionic exclusion principle.

So far, we have actually without explicitly mentioning it investigated such quantum mechanical systems that only describe a single wave function and, thus, a single particle problem. The concepts introduced above, however, may be easily generalized for the description of many-body systems. Consider a system of L sites, each one describing a single particle problem. The quantum state is then given by the tensor product

$$|\psi\rangle = |\psi_0\rangle \otimes |\psi_1\rangle \otimes \cdots \otimes |\psi_{L-2}\rangle \otimes |\psi_{L-1}\rangle, \tag{2.15}$$

the state $|\psi_i\rangle$ describing the system at site i. In this case, we also differentiate between local and global operators, the former acting on only a single, while the latter modifying several or all sites.

Most often, the site a local operator acts on is indicated by an index. Crucial to many-body systems is the presence of some sort of interaction between the individual sites since otherwise it would be possible to solve the single particle problems individually. As we shall see below in section 7.1.1 an apparent many-body problem in a certain representation may be converted into a set of single particle problems in another representation, a common example being the tight-binding model. This class of problems is, however, very small.

2.2 The Hilbert Space

As we have learned in the previous section, the Hilbert space incorporates all quantum states a physical system can take. Since the Hilbert space is a vector space, to each such Hilbert space there corresponds a basis defining its dimension. This dimension may either be finite or infinite. As for the former, consider a single spin-1/2 particle. Classically it may either be in the state $|\uparrow\rangle$ or $|\downarrow\rangle$. Quantum mechanically, these two states form a basis of its Hilbert space, such that a general state will be determined by a superposition

$$|\psi\rangle = c_\uparrow |\uparrow\rangle + c_\downarrow |\downarrow\rangle, \quad c_\uparrow, c_\downarrow \in \mathbb{C} \tag{2.16}$$

with the additional constraint

$$c_\uparrow^2 + c_\downarrow^2 = 1 \tag{2.17}$$

if $|\psi\rangle$ is normalized. The prime example of an infinitely dimensional Hilbert space is the quantum mechanical harmonic oscillator, where the states counting the number of modes $|n\rangle$ form the basis, $n \in \{0, \dots, \infty\}$, such that a general state in this case is given by

$$|\psi\rangle = \sum_n c_n |n\rangle \quad c_n \in \mathbb{C}. \tag{2.18}$$

As for many-body systems, the total Hilbert space is determined by $\mathscr{H} = \bigotimes_i \mathscr{H}_i$, $\mathscr{H}_i$ being the so-called local Hilbert space at site i. If we suppose all local Hilbert spaces to be identical, the total Hilbert space is commonly called $\mathscr{H}^L$. Let d be the local Hilbert space dimension. We, thus, obtain

$$\mathbf{dim}\big(\mathscr{H}^L\big) = d^L, \tag{2.19}$$

that is the Hilbert space grows exponentially with system size. As we shall further elaborate on in section 2.6 this particular property severely limits computational possibilities to a complete treatment of such systems. The total Hilbert space of a many-body system may be divided into sectors according to the total number of particles in the system summed over all sites. A Hilbert space with such a property is called a Fock space.

2.3 The (Time-dependent) Schrödinger Equation

In quantum mechanics a quantum system is described by its possibly time-dependent Hamiltonian $\hat{H}(t)$, which contains all information about the system's properties. We further introduce the quantum state $|\psi(t)\rangle$ to describe the system at a certain time t at zero temperature $T = 0$.

Conveniently, $|\psi(t)\rangle$ is thus referred to as the state of the system at time t. All these states satisfy the time-dependent Schrödinger equation [322, 323, 324, 325]

$$\mathrm{i}\hbar\frac{\mathrm{d}}{\mathrm{d}t}\,|\psi(t)\rangle = \hat{H}(t)\,|\psi(t)\rangle, \tag{2.20}$$

which clearly determines the time evolution of $|\psi(t)\rangle$. The time-dependent Schrödinger equation has the following properties:

1. It is linear, that is if $|\psi_a(t)\rangle$ and $|\psi_b(t)\rangle$ solve (2.20), so does

$$|\psi(t)\rangle = a\,|\psi_a(t)\rangle + b\,|\psi_b(t)\rangle\,, \quad a, b \in \mathbb{C}. \tag{2.21}$$

   Phrased differently, this property states that to any state $|\psi(t_0)\rangle = a\,|\psi_a(t_0)\rangle + b\,|\psi_b(t_0)\rangle$ at time t_0 the corresponding state at time t is given by equation (2.21).

2. It is homogeneous in $|\psi(t)\rangle$. This feature is of particular importance if it is expressed as a differential equation of wave functions.

3. It is non-relativistic. The relativistic generalization is given by the Dirac equation. Since the treatment of relativistic systems goes far beyond the scope of this thesis we refer to some standard textbooks, e.g. [130], at this point for further reading.

If we are to describe the state $|\psi(t)\rangle$ of the quantum system at any time t, thus, the "only" thing we need to do is to solve the time-dependent Schrödinger equation (2.20).

An important special case is obtained if the Hamiltonian is time-independent, i.e.

$$\hat{H}(t) = \hat{H}, \tag{2.22}$$

which is of particular importance in the description of quantum systems in equilibrium. In this case, the time-dependent Schrödinger equation (2.20) can easily be shown to be (partially) solved by the ansatz

$$\big|\psi_{n,j}(t)\big\rangle = \mathrm{e}^{-\mathrm{i}\omega_n t}\,\big|\psi_{n,j}(t_0)\big\rangle, \tag{2.23}$$

where t_0 is to be kept fix. Inserting into equation (2.20) we obtain

$$\hbar\omega_n\,\big|\psi_{n,j}(t_0)\big\rangle = \hat{H}\,\big|\psi_{n,j}(t_0)\big\rangle. \tag{2.24}$$

Identifying the prefactor in the left-hand side of the above equation to correspond to an energy

$$E_n = \hbar\omega_n, \tag{2.25}$$

we obtain the time-independent Schrödinger equation

$$\hat{H}\,\big|\psi_{n,j}(t_0)\big\rangle = E_n\,\big|\psi_{n,j}(t_0)\big\rangle, \tag{2.26}$$

which describes an eigenvalue problem. Hence, the states $|n,j\rangle = \big|\psi_{n,j}(t_0)\big\rangle$ are called the eigenstates of $\hat{H}$, which we shall sort according to their eigenenergies

$$E_0 < E_1 < \cdots < E_m. \tag{2.27}$$

The index j was simply introduced to count possibly degenerate eigenstates. Should all eigenstates be non-degenerate, it may safely be disregarded. All eigenstates corresponding to the lowest energy E_0 are called the ground state of $\hat{H}$

$$|\mathrm{GS}\rangle = |0,j\rangle. \tag{2.28}$$

Hence, E_0 is referred to as the ground state energy. Any system in equilibrium will stay in this state and have this energy. Note that with setting up the time-independent Schrödinger equation (2.26) we have transformed the problem of solving a linear differential equation into an algebraic problem.

From the time-independent Schrödinger equation (2.26) we may further illustrate that the expectation value of the Hamiltonian yields the energy of the system. This relation actually holds true in general, i.e.

$$E(t) = \langle\psi(t)|\,\hat{H}(t)\,|\psi(t)\rangle. \tag{2.29}$$

2.4 The Time Evolution Operator

Consider an arbitrary quantum state $|\psi(t_0)\rangle$ at time t_0. We define the time evolution operator $U(t, t_0)$ which transforms the state $|\psi(t_0)\rangle$ into $|\psi(t)\rangle$ at time t via

$$|\psi(t)\rangle = U(t, t_0)\,|\psi(t_0)\rangle. \tag{2.30}$$

Inserting the above into the time-dependent Schrödinger equation (2.20) we find

$$\mathrm{i}\hbar\frac{\mathrm{d}}{\mathrm{d}t}U(t, t_0)\,|\psi(t_0)\rangle = \hat{H}(t)\,U(t, t_0)\,|\psi(t_0)\rangle. \tag{2.31}$$

Since $|\psi(t_0)\rangle$ was chosen to be arbitrary, for the time evolution operator

$$\mathrm{i}\hbar\frac{\mathrm{d}}{\mathrm{d}t}U(t, t_0) = \hat{H}(t)\,U(t, t_0) \tag{2.32}$$

must hold true. This equation can be formally solved, yielding

$$U(t, t_0) = \mathscr{T}\exp\left(-\frac{\mathrm{i}}{\hbar}\int_{t_0}^{t}\mathrm{d}t'\,\hat{H}(t')\right), \tag{2.33}$$

where $\mathscr{T}$ is the time ordering operator. If the Hamiltonian at different times commutes, i.e. $\left[\hat{H}(t'), \hat{H}(t'')\right] = 0$, the time ordering operator may be dropped from equation (2.33). Note that the Hamiltonian $\hat{H}(t)$ is crucial to the definition of the time evolution operator $U(t, t_0)$. Therefore, in complete rigor we should refer to $U(t, t_0)$ as the time evolution operator with respect to $\hat{H}(t)$.

If the Hamiltonian is time-independent, the time evolution operator takes the simple form

$$U(t, t_0) = \mathrm{e}^{-\mathrm{i}\hat{H}\cdot(t-t_0)/\hbar}. \tag{2.34}$$

The time evolution operator has the following properties.

1. It is unitary, i.e.
$$U^\dagger(t, t_0)\,U(t, t_0) = \mathbb{1}. \tag{2.35}$$

2. For $t = t_0$ it is the identity
$$U(t_0, t_0) = \mathbb{1}. \tag{2.36}$$

3. It satisfies
$$U(t,t_0) = U(t,t')\,U(t',t_0) \quad \forall t'. \tag{2.37}$$

From the above properties it is easy to deduce that
$$U^\dagger(t,t_0) = U(t_0,t)\,. \tag{2.38}$$

Often times we have $t_0 = 0$. In this case we write
$$U(t) = U(t,0) \tag{2.39}$$
for short, such that the adjoint is given by
$$U^\dagger(t) = U(-t). \tag{2.40}$$

2.5 Schrödinger vs. Heisenberg vs. Dirac Picture and Their Transitions

So far, in order to describe quantum mechanical systems, we have encountered time-dependent quantum states $|\psi(t)\rangle_{\mathrm{S}}$ of which the time evolution is governed by the Schrödinger equation (2.20). The quantum states may be altered through the application of operators $\hat{O}_{\mathrm{S}}(t)$, which may likewise be time-dependent. All the above mentioned properties characterize the so-called Schrödinger picture. We shall indicate for the remainder of this section states and operators belonging to this particular picture with the subscript $_{\mathrm{S}}$.

The mathematics of quantum mechanics, however, may be conducted in different ways. We define the Heisenberg picture, in which the entire time-dependence is shifted to the operators, leaving the quantum states time-independent. We will use the subscript $_{\mathrm{H}}$ to tell operators and states in this picture apart from the Schrödinger picture. Let t_0 be fix. We introduce the time-independent quantum state in the Heisenberg picture as
$$|\psi(t_0)\rangle_{\mathrm{H}} = U_{\mathrm{S}}^\dagger(t,t_0)\,|\psi(t)\rangle_{\mathrm{S}}\,. \tag{2.41}$$

Accordingly, an operator in the Heisenberg picture is related to its counterpart in the Schrödinger picture via
$$\hat{O}_{\mathrm{H}}(t) = U_{\mathrm{S}}^\dagger(t,t_0)\,\hat{O}_{\mathrm{S}}(t)\,U_{\mathrm{S}}(t,t_0). \tag{2.42}$$

Differentiating this equation, we find the Heisenberg equation of motion
$$\frac{\mathrm{d}}{\mathrm{d}t}\hat{O}_{\mathrm{H}}(t) = \mathrm{i}\left[\hat{H}_{\mathrm{H}}(t)\,,\hat{O}_{\mathrm{H}}(t)\right] + \left(\partial_t \hat{O}_{\mathrm{S}}(t)\right)_{\mathrm{H}} = \mathrm{i}\left[\hat{H}_{\mathrm{H}}(t)\,,\hat{O}_{\mathrm{H}}(t)\right] + U_{\mathrm{S}}^\dagger(t,t_0)\left(\partial_t \hat{O}_{\mathrm{S}}(t)\right)U_{\mathrm{S}}(t,t_0) \tag{2.43}$$
describing the time evolution of operators in the Heisenberg picture. With $[\cdot,\cdot]$ we describe the commutator. Note that certain operators are independent of their representation in Heisenberg or Schrödinger picture, most notably the Hamiltonian $\hat{H}$ and its corresponding time evolution operator $U^\dagger(t,t_0)$ themselves since the Hamiltonian commutes with itself as can be easily verified from inserting into equation (2.42).

For the sake of completeness we mention a third commonly applied dynamical picture, the interaction or Dirac picture, which in some sense can be interpreted as a combination of the Schrödinger and the Dirac picture. In its definition we decompose in the Schrödinger picture the Hamiltonian into
$$\hat{H}_{\mathrm{S}}(t) = \hat{H}_{0,\mathrm{S}}(t) + \hat{H}_{1,\mathrm{S}}(t), \tag{2.44}$$

where we consider $\hat{H}_{1,\mathrm{S}}(t)$ to be a perturbation of an otherwise easily solvable system specified by $\hat{H}_{0,\mathrm{S}}(t)$. Note that in most applications $\hat{H}_{0,\mathrm{S}}(t)$ is chosen to be time-independent. This, however, is not required by its definition. We will use the subscript $_{\mathrm{D}}$ to mark states and operators given in the Dirac picture. We define a quantum state in the Dirac picture via

$$|\psi(t)\rangle_{\mathrm{D}} = U^{\dagger}_{0,\mathrm{S}}(t,t_0)\,|\psi(t)\rangle_{\mathrm{S}} \tag{2.45}$$

and an operator via

$$\hat{O}_{\mathrm{D}}(t) = U^{\dagger}_{0,\mathrm{S}}(t,t_0)\,\hat{O}_{\mathrm{S}}(t)\,U_{0,\mathrm{S}}(t,t_0), \tag{2.46}$$

where $U_{0,\mathrm{S}}(t,t_0)$ is the time evolution operator in the Schrödinger picture with respect to only $\hat{H}_{0,\mathrm{S}}(t)$. The time evolution of the states and operators is then given by

$$\mathrm{i}\hbar\frac{\mathrm{d}}{\mathrm{d}t}\,|\psi(t)\rangle_{\mathrm{D}} = \hat{H}_{1,\mathrm{S}}(t)\,|\psi(t)\rangle_{\mathrm{D}} \tag{2.47}$$

and

$$\frac{\mathrm{d}}{\mathrm{d}t}\hat{O}_{\mathrm{D}}(t) = \mathrm{i}\left[\hat{H}_{0,\mathrm{S}}(t)\,,\hat{O}_{\mathrm{D}}(t)\right] + \left(\partial_t\hat{O}_{\mathrm{S}}(t)\right)_{\mathrm{D}} \tag{2.48a}$$

$$= \mathrm{i}\left[\hat{H}_{0,\mathrm{S}}(t)\,,\hat{O}_{\mathrm{D}}(t)\right] + U^{\dagger}_{0,\mathrm{S}}(t,t_0)\left(\partial_t\hat{O}_{\mathrm{S}}(t)\right)U_{0,\mathrm{S}}(t,t_0), \tag{2.48b}$$

respectively. Equation (2.47) bears similarities to the Schrödinger equation (2.20), while equation (2.48) is essentially the Heisenberg equation of motion (2.43). Note that in the Dirac picture the Hamiltonian is not necessarily equal to its expression in the Schrödinger or Heisenberg picture, this being only the case if $\hat{H}_{0,\mathrm{S}}(t)$ and $\hat{H}_{1,\mathrm{S}}(t)$ commute, i.e. $\left[\hat{H}_{0,\mathrm{S}}(t)\,,\hat{H}_{1,\mathrm{S}}(t)\right] = 0$.

Although in these three dynamical pictures that we have introduced above the states and operators have in general different properties depending on their respective representation, certain features are invariant. First, the quantum state at t_0 is independent of the picture,

$$|\psi(t_0)\rangle_{\mathrm{S}} = |\psi(t_0)\rangle_{\mathrm{H}} = |\psi(t_0)\rangle_{\mathrm{D}} = |\psi(t_0)\rangle. \tag{2.49}$$

Second, expectation values are likewise picture-independent,

$${}_{\mathrm{S}}\langle\psi(t)|\,\hat{O}_{\mathrm{S}}(t)\,|\psi(t)\rangle_{\mathrm{S}} = {}_{\mathrm{H}}\langle\psi(t_0)|\,\hat{O}_{\mathrm{H}}(t)\,|\psi(t_0)\rangle_{\mathrm{H}} = {}_{\mathrm{D}}\langle\psi(t)|\,\hat{O}_{\mathrm{D}}(t)\,|\psi(t)\rangle_{\mathrm{D}} = \langle\psi(t)|\,\hat{O}(t)\,|\psi(t)\rangle \tag{2.50}$$

Hence, we may drop the subscript in the above equations. Taking the expectation value with respect to a state $|\psi(t')\rangle$ of the Heisenberg equation of motion (2.43) we may exploit equation (2.50), such that we obtain the picture-independent result

$$\frac{\mathrm{d}}{\mathrm{d}t}\,\langle\psi(t')|\,\hat{O}(t)\,|\psi(t')\rangle = \mathrm{i}\,\langle\psi(t')|\left[\hat{H}(t)\,,\hat{O}(t)\right]|\psi(t')\rangle + \langle\psi(t')|\left(\partial_t\hat{O}_{\mathrm{S}}(t)\right)|\psi(t')\rangle. \tag{2.51}$$

The above equation is referred to as the Heisenberg equation of motion for expectation values. Nevertheless, we shall simply call both, equation (2.43) just like equation (2.51), the Heisenberg equation of motion. If the state we are computing the expectation value with reference to is clear, we may write equation (2.51) in short as

$$\frac{\mathrm{d}}{\mathrm{d}t}\left\langle\hat{O}\right\rangle(t) = \mathrm{i}\left\langle\left[\hat{H}(t)\,,\hat{O}(t)\right]\right\rangle + \left\langle\left(\partial_t\hat{O}_{\mathrm{S}}(t)\right)\right\rangle. \tag{2.52}$$

Should the operator $\hat{O}_{\mathrm{S}}(t)$ further be time-independent, i.e. $\partial_t\hat{O}_{\mathrm{S}}(t) = 0$, we obtain the even easier form

$$\frac{\mathrm{d}}{\mathrm{d}t}\left\langle\hat{O}\right\rangle(t) = \mathrm{i}\left\langle\left[\hat{H}(t)\,,\hat{O}(t)\right]\right\rangle. \tag{2.53}$$

2.6 Exact / Full Diagonalization

Let us go back to the problem of solving the time-independent Schrödinger equation (2.26). As we have already pointed out in section 2.3 we face an eigenvalue problem. Here the quantum states take the role of vectors and accordingly may the operators be expressed as matrices. Let us by $|b_i\rangle$ denote a basis state of the Hilbert space $\mathscr{H}$, irrespective of whether it may be finite or not, of the Hamiltonian $\hat{H}$. The index i labeling the basis states, hence, takes values $i \in \{0, \dots, \dim(\mathscr{H})\}$. It is, thus, possible to set up a $\dim(\mathscr{H}) \times \dim(\mathscr{H})$-size Hamilton matrix H, which is determined by

$$H_{i,j} = \langle b_i | \hat{H} | b_j \rangle. \tag{2.54}$$

Diagonalizing this matrix

$$H = S \cdot D \cdot S^\dagger, \tag{2.55}$$

where D is diagonal and S Hermitian, we find the eigenstates of $\hat{H}$ to be determined by

$$|n, j\rangle = \sum_l S^*_{l,(n,j)} |b_l\rangle. \tag{2.56}$$

Their corresponding eigenenergies are given by

$$E_n = D_{(n,j),(n,j)}. \tag{2.57}$$

Consider now an arbitrary quantum state $|\psi(t_0)\rangle$ at fixed time t_0. If we express this state in terms of the previously found eigenstates

$$|\psi(t_0)\rangle = \sum_n c_{(n,j)}(t_0) |n, j\rangle, \tag{2.58}$$

its time evolution is completely determined by

$$|\psi(t)\rangle = \sum_{(n,j)} c_{(n,j)}(t_0)\, \mathrm{e}^{-\mathrm{i}E_n t} |n, j\rangle. \tag{2.59}$$

Hence, we have complete knowledge of the entire quantum system.

While this result in theory appears to be satisfactory, in practice this procedure of what is commonly called exact (or full [234]) diagonalization, ED or FD, is severely limited, compare for instance [167, 20], the problem being that the size of the Hilbert space grows exponentially with the system size L in case of a many-body system. Clearly, if the Hilbert space is of infinite dimensions this methods cannot be applied at all without modifications. With modern super computers system sizes of some tens of particles may be solved by means of exact diagonalization. There exist numerous specified algorithms to facilitate the actual diagonalization routine, see e.g. reference [21] for further reading. We shall describe one method, the Lanczos algorithm in section 3.4. Yet still, the problem of the exponentially growing Hilbert space cannot be tackled with conventional computers as advanced as they may be or become. Thus, the need for approximative methods is evident. Over the last decades several such methods have been developed each coming with their strengths and weaknesses. Such methods include density functional theory (DFT) [83], dynamical mean field theory (DMFT) [114], or quantum Monte Carlo methods (QMC) [258]. In this thesis we shall make use of the density matrix renormalization group (DMRG), to which we devote section 4.1, c.f. [259] for a comparison to ED. For a more comprehensive overview see for instance [101]. All these methods allow with certain restrictions the evaluation of systems with larger Hilbert spaces. Their quality may be then judged from reference data produced with ED for smaller systems.

3 Typical Numerical Methods in Tensor Network Computations

Before we begin with describing the key algorithms used in this thesis, we first set a base in introducing underlying concepts. The language of matrix-product states (MPSs) requires a tensor-based formulation. Hence, we will first introduce the concept of tensors in the first section of this chapter. Next, we will explain their pictorial notation. As will become obvious, a purely mathematical handling of tensors in terms of formulas becomes quite cumbersome and difficult to process even for rather simple structures. Just like Feynman diagrams sketching the associated relations provides an enormous benefit in understanding the corresponding calculations, plus in the case of tensors or tensor networks to be more precise this notation by design enforces correctness.

The next two sections deal with decomposing matrices in terms of the QR decomposition and the singular value decomposition (SVD), respectively. Both of these schemes are frequently applied in MPS-based algorithms, the SVD being of particluar importance to achieve reasonable computational times. We also elaborate on matrix operations focusing on their diagonalization. This procedure is of particular importance in so-called exact diagonalization (ED) methods in physics. Therefore, we introduce two algorithms in more detail, namely the QR algorithm in the former of the two sections and the Lanczos algorithm to which we devote an additional section. The Lanczos algorithm will become of crucial importance in DMRG algorithms to be presented in chapter 5.

Finite state machines will seem a rather stand-alone topic in this chapter. However, they are advantageous to use when it comes to the systematic construction of matrix-product operators (MPOs). It should further be mentioned that the concept of finite state machines itself largely extends the application presented in this thesis, playing an important role in theoretical computer science as well as in graph theory.

We will close this chapter with an extensive discussion of the discrete Fourier transform and its various pitfalls compared to the analytic Fourier transform. In physics the application of Fourier transforms is widespread as this scheme allows the transition from real space to momentum space in which many quantities are defined. In the case of this thesis, they will become necessary in order to calculate spectral functions. Although the analytical Fourier transform is quite easy to apply and interpret this does not apply to its discrete analog, which exhibits a wide range of sources of errors. Finally, we will introduce a Fourier-related transform, the sine transform, which is sometime also referred to as the Fourier sine transform.

This entire chapter is based on various textbooks [125, 297, 378, 139, 118, 153, 154, 62, 39, 45]. We shall also give the respective sources at points in the text where we feel them to fit best, which does not mean, however, that they do not contain information on later or previously presented topics.

3.1 Tensors, Their Notation and Pictorial Representation

In simple words a tensor is nothing more than a well-ordered arrangement of numbers, that is for a tensor T of rank r there is assigned a single number to every tuple $i_0, i_1, \dots, i_{r-2}, i_{r-1}$ of indices, with $i_k \in \{0, \dots, N_k - 1\}$ which makes the entire tensor an object of dimensions $N_0 \times N_1 \times \cdots \times N_{r-2} \times N_{r-1}$. Hence, a tensor of rank 0 is a simple scalar, a rank-1 tensor is a vector, and a rank-2 tensor a matrix. In analogy to their notation, we denote the elements of T by $T_{i_0, i_1, \dots, i_{r-2}, i_{r-1}}$. Since this notation, albeit strictly logical and correct, tends to be quite confusing in longer equations in 1971 Roger Penrose introduced a graphical notation [290] in which a rank-r tensor T is represented by a geometrical shape with r legs for its indices. Thus, more accurately what we actually have is a general depiction of its elements $T_{i_0, i_1, \dots, i_{r-2}, i_{r-1}}$. We show examples of these representations in figure 3.1.

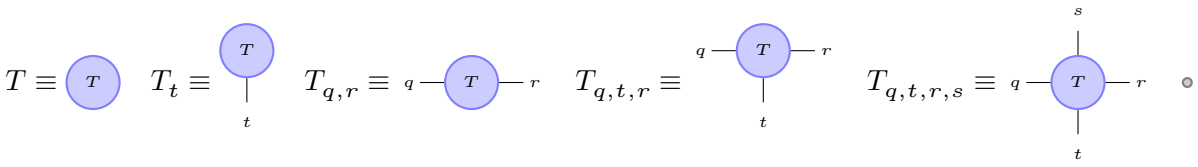

Figure 3.1: Pictorial representation of tensors T of different ranks r in Penrose notation. From left to right we have $r = 0, 1, 2, 3, 4$, T thus has the elements T, i.e. it is a scalar, T_t, i.e. it is a vector, $T_{q,r}$, i.e. it is a matrix, $T_{q,t,r}$, and $T_{q,t,r,s}$, respectively. At the very right we show the dummy tensor which may be of any rank r but with $N_k = 1 \forall k \in \{0, \dots, r-1\}$. We will occasionally use this dummy tensor as a Kronecker delta.

Mathematically tensors are understood as multi-linear maps between an input and an output vector space and the notation changes slightly the indices of the former and latter being denoted as sub- and superindices, respectively. Furthermore, dual vector spaces can be formally introduced. For the sake of simplicity we shall not concern ourselves with these issues in this work, which makes the use of super- or subindices arbitrary from a mathematical point of view. For a more rigorous treatment, see for instance [165].

Tensors can be manipulated by contracting them with other tensors, i.e. by summing over a common index. In Penrose notation this procedure is indicated by connecting the respective legs, c.f. figure 3.2 for an example.

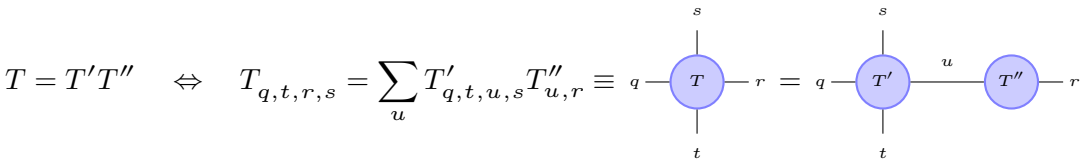

Figure 3.2: Example pictorial representation of a tensor contraction of a rank-4 and a rank-2 tensor, T' and T'', to a new rank-4 tensor T.

By regrouping the indices, we can furthermore change the shape of a tensor, that is we may either absorb several indices into a new superindex (which we then give in parentheses) or decompose an index into several subindices. Figure 3.3 shows an example of such a procedure.

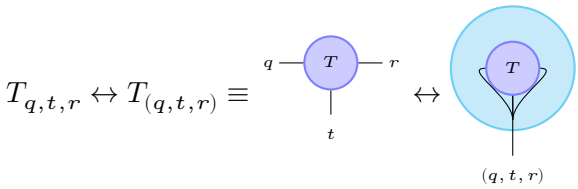

Figure 3.3: Example pictorial representation of reshaping a tensor T rank-3 tensor into a rank-1 tensor and vice versa.

In principle, the shape to represent the tensor may be chosen arbitrarily. In the remainder of this work we shall associate with different shapes different properties of a tensor which will hopefully become self-explaining from their respective introductions.

3.2 QR Decomposition

As a convenience for the reader we briefly review the QR decomposition, which will appear as a subroutine in many of the algorithms presented in chapters 4 and 5, and the QR algorithm, which may be used in ED computations, at this point. Here we focus on aspects important to keep in mind for the particular applications in the remainder of this thesis rather than providing a complete overview. For further reading we refer to [125] which also serves as the primary source for this section.

Let $M \in \mathbb{C}^{a\times b}$ be a complex matrix of rank r, then there exists a decomposition

$$M = Q \cdot R \equiv M_{\alpha,\beta} = \sum_{\gamma} Q_{\alpha,\gamma} R_{\gamma,\beta} \tag{3.1}$$

with a unitary matrix $Q \in \mathbb{C}^{a\times d}$, i.e.

$$Q^\dagger \cdot Q = \mathbb{1} \tag{3.2}$$

and an upper triangular – or right – matrix $R \in \mathbb{C}^{d\times b}$, where $d = \min(a, b)$. A sketch is provided in figure 3.4. Figure 3.5 shows equation (3.1) in tensor notation as defined in the above section.

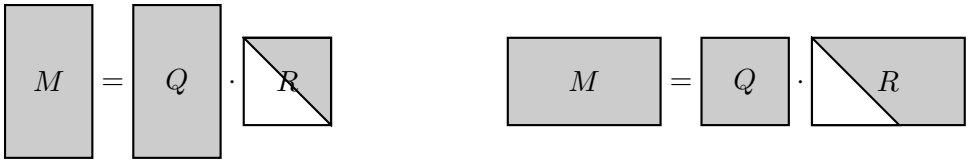

Figure 3.4: Sketch of the QR decomposition as in equation (3.1) in case $a \geq b$ (left) or $a < b$ (right).

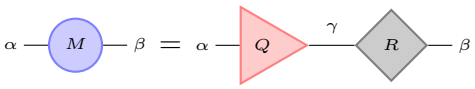

Figure 3.5: Pictorial representation of the QR decomposition, c.f. equation (3.1), in tensor network notation.

In case $a \geq b$ and $r = b = d$, i.e. the matrix M is of full rank, this decomposition is also unique. We should note that as defined above Q and R provide the so-called reduced or thin QR decomposition of M. For $a \geq b$ it is possible to enhance Q by $a - b$ orthonormal column vectors of dimension $\mathbb{C}^a$ and R by $a - b$ lines of zeros, thereby obtaining $Q' \in \mathbb{C}^{a \times a}$ and $R' \in \mathbb{C}^{a \times b}$ which yield a full QR decomposition. This variant is sketched in figure 3.6. However, for our application the reduced QR decomposition will prove to be sufficient.

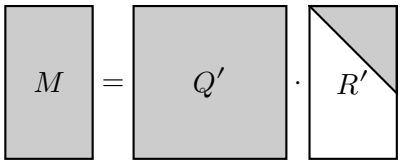

Figure 3.6: Sketch of the full QR decomposition.

As the QR decomposition lies at the core of many numerical algorithms, there exits a number of variations in their computation, including optimizations for matrices M with special properties to speed up calculations. A common method to determine the QR decomposition of a matrix M is via the application of unitary Householder matrices

$$H = \mathbb{1} - 2hh^\dagger \tag{3.3}$$

where h are unit vectors $h^\dagger h = 1$. It can be shown that a subsequent application of Householder matrices H to the original matrix M turns it into an upper triangular matrix. Thus, Q and R are given by

$$Q = H^1 \cdots H^r, \quad \text{and} \tag{3.4}$$
$$R = H^r \cdots H^1 \cdot M, \tag{3.5}$$

respectively. Here H^i describes the i^{th} Householder matrix. The total computational effort for computing the QR decomposition is, hence, determined by $\mathcal{O}(abr)$. Note that optimizations for matrices with special properties will perform much better [297].

To further outline applications of the QR decomposition, we now turn our attention to the QR algorithm, which, although it is not applied directly in MPS computations, is of great importance nonetheless, both in comparison to as well as a subroutine of the Lanczos algorithm to be presented in section 3.4. In addition the already mentioned material in this section we refer to [139] for further reading on this very broad topic.

The QR algorithm computes all eigenvalues and if desired their corresponding eigenvectors of a quadratic matrix $M \in \mathbb{C}^{a \times a}$. The principle idea is to start from the initial matrix $M_0 \coloneqq M$ and

calculate for each step i the QR decomposition $M_i = Q_i \cdot R_i$, then defining a new matrix

$$M_{i+1} = R_i \cdot Q_i. \tag{3.6}$$

By construction we have

$$M_{i+1} = R_i \cdot Q_i = Q_i^\dagger \cdot Q_i \cdot R_i \cdot Q_i = Q_i^\dagger \cdot M_i \cdot Q_i = Q_i^\dagger \cdot \cdots \cdot Q_0 \cdot M_0 \cdot Q_0 \cdot \cdots \cdot Q_i, \tag{3.7}$$

i.e. M_{i+1} is similar to the original matrix $M_0 = M$, thus having the same eigenvalues. The above sequence of matrices M_i can be shown to converge to an upper triangular matrix, the Schur form of M, which exhibits its eigenvalues on its diagonal [125].

In practice however, the above scheme is not applied as it is numerically inefficient. Instead, M is first converted into an upper Hessenberg matrix $\tilde{M}$, such that by definition all entries $\tilde{M}_{\alpha,\beta}$ with $\alpha < \beta - 1$ vanish. Hence, $\tilde{M}$ is an upper triangular matrix with a non-zero first subdiagonal. This conversion is achieved through the application of $a-2$ Householder matrices H_i, such that

$$\tilde{M} = H_{a-2}^\dagger \cdot \cdots \cdot H_1^\dagger \cdot M \cdot H_1 \cdot \cdots \cdot H_{a-2} \tag{3.8}$$

is again similar to M. The almost upper triangular matrix $\tilde{M}$ can finally be transformed into an actual upper triangular matrix via the subsequent application of so-called Givens matrices. A Givens matrix $G(\alpha, \beta; c, s)$ with $|c|^2 + |s|^2 = 1$, $c, s \in \mathbb{C}$ is of the form

$$G(\alpha,\beta;c,s) = \begin{pmatrix} 1 & & & & & & & & & \\ & \ddots & & & & & & & & \\ & & 1 & & & & & & & \\ & & & c^* & & & & s^* & & \\ & & & & 1 & & & & & \\ & & & & & \ddots & & & & \\ & & & & & & 1 & & & \\ & & & -s & & & & c & & \\ & & & & & & & & 1 & \\ & & & & & & & & & \ddots \\ & & & & & & & & & & 1 \end{pmatrix}, \tag{3.9}$$

that is it is an identity matrix $\mathbb{1}$ with the exceptions $G_{\alpha,\alpha} = c^*$, $G_{\beta,\beta} = c$, $G_{\alpha,\beta} = s^*$, and $G_{\beta,\alpha} = -s$. After the application of $a-1$ Givens matrices defining $\tilde{M}_i = G(i, i+1; c_i, s_i)\, \tilde{M}_{i-1}$ and $\tilde{M}_0 = \tilde{M}$, the matrix

$$\tilde{M}_{a-1} = G(a-1, a; c_{a-1}, s_{a-1}) \cdot \cdots \cdot G(1, 2; c_1, s_1) \cdot \tilde{M} \tag{3.10}$$

can be shown to be upper triangular containing the same eigenvalues as $\tilde{M}$ and, thus, M. The Givens coefficients c_i and s_i are given by

$$c_i = \frac{\left(\tilde{M}_{i-1}\right)_{i,i}}{\sqrt{\left|\left(\tilde{M}_{i-1}\right)_{i,i}\right|^2 + \left|\left(\tilde{M}_{i-1}\right)_{i+1,i}\right|^2}}, \quad \text{and} \tag{3.11}$$

$$s_i = \frac{\left(\tilde{M}_{i-1}\right)_{i+1,i}}{\sqrt{\left|\left(\tilde{M}_{i-1}\right)_{i,i}\right|^2 + \left|\left(\tilde{M}_{i-1}\right)_{i+1,i}\right|^2}} \tag{3.12}$$

respectively.

Note, that in this modern implementation of the QR algorithm the QR decomposition is actually not applied anymore. Only the name of the method remains.

With the calculations of eigenvalues being pivotal in numerics there exits a variety of modifications and optimizations for this algorithm for input matrices M with special properties. It is worth noticing that the second step of the application of Givens matrices requires $\mathcal{O}(a^2)$ operations, such that the computational cost of the algorithm decreases by one order of a if an initial Hessenberg matrix M is given as an input. In particular if M is tridiagonal, and thus Hessenberg, the computational cost reduces to just $\mathcal{O}(a)$ [297].

3.3 Singular Value Decomposition (SVD)

As we will learn in chapter 4 the SVD is needed in the MPS framework as one of the central routines. Hence, we will outline its basic properties in this section.

Consider again a matrix $M \in \mathbb{C}^{a\times b}$ of rank r. For any matrix of this kind there exists at least one decomposition such that

$$M = U \cdot \Gamma \cdot V^\dagger \equiv M_{\alpha,\beta} = \sum_\gamma U_{\alpha,\gamma}\Gamma_{\gamma,\gamma}V^*_{\beta,\gamma} \tag{3.13}$$

where the matrices U, Γ and V have the following properties: U and V are unitary matrices in $\mathbb{C}^{a\times d}$ and $\mathbb{C}^{b\times d}$, respectively, with $d = \min(a, b)$, and Γ is a real diagonal matrix of dimension $d \times d$ containing $r \leq d$ positive entires, which we label by $\lambda_i, i \in \{1, \dots, r\}$. Clearly, if M is of full rank, we have $d = r$. These r positive coefficients λ_i are called the *singular values* of M, while the entire scheme is dubbed the singular value decomposition (SVD) of matrix M. Note that the use of the adjoint matrix of V in the above definition is pure convention. A sketch of an SVD is given in figure 3.7, and figure 3.8 depicts equation (3.13) in tensor network notation as introduced above.

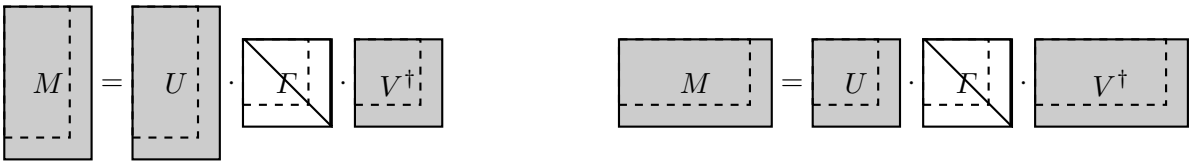

Figure 3.7: Sketch of the SVD as in equation (3.13) in case $a \geq b$ (left) or $a < b$ (right). Dashed lines: Dimensions after a truncation; data outside thes lines will be discarded.

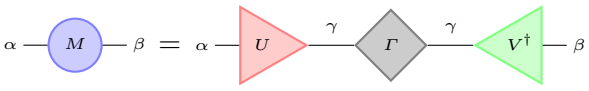

Figure 3.8: Pictorial representation of the SVD, c.f. equation (3.13), in tensor network notation.

The key feature of the SVD in terms of this work is its application to data compression, c.f. also [320]. Therefore, the matrices U, Γ, and V need to be computed in such a way that the singular values λ_i in Γ are arranged descendingly, i.e. $\lambda_1 \geq \lambda_2 \geq \cdots \geq \lambda_r > 0$. In order to perform a compression of M one now introduces a maximum dimension (cutoff) $\chi_{\max} \leq r$ to Γ, that is one discards all entries $\Gamma_{\gamma,\gamma} < \Gamma_{\chi_{\max},\chi_{\max}}$, and, if $\chi_{\max} < r$, all singular values $\lambda_i < \lambda_{\chi_{\max}}$ are neglected. That way, one obtains new truncated matrices $U'_{\chi_{\max}} \in \mathbb{C}^{a \times \chi_{\max}}$, $V'_{\chi_{\max}} \in \mathbb{C}^{b \times \chi_{\max}}$, and $\Gamma'_{\chi_{\max}} \in \mathbb{R}^{\chi_{\max} \times \chi_{\max}}$ which yield the compressed matrix $M'_{\chi_{\max}} = U'_{\chi_{\max}} \cdot \Gamma'_{\chi_{\max}} \cdot V'^{\dagger}_{\chi_{\max}}$. The accuracy of the approximation of $M'_{\chi_{\max}}$ to M now largely depends on the behavior of the singular values λ_i. If one chooses $\chi_{\max} = r$, that is one only discards zeros in Γ keeping all the singular values λ_i, obviously $M'_{\chi_{\max}} = M$ will hold. If the singular values λ_i decay exponentially for increasing i, then a non-trivial truncation will not have a too large effect on $M'_{\chi_{\max}}$. However, if the singular values λ_i are of similar size or in the worst case all equal, the SVD will change the original matrix M dramatically, with $M'_{\chi_{\max}}$ only vaguely mirroring its properties.

We illustrate these considerations in figure 3.9, where we plot different matrices $M \in \mathbb{R}^{480 \times 480}$ and compressed matrices $M'_{\chi_{\max}}$ for different cutoffs $\chi_{\max}$. For all matrices M we have

$$0 \leq M_{\alpha,\beta} \leq 1 \quad \forall \quad \alpha, \beta. \tag{3.14}$$

We plot all these matrices M in black and white with black corresponding to a value of $M_{\alpha,\beta}$ of 1 and white corresponding to a value of 0. Values between 1 and 0 are depicted by shades of gray with increasing lightness. We further define

$$\mathbf{1} \coloneqq M \,|\, M_{\alpha,\beta} = 1 \quad \forall \quad \alpha, \beta \tag{3.15}$$

and

$$\mathbf{0} \coloneqq M \,|\, M_{\alpha,\beta} = 0 \quad \forall \quad \alpha, \beta \tag{3.16}$$

as matrices containing only values of 1 or 0, respectively, and

$$D_j \coloneqq M \,|\, M_{\alpha,\beta} = \begin{cases} 1 & \text{if } \alpha \leq \beta \pm j \\ 0 & \text{else} \end{cases} \tag{3.17}$$

i.e. D_1 is a tridiagonal matrix with all entries 1. Finally we define

$$C_j \coloneqq M \,|\, M_{\alpha,\beta} = \begin{cases} 1 & \text{if } \alpha + \beta \leq j \\ 0 & \text{else} \end{cases}. \tag{3.18}$$

In figure 3.9a we now show SVDs for $M = \mathbb{1}$. As is evident from the singular value spectrum on the right, for this matrix M all the singular values λ_i are equal. Hence none of the approximations $M'_{\chi_{\max}}$ come close to the original matrix M, with even for a large cutoff of $\chi_{\max} = 120$ the difference is obvious. This example is of course very trivial as for the identity matrix $\mathbb{1}$ we have $U = V = \Gamma = \mathbb{1}$ such that it is obvious that all singular values are given by $\lambda_i = 1$ and a cutoff of $\chi_{\max}$ will only keep $\chi_{\max}$ ones instead of the total r ones, explaining the missing signature in the diagonal of the compressed matrices $M'_{\chi_{\max}}$. Next, in figure 3.9b we have the case $M = D_3$. Here, the singular values λ_i decay, however only polynomially. While the approximation of the compressions $M'_{\chi_{\max}}$ arguably matches the original matrix M much better for a large cutoff of $\chi_{\max} = 120$, it still exhibits a distinct shade of gray contrary to the original white. However, for an extremely low cutoff $\chi_{\max} = 5$ the original structure already surfaces. These observations intensity in figure 3.9c

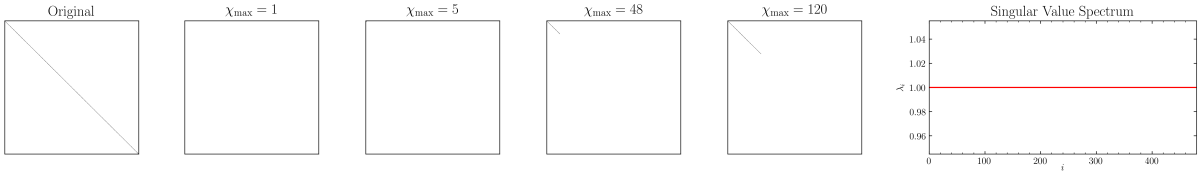

(a) $M = \mathbb{1}$.

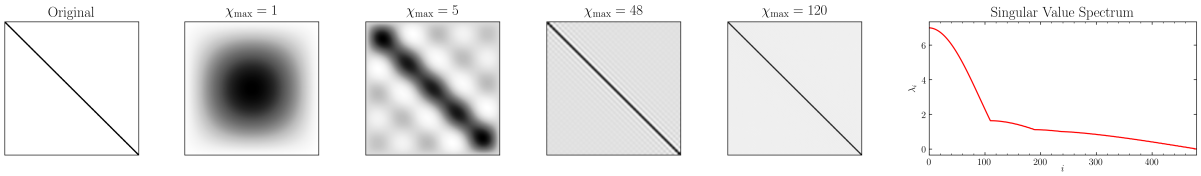

(b) $M = D_3$.

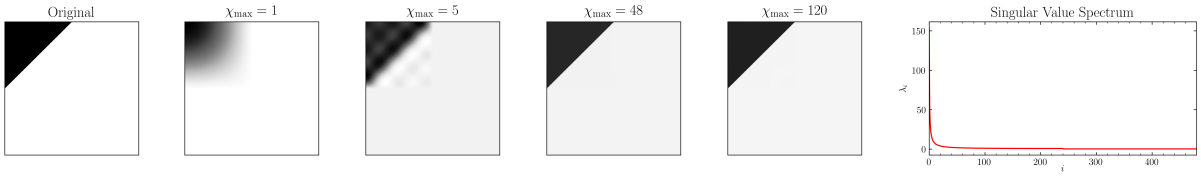

(c) $M = C_{120}$.

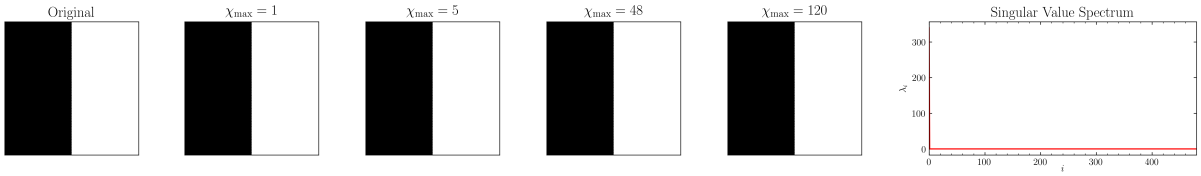

(d) $M = (M_l, M_r)\,, M_l = \mathbf{1} \in \mathbb{R}^{480\times240}, M_r = \mathbf{0} \in \mathbb{R}^{480\times240}$.

(e) M encoding an image of Gauß.

Figure 3.9: Illustration of data compression via SVD. For several matrices $M \in \mathbb{R}^{480\times480}$ the compressed matrices $M'_{\chi_{max}}$ are shown. From left to right we have M (original matrix), M'_1, M'_5, M'_{48}, M'_{120}, and the corresponding singular value spectrum. To all entires $0 \leq M_{\alpha,\beta} \leq 1$ applies. A value of 1 corresponds to black, a value of 0 to white, values between 1 and 0 are depicted by shades of gray with increasing lightness.

where we show SVDs of $M = C_{120}$ which has exponentially decaying singular values λ_i. Note that here, for $\chi_{\max} = 48$, i.e. only a tenth of the original matrix dimension, the principal structure of M has already fully emerged and there is only a slight difference visible compared to the compression for the significantly larger cutoff of $\chi_{\max} = 120$. Figure 3.9d shows the optimum case for an SVD. When $M = (M_l, M_r)\,, M_l = \mathbf{1} \in \mathbb{R}^{480\times 240}, M_r = \mathbf{0} \in \mathbb{R}^{408\times 240}$, there is only one singular value λ_1, such that all the compressions $M'_{\chi_{\max}}$ model the original matrix M exactly. Finally, in figure 3.9e we provide a classical visualization of the SVD's usefulness in practice. An image of Gauß is encoded as a matrix M and subject to an SVD. Again, the singular values decay exponentially and already for a maximum dimension of $\chi_{\max} = 48$ all the principal features of M have developed, just like in the previous example in figure 3.9c. Note that, of course, the same procedure could also be applied to a colored image where three SVDs would have to be performed, one for each color channel red, green, and blue.

We briefly mention that there also exist alternate definitions of the SVD regarding the dimensions of the matrices U, Γ, and V, such that $U' \in \mathbb{C}^{a\times a}$, $V' \in \mathbb{C}^{b\times b}$, and $\Gamma' \in \mathbb{R}^{a\times b}$, with Γ still holding the singular values λ_i in its diagonal entries. A sketch of this constellation is depicted in figure 3.10. In analogy to the QR decomposition, we may refer to this SVD as a full SVD, and accordingly

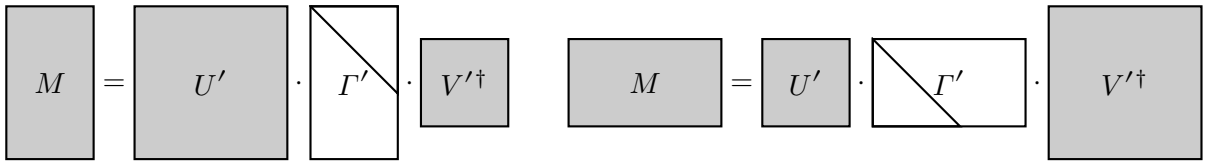

Figure 3.10: Sketch of the full SVD in case $a \geq b$ (left) or $a < b$ (right).

to our previous definition as a thin or reduced SVD. In our numerical computations we shall only make use of the latter.

In order to compute the singular values λ_i in practice, one uses the similarity of $\Gamma^\top \cdot \Gamma$ with $M^\dagger \cdot M$ which becomes evident trough the identity

$$M^\dagger \cdot M = \left(V \cdot \Gamma^\top \cdot U^\dagger\right) \cdot U \cdot \Gamma \cdot V^\dagger = V \cdot \Gamma^\top \cdot \Gamma \cdot V^\dagger. \tag{3.19}$$

From this observation it is clear that the singular values λ_i of M are determined by the square roots of the positive eigenvalues of $M^\dagger \cdot M$. Hence, from these considerations, it would seem feasible to calculate the eigenvalues of $M^\dagger \cdot M$, e.g. using the QR algorithm or the Lanczos algorithm which will be discussed in the subsequent sections. However, in order to achieve numerical stability, instead of performing this computation directly, the block matrix

$$\tilde{M} = \begin{pmatrix} \mathbf{0} & M \\ M^\dagger & \mathbf{0} \end{pmatrix} \tag{3.20}$$

is used [124]. After being subject to a Householder transformation where the same Householder matrices H we already encountered in the previous section are applied to it, it serves as an input to an optimization of the QR algorithm, which then yields the desired quantities [123, 378].

The computational cost of calculating an SVD is given by $\mathcal{O}(abr)$, hence theoretically it scales the same as the QR decomposition. However, in practice the latter is roughly twice as fast. Therefore, if one is not interested in the singular values themselves, when it comes to decomposing a matrix

the QR decomposition should be favoured over the SVD. For more details on how to numerically conduct an SVD see for instance [125, 378].

3.4 Lanczos Algorithm

When it comes to the computation of ground states in the MPS framework, which we will discuss in section 5.1, the Lanczos algorithm [207, 125, 2] is one of the frequently applied subroutines. As we already learned in section 2.6 it is also used in ED calculations. Since we will encounter it as a (possible) subroutine in other MPS algorithms in chapter 5 we devote this section to it.

While the QR algorithm can be used to compute the eigenvalues and eigenvectors of quadratic but otherwise generic matrices, the Lanczos algorithm requires the matrix $M \in \mathbb{C}^{a\times a}$ to also be hermitian, i.e.

$$M = M^\dagger. \tag{3.21}$$

For matrices of this type the eigenvalues and eigenvectors are computed by means of the so-called Krylov subspace

$$\mathscr{K}^b \equiv \text{span}\{\vec{v}_0, M\vec{v}_0, M^2\vec{v}_0, \dots, M^b\vec{v}_0\}, \tag{3.22}$$

which is created by successive application of the matrix M to be investigated to an initial non-trivial vector $\vec{v}_0 \in \mathbb{C}^a$ that can be chosen arbitrarily. The total number of applications b of the matrix M to the initial vector $\vec{v}_0$ determines the dimension of the Krylov space as $b+1$.

From the set $\{\vec{v}_0, M\vec{v}_0, M^2\vec{v}_0, \dots, M^b\vec{v}_0\}$ an orthogonal basis is constructed iteratively for $i \in \{1, \dots, b\}$ through

$$\vec{v}_{i+1} = M\vec{v}_i - \alpha_i\vec{v}_i - \beta_i^2\vec{v}_{i-1} \tag{3.23}$$

introducing

$$\alpha_i = \frac{\vec{v}_i^\dagger M\vec{v}_i}{\|\vec{v}_i\|^2}, \quad \text{and} \tag{3.24}$$

$$\beta_i = \frac{\|\vec{v}_i\|}{\|\vec{v}_{i-1}\|} \tag{3.25}$$

and setting $\beta_0 = 0$. The so-obtained vectors $\vec{v}_i$ are called Lanczos vectors, from which a matrix

$$V = (\vec{v}_0, \vec{v}_1, \dots, \vec{v}_{b-1}, \vec{v}_b) \in \mathbb{C}^{a\times b+1} \tag{3.26}$$

can be constructed.

While Lanczos in his original work [207] multiplied this matrix V with a vector he had generated from polynomials and their roots obtaining all eigenvalues and eigenvectors, due to this procedure being numerically unstable, modern implementations exploit the identity [125]

$$M = V \cdot \tilde{M} \cdot V^\dagger, \tag{3.27}$$

i.e. M is similar to

$$\tilde{M} = \begin{pmatrix} \alpha_0 & \beta_1 & 0 & \cdots & \cdots & 0 \\ \beta_1 & \alpha_1 & \beta_2 & \ddots & & \vdots \\ 0 & \beta_2 & \ddots & \ddots & \ddots & \vdots \\ \vdots & \ddots & \ddots & \ddots & \beta_{b-1} & 0 \\ \vdots & & \ddots & \beta_{b-1} & \alpha_{b-1} & \beta_b \\ 0 & \cdots & \cdots & 0 & \beta_b & \alpha_b \end{pmatrix}, \tag{3.28}$$

which is obviously tridiagonal since the Lanczos vectors $\vec{v}_i$ are orthogonal to one another. This matrix $\tilde{M}$ is then passed on to another algorithm which does the actual computations of its eigenvalues and eigenvectors. Often times an optimized version of the QR algorithm is used, where the computation of the eigenvalues is particularly efficient as discussed in the previous section. If the eigenvectors are also to be calculated, the transition matrix V needs to be saved to transform the eigenvectors of the tridiagonal matrix $\tilde{M}$ to those of the original matrix M. Otherwise it can be discarded.

Note that in modern versions of the Lanczos algorithm it is also common to work with an orthonormal Lanczos basis [2]. Therefore, one starts with a normalized initial vector $\vec{w}'_0$, which other than this constraint can be chosen freely, and the recursion relation (3.23) changes to

$$\vec{w}_{i+1} = M\vec{w}'_i - \alpha_i \vec{w}'_i - \beta_i \vec{w}'_{i-1} \tag{3.29}$$

with

$$\alpha_i = \vec{w}_i'^{\dagger} M \vec{w}'_i = \frac{\vec{w}_i^{\dagger} M \vec{w}_i}{\|\vec{w}_i\|^2}, \quad \text{and} \tag{3.30}$$

$$\beta_i = \|\vec{w}_i\|. \tag{3.31}$$

We use the prime to describe normalized vectors, i.e.

$$\vec{w}'_i = \frac{\vec{w}_i}{\|\vec{w}_i\|}, \tag{3.32}$$

furthermore the transition matrix V is now composed of the normalized vectors

$$V = \left(\vec{w}'_0, \vec{w}'_1, \ldots, \vec{w}'_{b-1}, \vec{w}'_b\right) \in \mathbb{C}^{a \times b+1}. \tag{3.33}$$

The transition from these orthonormal Lanczos vectors to the solely orthogonal Lanczos vectors discussed above is given by

$$\vec{v}_i = \prod_{j=1}^{i} \|\vec{w}_j\| \, \vec{w}'_i. \tag{3.34}$$

By construction $b \leq a$ always holds true as the Lanczos vectors $\vec{v}_i$ or $\vec{w}_i$ can be shown to converge to the respective zero element $\vec{0} \in \mathbb{C}^a$ for increasing i, that is

$$\vec{v}_{a+1} = \vec{w}_{a+1} = \vec{0}. \tag{3.35}$$

However, in most implementations one defines a cutoff $b = i_{\max}$ through

$$\left\|\vec{v}_{i_{\max}}\right\| \leq \varepsilon \ll 1, \quad \text{or} \tag{3.36}$$

$$\left\|\vec{w}_{i_{\max}}\right\| \leq \varepsilon \ll 1, \tag{3.37}$$

respectively.

3.5 Finite State Machines (FSMs)

Based on [153, 154] we give a brief outline and background information to finite state machines (FSMs) which we exploit in section 4.3.2 for setting up MPOs.

In theoretical computer science the study of models for computations and algorithms is governed by the field of automata theory. The descriptions of the computer to be modeled is achieved through the introduction of abstract machines, which come with distinct properties and rules on how and when to apply changes to them.

The perhaps most common abstract machine is the Turing machine introduced by British mathematician Alan Turing in 1937 [381]. Its invention dramatically changed the perception of the modeling of algorithms and therefore has manifested its pivotal position in both mathematics and computer science. A Turing machine which by definition cannot be realized in real life is in principle able to model the logic of any algorithm. Vice versa when giving a certain input, a so-called language, to a Turing machine it can classify in how far it allows to construct any algorithm from the given language. Such languages that can model any algorithm are called Turing complete, relating the field of automata theory to the related problem of language theory.

FSMs in this context provide a subclass of abstract machines, that model algorithms which only require a finite memory, that is so-called states. In mathematical rigor the most primitive FSM $\mathscr{M}$ is defined by a quintuple $(Q, q_0, \Sigma, \delta, F)$ where

- Q is a finite set of states $Q = \{q_0, q_1, \dots, q_n\}$, $|Q| < \infty$, the states $q_0, q_1, \dots, q_n$ being abstract quantities describing $\mathscr{M}$ and its properties at a given time. Note that these states $q_0, q_1, \dots, q_n$ are in no way associated with quantum mechanical states, e.g. $|\Psi\rangle$, we encountered in previous chapters, and that the notion of time in the context of FSMs is likewise not to be identified with a physical time, it merely provides an order to the procedure of the simulation,
- $q_0 \in Q$ is the initial state, i.e. the state from which $\mathscr{M}$ starts its simulation,
- Σ is the FSM's (input) alphabet, i.e. a set of symbols that $\mathscr{M}$ knows to interpret and depending on which it changes its state,
- $\delta \colon Q \times \Sigma \to \mathscr{P}(Q)$ is the state-transition function defining the above mentioned changes of states depending on a given input from the alphabet Σ
- $F \subset Q$ is a subset of allowed or accepted final states for $\mathscr{M}$ to end its simulation in. Note that F may also be empty.

Note, however, that there are also slightly different definitions [118]. FSMs can be conveniently represented as graphs with its states $q_0, q_1, \dots, q_n$ as the graph's nodes and edges representing the state transition function δ connecting the nodes. The quantity $\mathscr{P}(Q)$ in the definition of the state-transition function δ defines a set of states as its co-domain. If $|\mathscr{P}(Q)| = 1$ the FSM $\mathscr{M}$ is called deterministic, i.e. for each transition $Q \times \Sigma$ there exists only one possible final state. In the case of $|\mathscr{P}(Q)| \geq 1$ the FSM $\mathscr{M}$ is conveniently dubbed non-deterministic, meaning that now different states may be reached for at least one transition $Q \times \Sigma$. The state-transition function δ may also only be partially defined, that is for some transitions $Q \times \Sigma$ one has $|\mathscr{P}(Q)| = 0$. In this, an FSM will halt when encountering an ill-defined transition $Q \times \Sigma$.

As defined above an FSM of this type is also called an acceptor, meaning that for a given word w composed of symbols from the alphabet Σ, the FSM will be in either a final state of F having read

the word w completely, such that w is called accepted, or it will end up on any other state. In this case, w is rejected by the FSM.

If the FSM is enhanced to a septuple $(Q, q_0, \Sigma, \Gamma, \delta, F, \omega)$ with

- Γ the output alphabet of the FSM $\mathscr{M}$, i.e. a set of symbols it prints depending on
- ω the output function of the FSM $\mathscr{M}$

and the other quantities defined as before, it is called a transducer. An FSM of this kind is characterized by its ability to transfer an input word w composed of symbols from the input alphabet Σ into a word w' composed of symbols from the output alphabet Γ. The output function may either be defined via $\omega\colon Q \to \Gamma^*$, i.e. the output symbol depends on the state of the FSM $\mathscr{M}$ or via $\omega\colon Q \times \Sigma \to \Gamma^*$, such that the output symbol depends on the transition of one state to another. By Γ^* we denote the language of Γ, that is all strings that can be composed of elements from Γ. In the former case the FSM is called a Moore automaton, in the latter a Mealy automaton [154]. Both kinds of FSMs can be converted into one another, i.e. they describe the same procedures by different means.

Note that, again, there exists different definitions in the literature. In certain cases, the set of finite states may be unimportant to the functioning of the FSM, so that it is disregarded in its definition. Another common variant is to combine the transition and output function, δ and ω to a transition function $\Delta\colon Q \times \Sigma \to \mathscr{P}(Q) \times \Gamma^*$. Note further, that for a non-deterministic transducer the input alphabet Σ, as well as the output alphabet Γ need to be expanded by the empty word ε, such that in the above definitions we need to replace Σ and Γ by $(\Sigma \cup \{\varepsilon\})$ and $(\Gamma \cup \{\varepsilon\})$, respectively.

Above the here explained automata there exist quite a few other specifications or generalizations. For more details, the interested reader is to be referred to e.g. [153, 154], which most of this section is based on. Over the course of this thesis, we will use deterministic FSMs of the Mealy type to provide a general scheme for the construction of MPOs. More details on the exact properties of these FSMs will be given in chapter 4.

3.6 The Discrete Fourier Transform

The spectral quantities we will discuss in chapter 6 rely in several aspects on Fourier transforms. Since there are various definitions we will first briefly review the continuous Fourier transform and therefrom its discretized counterpart putting particular focus on its application, as well as the consequences of the discretization which are not encountered in pure analysis. A good overview of many of the concepts we will discuss is given in reference [62].

Discrete Fourier transforms are, despite their seemingly simple definitions, a rather complex topic. We provide a more detailed discussion of some of their properties, which are relevant for this work, in appendix A.1.

3.6.1 The Fourier Transform

Let $f : \mathbb{R}^N \mapsto \mathbb{C}$ be an integrable function. Its Fourier transform is then given by

$$\mathscr{F}[f(\vec{x})](\vec{y}) = \int_{\mathbb{R}^N} f(\vec{x})\, \mathrm{e}^{-\mathrm{i}\vec{y}\cdot\vec{x}} \mathrm{d}\vec{x} \tag{3.38}$$

and, provided it is itself integrable, the inverse transform is defined by

$$f(\vec{x}) = \mathscr{F}^{-1}[\mathscr{F}[f(\vec{x})](\vec{y})](\vec{x}) = \frac{1}{(2\pi)^N} \int_{\mathbb{R}^N} \mathscr{F}[f(\vec{x})](\vec{y})\, \mathrm{e}^{\mathrm{i}\vec{x}\cdot\vec{y}} \mathrm{d}\vec{y}. \tag{3.39}$$

We note that there exist alternative definitions, this one regarding the prefactor

$$\mathscr{F}[f(\vec{x})](\vec{y}) = \frac{1}{(2\pi)^{N/2}} \int_{\mathbb{R}^N} f(\vec{x})\, \mathrm{e}^{-\mathrm{i}\vec{y}\cdot\vec{x}} \mathrm{d}\vec{x}, \tag{3.40}$$

$$f(\vec{x}) = \mathscr{F}^{-1}[\mathscr{F}[f(\vec{x})](\vec{y})](\vec{x}) = \frac{1}{(2\pi)^{N/2}} \int_{\mathbb{R}^N} \mathscr{F}[f(\vec{x})](\vec{y})\, \mathrm{e}^{\mathrm{i}\vec{x}\cdot\vec{y}} \mathrm{d}\vec{y}, \tag{3.41}$$

of which the advantage is to be unitary, and

$$\mathscr{F}[f(\vec{x})](\vec{y}) = \int_{\mathbb{R}^N} f(\vec{x})\, \mathrm{e}^{-2\pi\mathrm{i}\vec{y}\cdot\vec{x}} \mathrm{d}\vec{x}, \tag{3.42}$$

$$f(\vec{x}) = \mathscr{F}^{-1}[\mathscr{F}[f(\vec{x})](\vec{y})](\vec{x}) = \int_{\mathbb{R}^N} \mathscr{F}[f(\vec{x})](\vec{y})\, \mathrm{e}^{2\pi\mathrm{i}\vec{x}\cdot\vec{y}} \mathrm{d}\vec{y}, \tag{3.43}$$

permitting the omission of the prefactors entirely. Note, however, that in this case the values $\vec{y}$ in Fourier space will be scaled, i.e. divided, by a factor of 2π compared to the two previously given definitions. The sign of the imaginary unit may also vary for other definitions. We will, for these discussions, stick with the definition from (3.38), and (3.39), respectively. In addition, we also mention the representation of the Dirac delta distribution most commonly encountered when operating with Fourier transforms

$$\delta(\vec{y}-\vec{z}) = \frac{1}{(2\pi)^N} \int_{\mathbb{R}^N} \mathrm{e}^{-\mathrm{i}(\vec{y}-\vec{z})\vec{x}} \mathrm{d}\vec{x} = \begin{cases} +\infty, & \vec{y}-\vec{z} = \vec{0} \\ 0, & \vec{y}-\vec{z} \neq \vec{0} \end{cases}. \tag{3.44}$$

Note that in this case the prefactor is fixed and only the sign of the imaginary unit may be altered. Therefore, using (3.38), and (3.39) factors of 2π are often encountered in Fourier transforms, but neglected in a sloppy notation.

The Fourier transform is the multidimensional continuous generalization of the Fourier series, introduced by Joseph Fourier, stating that any integrable function $f\colon \mathscr{X} \in \mathbb{R} \mapsto \mathbb{C}$ of period X may be decomposed as

$$f(x) = \sum_{\mu=-\infty}^{\infty} c_\mu \mathrm{e}^{\mathrm{i}2\pi\frac{\mu x}{X}} \tag{3.45}$$

the Fourier or spectral coefficients given by

$$c_\mu = \frac{1}{X} \int_0^X f(x)\, \mathrm{e}^{-\mathrm{i}2\pi\frac{\mu x}{X}} \mathrm{d}x = \frac{1}{X} \int_{-X/2}^{X/2} f(x)\, \mathrm{e}^{-\mathrm{i}2\pi\frac{\mu x}{X}} \mathrm{d}x. \tag{3.46}$$

Fourier's aim was to show that f being of period X may be constructed as a superposition of sine and cosine functions, thereby finding its spectrum. He, thus, decomposed

$$f(x) = \frac{a_0}{2} + \sum_{\mu=1}^{\infty} \left(a_\mu \cos\left(2\pi \frac{\mu x}{X}\right) + b_\mu \sin\left(2\pi \frac{\mu x}{X}\right)\right) \tag{3.47}$$

with spectral coefficients

$$a_\mu = \frac{1}{X} \int_{-X/2}^{X/2} f(x) \cos\left(2\pi \frac{\mu x}{X}\right) \mathrm{d}x, \quad \mu \geq 0, \tag{3.48}$$

$$b_\mu = \frac{1}{X} \int_{-X/2}^{X/2} f(x) \sin\left(2\pi \frac{\mu x}{X}\right) \mathrm{d}x, \quad \mu \geq 1. \tag{3.49}$$

The representation (3.45) and (3.46) was then later found alongside with the transition

$$a_\mu = c_\mu + c_{-\mu}, \quad \mu \geq 0, \tag{3.50}$$

$$b_\mu = \mathrm{i}\left(c_\mu - c_{-\mu}\right), \quad \mu \geq 1. \tag{3.51}$$

Note that while x is a continuous variable, μ takes only integer values. Thus, the Fourier series yield a discrete, however in general infinite, spectrum.

The transition from the Fourier series to the Fourier transform requires two steps. We first take the period to become infinite, i.e. $X \to \infty$. Therefore, the output spectrum will become more and more fine grained and eventually continuous. Hence, a representation by coefficients with integer numbers will become unfeasible, which yields to the definition of the spectral variable

$$y_\mu = 2\pi \frac{\mu}{X} \tag{3.52}$$

becoming likewise continuous taking the limit to infinity alongside the introduction of an integral. The inclusion of the factor 2π depends on convention, as is evident from comparing (3.38) and (3.39) to (3.42) and (3.43). If chosen to be part of the Fourier space, as in (3.52), it will reappear in terms of the prefactor, where it may, however be distributed freely, c.f. (3.38) and (3.39) or (3.40) and (3.41). The extension from one to multiple dimensions is then only a formality replacing the one dimensional scalars and volume forms in the integral by their multidimensional counterparts. The Fourier transform, thus, maps functions between two different function spaces.

3.6.2 Discretization of the Fourier Transform

The Fourier transform being defined for functions of infinitely long periods, its discretization is in general obviously erroneous. Additionally, instead of a function only a representation of finite length may serve as an input. We will call this representation the input signal in the following. Without any further physical interpretation the discrete Fourier transform is best understood as two functions, one mapping a given input signal $\vec{c}_{\vec{x}}$ with

$$c_{\vec{x}_m} = f(\vec{x}_m) \tag{3.53}$$

of length L from one space $\mathscr{X} \subset \mathbb{C}^{L \cdot N}$ to another signal $\vec{c}_{\vec{y}}$ of the same length L to another space $\mathscr{Y} \subset \mathbb{C}^{L \cdot N}$, and a second function mapping the representatives of the input space $\vec{x}_m \in \mathbb{R}^N$ to their

counterparts in the output or Fourier space $\vec{y}_\mu \in \mathbb{R}^N$. Note that in numerical implementations only the former function is explicitly implemented. In simple words this means that a complex vector is mapped onto another complex vector. In these notes we define the discrete Fourier transform via:

$$\mathscr{F} : \vec{c}_{\vec{x}} \in \mathscr{X} \subset \mathbb{C}^{L \cdot N} \mapsto \vec{c}_{\vec{y}} \in \mathscr{Y} \subset \mathbb{C}^{L \cdot N}, \quad c_{\vec{y}_\mu} = \sum_{\vec{x}_m} \mathrm{e}^{-\mathrm{i}\vec{y}_\mu \vec{x}_m} c_{\vec{x}_m}. \tag{3.54}$$

The inverse or back(ward) transform is given by

$$\mathscr{F}^{-1} : \vec{c}_{\vec{y}} \in \mathscr{Y} \subset \mathbb{C}^{L \cdot N} \mapsto \vec{c}_{\vec{x}} \in \mathscr{X} \subset \mathbb{C}^{L \cdot N}, \quad c_{\vec{x}_m} = \frac{1}{L} \sum_{\vec{y}_\mu} \mathrm{e}^{\mathrm{i}\vec{x}_m \vec{y}_\mu} c_{\vec{y}_\mu}. \tag{3.55}$$

Note that in this general multi-dimensional definition the indices of the input and output vectors $\vec{c}_{\vec{x}}$ and $\vec{c}_{\vec{y}}$ are vectors itself. Therefore, when it comes to the application on the computer one at first needs to map these vectors to a one dimensional string of numbers, i.e.

$$\sum_{\vec{x}_m} \coloneqq \sum_{m=0}^{L-1} \sum_{\vec{x}_m} \coloneqq \sum_{m=0}^{L-1} \sum_{m'=0}^{N-1}, \tag{3.56}$$

explaining why the total dimension of the in- and output vectors, $\vec{c}_{\vec{x}}$ and $\vec{c}_{\vec{y}}$, is actually $L \cdot N$.

More importantly, we emphasize that in applications each index of the in- and output signal, $\vec{x}$ and $\vec{y}$, corresponds to a physical quantity, i.e. the indices being discretizations themselves. The input and output signals are, thus, to be understood as the values corresponding to an instance the index encodes, c.f. again (3.53).

The (continuous or analytical) Fourier transform being defined for functions of infinite period, the discrete Fourier transform is best to be seen as a generalization of the original Fourier series, which is also apparent when comparing (3.54) to (3.46). Consequently, the input signal of the discrete Fourier transform will be interpreted to be periodic, which generalizing (3.52) to also hold in multiple dimensions will lead to a definition of the Fourier space. Introducing the Kronecker delta

$$\delta_{\mu,\nu} = \frac{1}{L} \sum_{m=0}^{L-1} \mathrm{e}^{-\mathrm{i}\frac{2\pi}{L}(\mu-\nu)m} = \begin{cases} 1, & \mu = \nu \\ 0, & \mu \neq \nu \end{cases}, \quad \mu, \nu \in \mathbb{Z}, \tag{3.57}$$

which may be interpreted as the discretization of the Dirac delta distribution (3.44) in one dimension, (3.55) can be shown to correctly define the inverse with the generalization of (3.55) to multiple dimensions

$$\delta_{\vec{\mu},\vec{\nu}} = \frac{1}{L^N} \sum_{\vec{m}} \mathrm{e}^{-\mathrm{i}\frac{2\pi}{L}(\vec{\mu}-\vec{\nu})\vec{m}} = \frac{1}{L^N} \sum_{m'=0}^{N-1} \mathrm{e}^{-\mathrm{i}\frac{2\pi}{L}(\vec{\mu}-\vec{\nu})_{m'}\vec{m}_{m'}} = \begin{cases} 1, & \vec{\mu} = \vec{\nu} \\ 0, & \vec{\mu} \neq \vec{\nu} \end{cases}, \quad \vec{\mu}, \vec{\nu} \in \mathbb{Z}^N. \tag{3.58}$$

Note that in this case, $\vec{m}$ is a vector holding indices.

3.6.3 Discrete Fourier Transform in One Dimension

The one-dimensional discrete Fourier transform is of particular importance as nearly any math library in computer science implements it as the default case. Here

$$N = 1, \tag{3.59}$$

thus, the vectors $\vec{x}_m$ and $\vec{y}_\mu$ turn to scalars x_m and y_μ. We emphasize that these components now form vectors $\vec{x}$ and $\vec{y}$ describing physical quantities, while m and μ are just integers running from 0 to $L-1$. The discrete forward and backward Fourier transform is then defined via

$$c_{y_\mu} = \sum_{x_m} \mathrm{e}^{-\mathrm{i}x_m y_\mu} c_{x_m}, \tag{3.60}$$

$$c_{x_m} = \frac{1}{L} \sum_{y_\mu} \mathrm{e}^{\mathrm{i}y_\mu x_m} c_{y_\mu}. \tag{3.61}$$

For the sake of completeness we mention that an alternative definition can be found in the literature concerning the prefactor,

$$c_{y_\mu} = \frac{1}{\sqrt{L}} \sum_{x_m} \mathrm{e}^{-\mathrm{i}x_m y_\mu} c_{x_m}, \tag{3.62}$$

$$c_{x_m} = \frac{1}{\sqrt{L}} \sum_{y_\mu} \mathrm{e}^{\mathrm{i}y_\mu x_m} c_{y_\mu}. \tag{3.63}$$

As we will explain later, neither of these definitions will suit our purposes, which calls for a slight modification. Until then, however, we shall operate with the former definitions (3.60) and (3.61), also because these are the standard implementations in most programming libraries, in particular Python (Numpy [141] and Scipy [393]) and C++ (e.g. FFTW [110]). Another variation to the above definitions is the choice of the sign in the exponential. This convention, however, does not play a role in the outcome of the transform's results. We, again, followed the definitions in most programming libraries.

In one dimension we consider a chain of length L and a sampling δ_x. The steps x_m at which we sample our input signal $\vec{c}_x$ are, thus, given by

$$x_m = \delta_x \cdot m, \quad m \in \{0, \dots, L-1\} \quad \Rightarrow \quad x_m \in \{0, \dots, (L-1) \cdot \delta_x\}. \tag{3.64}$$

We already discussed in section 3.6.1 that the analytical Fourier transform in its original form is defined for periodic signals of infinite length only. The latter constraint can obviously not be realized in numerical calculations. Hence, by design, the discrete Fourier transform will *assume* for the input signal $\vec{c}_x$ to be periodic in L, that is

$$c_{x_m} \overset{!}{=} c_{x_m + x_L}. \tag{3.65}$$

Inserting (3.61), we find a constraint for the vector y in reciprocal space,

$$c_{x_m + x_L} = \frac{1}{L} \sum_{y_\mu} \mathrm{e}^{\mathrm{i}y_\mu (x_m + x_L)} c_{y_\mu} = \frac{1}{L} \sum_{y_\mu} \mathrm{e}^{\mathrm{i}y_\mu \delta_x m} c_{y_\mu} \mathrm{e}^{\mathrm{i}y_\mu \delta_x L} \tag{3.66a}$$

$$= c_{x_m} = \frac{1}{L} \sum_{y_\mu} \mathrm{e}^{\mathrm{i}y_\mu x_m} c_{y_\mu} = \frac{1}{L} \sum_{y_\mu} \mathrm{e}^{\mathrm{i}y_\mu \delta_x m} c_{y_\mu} \tag{3.66b}$$

$$\Rightarrow \mathrm{e}^{\mathrm{i}\delta_x L y_\mu} \overset{!}{=} 1 \quad \forall \quad y_\mu \tag{3.66c}$$

$$\Rightarrow y_\mu \delta_x L \overset{!}{=} 2\pi \cdot \mu. \tag{3.66d}$$

We, thus, define the sampling of the output signal $\vec{c}_y$ via

$$y_\mu = \frac{2\pi\mu}{\delta_x L}, \quad \mu \in \{0, \dots, L-1\} \quad \Rightarrow \quad y_\mu \in \left\{0, \dots, (L-1) \cdot \frac{2\pi}{\delta_x L}\right\}. \tag{3.67}$$

Hence, the step size for sampling of the output signal is given by

$$\delta_y = \frac{2\pi}{\delta_x L}. \tag{3.68}$$

In order to decrease the step size, i.e. to obtain a higher resolution in the reciprocal space, one has to either increase the length L of the input signal or the corresponding step size δ_x. Choosing δ_x too large, however, poses the danger of undersampling, i.e. missing contributions to the input signal, and aliasing meaning the misinterpretation of the output signal. Increasing L on the other hand may be numerically expensive. An appropriate choice of these two quantities is, thus, always a problem specific tradeoff. We stress in addition that only the step size of the input signal δ_x determines the range of the output signal y_μ as is evident from the above equation. We compute

$$c_{y_\mu + y_L} = \sum_{x_m} \mathrm{e}^{-\mathrm{i}x_m(y_\mu + y_L)} c_{x_m} = \sum_{x_m} \mathrm{e}^{-\mathrm{i}x_m y_\mu} \mathrm{e}^{-\mathrm{i}x_m y_L} c_{x_m} = \sum_{x_m} \mathrm{e}^{-\mathrm{i}x_m y_\mu} \mathrm{e}^{-\mathrm{i}\delta_x m \cdot \frac{2\pi L}{\delta_x L}} c_{x_m} \tag{3.69a}$$

$$= \sum_{x_m} \mathrm{e}^{-\mathrm{i}x_m y_\mu} \mathrm{e}^{-\mathrm{i}2\pi m} c_{x_m} = \sum_{x_m} \mathrm{e}^{-\mathrm{i}x_m y_\mu} c_{x_m} = c_{y_\mu}, \tag{3.69b}$$

to find that the output signal is of period L as well.

Introducing the common but quite misleading abbreviations

$$c_m \coloneqq c_{x_m} \tag{3.70}$$

$$c_\mu \coloneqq c_{y_\mu} \tag{3.71}$$

we obtain for the discrete forward and backward Fourier transform

$$c_\mu = \sum_{m=0}^{L-1} \mathrm{e}^{-\mathrm{i}\frac{2\pi}{\delta_x L} \cdot \mu \cdot \delta_x \cdot m} c_m = \sum_{m=0}^{L-1} \mathrm{e}^{-\mathrm{i}\frac{2\pi}{L}\mu \cdot m} c_m, \quad \mu \in \{0, \dots, L-1\}, \tag{3.72}$$

$$c_m = \frac{1}{L} \sum_{\mu=0}^{L-1} \mathrm{e}^{\mathrm{i}\frac{2\pi}{\delta_x L} \cdot \mu \cdot \delta_x \cdot m} c_\mu = \frac{1}{L} \sum_{\mu=0}^{L-1} \mathrm{e}^{\mathrm{i}\frac{2\pi}{L}\mu \cdot m} c_\mu, \quad m \in \{0, \dots, L-1\} \tag{3.73}$$

which matches the definition in programming libraries. Note that these equations resemble the discretization of (3.46), the only difference being the prefactor now being assigned to the backward Fourier transform. Furthermore do we stress that the phase does not depend on the sampling of the input signal δ_x, which cancels out due to the determination of the output sampling δ_y as a result of (3.65). Therefore, may the discrete Fourier transform may be applied in the same way for two input signals covering the same range with different samplings.

For a discrete Fourier transform from real to reciprocal space, we identify $x = r$ and $y = k$, whilst for a transfrom from time to frequency space we have $x = t$ and $y = \omega$. We discuss these procedures alongside other important properties of the discrete Fourier transform in appendix A.1 in great detail.

3.7 The Discrete Sine Transform

Now that we have gained an overview of the discrete Fourier transform and its properties, we discuss a related integral transform, the sine transform. We shall proceed as before, presenting at first the continuous case and then deriving the discretization.

3.7.1 The Sine (and Cosine) Transform

For integrable functions $f : \mathbb{R}^N \mapsto \mathbb{R}$ from the definition of the Fourier transform (3.38) employing Euler's formula

$$\mathscr{F}[f(\vec{x})](\vec{y}) = \int_{\mathbb{R}^N} f(\vec{x})\, \mathrm{e}^{-\mathrm{i}\vec{y}\cdot\vec{x}} \mathrm{d}\vec{x} = \int_{\mathbb{R}^N} f(\vec{x}) \cos(\vec{y}\cdot\vec{x})\, \mathrm{d}\vec{x} - \mathrm{i} \int_{\mathbb{R}^N} f(\vec{x}) \sin(\vec{y}\cdot\vec{x})\, \mathrm{d}\vec{x} \tag{3.74}$$

we define the sine and consine transform via

$$\mathscr{S}[f(\vec{x})](\vec{y}) = \int_{\mathbb{R}^N} f(\vec{x}) \sin(\vec{y}\cdot\vec{x})\, \mathrm{d}\vec{x} \tag{3.75}$$

$$\mathscr{C}[f(\vec{x})](\vec{y}) = \int_{\mathbb{R}^N} f(\vec{x}) \cos(\vec{y}\cdot\vec{x})\, \mathrm{d}\vec{x}. \tag{3.76}$$

In case that both, $\mathscr{S}[f(\vec{x})](\vec{y})$ and $\mathscr{C}[f(\vec{x})](\vec{y})$, are integrable themselves, the original function f can be obtained through

$$f(\vec{x}) = \int_{\mathbb{R}^N} \mathscr{C}[f(\vec{x})](\vec{y}) \cos(\vec{x}\cdot\vec{y})\, \mathrm{d}\vec{y} + \int_{\mathbb{R}^N} \mathscr{S}[f(\vec{x})](\vec{y}) \sin(\vec{x}\cdot\vec{y})\, \mathrm{d}\vec{y}, \tag{3.77}$$

that is there exists no separate inverse for either transformation.

If, however, f is one-dimensional and meets some symmetry criteria, the definitions (3.75) and (3.76), as well as the inversion formula (3.77) simplify significantly. Let $f\colon \mathbb{R} \mapsto \mathbb{R}$ be integrable and odd, i.e. $-f(x) = f(-x)$, its sine transform is given by

$$\mathscr{S}[f(x)](y) = \int_0^\infty f(x) \sin(y\cdot x)\, \mathrm{d}x \tag{3.78}$$

and given $\mathscr{S}[f(x)](y)$ is also integrable an inversion is determined by

$$\mathscr{S}^{-1}[\mathscr{S}[f(x)](y)](x) = \frac{2}{\pi} \int_0^\infty \mathscr{S}[f(x)](y) \sin(y\cdot x)\, \mathrm{d}y \tag{3.79}$$

Likewise, if $f\colon \mathbb{R} \mapsto \mathbb{R}$ be integrable and even, i.e. $f(x) = f(-x)$, its cosine transform is given by

$$\mathscr{C}[f(x)](y) = \int_0^\infty f(x) \cos(y\cdot x)\, \mathrm{d}x, \tag{3.80}$$

which should it be integrable yields

$$\mathscr{C}^{-1}[\mathscr{C}[f(x)](y)](x) = \frac{2}{\pi} \int_0^\infty \mathscr{C}[f(x)](y) \cos(y\cdot x)\, \mathrm{d}y \tag{3.81}$$

as the inverse. Sometimes the sine and cosine transform are only defined via (3.78) to (3.81) for functions satisfying the above mentioned restrictions [39].

As for the case of Fourier transforms, there exists a number of slightly different definitions for the sine and cosine transforms as well. First, some definitions of the sine transform include the imaginary unit i. Second, (3.78) to (3.81) may all come with the prefactor $\sqrt{\frac{2}{\pi}}$, another convention being multiplying only (3.78) and (3.80) by 2. Finally, in analogy to (3.40) a factor of $\frac{1}{(2\pi)^{N/2}}$ is occasionally added in (3.75) and (3.76). In all these cases, the inverse formulas modify accordingly.

3.7.2 Discretization of the One-dimensional Sine Transform

Just like for Fourier transforms the discretization of both sine and cosine transform is erroneous in general, the same problem being that instead of a function only a representation of finite length can serve as the input signal. The principle understanding for both transforms of two functions, one mapping a given input signal $\vec{c}_{\vec{x}}$ with

$$c_{\vec{x}_m} = f(\vec{x}_m) \tag{3.82}$$

of length L from one space $\mathscr{X} \subset \mathbb{R}^{L \cdot N}$ to another signal $\vec{c}_{\vec{y}}$ of the same length L to another space $\mathscr{Y} \subset \mathbb{R}^{L \cdot N}$, and a second function mapping the representatives of the input space $\vec{x}_m \in \mathbb{R}^N$ to their counterparts in the output or Fourier space $\vec{y}_\mu \in \mathbb{R}^N$ also remains valid. Note, however, that due to the restriction of its definition, now a real vector is mapped onto another real vector.

The analytical Fourier transform in its original form being defined for periodic signals of infinite length, this by construction also holds true for the analytical sine and cosine transform. Hence, it is only logical that also their discretizations, just like the one of the Fourier transform, by design need to make assumptions regarding the input signal. These assumptions are, indeed, the requirements in the definitions of (3.78) and (3.80), i.e. the input signal of the discrete sine transform will be taken to stem from an odd function, while the input signal of the discrete cosine transform will be taken to stem from an even function. This observations yields two consequences. First, the discrete sine and cosine transforms are best understood in one dimension, i.e. $N = 1$, such that the vectors $\vec{x}_m$ and $\vec{y}_\mu$ turn to scalars x_m and y_μ, as here the meaning of even and odd is clearest, and second can these constraints be implemented in different fashions each one altering the definitions slightly. Thus, there are in total eight definitions for the discrete sine and cosine transforms each. We will therefore proceed discussing only one definitions of the discrete sine transform, commonly known as DST-I in the literature, and refer the interested reader to, e.g. [45] for further information. In the remainder of this text we shall also refer to the discrete sine transform by means of a DST-I.

So, we define the discrete sine transform and its inverse through

$$c_{\tilde{y}_\mu} = \sum_{\tilde{x}_m} \sin(\tilde{x}_m \tilde{y}_\mu)\, c_{\tilde{x}_m}, \tag{3.83}$$

$$c_{\tilde{x}_m} = \frac{2}{L+1} \sum_{\tilde{y}_\mu} \sin(\tilde{x}_m \tilde{y}_\mu)\, c_{\tilde{y}_\mu}. \tag{3.84}$$

Regarding the prefactor there is again an alternative definition

$$c_{\tilde{y}_\mu} = \sqrt{\frac{2}{L+1}} \sum_{\tilde{x}_m} \sin(\tilde{x}_m \tilde{y}_\mu)\, c_{\tilde{x}_m}, \tag{3.85}$$

$$c_{\tilde{x}_m} = \sqrt{\frac{2}{L+1}} \sum_{\tilde{y}_\mu} \sin(\tilde{x}_m \tilde{y}_\mu)\, c_{\tilde{y}_\mu}. \tag{3.86}$$

These definitions implicitly construct an odd signal from the given input signal $\vec{c}_x$ in the following way: Let again L be the length of the input signal δ_x its sampling. This signal is first taken to be enhanced by a data point corresponding to be at position zero, of which the value also is zero. Next, this signal which now is of length $L+1$ is enhanced by another data point at its end also being zero. Finally, the original input signal is added to the end in inverted order and with inverted sign. The so-obtained data string of length $2(L+1)$ is then taken as one period of an infinitely long signal.

We may now introduce quasi steps $\tilde{x}_m$ given by

$$\tilde{x}_m = \delta_x \cdot m, \quad m \in \{1, \dots, L\}, \quad \Rightarrow \quad \tilde{x}_m \in \{1, \dots, L \cdot \delta_x\} \tag{3.87}$$

due to the introduction of extra values to the original input signal, in particular

$$c_{\tilde{x}_0} = 0 \tag{3.88}$$

$$c_{\tilde{x}_{L+1}} = 0. \tag{3.89}$$

The assumed symmetry

$$c_{\tilde{x}_m} = -c_{\tilde{x}_{-m}} \tag{3.90}$$

further implies considering periodicity

$$c_{\tilde{x}_m} \overset{!}{=} c_{\tilde{x}_m + \tilde{x}_{2(L+1)}}. \tag{3.91}$$

Using (3.84) yields the step size in quasi reciprocal space

$$\begin{aligned} c_{\tilde{x}_m + \tilde{x}_{2(L+1)}} &= \frac{2}{L+1} \sum_{\tilde{y}_\mu} \sin\Big(\big(\tilde{x}_m + \tilde{x}_{2(L+1)}\big) \cdot \tilde{y}_\mu\Big)\, c_{\tilde{y}_\mu} && \text{(3.92a)} \\ &= \frac{2}{L+1} \sum_{\tilde{y}_\mu} \sin\big(\tilde{x}_m \cdot \tilde{y}_\mu\big) \cos\Big(\tilde{x}_{2(L+1)} \cdot \tilde{y}_\mu\Big)\, c_{\tilde{y}_\mu} \\ &\quad + \frac{2}{L+1} \sum_{\tilde{y}_\mu} \sin\Big(\tilde{x}_{2(L+1)} \cdot \tilde{y}_\mu\Big) \cos\big(\tilde{x}_m \cdot \tilde{y}_\mu\big)\, c_{\tilde{y}_\mu} && \text{(3.92b)} \\ = c_{\tilde{x}_m} &= \frac{2}{L+1} \sum_{\tilde{y}_\mu} \sin\big(\tilde{x}_m \cdot \tilde{y}_\mu\big)\, c_{\tilde{y}_\mu} && \text{(3.92c)} \\ \Rightarrow \quad \cos\Big(\tilde{x}_{2(L+1)} \cdot \tilde{y}_\mu\Big) &= \cos\big(2\,(L+1)\,\delta_x \cdot \tilde{y}_\mu\big) \overset{!}{=} 1 \quad \forall \quad y_\mu && \text{(3.92d)} \\ \wedge \quad \sin\Big(\tilde{x}_{2(L+1)} \cdot \tilde{y}_\mu\Big) &= \sin\big(2\,(L+1)\,\delta_x \cdot \tilde{y}_\mu\big) \overset{!}{=} 0 \quad \forall \quad y_\mu. && \text{(3.92e)} \end{aligned}$$

The sampling of the output signal $\vec{c}_{\tilde{y}}$ is, hence, determined by

$$\tilde{y}_\mu = \frac{\pi}{(L+1)\,\delta_x} \cdot \mu, \quad \mu \in \{1, \dots, L\}, \quad \Rightarrow \quad \tilde{y}_\mu \in \left\{ \frac{\pi}{(L+1)\,\delta_x}, \dots, \frac{\pi}{(L+1)\,\delta_x} \cdot L \right\}, \tag{3.93}$$

the sampling being

$$\delta_y = \frac{\pi}{(L+1)\,\delta_x}. \tag{3.94}$$

From definition (3.83), we find the enhancements (3.88) to (3.90) to also hold for the output signal in quasi reciprocal space and from computing

$$\begin{aligned} c_{\tilde{y}_\mu + \tilde{y}_{2(L+1)}} &= \sum_{\tilde{x}_m} \sin\Big(\tilde{x}_m \left(\tilde{y}_\mu + \tilde{y}_{2(L+1)}\right)\Big)\, c_{\tilde{x}_m} = \sum_{\tilde{x}_m} \sin\Big(\tilde{x}_m \tilde{y}_\mu + \tilde{x}_m \tilde{y}_{2(L+1)}\Big)\, c_{\tilde{x}_m} && \text{(3.95a)} \\ &= \sum_{\tilde{x}_m} \sin\left(\tilde{x}_m \tilde{y}_\mu + \delta_x m \cdot \frac{\pi}{(L+1)\,\delta_x} 2\,(L+1)\right) c_{\tilde{x}_m} = \sum_{\tilde{x}_m} \sin\big(\tilde{x}_m \tilde{y}_\mu + 2\pi m\big)\, c_{\tilde{x}_m} && \text{(3.95b)} \\ &= \sum_{\tilde{x}_m} \sin\big(\tilde{x}_m \tilde{y}_\mu\big)\, c_{\tilde{x}_m} = c_{\tilde{y}_\mu}, && \text{(3.95c)} \end{aligned}$$

the output signal to be of period $2\,(L+1)$ as well.

With the common abbreviations

$$c_m \coloneqq c_{\tilde{x}_m} \tag{3.96}$$

$$c_\mu \coloneqq c_{\tilde{y}_\mu} \tag{3.97}$$

we find the standard definition of the discrete forward and backward sine transform

$$c_\mu = \sum_{m=1}^{L} \sin\!\left(\frac{\delta_x \cdot m \cdot \pi}{(L+1)\,\delta_x} \cdot \mu\right) c_m = \sum_{m=1}^{L} \sin\!\left(\frac{\pi \mu m}{(L+1)}\right) c_m, \quad \mu \in \{1, \ldots, L\}\,, \tag{3.98}$$

$$c_m = \frac{2}{L+1} \sum_{\mu=1}^{L} \sin\!\left(\frac{\delta_x \cdot m \cdot \pi}{(L+1)\,\delta_x} \cdot \mu\right) c_\mu = \frac{2}{L+1} \sum_{\mu=1}^{L} \sin\!\left(\frac{\pi \mu m}{(L+1)}\right) c_\mu, \quad m \in \{1, \ldots, L\}\,. \tag{3.99}$$

We note that in contrast to the discrete Fourier transform discussed in section 3.6.2 due to assumption (3.90) in order to create an odd input signal, the output signal in quasi reciprocal space of the discrete sine transform will only cover half of the range of its analog in the discrete Fourier transform, c.f. (3.67) and (3.93).

For a discrete sine transform in one dimension from real space to reciprocal space, we identify $x = r$ and $y = k$, as before. Again, a more detailed discussion can be found in appendix A.1.

4 Matrix Product States and Matrix Product Operators

With the exponential growth of the Hilbert space as pointed out previously it is quite evident that one needs to find ways to approximate these systems in such a way that one can investigate their behavior in a reasonable time using reasonably many computational resources. Matrix product states (MPSs) provide such an approximation. Although having been known in mathematics as well as in physics for quite a long time [26, 9, 10, 274, 226], they have been rediscovered in the 1990s over the development of the density matrix renormalization group (DMRG).

Ever since they have become a de-facto standard tool for describing the physics of one-dimensional systems with short-range interaction due to their versatility and good scaling behavior.

Since the vast majority of the results to be presented in later chapters of this work is obtained from computations based on matrix product states (MPSs) and matrix product operators (MPOs), we give a rather detailed introduction to this topic in this chapter. This should, furthermore, allow the reader to judge the validity of our results. We will first summarize the development of DMRG in order to pave the way towards the introduction of MPSs and MPOs. We will then proceed with a detailed description of their construction and key properties and close with a discussion of the calculus, thereby outlining strengths and weaknesses of the approaches discussed. Note that matrix product states are most powerful for system with open boundaries. Hence, unless stated otherwise, we will only consider such systems. For a generalization to periodic boundary conditions c.f. [320], which serves alongside [195, 280] as the primary source of this entire chapter. We mention that there exist also extensions for the treatment of systems in the thermodynamic limit, so-called infinite system MPSs, iMPSs, which we do not discuss here. Instead we refer, for instance, to [183, 272, 390, 275].

Standard algorithms involving MPSs and MPOs will be discussed in the following chapter.

4.1 A Very Brief History of DMRG

Based on Wilson's numerical renormalization group (NRG) [409], in 1992 Steven White proposed [406] and later expanded [407] the density matrix renormalization group, DMRG, for one-dimensional systems which allowed him to compute the ground state and other observables of the Heisenberg spin $S = 1$ chain to a surprising accuracy surpassing other methods. The power of this new method was quickly acknowledged in the community and further developed [279]. The DMRG served a great deal when it came to the calculation of phase diagrams, c.f. for instance [319]. However, its powers in other fields, namely in quantum information [387], were also discovered indicating it to be applicable to more problems than "only" ground state computations.

In the early 2000s, several enhancements were introduced. In 2002 Eric Jeckelmann invented the dynamical DMRG [171], or DDMRG for short, which allowed him to compute (equilibrium) dynamical properties, like spectral functions or optical conductivities. At around the same time, several extensions allowing the computation of time evolutions, then to be called tDMRG, were

introduced [392, 70, 408] and the description of thermal quantum states was developed [386, 432]. From an early stage on it was noted [84] that the scheme of the DMRG can be formulated in terms of tensor arithmetics [273] such that eventually the language of matrix product states, MPSs, amongst other tensor-based algorithms like tree tensor networks [339] or fork tensor networks [24], was developed.

The concept of MPSs has been adapted to two dimensions under the name of projected entangled pair states (PEPSs) [385] and arbitrary dimensions as the multiscale entanglement renormalization ansatz (MERA) [389]. For an introduction to the former see for instance [272]. In restricted cases MPSs have been shown to obey to an area law [144, 384] as have PEPSs [388]. Thus, due to their increased dimensions, handling the latter is significantly more complex such that they are not as frequently applied as MPSs yet the focus lying rather on conceptional improvements, see for instance [316].

Nowadays, MPSs have become a standard in describing one-dimensional quantum systems. Of the many works dedicated to this topic we only named a few here. We should mention the comprehensive reviews of Ulrich Schollwöck, both for classical DMRG [319], as well as for its re-expression in terms of MPSs [320]. Since both these works are rather extensive for beginners we also refer to the introductory courses [1] and [4].

As will become clear below, for systems with large local Hilbert spaces MPS computations also become challenging, which necessitates the introduction of further methods, c.f. for instance [82, 354, 169]. To tackle these obstacles, recently an MPS-based extension to the DMRG, the so-called projected purified DMRG (ppDMRG) has been introduced [196, 355, 353].

4.2 Matrix Product States

Consider any arbitrary many-body quantum state describing a system with L sites

$$|\psi\rangle = \sum_{\sigma_1,\sigma_2,\dots,\sigma_{L-1},\sigma_L} c_{\sigma_1,\sigma_2,\dots,\sigma_{L-1},\sigma_L} |\sigma_1,\sigma_2,\dots,\sigma_{L-1},\sigma_L\rangle \tag{4.1}$$

with $c \in \mathbb{C}$ and

$$|\sigma_1,\sigma_2,\dots,\sigma_{L-1},\sigma_L\rangle \equiv |\sigma_1\rangle\,|\sigma_2\rangle\cdots|\sigma_{L-1}\rangle\,|\sigma_L\rangle \equiv |\sigma_1\rangle \otimes |\sigma_2\rangle \otimes \cdots \otimes |\sigma_{L-1}\rangle \otimes |\sigma_L\rangle\,. \tag{4.2}$$

Let d now be the local dimension of each state space on site $i = 1,\dots,L$, i.e. $\mathrm{card}\,\{\sigma_i\} = d\,\forall i \in \{1,\dots,L\}$. The number of coefficients $c_{\sigma_1,\sigma_2,\dots,\sigma_{L-1},\sigma_L}$ is then determined by d^L reflecting the exponential nature of the problem.

The idea of matrix product states is now to encode these d^L coefficients in a product of just $d \cdot L$ matrices M^{σ_i} where each matrix only affects its assigned state space at site i. Thus, the arbitrary quantum state in equation (4.1) is then given by

$$|\psi\rangle = \sum_{\sigma_1,\sigma_2,\dots,\sigma_{L-1},\sigma_L} M_1^{\sigma_1} \cdot M_2^{\sigma_2} \cdot \dots \cdot M_{L-1}^{\sigma_{L-1}} \cdot M_L^{\sigma_L} |\sigma_1,\sigma_2,\dots,\sigma_{L-1},\sigma_L\rangle\,. \tag{4.3}$$

Written down in this manner the state $|\psi\rangle$ is now conveniently called a matrix product state (MPS). A graphical representation using the notation introduced in section 3.1 is given in figure 4.1. Note

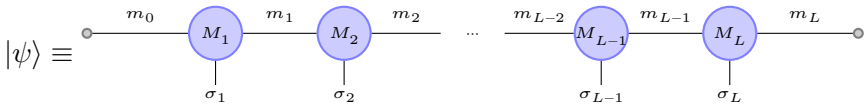

Figure 4.1: Pictorial representation of a general MPS $|\psi\rangle$, c.f. equation (4.3).

that this decomposition of coefficients into matrices is far from being unique as can be envisaged when thinking of an arbitrary invertible matrix X (of proper dimension) such that

$$M_i^{\sigma_i} \to M_i^{\sigma_i} \cdot X, \quad M_{i+1}^{\sigma_{i+1}} \to X^{-1} \cdot M_{i+1}^{\sigma_{i+1}}. \tag{4.4}$$

Hence, not even the dimensions of the matrices $M_i^{\sigma_i}$ in equation (4.3) need to be the same for different decompositions. Therefore, it is quite naive to believe to have reduced the problem from an exponential to a linear one just by rewriting the coefficients in termes of matrices. Obviously, however, it is clear that one has no need to make any of these dimension unnecessarily large. To cover the coefficients exactly, the matrices need to be of the following dimensions:

$M_1^{\sigma_1}$	$M_2^{\sigma_2}$	$\cdots$	$M_{L/2}^{\sigma_{L/2}}$	$M_{L/2+1}^{\sigma_{L/2+1}}$	$\cdots$	$M_{L-1}^{\sigma_{L-1}}$	$M_L^{\sigma_L}$
$(1 \times d)$	$(d \times d^2)$	$\cdots$	$(d^{L/2-1} \times d^{L/2})$	$(d^{L/2} \times d^{L/2-1})$	$\cdots$	$(d^2 \times d)$	$(d \times 1)$

if L is even,

$M_1^{\sigma_1}$	$M_2^{\sigma_2}$	$\cdots$	$M_{\lfloor L/2 \rfloor}^{\sigma_{\lfloor L/2 \rfloor}}$	$M_{\lceil L/2 \rceil}^{\sigma_{\lceil L/2 \rceil}}$	$M_{\lceil L/2 \rceil+1}^{\sigma_{\lceil L/2 \rceil+1}}$	$\cdots$	$M_{L-1}^{\sigma_{L-1}}$	$M_L^{\sigma_L}$
$(1 \times d)$	$(d \times d^2)$	$\cdots$	$(d^{\lfloor L/2 \rfloor-1} \times d^{\lfloor L/2 \rfloor})$	$(d^{\lfloor L/2 \rfloor} \times d^{\lfloor L/2 \rfloor})$	$(d^{\lfloor L/2 \rfloor} \times d^{\lfloor L/2 \rfloor-1})$	$\cdots$	$(d^2 \times d)$	$(d \times 1)$

if L is odd. Note that from this visualization it is obvious that $M_1^{\sigma_1}$ and $M_L^{\sigma_L}$ are actually vectors rather than matrices to ensure that the final product of all the matrices $M_i^{\sigma_i}$ in the end yields a scalar. Often times, however a dummy index is added to these vectors in order to be able to treat them as ordinary matrices. Furthermore, it is at this point worth mentioning that what we have called "matrices" in this section so far are actually rank-3 tensors, whilst what we have called "vectors" are actually rank-2 tensors, c.f. again figure 3.1 for further explanation of these issues.

Regarding the notation, we shall always denote physical indices as superindices, while we will be using subindices for numerical or bond indices. In order to differentiate $M_j^{\sigma_j\dagger}$ from $M_j^{\sigma_j}$ we shall further denote the bond indices of the former with bars, as well as its tag. We present these conventions in figure 4.2.

Figure 4.2: Pictorial representation of an MPS $M_j^{\sigma_j}$ and its adjoint $M_j^{\sigma_j\dagger}$.

Summing up over all the matrices $M_i^{\sigma_i}$ one realizes that in order to represent the state $|\psi\rangle$ accurately one needs to calculate $2\sum_{i=1}^{\lfloor L/2 \rfloor} d^{2i} + (L \mod 2)\, d^{2\lfloor L/2 \rfloor + 1}$ matrix elements, which is more than the d^L coefficients one originally intended to decrease in number. It is at this point when the true power of matrix product states comes into play: Instead of having the matrices grow in size such that the total number of elements exceeds the number of coefficients one introduces a maximum dimension $\chi_{\max}$ the matrices can assume and truncates all the matrices to this dimension of $(\chi_{\max} \times \chi_{\max})$ that otherwise would be larger. In certain cases, however, it is actually possible to construct an MPS with matrices of lower dimensions than the one presented above in the first place. A trivial example are product states, where all matrices need only be of dimensions 1×1. We elaborate on these issues in appendix B with the help of three example MPSs.

The above considerations illustrate that we are in need of

1. a procedure to construct an MPS efficiently, using only a minimum number of matrix elements,
2. a procedure to truncate the matrices efficiently if necessary, keeping the difference to the uncompressed state as small a possible,
3. a measure to quantify the approximation of the MPS, and
4. a criterion to judge in how far a certain state of a certain problem with certain properties is suitable for an MPS treatment.

We will address each of these issues in a subsequent section. Beginning with the first problem we will show that an SVD introduced in section 3.3 will do the trick of an efficient construction of MPSs. We will proceed showing that using an SVD will also provide a natural mechanism for truncation of too large matrices, furthermore introducing a very convenient measure of this approximation, the so-called discarded weight. Finally we will identify the entanglement entropy and its associated area law as an appropriate measure to judge the use of MPSs and discuss different representations of MPSs, which will become useful when developing MPS-based algorithms.

4.2.1 Construction of Matrix-Product-States via SVD

Let

$$|\psi\rangle = \sum_{\sigma_1, \sigma_2, \ldots, \sigma_{L-1}, \sigma_L} c_{\sigma_1, \sigma_2, \ldots, \sigma_{L-1}, \sigma_L} |\sigma_1, \sigma_2, \ldots, \sigma_{L-1}, \sigma_L\rangle \tag{4.5}$$

with $c \in \mathbb{C}$ and L the number of sites in the system under consideration again be the state we wish to express as an MPS, c. f. equation (4.1). The goal is now to express this state in terms of a matrix product as efficiently as possible.

We begin by interpreting the coefficients $c_{\sigma_1, \sigma_2, \ldots, \sigma_{L-1}, \sigma_L}$ as a tensor of rank L, calling each index σ_i a physical index, c.f. figure 4.3 for a graphical representation. This tensor can now be reshaped into a matrix via

$$\Psi_{\sigma_1, (\sigma_2, \ldots, \sigma_{L-1}, \sigma_L)} = c_{\sigma_1, \sigma_2, \ldots, \sigma_{L-1}, \sigma_L}. \tag{4.6}$$

If the matrix Ψ in the above equation is subject to an SVD, we obtain

$$\Psi_{\sigma_1, (\sigma_2, \ldots, \sigma_L)} = \sum_{m_1} U_{\sigma_1, m_1} \Gamma_{m_1, m_1} \left(V^\dagger\right)_{m_1, (\sigma_2, \ldots, \sigma_{L-1}, \sigma_L)}. \tag{4.7}$$

Figure 4.3: Pictorial representation of the interpretation of a quantum state $|\psi\rangle$ as a multi-dimensional tensor, c.f. equation (4.5).

Introducing

$$A^{\sigma_1}_{1;m_0,m_1} = U_{\sigma_1,m_1} \tag{4.8}$$

and reshaping

$$\sum_{m_1} \Gamma_{m_1,m_1} \left(V^\dagger\right)_{m_1,(\sigma_2,\ldots,\sigma_{L-1},\sigma_L)} = \left(\tilde{V}^\dagger\right)_{m_1,(\sigma_2,\ldots,\sigma_{L-1},\sigma_L)} = c_{m_1,\sigma_2,\ldots,\sigma_{L-1},\sigma_L} \tag{4.9}$$

we obtain

$$c_{\sigma_1,\sigma_2,\ldots,\sigma_{L-1},\sigma_L} = \sum_{m_1} A^{\sigma_1}_{1;m_1} c_{m_1,\sigma_2,\ldots,\sigma_{L-1},\sigma_L} \tag{4.10}$$

where $A^{\sigma_1}_{1;m_1}$ may be interpreted as a rank-2 tensor with a physical index σ_1 and a bond index m_1 and $c_{m_1,\sigma_2,\ldots,\sigma_{L-1},\sigma_L}$ as a tensor of rank L with bond index m_1 and physical indices $\sigma_2,\ldots,\sigma_{L-1},\sigma_L$. We proceed by reshaping $c_{m_1,\sigma_2,\ldots,\sigma_{L-1},\sigma_L}$ into a matrix

$$\Psi_{(m_1,\sigma_2),(\sigma_3,\ldots,\sigma_{L-1},\sigma_L)} = c_{m_1,\sigma_2,\ldots,\sigma_{L-1},\sigma_L} \tag{4.11}$$

and subsequently decomposing the result which yields

$$\Psi_{(m_1,\sigma_2),(\sigma_3,\ldots,\sigma_{L-1},\sigma_L)} = \sum_{m_2} U_{(m_1,\sigma_2),m_2} \Gamma_{m_2,m_2} \left(V^\dagger\right)_{m_2,(\sigma_3,\ldots,\sigma_{L-1},\sigma_L)}. \tag{4.12}$$

Analogously to the above we define

$$A^{\sigma_2}_{2;m_1,m_2} = U_{(m_1,\sigma_2),m_2} \tag{4.13}$$

and reshape

$$\sum_{m_2} \Gamma_{m_2,m_2} \left(V^\dagger\right)_{m_2,(\sigma_3,\ldots,\sigma_{L-1},\sigma_L)} = \left(\tilde{V}^\dagger\right)_{m_2,(\sigma_3,\ldots,\sigma_{L-1},\sigma_L)} = c_{m_2,\sigma_3,\ldots,\sigma_{L-1},\sigma_L} \tag{4.14}$$

such that

$$c_{\sigma_1,\sigma_2,\ldots,\sigma_{L-1},\sigma_L} = \sum_{m_1,m_2} A^{\sigma_1}_{1;m_1} A^{\sigma_2}_{2;m_1,m_2} c_{m_2,\sigma_3,\ldots,\sigma_{L-1},\sigma_L}. \tag{4.15}$$

This procedure may now be repeated until the last site L resulting in

$$c_{\sigma_1,\sigma_2,\ldots,\sigma_{L-2},\sigma_{L-1}} = \sum_{m_1,m_2,\ldots,m_{L-2},m_{L-1}} A^{\sigma_1}_{1;m_1} A^{\sigma_2}_{2;m_1,m_2} \cdots A^{\sigma_{L-1}}_{L-1;m_{L-2},m_{L-1}} A^{\sigma_L}_{L;m_{L-1}}. \tag{4.16}$$

With the exception of the first and last tensors $A^{\sigma_1}_1$ and $A^{\sigma_L}_L$ all the other "matrices" $A^{\sigma_i}_i$ are rank-3 tensors with one physical index σ_i and two bond indices m_{i-1} and m_i. For the sake of brevity and uniformity, one often introduces dummy indices m_0 and m_L, which may only take the value of 1, on the edges, such that equation (4.16) reads

$$c_{\sigma_1,\sigma_2,\ldots,\sigma_{L-1},\sigma_L} = \sum_{m_0,m_1,\ldots,m_{L-1},m_L} A^{\sigma_1}_{1;m_0,m_1} A^{\sigma_2}_{2;m_1,m_2} \cdots A^{\sigma_{L-1}}_{L-1;m_{L-2},m_{L-1}} A^{\sigma_L}_{L;m_{L-1},m_L}, \tag{4.17}$$

or in short

$$c_{\sigma_1,\sigma_2,\dots,\sigma_{L-1},\sigma_L} = A_1^{\sigma_1} A_2^{\sigma_2} \cdots A_{L-1}^{\sigma_{L-1}} A_L^{\sigma_L}. \tag{4.18}$$

Inserting this result into the original equation (4.5) we find

$$|\psi\rangle = \sum_{\sigma_1,\sigma_2,\dots,\sigma_{L-1},\sigma_L} A_1^{\sigma_1} A_2^{\sigma_2} \cdots A_{L-1}^{\sigma_{L-1}} A_L^{\sigma_L} \left|\sigma_1, \sigma_2, \dots, \sigma_{L-1}, \sigma_L\right\rangle, \tag{4.19}$$

which is the (or rather a) decomposition of $|\psi\rangle$ into an MPS we were in search of.

For each element of the on-site local Hilbert space σ_i we now have a matrix $A_i^{\sigma_i}$ with bond indices m_{i-1} and m_i. The dimensions of these matrices are determined by the SVD, i.e.

$$A_i^{\sigma_i} \in \mathbb{C}^{(r_{i-1}, r_i)}, \tag{4.20}$$

c.f. section 3.3, with the special cases $r_0 = r_L = 1$. However the dimension will by construction never exceed the numbers presented in the previous section. Note that so far we have not made any remarks on truncation, i.e. up to this point the would obtain an exact representation of the state $|\psi\rangle$, which is numerically even more costly as we have already seen.

4.2.2 Normalization and MPS Representations

Consider again the problem of constructing an MPS for a given state

$$|\psi\rangle = \sum_{\sigma_1,\sigma_2,\dots,\sigma_{L-1},\sigma_L} c_{\sigma_1,\sigma_2,\dots,\sigma_{L-1},\sigma_L} \left|\sigma_1, \sigma_2, \dots, \sigma_{L-1}, \sigma_L\right\rangle, \tag{4.21}$$

$c \in \mathbb{C}$ and L the system size, c.f. (4.5), as discussed in section 4.2.1.

The choice of reshaping the rank-L tensor $c_{\sigma_1,\sigma_2,\dots,\sigma_{L-1},\sigma_L}$ beginning from site 1 was entirely arbitrary. The procedure works just as well starting from the last site L, reshaping

$$\Psi_{(\sigma_1,\sigma_2,\dots,\sigma_{L-1}),\sigma_L} = c_{\sigma_1,\sigma_2,\dots,\sigma_{L-1},\sigma_L} \tag{4.22}$$

and performing an SVD on the matrix Ψ yielding

$$\Psi_{(\sigma_1,\dots,\sigma_{L-1}),\sigma_L} = \sum_{m_{L-1}} U_{(\sigma_1,\dots,\sigma_{L-1}),m_{L-1}} \Gamma_{m_{L-1},m_{L-1}} \left(V^\dagger\right)_{m_{L-1},\sigma_L}. \tag{4.23}$$

If we now define

$$B_{L;m_{L-1},m_L}^{\sigma_L} = \left(V^\dagger\right)_{m_{L-1},\sigma_L}, \tag{4.24}$$

m_L again being a dummy index, we may in analogy to the procedure in 4.2.1 reshape

$$\sum_{m_{L-1}} U_{(\sigma_1,\dots,\sigma_{L-1}),m_{L-1}} \Gamma_{m_{L-1},m_{L-1}} = \tilde{U}_{(\sigma_1,\dots,\sigma_{L-1}),m_{L-1}} = c_{\sigma_1,\sigma_2,\dots,\sigma_{L-1},m_{L-1}} \tag{4.25}$$

to have

$$c_{\sigma_1,\sigma_2,\dots,\sigma_{L-1},\sigma_L} = \sum_{m_{L-1},m_L} c_{\sigma_1,\sigma_2,\dots,\sigma_{L-1},m_{L-1}} B_{L;m_{L-1},m_L}^{\sigma_L} \tag{4.26}$$

from which we can then construct

$$\Psi_{(\sigma_1,\sigma_2,\dots,\sigma_{L-2}),(\sigma_{L-1},m_{L-1})} = c_{\sigma_1,\sigma_2,\dots,\sigma_{L-1},m_{L-1}} \tag{4.27}$$

to continue SV decomposing and reshaping into tensors until we have

$$|\psi\rangle = \sum_{\sigma_1,\sigma_2,\dots,\sigma_{L-1},\sigma_L} B_1^{\sigma_1} B_2^{\sigma_2} \cdots B_{L-1}^{\sigma_{L-1}} B_L^{\sigma_L} |\sigma_1,\sigma_2,\dots,\sigma_{L-1},\sigma_L\rangle . \tag{4.28}$$

We have, thus, found another way of decomposing $|\psi\rangle$ into an MPS.

The crucial observation at this point is that all the matrices A and B in the procedures introduced above were constructed from matrices U and $V^\dagger$ of the SVD, respectively, which we know to be unitary from section 3.3. Thus, we find

$$\delta_{m_l,m_l'} = \sum_{m_{l-1},\sigma_l} \left(U^\dagger\right)_{m_l,(m_{l-1},\sigma_l)} U_{(m_{l-1},\sigma_l),m_l'} = \sum_{m_{l-1},\sigma_l} \left(A_l^{\sigma_l\dagger}\right)_{m_l,m_{l-1}} A^{\sigma_l}_{l;m_{l-1},m_l'} \tag{4.29}$$

$$= \sum_{\sigma_l} \left(A_l^{\sigma_l\dagger} A_l^{\sigma_l}\right)_{m_l,m_l'}, \tag{4.30}$$

$$\delta_{m_{l-1},m_{l-1}'} = \sum_{\sigma_l,m_l} \left(V^\dagger\right)_{m_{l-1},(\sigma_l,m_l)} V_{(\sigma_l,m_l),m_{l-1}'} \tag{4.31}$$

$$= \sum_{\sigma_l,m_l} B^{\sigma_l}_{l;m_{l-1},m_l} \left(B_l^{\sigma_l\dagger}\right)_{m_l,m_{l-1}'} = \sum_{\sigma_l} \left(B_l^{\sigma_l} B_l^{\sigma_l\dagger}\right)_{m_{l-1},m_{l-1}'} \tag{4.32}$$

or in short

$$\sum_{\sigma_l} A_l^{\sigma_l\dagger} A_l^{\sigma_l} = \mathbb{1}, \tag{4.33}$$

$$\sum_{\sigma_l} B_l^{\sigma_l} B_l^{\sigma_l\dagger} = \mathbb{1}, \tag{4.34}$$

c.f. figure 4.4 or 4.5, respectively. Note that the converse is in general not true, i.e.

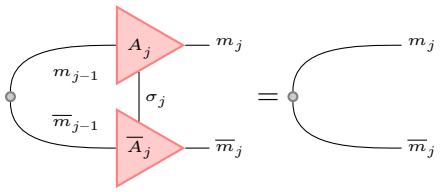

Figure 4.4: Pictorial representation of equation (4.33).

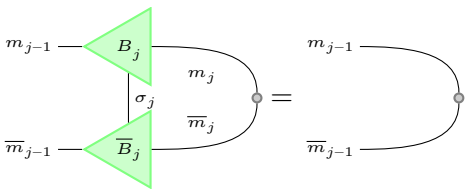

Figure 4.5: Pictorial representation of equation (4.34).

$$\sum_{\sigma_l} A_l^{\sigma_l} A_l^{\sigma_l\dagger} \neq \mathbb{1}, \tag{4.35}$$

$$\sum_{\sigma_l} B_l^{\sigma_l \dagger} B_l^{\sigma_l} \neq \mathbb{1}. \tag{4.36}$$

Due to the properties (4.33) and (4.34), the matrices $A_l^{\sigma_l}$ (A-matrices) and $B_l^{\sigma_l}$ (B-matrices) are called *left-* or *right-normalized*, respectively. Analogously, an MPS consisting of only A-matrices

$$|\psi\rangle = \sum_{\sigma_1,\sigma_2,\dots,\sigma_{L-1},\sigma_L} A_1^{\sigma_1} A_2^{\sigma_2} \cdots A_{L-1}^{\sigma_{L-1}} A_L^{\sigma_L} \, |\sigma_1, \sigma_2, \dots, \sigma_{L-1}, \sigma_L\rangle \tag{4.37}$$

is referred to as *left-canonical*, while one entirely composed of B-matrices

$$|\psi\rangle = \sum_{\sigma_1,\sigma_2,\dots,\sigma_{L-1},\sigma_L} B_1^{\sigma_1} B_2^{\sigma_2} \cdots B_{L-1}^{\sigma_{L-1}} B_L^{\sigma_L} \, |\sigma_1, \sigma_2, \dots, \sigma_{L-1}, \sigma_L\rangle \,, \tag{4.38}$$

is called *right-canonical*. In figures 4.6 and 4.7 we present graphical representations of both these cases.

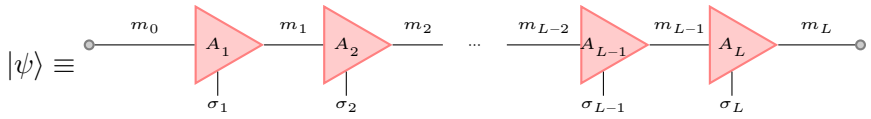

Figure 4.6: Pictorial representation of a left-canonical MPS $|\psi\rangle$, c.f. equation (4.37).

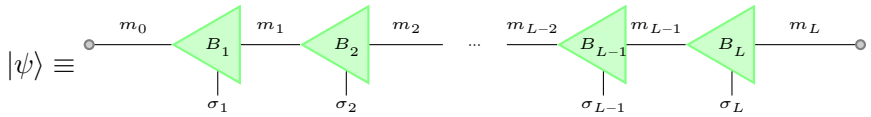

Figure 4.7: Pictorial representation of a right-canonical MPS $|\psi\rangle$, c.f. equation (4.38).

The task of normalizing a general MPS

$$|\psi\rangle = \sum_{\sigma_1,\sigma_2,\dots,\sigma_{L-1},\sigma_L} M_1^{\sigma_1} M_2^{\sigma_2} \cdots M_{L-1}^{\sigma_{L-1}} M_L^{\sigma_L} \, |\sigma_1, \sigma_2, \dots, \sigma_{L-1}, \sigma_L\rangle \,, \tag{4.39}$$

composed of general matrices $M_l^{\sigma_l}$ is, hence, reduced to bringing it either into left- or right-canonical form. In order to obtain a left-canonical MPS, beginning from $l = 1$ the matrix $M_l^{\sigma_l}$, i.e. the rank-3 tensor $M^{\sigma_l}_{l;m_{l-1},m_l}$, is reshaped into an actual matrix $M'_{l;(m_{l-1},\sigma_l),m_l}$ and then decomposed

$$M'_{l;(m_{l-1},\sigma_l),m_l} = \sum_{m'_l} \Theta_{(m_{l-1},\sigma_l),m'_l} \Xi_{m'_l,m_l}. \tag{4.40}$$

where we require Θ to be unitary, i.e. $\Theta = \Theta^\dagger$. Next, we reshape

$$\Theta_{(m_{l-1},\sigma_l),m'_l} = A^{\sigma_l}_{l;m_{l-1},m'_l} \tag{4.41}$$

and take the next 3-tensor $M^{\sigma_{l+1}}_{l+1;m_l,m_{l+1}}$ converting it into a matrix $\tilde{M}_{l+1;m_l,(\sigma_{l+1},m_{l+1})}$ which we then update by

$$M'_{l+1;m'_l,(\sigma_{l+1},m_{l+1})} = \sum_{m_l} \Xi_{m'_l,m_l} \tilde{M}_{l+1;m_l,(\sigma_{l+1},m_{l+1})}. \tag{4.42}$$

After renaming the index m'_l to m_l and reshaping $M'_{l+1;m_l,(\sigma_{l+1},m_{l+1})}$ to $M'_{l+1;(m_l,\sigma_{l+1}),m_{l+1}}$ steps (4.40) to (4.42) may be repeated for this matrix, such that when $l = L$ the MPS takes the desired form. Note that for the decomposition into Θ and Ξ several routines may be applied. In principle, it is possible to again make use of an SVD, c.f. section 3.3, which would mean $\Theta = U$ and $\Xi = \Gamma V^\dagger$. However, in most applications it is more desirable to instead do a QR decomposition, c.f. section 3.2, as it is numerically less costly. This then means $\Theta = Q$ and $\Xi = R$. The disadvantage of the QR-decomposition is that it does not allow for an efficient truncation. When it comes to normalizing an MPS, however, there is usually no need to do so. Thus, in general, when it comes to the pure construction of A- or B-matrices the QR-decomposition is preferred.

Normalizing an MPS into a right-canonical form involves in general one extra step. Starting from $l = L$ we reshape $M^{\sigma_l}_{l;m_{l-1},m_l}$ into $M'_{l;m_{l-1},(\sigma_l,m_l)}$ and decompose the complex conjugate

$$\overline{M}'_{l;(\sigma_l,m_l),m_{l-1}} = \sum_{m'_{l-1}} \Theta_{(\sigma_l,m_l),m'_{l-1}} \Xi_{m'_{l-1},m_{l-1}} \tag{4.43}$$

allowing us to construct

$$\overline{\Theta}_{m'_{l-1},(\sigma_l,m_l)} = B^{\sigma_l}_{l;m'_{l-1},m_l}. \tag{4.44}$$

Then we take $M^{\sigma_{l-1}}_{l-1;m_{l-2},m_{l-1}}$ which we first reshape into $\tilde{M}_{l-1;(m_{l-2},\sigma_{l-1}),m_{l-1}}$ and update via

$$M'_{l-1;(m_{l-2},\sigma_{l-1}),m'_{l-1}} = \sum_{m_{l-1}} \tilde{M}_{l-1;(m_{l-2},\sigma_{l-1}),m_{l-1}} \overline{\Xi}_{m_{l-1},m'_{l-1}}. \tag{4.45}$$

Renaming the index m'_{l-1} to m_{l-1} and reshaping $M'_{l-1;(m_{l-2},\sigma_{l-1}),m_{l-1}}$ to $M'_{l-1;m_{l-2},(\sigma_{l-1},m_{l-1})}$ allows us to repeat (4.43) to (4.45) until $l = 1$. Note that working with the complex conjugate in the procedure is not strictly necessary when applying the SVD. In that case it would be possible constructing the B-matrices from matrices $V^\dagger$ and update $\tilde{M}$ by $U\Gamma$ similar to the construction of a right-canonical MPS presented in the beginning of this section, as for the SVD U, as well as V are unitary. Consequently, QR- instead of SV-decomposing would have worked equally fine in section 4.2.1, the substitution simply being $U \equiv Q$ and $\Gamma V^\dagger \equiv R$. Likewise would QR-decomposing the complex conjugated matrices Ψ in the construction of the right canonical MPS have been possible, the drawback again being that this way no reasonable truncation is possible.

The concept of iteratively running through an MPS manipulating each matrix separately is known as sweeping, where more precisely we call running from left to right a right-sweep and going from right to left we refer to as left-sweeping. Beginning now with a left-normalized MPS performing a right-sweep or equally beginning with a right-normalized MPS performing a left-sweep during this procedure we will encounter MPSs of the form

$$|\psi\rangle = \sum_{\sigma_1,\sigma_2,\dots,\sigma_{L-1},\sigma_L} A^{\sigma_1}_1 A^{\sigma_2}_2 \cdots A^{\sigma_{j-1}}_{j-1} M^{\sigma_j}_j B^{\sigma_{j+1}}_{j+1} \cdots B^{\sigma_{L-1}}_{L-1} B^{\sigma_L}_L |\sigma_1, \sigma_2, \dots, \sigma_{L-1}, \sigma_L\rangle, \tag{4.46}$$

c.f. figure 4.8 for a sketch. This representation of an MPS is conveniently called *mixed-canonical* and the site j which is described by the only non-normalized matrix is referred to as the *active site* or *orthogonality center*. As most intrinsically MPS-based algorithms rely on the above described sweeping procedures, mixed-canonical MPSs are regularly encountered. Shifting the orthogonality center works just like a single step in a normalization sweep. Depending on whether the orthogonality center is to be moved form $M^{\sigma_j}_j$ to the left or right, first M_j needs to be decomposed and then

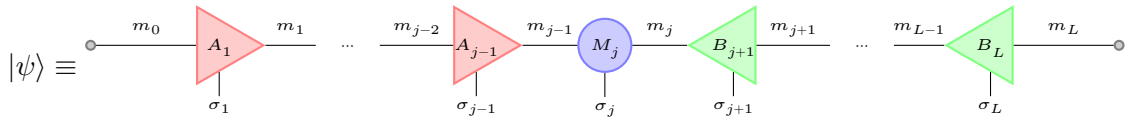

Figure 4.8: Pictorial representation of a mixed-canonical MPS $|\psi\rangle$ with orthogonality center at site j, c.f. equation (4.46).

reshaped according to equation (4.43) and (4.44) or (4.40) and (4.41), respectively. Afterwards $M_{j-1}^{\sigma_{j-1}}$ is updated according to equation (4.45), or $M_{j+1}^{\sigma_{j+1}}$ as in (4.42), and eventually recast into a rank-3 tensor.

At this point, also the connection to classical DMRG becomes evident. Considering the entire left-normalized matrices of a mixed-canonical MPS as one entity and all the right-normalized matrices as another one, we reobtain the typical splitting of a physical state into two subsystems native to DMRG consisting of a left part, a right part and a center site on which operations may be performed on.

For the sake of completeness we mention that there is also an alternative representation of MPSs introduced by Vidal decomposing into

$$|\psi\rangle = \sum_{\sigma_1,\dots,\sigma_L} \Gamma_{V,1}^{\sigma_1} \Lambda_{V,1} \Gamma_{V,2}^{\sigma_2} \Lambda_{V,2} \cdots \Lambda_{V,L-2} \Gamma_{V,L-1}^{\sigma_{L-1}} \Lambda_{V,L-1} \Gamma_{V,L}^{\sigma_L} |\sigma_1, \sigma_2, \dots, \sigma_{L-1}, \sigma_L\rangle, \tag{4.47}$$

which can be constructed from SVDs. In this representation all matrices $\Lambda_{V,l}$ contain the singular values of the respective SVD, thus, they are diagonal, and the $\Lambda_{V,l}$ are unitary matrices. Introducing the 1×1 dummy matrix $\Lambda_{V,0} = 1$ or $\Lambda_{V,L} = 1$ Vidal's representation can be transformed into a left- or right-canonical representation via

$$A_{l;m_{l-1},m_l}^{\sigma_l} = \sum_{m_{l-1}} \Lambda_{V,l-1;m_{l-1},m_{l-1}} \Gamma_{V,l;m_{l-1},m_l}^{\sigma_l}, \quad \text{or} \tag{4.48}$$

$$B_{l;m_{l-1},m_l}^{\sigma_l} = \sum_{m_l} \Gamma_{V,l;m_{l-1},m_l}^{\sigma_l} \Lambda_{V,l;m_l,m_l}, \tag{4.49}$$

respectively. As we will hardly make use of this representation in the remainder of this work, apart from presenting a sketch in figure 4.9, we refer to Vidal's original work [391] or [320] for further reading.

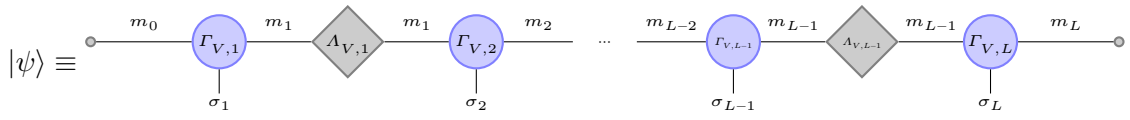

Figure 4.9: Pictorial representation of an MPS $|\psi\rangle$ in Vidal's notation, c.f. equation (4.47).

Note that while all the MPS representations introduced in this section have different properties, they still describe the same physical state and, thus, the same physics. What representation will be used depends on the respective algorithm manipulating the MPS as we will outline in chapter 5.

4.2.3 Truncation and Discarded Weight

In this section we will discuss the compression of an MPS applying an SVD. This procedure leads to the introduction of the important quantity of the discarded weight quite naturally. Note, however that in practice this method is not applied as it does not yield an optimum truncation. Instead one makes use of a variational approach. For pedagogical reasons we will nevertheless review the naive compression via an SVD first and postpone the discussion of the variational approach to the next section for it also requires a deeper understanding of MPSs.

The actual truncation of an MPS happens applying the SVD. As explained in detail in section 3.3 the matrix Γ is diagonal containing the singular values of the decomposed matrix sorted from large to small. The crucial point of the MPS representation is now to only take the $\chi_{\max}$ largest singular values into account by restricting Γ to be at most of size $(\chi_{\max} \times \chi_{\max})$ if $r_i > \chi_{\max}$. Truncating an MPS is thus achieved by applying the normalization routine we presented in the preceding section, the only difference being that now the SVD needs to be applied in order to then contract Γ and adjust U and $V^\dagger$ accordingly. For this routine either a single left- or right-sweep may be performed.

Clearly, the so-obtained approximation may be a rather drastic. However, from inspecting the singular value spectra shown for the compression of images in figure 3.9 we also know that the size of the singular values may also decrease exponentially. In order to quantify the error one has made by enforcing this restriction, we define the discarded weight

$$\delta_i = 1 - \sum_{m_i=1}^{\chi_{\max}} \lambda_{m_i}^2 \tag{4.50}$$

where the λ_{m_i} are the singular values of the matrix $\Psi_{(m_{i-1},\sigma_i),(\sigma_{i+1},\ldots,\sigma_{L-1},\sigma_L)}$. It is now obvious that the quality of the approximation depends largely on the properties of the system or state under consideration:

- In the most trivial case all singular values but one vanish. This is for example the case of all the matrices A^{σ_i} of a product state like in the examples presented in appendix B.
- If the singular values decay exponentially the approximation will only slightly change the physical content of the state $|\psi\rangle$ but provide an enormous computational simplification. In practice for systems of length $L \in \mathcal{O}(10)$ with a local Hilbert space dimension of $d \leq 4$, often a few hundred or thousand singular values suffice to represent the physics almost perfectly with a discarded weight of an order up to $\mathcal{O}\left(10^{-10}\right)$.
- For a non-exponential decay of the singular values things start to get difficult. Depending on the exact behavior the problem may be solvable to a satisfying precision, which is, however, often at the cost of an increased computation time and memory usage.
- In case the singular values are of similar size, the approximation will obviously introduce a significant error to the calculations such that further computations become obsolete and other methods need to be applied.
- Hence, the worst case is that all singular value are equal. This is the case in the third example we show in appendix B. Here, the truncation changes the state and consequently the physics entirely, making MPSs entirely unsuitable for the problem.

If one encounters a well-behaved case with reasonably fast decaying singular values the truncated state may be renormalized afterwards such that

$$\sum_{m_i=1}^{\chi_{\max}} \lambda_{m_i}^2 = 1 \tag{4.51}$$

for further computation.

It has been shown that one-dimensional systems with short-range interactions behave particularly well, i.e. here the singular values decay exponentially, explaining the success and widespread application of MPSs for such problems, c.f. reference [320]. In section 4.2.5 we will further elaborate on the causes of this property.

4.2.4 Variational MPS Truncation

The SVD-based MPS truncation presented in the preceding section comes with the huge disadvantage of never being optimal, its primary advantage being the speediness of its application. Hence, to more accurately truncate an MPS a more evolved scheme is necessary. Such an algorithm is given in terms of the variational truncation. We will present this procedure here in greater detail as it also nicely illustrates the repeated application of sweeping through the chain.

Let $|\psi'\rangle$ be a given MPS which we wish to truncate into an MPS $|\psi\rangle$ of freely chosen maximum bond dimension $\chi_{\max}$ smaller than the maximum bond dimension χ of $|\psi'\rangle$. The principal idea is to minimize the distance

$$\| |\psi'\rangle - |\psi\rangle \|_2^2 = \langle\psi'|\psi'\rangle - \langle\psi'|\psi\rangle - \langle\psi|\psi'\rangle + \langle\psi|\psi\rangle \tag{4.52}$$

with respect to $|\psi\rangle$ between both these states by iteratively running through the system computing just the minimum with respect to a single site tensor $\overline{M}_j^{\sigma_j}$ and updating the MPS in the process. The hope then is that after a certain number of these sweeps an optimum truncation is actually found. We begin by formally writing out the necessary condition for the distance $\| |\psi'\rangle - |\psi\rangle \|_2^2$ to fulfill when minimized with respect to an entry of a single site tensor $\overline{M}_j^{\sigma_j}$

$$\frac{\partial}{\partial \overline{M}^{\sigma_j}_{j;\overline{m}_j,\overline{m}_{j-1}}} \| |\psi'\rangle - |\psi\rangle \|_2^2 = \frac{\partial}{\partial \overline{M}^{\sigma_j}_{j;\overline{m}_j,\overline{m}_{j-1}}} \langle\psi|\psi\rangle - \frac{\partial}{\partial \overline{M}^{\sigma_j}_{j;\overline{m}_j,\overline{m}_{j-1}}} \langle\psi|\psi'\rangle = 0. \tag{4.53}$$

Let us now assume that $|\psi\rangle$ is given in a mixed-canonical form with orthogonality center at site j, such that we have

$$\frac{\partial}{\partial \overline{M}^{\sigma_j}_{j;\overline{m}_j,\overline{m}_{j-1}}} \langle\psi|\psi\rangle = \frac{\partial}{\partial \overline{M}^{\sigma_j}_{j;\overline{m}_j,\overline{m}_{j-1}}} \left(\sum_{\substack{\sigma_j,\\ \overline{m}_{j-1},\overline{m}_j,\\ m_{j-1},m_j}} \overline{M}^{\sigma_j}_{j;\overline{m}_j,\overline{m}_{j-1}} M^{\sigma_j}_{j;m_{j-1},m_j} \right) = M^{\sigma_j}_{j;m_{j-1},m_j}. \tag{4.54}$$

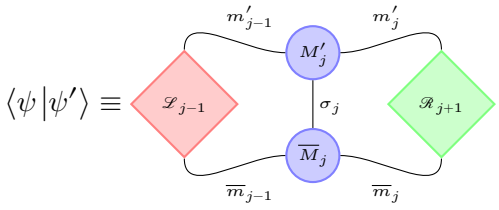

Figure 4.10: Pictorial representation of the overlap of two MPSs $|\psi'\rangle$ and $|\psi\rangle$, c.f. equation (4.55).

If we express the overlap $\langle\psi|\psi'\rangle$ in terms of newly defined left and right tensors, i.e.

$$\langle\psi|\psi'\rangle = \sum_{\substack{\sigma_j,\\ \overline{m}_{j-1},\overline{m}_j,\\ m'_{j-1},m'_j}} \mathscr{L}_{j-1;\overline{m}_{j-1},m'_{j-1}} \overline{M}^{\sigma_j}_{j;\overline{m}_j,\overline{m}_{j-1}} M'^{\sigma_j}_{j;m'_{j-1},m'_j} \mathscr{R}_{j+1;m'_j,\overline{m}_j}, \tag{4.55}$$

c.f. figure 4.10, with the left tensor

$$\mathscr{L}_{j-1;\overline{m}_{j-1},m'_{j-1}} = \sum_{\substack{\overline{m}_{j-2},m'_{j-2},\\ \sigma_{j-1}}} \left(\overline{A}^{\sigma_{j-1}}_{j-1;\overline{m}_{j-1},\overline{m}_{j-2}} \left(\cdots \left(\sum_{\substack{\overline{m}_0,m'_0,\\ \sigma_1}} \left(\overline{A}^{\sigma_1}_{1;\overline{m}_1,\overline{m}_0} M'^{\sigma_1}_{1;m'_0,m'_1} \right) \right) \cdots \right) M'^{\sigma_{j-1}}_{j-1;m'_{j-2},m'_{j-1}} \right), \tag{4.56}$$

c.f. figure 4.11, and similarly the right tensor

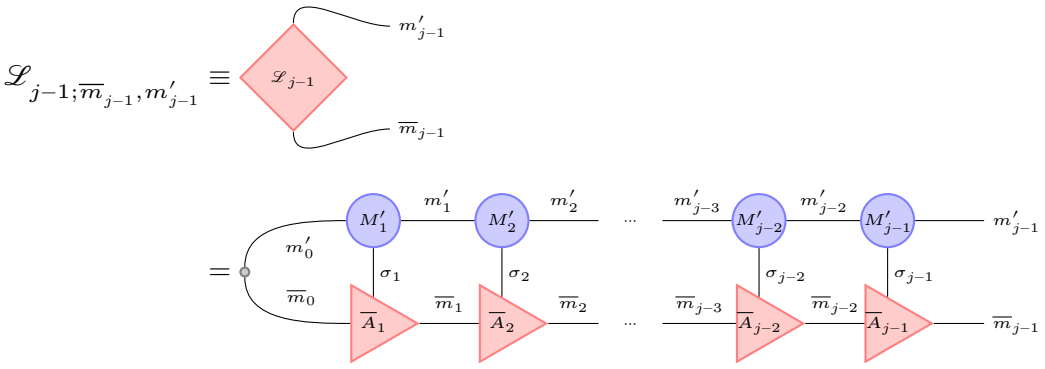

Figure 4.11: Pictorial representation of the left tensor $\mathscr{L}_{j-1;\overline{m}_{j-1},m'_{j-1}}$, c.f. equation (4.56).

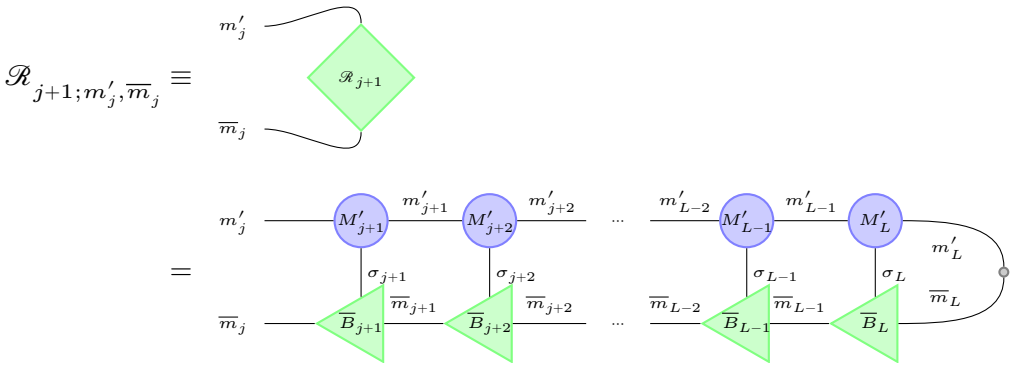

Figure 4.12: Pictorial representation of the right tensor $\mathscr{R}_{j+1;m'_j,\overline{m}_j}$, c.f. equation (4.57).

$$\mathscr{R}_{j+1;m'_j,\overline{m}_j} = \sum_{\substack{\overline{m}_{j+1},m'_{j+1},\\ \sigma_{j+1}}} \left(M'^{\sigma_{j+1}}_{j+1;m'_j,m'_{j+1}} \left(\cdots \left(\sum_{\substack{\overline{m}_L,m'_L,\\ \sigma_L}} \left(M'^{\sigma_L}_{L;m'_{L-1},m'_L} \overline{B}^{\sigma_L}_{L;\overline{m}_L,\overline{m}_{L-1}} \right) \right) \cdots \right) \overline{B}^{\sigma_{j+1}}_{j+1;\overline{m}_{j+1},\overline{m}_j} \right), \tag{4.57}$$

c.f. figure 4.12, we find for the second part in equation (4.53)

$$\frac{\partial}{\partial \overline{M}^{\sigma_j}_{j;\overline{m}_j,\overline{m}_{j-1}}} \langle \psi | \psi' \rangle = \frac{\partial}{\partial \overline{M}^{\sigma_j}_{j;\overline{m}_j,\overline{m}_{j-1}}} \left(\sum_{\substack{\sigma_j,\\ \overline{m}_{j-1},\overline{m}_j,\\ m'_{j-1},m'_j}} \mathscr{L}_{j-1;\overline{m}_{j-1},m'_{j-1}} \overline{M}^{\sigma_j}_{j;\overline{m}_j,\overline{m}_{j-1}} M'^{\sigma_j}_{j;m'_{j-1},m'_j} \right.$$
$$\left. \mathscr{R}_{j+1;m'_j,\overline{m}_j} \right) = \sum_{m'_{j-1},m'_j} \mathscr{L}_{j-1;\overline{m}_{j-1},m'_{j-1}} M'^{\sigma_j}_{j;m'_{j-1},m'_j} \mathscr{R}_{j+1;m'_j,\overline{m}_j}. \tag{4.58}$$

Thus, using these simplifying expressions (4.53) reduces to the rather simple form

$$M^{\sigma_j}_{j;m_{j-1},m_j} = \sum_{m'_{j-1},m'_j} \mathscr{L}_{j-1;\overline{m}_{j-1},m'_{j-1}} M'^{\sigma_j}_{j;m'_{j-1},m'_j} \mathscr{R}_{j+1;m'_j,\overline{m}_j}, \tag{4.59}$$

c.f. figure 4.13, that is we have found an expression to obtain all matrices of the truncated MPS $|\psi\rangle$ from the given MPS $|\psi'\rangle$.

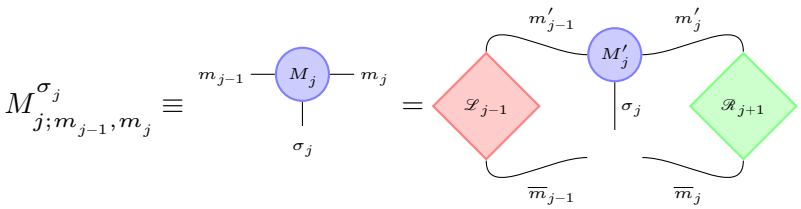

Figure 4.13: Pictorial representation of equation (4.59).

The idea for the truncation routine now is for a given trail MPS $|\psi\rangle$ to iteratively optimize each of its site tensors according to equation (4.59). While in principle any mixed-canonical MPS can serve as the initial trial MPS, it is most recommendable to use a roughly SVD-truncated MPS as obtained from the algorithm introduced in the preceding section the reason being that variational methods may become quite slow for improperly chosen initial states. Realizing that we may construct the left and right tensors recursively via

$$\mathscr{L}_{j;\overline{m}_j,m'_j} = \sum_{\substack{\overline{m}_{j-1},m'_{j-1},\\ \sigma_j}} \left(\overline{A}^{\sigma_j}_{j;\overline{m}_j,\overline{m}_{j-1}} \mathscr{L}_{j-1;\overline{m}_{j-1},m'_{j-1}} M'^{\sigma_j}_{j;m'_{j-1},m'_j} \right), \tag{4.60}$$

$$\mathscr{R}_{j;m'_{j-1},\overline{m}_{j-1}} = \sum_{\substack{\overline{m}_j,m'_j,\\ \sigma_j}} \left(M'^{\sigma_j}_{j;m'_{j-1},m'_j} \mathscr{R}_{j+1;m'_j,\overline{m}_j} \overline{B}^{\sigma_j}_{j;\overline{m}_j,\overline{m}_{j-1}} \right), \tag{4.61}$$

c.f. figures 4.14 and 4.15, with the 1×1 dummy tensors $\mathscr{L}_0$ and $\mathscr{R}_{L+1}$ we execute the sweeping procedure as follows. We begin the trial MPS $|\psi\rangle$ of which we suppose its active site to be at $j = 1$. To all its M-matrices we add an extra subscript in square brackets indicating the number of the sweep, thus in the beginning this subscript is [0]. We further need to have constructed all $\mathscr{R}^{[0]}_j$ according to equation (4.57). Starting from $j = 1$, we now for each j first update the matrix $M^{[0]\sigma_j}_j$ to $M^{[1]\sigma_j}_j$ as described by equation (4.59). Next, the orthogonality center of $|\psi\rangle$ is shifted to site $j+1$ through an SVD as described in section 4.2.2, $\mathscr{R}^{[0]}_{j+1}$ is discarded and $\mathscr{L}^{[1]}_j$ is constructed from $M^{[1]\sigma_j}_j$ according to equation (4.60). At $j = L$ this right sweep is completed and the distance which

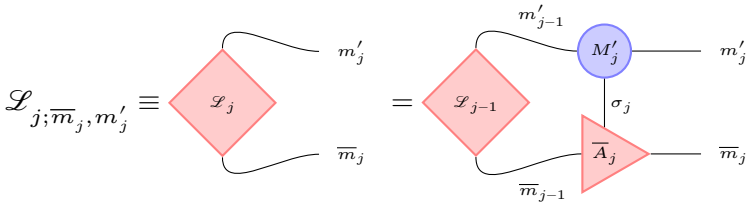

Figure 4.14: Pictorial representation of the recursive construction of the left tensor $\mathscr{L}_{j;\overline{m}_j,m'_j}$, c.f. equation (4.60).

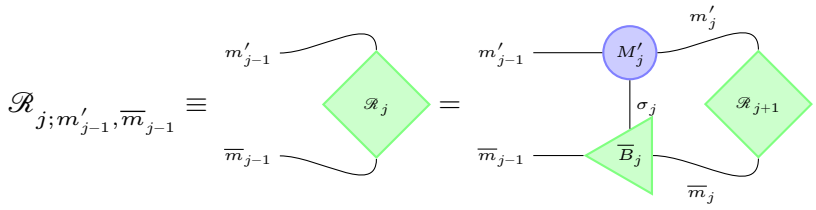

Figure 4.15: Pictorial representation of the recursive construction of the right tensor $\mathscr{R}_{j;m'_{j-1},\overline{m}_{j-1}}$, c.f. equation (4.61).

is now given by

$$\left\| |\psi'\rangle - |\psi\rangle \right\|_2^2 = 1 - \langle\psi|\psi\rangle \tag{4.62}$$

is evaluated. In case it has reached a certain threshold, the procedure is stopped. Otherwise a left sweep is performed. Beginning with $j = L$, for each j the matrix $M_j^{[1]\sigma_j}$ is updated to $M_j^{[2]\sigma_j}$ as in equation (4.59). Then, the orthogonality center of $|\psi\rangle$ is shifted to site $j-1$ through an SVD, $\mathscr{L}_{j-1}^{[1]}$ is discarded and $\mathscr{R}_j^{[2]}$ is constructed from $M_j^{[2]\sigma_j}$ as specified by equation (4.60). At $j = 0$ the sweep is completed and the distance can be computed again. This procedure of right and left sweeps is repeated until the desired distance or a maximum number of sweeps is reached. Clearly we could have also started with an initial state with its active site at $j = L$. In that case, we would have started with a left sweep having constructed all $\mathscr{L}_j^{[0]}$ as in equation (4.56) prior the the beginning of the procedure.

Note that in case the algorithm converges too slowly the maximally allowed bond dimension $\chi_{\max}$ might need to be chosen larger. An important caveat to keep in mind is that this scheme is not guaranteed to yield the absolute minimum, that is, it is indeed possible for it to get stuck in a local minimum. While in general, there is no ideal solution to this obstacle it can nevertheless, often times be overcome by optimizing with respect to two sites. Such two-site variants are quite frequent in variational approaches as we shall discuss in section 5.3.

4.2.5 Entanglement Entropy and the Area Law of Entanglement

So far we have learned how to truncate an MPS and identified the discarded weight as the principal quantity to track when judging the accuracy of the approximation. The question remains, whether the discarded weight is guaranteed to remain small. Indeed, such a theorem exists by means of the area law of entanglement. However, it should be pointed out, that it has only been proven conclusively for rather restricted cases. Nevertheless, it still provides a good intuition to what systems are manageable and which are problematic to treat using MPSs.

We begin by remembering that for product states an efficient MPS representation will consist of only 1×1 matrices. The reason for which we need to increase the matrices in dimension is due to entanglement of an MPS. Hence, the more entangled a state is, the larger need the bond dimensions be, the more urgent is our need to truncate this state and, evidently, the larger is the error we make

during the truncation. Conversely, if the entanglement is guaranteed to stay small, we will only make reasonably small errors when truncating an MPS.

In order to judge how entangled a quantum state is we are in need of a measure of entanglement. While there exist numerous such quantities [47], in case of MPSs usually the entanglement entropy, also known as von Neumann entropy is employed. For MPSs, this quantity can best be derived from Vidal's notation (4.47). We therefore start with an MPS

$$|\psi\rangle = \sum_{\sigma_1,\dots,\sigma_L} \Gamma^{\sigma_1}_{V,1} \Lambda_{V,1} \Gamma^{\sigma_2}_{V,2} \Lambda_{V,2} \cdots \Lambda_{V,L-2} \Gamma^{\sigma_{L-1}}_{V,L-1} \Lambda_{V,L-1} \Gamma^{\sigma_L}_{V,L} \, |\sigma_1, \sigma_2, \dots, \sigma_{L-1}, \sigma_L\rangle, \tag{4.63}$$

which we decompose into two parts, i and ii, describing two subsystems introducing

$$|\alpha_l\rangle_{\mathrm{i}} = \sum_{\sigma_1,\dots,\sigma_l} \left(\Gamma^{\sigma_1}_{V,1} \Lambda_{V,1} \Gamma^{\sigma_2}_{V,2} \Lambda_{V,2} \cdots \Lambda_{V,l-2} \Gamma^{\sigma_{l-1}}_{V,l-1} \Lambda_{V,l-1} \Gamma^{\sigma_l}_{V,l}\right)_{\alpha_l} |\sigma_1, \sigma_2, \dots, \sigma_{l-1}, \sigma_l\rangle, \tag{4.64}$$

$$|\alpha_l\rangle_{\mathrm{ii}} = \sum_{\sigma_{l+1},\dots,\sigma_L} \left(\Gamma^{\sigma_{l+1}}_{V,l+1} \Lambda_{V,l+1} \Gamma^{\sigma_{l+2}}_{V,l+2} \Lambda_{V,l+2} \cdots \Lambda_{V,L-2} \Gamma^{\sigma_{L-1}}_{V,L-1} \Lambda_{V,L-1} \Gamma^{\sigma_L}_{V,L}\right)_{\alpha_l} \big|\sigma_{l+1}, \sigma_{l+2}, \dots, \sigma_{L-1}, \sigma_L\big\rangle, \tag{4.65}$$

such that the entire state is given by

$$|\psi\rangle = \sum_{\alpha_l} \Lambda_{V,l;\alpha_l,\alpha_l} \, |\alpha_l\rangle_{\mathrm{i}} \, |\alpha_l\rangle_{\mathrm{ii}} = \sum_{\alpha_l} \lambda_{\alpha_l} \, |\alpha_l\rangle_{\mathrm{i}} \, |\alpha_l\rangle_{\mathrm{ii}} \, . \tag{4.66}$$

This representation of $|\psi\rangle$ is commonly known as the Schmidt decomposition. Because it makes use of the system's eigenbasis, the density operator takes the rather simple form

$$\rho \coloneqq |\psi\rangle\langle\psi| = \left(\Lambda_{V,l}\right)^2 , \tag{4.67}$$

from which the von Neumann entropy can be computed via

$$S_{\mathrm{vN}} \coloneqq -\mathrm{Tr}(\rho \ln(\rho)) = -\mathrm{Tr}\Big(\left(\Lambda_{V,l}\right)^2 \ln\Big(\left(\Lambda_{V,l}\right)^2\Big)\Big) = -\sum_{\alpha_l} \Big(\lambda^2_{\alpha_l} \ln\Big(\lambda^2_{\alpha_l}\Big)\Big) \tag{4.68}$$

to tell us, how much the two subsystems we divided the system into are entangled with each other.

The crucial observation now is that for a gapped system $\mathcal{S}$ of arbitrary size and dimensions, the von Neumann entropy roughly scales as [388]

$$S_{\mathrm{vN}} \sim \mathcal{O}(\partial\mathcal{S}) \, , \tag{4.69}$$

that is the edge of the system. This expression is known as the area law of entanglement. Its consequences for one-dimensional systems are of particular importance. Irrespective of its size L the edge $\partial\mathcal{S}$ will always stay constant. Hence, for one-dimensional gapped systems the entanglement entropy stays constant with growing system size, which as a consequence tells us that such systems can be efficiently truncated as the discarded weight stays small. Thus, the area law of entanglement shows, why MPSs are such a powerful method in one dimension, and also why their extensions to multiple dimensions, namely PEPS and MERA, are far more restricted in their versatility. Note again, however, that the area law of entanglement (4.69) was actually only proven to exactly hold for ground state searches of one-dimensional gapped systems [144, 50], which are rather strict constraints, and to be violated for gapless fermionic systems [410, 120]. In particular the behavior of time evolutions is not governed. Still, it serves as a good point of reference to judge how promising an MPS treatment of a physical system is in the first place.

4.3 Matrix Product Operators

The extension of the procedures we discussed in the preceding section regarding the construction of MPSs in order to describe physical states to operators is rather convenient. Let $\hat{O}\colon \mathscr{H} \mapsto \mathscr{H}$ be a quantum mechanical operator mapping states of an L-site system with local dimension d to one another, i.e. $\dim(\mathscr{H}) = d^L$. Thus, in its most general form $\hat{O}$ may be represented as

$$\hat{O} = \sum_{\substack{\sigma_1,\dots,\sigma_L,\\ \sigma'_1,\dots,\sigma'_L}} c_{(\sigma_1,\sigma_2,\dots,\sigma_{L-1},\sigma_L),(\sigma'_1,\sigma'_2,\dots,\sigma'_{L-1},\sigma'_L)} \left|\sigma_1,\sigma_2,\dots,\sigma_{L-1},\sigma_L\right\rangle\left\langle\sigma'_1,\sigma'_2,\dots,\sigma'_{L-1},\sigma'_L\right|. \tag{4.70}$$

Hence, the goal is to express the coefficients $c_{(\sigma_1,\sigma_2,\dots,\sigma_{L-1},\sigma_L),(\sigma'_1,\sigma'_2,\dots,\sigma'_{L-1},\sigma'_L)} \in \mathbb{C}$ as a product of matrices analogously to the treatment of quantum states, such that in the end we have

$$\begin{aligned}\hat{O} = \sum_{\substack{\sigma_1,\dots,\sigma_L,\\ \sigma'_1,\dots,\sigma'_L}} & W_1^{\sigma_1,\sigma'_1} \cdot W_2^{\sigma_2,\sigma'_2} \cdot \dots \cdot W_{L-1}^{\sigma_{L-1},\sigma'_{L-1}} \cdot W_L^{\sigma_L,\sigma'_L} \\ & \left|\sigma_1,\sigma_2,\dots,\sigma_{L-1},\sigma_L\right\rangle\left\langle\sigma'_1,\sigma'_2,\dots,\sigma'_{L-1},\sigma'_L\right|,\end{aligned} \tag{4.71}$$

c.f. figure 4.16 for a graphical representation. The principal difference towards the MPS representation

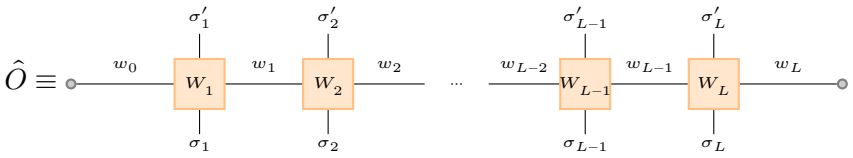

Figure 4.16: Pictorial representation of a general MPO $\hat{O}$, c.f. equation (4.71).

is that for the case of MPOs the W-tensors are of rank 4 unlike the M- (or A- or B-) tensors, which were of rank 3. Further, the number of coefficients $c_{(\sigma_1,\sigma_2,\dots,\sigma_{L-1},\sigma_L),(\sigma'_1,\sigma'_2,\dots,\sigma'_{L-1},\sigma'_L)}$ increases to d^{2L} illustrating that the number of possible MPO representations is even larger than for MPSs. Nevertheless, it is in principle possible to construct MPOs from SV decomposing the reshaped coefficients as explained in section 4.2.1 for MPSs the only differences being that for the SVDs double indices $\left(\sigma_l,\sigma'_l\right)$ take the place single indices σ_l and accordingly in the end the matrices U or $V^\dagger$ need to be reshaped into rank-4 tensors.

In the following two sections we will outline shortly, how MPOs can be conveniently constructed, starting with single site operators and then extending to more complex ones.

4.3.1 Single site MPOs

In many body physics one frequently encounters operators that only act on one single site, $\hat{o}_j(j)$, j being the site and $\hat{o}(j)$ the possibly site-dependent operator that acts on the local Hilbert space only. Note that in a many body problem this local Hilbert space is orders of magnitudes smaller

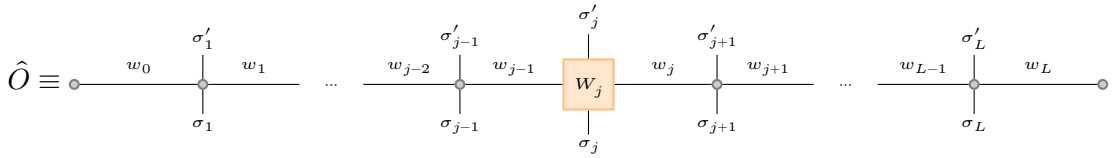

Figure 4.17: Pictorial representation of a single site MPO $\hat{O}$, c.f. equation (4.72).

than the total one which allows a rather efficient implementation as an MPO without truncations. We begin by noting that any local operator $\hat{o}_j(j)$ can be extended to a formally global one via

$$\hat{O} = \hat{I}_1 \otimes \hat{I}_2 \otimes \cdots \otimes \hat{I}_{j-1} \otimes \hat{o}_j(j) \otimes \hat{I}_{j+1} \otimes \cdots \otimes \hat{I}_{L-1} \otimes \hat{I}_L, \tag{4.72}$$

c.f. figure 4.17, where $\hat{I}$ is the local identity. The rank-4 W-tensor thus simplifies dramatically, being simply determined by

$$W^{\sigma_l,\sigma'_l}_{l;w_{l-1},w_l} = \delta_{l,j} \langle \sigma_l | \hat{o}_l(l) | \sigma'_l \rangle + (1 - \delta_{l,j}) \delta_{\sigma_l,\sigma'_l}. \tag{4.73}$$

Note that for this case the bond indices w_{l-1} and w_l are dummy indices taking only one value. Hence, the total W-tensor is of dimension d^2.

4.3.2 Construction of Matrix-Product Operators from FSMs

In most cases complex operators are combinations of usually only a few local ones. We will call the set containing these local operators Ω. Thus, a general operator may be expressed as

$$\hat{O} = \sum_{\mathscr{P}} \mathscr{P} \left(\bigotimes_{l=1}^{L} \hat{o}_l(l) \right), \tag{4.74}$$

that is the sum over all paths $\mathscr{P}$ consisting of successively applied local operators $\hat{o}(l) \in \Omega$ at all sites l of the system. Note that evidently $\hat{I}_l \in \Omega$. In order to construct an MPO, we decompose the operator into

$$\hat{O} = \hat{W}_1 \cdot \hat{W}_2 \cdot \cdots \cdot \hat{W}_{L-1} \cdot \hat{W}_L \tag{4.75}$$

introducing operator-valued matrices $\hat{W}_l$ containing local operators $\hat{o}_l(l) \in \Omega$. Once this decomposition is known, the MPO can be constructed from these operator valued matrices through

$$W^{\sigma_l,\sigma'_l}_{l;w_{l-1},w_l} = \langle \sigma_l | \hat{W}_{l;w_{l-1},w_l} | \sigma'_l \rangle . \tag{4.76}$$

Note that for the operator in equation (4.75) to give a string of local operators, $\hat{W}_1$ and $\hat{W}_L$ need to be a row or column vector, respectively. Note further that for an single site MPO $\hat{o}(j)$ equation (4.72) already specifies the operator-valued matrices $\hat{W}_l$ via

$$\hat{W}_l = \begin{cases} \hat{o}_j(j) & \text{if} \quad l = j \\ \hat{I}_j & \text{else} \end{cases}, \tag{4.77}$$

which implies that in this case all indices w_l are dummy indices taking only the value of 1.

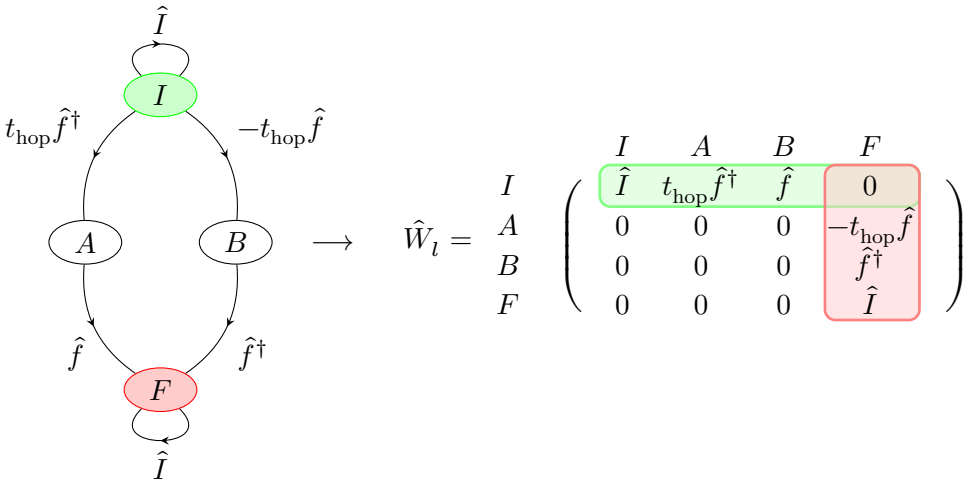

Figure 4.18: Example illustration of the generation of operator-valued matrices $\hat{W}_l$ from an FSM in case of the tight binding model, c.f. section 7.1.1. The green and red boxes show $\hat{W}_1$ and $\hat{W}_L$, respectively. This plot was generated adapting LaTeX code by Thomas Köhler and Sebastian Paeckel which was used to create figures 3(a) and 4(b) in reference [282].

The crucial observation reported by Crosswhite et al. [67, 68] is that these operator valued matrices $\hat{W}_l$ can be constructed from FSMs which we introduced in section 3.5. The idea is to encode the summands in equation (4.74) by means of a Mealy automaton. Starting from an initial state I going over arbitrarily many intermediate states until finally reaching the final state F each edge in the FSM corresponds to the application of one local operator $\hat{o}_l(l)$. The use of loops in the FSM is explicitly wanted at this point to keep the structure as simple as possible. Hence, for an L-site system each path through the FSM consisting of exactly L edges beginning at the initial state I and ending at the final state F will correspond to one path in $\mathscr{P}$ from equation (4.74). All these paths in sum then describe the total operator $\hat{O}$. The transition from such an FSM to the operator-valued $\hat{W}$-matrices is straight forward: Let f be the number of states in the FSM. Thus $\hat{W}_l$ is a matrix of dimension $f \times f$ each line and column corresponding to one particular state of the FSM. In a next step the local operators $\hat{o}_l(l)$ from the edges of the FSM are inserted into $\hat{W}_l$ such that for an operator $\hat{o}_j(j)$ connecting states S_1 and S_2 of the FSM

$$\hat{W}_{j;S_1,S_2} = \hat{o}_j(j) \tag{4.78}$$

holds. Note that the FSM is best constructed exploiting as many symmetries of the operator $\hat{O}$ to encode as possible, such that the dimensions f of $\hat{W}_l$ are kept small. We mention that at the edges $\hat{W}_1$ and $\hat{W}_L$ are determined by the first row and last column of the general, i.e. the bulk matrices $\hat{W}_l$, respectively. We illustrate these rather abstract explanations with an example in figure 4.18.

Note that FSMs will simply provide a systematic approach to finding a decomposition of $\hat{O}$ according to equation (4.75). The task of decomposing $\hat{O}$ efficiently into a product of operator-valued matrices is therefore just shifted to constructing an efficient FSM. Clearly, there are many ways to set up an FSM describing an operator. Other than trying to keep the FSM as small as possible, i.e. reduce the number of nodes to its minimum value, thereby reusing as many subpaths as possible, there is no general algorithm to constructing an efficient FSM. Hence, at this point most care needs to be taken in order to achieve satisfactory speed in the computations with the so-generated MPOs.

More details on how to proceed and further properties regarding the constructions of MPOs from FSMs are given in references [282, 195, 280].

4.4 MPS-MPO Calculus

Now that we have gained a basic understanding of MPSs and MPOs and their respective individual properties and construction schemes, in this section we will learn how to manipulate and how to perform calculations with both of them.

4.4.1 Computation of Scalar Products and Expectation Values

In order to calculate the overlap of two MPSs, $|\psi\rangle$ and $|\psi'\rangle$ care needs to be taken regarding the order of the contractions. We have to compute

$$\langle\psi'|\psi\rangle = \sum_{\substack{\sigma_1,\dots,\sigma_L,\\ \sigma'_1,\dots,\sigma'_L}} \left(M'^{\sigma'_L\dagger}_L \cdots M'^{\sigma'_1\dagger}_1\right) \cdot \left(M^{\sigma_1}_1 \cdots M^{\sigma_L}_L\right) \langle\sigma'_1,\dots,\sigma'_L|\sigma_1,\dots,\sigma_L\rangle \tag{4.79a}$$

$$= \sum_{\sigma_1,\dots,\sigma_L} \sum_{\substack{m_0,\dots,m_L,\\ \overline{m}'_0,\dots,\overline{m}'_L}} \overline{M}'^{\sigma_L}_{L;\overline{m}'_L,\overline{m}'_{L-1}} \cdots \overline{M}'^{\sigma_1}_{1;\overline{m}'_1,\overline{m}'_0} M^{\sigma_1}_{1;m_0,m_1} \cdots M^{\sigma_L}_{L;m_{L-1},m_L}. \tag{4.79b}$$

Suppose now we first evaluated the sums over the bond indices, m_l and m'_l. That way, before actually computing an overlap, we would undo the decomposition introduced by the MPS formulation, and could have, likewise just naively evaluated an overlap of two general states (4.5). Hence, it is much more efficient to rearrange the tensors and evaluate the sums iteratively by site, starting from 1 or analogously L. This procedure yields

$$\langle\psi'|\psi\rangle = \sum_{\substack{m_{L-1},\overline{m}'_{L-1},\\ \sigma_L,\\ m_L,\overline{m}'_L}} \left(\overline{M}^{L;\prime\sigma_L}_{\overline{m}'_L,\overline{m}'_{L-1}} \left(\cdots \left(\sum_{\substack{m_0,\overline{m}'_0,\\ \sigma_1}} \left(\overline{M}'^{\sigma_1}_{1;\overline{m}'_1,\overline{m}'_0} M^{\sigma_1}_{1;m_0,m_1}\right)\right)\cdots\right) M^{\sigma_L}_{L;m_{L-1},m_L}\right) \tag{4.80a}$$

$$= \sum_{\sigma_L} \left(M'^{\sigma_L\dagger}_L \left(\cdots \left(\sum_{\sigma_2} \left(M'^{\sigma_2\dagger}_2 \left(\sum_{\sigma_1} \left(M'^{\sigma_1\dagger}_1 M^{\sigma_1}_1\right)\right) M^{\sigma_2}_2\right)\right)\cdots\right) M^{\sigma_L}_L\right), \tag{4.80b}$$

c.f. figure 4.19, or

$$\langle\psi'|\psi\rangle = \sum_{\substack{m_1,\overline{m}'_1,\\ \sigma_1,\\ m_0,\overline{m}'_0}} \left(M^{\sigma_1}_{1;m_0,m_1} \left(\cdots \left(\sum_{\substack{m_L,\overline{m}'_L,\\ \sigma_L}} \left(M^{\sigma_L}_{L;m_{L-1},m_L} \overline{M}'^{\sigma_L}_{L;\overline{m}'_L,\overline{m}'_{L-1}}\right)\right)\cdots\right) \overline{M}'^{\sigma_1}_{1;\overline{m}'_1,\overline{m}'_0}\right) \tag{4.81a}$$

$\langle\psi'|\psi\rangle \equiv$

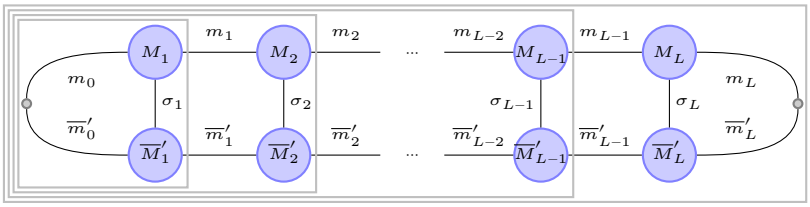

Figure 4.19: Pictorial representation of the successive computation of the overlap $\langle\psi'|\psi\rangle$ according to equation (4.80).

$$= \sum_{\sigma_1} \left(M_1^{\sigma_1} \left(\cdots \left(\sum_{\sigma_{L-1}} \left(M_{L-1}^{\sigma_{L-1}} \left(\sum_{\sigma_L} \left(M_L^{\sigma_L} M_L'^{\sigma_L\dagger} \right) \right) M_{L-1}'^{\sigma_{L-1}\dagger} \right) \right) \cdots \right) M_1'^{\sigma_1\dagger} \right), \tag{4.81b}$$

c.f. figure 4.20, respectively. Mind that in this representation exploiting (4.33) or (4.34) the result is obviously 1, if $|\psi\rangle = |\psi'\rangle$ and both are left- or right-normalized, respectively. In doing so, we have decreased the numerical cost of the entire computation from $\mathcal{O}(d^L)$ to just $\mathcal{O}(dL\chi_{\max}^3)$.

Computing the expectation value for an MPO $\hat{O}$ works similarly. We now have to evaluate

$$\langle\psi'|\hat{O}|\psi\rangle = \sum_{\substack{\sigma_1,\ldots,\sigma_L,\\ \sigma'_1,\ldots,\sigma'_L,\\ \sigma''_1,\ldots,\sigma''_L,\\ \sigma'''_1,\ldots,\sigma'''_L}} \left(M_L'^{\sigma'_L\dagger} \cdots M_1'^{\sigma'_1\dagger} \right) \cdot \left(W_1^{\sigma''_1,\sigma'''_1} \cdots W_L^{\sigma''_L,\sigma'''_L} \right) \cdot \left(M_1^{\sigma_1} \cdots M_L^{\sigma_L} \right) \tag{4.82a}$$

$$\langle\sigma'_1,\ldots,\sigma'_L|\sigma''_1,\ldots,\sigma''_L\rangle \langle\sigma'''_1,\ldots,\sigma'''_L|\sigma_1,\ldots,\sigma_L\rangle \tag{4.82b}$$

$$= \sum_{\substack{\sigma_1,\ldots,\sigma_L,\\ \sigma'_1,\ldots,\sigma'_L}} \sum_{\substack{m_1,\ldots,m_L,\\ \overline{m}'_1,\ldots,\overline{m}'_L,\\ w_1,\ldots,w_L,\\ w'_1,\ldots,w'_L}} \overline{M}'^{\sigma'_L}_{L;\overline{m}'_L,\overline{m}'_{L-1}} \cdots \overline{M}'^{\sigma'_1}_{1;\overline{m}'_1,\overline{m}'_0} W^{\sigma'_1,\sigma_1}_{w_0,w_1} \cdots W^{\sigma'_L,\sigma_L}_{w_{L-1},w_L}$$

$$M^{\sigma_1}_{1;m_0,m_1} \cdots M^{\sigma_L}_{L;m_{L-1},m_L}, \tag{4.82c}$$

which is again orders of magnitude faster when contracting over the physical indices first starting

$\langle\psi'|\psi\rangle \equiv$

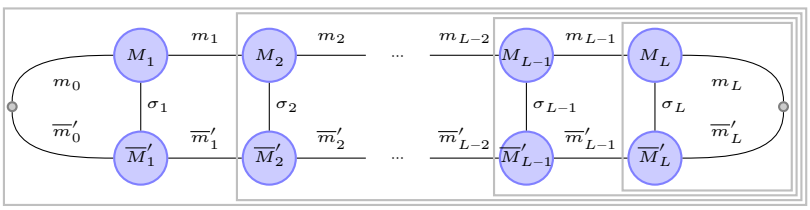

Figure 4.20: Pictorial representation of the successive computation of the overlap $\langle\psi'|\psi\rangle$ according to equation (4.81).

$\langle\psi'|\hat{O}|\psi\rangle \equiv$

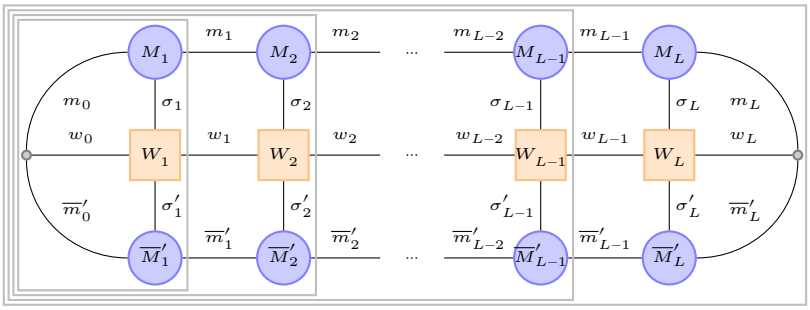

Figure 4.21: Pictorial representation of the successive computation of the expectation value $\langle\psi'|\hat{O}|\psi\rangle$ according to equation (4.83).

from 1 or L. The former option gives

$$\langle\psi'|\hat{O}|\psi\rangle = \sum_{\substack{m_{L-1},\overline{m}'_{L-1},\\ w_{L-1},w_L,\\ \sigma_L,\sigma'_L,\\ m_L,\overline{m}'_L}} \left(\overline{M}'^{\sigma'_L}_{L;\overline{m}'_L,\overline{m}'_{L-1}} W^{\sigma'_L,\sigma_L}_{L;w_{L-1},w_L} \right. \left(\cdots \left(\sum_{\substack{m_0,\overline{m}'_0,\\ w_0,\\ \sigma_1,\sigma'_1}} \left(\overline{M}'^{\sigma'_1}_{1;\overline{m}'_1,\overline{m}'_0} W^{\sigma'_1,\sigma_1}_{1;w_0,w_1} M^{\sigma_1}_{1;m_0,m_1} \right) \right) \cdots \right) \left. M^{\sigma_L}_{L;m_{L-1},m_L} \right), \tag{4.83}$$

c.f. figure 4.21, while the latter one yields

$$\langle\psi'|\hat{O}|\psi\rangle = \sum_{\substack{m_1,\overline{m}'_1,\\ w_1,w_0,\\ \sigma_1,\sigma'_1,\\ m_0,\overline{m}'_0}} \left(M^{\sigma_1}_{1;m_0,m_1} \left(\cdots \left(\sum_{\substack{m_L,\overline{m}'_L,\\ w_L,\\ \sigma_L,\sigma'_L}} \left(M^{\sigma_L}_{L;m_{L-1},m_L} W^{\sigma'_L,\sigma_L}_{L;w_{L-1},w_L} \overline{M}'^{\sigma'_L}_{L;\overline{m}'_L,\overline{m}'_{L-1}} \right) \right) \cdots \right) \right. \left. W^{\sigma'_1,\sigma_1}_{1;w_0,w_1} \overline{M}'^{\sigma'_1}_{1;\overline{m}'_1,\overline{m}'_0} \right), \tag{4.84}$$

c.f. figure 4.22, We note, however, that there exists an alternative. The expectation value may also

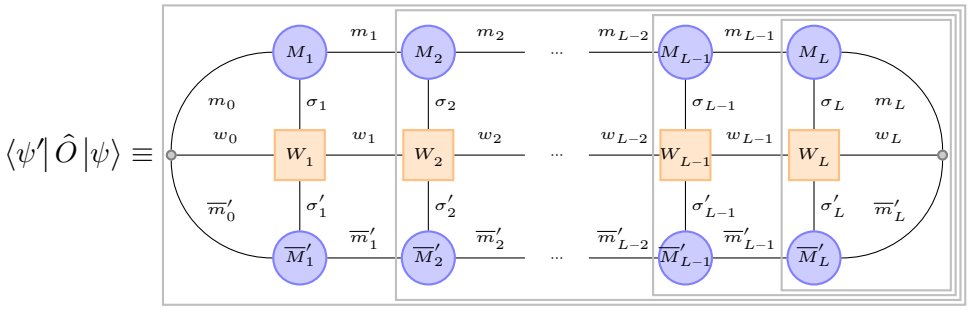

Figure 4.22: Pictorial representation of the successive computation of the expectation value $\langle\psi'|\hat{O}|\psi\rangle$ according to equation (4.84).

be computed contracting the recursively defined left and right tensor

$$\mathscr{W}^{\mathscr{L}}_{j;m_j,w_j,\overline{m}'_j} = \sum_{\substack{\overline{m}_{j-1},m'_{j-1},\\ \sigma_j,\sigma'_j,\\ w_{j-1}}} \left(\overline{M}'^{\sigma'_j}_{j;\overline{m}'_j,\overline{m}'_{j-1}} \mathscr{W}^{\mathscr{L}}_{j-1;\overline{m}'_{j-1},w_{j-1},m_{j-1}} W^{\sigma'_j,\sigma_j}_{j;w_{j-1},w_j} M^{\sigma_j}_{j;m_{j-1},m_j}\right), \tag{4.85}$$

$$\mathscr{W}^{\mathscr{R}}_{j;\overline{m}'_{j-1},w_{j-1},m_{j-1}} = \sum_{\substack{\overline{m}_j,m'_j,\\ \sigma_j,\sigma'_j,\\ w_j}} \left(W^{\sigma'_j,\sigma_j}_{j;w_{j-1},w_j} M^{j;\sigma_j}_{m_{j-1},m_j} \mathscr{W}^{\mathscr{R}}_{j+1;m_j,w_j,\overline{m}'_j} \overline{M}'^{\sigma'_j}_{j;\overline{m}'_j,\overline{m}'_{j-1}}\right), \tag{4.86}$$

c.f. figures 4.23 and 4.24, which gives

$$\langle\psi'|\hat{O}|\psi\rangle = \sum_{m_{L/2},w_{L/2},\overline{m}'_{L/2}} \mathscr{W}^{\mathscr{L}}_{L/2;m_{L/2},w_{L/2},\overline{m}'_{L/2}} \mathscr{W}^{\mathscr{R}}_{L/2+1;\overline{m}'_{L/2},w_{L/2},m_{L/2}}, \tag{4.87}$$

c.f. figure 4.25. Here $\mathscr{W}^{\mathscr{L}}_0$ and $\mathscr{W}^{\mathscr{R}}_{L+1}$ are $1\times1\times1$ dummy tensors. The advantage of this approach

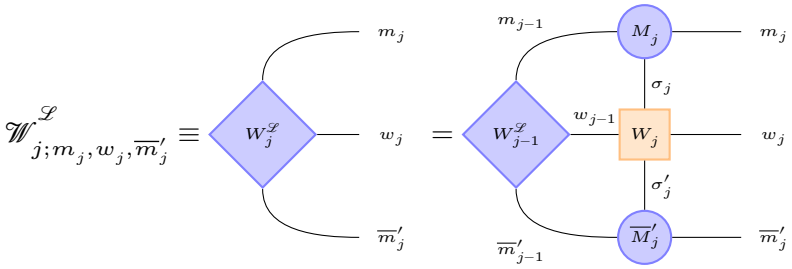

Figure 4.23: Pictorial representation of the recursive construction of the left tensor $\mathscr{W}^{\mathscr{L}}_{j;m_j,w_j,\overline{m}'_j}$, c.f. equation (4.85).

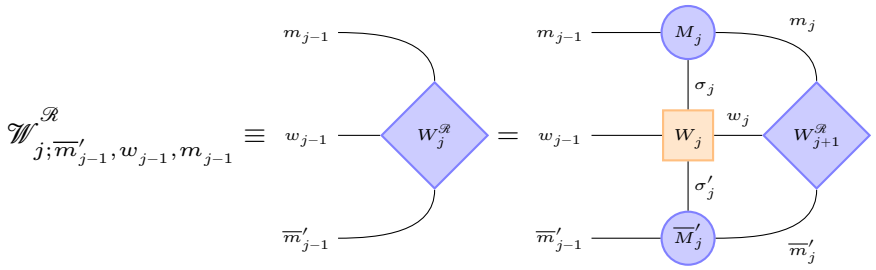

Figure 4.24: Pictorial representation of the recursive construction of the right tensor $\mathscr{W}^{\mathscr{R}}_{j;\overline{m}'_{j-1},w_{j-1},m_{j-1}}$, c.f. equation (4.86).

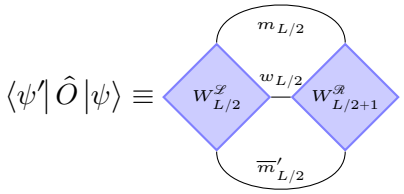

Figure 4.25: Pictorial representation of the computation of the overlap $\langle\psi'|\hat{O}|\psi\rangle$ by means of the left tensor $\mathscr{W}^{\mathscr{L}}_{L/2;m_{L/2},w_{L/2},\overline{m}'_{L/2}}$ and the right tensor $\mathscr{W}^{\mathscr{R}}_{L/2+1;\overline{m}'_{L/2},w_{L/2},m_{L/2}}$, c.f. equation (4.87).

is that it allows for a parallelization of the procedure as $\mathscr{W}^{\mathscr{L}}_{L/2}$ and $\mathscr{W}^{\mathscr{R}}_{L/2+1}$ can be computed individually according to (4.85) or (4.86), respectively, so that in the end only the final contraction (4.87) needs to be performed.

We close this section with the remark that for single site MPOs, i.e. $\hat{O} = \hat{o}(j)$, as introduced in section 4.3.1, the computation of the expectation value reduces to just two tensor contractions

$$\langle\psi|\hat{O}|\psi\rangle = \sum_{\substack{m_{j-1},m'_{j-1},\\ m_j,m'_j,\\ w_{j-1},w_j,\\ \sigma_j,\sigma'_j}} \left(\overline{M}^{\sigma'_j}_{j;m_j,m'_{j-1}} W^{\sigma'_j,\sigma_j}_{j;w_{j-1},w_j} M^{\sigma_j}_{j;m_{j-1},m_j}\right), \tag{4.88}$$

c.f. figure 4.26, where we used a mixed-canonical representation for both MPSs, $|\psi\rangle$ and $|\psi'\rangle$ allowing us to exploit (4.33) and (4.34).

4.4.2 Manipulation of MPSs and MPOs

In this section we will discuss manipulations of MPSs and MPOs which do not involve the respective other.

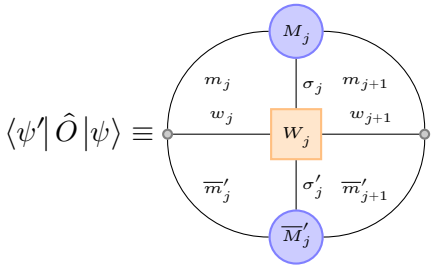

Figure 4.26: Pictorial representation of the computation of the overlap $\langle\psi'|\hat{O}|\psi\rangle$ for a single site MPO, c.f. equation (4.88).

The by far easiest procedure is the multiplication with a scalar $\lambda \in \mathbb{C}$. For both, the scalar-MPS as well as the scalar-MPO multiplication the factor λ may be incorporated in one freely chosen tensor, i.e. in order to compute

$$|\psi\rangle = \lambda \cdot |\psi'\rangle \tag{4.89}$$

we have

$$M_j^{\sigma_j} = \lambda \cdot M_j'^{\sigma'_j}, \tag{4.90}$$

while

$$\hat{O} = \lambda \cdot \hat{O}' \tag{4.91}$$

is computed through

$$W_j^{\sigma'_j,\sigma_j} = \lambda \cdot W_j'^{\sigma'_j,\sigma_j}. \tag{4.92}$$

Due to numerical efficiency usually $j = 1$ or $j = L$ is chosen. A distribution of λ over all tensors is equally unorthodox.

Another rarely occurring manipulation is the bare multiplication of two MPOs. Its computation, however is rather simple involving only the contraction over shared physical indices:

$$\begin{aligned}
\hat{O} = \hat{O}'\hat{O}'' = & \sum_{\substack{\sigma_1,\dots,\sigma_L,\\ \sigma'_1,\dots,\sigma'_L,\\ \sigma''_1,\dots,\sigma''_L,\\ \sigma'''_1,\dots,\sigma'''_L}} \left(W_1'^{\sigma_1,\sigma''_1} \cdots W_L'^{\sigma_L,\sigma''_L}\right) \cdot \left(W_1''^{\sigma'''_1,\sigma'_1} \cdots W_L''^{\sigma'''_L,\sigma'_L}\right) \\
& |\sigma_1,\dots,\sigma_L\rangle \langle\sigma''_1,\dots,\sigma''_L| \, |\sigma'''_1,\dots,\sigma'''_L\rangle \langle\sigma'_1,\dots,\sigma'_L| \qquad (4.93a) \\
= & \sum_{\substack{w'_0,\dots,w'_L,\\ w''_0,\dots,w''_L,\\ \sigma_1,\dots,\sigma_L,\\ \sigma'_1,\dots,\sigma'_L,\\ \sigma''_1,\dots,\sigma''_L}} W'^{\sigma_1,\sigma''_1}_{1;w'_0,w'_1} \cdots W'^{\sigma_L,\sigma''_L}_{L;w'_{L-1},w'_L} W''^{\sigma''_1,\sigma'_1}_{1;w''_0,w''_1} \cdots W''^{\sigma''_L,\sigma'_L}_{L;w''_{L-1},w''_L} \\
& |\sigma_1,\dots,\sigma_L\rangle \langle\sigma'_1,\dots,\sigma'_L| \qquad (4.93b) \\
= & \sum_{\substack{w'_0,\dots,w'_L,\\ w''_0,\dots,w''_L,\\ \sigma_1,\dots,\sigma_L,\\ \sigma'_1,\dots,\sigma'_L}} \left(\sum_{\sigma''_1} W'^{\sigma_1,\sigma''_1}_{1;w'_0,w'_1} W''^{\sigma''_1,\sigma'_1}_{1;w''_0,w''_1}\right) \cdots \left(\sum_{\sigma''_L} W'^{\sigma_L,\sigma''_L}_{L;w'_{L-1},w'_L} W''^{\sigma''_L,\sigma'_L}_{L;w''_{L-1},w''_L}\right)
\end{aligned}$$

$$\left|\sigma_1,\dots,\sigma_L\right\rangle\left\langle\sigma'_1,\dots,\sigma'_L\right| \tag{4.93c}$$

$$= \sum_{\substack{w_0,\dots,w_L,\\ \sigma_1,\dots,\sigma_L,\\ \sigma'_1,\dots,\sigma'_L}} W^{\sigma_1,\sigma'_1}_{1;w_0,w_1}\cdots W^{\sigma_L,\sigma'_L}_{L;w_{L-1},w_L}\left|\sigma_1,\dots,\sigma_L\right\rangle\left\langle\sigma'_1,\dots,\sigma'_L\right| \tag{4.93d}$$

$$= \sum_{\substack{\sigma_1,\dots,\sigma_L,\\ \sigma'_1,\dots,\sigma'_L}} W_1^{\sigma_1,\sigma'_1}\cdots W_L^{\sigma_L,\sigma'_L}\left|\sigma_1,\dots,\sigma_L\right\rangle\left\langle\sigma'_1,\dots,\sigma'_L\right|, \tag{4.93e}$$

c.f. figure 4.27, where we have introduced the compact tensors

$$W^{\sigma_l,\sigma'_l}_{l;w_{l-1},w_l} = W^{\sigma_l,\sigma'_l}_{l;(w'_{l-1},w''_{l-1}),(w'_l,w''_l)} = \sum_{\sigma''_l} W'^{\sigma_l,\sigma''_l}_{l;w'_{l-1},w'_l} W''^{\sigma''_l,\sigma'_l}_{l;w''_{l-1},w''_l}. \tag{4.94}$$

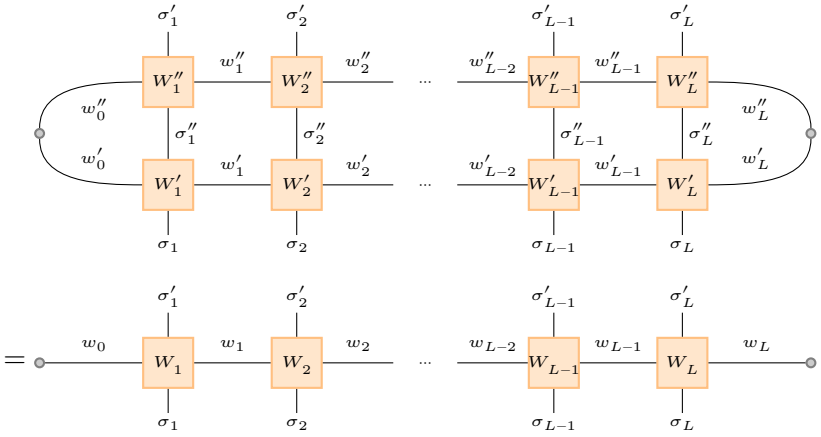

Figure 4.27: Pictorial representation of equation (4.93).

Note that now the bond dimension of $\hat{O}$ is determined by the product of the bond dimensions of $\hat{O}'$ and $\hat{O}''$. Hence, in practice, most often this construction of an MPO is rather inefficient necessitating a subsequent truncation, c.f. chapter 4.3. Instead $\hat{O}$ should rather be implemented individually, i.e. through an extra FSM as described in section 4.3.2. In practice, a product of two MPOs will be encountered either when it comes to the application to an MPS, $\hat{O}'\hat{O}''\left|\psi\right\rangle$, or the computation of a scalar product, $\left\langle\psi'\right|\hat{O}'\hat{O}''\left|\psi\right\rangle$. In these cases it is more efficient to apply the MPOs one after another to $\left|\psi\right\rangle$, which we will discuss in the upcoming sections, or in case of the latter, the scalar product of $\hat{O}''\left|\psi\right\rangle$ and $\hat{O}'\left|\psi'\right\rangle$ may be computed.

As there is no reasonable definition of a multiplication of two MPSs, that is two Ket vectors, we now turn our attention to the evaluation of sums of MPSs and MPOs. While multiplications are rather straight forward to compute in the MPS and MPO representation, taking the sum is somewhat more tedious as it requires the entire construction of new tensors. Let us begin with the sum of two MPSs, i.e. we wish to calculate

$$\left|\psi\right\rangle = \sum_{\sigma_1,\dots,\sigma_L} M_1^{\sigma_1}\cdots M_L^{\sigma_L}\left|\sigma_1,\sigma_2,\dots,\sigma_{L-1},\sigma_L\right\rangle = \left|\psi'\right\rangle + \left|\psi''\right\rangle. \tag{4.95}$$

Here, no direct contraction is possible such that we need to set up new M-matrices

$$M^{\sigma_l}_{l;m_{l-1},m_l} = \left[\begin{pmatrix} M_l^{\prime\sigma_l} & 0 \\ 0 & M_l^{\prime\prime\sigma_l} \end{pmatrix} \right]_{m_{l-1},m_l} = \left[M_l^{\prime\sigma_l} \oplus M_l^{\prime\prime\sigma_l} \right]_{m_{l-1},m_l} \tag{4.96}$$

for $l = 2, \dots, L-1$ and the special cases

$$M^{\sigma_1}_{1;m_0,m_1} = \left[\begin{pmatrix} M_1^{\prime\sigma_1} & M_1^{\prime\prime\sigma_1} \end{pmatrix} \right]_{m_0,m_1}, \tag{4.97}$$

$$M^{\sigma_L}_{L;m_{L-1},m_L} = \left[\begin{pmatrix} M_L^{\prime\sigma_L} \\ M_L^{\prime\prime\sigma_L} \end{pmatrix} \right]_{m_{L-1},m_L}. \tag{4.98}$$

Clearly, with the exception of the edges, the bond dimensions of the MPS $|\psi\rangle$ are now given by the sum of the bond dimensions of $|\psi'\rangle$ and $|\psi''\rangle$ which might require a subsequent truncation, c.f. section 4.2 which certainly increases computational costs and might lead to loss of accuracy. Therefore MPS additions should be applied cautiously. An extreme example is the explicit addition of identical MPSs instead of a multiplication. The addition of two MPOs

$$\hat{O} = \sum_{\substack{\sigma_1,\dots,\sigma_L,\\ \sigma_1',\dots,\sigma_L'}} W_1^{\sigma_1,\sigma_1'} \cdots W_L^{\sigma_L,\sigma_L'} |\sigma_1,\dots,\sigma_L\rangle\langle\sigma_1',\dots,\sigma_L'| = \hat{O}' + \hat{O}'' \tag{4.99}$$

works entirely analogously introducing

$$W^{\sigma_l,\sigma_l'}_{l;w_{l-1},w_l} = \left[\begin{pmatrix} W_l^{\prime\sigma_l,\sigma_l'} & 0 \\ 0 & W_l^{\prime\prime\sigma_l,\sigma_l'} \end{pmatrix} \right]_{w_{l-1},w_l} = \left[W_l^{\prime\sigma_l,\sigma_l'} \oplus W_l^{\prime\prime\sigma_l,\sigma_l'} \right]_{w_{l-1},w_l} \tag{4.100}$$

for $l = 2, \dots, L-1$ and

$$W^{\sigma_1,\sigma_1'}_{1;w_0,w_1} = \left[\begin{pmatrix} W_1^{\prime\sigma_1,\sigma_1'} & W_1^{\prime\prime\sigma_1,\sigma_1'} \end{pmatrix} \right]_{w_0,w_1}, \tag{4.101}$$

$$W^{\sigma_L,\sigma_L'}_{L;w_{L-1},w_L} = \left[\begin{pmatrix} W_L^{\prime\sigma_L,\sigma_L'} \\ W_L^{\prime\prime\sigma_L,\sigma_L'} \end{pmatrix} \right]_{w_{L-1},w_L}. \tag{4.102}$$

4.4.3 Direct Application of an MPO to an MPS

Consider a quantum state $|\psi\rangle$ encoded as an MPS and an operator $\hat{O}$ described by an MPO. In principle the computation of the state $\hat{O}|\psi\rangle$ can be conducted in a straight forward fashion via

$$\hat{O}|\psi\rangle = \sum_{\substack{\sigma_1,\dots,\sigma_L,\\ \sigma_1',\dots,\sigma_L',\\ \sigma_1'',\dots,\sigma_L''}} \left(W_1^{\sigma_1,\sigma_1'} \cdots W_L^{\sigma_L,\sigma_L'} \right) \left(M_1^{\sigma_1''} \cdots M_L^{\sigma_L''} \right) |\sigma_1,\dots,\sigma_L\rangle \langle\sigma_1',\dots,\sigma_L'|\sigma_1'',\dots,\sigma_L''\rangle \tag{4.103a}$$

$$= \sum_{\substack{\sigma_1,\dots,\sigma_L,\\ \sigma_1',\dots,\sigma_L'}} \sum_{\substack{m_0,\dots,m_L\\ w_0,\dots,w_L}} W^{\sigma_1,\sigma_1'}_{1;w_0,w_1} \cdots W^{\sigma_L,\sigma_L'}_{L;w_{L-1},w_L} \cdot M^{\sigma_1'}_{1;m_0,m_1} \cdots M^{\sigma_L'}_{L;m_{L-1},m_L} |\sigma_1,\dots,\sigma_L\rangle \tag{4.103b}$$

$$= \sum_{\substack{\sigma_1,\dots,\sigma_L,\\ \sigma'_1,\dots,\sigma'_L}} \sum_{\substack{m_0,\dots,m_L\\ w_0,\dots,w_L}} \left(W^{\sigma_1,\sigma'_1}_{1;w_0,w_1} M^{\sigma'_1}_{1;m_0,m_1}\right) \cdots \left(W^{\sigma_L,\sigma'_L}_{L;w_{L-1},w_L} M^{\sigma'_L}_{L;m_{L-1},m_L}\right) |\sigma_1,\dots,\sigma_L\rangle \tag{4.103c}$$

$$= \sum_{\substack{\sigma_1,\dots,\sigma_L,\\ m_0,\dots,m_L\\ w_0,\dots,w_L}} \tilde{M}^{\sigma_1}_{1;(w_0,m_0),(w_1,m_1)} \cdots \tilde{M}^{\sigma_L}_{L;(w_{L-1},m_{L-1}),(w_L,m_L)} |\sigma_1,\dots,\sigma_L\rangle \tag{4.103d}$$

$$= \sum_{\sigma_1,\dots,\sigma_L} \tilde{M}^{\sigma_1}_1 \cdots \tilde{M}^{\sigma_L}_L |\sigma_1,\dots,\sigma_L\rangle = |\tilde{\psi}\rangle, \tag{4.103e}$$

c.f. figure 4.28, introducing new rank-3 tensors

$$\tilde{M}^{\sigma_l}_{l;(w_{l-1},m_{l-1}),(w_l,m_l)} = \sum_{\sigma'_l} W^{\sigma_l,\sigma'_l}_{l;w_{l-1},w_l} M^{\sigma'_l}_{l;m_{l-1},m_l}. \tag{4.104}$$

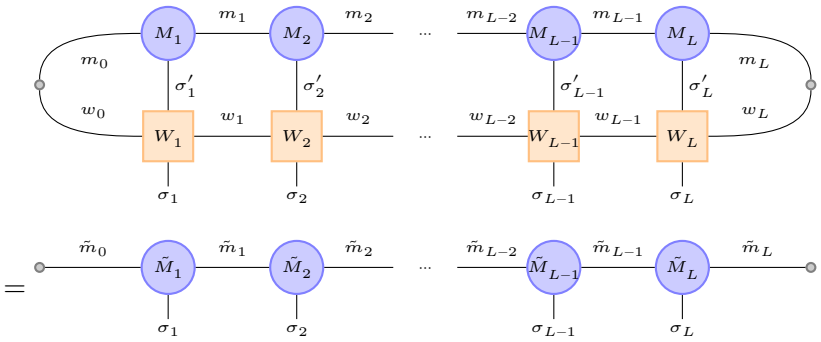

Figure 4.28: Pictorial representation of equation (4.103).

Thus, we have created a new MPS $|\tilde{\psi}\rangle$ which is now of the larger dimension $\tilde{m} = m \cdot w$. Obviously, a repeated application of MPOs to an MPS therefore will lead to a dramatic and in most cases unnecessary increase in the bond dimension, which then raises the need for truncating $|\tilde{\psi}\rangle$ as described in section 4.2.4. The entire procedure of direct application and subsequent truncation, however, is numerically costly, making it impractical to use. Therefore MPO-application schemes are desirable that keep the bond dimension comparably low. We will present two such mechanisms in the next sections.

4.4.4 Variational Application of an MPO to an MPS

Given the local structure of MPSs a site-wise optimization forced itself quasi onto us when we start to think harder about possible alternatives. We have already encountered the variational truncation of an MPS in section 4.2.4, and indeed the procedure to the variational MPO application does not differ too much from it. Nevertheless, we will give a detailed presentation of the algorithm at this point to further illustrate the advantages of variational sweeping.

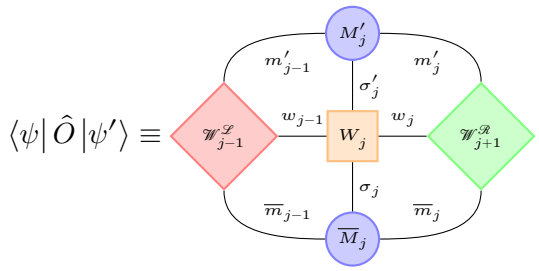

Figure 4.29: Pictorial representation of the overlap $\langle\psi|\hat{O}|\psi'\rangle$, c.f. equation (4.108).

We begin an MPS $|\psi'\rangle$ onto which we intend to apply an MPO $\hat{O}$ to obtain a new MPS $|\psi\rangle$. Thus, in this case the distance

$$\left\|\hat{O}|\psi'\rangle - |\psi\rangle\right\|_2^2 = \langle\psi'|\hat{O}^\dagger\hat{O}|\psi'\rangle - \langle\psi'|\hat{O}^\dagger|\psi\rangle - \langle\psi|\hat{O}|\psi'\rangle + \langle\psi|\psi\rangle \tag{4.105}$$

needs to be minimized with respect to $|\psi\rangle$. The formal minimization constraint with respect to an entry of a single site tensor $\overline{M}^{\sigma_j}_j$ then reads

$$\frac{\partial}{\partial \overline{M}^{\sigma_j}_{j;\overline{m}_j,\overline{m}_{j-1}}}\left\|\hat{O}|\psi'\rangle - |\psi\rangle\right\|_2^2 = \frac{\partial}{\partial \overline{M}^{\sigma_j}_{j;\overline{m}_j,\overline{m}_{j-1}}}\langle\psi|\psi\rangle - \frac{\partial}{\partial \overline{M}^{\sigma_j}_{j;\overline{m}_j,\overline{m}_{j-1}}}\langle\psi|\hat{O}|\psi'\rangle = 0. \tag{4.106}$$

Just like in the truncation routine we note that if $|\psi\rangle$ is given in a mixed-canonical form with orthogonality center at site j we obtain

$$\frac{\partial}{\partial \overline{M}^{\sigma_j}_{j;\overline{m}_j,\overline{m}_{j-1}}}\langle\psi|\psi\rangle = \frac{\partial}{\partial \overline{M}^{\sigma_j}_{j;\overline{m}_j,\overline{m}_{j-1}}}\left(\sum_{\substack{\sigma_j,\\ \overline{m}_{j-1},\overline{m}_j,\\ m_{j-1},m_j}} \overline{M}^{\sigma_j}_{j;\overline{m}_j,\overline{m}_{j-1}} M^{\sigma_j}_{j;m_{j-1},m_j}\right) = M^{\sigma_j}_{j;m_{j-1},m_j}, \tag{4.107}$$

c.f. equation (4.54). In strict analogy to the truncation scheme the overlap $\langle\psi|\hat{O}|\psi'\rangle$ is expressed with the help of newly defined left and right tensors, i.e.

$$\langle\psi|\hat{O}|\psi'\rangle = \sum_{\substack{\sigma_j,\sigma'_j,\\ \overline{m}_{j-1},\overline{m}_j,\\ w_{j-1},w_j,\\ m'_{j-1},m'_j}} \mathscr{W}^{\mathscr{L}}_{j1-;\overline{m}_{j-1},w_{j-1},m'_{j-1}} \overline{M}^{\sigma_j}_{j;\overline{m}_j,\overline{m}_{j-1}} W^{\sigma_j,\sigma'_j}_{j;w_{j-1},w_j} M'^{\sigma'_j}_{j;m'_{j-1},m'_j} \mathscr{W}^{\mathscr{R}}_{j+1;m'_j,w_j,\overline{m}_j}, \tag{4.108}$$

c.f. figure 4.29, where

$$\mathscr{W}^{\mathscr{L}}_{j-1;\overline{m}_{j-1},w_{j-1},m'_{j-1}} = \sum_{\substack{\overline{m}_{j-2},m'_{j-2},\\ w_{j-2},\\ \sigma_{j-1},\sigma'_{j-1}}} \left(\overline{A}^{\sigma_{j-1}}_{j-1;\overline{m}_{j-1},\overline{m}_{j-2}} \right.$$

$$\left(\cdots \left(\sum_{\substack{\overline{m}_0, m'_0, \\ w_0, \\ \sigma_1, \sigma'_1}} \left(\overline{A}^{\sigma_1}_{1;\overline{m}_1,\overline{m}_0} W^{\sigma_1,\sigma'_1}_{1;w_0,w_1} M'^{\sigma'_1}_{1;m'_0,m'_1} \right) \right) \cdots \right) W^{\sigma_{j-1},\sigma'_{j-1}}_{j-1;w_{j-2},w_{j-1}} M'^{\sigma'_{j-1}}_{j-1;m'_{j-2},m'_{j-1}} \Bigg), \quad (4.109)$$

c.f. figure 4.30, is just the left tensor and

$$\mathscr{W}^{\mathscr{R}}_{j+1;m'_j,w_j,\overline{m}_j} = \sum_{\substack{\overline{m}_{j+1}, m'_{j+1}, \\ w_{j+1}, \\ \sigma_{j+1}, \sigma'_{j+1}}} \Bigg(W^{\sigma_{j+1},\sigma'_{j+1}}_{j+1;w_j,w_{j+1}} M'^{\sigma'_{j+1}}_{j+1;m'_j,m'_{j+1}} \left(\cdots \left(\sum_{\substack{\overline{m}_L, m'_L, \\ w_L, \\ \sigma_L, \sigma'_L}} \left(W^{\sigma_L,\sigma'_L}_{L;w_{L-1},w_L} M'^{\sigma'_L}_{L;m'_{L-1},m'_L} \overline{B}^{\sigma_1}_{1;\overline{m}_L,\overline{m}_{L-1}} \right) \right) \cdots \right) \overline{B}^{\sigma_{j+1}}_{j+1;\overline{m}_{j+1},\overline{m}_j} \Bigg), \quad (4.110)$$

c.f. figure 4.31, is just the right tensor we defined for the computation of the operator expectation value, c.f. section 4.4.1, the only difference being that in this case the usage of A- and B-matrices is

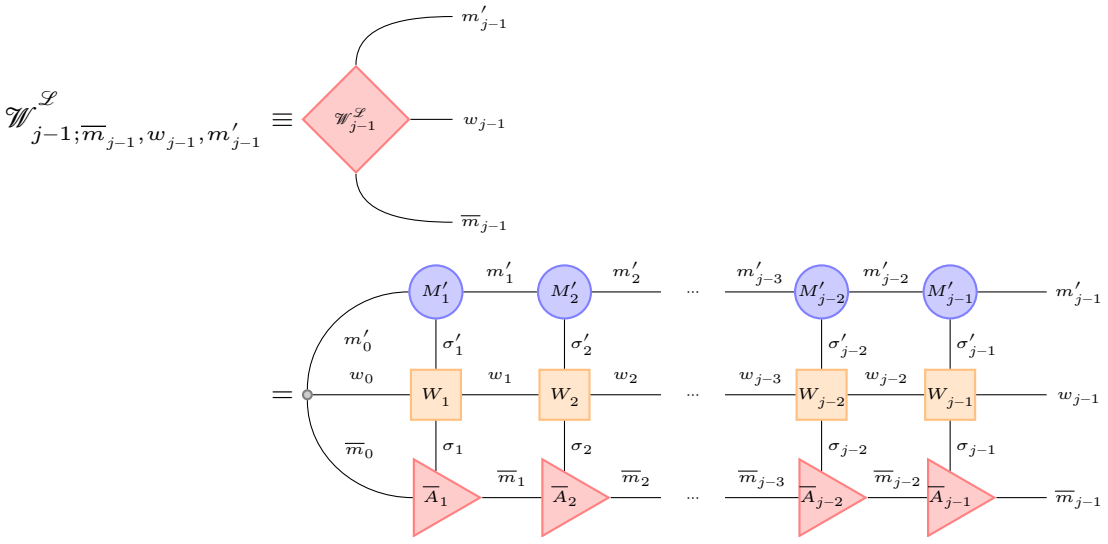

Figure 4.30: Pictorial representation of the left tensor $\mathscr{W}^{\mathscr{L}}_{j-1;\overline{m}_{j-1},w_{j-1},m'_{j-1}}$, c.f. equation (4.109).

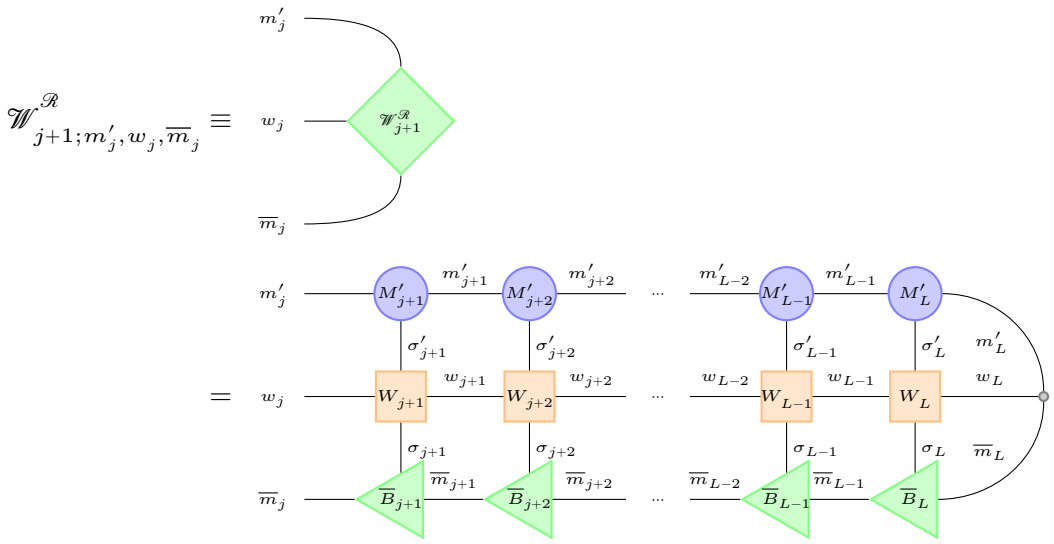

Figure 4.31: Pictorial representation of the right tensor $\mathscr{W}^{\mathscr{R}}_{j+1;m'_j,w_j,\overline{m}_j}$, c.f. equation (4.110).

essential to the routine. Thus, the second part in equation (4.106) is given by

$$\frac{\partial}{\partial \overline{M}^{\sigma_j}_{j;\overline{m}_j,\overline{m}_{j-1}}} \langle\psi|\hat{O}|\psi'\rangle = \frac{\partial}{\partial \overline{M}^{\sigma_j}_{j;\overline{m}_j,\overline{m}_{j-1}}} \left(\sum_{\substack{\sigma_j,\sigma'_j,\\ \overline{m}_{j-1},\overline{m}_j,\\ w_{j-1},w_j,\\ m'_{j-1},m'_j}} \mathscr{W}^{\mathscr{L}}_{j-1;\overline{m}_{j-1},w_{j-1},m'_{j-1}} \overline{M}^{\sigma_j}_{j;\overline{m}_j,\overline{m}_{j-1}} W^{\sigma_j,\sigma'_j}_{j;w_{j-1},w_j} M'^{\sigma'_j}_{j;m'_{j-1},m'_j} \mathscr{W}^{\mathscr{R}}_{j+1;m'_j,w_j,\overline{m}_j} \right) \tag{4.111a}$$

$$= \sum_{\substack{\sigma'_j,\\ w_{j-1},w_j,\\ m'_{j-1},m'_j}} \mathscr{W}^{\mathscr{L}}_{j-1;\overline{m}_{j-1},w_{j-1},m'_{j-1}} W^{\sigma_j,\sigma'_j}_{j;w_{j-1},w_j} M'^{\sigma'_j}_{j;m'_{j-1},m'_j} \mathscr{W}^{\mathscr{R}}_{j+1;m'_j,w_j,\overline{m}_j}, \tag{4.111b}$$

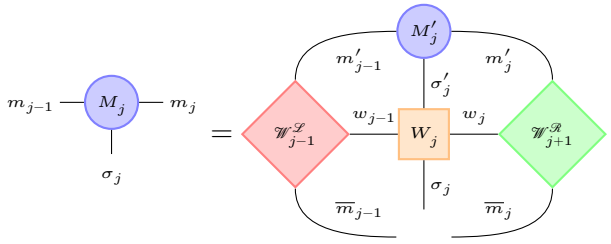

Figure 4.32: Pictorial representation of equation (4.112).

which yields for equation (4.106)

$$M^{\sigma_j}_{j;m_{j-1},m_j} = \sum_{\substack{\sigma'_j,\\ w_{j-1},w_j,\\ m'_{j-1},m'_j}} \mathscr{W}^{\mathscr{L}}_{j-1;\overline{m}_{j-1},w_{j-1},m'_{j-1}} W^{\sigma_j,\sigma'_j}_{j;w_{j-1},w_j} M'^{\sigma'_j}_{j;m'_{j-1},m'_j} \mathscr{W}^{\mathscr{R}}_{j+1;m'_j,w_j,\overline{m}_j}, \tag{4.112}$$

c.f. figure 4.32. Obviously, the left and right tensors can be constructed recursively, c.f. equations (4.85) and (4.86),

$$\mathscr{W}^{\mathscr{L}}_{j;\overline{m}_j,w_j,m'_j} = \sum_{\substack{\overline{m}_{j-1},m'_{j-1},\\ \sigma_j,\sigma'_j,\\ w_{j-1}}} \left(\overline{A}^{\sigma_j}_{j;\overline{m}_j,\overline{m}_{j-1}} \mathscr{W}^{\mathscr{L}}_{j-1;\overline{m}_{j-1},w_{j-1},m'_{j-1}} W^{\sigma_j,\sigma'_j}_{j;w_{j-1},w_j} M'^{\sigma'_j}_{j;m'_{j-1},m'_j}\right) \tag{4.113}$$

$$\mathscr{W}^{\mathscr{R}}_{j;m'_{j-1},w_{j-1},\overline{m}_{j-1}} = \sum_{\substack{\overline{m}_j,m'_j,\\ \sigma_j,\sigma'_j,\\ w_j}} \left(W^{\sigma_j,\sigma'_j}_{j;w_{j-1},w_j} M'^{\sigma'_j}_{j;m'_{j-1},m'_j} \mathscr{W}^{\mathscr{R}}_{j+1;m'_j,w_j,\overline{m}_j} \overline{B}^{\sigma_j}_{j;\overline{m}_j,\overline{m}_{j-1}}\right), \tag{4.114}$$

c.f. figures 4.33 and 4.34, with $\mathscr{W}^{\mathscr{L}}_0$ and $\mathscr{W}^{\mathscr{R}}_{L+1}$ being $1\times1\times1$ dummy tensors.

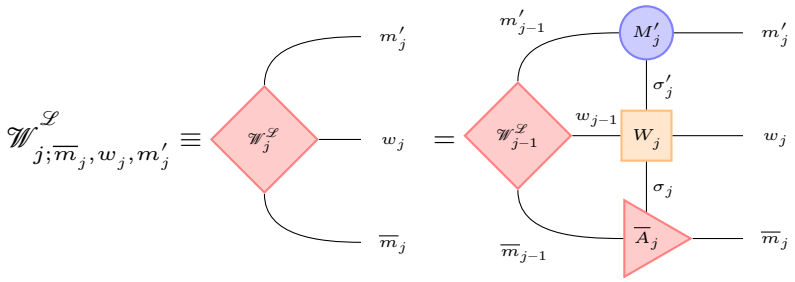

Figure 4.33: Pictorial representation of the recursive construction of the left tensor $\mathscr{W}^{\mathscr{L}}_{j;\overline{m}_j,w_j,m'_j}$, c.f. equation (4.113).

With the above considerations we may set up the scheme for variationally sweeping through the MPS as follows: Starting from a trial MPS $|\psi\rangle$ with its active site at $j=1$ and all $\mathscr{W}^{\mathscr{R}[0]}_j$ constructed

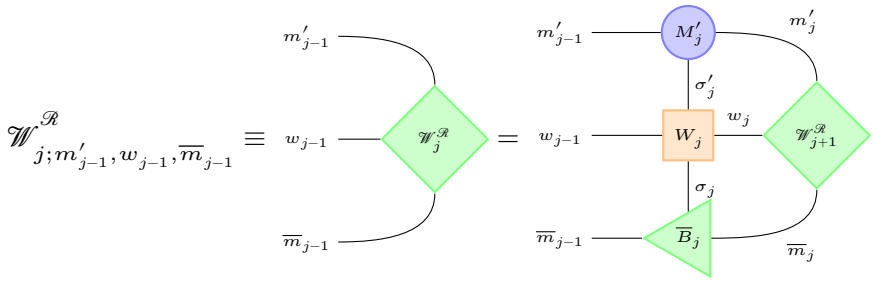

Figure 4.34: Pictorial representation of the recursive construction of the right tensor $\mathscr{W}^{\mathscr{R}}_{j;m'_{j-1},w_{j-1},\overline{m}_{j-1}}$, c.f. equation (4.114).

according to equation (4.110) we update the matrix $M_j^{[0]\sigma_j}$ to $M_j^{[1]\sigma_j}$ as described by equation (4.112). We have again added the extra subscript in square brackets indicating the number of the sweep. Then, the orthogonality center of $|\psi\rangle$ is shifted to site $j+1$, c.f. section 4.2.2, $\mathscr{W}^{\mathscr{R}[0]}_{j+1}$ is discarded and $\mathscr{W}^{\mathscr{L}[1]}_{j}$ is constructed from $M_j^{[1]\sigma_j}$ according to equation (4.113). As $j = L$ is reached this right sweep is completed, the distance

$$\left\| \hat{O} |\psi'\rangle - |\psi\rangle \right\|_2^2 = 1 - \langle \psi | \psi \rangle \tag{4.115}$$

is computed, and, should it have reached a certain threshold, the algorithm terminates, otherwise it continues with a left sweep. Therewith starting from $j = L$, for each j the matrix $M_j^{[1]\sigma_j}$ is updated to $M_j^{[2]\sigma_j}$ as in equation (4.112), the orthogonality center of $|\psi\rangle$ is shifted to site $j-1$, $\mathscr{W}^{\mathscr{L}[1]}_{j-1}$ is discarded, and $\mathscr{W}^{\mathscr{R}[2]}_{j}$ is constructed from $M_j^{[2]\sigma_j}$ according to equation (4.113) until $j = 0$ is reached. Then the distance can be computed again and the procedure of right and left sweeps may be repeated until the desired distance or a maximum number of sweeps is reached. Just like for the truncation scheme, we could have also started with an initial state with its active site at $j = L$, which would have necessitated the construction of all $\mathscr{W}^{\mathscr{L}[0]}_{j}$, c.f. equation (4.109), to begin with a left sweep.

4.4.5 Zip-up Application of an MPO to an MPS

So far we have encountered two methods to compute the application of an MPO to an MPS. While the direct application comes with the disadvantage of significantly increasing the MPS's bond dimension, the variational application may suffer from convergence problems. It would therefore be beneficial to come up with a scheme that is reasonably exact as the direct application keeping the bond dimension comparably low. Indeed, such a mechanism exists by means of the zip-up method as introduced by Stoudenmire et al. in [356]. The principal idea is to site-wise contract the MPS- and MPO-matrices and to directly perform an SVD as part of the MPS-MPO contraction allowing an immediate truncation. Note, however, that this method operates under the assumption that the application of the MPO will only mildly destroy the MPS's canonical form, which justifies a truncation as part of the contraction process. A typical example of an MPO to meet this assumption is the time-evolution operator (with a significantly small time step of course.)

Let us assume that we have a given right-normalized MPS $|\psi\rangle$ to which we want to apply the MPO $\hat{O}$. We begin by constructing a new tensor from the contributions of $|\psi\rangle$ and $\hat{O}$ at site $j = 1$ via

$$N^{\sigma_1}_{1;n_0,(w_1,m_1)} = \sum_{\sigma_1',n_0,m_0,w_0} \Gamma_{0;n_0,n_0} \left(V_0^\dagger\right)_{n_0,(w_0,m_0)} W^{\sigma_1,\sigma_1'}_{1;w_0,w_1} B^{\sigma_1'}_{1;m_0,m_1}, \tag{4.116}$$

where we for the sake of generalization have introduced the 1×1 dummy tensors Γ_0 and $V_0^\dagger$. Now, for all j, first the new tensor is SV decomposed

$$N^{\sigma_j}_{j;n_{j-1},(w_j,m_j)} = \sum_{n_j} U^{\sigma_j}_{j;n_{j-1},n_j} \Gamma_{j;n_j,n_j} \left(V_j^\dagger\right)_{n_j,(w_j,m_j)}, \tag{4.117}$$

the matrix U of the SVD is identified with an A-matrix

$$A^{\sigma_j}_{j;n_{j-1},n_j} = U^{\sigma_j}_{j;n_{j-1},n_j}, \tag{4.118}$$

and the remaining matrices of the SVD are fused with the subsequent M- and W-matrices to form

$$N^{\sigma_{j+1}}_{j+1;n_j,(w_{j+1},m_{j+1})} = \sum_{\sigma_{j+1}',n_j,m_j,w_j} \Gamma_{j;n_j,n_j} \left(V_j^\dagger\right)_{n_j,(w_j,m_j)} W^{\sigma_{j+1},\sigma_{j+1}'}_{j+1;w_j,w_{j+1}} B^{\sigma_{j+1}'}_{j+1;m_j,m_{j+1}}, \tag{4.119}$$

such that we obtain a left-normalized MPS as $j = L$ is reached. If necessary this resulting MPS may then be subject to a further truncation as explained in section 4.2.3 or 4.2.4.

Clearly we could have just as well started from a left-normalized MPS. In that case we begin at site $j = L$ with the construction of the new tensor

$$N^{\sigma_L}_{L;(w_{L-1},m_{L-1}),n_L} = \sum_{\sigma_L',n_L,m_L,w_L} W^{\sigma_L,\sigma_L'}_{L;w_{L-1},w_L} A^{\sigma_L'}_{L;m_{L-1},m_L} U_{L;(w_L,m_L),n_L} \Gamma_{L;n_L,n_L}, \tag{4.120}$$

where this time U_L and Γ_L are 1×1 dummy tensors. Then, for all j, the SVD runs as

$$N^{\sigma_j}_{j;(w_{j-1},m_{j-1}),n_j} = \sum_{n_{j-1}} U_{j-1;(w_{j-1},m_{j-1}),n_{j-1}} \Gamma_{j-1;n_{j-1},n_{j-1}} \left(V_j^\dagger\right)^{\sigma_j}_{n_{j-1},n_j}, \tag{4.121}$$

$V^\dagger$ is identified with a B-matrix

$$B^{\sigma_j}_{j;n_{j-1},n_j} = \left(V_j^\dagger\right)^{\sigma_j}_{n_{j-1},n_j}, \tag{4.122}$$

and the remaining matrices are fused with the preceding M- and W-matrices giving

$$N^{\sigma_{j-1}}_{j-1;(w_{j-2},m_{j-2}),n_{j-1}} = \sum_{\sigma_{j-1}',n_{j-1},m_{j-1},w_{j-1}} W^{\sigma_{j-1},\sigma_{j-1}'}_{j-1;w_{j-2},w_{j-1}} A^{\sigma_{j-1}'}_{j-1;m_{j-2},m_{j-1}} U_{j-1;(w_{j-1},m_{j-1}),n_{j-1}} \Gamma_{j-1;n_{j-1},n_{j-1}}. \tag{4.123}$$

Thus, at $j = 1$ a right-normalized MPS is obtained.

5 Algorithms Using Matrix Product States

Having gained a basic understanding of MPSs and their properties, we now present the algorithms used to obtain the results presented in this work. We begin with an explanation of the the ground state search which was derived from classical DMRG algorithms. Here we follow the excellent review by Schollwöck [320] also incorporating ideas from [280]. Second, we introduce several time evolution routines, where regarding both the style of presentation, as well as terminology we stick close to the review article by Paeckel et al. [283], or equally [280] and [195]. References for further reading in the following sections are also to a large extend taken from these primary sources.

5.1 DMRG Ground State Search

The original aim of DMRG computations being to find ground states, this algorithm has, obviously, been reformulated in terms of the newer language of MPSs. In this chapter we will set up yet another variational scheme, which transfers the original DMRG routine to the MPS framework. Mathematically this procedure is a non-linear Gauß–Seidel method, c.f. for instance [271]. Again, we will encounter very familiar concepts from the variational MPS truncation, as well as the variational MPO application, c.f. sections 4.2.4 and 4.4.4, respectively.

Let $\hat{H}$ be the Hamiltonian to consider. If $|\psi\rangle$ is the (or a in case of degeneracy) ground state of $\hat{H}$ then it minimizes the expression

$$E_0 = \frac{\langle\psi|\,\hat{H}\,|\psi\rangle}{\langle\psi\,|\psi\rangle} \tag{5.1}$$

with the ground state energy E_0 and $\langle\psi|\psi\rangle$ ensuring normalization. Based on this observation we may set up the following functional

$$\mathscr{L} = \langle\psi|\,\hat{H}\,|\psi\rangle - \lambda\,\langle\psi|\psi\rangle, \tag{5.2}$$

which we need to minimized with respect to $|\psi\rangle$ in order to find the ground state. Here λ is a Lagrange multiplier, which will, once the routine is done, hold the ground state energy. As for the variational schemes we discussed so far, we will optimize $|\psi\rangle$ site wise. We, hence, begin with minimizing the functional with respect to an entry of a single site tensor $\overline{M}_j^{\sigma_j}$

$$\frac{\partial\mathscr{L}}{\partial\overline{M}^{\sigma_j}_{j;\overline{m}_j,\overline{m}_{j-1}}} = \frac{\partial}{\partial\overline{M}^{\sigma_j}_{j;\overline{m}_j,\overline{m}_{j-1}}}\,\langle\psi|\,\hat{H}\,|\psi\rangle - \lambda\frac{\partial}{\partial\overline{M}^{\sigma_j}_{j;\overline{m}_j,\overline{m}_{j-1}}}\,\langle\psi|\psi\rangle = 0. \tag{5.3}$$

As usual, c.f. (4.54) or (4.107), we take $|\psi\rangle$ to be given in a mixed-canonical form with orthogonality center at site j such that we have

$$\frac{\partial}{\partial \overline{M}^{\sigma_j}_{j;\overline{m}_j,\overline{m}_{j-1}}} \langle\psi|\psi\rangle = \frac{\partial}{\partial \overline{M}^{\sigma_j}_{j;\overline{m}_j,\overline{m}_{j-1}}} \left(\sum_{\substack{\sigma_j,\\ \overline{m}_{j-1},\overline{m}_j,\\ m_{j-1},m_j}} \overline{M}^{\sigma_j}_{j;\overline{m}_j,\overline{m}_{j-1}} M^{\sigma_j}_{j;m_{j-1},m_j} \right) = M^{\sigma_j}_{j;m_{j-1},m_j}. \quad (5.4)$$

Furthermore, $\langle\psi|\hat{H}|\psi\rangle$ is once again expressed in terms of left and right tensors

$$\langle\psi|\hat{H}|\psi\rangle = \sum_{\substack{\sigma_j,\sigma'_j,\\ \overline{m}_{j-1},\overline{m}_j,\\ w_{j-1},w_j,\\ m_{j-1},m_j}} \mathscr{W}^{\mathscr{L}}_{j-1;\overline{m}_{j-1},w_{j-1},m_{j-1}} \overline{M}^{\sigma_j}_{j;\overline{m}_j,\overline{m}_{j-1}} W^{\sigma_j,\sigma'_j}_{j;w_{j-1},w_j} M^{\sigma'_j}_{j;m_{j-1},m_j} \mathscr{W}^{\mathscr{R}}_{j+1;m_j,w_j,\overline{m}_j} \quad (5.5)$$

with

$$\mathscr{W}^{\mathscr{L}}_{j-1;\overline{m}_{j-1},w_{j-1},m_{j-1}} = \sum_{\substack{\overline{m}_{j-2},m_{j-2},\\ w_{j-2},\\ \sigma_{j-1},\sigma'_{j-1}}} \left(\overline{A}^{\sigma_{j-1}}_{j-1;\overline{m}_{j-1},\overline{m}_{j-2}} \left(\cdots \left(\sum_{\substack{\overline{m}_0,m_0,\\ w_0,\\ \sigma_1,\sigma'_1}} \left(\overline{A}^{\sigma_1}_{1;\overline{m}_1,\overline{m}_0} W^{\sigma_1,\sigma'_1}_{1;w_0,w_1} A^{\sigma'_1}_{1;m_0,m_1} \right) \right) \cdots \right) W^{\sigma_{j-1},\sigma'_{j-1}}_{j-1;w_{j-2},w_{j-1}} A^{\sigma'_{j-1}}_{j-1;m_{j-2},m_{j-1}} \right) \quad (5.6)$$

$$\mathscr{W}^{\mathscr{R}}_{j+1;m_j,w_j,\overline{m}_j} = \sum_{\substack{\overline{m}_{j+1},m_{j+1},\\ w_{j+1},\\ \sigma_{j+1},\sigma'_{j+1}}} \left(W^{\sigma_{j+1},\sigma'_{j+1}}_{j+1;w_j,w_{j+1}} B^{\sigma'_{j+1}}_{j+1;m_j,m_{j+1}} \left(\cdots \left(\sum_{\substack{\overline{m}_L,m_L,\\ w_L,\\ \sigma_L,\sigma'_L}} \left(W^{\sigma_L,\sigma'_L}_{L;w_{L-1},w_L} B^{\sigma'_L}_{L;m_{L-1},m_L} \overline{B}^{\sigma_1}_{L;\overline{m}_L,\overline{m}_{L-1}} \right) \right) \cdots \right) \overline{B}^{\sigma_{j+1}}_{j+1;\overline{m}_{j+1},\overline{m}_j} \right) \quad (5.7)$$

as in (4.109) and (4.110) with the difference that in this case both MPSs are the same and expressed in the mixed-canonical representation, c.f. figures 5.1 and 5.2. In the actual algorithm, these

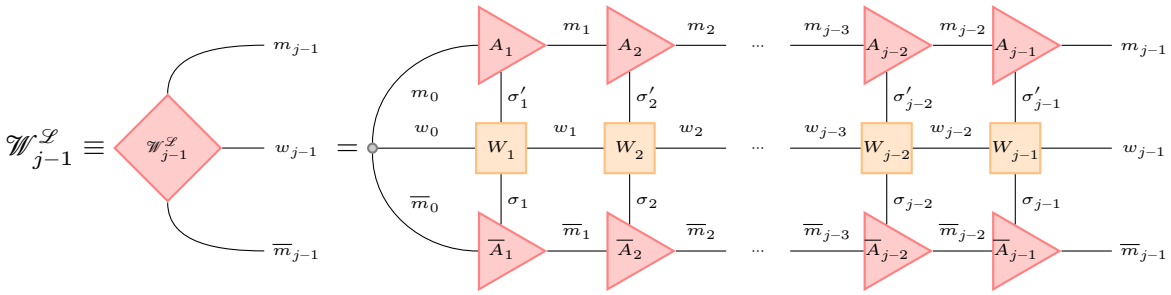

Figure 5.1: Pictorial representation of the left tensor $\mathscr{W}^{\mathscr{L}}_{j-1}$, c.f. equation (5.6).

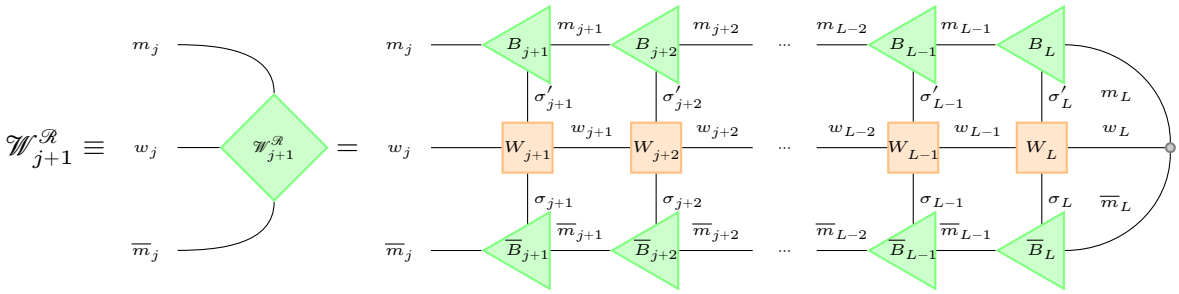

Figure 5.2: Pictorial representation of the right tensor $\mathscr{W}^{\mathscr{R}}_{j+1}$, c.f. equation (5.7).

tensors are again constructed recursively, c.f. equations (4.85) and (4.86) or (4.113) and (4.114),

$$\mathscr{W}^{\mathscr{L}}_{j;\overline{m}_j,w_j,m_j} = \sum_{\substack{\overline{m}_{j-1},m_{j-1},\\ \sigma_j,\sigma'_j,\\ w_{j-1}}} \left(\overline{A}^{\sigma_j}_{j;\overline{m}_j,\overline{m}_{j-1}} \mathscr{W}^{\mathscr{L}}_{j-1;\overline{m}_{j-1},w_{j-1},m_{j-1}} W^{\sigma_j,\sigma'_j}_{j;w_{j-1},w_j} A^{\sigma'_j}_{j;m_{j-1},m_j} \right) \tag{5.8}$$

$$\mathscr{W}^{\mathscr{R}}_{j;m_{j-1},w_{j-1},\overline{m}_{j-1}} = \sum_{\substack{\overline{m}_j,m_j,\\ \sigma_j,\sigma'_j,\\ w_j}} \left(W^{\sigma_j,\sigma'_j}_{j;w_{j-1},w_j} B^{\sigma'_j}_{j;m_{j-1},m_j} \mathscr{W}^{\mathscr{R}}_{j+1;m_j,w_j,\overline{m}_j} \overline{B}^{\sigma_j}_{j;\overline{m}_j,\overline{m}_{j-1}} \right) \tag{5.9}$$

with $1 \times 1 \times 1$ dummy tensors $\mathscr{W}^{\mathscr{L}}_0$ and $\mathscr{W}^{\mathscr{R}}_L$. We show schematics of these procedures in figures 5.3 and 5.4, respectively. The second part in equation (5.3) now takes the rather familiar form

$$\frac{\partial}{\partial \overline{M}^{\sigma_j}_{j;\overline{m}_j,\overline{m}_{j-1}}} \langle\psi|\hat{H}|\psi\rangle = \frac{\partial}{\partial \overline{M}^{\sigma_j}_{j;\overline{m}_j,\overline{m}_{j-1}}} \left(\sum_{\substack{\sigma_j,\sigma'_j,\\ \overline{m}_{j-1},\overline{m}_j,\\ w_{j-1},w_j,\\ m_{j-1},m_j}} \mathscr{W}^{\mathscr{L}}_{j-1;\overline{m}_{j-1},w_{j-1},m_{j-1}} \overline{M}^{\sigma_j}_{j;\overline{m}_j,\overline{m}_{j-1}} \right.$$

$$W^{\sigma_j,\sigma'_j}_{j;w_{j-1},w_j} M^{\sigma'_j}_{j;m_{j-1},m_j} \mathscr{W}^{\mathscr{R}}_{j+1;m_j,w_j,\overline{m}_j} \Bigg) \tag{5.10a}$$

$$= \sum_{\substack{\sigma'_j,\\ w_{j-1},w_j,\\ m_{j-1},m_j}} \mathscr{W}^{\mathscr{L}}_{j-1;\overline{m}_{j-1},w_{j-1},m_{j-1}} W^{\sigma_j,\sigma'_j}_{j;w_{j-1},w_j} M^{\sigma'_j}_{j;m_{j-1},m_j} \mathscr{W}^{\mathscr{R}}_{j+1;m_j,w_j,\overline{m}_j} \tag{5.10b}$$

$$= \sum_{\sigma'_j,m_{j-1},m_j} \mathscr{O}^{\sigma_j,\sigma'_j}_{j;\overline{m}_{j-1},m_{j-1},m_j,\overline{m}_j} M^{\sigma'_j}_{j;m_{j-1},m_j}, \tag{5.10c}$$

where we have introduced the new tensor

$$\mathscr{O}^{\sigma_j,\sigma'_j}_{j;\overline{m}_{j-1},m_{j-1},m_j,\overline{m}_j} = \sum_{w_{j-1},w_j} \mathscr{W}^{\mathscr{L}}_{j-1;\overline{m}_{j-1},w_{j-1},m_{j-1}} W^{\sigma_j,\sigma'_j}_{j;w_{j-1},w_j} \mathscr{W}^{\mathscr{R}}_{j+1;m_j,w_j,\overline{m}_j}, \tag{5.11}$$

which we show in figure 5.5. Thus, equation (5.3) reduces to

$$\lambda M^{\sigma_j}_{j;\overline{m}_{j-1},\overline{m}_j} = \sum_{\sigma'_j,m_{j-1},m_j} \mathscr{O}^{\sigma_j,\sigma'_j}_{j;\overline{m}_{j-1},m_{j-1},m_j,\overline{m}_j} M^{\sigma'_j}_{j;m_{j-1},m_j}, \tag{5.12}$$

c.f. figure 5.6. Reshaping the tensors M and $\mathscr{O}$ into bare vectors, we find equation (5.12) to simply reflect an eigenvalue problem

$$\lambda M_{j;(\sigma_j,m_{j-1},m_j)} = \sum_{(\sigma'_j,m_{j-1},m_j)} \mathscr{O}_{j;(\sigma_j,\overline{m}_{j-1},\overline{m}_j),(\sigma'_j,m_{j-1},m_j)} M_{j;(\sigma'_j,m_{j-1},m_j)}, \tag{5.13}$$

for which efficient numerical solvers exist, for instance by means of the Lanczos algorithm [207] we introduced in section 3.4. Other frequently applied schemes are the Jacobi-Davidson [76, 343] routine or the Arnoldi iteration [16].

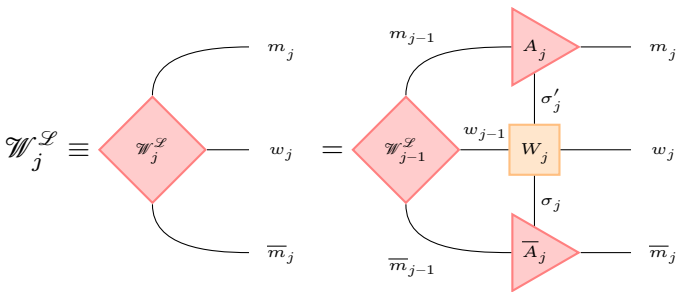

Figure 5.3: Pictorial representation of the recursive construction of the left tensor $\mathscr{W}^{\mathscr{L}}_j$, c.f. equation (5.8).

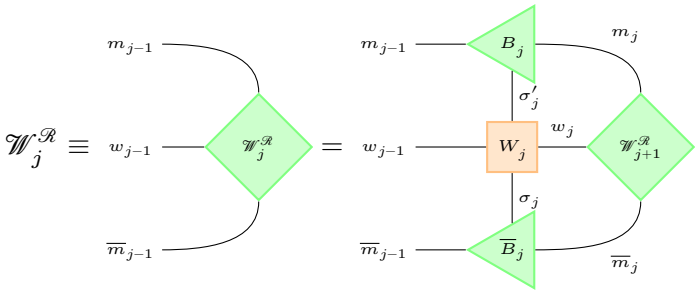

Figure 5.4: Pictorial representation of the recursive construction of the right tensor $\mathscr{W}_j^{\mathscr{R}}$, c.f. equation (5.9).

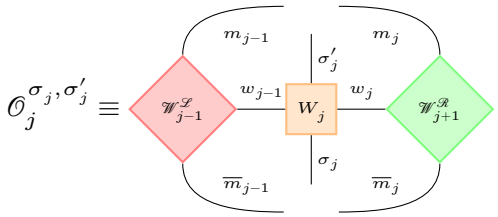

Figure 5.5: Pictorial representation of the tensor $\mathscr{O}_j^{\sigma_j,\sigma'_j}$, c.f. equation (5.11).

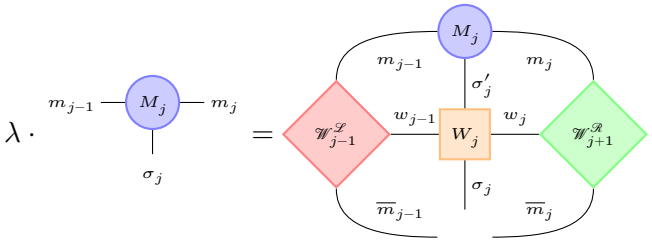

Figure 5.6: Pictorial representation of equation (5.12).

Based on the above observation we may now set up an iterative sweeping procedure to conduct an MPS-based DMRG ground state search. We begin with an initial MPS $|\psi\rangle$ which has its active site at $j = 1$ having constructed all right tensors $\mathscr{W}_j^{\mathscr{R}[0]}$ according to equation (5.7). As usual, the extra subscript in square brackets indicates the number of the sweep. For all j we now first construct the tensor $\mathcal{O}_j^{[1]}$ according to equation (5.11) to set up the eigenvalue problem (5.13). Then, $M_j^{[0]}$ is replaced by $M_j^{[1]}$, which is reshaped from the eigenvector of the previously set up eigenvalue problem corresponding to the smallest eigenvalue, which itself is taken as the new ground state energy $E_0^{[1]}$. Next, the orthogonality center of $|\psi\rangle$ is shifted to site $j+1$ as described in section 4.2.2, $\mathscr{W}_{j+1}^{\mathscr{R}[0]}$ is discarded and $\mathscr{W}_j^{\mathscr{L}[1]}$ is constructed from $M_j^{[1]}$ according to equation (5.8). At $j = L$ this right sweep is finished and

$$\epsilon = \langle\psi| \hat{H}^2 |\psi\rangle - \left(\langle\psi| \hat{H} |\psi\rangle\right)^2 \tag{5.14}$$

is evaluated to check for convergence. If $|\psi\rangle$ really is a ground state ϵ will take a value close to zero. Thus, in case it has reached a certain threshold, the algorithm terminates, otherwise it continues with a left sweep: Starting from $j = L$, for each j the tensor $\mathcal{O}_j^{[2]}$ is constructed, the corresponding eigenvalue problem is solved to replace $M_j^{[1]}$ by $M_j^{[2]}$, which is generated from the eigenvector corresponding to the smallest eigenvalue, that serves as the new ground state energy $E_0^{[2]}$. The orthogonality center of $|\psi\rangle$ is then shifted to $j-1$, $\mathscr{W}_j^{\mathscr{L}[1]}$ is discarded, and $\mathscr{W}_{j+1}^{\mathscr{R}[2]}$ is constructed from $M_j^{[2]}$. When $j = 1$ is reached ϵ can be computed again and the procedure of right and left sweeps continues until ϵ is sufficiently small or a maximum number of sweeps is achieved. We could have, of course, also started with an initial MPS with its active site at $j = L$ and having constructed all $\mathscr{W}_j^{\mathscr{L}[0]}$ according to equation (5.6) to begin with a left sweep.

As ground states are most often the basis for further computations, for example observables, their accuracy is of particular importance. However, unfortunately, there is again no guarantee for the procedure to converge to a global minimum. Therefore, the choice of the initial state is of great importance. A quite naive way is to start with a randomly generated MPS. In more elaborate schemes one tries to manually create an MPS that to a certain degree already fulfills certain properties known of the ground state. Still in some cases one might actually have to start with random MPSs. Nevertheless, in such cases it is often useful to conduct the ground state search stage wise, that is one performs several ground state searches, where in each stage the Hamiltonian is made more and more complex until its final form is implemented each time using the resulting MPS of the previous stage – which by no means needs to be converged – as the initial state for the current stage. It is likewise possible to increase the Hamiltonian's complexity with each sweep. Conducting the ground state search by means of these so-called warm-up sweeps is a standard approach. More details are discussed by Paeckel in great detail in [280]. Again, there is no general routine for this procedure and finding the best scheme to reliably converge an MPS to the ground state often requires a good portion of intuition. After the ground state search is done, it is highly recommendable to run sanity checks by means of computing local observables to test for the fulfillment of certain symmetries, if they are known to exist in the system under investigation. Possible observables could for instance be the local particle density, to find out if all particles in the system are equally distributed, in case this is expected from the ground state, or a certain spin configuration.

5.2 Time Evolution

When it comes to the numerical time-evolution of a quantum state, the problem usually boils down to compute

$$\left|\psi(t+\delta t)\right\rangle = U(t+\delta t,t)\left|\psi(t)\right\rangle = \mathrm{e}^{-\mathrm{i}\hat{H}(t)\delta t}\left|\psi(t)\right\rangle, \tag{5.15}$$

that is for a given quantum state $\left|\psi(t)\right\rangle$ at time t, we want to compute the quantum state at a subsequent time $\left|\psi(t+\delta t)\right\rangle$, δt being the time step of our sampling. This choice allows us to express the time evolution operator $U(t+\delta t,t)$ explicitly in the last equality of equation (5.15).

The computation of a full time evolution from $t=0$ to $t=t_{\max}$ is then nothing more than subsequently solving equation (5.15) $t_{\max}/\delta t$ times. Note that due to the discretization all numerical time evolution schemes will inevitably introduce an error in each iteration. In order to judge in how far the obtained results are trustworthy it is therefore most recommendable to, if accessible, measure appropriate observables for each time step. Furthermore it is obvious that there is a maximally accessible time for each such algorithm. There is no generically superior time evolution method, by contrast does the success of each scheme depend greatly on the properties of the system it is applied to. We will therefore shortly review several commonly used time evolution methods also dealing with assumptions they make and which systems they are best used for.

In general there exist two types of time evolution schemes, those to approximate the time evolution operator $U(t+\delta t,t)$ which then is applied to the initial state $\left|\psi(t)\right\rangle$, and those to directly compute the time evolved state $\left|\psi(t+\delta t)\right\rangle$. Amongst the former are the time-evolving block decimation (TEBD) or Trotter-Suzuki algorithm, as well as the W-I and W-II method, while the global and local Krylov method, and the time-dependent variational principle (TDVP) are representatives of the latter.

This differentiation being made, it is worth mentioning that the second class of solvers itself falls into two subgroups. In the first one, represented by the global Krylov method, $U(t+\delta t,t)\left|\psi(t)\right\rangle$ is approximated as a whole according to equation (5.15). The second subgroup does the time evolution iteratively by solving a sequence of local ones. Therefore, a Lie-Trotter decomposition of the time-dependent Schrödinger equation (2.20) is performed, which involves expressing the total Hamiltonian as a sum of n local Hamiltonians $\hat{H}_n(t)$, i.e.

$$\hat{H}(t) = \sum_n \hat{H}_n(t). \tag{5.16}$$

Whilst in general it is not possible to solve this problem as a whole, to a first order approximation a solution may be obtained from solving a string of equations

$$\left|\psi_{n,n-1}(t+\delta t,t)\right\rangle = U_n(t+\delta t,t)\left|\psi_{n-1}(t+\delta t,t)\right\rangle = \mathrm{e}^{-\mathrm{i}\hat{H}_n(t)\delta t}\left|\psi_{n-1}(t+\delta t,t)\right\rangle, \tag{5.17}$$

where each subsequent initial state is constructed from its predecessor

$$\left|\psi_n(t+\delta t,t)\right\rangle = \left|\psi_n(t+\delta t,t)\right\rangle\left(\left|\psi_{n,n-1}(t+\delta t,t)\right\rangle\right). \tag{5.18}$$

which recursively defines the partially evolved states $\left|\psi_n(t+\delta t,t)\right\rangle$ together with

$$\left|\psi_0(t+\delta t,t)\right\rangle = \left|\psi(t)\right\rangle, \tag{5.19}$$

$$\left|\psi_L(t+\delta t,t)\right\rangle = \left|\psi(t+\delta t)\right\rangle, \tag{5.20}$$

in case the procedure starts from $n = 1$. In case we begin at $n = L$, we have

$$\left|\psi_{n,n+1}(t+\delta t,t)\right\rangle = U_n(t+\delta t,t)\left|\psi_{n+1}(t+\delta t,t)\right\rangle = \mathrm{e}^{-\mathrm{i}\hat{H}_n(t)\delta t}\left|\psi_{n+1}(t+\delta t,t)\right\rangle, \tag{5.21}$$

$$\left|\psi_n(t+\delta t,t)\right\rangle = \left|\psi_n(t+\delta t,t)\right\rangle\left(\left|\psi_{n,n+1}(t+\delta t,t)\right\rangle\right) \tag{5.22}$$

and

$$\left|\psi_{L+1}(t+\delta t,t)\right\rangle = \left|\psi(t)\right\rangle, \tag{5.23}$$

$$\left|\psi_1(t+\delta t,t)\right\rangle = \left|\psi(t+\delta t)\right\rangle. \tag{5.24}$$

This iterative computation of the time-evolved state $\left|\psi(t+\delta t)\right\rangle$ is carried out in the global Krylov method, as well as in the TDVP. In terms of the MPS language in very simple words these two algorithms solve the time-dependent Schrödinger equation for all site-tensors individually and fuse the so-obtained solutions into a whole by means of a projection for the former and a backward time evolution for the latter algorithm, respectively.

5.2.1 The Time-evolving Block Decimation (TEBD)

For this algorithm [392, 408, 70, 386] a Trotter-Suzuki decomposition [362, 360, 361] of the Hamiltonian $\hat{H}(t)$ needs to be found manually. Therewith $\hat{H}(t)$ is expressed as a sum of internally commuting parts, that is

$$\hat{H}(t) = \sum_{n=1}^{N_H} \hat{H}_n(t), \tag{5.25a}$$

$$\hat{H}_n(t) = \sum_{m=1}^{M_n} \hat{h}_{n,m}(t), \tag{5.25b}$$

$$0 = \left[\hat{h}_{n,m}(t)\,,\hat{h}_{n,m'}(t)\right]. \tag{5.25c}$$

The important observation is that because of equation (5.25c), the time evolution of each part is given by simply taking the exponentials of the individual summands

$$\mathrm{e}^{-\mathrm{i}\hat{H}_n(t)\delta t} = \prod_{m=1}^{M_n} \mathrm{e}^{-\mathrm{i}\hat{h}_{n,m}(t)\delta t} \tag{5.26}$$

as follows from the Baker–Campbell–Hausdorff formula. Using the commuting parts (5.25b), the time evolution operator in equation (5.15) is to first order approximated by

$$U(t+\delta t,t) = U^{\mathrm{TEBD1}}(t+\delta t,t) + \mathcal{O}(\delta t) \approx \prod_{n=1}^{N_H} \mathrm{e}^{-\mathrm{i}\hat{H}_n(t)\delta t}, \tag{5.27}$$

where the exact error is determined by the commutator of the Baker–Campbell–Hausdorff formula. Halving the time step δt and rearranging the order of the commuting parts the scheme may be improved to a second order approximation

$$U(t+\delta t,t) = U^{\mathrm{TEBD2}}(t+\delta t,t) + \mathcal{O}\left(\delta t^3\right) \approx \prod_{n=1}^{N_H} \mathrm{e}^{-\mathrm{i}\hat{H}_n(t)\delta t/2} \prod_{n=N_H}^{1} \mathrm{e}^{-\mathrm{i}\hat{H}_n(t)\delta t/2}, \tag{5.28}$$

and even a fourth order approximation can be constructed by

$$U(t+\delta t,t) = U^{\mathrm{TEBD4}}(t+\delta t,t) + \mathcal{O}\big(\delta t^5\big) \approx U^{\mathrm{TEBD2}}(t+\delta t_1,t)\, U^{\mathrm{TEBD2}}(t+\delta t_1,t) \\ U^{\mathrm{TEBD2}}(t+\delta t_2,t)\, U^{\mathrm{TEBD2}}(t+\delta t_1,t)\, U^{\mathrm{TEBD2}}(t+\delta t_1,t), \tag{5.29}$$

where we have introduced

$$\delta t_1 = \frac{1}{4-4^{1/3}}\delta t \quad \text{and} \quad \delta t_2 = (1-4\delta t_1)\,\delta t. \tag{5.30}$$

The TEBD algorithm is rather simple to implement once the decomposition of $\hat{H}(t)$ is found. Based on these internally commutating parts, first the respective parts of the time evolution operator are constructed as MPOs according to equation (5.26). Depending on what approximation is to be applied, these MPOs are applied successively to the initial MPS $\big|\psi(t)\big\rangle$ as specified by equation (5.27), (5.28), or (5.29), respectively. Therefore, the algorithms discussed in sections 4.4.3, 4.4.4, or 4.4.5 may be applied. Clearly, for the bond dimension not to dramatically increase truncation needs to be applied.

Note that the commuting parts (5.26) are particularly easy to encode as MPOs if their respective summands act on sites close to one another. If this is not the case depending on the problems in between the application of these commuting parts swap gates may be applied to move the affected sites closer together. After their time evolution, the same swap gates need to be applied in reverse order to undo this alteration. Generally speaking, the TEBD requires quite some additional thought before it may be applied successfully. Any alterations and even the choice, which approximation to use, are often rather problem specific. Depending on the value of the time step δt it might even not be useful to construct a fourth order TEBD scheme as it requires five times as many operator applications as the second order variant. For systems with only nearest-neighbor interactions, however, the decomposition is quickly found, c.f. for instance [165].

5.2.2 W-I / W-II

The W-I and W-II methods as introduced by Zaletel et al. [420] are generalizations of the Euler approximation of the time evolution operator $U(t+\delta t,t)$ which make particular use of decomposing the Hamiltonian as

$$\hat{H}(t) = \sum_n \hat{H}_n(t). \tag{5.31}$$

To second order $U(t+\delta t,t)$ then approximates to

$$U(t+\delta t,t) \approx 1 - \mathrm{i}\delta t \sum_n \hat{H}_n(t) - \frac{1}{2}\,(\delta t)^2 \sum_{n,m} \hat{H}_n(t)\,\hat{H}_m(t), \tag{5.32}$$

which itself will be subject to further approximations.

Beforehand, however, we recall the possibility to express any operator which naturally includes Hamiltonians as a product of operator-valued matrices, c.f. equation (4.75)

$$\hat{H}(t) = \hat{W}_1(t) \cdot \hat{W}_2(t) \cdot \cdots \cdot \hat{W}_{L-1}(t) \cdot \hat{W}_L(t). \tag{5.33}$$

We proceed by realizing that we may express these matrices as follows

$$\hat{W}_l(t) = \begin{matrix} & {\scriptstyle 1} & {\scriptstyle N_l} & {\scriptstyle 1} \\ {\scriptstyle 1} \\ {\scriptstyle N_{l-1}} \\ {\scriptstyle 1} \end{matrix} \begin{pmatrix} \mathbb{1} & \hat{C}_l(t) & \hat{D}_l(t) \\ \mathbb{0} & \hat{A}_l(t) & \hat{B}_l(t) \\ \mathbb{0} & \mathbb{0} & \mathbb{1} \end{pmatrix}, \tag{5.34a}$$

$$\hat{W}_1(t) = \begin{matrix} & {\scriptstyle 1} & {\scriptstyle N_1} & {\scriptstyle 1} \\ {\scriptstyle 1} \end{matrix} \begin{pmatrix} \mathbb{1} & \hat{C}_1(t) & \hat{D}_1(t) \end{pmatrix}, \quad \hat{W}_L(t) = \begin{matrix} & {\scriptstyle 1} \\ {\scriptstyle 1} \\ {\scriptstyle N_{L-1}} \\ {\scriptstyle 1} \end{matrix} \begin{pmatrix} \hat{D}_L(t) \\ \hat{B}_L(t) \\ \mathbb{1} \end{pmatrix} \tag{5.34b}$$

with operator valued matrices $\hat{A}_l(t)$, $\hat{B}_l(t)$, $\hat{C}_l(t)$, and $\hat{D}_l(t)$ of dimensions as specified in the above equations. Expressing equation (5.33) by means of these matrices, we find

$$\hat{H}(t) = \sum_j \hat{D}_j(t) + \sum_j \hat{C}_j(t)\,\hat{B}_{j+1}(t) + \sum_{j,l} \hat{C}_j(t) \left(\prod_{j<k<l} \hat{A}_k(t) \right) \hat{B}_l(t) = \sum_n \hat{H}_n(t), \tag{5.35}$$

which gives a rather clear interpretation of its components. The $\hat{D}_l(t)$ describe local parts of the Hamiltonian, $\hat{C}_l(t)$ and $\hat{B}_l(t)$ mark the beginning and end of an action, respectively, and the $\hat{A}_l(t)$ are used to express longer-ranged actions, an important case being long-range interactions. Note that $\hat{A}_l(t) = \mathbb{0}$ if there are no long-range components to the Hamiltonian.

In order to approximate equation (5.32), we restrict its double sum to incorporate only such $\hat{H}_n(t)$ and $\hat{H}_m(t)$ that do not overlap

$$U^I(t+\delta t, t) = 1 - \mathrm{i}\delta t \sum_n \hat{H}_n(t) - (\delta t)^2 \sum_{n,m}{}' \hat{H}_n(t)\,\hat{H}_m(t) \approx \prod_n \left(1 - \mathrm{i}\delta t \hat{H}_n(t)\right), \tag{5.36}$$

which we indicate by the primed sum. We have also neglected the factor of $1/2$ at this point, which will, however not significantly influence the error that we make as it is of the same order as the original approximation. This approximate operator may be expressed as a product of operator-valued matrices $\hat{W}_l^I(t, \delta t)$ which themselves are constructed from the previously introduced matrices $\hat{A}_l(t)$, $\hat{B}_l(t)$, $\hat{C}_l(t)$, and $\hat{D}_l(t)$ via

$$\hat{W}_l^I(t, \delta t) = \begin{pmatrix} \mathbb{1} + \mathrm{i}\delta t \hat{D}_l(t) & \hat{C}_l(t) \\ \mathrm{i}\delta t \hat{B}_l(t) & \hat{A}_l(t) \end{pmatrix}, \tag{5.37a}$$

$$\hat{W}_1^I(t, \delta t) = \begin{pmatrix} \mathbb{1} + \mathrm{i}\delta t \hat{D}_1(t) & \hat{C}_1(t) \end{pmatrix}, \quad \hat{W}_L^I(t, \delta t) = \begin{pmatrix} \mathbb{1} + \mathrm{i}\delta t \hat{D}_L(t) \\ \mathrm{i}\delta t \hat{B}_L(t) \end{pmatrix}, \tag{5.37b}$$

which serve as the basis for constructing an MPO by means of an FSM as described in section 4.3.2. Unfortunately, this approximation is not very good as it already fails to describe purely local Hamiltonians. Therefore, we relax the constraint in equation (5.36) a bit by allowing the double sum to also include $\hat{H}_n(t)$ and $\hat{H}_m(t)$ that overlap by at most one site, thereby introducing

$$U^{II}(t+\delta t, t) = 1 - \mathrm{i}\delta t \sum_n \hat{H}_n(t) - (\delta t)^2 \sum_{n,m}{}'' \hat{H}_n(t)\,\hat{H}_m(t) \approx \prod_n \left(1 - \mathrm{i}\delta t \hat{H}_n(t)\right). \tag{5.38}$$

Here the doubly primed sum indicates the less strict approximation. Analogously to the previous approximation, we intend to express $U^{II}(t+\delta t,t)$ as a product of operator-valued matrices. In this case, however, there exists no closed form to write down these matrices. Instead, we begin by generally defining

$$\hat{W}_l^{II}(t,\delta t) = \begin{pmatrix} \hat{W}_{D_l}^{II}(t,\delta t) & \hat{W}_{C_l}^{II}(t,\delta t) \\ \hat{W}_{B_l}^{II}(t,\delta t) & \hat{W}_{A_l}^{II}(t,\delta t) \end{pmatrix}, \tag{5.39a}$$

$$\hat{W}_1^{II}(t,\delta t) = \begin{pmatrix} \hat{W}_{D_1}^{II}(t,\delta t) & \hat{W}_{C_1}^{II}(t,\delta t) \end{pmatrix}, \quad \hat{W}_L^{II}(t,\delta t) = \begin{pmatrix} \hat{W}_{D_L}^{II}(t,\delta t) \\ \hat{W}_{B_L}^{II}(t,\delta t) \end{pmatrix}, \tag{5.39b}$$

of which the entries are determined by

$$\begin{aligned} \hat{W}_{S_l;n,m}^{II}(t,\delta t) = {} & \begin{pmatrix} \delta_{S_l,D_l} & \delta_{S_l,C_l} & \delta_{S_l,B_l} & \delta_{S_l,A_l} \end{pmatrix} \\ & \exp\left[\begin{pmatrix} \mathrm{i}\delta t \hat{D}_l(t) & 0 & 0 & 0 \\ \hat{C}_{l;m}(t) & \mathrm{i}\delta t \hat{D}_l(t) & 0 & 0 \\ \mathrm{i}\delta t \hat{B}_{l;n}(t) & 0 & \mathrm{i}\delta t \hat{D}_l(t) & 0 \\ \hat{A}_{l;n,m}(t) & \mathrm{i}\delta t \hat{B}_{l;n}(t) & \hat{C}_{l;m}(t) & \mathrm{i}\delta t \hat{D}_l(t) \end{pmatrix} \right] \begin{pmatrix} 1 \\ 0 \\ 0 \\ 0 \end{pmatrix}, \end{aligned} \tag{5.40}$$

with $S_l \in \{A_l, B_l, C_l, D_l\}$. As the derivation of the above equation is rather involved, we refer the interested reader to [283] or [280]. We close this section with two remarks on the usage of the newly defined schemes. First do we note that both approximations are of the same accuracy, yet the error of $U^{II}(t+\delta t,t)$ is smaller than the one of $U^{I}(t+\delta t,t)$. Therefore, the W-II method should always be preferred over W-I. Second, we emphasize that this method is particularly suited for Hamiltonians with long-ranged interactions and should, hence, be applied preferentially for such systems.

5.2.3 Global Krylov

The principal idea of the global Krylov method [286, 201, 111, 72, 396, 311] is to project the initial quantum state $|\psi(t)\rangle$ onto a Krylov subspace, c.f. section 3.4, and then construct the subsequent state $|\psi(t+\delta t)\rangle$ within this subspace.

Setting up a $K+1$-dimensional Krylov subspace of orthonormal Krylov vectors is achieved similarly to equation (3.22) via

$$\mathscr{K}^K \equiv \mathrm{span}\Big\{|v_0\rangle, \hat{H}|v_0\rangle, \hat{H}^2|v_0\rangle, \dots, \hat{H}^K|v_0\rangle\Big\} = \mathrm{span}\{|v_0\rangle, |v_1\rangle, |v_2\rangle, \dots, |v_K\rangle\}, \tag{5.41}$$

where we start from

$$|v_0\rangle = \frac{|\psi(t)\rangle}{\||\psi(t)\rangle\|}. \tag{5.42}$$

Next, we construct a projector onto this subspace through

$$\hat{P}^K = \sum_{k=0}^{K} |v_k\rangle\langle v_k| = V_K^\dagger V_K, \tag{5.43}$$

which we formally express in terms of the state vector

$$V_K = \begin{pmatrix} \langle v_0| \\ \langle v_1| \\ \vdots \\ \langle v_{K-1}| \\ \langle v_K| \end{pmatrix}. \tag{5.44}$$

Applying this projection to equation (5.15) then yields

$$|\psi(t+\delta t)\rangle = \hat{P}^K \mathrm{e}^{-\mathrm{i}\hat{H}(t)\delta t}\hat{P}^K |\psi(t)\rangle = V_K^\dagger \sum_{n=0}^{\infty} \left(\frac{(-\mathrm{i}\delta t)^n}{n!} V_K \hat{H}(t)^n V_K^\dagger \right) V_K |\psi(t)\rangle. \tag{5.45}$$

Defining

$$T_K = V_K \hat{H}(t) V_K^\dagger, \tag{5.46}$$

that is

$$\left(T_K\right)_{k,l} = \langle v_k| \hat{H}(t) |v_l\rangle, \tag{5.47}$$

we introduce the following approximation

$$V_K \hat{H}(t)^n V_K^\dagger \approx T_K^n, \tag{5.48}$$

which is only exact for $n \leq K$. Thus, equation (5.45) simplifies to

$$|\psi(t+\delta t)\rangle \approx V_K^\dagger \sum_{n=0}^{\infty} \left(\frac{(-\mathrm{i}\delta t)^n}{n!} T_K^n \right) V_K |\psi(t)\rangle = V_K^\dagger \mathrm{e}^{-\mathrm{i}\delta t T_K} V_K |\psi(t)\rangle \tag{5.49a}$$

$$= \sum_{k,l} |v_k\rangle \left(\mathrm{e}^{-\mathrm{i}\delta t T_K}\right)_{k,l} \langle v_l |\psi(t)\rangle \tag{5.49b}$$

$$= \| |\psi(t)\rangle \| \sum_k \left(\mathrm{e}^{-\mathrm{i}\delta t T_K}\right)_{k,0} |v_k\rangle. \tag{5.49c}$$

In the last equality we have used that

$$\langle v_l |\psi(t)\rangle = \delta_{l,0} \| |\psi(t)\rangle \| \tag{5.50}$$

bearing in mind the definition of $|v_0\rangle$ (5.42) and the orthonormality of the Krylov vectors. The matrix exponential in equation (5.49) is easily computed through diagonalizing

$$T_K = Q_K^\dagger D_K Q_K, \tag{5.51}$$

with D_K being diagonal, such that

$$\mathrm{e}^{-\mathrm{i}\delta t T_K} = Q_K^\dagger \mathrm{e}^{-\mathrm{i}\delta t D_K} Q_K. \tag{5.52}$$

A few remarks are in order. First note that the error in equation (5.48) scales as $\delta t^n/n!$ and can, hence, be made very small for a sufficient number of iterations. Second, we emphasize that until this point we did not exploit any MPS properties in the derivation of this method. Indeed, the global Krylov solver may just as well be implemented by means of other numerical techniques, such as exact diagonalization. When it comes to the use of MPSs due to their inherent truncation,

setting up the Krylov space is particularly tedious. With the truncation absent, its construction would be analogous to the procedure described in the discussion of the Lanczos algorithm in section 3.4, that is the orthogonalization of subsequent Krylov vectors would only need to be performed considering its two predecessors. For truncated, i.e. regular, MPSs, this inherent orthogonalization is unfortunately lost. Therefore any additional Krylov state needs to be orthogonalized with respect to all its predecessors. In practice this is achieved by variationally minimizing the functional

$$F = \left\| \hat{H}(t) \left| v_k \right\rangle - \left| v_{k+1} \right\rangle \right\|^2 + \sum_{l<k} \lambda_l \left\langle v_{k+1} \middle| v_l \right\rangle , \tag{5.53}$$

where the λ_l are Lagrange multipliers ensuring that

$$\left\langle v_{k+1} \middle| v_l \right\rangle = 0, 0 \leq l \leq k. \tag{5.54}$$

Once the Krylov states are constructed, however, the huge advantage of MPSs come into play, that is the construction of T_K according to equation (5.47). With MPSs, it is not necessary to explicitly construct states $\hat{H}(t) \left| v_k \right\rangle$ as part of the computation of $\left\langle v_k \right| \hat{H}(t) \left| v_l \right\rangle$, but instead is it possible to directly evaluate these terms at a much lower computational cost.

All the mentioned advantages and disadvantages aside, the global Krylov method is still a rather general scheme that does not make efficient use of MPS specific properties, in particular their locality. This observation motivates the introduction of algorithms more natural to MPSs, as for example the local Krylov method or TDVP which will be discussed in the following sections.

5.2.4 Local Krylov

What hereafter is referred to as the local Krylov method is a reformulation of time-step targeting DMRG [111, 102, 235, 305, 307] in terms of the MPS framework. This analogy was elaborated extensively on by Paeckel et al. in reference [283] and also [280]. It should be noted that despite the method's name, the local solver need not be a Krylov method, also Runge-Kutta solvers have been applied. In these explanations, however, we stick close to [283] and go with Krylov solvers. The main idea of the local Krylov method is to site-wise time-evolve a given MPS $\left| \psi(t) \right\rangle$ to $\left| \psi(t + \delta t) \right\rangle$ and for each subsequent site to first express the updated M-matrices in terms of the initial time t. In short this means that tensors at time t are expressed in terms of tensors at time $t + \delta t$. This is achieved using projectors which we will define in the following.

We begin with the left projector onto $\left| \psi(t) \right\rangle$

$$\begin{aligned} \mathscr{P}_j^{|\psi\rangle\mathscr{L}}(t) = & \left(\sum_{\substack{\sigma_1,\dots,\sigma_j, \\ \sigma'_1,\dots,\sigma'_j}} A_1^{\sigma_1}(t) \cdots A_j^{\sigma_j}(t)\, A_j^{\dagger\sigma'_j}(t) \cdots A_1^{\dagger\sigma'_1}(t) \left| \sigma_1, \dots, \sigma_j \right\rangle \left\langle \sigma'_1, \dots, \sigma'_j \right| \right) \\ & \otimes \left(\bigotimes_{l=j+1}^{L} \hat{\mathbb{1}}_l \right) \qquad (5.55a) \\ = & \left(\mathscr{P}_j^{|\psi\rangle A}(t)\, \mathscr{P}_j^{|\psi\rangle A\dagger}(t) \right) \otimes \left(\bigotimes_{l=j+1}^{L} \hat{\mathbb{1}}_l \right) \qquad (5.55b) \end{aligned}$$

and its counterpart, the right projector onto $|\psi(t)\rangle$

$$\mathscr{P}_j^{|\psi\rangle\mathscr{R}}(t) = \left(\bigotimes_{l=1}^{j-1} \hat{\mathbb{1}}_l\right) \otimes \left(\sum_{\substack{\sigma_j,\dots,\sigma_L,\\ \sigma'_j,\dots,\sigma'_L}} B_j^{\dagger\sigma_j}(t)\cdots B_L^{\dagger\sigma_L}(t)\, B_L^{\sigma'_L}(t)\cdots B_j^{\sigma'_j}(t)\,|\sigma_j,\dots,\sigma_L\rangle\langle\sigma'_j,\dots,\sigma'_L|\right) \tag{5.56a}$$

$$= \left(\bigotimes_{l=1}^{j-1} \hat{\mathbb{1}}_l\right) \otimes \left(\mathscr{P}_j^{|\psi\rangle B}(t)\,\mathscr{P}_j^{|\psi\rangle B\dagger}(t)\right) \tag{5.56b}$$

with

$$\mathscr{P}_j^{|\psi\rangle A}(t) = \sum_{\sigma_1,\dots,\sigma_j} A_1^{\sigma_1}(t)\cdots A_j^{\sigma_j}(t)\,|\sigma_1,\dots,\sigma_j\rangle, \tag{5.57}$$

$$\mathscr{P}_j^{|\psi\rangle B}(t) = \sum_{\sigma_j,\dots,\sigma_L} B_L^{\sigma_L}(t)\cdots B_j^{\sigma_j}(t)\,|\sigma_j,\dots,\sigma_L\rangle, \tag{5.58}$$

c.f. figures 5.7 to 5.10 for the respective sketches.

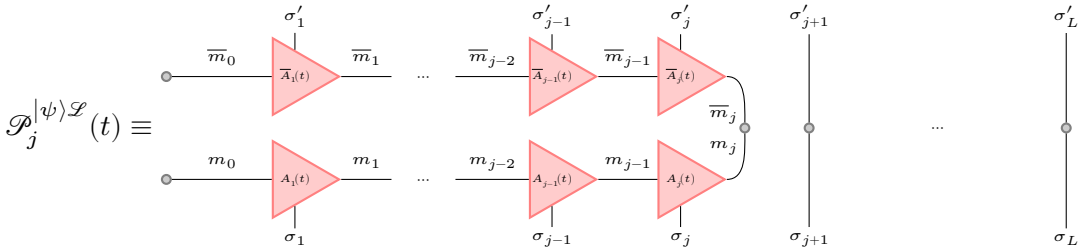

Figure 5.7: Pictorial representation of the left projector $\mathscr{P}_j^{|\psi\rangle\mathscr{L}}(t)$, c.f. equation (5.55).

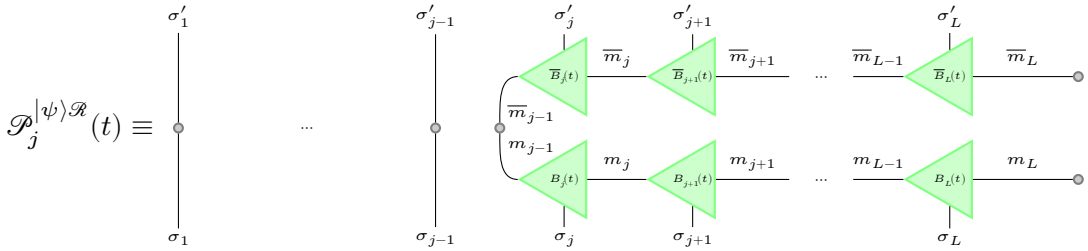

Figure 5.8: Pictorial representation of the right projector $\mathscr{P}_j^{|\psi\rangle\mathscr{R}}(t)$, c.f. equation (5.56).

Therefrom we first construct the isolation operator

$$\mathscr{I}_j^{|\psi\rangle}(t,t') = \mathscr{P}_{j-1}^{|\psi\rangle A}(t) \otimes \hat{\mathbb{1}}_j \otimes \mathscr{P}_{j+1}^{|\psi\rangle B}(t'), \tag{5.59}$$

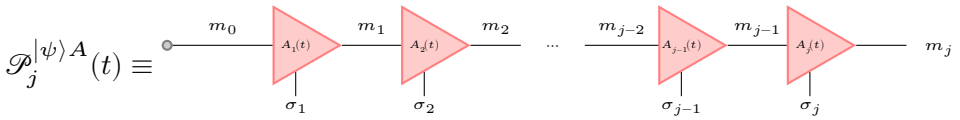

Figure 5.9: Pictorial representation of the projector $\mathscr{P}_j^{|\psi\rangle A}(t)$, c.f. equation (5.57).

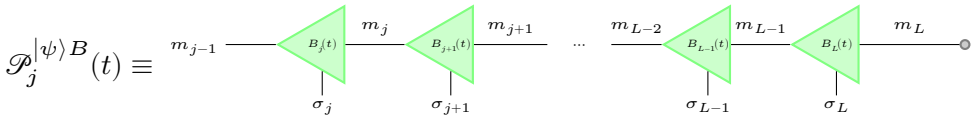

Figure 5.10: Pictorial representation of the projector $\mathscr{P}_j^{|\psi\rangle B}(t)$, c.f. equation (5.58).

c.f. figure 5.11, and, hence, another projector, which we depict in figure 5.12, onto the reduced site-space at site j through

$$\hat{\Pi}_j^{|\psi\rangle}(t,t') = \mathscr{P}_{j-1}^{|\psi\rangle\mathscr{L}}(t) \otimes \hat{\mathbb{1}}_j \otimes \mathscr{P}_{j+1}^{|\psi\rangle\mathscr{R}}(t') \tag{5.60a}$$

$$= \left(\mathscr{P}_{j-1}^{|\psi\rangle A}(t) \otimes \hat{\mathbb{1}}_j \otimes \mathscr{P}_{j+1}^{|\psi\rangle B}(t')\right) \cdot \left(\mathscr{P}_{j-1}^{|\psi\rangle A\dagger}(t) \otimes \hat{\mathbb{1}}_j \otimes \mathscr{P}_{j+1}^{|\psi\rangle B\dagger}(t')\right) \tag{5.60b}$$

$$= \mathscr{I}_j^{|\psi\rangle}(t,t')\,\mathscr{I}_j^{|\psi\rangle\dagger}(t,t') \tag{5.60c}$$

and we define the short notations

$$\hat{\Pi}_j^{|\psi\rangle}(t) = \hat{\Pi}_j^{|\psi\rangle}(t,t), \tag{5.61}$$

$$\mathscr{I}_j^{|\psi\rangle}(t) = \mathscr{I}_j^{|\psi\rangle}(t,t). \tag{5.62}$$

The crucial observation now is that with

$$\hat{H}_n(t) = \frac{1}{L\,\||\psi(t)\rangle\|}\hat{\Pi}_n^{|\psi\rangle}(t)\,\hat{H}(t)\,\hat{\Pi}_n^{|\psi\rangle}(t) \tag{5.63}$$

indeed an approximate Lie-Trotter decomposition of the time-dependent Schrödinger equation is obtained assuming that $\||\psi(t)\rangle\|$ is invariant under the time evolution. In a further approximation, we may, thus, conduct the time evolution sequentially.

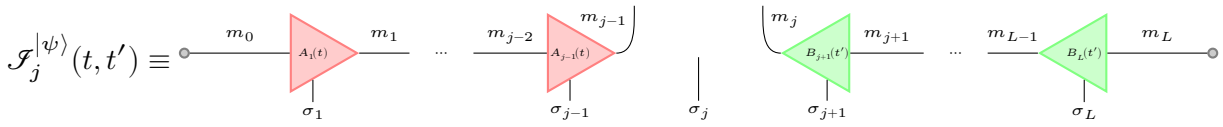

Figure 5.11: Pictorial representation of the isolation operator $\mathscr{I}_j^{|\psi\rangle}(t,t')$, c.f. equation (5.59).

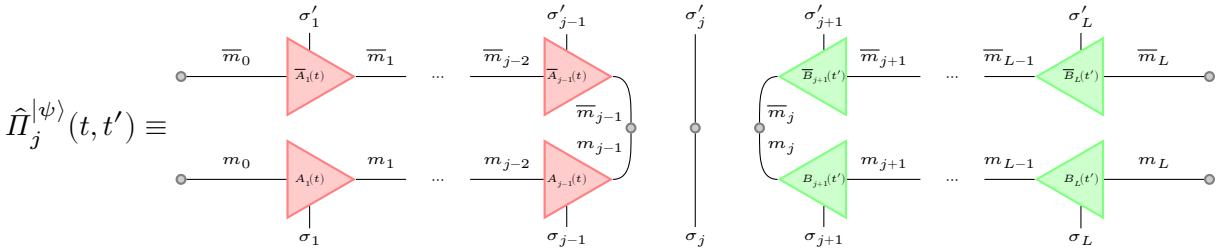

Figure 5.12: Pictorial representation of the projector $\hat{\Pi}_j^{|\psi\rangle}(t,t')$, c.f. equation (5.60).

Let us therefore consider the general partially time-evolved state in MPS mixed-canonical representation with active site j

$$\left|\psi_j(t',t,t'')\right\rangle = \sum_{\sigma_1,\ldots,\sigma_L} A_1^{\sigma_1}(t')\cdots A_{j-1}^{\sigma_{j-1}}(t')\, M_j^{\sigma_j}(t)\, B_{j+1}^{\sigma_{j+1}}(t'')\cdots B_L^{\sigma_L}(t'')\left|\sigma_1,\ldots,\sigma_L\right\rangle, \tag{5.64}$$

see figure 5.13. We now compute the time evolution according to equation (5.17) or (5.21) using

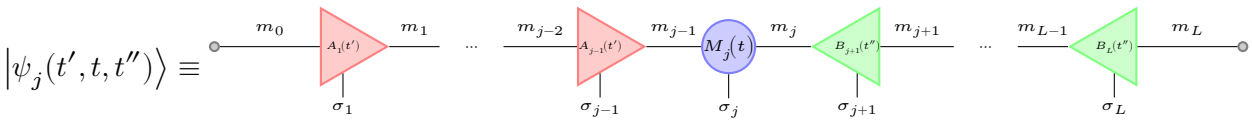

Figure 5.13: Pictorial representation of the general partially time-evolved state in MPS mixed-canonical representation with active site j, $\left|\psi_j(t',t,t'')\right\rangle$, c.f. equation (5.64).

the single-site Hamiltonian (5.63) obtained from the Lie-Trotter decomposition of the Schrödinger equation and find

$$\left|\psi_j(t',t+\delta t,t'')\right\rangle = U_j(t+\delta t,t)\left|\psi_j(t',t,t'')\right\rangle = \mathrm{e}^{-\mathrm{i}\hat{H}_j(t)\delta t}\left|\psi_j(t',t,t'')\right\rangle \tag{5.65a}$$

$$= \mathrm{e}^{-\mathrm{i}\frac{1}{L\||\psi(t)\rangle\|}\hat{\Pi}_j^{|\psi\rangle}(t',t'')\hat{H}(t)\hat{\Pi}_j^{|\psi\rangle}(t',t'')\delta t}\left|\psi_j(t',t,t'')\right\rangle \tag{5.65b}$$

$$= \mathscr{I}_j^{|\psi\rangle}(t',t'')\,\mathrm{e}^{-\mathrm{i}\frac{1}{L\||\psi(t)\rangle\|}\mathscr{I}_j^{|\psi\rangle\dagger}(t',t'')\hat{H}(t)\mathscr{I}_j^{|\psi\rangle}(t',t'')\delta t}\,\mathscr{I}_j^{|\psi\rangle\dagger}(t',t'')\left|\psi_j(t',t,t'')\right\rangle. \tag{5.65c}$$

Note that the argument in the exponential has a very familiar structure, namely

$$\mathscr{O}_j(t',t,t'') = \mathscr{I}_j^{|\psi\rangle\dagger}(t',t'')\,\hat{H}(t)\,\mathscr{I}_j^{|\psi\rangle}(t',t'') = \mathscr{W}_{j-1}^{\mathscr{L}}(t',t)\,W_j^{\sigma_j,\sigma_j'}(t)\,\mathscr{W}_{j+1}^{\mathscr{R}}(t'',t), \tag{5.66}$$

c.f. figure 5.14, which is the exact same tensor as defined in equation (5.11), including the left and right tensors from equation (5.6) and (5.7), respectively, the only difference being the time dependence of the tensors. All W-matrices of the Hamiltonian $\hat{H}(t)$, which for the sufficiently small chosen step size in the discretization is taken to be fairly constant, will of course all invariably depend on t, all A-matrices in $\mathscr{W}_{j-1}^{\mathscr{L}}(t',t)$ then depend on t', and, likewise, all B-matrices in $\mathscr{W}_{j-1}^{\mathscr{R}}(t'',t)$ on t''. We stress that the t-dependence in both, $\mathscr{W}_{j-1}^{\mathscr{L}}(t',t)$ and $\mathscr{W}_{j-1}^{\mathscr{R}}(t'',t)$, is solely due to the

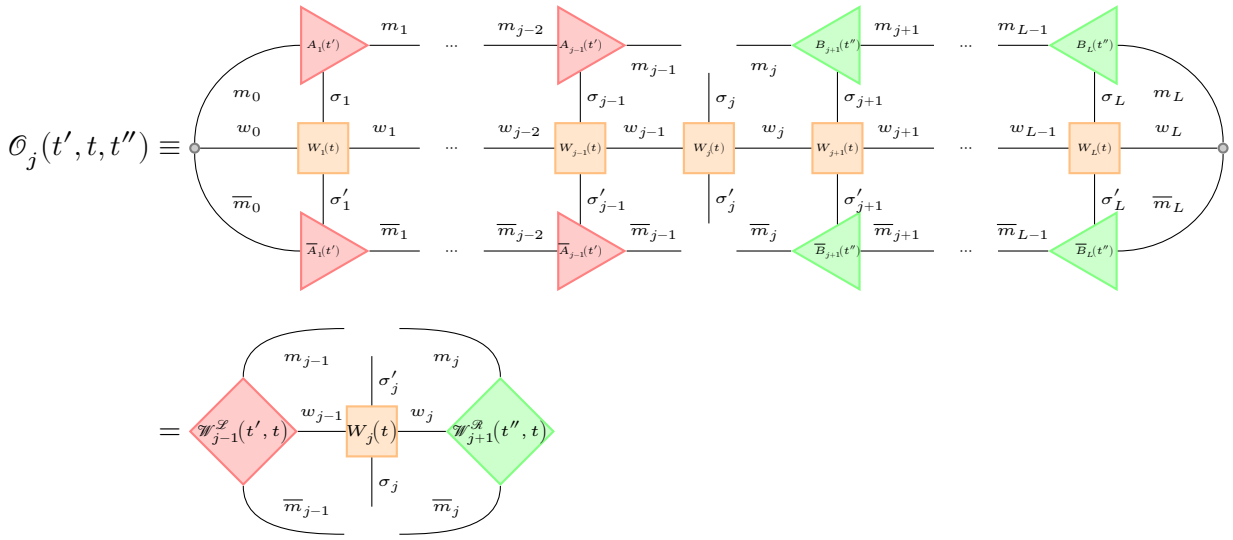

Figure 5.14: Pictorial representation of equation (5.66).

W-matrices of the Hamiltonian. Bearing in mind equations (5.8) and (5.9), we note that these tensors can efficiently be constructed recursively making them accessible at a reasonable cost in a site-wise integration scheme.

Realizing that

$$\mathscr{I}_j^{|\psi\rangle\dagger}(t',t'')\left|\psi_j(t',t,t'')\right\rangle = M_j^{\sigma_j}(t)\left|\sigma_j\right\rangle, \tag{5.67}$$

see also figure 5.15, applying $\mathscr{I}_j^{|\psi\rangle\dagger}(t',t'')$ to both sides we may greatly simplify equation (5.65) to just

$$M_j^{\sigma_j}(t+\delta t) = \mathrm{e}^{-\mathrm{i}\frac{1}{L\||\psi(t)\rangle\|}\mathscr{O}_j(t',t,t'')\delta t} M_j^{\sigma_j}(t), \tag{5.68}$$

where we have neglected the physical state $\left|\sigma_j\right\rangle$ as we are now facing a single site problem. This equation is of the exact type as equation (5.15) with $\frac{1}{L\||\psi(t)\rangle\|}\mathscr{O}_j(t',t,t'')$ taking the role of $\hat{H}(t)$

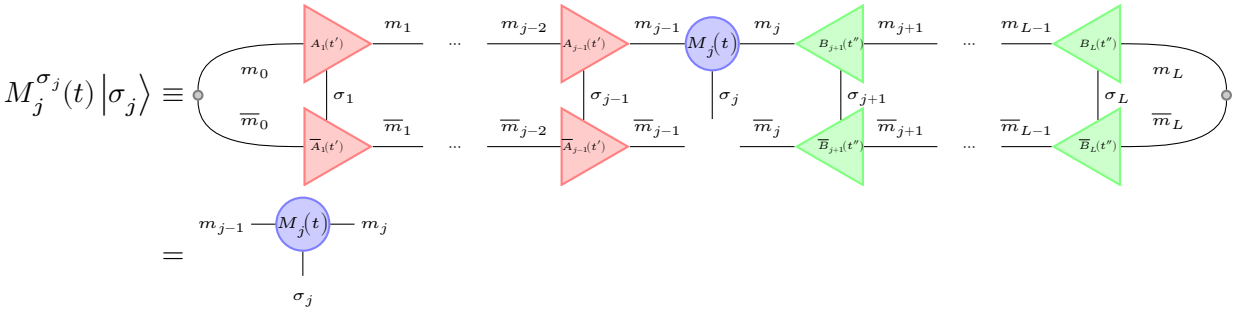

Figure 5.15: Pictorial representation of equation (5.67).

and $M_j^{\sigma_j}$ the one of $|\psi(t)\rangle$. Hence, if $M_j^{\sigma_j}$ is reshaped into a vector and $\frac{1}{L\|\psi(t)\|}\mathcal{O}_j\left(t', t, t''\right)$ into a matrix the Krylov method as explained in section 5.2.3 may be applied to obtain a vector describing $M_j^{\sigma_j}(t+\delta t)$ which can then be reshaped back into a proper M-matrix.

We conclude that we indeed succeeded in reformulating the time evolution of the entire MPS $|\psi(t)\rangle$ into a series of local problems. However, one obstacle remains. We cannot simply shift the orthogonality center from j to $j \pm 1$ (depending on whether we perform a left or a right sweep) as the time evolved M-matrices at time $t+\delta t$ are in general given in a different basis as the initial A- or B-matrices at time t. Instead, we first need to express these tensors in terms of the new basis at time $t+\delta t$. We therefore introduce the basis transformation tensors

$$\mathcal{Q}^{\mathscr{L}}_{j;\overline{m}_j,m_j}(t+\delta t,t) = \sum_{\overline{m}_{j-1},m_{j-1},\sigma_j} \Bigg(\overline{A}^{\sigma_j}_{j;\overline{m}_j,\overline{m}_{j-1}}(t+\delta t) \Bigg(\cdots \Bigg(\sum_{\overline{m}_0,m_0,\sigma_1} \left(\overline{A}^{\sigma_1}_{1;\overline{m}_1,\overline{m}_0}(t+\delta t)\, A^{\sigma_1}_{1;m_0,m_1}(t) \right) \Bigg) \cdots \Bigg) A^{\sigma_j}_{j;m_{j-1},m_j}(t) \Bigg), \tag{5.69}$$

$$\mathcal{Q}^{\mathscr{R}}_{j;m_{j-1},\overline{m}_{j-1}}(t+\delta t,t) = \sum_{\overline{m}_j,m_j,\sigma_j} \Bigg(B^{\sigma_j}_{j;m_{j-1},m_j}(t) \Bigg(\cdots \Bigg(\sum_{\overline{m}_L,m_L,\sigma_L} \left(B^{\sigma_L}_{L;m_{L-1},m_L}(t)\, \overline{B}^{\sigma_L}_{L;\overline{m}_L,\overline{m}_{L-1}}(t+\delta t) \right) \Bigg) \cdots \Bigg) \overline{B}^{\sigma_j}_{j;\overline{m}_j,\overline{m}_{j-1}}(t+\delta t) \Bigg), \tag{5.70}$$

c.f. also figures 5.16 and 5.17, which also may be constructed recursively, c.f. figures 5.18 and 5.19,

$$\mathcal{Q}^{\mathscr{L}}_{j;\overline{m}_j,m_j}(t+\delta t,t) = \sum_{\overline{m}_{j-1},m_{j-1},\sigma_j} \Big(\overline{A}^{\sigma_j}_{j;\overline{m}_j,\overline{m}_{j-1}}(t+\delta t)\, \mathcal{Q}^{\mathscr{L}}_{j-1;\overline{m}_{j-1},m_{j-1}}(t+\delta t,t)\, A^{\sigma_j}_{j;m_{j-1},m_j}(t) \Big), \tag{5.71}$$

$$\mathcal{Q}^{\mathscr{R}}_{j;m_{j-1},\overline{m}_{j-1}}(t+\delta t,t) = \sum_{\overline{m}_j,m_j,\sigma_j} \left(B^{\sigma_j}_{j;m_{j-1},m_j}(t)\, \mathcal{Q}^{\mathscr{R}}_{j+1;m_j,\overline{m}_j}(t+\delta t,t)\, \overline{B}^{\sigma_j}_{j;\overline{m}_j,\overline{m}_{j-1}}(t+\delta t) \right) \tag{5.72}$$

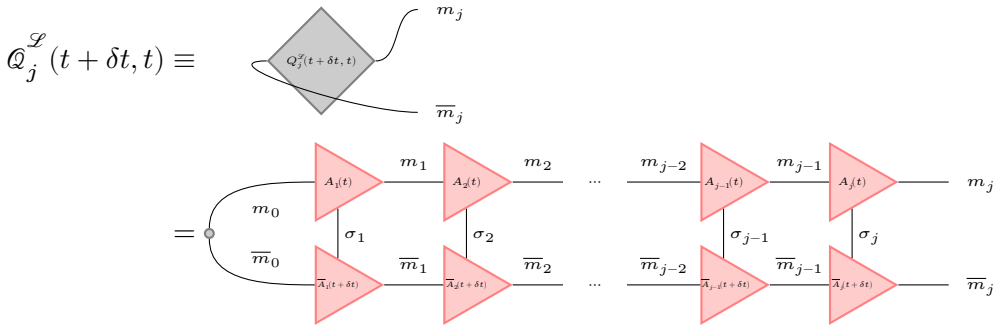

Figure 5.16: Pictorial representation of the left basis transformation tensor $\mathcal{Q}^{\mathscr{L}}_j(t+\delta t,t)$, c.f. equation (5.69).

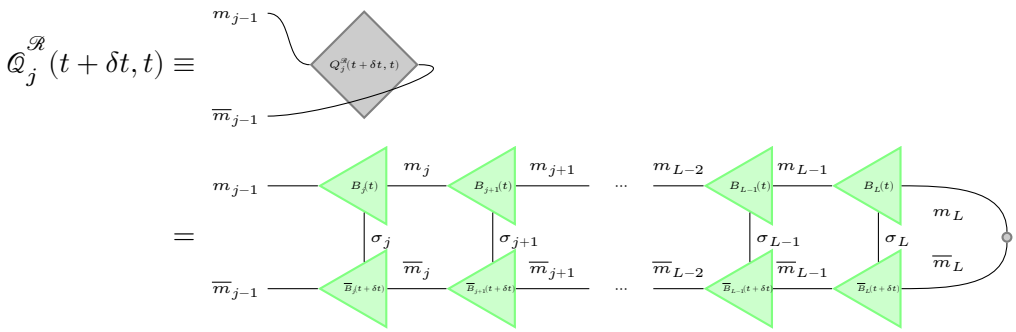

Figure 5.17: Pictorial representation of the left basis transformation tensor $\mathcal{Q}_j^{\mathscr{R}}(t+\delta t, t)$, c.f. equation (5.70).

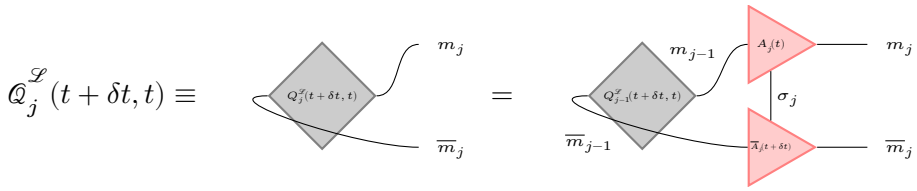

Figure 5.18: Pictorial representation of the recursive construction of the left basis transformation tensor $\mathcal{Q}_j^{\mathscr{L}}(t+\delta t, t)$, c.f. equation (5.71).

with $\mathcal{Q}_0^{\mathscr{L}}(t+\delta t, t)$ and $\mathcal{Q}_{L+1}^{\mathscr{R}}(t+\delta t, t)$ being 1×1 dummy tensors. Then we update the subsequent tensor via

$$M^{\sigma_{j+1}}_{j+1;m_j,m_{j+1}}(t) = \sum_{m_j} \mathcal{Q}^{\mathscr{L}}_{j;\overline{m}_j,m_j}(t+\delta t, t)\, B^{\sigma_{j+1}}_{j+1;m_j,m_{j+1}}(t), \tag{5.73}$$

$$M^{\sigma_{j-1}}_{j-1;m_{j-1},m_j}(t) = \sum_{m_j} A^{\sigma_{j-1}}_{j-1;m_{j-1},m_j}(t)\, \mathcal{Q}^{\mathscr{R}}_{j;m_j,\overline{m}_j}(t+\delta t, t), \tag{5.74}$$

c.f. figures 5.20 and 5.21, in case a right or left sweep is performed, respectively.

In total, the entire algorithm to time evolve an MPS $|\psi(t)\rangle$ to $|\psi(t+\delta t)\rangle$ reads as follows: For a right sweep we require $|\psi(t)\rangle$ to have its active site at $j = 1$ and first need to construct all tensors

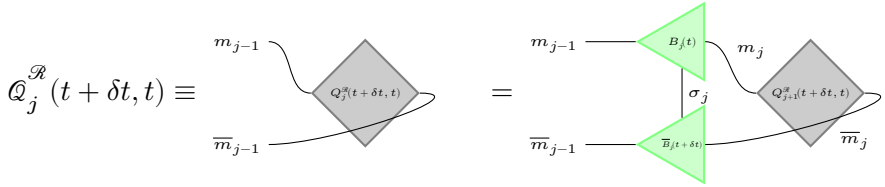

Figure 5.19: Pictorial representation of the recursive construction of the left basis transformation tensor $\mathcal{Q}_j^{\mathscr{R}}(t+\delta t, t)$, c.f. equation (5.72).

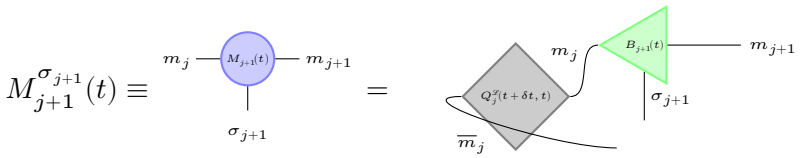

Figure 5.20: Pictorial representation of equation (5.73).

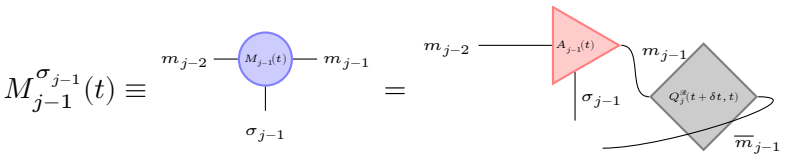

Figure 5.21: Pictorial representation of equation (5.74).

$\mathscr{W}_j^{\mathscr{R}[0]}(t,t)$ according to equation (5.7) unless of course we have access to them from a previous sweep. At this point, we only use B- and W-matrices from $\left|\psi(t)\right\rangle$ and $\hat{H}(t)$, respectively. Then, the steps are as follows (As usual the index in square brackets indicates the number of the sweep.):

1. From $j = 1$ on

   a) From $\left|\psi_j(t+\delta t,t,t)\right\rangle$ construct $\mathscr{O}_j^{[1]}(t+\delta t,t,t)$ according to equation (5.66).

   - Remark: We may identify $\left|\psi_j(t+\delta t,t,t)\right\rangle$ as from equation (5.64) with $\left|\psi_j(t+\delta t,t)\right\rangle$ from equation (5.18).

   b) Solve equation (5.68) to find $M_j^{[1]\sigma_j}(t+\delta t)$ and obtain, hence, $\left|\psi_j(t+\delta t,t+\delta t,t)\right\rangle$.

   - Remark 1: Solving equation (5.68) may, for example be achieved by applying the Krylov method described in section 5.2.3.
   - Remark 2: The state $\left|\psi_j(t+\delta t,t+\delta t,t)\right\rangle$ corresponds to $\left|\psi_{j+1,j}(t+\delta t,t)\right\rangle$ in equation (5.17).

   c) Decompose $M_j^{[1]\sigma_j}(t+\delta t)$ to obtain $A_j^{[1]\sigma_j}(t+\delta t)$.

   - Remark 1: This and the following steps are necessary as the MPS needs to be updated to continue the time evolution as specified by equation (5.18).
   - Remark 2: Either a QR decomposition or an SVD may be applied depending on whether or not truncation is desired similarly to what was explained in section 4.2.2.

   d) Construct $\mathscr{Q}_j^{\mathscr{L}[1]}(t+\delta t,t)$ alongside with $\mathscr{W}_{j-1}^{\mathscr{L}[1]}(t+\delta t,t)$ as defined by equations (5.71) and (5.9), respectively.

   - Remark 1: The remaining part of the decomposition from the previous step is discarded.
   - Remark 2: For the construction of $\mathscr{W}_{j-1}^{\mathscr{L}[1]}(t+\delta t,t)$ we use $A_j^{[1]\sigma_j}(t+\delta t)$ and $W_j^{\sigma_j,\sigma_j'}(t)$.

   e) Update the subsequent tensor $B_{j+1}^{[0]\sigma_{j+1}}(t)$ with the help of $\mathscr{Q}_{j;\overline{m}_j,m_j}^{\mathscr{L}[1]}(t+\delta t,t)$ according to equation (5.73) to obtain $M_{j+1}^{[1]\sigma_{j+1}}(t)$ and, thus, $\left|\psi_{j+1}(t+\delta t,t,t)\right\rangle$.

- Remark: The state $\left|\psi_{j+1}(t+\delta t,t,t)\right\rangle$ then corresponds to $\left|\psi_{j+1}(t+\delta t,t)\right\rangle$ in equation (5.18).

This procedure is repeated until $j=L$ is reached.

For a left sweep we start with $\left|\psi(t)\right\rangle$ to having its active site at $j=L$ and constructing all tensors $\mathscr{W}_j^{\mathscr{L}[0]}(t,t)$ according to equation (5.6) unless they are already known from a previous sweep. We solely use A- and W-matrices from $\left|\psi(t)\right\rangle$ and $\hat{H}(t)$, respectively. Then the procedure goes like this:

1. From $j=L$ on

   a) From $\left|\psi_j(t,t,t+\delta t)\right\rangle$ construct $\mathscr{O}_j^{[1]}(t,t,t+\delta t)$ according to equation (5.66).

   - Remark: We may identify $\left|\psi_j(t,t,t+\delta t)\right\rangle$ as from equation (5.64) with $\left|\psi_j(t+\delta t,t)\right\rangle$ from equation (5.18).

   b) Solve equation (5.68) to find $M_j^{[1]\sigma_j}(t+\delta t)$ and obtain, hence, $\left|\psi_j(t,t+\delta t,t+\delta t)\right\rangle$.

   - Remark 1: As before, solving equation (5.68) may, for example be achieved by applying the Krylov method described in section 5.2.3.
   - Remark 2: The state $\left|\psi_j(t,t+\delta t,t+\delta t)\right\rangle$ corresponds to $\left|\psi_{j-1,j}(t+\delta t,t)\right\rangle$ from equation (5.21).

   c) Decompose $M_j^{[1]\sigma_j}(t+\delta t)$ to obtain $B_j^{[1]\sigma_j}(t+\delta t)$.

   - Remark 1: This and the following steps are necessary as the MPS needs to be updated to continue the time evolution as specified by equation (5.18)..
   - Remark 2: Either a QR decomposition or an SVD may be applied depending on whether or not truncation is desired similarly to what was explained in section 4.2.2.

   d) Construct $\mathscr{Q}_{j;\overline{m}_j,m_j}^{\mathscr{R}[1]}(t+\delta t,t)$ alongside with $\mathscr{W}_{j-1}^{\mathscr{R}[1]}(t+\delta t,t)$ as defined by equations (5.72) and (5.8), respectively.

   - Remark 1: The remaining part of the decomposition from the previous step is discarded.
   - Remark 2: For the construction of $\mathscr{W}_{j-1}^{\mathscr{R}[1]}(t+\delta t,t)$ we use $B_j^{[1]\sigma_j}(t+\delta t)$ and $W_j^{\sigma_j,\sigma_j'}(t)$.

   e) Update the subsequent tensor $A_{j-1}^{[0]\sigma_{j-1}}(t)$ with the help of $\mathscr{Q}_{j;\overline{m}_j,m_j}^{\mathscr{R}[1]}(t+\delta t,t)$ according to (5.74) to obtain $M_{j-1}^{[1]\sigma_{j+1}}(t)$ and, thus, $\left|\psi_{j-1}(t,t,t+\delta t)\right\rangle$.

   - Remark: The state $\left|\psi_{j-1}(t,t,t+\delta t)\right\rangle$ then corresponds to $\left|\psi_{j-1}(t+\delta t,t)\right\rangle$ in equation (5.22).

The sweep ends when $j=1$ is reached.

In a complete time evolution from $t=0$ to $t=t_{\max}$ left and right sweeps are conducted alternately until $t_{\max}$ is reached and after each sweep $\hat{H}(t)$ is updated according to the discretization δt.

5.2.5 The Time-dependent Variational Principle (TDVP)

The principal idea of the TDVP [135, 136] can easily be understood under the assumption that the quantum state $|\psi(t+\delta t)\rangle$ will not differ too much from the original one $|\psi(t)\rangle$. Therefore, instead of projecting $|\psi(t)\rangle$ onto $|\psi(t+\delta t)\rangle$ as does the local Krylov, before the time evolution is conducted, the Hamiltonian $\hat{H}(t)$ is projected onto the tangent space of $|\psi(t)\rangle$ and the solution of the time-dependent Schrödinger equation is only computed on the so-obtained manifold of MPSs.

We therefore define the projector onto the tangent space of $|\psi(t+\delta t)\rangle$ through [283]

$$\mathscr{T}^{|\psi\rangle}(t) = \sum_{j=1}^{L} \mathscr{P}_{j-1}^{|\psi\rangle\mathscr{L}}(t) \otimes \hat{\mathbb{1}}_j \otimes \mathscr{P}_{j+1}^{|\psi\rangle\mathscr{R}}(t) - \sum_{j=1}^{L-1} \mathscr{P}_{j}^{|\psi\rangle\mathscr{L}}(t) \otimes \mathscr{P}_{j+1}^{|\psi\rangle\mathscr{R}}(t) \tag{5.75a}$$

$$= \sum_{j=1}^{L} \mathscr{J}_j^{|\psi\rangle}(t)\, \mathscr{J}_j^{|\psi\rangle\dagger}(t) - \sum_{j=1}^{L-1} \mathscr{J}_j^{|\psi\rangle}(t)\, \mathscr{J}_j^{|\psi\rangle\dagger}(t), \tag{5.75b}$$

where we have introduced

$$\mathscr{J}_j^{|\psi\rangle}(t,t') = \mathscr{P}_j^{|\psi\rangle A}(t) \otimes \mathscr{P}_{j+1}^{|\psi\rangle B}(t'), \tag{5.76}$$

$$\mathscr{J}_j^{|\psi\rangle}(t) = \mathscr{J}_j^{|\psi\rangle}(t,t), \tag{5.77}$$

c.f. figure 5.22. Note that for this construction we used the projectors from the previous section, c.f.

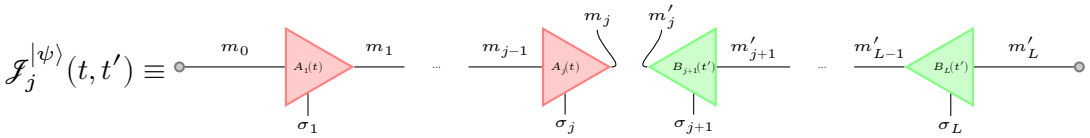

Figure 5.22: Pictorial representation of the projector $\mathscr{J}_j^{|\psi\rangle}(t,t')$, c.f. equation (5.76).

equations (5.55) to (5.62) or equally figures 5.7 to 5.12. The tangent space operator $\mathscr{T}^{|\psi\rangle}(t)$ from equation (5.75) has a rather intuitive interpretation. The first term gives all MPSs that differ in at most one site from the original MPS $|\psi(t)\rangle$ while the second term removes all those MPSs that by coincidence coincide with $|\psi(t)\rangle$. Hence, the tangent space of $|\psi(t)\rangle$ is constructed from MPSs that differ in one site from $|\psi(t)\rangle$, that is $M_j^{\sigma_j}$ is replaced by $\tilde{M}_j^{\sigma_j}$ with [151]

$$M_j^{\sigma_j} \cdot \tilde{M}_j^{\dagger\sigma_j} = 0. \tag{5.78}$$

Thus, instead of solving equation (5.15), we restrict ourselves to only doing the computation on the above defined tangent space, i.e.

$$|\psi(t+\delta t)\rangle = U_{\mathscr{T}^{|\psi\rangle}(t)}(t+\delta t, t)\,|\psi(t)\rangle = \mathrm{e}^{-\mathrm{i}\mathscr{T}^{|\psi\rangle}(t)\hat{H}(t)\delta t}\,|\psi\,(t)\rangle, \tag{5.79}$$

$$= \mathrm{e}^{-\mathrm{i}\left(\sum_{j=1}^{L} \mathscr{J}_j^{|\psi\rangle}(t)\mathscr{J}_j^{|\psi\rangle\dagger}(t) - \sum_{j=1}^{L-1} \mathscr{J}_j^{|\psi\rangle}(t)\mathscr{J}_j^{|\psi\rangle\dagger}(t)\right)\hat{H}(t)\delta t}\,|\psi\,(t)\rangle. \tag{5.80}$$

As this problem, still, is not solvable in general, we in a first order approximation decompose the above equation into $2L-1$ individual problems

$$\left|\psi(t+\delta t)\right\rangle = \mathrm{e}^{-\mathrm{i}\mathscr{F}_j^{|\psi\rangle}(t)\mathscr{F}_j^{|\psi\rangle\dagger}(t)\hat{H}(t)\delta t}\left|\psi\,(t)\right\rangle, \tag{5.81}$$

$$\left|\psi(t+\delta t)\right\rangle = \mathrm{e}^{+\mathrm{i}\mathscr{F}_j^{|\psi\rangle}(t)\mathscr{F}_j^{|\psi\rangle\dagger}(t)\hat{H}(t)\delta t}\left|\psi\,(t)\right\rangle, \tag{5.82}$$

which we solve sequentially having again split the original problem into a series of local ones. Note in particular that of those $2L-1$ problems we have L forward time evolutions (5.81) and $L-1$ backward time evolutions (5.82).

Let us therefore again begin with the general partially time-evolved quantum state in MPS mixed-canonical representation with active site j, c.f. also equation (5.64) or figure 5.13,

$$\left|\psi_j(t',t,t'')\right\rangle = \sum_{\sigma_1,\ldots,\sigma_L} A_1^{\sigma_1}(t')\cdots A_{j-1}^{\sigma_{j-1}}(t')\,M_j^{\sigma_j}(t)\,B_{j+1}^{\sigma_{j+1}}(t'')\cdots B_L^{\sigma_L}(t'')\left|\sigma_1,\ldots,\sigma_L\right\rangle. \tag{5.83}$$

For sequentially solving the individual problems, equation (5.81) takes the form

$$\left|\psi_j(t',t+\delta t,t'')\right\rangle = \mathrm{e}^{-\mathrm{i}\mathscr{F}_j^{|\psi\rangle}(t',t'')\mathscr{F}_j^{|\psi\rangle\dagger}(t',t'')\hat{H}(t)\delta t}\left|\psi_j(t',t,t'')\right\rangle \tag{5.84a}$$

$$= \mathrm{e}^{-\mathrm{i}\mathscr{F}_j^{|\psi\rangle}(t',t'')\mathscr{F}_j^{|\psi\rangle\dagger}(t',t'')\hat{H}(t)\delta t}\mathscr{F}_j^{|\psi\rangle}(t',t'')\,\mathscr{F}_j^{|\psi\rangle\dagger}(t',t'')\left|\psi_j(t',t,t'')\right\rangle \tag{5.84b}$$

$$= \mathscr{F}_j^{|\psi\rangle}(t',t'')\,\mathrm{e}^{-\mathrm{i}\mathscr{F}_j^{|\psi\rangle\dagger}(t',t'')\hat{H}(t)\mathscr{F}_j^{|\psi\rangle}(t',t'')\delta t}\mathscr{F}_j^{|\psi\rangle\dagger}(t',t'')\left|\psi_j(t',t,t'')\right\rangle, \tag{5.84c}$$

which, with the exception of the prefactor $\frac{1}{L\||\psi(t)\rangle\|}$, is exactly the same as equation (5.65). Thus, c.f. equation (5.66) or figure 5.14, we again identify the exponential with

$$\mathscr{O}_j(t',t,t'') = \mathscr{F}_j^{|\psi\rangle\dagger}(t',t'')\,\hat{H}\,(t)\,\mathscr{F}_j^{|\psi\rangle}(t',t'') = \mathscr{W}_{j-1}^{\mathscr{L}}(t',t)\,W_j^{\sigma_j,\sigma_j'}(t)\,\mathscr{W}_{j+1}^{\mathscr{R}}(t'',t) \tag{5.85}$$

thereby obtaining the tensor (5.11) with time-dependent left and right tensors from equation (5.6) and (5.7), respectively. Bearing in mind equation (5.67) and multiplying both sides of equation (5.84) by $\mathscr{F}_j^{|\psi\rangle\dagger}(t',t'')$ we find neglecting the physical state $\left|\sigma_j\right\rangle$

$$M_j^{\sigma_j}(t+\delta t) = \mathrm{e}^{-\mathrm{i}\mathscr{O}_j(t',t,t'')\delta t}M_j^{\sigma_j}(t), \tag{5.86}$$

in strict analogy to equation (5.68). Hence, this problem may be solved by means of the Krylov method as explained in section 5.2.3.

In order to derive a similar single-site problem for the backward time evolution (5.82) we proceed analogously. First, we introduce the general partially time-evolved transition state with active site j

$$\left|\psi_{C;j}(t',t,t'')\right\rangle = \sum_{\sigma_1,\ldots,\sigma_L} A_1^{\sigma_1}(t')\cdots A_j^{\sigma_j}(t')\,C_j(t)\,B_{j+1}^{\sigma_{j+1}}(t'')\cdots B_L^{\sigma_L}(t'')\left|\sigma_1,\ldots,\sigma_L\right\rangle, \tag{5.87}$$

c.f. figure 5.23, allowing us similarly to the derivation of problem (5.84) to transform equation (5.82) into

$$\left|\psi_{C;j}(t',t,t'')\right\rangle = \mathrm{e}^{\mathrm{i}\mathscr{F}_j^{|\psi_C\rangle}(t',t'')\mathscr{F}_j^{|\psi_C\rangle\dagger}(t',t'')\hat{H}(t)\delta t}\left|\psi_{C;j}(t',t+\delta t,t'')\right\rangle \tag{5.88a}$$

$\left|\psi_{C;j}(t',t,t'')\right\rangle \equiv$

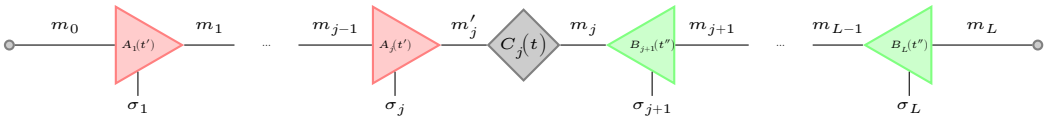

Figure 5.23: Pictorial representation of the general partially time-evolved transition state with active site j, $\left|\psi_{C;j}(t',t,t'')\right\rangle$, c.f. equation (5.87).

$$= \mathrm{e}^{\mathrm{i}\mathscr{J}_j^{|\psi_C\rangle}(t',t'')\mathscr{J}_j^{|\psi_C\rangle\dagger}(t',t'')\hat{H}(t)\delta t}\,\mathscr{J}_j^{|\psi_C\rangle}(t',t'')\,\mathscr{J}_j^{|\psi_C\rangle\dagger}(t',t'')\left|\psi_{C;j}(t',t+\delta t,t'')\right\rangle \tag{5.88b}$$

$$= \mathscr{J}_j^{|\psi_C\rangle}(t',t'')\,\mathrm{e}^{\mathrm{i}\mathscr{J}_j^{|\psi_C\rangle\dagger}(t',t'')\hat{H}(t)\mathscr{J}_j^{|\psi_C\rangle}(t',t'')\delta t}\,\mathscr{J}_j^{|\psi_C\rangle\dagger}(t',t'')\left|\psi_{C;j}(t',t+\delta t,t'')\right\rangle, \tag{5.88c}$$

The argument in the exponential for this computation can be expressed via

$$\mathscr{O}_{C;j}(t',t,t'') = \mathscr{J}_j^{|\psi_C\rangle\dagger}(t',t'')\,\hat{H}(t)\,\mathscr{J}_j^{|\psi_C\rangle}(t',t'') = \mathscr{W}_j^{\mathscr{L}}(t',t)\,\mathscr{W}_{j+1}^{\mathscr{R}}(t'',t), \tag{5.89}$$

c.f. figure 5.24, using again time-dependent versions of the left and right tensors from equation

$\mathscr{O}_{C;j}(t',t,t'') \equiv$

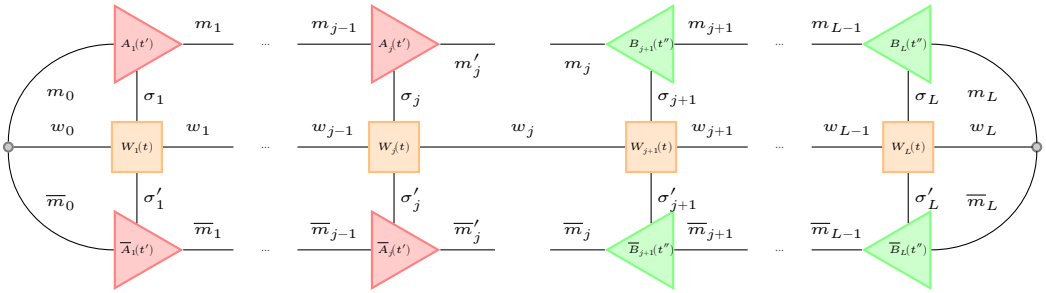

$=$

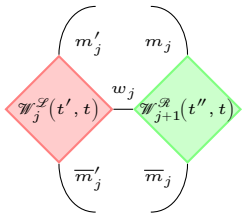

Figure 5.24: Pictorial representation of equation (5.89).

(5.6) and (5.7), respectively, where all A-matrices in $\mathscr{W}_{j-1}^{\mathscr{L}}(t',t)$ depend on t', all B-matrices in $\mathscr{W}_{j-1}^{\mathscr{R}}(t'',t)$ on t'', and the dependence on time t is only due to the W-matrices of the Hamiltonian. Evidently $\mathscr{O}_{C;j}(t',t,t'')$ can, thus, be constructed recursively as follows from equations (5.8) and (5.9). We compute

$$\mathscr{J}_j^{|\psi_C\rangle\dagger}(t',t'')\left|\psi_{C;j}(t',t,t'')\right\rangle = C_j(t), \tag{5.90}$$

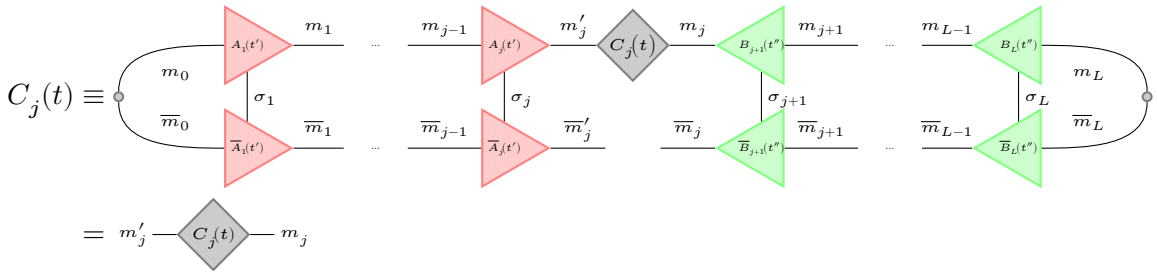

Figure 5.25: Pictorial representation of equation (5.90).

c.f. figure 5.25, and apply $\mathscr{J}_j^{|\psi_C\rangle\dagger}(t',t'')$ to both sides of equation (5.88) to find

$$C_j(t) = \mathrm{e}^{\mathrm{i}\mathscr{O}_{C;j}(t',t,t'')\delta t} C_j(t+\delta t), \tag{5.91}$$

which, as before, is of type (5.15) with $\mathscr{O}_{C;j}(t',t,t'')$ as $\hat{H}(t)$ and C_j as $|\psi(t)\rangle$, its solution being obtained from the Krylov method explained in section 5.2.3.

Now we have all the ingredients to formulate the TDVP algorithm in its entirety: For a right sweep we start with $|\psi(t)\rangle$ with its active site at $j=1$ and construct all tensors $\mathscr{W}_j^{\mathscr{R}[0]}(t,t)$ according to equation (5.7) in case we do not have access to them from a previous sweep using only B- and W-matrices from $|\psi(t)\rangle$ and $\hat{H}(t)$, respectively. Then the routine goes as follows, the index in square brackets specifies again the number of the sweep:

1. From $j=1$ on

   a) From $|\psi_j(t+\delta t,t,t)\rangle$ construct $\mathscr{O}_j^{[1]}(t+\delta t,t,t)$ according to equation (5.85).

   - Remark: We may identify $|\psi_j(t+\delta t,t,t)\rangle$ as from equation (5.83) with $|\psi_j(t+\delta t,t)\rangle$ from equation (5.18).

   b) Solve equation (5.86) to find $M_j^{[1]\sigma_j}(t+\delta t)$ and obtain, hence, $|\psi_j(t+\delta t,t+\delta t,t)\rangle$.

   - Remark 1: Solving equation (5.86) may, for example, be achieved by applying the Krylov method described in section 5.2.3
   - Remark 2: The state $|\psi_j(t+\delta t,t+\delta t,t)\rangle$ corresponds to $|\psi_{j+1,j}(t+\delta t,t)\rangle$ in equation (5.17).

   c) Decompose

   $$M_j^{[1]\sigma_j}(t+\delta t) = A_j^{[1]\sigma_j}(t+\delta t)\cdot C_j^{[1]}(t+\delta t), \tag{5.92}$$

   c.f. figure 5.26, yielding the state $|\psi_{C;j}(t+\delta t,t+\delta t,t)\rangle$, c.f. equation (5.87).

   - Remark: Here, a QR decomposition rather than an SVD is preferably applied as that way both, the norm as, well as the energy of the state are conserved.

   d) Construct $\mathscr{W}_j^{\mathscr{L}[1]}(t+\delta t,t)$ and therefrom $\mathscr{O}_{C;j}(t+\delta t,t+\delta t,t)$ as defined by equations (5.9) and (5.89), respectively.

   e) Solve equation (5.91) to obtain $C_j^{[1]}(t)$.

   - Remark: Again, the Krylov method, c.f. section 5.2.3, may be applied here.

f) Contract

$$M_{j+1}^{[1]\sigma_j}(t) = C_j^{[1]}(t) \cdot B_{j+1}^{[0]\sigma_{j+1}}(t), \tag{5.93}$$

5.27, to end up with $\left|\psi_{j+1}(t+\delta t, t, t)\right\rangle$.

- Remark 1: Now, $\left|\psi_{j+1}(t+\delta t, t, t)\right\rangle$ corresponds to $\left|\psi_{j+1}(t+\delta t, t)\right\rangle$ in equation (5.18).
- Remark 2: Only by means of this second backward time evolution equation (5.18) is satisfied.

At $j = L$ the sweep has ended and we have time evolved $\left|\psi(t+\delta t)\right\rangle$ from $\left|\psi(t)\right\rangle$.

$$M_j^{[1]\sigma_j}(t+\delta t) \equiv$$

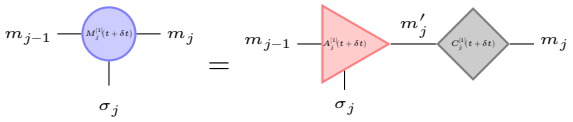

Figure 5.26: Pictorial representation of equation (5.92).

$$M_{j+1}^{[1]\sigma_{j+1}}(t) \equiv$$

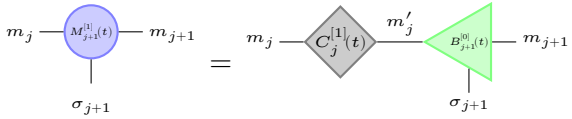

Figure 5.27: Pictorial representation of equation (5.93).

The procedure for a left sweep works quite analogously. We begin with $\left|\psi(t)\right\rangle$, the active site being $j = L$ and might need to construct all tensors $\mathscr{W}_j^{\mathscr{L}[0]}(t,t)$ defined by equation (5.6). Only A- and W-matrices from $\left|\psi(t)\right\rangle$ and $\hat{H}(t)$, respectively, are incorporated at this point. Then the algorithm goes

1. From $j = L$ on

   a) From $\left|\psi_j(t, t, t+\delta t)\right\rangle$ construct $\mathscr{O}_j^{[1]}(t, t, t+\delta t)$ according to equation (5.85).

   - Remark: We may identify $\left|\psi_j(t, t, t+\delta t)\right\rangle$ as from equation (5.83) with $\left|\psi_j(t+\delta t, t)\right\rangle$ from equation (5.18).

   b) Solve equation (5.86) to find $M_j^{[1]\sigma_j}(t+\delta t)$ and obtain, hence, $\left|\psi_j(t, t+\delta t, t+\delta t)\right\rangle$.

   - Remark 1: As before, solving equation (5.86) may, for example, be achieved by applying the Krylov method described in section 5.2.3
   - Remark 2: The state $\left|\psi_j(t, t+\delta t, t+\delta t)\right\rangle$ corresponds to $\left|\psi_{j-1,j}(t+\delta t, t)\right\rangle$ in equation (5.21).

   c) Decompose

$$M_j^{[1]\sigma_j}(t+\delta t) = C_{j-1}^{[1]}(t+\delta t) \cdot B_j^{[1]\sigma_j}(t+\delta t), \tag{5.94}$$

   c.f. figure 5.28, yielding the state $\left|\psi_{C;j}(t, t+\delta t, t+\delta t)\right\rangle$, c.f. equation (5.87).

   - Remark: Here, a QR decomposition rather than an SVD is preferably applied as that way both, the norm as, well as the energy of the state are conserved.

d) Construct $\mathscr{W}_j^{\mathscr{R}[1]}(t+\delta t, t)$ and therefrom $\mathscr{O}_{C;j}(t, t+\delta t, t+\delta t)$ as defined by equations (5.8) and (5.89), respectively.

e) Solve equation (5.91) to obtain $C_{j-1}^{[1]}(t)$.

- Remark: Again, the Krylov method, c.f. section 5.2.3, may be applied here.

f) Contract

$$M_{j-1}^{[1]\sigma_{j-1}}(t) = A_{j-1}^{[0]\sigma_{j-1}}(t) \cdot C_{j-1}^{[1]}(t), \tag{5.95}$$

c.f. figure 5.29, to end up with $\left|\psi_{j-1}(t, t, t+\delta t)\right\rangle$.

- Remark 1: Now, $\left|\psi_{j-1}(t, t, t+\delta t)\right\rangle$ corresponds to $\left|\psi_{j-1}(t+\delta t, t)\right\rangle$ in equation (5.22).
- Remark 2: Only by means of this second backward time evolution equation (5.22) is satisfied.

The sweep is complete when $j = 1$ is reached.

$M_j^{[1]\sigma_j}(t+\delta t) \equiv$ 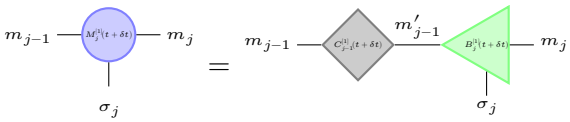 $=$

Figure 5.28: Pictorial representation of equation (5.94).

$M_{j-1}^{[1]\sigma_{j-1}}(t) \equiv$ 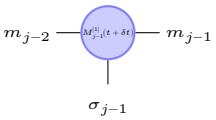 $=$ 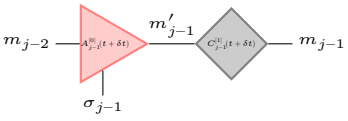

Figure 5.29: Pictorial representation of equation (5.95).

Just like for the local Krylov method in a complete time evolution left and right sweeps are conducted alternately until the maximum time is reached and after each sweep $\hat{H}(t)$ is updated according to the discretization δt.

5.3 One-site Vs. Two-site Implementations

For all variational methods from the above chapters, including the variational compression and the variational MPO application, as well as the local Krylov algorithm, we have presented the so-called one-site variant only. An extension to all these methods is provided by a two-site variant, where instead of one active site, two neighboring active sites are modified in each step of each sweep. In case of a right sweep, we construct a two-site active tensor by reshaping

$$M_{j,j+1}^{\sigma_j,\sigma_{j+1}} = M_j^{\sigma_j} B_{j+1}^{\sigma_{j+1}}, \tag{5.96}$$

for a left sweep, we have

$$M_{j-1,j}^{\sigma_{j-1},\sigma_j} = A_{j-1}^{\sigma_{j-1}} M_j^{\sigma_j}, \tag{5.97}$$

and clearly, the left and right tensors need to be adjusted accordingly. The principal ideas of the respective algorithms, however, remain the same. Once the two-site active tensor is updated, it is decomposed to obtain the new A- or B-matrix, respectively. At this point, the algorithms proceed slightly differently. The two-site local Krylov method discards the remainder of the SVD of the time-evolved two-site active tensor and projects the two subsequent sites from j on into the new basis. The two-site implementation of the TDVP, instead, uses the remainder to construct an M-matrix at site $j \pm 1$ and then does the backward time evolution as in the one-site implementation. In DMRG the procedure is similar: After solving the local problem, e.g. by means of applying the Lanczos algorithm, for the two-site active tensor, the result is SV decomposed and the remainder is simply fused to the subsequent tensor which corresponds to an ordinary shift of the active site. The extension for the variational MPS truncation and the variational MPO application is by far the easiest. After the SVD, the remainder is discarded and the next two-site active tensor is constructed.

With more operations required the two-site variants for all the algorithms are obviously slower than their one-site counterparts. Nevertheless, most often the two-site variants are preferred as they allow through the SVD for flexibility regarding the bond dimensions, that is it can be enhanced, if during the algorithm the originally chosen one turns out to be too small. Yet still, another disadvantage is that the extra SVD will, provided truncation is applied, introduce an additional error. Especially when it comes to the TDVP its two-site variant is disadvantageous in the sense that unlike for the one-site implementation both, the norm and the energy, of the time-evolved MPS are no conserved quantities anymore. Hence, often times a hybrid scheme is employed. First the time evolution is computed using the two-site variant until the bond dimension saturates or a previously specified maximum value is reached, afterwards the scheme is changed to the one-site implementation, c.f. references [283, 280, 127] for further reading.

6 Single Particle Spectral Functions and Optical Conductivities In and Out-of-equilibrium and Excitation Protocols

We present the spectral function, as well as the optical conductivity as the principle observables for our investigations. We will show that these quantities are related to one another. Since both are measured in different types of experiments, we will, hence, also discuss and later compute both. Here we proceed similarly as is done in reference [284] which served as the basis for this chapter. However, we shall also go beyond and explore several variants for the theoretical description of out-of-equilibrium setups. As we shall learn there is no single general theory. Instead, depending on the particular problem different approaches have been proposed of which we will give a brief overview at the end of this chapter.

6.1 Spectral Functions

Spectral functions have already been described in great detail, where, at this point we refer to two examples [48, 178] for detailed explanations and [357] for a quick introduction. All these works have in common, however, that they concern equilibrium, both thermal and non-thermal, systems, c.f. for instance [260]. Even in these cases, however, the computation of spectral functions is a non-trivial task when it comes to many-body problems. Here, often only an approximative solution is possible. A standard approach would be the application of perturbation theory as for example in references [75, 113, 430, 230]. Still, spectral functions have already been computed numerically applying the DMRG, see for instance [203, 414]. Spectral functions are of great importance when it comes to the theoretical explanation of equilibrium [71], as well as non-equilibrium [184] ARPES-type experiments.

However, when it comes to a description of out-of-equilibrium phenomena, the situation is quite confusing since instead of a single clear approach there exists a plethora of different definitions depending on the particular problem at hand. The theoretical challenge, as we shall particularly elaborate on in section 6.1.2, is how to transform a two-time Green's function into a single-frequency spectral function. Indeed, this problems is only hardly covered even in modern textbooks, see for instance [347]. While some approaches conduct two partial transformations, c.f. for example [266], others only do one. This path has, for instance, been chosen in references [15, 51, 255, 256, 257] and shall also be our method of choice. Thus, in this section we shall first present our definition of Green's functions to then directly derive time-dependent non-equilibrium spectral functions from which their equilibrium analog may be derived as a special case. We will predominantly focus on a Fourier transform-based approach to obtain the spectral functions, but also briefly outline how to construct them from a frequency space approach, namely the Chebyshev formalism followed by an explanation of why this procedure is impractical to a treatment of non-equilibrium problems. We only mention at this point that there do exist other methods, for instance the band Lanczos

algorithm, c.f. [213], but will refrain from further explanations at this point. While the topic of non-equilibrium spectral functions is in general rather wide, we refer to [5] for a brief introduction. We will devote section 6.3 to discussing more complex problems.

6.1.1 Green's Functions

We define the lesser and greater Green's function for operators $\hat{A}$ and $\hat{B}$ and times t_1 and t_2 with respect to state $|\psi\rangle$ via

$$\mathscr{G}^{<}_{\hat{A},\hat{B}}(t_1,t_2) = \langle\psi|\,\hat{A}(t_1)\,\hat{B}(t_2)\,|\psi\rangle, \tag{6.1}$$

$$\mathscr{G}^{>}_{\hat{A},\hat{B}}(t_1,t_2) = \langle\psi|\,\hat{B}(t_2)\,\hat{A}(t_1)\,|\psi\rangle. \tag{6.2}$$

Employing a mixture of the Heisenberg and the Schrödinger picture, exploiting basic properties of the time evolution operator $U(t_2,t_1)$, c.f. sections 2.4 and 2.5, respectively, we find these functions to fulfill the following identities

$$\begin{aligned}
\mathscr{G}^{<}_{\hat{A},\hat{B}}(t_1,t_2) &= \langle\psi|\,\hat{A}(t_1)\,\hat{B}(t_2)\,|\psi\rangle = \langle\psi|\,U^\dagger(t_1,0)\,\hat{A}U(t_1,0)\,U^\dagger(t_2,0)\,\hat{B}U(t_2,0)\,|\psi\rangle && \text{(6.3a)}\\
&= \langle\psi|\,U^\dagger(t_2,0)\,U(t_2,0)\,U^\dagger(t_1,0)\,\hat{A}U(t_1,0)\,U^\dagger(t_2,0)\,\hat{B}U(t_2,0)\,|\psi\rangle && \text{(6.3b)}\\
&= \langle\psi(t_2)|\,\hat{A}(t_1-t_2)\,\hat{B}\,|\psi(t_2)\rangle && \text{(6.3c)}\\
&= \langle\psi|\,U^\dagger(t_1,0)\,\hat{A}U(t_1,0)\,U^\dagger(t_2,0)\,\hat{B}U(t_2,0)\,U^\dagger(t_1,0)\,U(t_1,0)\,|\psi\rangle && \text{(6.3d)}\\
&= \langle\psi(t_1)|\,\hat{A}\hat{B}(t_2-t_1)\,|\psi(t_1)\rangle, && \text{(6.3e)}\\
\mathscr{G}^{>}_{\hat{A},\hat{B}}(t_1,t_2) &= \langle\psi|\,\hat{B}(t_2)\,\hat{A}(t_1)\,|\psi\rangle = \langle\psi|\,U^\dagger(t_2,0)\,\hat{B}U(t_2,0)\,U^\dagger(t_1,0)\,\hat{A}U(t_1,0)\,|\psi\rangle && \text{(6.4a)}\\
&= \langle\psi|\,U^\dagger(t_1,0)\,U(t_1,0)\,U^\dagger(t_2,0)\,\hat{B}U(t_2,0)\,U^\dagger(t_1,0)\,\hat{A}U(t_1,0)\,|\psi\rangle && \text{(6.4b)}\\
&= \langle\psi(t_1)|\,\hat{B}(t_2-t_1)\,\hat{A}\,|\psi(t_1)\rangle && \text{(6.4c)}\\
&= \langle\psi|\,U^\dagger(t_2,0)\,\hat{B}U(t_2,0)\,U^\dagger(t_1,0)\,\hat{A}U(t_1,0)\,U^\dagger(t_2,0)\,U(t_2,0)\,|\psi\rangle && \text{(6.4d)}\\
&= \langle\psi(t_2)|\,\hat{B}\hat{A}(t_1-t_2)\,|\psi(t_2)\rangle. && \text{(6.4e)}
\end{aligned}$$

Note that compared to most standard textbooks we have neglected the imaginary unit i and (different) signs in our definitions of $\mathscr{G}^{<}_{\hat{A},\hat{B}}(t_1,t_2)$ and $\mathscr{G}^{>}_{\hat{A},\hat{B}}(t_1,t_2)$.

6.1.2 Derivation of the Spectral Function

Based on the definition of the lesser and greater Green's functions, (6.1) and (6.2), from the above section, we define momentum-dependent specifications

$$\mathscr{G}^{<}(k,t_1,t_2) = \mathscr{G}^{<}_{\hat{c}_k^\dagger,\hat{c}_k}(t_1,t_2) = \langle\psi|\,\hat{c}_k^\dagger(t_1)\,\hat{c}_k(t_2)\,|\psi\rangle, \tag{6.5}$$

$$\mathscr{G}^{>}(k,t_1,t_2) = \mathscr{G}^{>}_{\hat{c}_k^\dagger,\hat{c}_k}(t_1,t_2) = \langle\psi|\,\hat{c}_k(t_2)\,\hat{c}_k^\dagger(t_1)\,|\psi\rangle\,, \tag{6.6}$$

where $\hat{c}_k^{(\dagger)}$ is the annihilation (creation) operator for a single fermion of momentum k. For the remainder of this chapter, we extend the notion of k not only to the physical momentum but also to other quantum numbers like spin or band indices. It may, thus, be also regarded as a superindex.

The momentum dependent Green's functions form the basis to introducing time-dependent lesser and greater spectral functions. Clearly, to obtain such spectral functions at this point a Fourier transform from time to frequency space needs to be performed, which, however, as there are two time variables, may be done in different ways. In principle, there exist two procedures yielding two similar yet in general different definitions. For further reading on this issue we refer, for instance, to [179].

We begin with the definition in so-called Wigner coordinates, where we have

$$\mathscr{A}^{<}(k,\omega,t) = \int_{-\infty}^{\infty} \mathrm{d}t' \mathrm{e}^{-\mathrm{i}\omega t'} \mathscr{G}^{<}(k, t + t'/2, t - t'/2) \tag{6.7a}$$

$$= \int_{-\infty}^{\infty} \mathrm{d}t' \mathrm{e}^{-\mathrm{i}\omega t'} \left\langle \psi(t - t'/2) \right| \hat{c}_k^{\dagger}(t')\, \hat{c}_k \left| \psi(t - t'/2) \right\rangle, \tag{6.7b}$$

$$\mathscr{A}^{>}(k,\omega,t) = \int_{-\infty}^{\infty} \mathrm{d}t' \mathrm{e}^{-\mathrm{i}\omega t'} \mathscr{G}^{>}(k, t + t'/2, t - t'/2) \tag{6.8a}$$

$$= \int_{-\infty}^{\infty} \mathrm{d}t' \mathrm{e}^{-\mathrm{i}\omega t'} \left\langle \psi(t - t'/2) \right| \hat{c}_k \hat{c}_k^{\dagger}(t') \left| \psi(t - t'/2) \right\rangle. \tag{6.8b}$$

In this case t is also called the average time, while t' is referred to as the relative time. Note that because the momentum-dependent Green's functions are Hermitian symmetric in t', that is

$$\mathscr{G}^{<,>}(k, t - t'/2, t + t'/2) = \mathscr{G}^{<,>*}(k, t + t'/2, t - t'/2), \tag{6.9}$$

we may compute the spectral functions through

$$\mathscr{A}^{<,>}(k,\omega,t) = 2\mathrm{Re}\left(\int_{0}^{\infty} \mathrm{d}t' \mathrm{e}^{-\mathrm{i}\omega t'} \mathscr{G}^{<,>}(k, t + t'/2, t - t'/2) \right). \tag{6.10}$$

An alternative is provided by means of using relative coordinates

$$\mathscr{A}^{<}(k,\omega,t) = \int_{-\infty}^{\infty} \mathrm{d}t' \mathrm{e}^{-\mathrm{i}\omega t'} \mathscr{G}^{<}(k, t + t', t) = \int_{-\infty}^{\infty} \mathrm{d}t' \mathrm{e}^{-\mathrm{i}\omega t'} \left\langle \psi(t) \right| \hat{c}_k^{\dagger}(t')\, \hat{c}_k \left| \psi(t) \right\rangle, \tag{6.11}$$

$$\mathscr{A}^{>}(k,\omega,t) = \int_{-\infty}^{\infty} \mathrm{d}t' \mathrm{e}^{-\mathrm{i}\omega t'} \mathscr{G}^{>}(k, t + t', t) = \int_{-\infty}^{\infty} \mathrm{d}t' \mathrm{e}^{-\mathrm{i}\omega t'} \left\langle \psi(t) \right| \hat{c}_k \hat{c}_k^{\dagger}(t') \left| \psi(t) \right\rangle, \tag{6.12}$$

where the Fourier transform is simply performed in the relative time t'. Note that in this case, the momentum-dependent Green's functions are not Hermitian symmetric in t' anymore, i.e. in general we have

$$\mathscr{G}^{<,>}(k, t - t', t) \neq \mathscr{G}^{<,>*}(k, t + t', t)\,. \tag{6.13}$$

If, however, we assume (6.13) to approximately hold for the problem under investigation, the computation of the spectral function reduces to

$$\mathscr{A}^{<,>}(k,\omega,t) = 2\mathrm{Re}\left(\int_{0}^{\infty} \mathrm{d}t' \mathrm{e}^{-\mathrm{i}\omega t'} \mathscr{G}^{<,>}(k, t + t', t) \right). \tag{6.14}$$

From a physical point of view, this assumption is particularly valid, if the system under consideration is expected to only slightly deviate from the equilibrium case. For further remarks on this issue see appendix C.

The choice of which of the above transformations to apply highly depends on the problem at hand. We will get back to this issue in section 6.3. Note further that in numerical computations we need to add an extra term enforcing convergence. This is achieved by means of an additional damping η, i.e. we change in the above Fourier transformations

$$\omega \to \omega - \mathrm{i}\eta, \quad \eta > 0 \tag{6.15}$$

The right choice of η is again a non-trivial task. Chosen too large it will result in a too strong broadening of the output signal such that smaller components might be suppressed. If, on the other hand, it is too weak it might not serve its original purpose.

In case we take equation (6.13) by heart the numerical evaluation of equations (6.11) and (6.12) becomes more difficult. Then, more care needs to be taken, see appendix A.1.6. We show how these approaches change the output data in appendix C. There we will find that for the numerical computations of spectral functions it is best to make use of Hermitian symmetry in t' when its application is physically reasonable. In other cases damping and zero padding the input signal may already lead to satisfactory results for the real part, while the absolute value should always be considered as interpretable in order to be able to rule out effects originating from spectral leaking. Note that we will restrict our discussions to time-independent Hamiltonians for which the spectral functions can be proven to be not only real but also positive, when relative coordinates are employed, as shown in appendix C.

In either case of choice of coordinates or Fourier transform, the total spectrum is given by

$$\mathscr{A}(k,\omega,t) = \mathscr{A}^{<}(k,\omega,t) + \mathscr{A}^{>}(k,\omega,t). \tag{6.16}$$

Note that spectral functions are conceptually closely related to dynamic structure factors for spin operators, compare for instance [359, 54, 27], so that these considerations should be applicable to these quantities as well.

6.1.3 Special Case of Non-interacting Time-independent Systems with Respect to an Eigenstate

In case the Hamiltonian of the system is time-independent and the state $|\psi\rangle$ the Green's functions are computed with reference to is an eigenstate of this very Hamiltonian, such that we have

$$U(t_2,t_1)\,|\psi\rangle = \mathrm{e}^{-\mathrm{i}\hat{H}(t_2-t_1)}\,|\alpha\rangle = \mathrm{e}^{-\mathrm{i}E_\alpha(t_2-t_1)}\,|\alpha\rangle, \tag{6.17}$$

the Green's functions will only depend on a time difference

$$\mathscr{G}^{<}_{\hat{A},\hat{B}}(t_1,t_2) = \langle\alpha|\,\hat{A}(t_1-t_2)\,\hat{B}\,|\alpha\rangle = \langle\alpha|\,\hat{A}\hat{B}(t_2-t_1)\,|\alpha\rangle, \tag{6.18}$$

$$\mathscr{G}^{>}_{\hat{A},\hat{B}}(t_1,t_2) = \langle\alpha|\,\hat{B}(t_2-t_1)\,\hat{A}\,|\alpha\rangle = \langle\alpha|\,\hat{B}\hat{A}(t_1-t_2)\,|\alpha\rangle, \tag{6.19}$$

and, thus, a single time variable $t' = t_1 - t_2$, i.e.

$$\mathscr{G}^{<}_{\hat{A},\hat{B}}(t') = \langle\alpha|\,\hat{A}(t')\,\hat{B}\,|\alpha\rangle = \langle\alpha|\,\hat{A}\hat{B}(-t')\,|\alpha\rangle, \tag{6.20}$$

$$\mathscr{G}^{>}_{\hat{A},\hat{B}}(t') = \langle\alpha|\,\hat{B}(-t')\,\hat{A}\,|\alpha\rangle = \langle\alpha|\,\hat{B}\hat{A}(t')\,|\alpha\rangle, \tag{6.21}$$

This follows directly from equations (6.1) and (6.2). Clearly, this property is inherited by the spectral functions, such that, as a consequence, both definitions using Wigner or relative coordinates collapse to the same expression

$$\mathscr{A}^{<,>}(k,\omega) = \int_{-\infty}^{\infty} \mathrm{d}t' \mathrm{e}^{-\mathrm{i}\omega t'} \mathscr{G}^{<,>}(k,t') = 2\mathrm{Re}\left(\int_{0}^{\infty} \mathrm{d}t' \mathrm{e}^{-\mathrm{i}\omega t'} \mathscr{G}^{<,>}(k,t') \right). \tag{6.22}$$

We can formally solve the above equation by employing the Lehmann representation of the momentum-dependent Green's functions

$$\begin{aligned}
\mathscr{G}^{<}(k,t') &= \langle \alpha | \, \hat{c}_k^\dagger(t') \, \hat{c}_k \, | \alpha \rangle = \sum_n \langle \alpha^M | \, \mathrm{e}^{\mathrm{i}\hat{H}t'} \hat{c}_k^\dagger \mathrm{e}^{-\mathrm{i}\hat{H}t'} \, | n^{M-1} \rangle \, \langle n^{M-1} | \, \hat{c}_k \, | \alpha^M \rangle, && \text{(6.23a)} \\
&= \sum_n \mathrm{e}^{\mathrm{i}(E_\alpha^M - E_n^{M-1})t'} \, \langle \alpha^M | \, \hat{c}_k^\dagger \, | n^{M-1} \rangle \, \langle n^{M-1} | \, \hat{c}_k \, | \alpha^M \rangle && \text{(6.23b)} \\
&= \sum_n \mathrm{e}^{\mathrm{i}(E_\alpha^M - E_n^{M-1})t'} \left| \langle n^{M-1} | \, \hat{c}_k \, | \alpha^M \rangle \right|^2, && \text{(6.23c)} \\
\mathscr{G}^{>}(k,t') &= \langle \alpha | \, \hat{c}_k \hat{c}_k^\dagger(t') \, | \alpha \rangle = \sum_n \langle \alpha^M | \, \hat{c}_k \, | n^{M+1} \rangle \, \langle n^{M+1} | \, \mathrm{e}^{\mathrm{i}\hat{H}t'} \hat{c}_k^\dagger \mathrm{e}^{-\mathrm{i}\hat{H}t'} \, | \alpha^M \rangle, && \text{(6.24a)} \\
&= \sum_n \mathrm{e}^{\mathrm{i}(E_n^{M+1} - E_\alpha^M)t'} \, \langle \alpha^M | \, \hat{c}_k \, | n^{M+1} \rangle \, \langle n^{M+1} | \, \hat{c}_k^\dagger \, | \alpha^M \rangle && \text{(6.24b)} \\
&= \sum_n \mathrm{e}^{-\mathrm{i}(E_\alpha^M - E_n^{M+1})t'} \left| \langle n^{M+1} | \, \hat{c}_k^\dagger \, | \alpha^M \rangle \right|^2. && \text{(6.24c)}
\end{aligned}$$

Here we have expanded our notation with a superscript of the particle number M to indicate the respective particle number sectors of the Hilbert space we operate in. Note also that by construction the momentum-dependent Green's functions are Hermitian symmetric in t'. Inserting the Lehmann representations into equation (6.22), we find for the spectral functions

$$\begin{aligned}
\mathscr{A}^{<}(k,\omega) &= \int_{-\infty}^{\infty} \mathrm{d}t' \sum_n \mathrm{e}^{-\mathrm{i}(\omega - (E_\alpha^M - E_n^{M-1}))t'} \left| \langle n^{M-1} | \, \hat{c}_k \, | \alpha^M \rangle \right|^2 && \text{(6.25a)} \\
&= 2\pi \sum_n \delta\big(\omega - (E_\alpha^M - E_n^{M-1})\big) \left| \langle n^{M-1} | \, \hat{c}_k \, | \alpha^M \rangle \right|^2, && \text{(6.25b)} \\
\mathscr{A}^{>}(k,\omega) &= \int_{-\infty}^{\infty} \mathrm{d}t' \sum_n \mathrm{e}^{-\mathrm{i}(\omega + (E_\alpha^M - E_n^{M+1}))t'} \left| \langle n^{M+1} | \, \hat{c}_k^\dagger \, | \alpha^M \rangle \right|^2 && \text{(6.26a)} \\
&= 2\pi \sum_n \delta\big(\omega + (E_\alpha^M - E_n^{M+1})\big) \left| \langle n^{M+1} | \, \hat{c}_k^\dagger \, | \alpha^M \rangle \right|^2. && \text{(6.26b)}
\end{aligned}$$

We learn that the lesser spectral function shows peaks at those energies that correspond to the energy differences of the reference state $|\alpha^M\rangle$ and all eigenstates of the sector of the Hilbert space with one less particle. Similarly, the greater spectral function has its peaks at energies corresponding to the differences of the energies of all eigenstates with one additional particle and the reference state $|\alpha^M\rangle$.

If we in addition to the assumptions of measuring with respect to an eigenstate and a time independence of the Hamiltonian suppose it to be bilinear, which implies also that it is non-interacting, i.e.

$$\hat{H} = \sum_k \varepsilon_k \hat{c}_k^\dagger \hat{c}_k, \tag{6.27}$$

the spectral functions have a very clear interpretation. From the Heisenberg equation of motion (2.43) we obtain

$$\frac{\mathrm{d}}{\mathrm{d}t}\hat{c}_k^\dagger(t) = \mathrm{i}\sum_{k'}\varepsilon_{k'}\left[\hat{c}_{k'}^\dagger\hat{c}_{k'},\hat{c}_k^\dagger\right] = \mathrm{i}\sum_{k'}\varepsilon_{k'}\hat{c}_{k'}^\dagger\left\{\hat{c}_k^\dagger,\hat{c}_{k'}\right\} = \mathrm{i}\sum_{k'}\varepsilon_{k'}\hat{c}_{k'}^\dagger\delta_{k,k'} = \mathrm{i}\varepsilon_k\hat{c}_k^\dagger \tag{6.28a}$$

$$\Rightarrow \quad \hat{c}_k^\dagger(t) = \mathrm{e}^{\mathrm{i}\varepsilon_k t}\hat{c}_k^\dagger, \tag{6.28b}$$

which yields

$$\mathscr{G}^<(k,t') = \langle\alpha|\,\hat{c}_k^\dagger(t')\,\hat{c}_k\,|\alpha\rangle = \mathrm{e}^{\mathrm{i}\varepsilon_k t'}\,\langle\alpha|\,\hat{c}_k^\dagger\hat{c}_k\,|\alpha\rangle, \tag{6.29}$$

$$\mathscr{G}^>(k,t') = \langle\alpha|\,\hat{c}_k\hat{c}_k^\dagger(t')\,|\alpha\rangle = \mathrm{e}^{\mathrm{i}\varepsilon_k t'}\,\langle\alpha|\,\hat{c}_k\hat{c}_k^\dagger\,|\alpha\rangle \tag{6.30}$$

and thus

$$\mathscr{A}^<(k,\omega) = \int_{-\infty}^{\infty}\mathrm{d}t'\mathrm{e}^{-\mathrm{i}\left(\omega-\varepsilon_k\right)t'}\,\langle\alpha|\,\hat{c}_k^\dagger\hat{c}_k\,|\alpha\rangle = 2\pi\delta\left(\omega-\varepsilon_k\right)\langle\alpha|\,\hat{c}_k^\dagger\hat{c}_k\,|\alpha\rangle, \tag{6.31}$$

$$\mathscr{A}^>(k,\omega) = \int_{-\infty}^{\infty}\mathrm{d}t'\mathrm{e}^{-\mathrm{i}\left(\omega-\varepsilon_k\right)t'}\,\langle\alpha|\,\hat{c}_k\hat{c}_k^\dagger\,|\alpha\rangle = 2\pi\delta\left(\omega-\varepsilon_k\right)\langle\alpha|\,\hat{c}_k\hat{c}_k^\dagger\,|\alpha\rangle. \tag{6.32}$$

Hence, in this special case the lesser spectral function reflects the dispersion relation ε_k at the occupied modes of the reference state $|\alpha\rangle$, while the greater spectral functions reflects those that are not. The eigenstates are equally simple, namely

$$|\alpha^M\rangle = \prod_{k\in K^M}\hat{c}_k^\dagger\,|\emptyset\rangle, \tag{6.33}$$

where K^M is a set of M ordered indices k, i.e. $\mathrm{card}\left(K^M\right) = M$ and $k_i < k_{i+1}\forall k_i \in K^M$ and $|\emptyset\rangle$ is the vacuum state. In simple words, the eigenstates are determined by successively adding M modes to the vacuum. The ordering of the indices is required to avoid fermionic sign problems.

Often times the reference state is the ground state, i.e. $|\alpha = 0\rangle = |\mathrm{GS}\rangle$. For this eigenstate the M indices k_i are chosen for which the dispersion relation ε_{k_i} takes the M smallest values, such that the lesser spectral function resembles the occupied part of the lowest energies of the dispersion and the greater spectral function the remaining unoccupied part. A frequent notation is

$$|\mathrm{GS}\rangle = \prod_{k\leq k_\mathrm{F}}\hat{c}_k^\dagger\,|\emptyset\rangle, \tag{6.34}$$

where k_F is called the Fermi wave vector.

6.1.4 Construction from MPSs

Evaluating the spectral functions in terms of MPSs poses several difficulties we shall address at this point. Suppose that the problem at hand is to compute the lesser or greater spectral function $\mathscr{A}^{<,>}(k,\omega,t)$ at a fixed time t. As we learned from section 6.1.2 this first requires calculating a momentum-dependent Green's function $\mathscr{G}^{<,>}(k,t_1,t_2)$. While this task is mathematically well defined care needs to be taken in its numerical evaluation.

The first problem is that in terms of their real space expressions the operators $\hat{c}_k^{(\dagger)}$ are of global type and need to be applied to (possibly) time-evolved states. Time-evolved MPSs, however, are in general already comparably strongly entangled. While the application of a global MPO, unless it is composed of a product of local operators, to an MPS alone leads to a rather strong increase in entanglement, applying it to a strongly entangled MPS is clearly problematic, especially as the so-obtained MPS needs to be subject to a further time evolution. We therefore exploit that the momentum-dependent operators can be expressed as a sum of local ones, that is

$$\hat{c}_k^{(\dagger)} = \sum_r S_{k,r}^{(*)} \hat{c}_r^{(\dagger)} \tag{6.35}$$

with local annihilation and creation operators $\hat{c}_r^{(\dagger)}$ and a unitary transformation matrix S, such that equations (6.5) and (6.6) become

$$\mathscr{G}^<(k, t_1, t_2) = \sum_{r,r'} S_{k,r'}^* S_{k,r} \langle\psi| \hat{c}_{r'}^\dagger(t_1)\, \hat{c}_r(t_2) |\psi\rangle, \tag{6.36}$$

$$\mathscr{G}^>(k, t_1, t_2) = \sum_{r,r'} S_{k,r'} S_{k,r}^* \langle\psi| \hat{c}_{r'}(t_2)\, \hat{c}_r^\dagger(t_1) |\psi\rangle. \tag{6.37}$$

The disadvantage of this procedure is evident. Instead of one computation L^2 need to be performed on the MPS level, L being the system size, which corresponds to a massive increase in computational resources. The so-obtained expectation values can then be fused into the entire momentum dependent Green's function in a post processing routine. If these L^2 computations can be conducted in parallel, roughly the same time will be required for the entire calculus. Our experience is that done so the MPO applications converge significantly faster so that it would be wrong to assume that the total computational time increases by a factor of L^2 compared to the naive approach.

The second problem lies in the obvious discretization of the time evolution and the therewith associated iterative computation of the expectation values in equations (6.36) and (6.37). Here, the computational effort depends massively on the coordinates chosen to perform the Fourier transform in.

We begin with the less demanding scenario of relative coordinates. Recalling equations (6.11) (6.12) and our above considerations, we need to compute the correlation matrices

$$C_{r',r}^<(t') = \langle\psi(t)| \hat{c}_{r'}^\dagger(t')\, \hat{c}_r |\psi(t)\rangle, \tag{6.38}$$

$$C_{r,r'}^>(t') = \langle\psi(t)| \hat{c}_r \hat{c}_{r'}^\dagger(t') |\psi(t)\rangle, \tag{6.39}$$

for $\mathscr{G}^<(k, t+t', t)$ and $\mathscr{G}^>(k, t+t', t)$, respectively. We have not indexed the time t in this notation as it is supposed to be constant. Furthermore, for these calculations we have $t' \geq 0$. Let us define

$$|\phi_r^<\rangle = \hat{c}_r |\psi(t)\rangle, \tag{6.40}$$

$$|\phi_r^>\rangle = \hat{c}_r^\dagger |\psi(t)\rangle, \tag{6.41}$$

$$\left|\phi_r^{<,>}\right\rangle_n = U(n\delta t', 0) \left|\phi^{<,>}\right\rangle = U(\delta t', 0) \left|\phi_r^{<,>}\right\rangle_{n-1}, \tag{6.42}$$

$$|\psi\rangle_n = U(n\delta t', 0) |\psi(t)\rangle = U(\delta t', 0) |\psi\rangle_{n-1}, \quad 0 \leq n \leq n_{\max}. \tag{6.43}$$

Here, $\delta t'$ is the time step of the discretized time evolution. The discretized correlation matrices may now be computed via

$$C_{r',r}^<(n\delta t') = {}_n\langle\psi| \hat{c}_{r'}^\dagger |\phi_r^<\rangle_n, \tag{6.44}$$

$$C^{>}_{r,r'}(n\delta t') = {}_n\langle \phi^{>}_r | \, \hat{c}^{\dagger}_{r'} \, | \psi \rangle_n \tag{6.45}$$

which yields a rather simple algorithm to compute the spectral functions:

1. For all r
   a) Compute $|\phi^{<}_r\rangle$ or $|\phi^{>}_r\rangle$ according to equation (6.40) or (6.41), respectively.
   b) While $n \leq n_{\max}$
      i. Compute $|\phi^{<}_r\rangle_n$ or $|\phi^{>}_r\rangle_n$ according to equation (6.42).
      ii. Compute $|\psi\rangle_n$ according to equation (6.43).
      iii. Compute the correlation matrix elements $C^{<}_{r',r}(n\delta t')$ or $C^{>}_{r,r'}(n\delta t')$ according to equation (6.44) or (6.45) for all r'.
2. Compute the momentum-dependent Green's function $\mathscr{G}^{<}(k, t+t', t)$ or $\mathscr{G}^{>}(k, t+t', t)$, which of course are now discretized, according to equation (6.36) or (6.37) .
3. Compute the spectral function $\mathscr{A}^{<}(k, \omega, t)$ or $\mathscr{A}^{>}(k, \omega, t)$ according to equation (6.11) or (6.12) or by means of equation (6.14) using a discrete Fourier transform, c.f. section 3.6, in all cases.

Hence, for a system of L sites we require $L\,(1 + 3\,(n_{\max} + 1)) + 2$ operations of which step 1, i.e. setting up the correlation matrix, with $L\,(1 + 3\,(n_{\max} + 1))$ operations is by far the most laborious one. Note that step 1(b)iii actually involves L computations, which however due to their local nature are significantly less costly than all the other ones, allowing us to count them as equally demanding to a single global operation. We also emphasize that the individual operations do not require the same amount of time, MPS time evolutions (especially for later times) being in general orders of magnitude more demanding than applications of local MPOs or computations of overlaps. Furthermore, we should mention that this algorithm is rather inefficient in the sense that the time evolution of $|\psi(t)\rangle$ is computed L times. However, the alternative of just doing the computation once would require storing all states $|\psi\rangle_n$ on disc. Depending on the system size, as well as MPS parameters like the maximum dimension and of course $n_{\max}$ this approach can quickly demand an enormous amount of disc space making this solution unfeasible. Supposing that in the approach we presented above all states that are not needed any more are either deleted or overwritten we only need disc space for storing $2L$ MPSs, which is for most computations of this kind substantially less than the $n_{\max} + 1 + L$ MPSs that needed to be saved otherwise, since typically $n_{\max} \gg L$.

In the case of Wigner coordinates the computations become more cumbersome. Based on equations (6.7) and (6.8) and our above considerations the correlation matrices take the forms

$$\begin{aligned}
C^{<}_{r',r}(t') &= \langle \psi(t - t'/2) | \, \hat{c}^{\dagger}_{r'}(t') \, \hat{c}_r \, | \psi(t - t'/2) \rangle && \text{(6.46a)} \\
&= \langle \psi(t + t'/2) | \, \hat{c}^{\dagger}_{r'} U^{\dagger}(0, t'/2) \, U(t'/2, 0) \, \hat{c}_r \, | \psi(t - t'/2) \rangle, && \text{(6.46b)} \\
C^{>}_{r,r'}(t') &= \langle \psi(t - t'/2) | \, \hat{c}_r \hat{c}^{\dagger}_{r'}(t') \, | \psi(t - t'/2) \rangle && \text{(6.47a)} \\
&= \langle \psi(t - t'/2) | \, \hat{c}_r U^{\dagger}(0, -t'/2) \, U(-t'/2, 0) \, \hat{c}^{\dagger}_{r'} \, | \psi(t + t'/2) \rangle, && \text{(6.47b)}
\end{aligned}$$

for $\mathscr{G}^{<}(k, t + t'/2, t - t'/2)$ and $\mathscr{G}^{>}(k, t + t'/2, t - t'/2)$, respectively. Again, we have not indexed t which we suppose to be constant. We continue by defining

$$|\psi\rangle_{\pm n} = U(\pm n\delta t', 0) \, |\psi(t)\rangle = U(\pm\delta t', 0) \, |\psi\rangle_{\pm n \mp 1}, \quad 0 \leq n \leq n_{\max}, \tag{6.48}$$

$$\left|\phi_r^{<}\right\rangle_{\pm n} = \hat{c}_r \left|\psi\right\rangle_{\pm n}, \tag{6.49}$$

$$\left|\phi_r^{>}\right\rangle_{\pm n} = \hat{c}_r^{\dagger} \left|\psi\right\rangle_{\pm n}, \tag{6.50}$$

$$\left|\xi_r^{<,>}\right\rangle_{\pm n,\mp m} = U(\mp m\delta t', 0) \left|\phi_r^{<,>}\right\rangle_{\pm n} = U(\mp\delta t', 0) \left|\xi_r^{<,>}\right\rangle_{\pm n,\mp m\pm 1}, \quad 0 \leq m \leq n, \tag{6.51}$$

such that we can express the correlation matrices through

$$C^{<}_{r',r}(n2\delta t') = {}_{+n,-n}\langle \xi^{<}_{r'} | \xi^{<}_{r} \rangle_{-n,+n}, \tag{6.52}$$

$$C^{>}_{r,r'}(n2\delta t') = {}_{-n,+n}\langle \xi^{>}_{r} | \xi^{>}_{r'} \rangle_{+n,-n}. \tag{6.53}$$

The algorithm to calculating the spectral functions then goes:

1. While $n \leq n_{\max}$
   a) Compute $\left|\psi\right\rangle_{-n}$ and $\left|\psi\right\rangle_{+n}$ according to equation (6.48).
   b) For all r
      i. Compute $\left|\phi_r^{<}\right\rangle_{+n}$ and $\left|\phi_r^{<}\right\rangle_{-n}$ or $\left|\phi_r^{>}\right\rangle_{+n}$ and $\left|\phi_r^{>}\right\rangle_{-n}$ according to equation (6.49) or (6.50).
      ii. While $m \leq n$
         A. Compute $\left|\xi_r^{<}\right\rangle_{-n,+m}$ and $\left|\xi_r^{<}\right\rangle_{+n,-m}$ or $\left|\xi_r^{>}\right\rangle_{-n,+m}$ and $\left|\xi_r^{>}\right\rangle_{+n,-m}$ according to equation (6.43).
   c) Compute the correlation matrix elements $C^{<}_{r',r}(n2\delta t')$ or $C^{>}_{r,r'}(n2\delta t')$ according to equation (6.52) or (6.53).
2. Compute the discretized momentum-dependent Green's function $\mathscr{G}^{<}(k, t + t'/2, t - t'/2)$ or $\mathscr{G}^{>}(k, t + t'/2, t - t'/2)$ according to equation (6.36) or (6.37) .
3. Compute the spectral function $\mathscr{A}^{<}(k, \omega, t)$ or $\mathscr{A}^{>}(k, \omega, t)$ according to equation (6.10) using a discrete Fourier transform, c.f. section 3.6.

For this procedure in total $(n_{\max} + 1)(2L + 3) + Ln_{\max}(n_{\max} + 1) + 2$ operations are necessary, which is an order of magnitude in $n_{\max}$ higher than for the computation for relative coordinates. Note that here we counted steps 1a, 1(b)i, and 1(b)iiA as containing two operations each due to the computation of two states. As before the construction of the correlation matrix is the computationally most demanding task. Regarding disk usage this algorithm will need to store $2Ln_{\max}$ MPSs again assuming that unneeded ones are either discarded or overwritten. Thus, also regarding this aspect the usage of Wigner coordinates performs one order of magnitude in $n_{\max}$ worse than the variant with relative coordinates. Note further that in order to achieve the same resolution as the calculus with relative coordinates we need to decrease the time step $\delta t'$ by a factor of 2.

While in theoretical calculations most often infinitely large systems are investigated for an infinite time, in numerical practice for the framework we have introduced so far clearly bounds to both quantities need to be introduced. Most obvious is the choice of a size L of the system under investigation, which may have an influence on other numerical measurements, a phenomenon known as finite size effects. Minimizing these effects is a rather artistic procedure in numerics since there is no algorithm to apply. Here we shall discuss the maximum time $t'_{\max}$ that should be reached in

the time evolutions. For a given interacting system we only consider the non-interacting part in equilibrium, i.e. such that the system in principle would be analytically solvable. Then we compute $C^{<}_{r',L/2}(t')$ (or equally $C^{>}_{r',L/2}(t')$) and plot the results with respect to both t' and r'. We will find a light cone-like structure beginning from the initial perturbation at site $L/2$ propagating through the system. This can be seen as a manifestation of Lieb-Robinson bounds [216, 251, 206], which state that even in non-relativistic quantum systems there is an upper limit of the speed information propagates with. Clearly in an infinitely large system the light cone would extend infinitely. In the L site system, however, it will reach the edges at a certain time, which we shall take as t'_{max} later on. For open boundaries, the information will be reflected at this edges while for periodic boundaries it will interfere with the branch coming from the other edge. These reflections or interferences will cause finite size effects and are therefore to be avoided as much as possible. Actually, one finds [276] that t' may be chosen so large that up to two times the edges of the system are reached without the appearance of noticeable finite size effects. This is a rather reassuring observation as $C^{<}_{r',r}(t')$ especially for $r \sim 0$ and $r \sim L_1$ one edge is reached (almost) instantly. In order to compare results for different interactions and and out-of equilibrium setups to one another, it is highly desirable to fix t'_{max} and also $\delta t'$ to a definite value. Here the time at which the edges are first reached in $C^{<}_{r',L/2}(t')$ (or $C^{>}_{r',L/2}(t')$) in the equilibrium system without interactions provides a good point of reference, especially since at least in this case it is known to be easily expandable.

We close this section with two remarks on frequently applied simplifications regarding the computation of spectral functions with MPSs. As we learned in chapter 4 open boundaries are preferred in most MPS applications. Still often times, even though the MPS computations are done with open boundary conditions the transformations (6.36) or (6.37) are often done with respect to periodic boundaries, that is technically an incorrect transformation matrix S is applied. While in many cases this procedure works amazingly well for equilibrium spectral functions, it must not be applied for time-dependent spectral functions in out-of-equilibrium setups, since then band occupations for non-interacting systems become time-dependent contrary to the analytically obtained results.

Another common approximation is to assume spatial translational invariance when it comes to computing the correlation matrices, i.e. to take

$$C^{<,>}_{r',r}(t') = C^{<,>}_{r',L/2}(t') \tag{6.54}$$

in equations (6.38), (6.39), (6.46), and (6.47). Although the computational effort is clearly decreased by a factor of L, for smaller systems this simplification may result in unphysical artifacts even in equilibrium spectral functions especially if the MPS calculus is done using open boundary conditions and even more so for systems with a non-trivial unit cell.

The quality of any numerical computation of spectral functions may be judged by computing the spectral moments [262] to which certain sum rules apply [200]. We will not compute any other moments than the zeroth one, which gives the particle number and, due to assuming equation (6.14) to hold, is correct at all times. For an analysis of (equlibrium) spectral functions and its moments see for instance [42, 41].

6.1.5 The Chebyshev Formalism

So far we have essentially computed spectral functions through Fourier transforming time-dependent Green's functions. As time-evolutions are numerically quite costly to perform and at least when it

comes to MPS computations always come with a certain error, it would be desirable to circumvent them wherever possible and to directly work in frequency space. Of course, the evaluation of time-dependent spectral functions will always require time evolutions. In this case, we would only want to avoid the second time evolution from which the spectrum is obtained.

Indeed, such frequency space methods do exist. However, they are most often restricted to time-independent systems with respect to an eigenstate, which in most cases is the ground state. Note further that only very recently an MPS recursion method for the computation of spectral function was proposed [368], so far, unfortunately also for equilibrium spectral functions only. In this section we will briefly explain the so-called Chebyshev method and illustrate why its generalization to non-equilibrium spectral functions is problematic. For an application see for instance [371, 370].

In principle, the Chebyshev formalism can be regarded as a further development of the DDMRG [369], which, nevertheless, relies on the same assumptions. Let us now consider a time-independent system where we aim at calculating Green's functions with respect to an eigenvector $|\alpha\rangle$. In this case, we can take equations (6.20) and (6.21) and express their Fourier transforms through

$$\int_{-\infty}^{\infty} \mathrm{d}t' \mathrm{e}^{-\mathrm{i}\omega t'} \mathscr{G}^{<}_{\hat{A},\hat{B}}(t') = \int_{-\infty}^{\infty} \mathrm{d}t' \mathrm{e}^{-\mathrm{i}\omega t'} \langle\alpha| \mathrm{e}^{\mathrm{i}E_\alpha t'} \hat{A} \mathrm{e}^{-\mathrm{i}\hat{H}t'} \hat{B} |\alpha\rangle \tag{6.55a}$$

$$= \int_{-\infty}^{\infty} \mathrm{d}t' \langle\alpha| \hat{A} \mathrm{e}^{-\mathrm{i}\left(\omega - E_\alpha + \hat{H}\right)t'} \hat{B} |\alpha\rangle = \langle\alpha| \hat{A}\delta\left(\omega - E_\alpha + \hat{H}\right) \hat{B} |\alpha\rangle, \tag{6.55b}$$

$$\int_{-\infty}^{\infty} \mathrm{d}t' \mathrm{e}^{-\mathrm{i}\omega t'} \mathscr{G}^{>}_{\hat{A},\hat{B}}(t') = \int_{-\infty}^{\infty} \mathrm{d}t' \mathrm{e}^{-\mathrm{i}\omega t'} \langle\alpha| \hat{B} \mathrm{e}^{\mathrm{i}\hat{H}t'} \hat{A} \mathrm{e}^{-\mathrm{i}E_\alpha t'} |\alpha\rangle \tag{6.56a}$$

$$= \int_{-\infty}^{\infty} \mathrm{d}t' \langle\alpha| \hat{A} \mathrm{e}^{-\mathrm{i}\left(\omega - \hat{H} + E_\alpha\right)t'} \hat{B} |\alpha\rangle = \langle\alpha| \hat{A}\delta\left(\omega - \hat{H} + E_\alpha\right) \hat{B} |\alpha\rangle, \tag{6.56b}$$

such that the spectral functions are given by

$$\mathscr{A}^{<}(k,\omega) = \langle\alpha| \hat{c}_k^\dagger \delta\left(\omega - E_\alpha + \hat{H}\right) \hat{c}_k |\alpha\rangle, \tag{6.57}$$

$$\mathscr{A}^{>}(k,\omega) = \langle\alpha| \hat{c}_k \delta\left(\omega - \hat{H} + E_\alpha\right) \hat{c}_k^\dagger |\alpha\rangle. \tag{6.58}$$

The delta functions may now be expressed by means of a Chebyshev expansion (and the kernel polynomial method [405]), which ultimately results in an iterative algorithm to compute the spectral functions to in principle arbitrary accuracy. We do not give the details here but rather refer to [152] for further reading regarding the exact algorithm. This approach has established itself for its respective class of problems and is particularly characterized by the excellent resolution of its results. As already mentioned, in most applications the state of reference is the ground state, such that for an MPS treatment the Chebyshev formalism can be conducted once the ground state and its energy are known, two quantities which we know from section 5.1 to be easily accessible.

We note that in order to set up equation (6.57) and (6.58) we exploited that we computed the expectation value with respect to an eigenvalue of which we know the time evolution, i.e.

$$\mathrm{e}^{-\mathrm{i}\hat{H}t'} |\alpha\rangle = \mathrm{e}^{-\mathrm{i}E_\alpha t'} |\alpha\rangle. \tag{6.59}$$

This is the crucial point in the derivation which we easily see from considering the opposite case, where the state of reference is explicitly no eigenstate, let us say $|\psi(t)\rangle$. If we wanted to set up an

equation analogously to (6.57) or (6.58) we would need to decompose

$$\mathrm{e}^{-\mathrm{i}\hat{H}t'}\left|\psi(t)\right\rangle = \sum_n \lambda_n(t)\,\mathrm{e}^{-\mathrm{i}E_n t'}\left|n^M\right\rangle, \tag{6.60}$$

such that for the spectral functions we would obtain

$$\mathscr{A}^<(k,\omega,t) = \sum_n \lambda_n^*(t)\left\langle n^M\right|\hat{c}_k^\dagger \delta\big(\omega - E_n + \hat{H}\big)\,\hat{c}_k\left|\psi(t)\right\rangle, \tag{6.61}$$

$$\mathscr{A}^>(k,\omega,t) = \sum_n \lambda_n(t)\left\langle\psi(t)\right|\hat{c}_k \delta\big(\omega - \hat{H} + E_n\big)\,\hat{c}_k^\dagger\left|n^M\right\rangle. \tag{6.62}$$

In these equations we could in principle use a Chebyshev expansion to evaluate the delta functions proceeding analogously as in the special case considered above. However, we would be required to know all eigenstates $\left|n^M\right\rangle$ and to perform the procedure for all these eigenstates. This is clearly unfeasible in practice since the number of eigenstates grows exponentially with the system size. Note that in the above description we implicitly assumed relative coordinates, c.f. section 6.1.2. As the Green's functions in Wigner coordinates come with a t' dependence in the states the expectation value is taken with respect to, for this case two decompositions would be necessary which would square the amount of computations to do. We conclude that while it is in principle possible to naively extend the Chebyshev formalism to general non-equilibrium setups, it cannot be applied in numerical practice, at least for reasonably large systems.

6.2 Optical Conductivity

We now present the optical conductivity as the second principal observable of the computations to be conducted in this thesis. As for the case of spectral functions, optical conductivities have been studied in great detail in equilibrium setups, c.f. for instance [372], and are at the core for Drude theory [431]. Here we follow references [212] and [336] to extend the formalism to non-equilibrium situations, which has been applied, e.g. in [225]. Another approach to computing the (equilibrium) optical conductivity through a quantum stochastic time evolution is presented in reference [31]. We shall also discuss the relation to the spectral function to gain a better grasp of how to interpret the optical conductivity.

6.2.1 Definition and Evaluation from Linear Response Theory

Unlike Green's functions, which are a quite general concept in many-body physics, from which the spectral functions are then derived, the optical conductivity is motivated directly from linear response theory. Consider a system which is subject to an external perturbation field $E(t)$. Assuming that under this perturbation the system remains sufficiently close to the ground state the so-induced current is given by

$$\left\langle\hat{\jmath}(t_1)\right\rangle = \int_{-\infty}^{\infty} \mathrm{d}t_2 \sigma(t_1,t_2)\,E(t_2). \tag{6.63}$$

Here we have introduced the current operator

$$\hat{\jmath} = -\mathrm{i}t_{\mathrm{hop}} \sum_r \big(\hat{c}_{r+1}^\dagger \hat{c}_r - \hat{c}_r^\dagger \hat{c}_{r+1}\big), \tag{6.64}$$

where just like in the previous chapter r is a general site index, i.e. it may contain additional quantum numbers like, for instance, the spin as well. Note that the current operator is explicitly defined by means of real space operators. We will at a later point turn to its expression in momentum space operators. The response function $\sigma(t_1, t_2)$ in equation (6.63), which measures the response of the current at time t_2 with respect to a perturbation at time t_1, is referred to as the optical conductivity. In general it is determined by

$$\sigma(t_1, t_2) = \theta(t_1 - t_2)\,\frac{1}{L}\left(\langle\psi(t_1)|\,\hat{s}\,|\psi(t_1)\rangle + \int_{-\infty}^{\infty} \mathrm{d}t_3 \chi(t_1, t_3)\right), \tag{6.65}$$

where we have introduced the stress tensor

$$\hat{s} = t_{\mathrm{hop}} \sum_r \left(\hat{c}_r^\dagger \hat{c}_{r+1} + \hat{c}_{r+1}^\dagger \hat{c}_r\right), \tag{6.66}$$

the two-time susceptibility

$$\chi(t_1, t_3) = -\mathrm{i}\theta(t_1 - t_3)\,\langle\psi|\,[\hat{\jmath}(t_1)\,, \hat{\jmath}(t_3)]\,|\psi\rangle, \tag{6.67}$$

and where θ is the Heaviside step function. Note that with all Heaviside functions applied the integral in equation (6.65) actually only runs from t_2 to t_1.

We will mostly be interested in a time- and frequency-dependent formulation of the optical conductivity. However, just like in the case of spectral functions discussed in the previous section, there is no general definition of how to perform the Fourier transform to frequency space. We therefore choose relative coordinates, thereby defining

$$\sigma(\omega, t) = \int_{-\infty}^{\infty} \mathrm{d}t' \mathrm{e}^{-\mathrm{i}\omega t'} \sigma(t + t', t). \tag{6.68}$$

Often times the optical conductivity is evaluated regarding its real and imaginary part, where we have

$$\sigma(\omega, t) = \sigma_1(\omega, t) + \mathrm{i}\sigma_2(\omega, t). \tag{6.69}$$

6.2.2 Special Case of Non-interacting Time-independent Systems with Respect to an Eigenstate

Let us again assume the Hamiltonian of the system to be time-independent and the reference state $|\psi\rangle$ be an eigenstate, c.f. equation (6.17). In this case the two-time susceptibility (6.67) becomes

$$\begin{aligned}
\chi(t_1, t_3) &= -\mathrm{i}\theta(t_1 - t_3)\left(\langle\alpha|\,\hat{\jmath}(t_1)\,\hat{\jmath}(t_3)\,|\alpha\rangle - \langle\alpha|\,\hat{\jmath}(t_3)\,\hat{\jmath}(t_1)\,|\alpha\rangle\right) && \text{(6.70a)}\\
&= -\mathrm{i}\theta(t_1 - t_3)\left(\langle\alpha|\,\mathrm{e}^{\mathrm{i}\hat{H}t_1}\hat{\jmath}\mathrm{e}^{-\mathrm{i}\hat{H}(t_1 - t_3)}\hat{\jmath}\mathrm{e}^{-\mathrm{i}\hat{H}t_3}\,|\alpha\rangle - \langle\alpha|\,\mathrm{e}^{\mathrm{i}\hat{H}t_3}\hat{\jmath}\mathrm{e}^{-\mathrm{i}\hat{H}(t_3 - t_1)}\hat{\jmath}\mathrm{e}^{-\mathrm{i}\hat{H}t_1}\,|\alpha\rangle\right) && \text{(6.70b)}\\
&= -\mathrm{i}\theta(t_1 - t_3)\left(\langle\alpha|\,\mathrm{e}^{\mathrm{i}\hat{H}(t_1 - t_3)}\hat{\jmath}\mathrm{e}^{-\mathrm{i}\hat{H}(t_1 - t_3)}\hat{\jmath}\,|\alpha\rangle - \langle\alpha|\,\hat{\jmath}\mathrm{e}^{\mathrm{i}\hat{H}(t_1 - t_3)}\hat{\jmath}\mathrm{e}^{-\mathrm{i}\hat{H}(t_1 - t_3)}\,|\alpha\rangle\right) && \text{(6.70c)}\\
&= -\mathrm{i}\theta(t_1 - t_3)\,\langle\alpha|\,[\hat{\jmath}(t_1 - t_3)\,, \hat{\jmath}(0)]\,|\alpha\rangle = \chi(t_1 - t_3), && \text{(6.70d)}
\end{aligned}$$

and, thus, only depends on the relative time $t_1 - t_3$. Together with

$$\langle\alpha(t_1)|\,\hat{s}\,|\alpha(t_1)\rangle = \langle\alpha|\,\mathrm{e}^{\mathrm{i}\hat{H}t_1}\hat{s}\mathrm{e}^{-\mathrm{i}\hat{H}t_1}\,|\alpha\rangle = \langle\alpha|\,\mathrm{e}^{\mathrm{i}E_\alpha t_1}\hat{s}\mathrm{e}^{-\mathrm{i}E_\alpha t_1}\,|\alpha\rangle = \langle\alpha|\,\hat{s}\,|\alpha\rangle \tag{6.71}$$

we find the optical conductivity from equation (6.65) to also only depend on the relative time $t_1 - t_2$

$$\sigma(t_1, t_2) = \theta(t_1 - t_2)\,\frac{1}{L}\left(\langle\alpha|\,\hat{s}\,|\alpha\rangle + \int_{-\infty}^{\infty} \mathrm{d}t_3 \chi(t_1 - t_3)\right) = \sigma(t_1 - t_2), \tag{6.72}$$

with the integral after the application of all Heaviside functions running from 0 to $t_1 - t_2$. As a consequence, the defining equation of the optical conductivity (6.63) turns into a convolution, of which the Fourier transform is known to yield

$$j(\omega) = \int_{-\infty}^{\infty} \mathrm{d}t_1 \mathrm{e}^{-\mathrm{i}\omega t_1}\,\langle\hat{j}(t_1)\rangle = \int_{-\infty}^{\infty} \mathrm{d}t_1 \mathrm{e}^{-\mathrm{i}\omega t_1} \int_{-\infty}^{\infty} \mathrm{d}t_2 \sigma(t_1 - t_2)\,E(t_2) \tag{6.73a}$$

$$= \left(\int_{-\infty}^{\infty} \mathrm{d}(t_1 - t_2)\,\mathrm{e}^{-\mathrm{i}\omega(t_1 - t_2)}\sigma(t_1 - t_2)\right)\left(\int_{-\infty}^{\infty} \mathrm{d}t_2 \mathrm{e}^{-\mathrm{i}\omega t_2} E(t_2)\right) = \sigma(\omega)\,E(\omega), \tag{6.73b}$$

that is in this case in frequency space the current is directly proportional to the perturbation with the optical conductivity taking the role of the proportionality constant. Evidently, we can compute

$$\sigma(\omega) = \frac{j(\omega)}{E(\omega)}. \tag{6.74}$$

In reference [336] the optical conductivity is derived to be given via

$$\sigma(\omega) = \frac{1}{\omega L}\int_{-\infty}^{\infty} \mathrm{d}t' \mathrm{e}^{-\mathrm{i}\omega t'}\,\langle\alpha|\,[\hat{j}(t'), \hat{j}(0)]\,|\alpha\rangle + \frac{\pi}{L}\,\langle\alpha|\,\hat{s}\,|\alpha\rangle\,\delta(\omega) = \sigma_1(\omega) + \mathrm{i}\sigma_2(\omega). \tag{6.75}$$

We compute the Lehmann representations

$$\langle\alpha^M|\,\hat{j}(t')\,\hat{j}(0)\,|\alpha^M\rangle = \sum_n \langle\alpha^M|\,\mathrm{e}^{\mathrm{i}\hat{H}t'}\hat{j}\mathrm{e}^{-\mathrm{i}\hat{H}t'}\,|n^M\rangle\,\langle n^M|\,\hat{j}\,|\alpha^M\rangle \tag{6.76a}$$

$$= \sum_n \mathrm{e}^{\mathrm{i}(E_\alpha^M - E_n^M)t'}\,\langle\alpha^M|\,\hat{j}\,|n^M\rangle\,\langle n^M|\,\hat{j}\,|\alpha^M\rangle \tag{6.76b}$$

$$= \sum_n \mathrm{e}^{\mathrm{i}(E_\alpha^M - E_n^M)t'}\,|\langle n^M|\,\hat{j}\,|\alpha^M\rangle|^2, \tag{6.76c}$$

$$\langle\alpha^M|\,\hat{j}(0)\,\hat{j}(t')\,|\alpha^M\rangle = \sum_n \langle\alpha^M|\,\hat{j}\,|n^M\rangle\,\langle n^M|\,\mathrm{e}^{\mathrm{i}\hat{H}t'}\hat{j}\mathrm{e}^{-\mathrm{i}\hat{H}t'}\,|\alpha^M\rangle \tag{6.77a}$$

$$= \sum_n \mathrm{e}^{\mathrm{i}(E_n^M - E_\alpha^M)t'}\,\langle\alpha^M|\,\hat{j}\,|n^M\rangle\,\langle n^M|\,\hat{j}\,|\alpha^M\rangle \tag{6.77b}$$

$$= \sum_n \mathrm{e}^{\mathrm{i}(E_n^M - E_\alpha^M)t'}\,|\langle n^M|\,\hat{j}\,|\alpha^M\rangle|^2, \tag{6.77c}$$

$$\langle\alpha^M|\,\hat{s}\,|\alpha^M\rangle = t_{\mathrm{hop}}\sum_r\sum_n \big(\langle\alpha^M|\,\hat{c}_r^\dagger\,|n^M\rangle\,\langle n^M|\,\hat{c}_{r+1}\,|\alpha^M\rangle + \langle\alpha^M|\,\hat{c}_{r+1}^\dagger\,|n^M\rangle\,\langle n^M|\,\hat{c}_r\,|\alpha^M\rangle\big) \tag{6.78a}$$

$$= t_{\mathrm{hop}}\sum_r\sum_n \big(\langle\alpha^M|\,\hat{c}_r^\dagger\,|n^M\rangle\,\langle n^M|\,\hat{c}_{r+1}\,|\alpha^M\rangle + \langle n^M|\,\hat{c}_{r+1}\,|\alpha^M\rangle^*\,\langle\alpha^M|\,\hat{c}_r^\dagger\,|n^M\rangle^*\big) \tag{6.78b}$$

$$= 2t_{\mathrm{hop}}\sum_r\sum_n \mathrm{Re}\big(\langle\alpha^M|\,\hat{c}_r^\dagger\,|n^M\rangle\,\langle n^M|\,\hat{c}_{r+1}\,|\alpha^M\rangle\big) \tag{6.78c}$$

where we have again used the general particle number M as a superscript, to confirm that the optical conductivity is actually a real number

$$\sigma(\omega) = \frac{1}{\omega L}\sum_n |\langle n^M|\,\hat{j}\,|\alpha^M\rangle|^2 \int_{-\infty}^{\infty} \mathrm{d}t' \left(\mathrm{e}^{-\mathrm{i}\omega - (E_\alpha^M - E_n^M)t'} - \mathrm{e}^{-\mathrm{i}\omega - (E_n^M - E_\alpha^M)t'}\right)$$

$$+ 2t_{\text{hop}} \frac{\pi}{L} \sum_r \sum_n \text{Re}\Big(\langle \alpha^M | \hat{c}_r^\dagger | n^M \rangle \langle n^M | \hat{c}_{r+1} | \alpha^M \rangle \Big) \delta(\omega) \tag{6.79a}$$

$$= \frac{1}{\omega L} \sum_n |\langle n^M | \hat{\jmath} | \alpha^M \rangle|^2 \left(\delta(\omega - (E_\alpha^M - E_n^M)) - \delta(\omega - (E_n^M - E_\alpha^M)) \right)$$

$$+ 2t_{\text{hop}} \frac{\pi}{L} \sum_r \sum_n \text{Re}\Big(\langle \alpha^M | \hat{c}_r^\dagger | n^M \rangle \langle n^M | \hat{c}_{r+1} | \alpha^M \rangle \Big) \delta(\omega). \tag{6.79b}$$

As this structure is clearly symmetric in ω, i.e.

$$\sigma(\omega) = \sigma(-\omega), \tag{6.80}$$

often times only frequencies $\omega > 0$ are regarded when it comes to its interpretation. In this case $\sigma(\omega > 0)$ is a common notation. In general, only the real part of the optical conductivity is interpreted since this is also the quantity that is measured in experiments. Then, $\sigma_1(\omega > 0)$ is referred to as the regular part, while $\sigma_1(\omega = 0)$ is called the Drude peak, the prefactor of the delta peak being known as the Drude weight [69, 209]. Its properties are discussed in Drude theory, where it is used to differentiate between insulators and metals [146, 182]. As for this work, we shall be more interested in the regular part.

Concerning the relation to the spectral function, it is worth to distinguish between systems with a trivial unit cell and such with a more complex structure, as well as between open and periodic boundaries. The case of a trivial unit cell and periodic boundaries is easily computed. We again assume the Hamiltonian to be bilinear

$$\hat{H} = \sum_k \varepsilon_k \hat{c}_k^\dagger \hat{c}_k, \tag{6.81}$$

where we explicitly assume the system to consist of one single band only. Only in this case, the current operator can be expressed in terms of momentum space operators as

$$\hat{\jmath} = \sum_k \tilde{\varepsilon}_k \hat{c}_k^\dagger \hat{c}_k, \tag{6.82}$$

with coefficients $\tilde{\varepsilon}_k$, which clearly commutes with the Hamiltonian. Thus, from the Heisenberg equation of motion (2.43) we learn that

$$\frac{\mathrm{d}}{\mathrm{d}t} \hat{\jmath}(t) = 0 \quad \Rightarrow \quad \hat{\jmath}(t) = c, \tag{6.83}$$

i.e. the current operator is constant in time. As a consequence, the Fourier transform in equation (6.75) will be applied to a constant function, which will result in a sole peak at $\omega = 0$.

If, however, the system is described in terms of complex unit cell, which will result in a multi-band structure, or if we consider open boundaries, the situation changes significantly. Here we give the explicit calculus for the former case. The Hamiltonian, whilst still bilinear, is determined by

$$\hat{H} = \sum_{k,\nu} \varepsilon_{k,\nu} \hat{c}_{k,\nu}^\dagger \hat{c}_{k,\nu}, \tag{6.84}$$

while the current operator takes the more complex form

$$\hat{\jmath} = \sum_{k,\nu,\nu'} \tilde{\varepsilon}_{k,\nu,\nu'} \hat{c}_{k,\nu}^\dagger \hat{c}_{k,\nu'}, \tag{6.85}$$

where we have introduced the band index ν. Two such examples will be presented in equations (7.84) and (7.85) in section 7.2.2. Note also that the $\tilde{\varepsilon}_{k,\nu,\nu'}$ are in general complex numbers. Now, analogously to equation (6.28) we can compute the time-dependent creation and annihilation operators through the Heisenberg equation of motion

$$\frac{\mathrm{d}}{\mathrm{d}t}\hat{c}^\dagger_{k,\nu}(t) = \mathrm{i}\sum_{k',\nu'}\varepsilon_{k',\nu'}\left[\hat{c}^\dagger_{k',\nu'}\hat{c}_{k',\nu'},\hat{c}^\dagger_{k,\nu}\right] = \mathrm{i}\sum_{k',\nu'}\varepsilon_{k',\nu'}\hat{c}^\dagger_{k',\nu'}\left\{\hat{c}^\dagger_{k,\nu},\hat{c}_{k',\nu'}\right\} \tag{6.86a}$$

$$= \mathrm{i}\sum_{k',\nu'}\varepsilon_{k',\nu'}\hat{c}^\dagger_{k',\nu'}\delta_{k,k'}\delta_{\nu,\nu'} = \mathrm{i}\varepsilon_{k,\nu}\hat{c}^\dagger_{k,\nu} \Rightarrow \hat{c}^\dagger_k(t) = \mathrm{e}^{\mathrm{i}\varepsilon_{k,\nu}t}\hat{c}^\dagger_{k,\nu}, \tag{6.86b}$$

$$\frac{\mathrm{d}}{\mathrm{d}t}\hat{c}_{k,\nu}(t) = \mathrm{i}\sum_{k',\nu'}\varepsilon_{k',\nu'}\left[\hat{c}^\dagger_{k',\nu'}\hat{c}_{k',\nu'},\hat{c}_{k,\nu}\right] = -\mathrm{i}\sum_{k',\nu'}\varepsilon_{k',\nu'}\left\{\hat{c}_{k,\nu},\hat{c}^\dagger_{k',\nu'}\right\}\hat{c}_{k',\nu'} \tag{6.87a}$$

$$= -\mathrm{i}\sum_{k',\nu'}\varepsilon_{k',\nu'}\hat{c}_{k',\nu'}\delta_{k,k'}\delta_{\nu,\nu'} = -\mathrm{i}\varepsilon_{k,\nu}\hat{c}_{k,\nu} \Rightarrow \hat{c}_k(t) = \mathrm{e}^{-\mathrm{i}\varepsilon_{k,\nu}t}\hat{c}_{k,\nu}, \tag{6.87b}$$

such that the time-dependent current operator takes the form

$$\hat{\jmath}(t) = \sum_{k,\nu,\nu'}\tilde{\varepsilon}_{k,\nu,\nu'}\hat{c}^\dagger_{k,\nu}(t)\,\hat{c}_{k,\nu'}(t) = \sum_{k,\nu,\nu'}\tilde{\varepsilon}_{k,\nu,\nu'}\mathrm{e}^{\mathrm{i}\left(\varepsilon_{k,\nu}-\varepsilon_{k,\nu'}\right)t}\hat{c}^\dagger_{k,\nu}\hat{c}_{k,\nu'}. \tag{6.88}$$

Inserting this result into equation (6.75) we find

$$\sigma_1(\omega) = \frac{1}{\omega L}\sum_{\substack{k,\nu,\nu',\\ \tilde{k},\tilde{\nu},\tilde{\nu}'}}\tilde{\varepsilon}_{k,\nu,\nu'}\tilde{\varepsilon}_{\tilde{k},\tilde{\nu},\tilde{\nu}'}\int_{-\infty}^{\infty}\mathrm{d}t'\mathrm{e}^{-\mathrm{i}\left(\omega-\left(\varepsilon_{k,\nu}-\varepsilon_{k,\nu'}\right)\right)t'}\left\langle\alpha\right|\left[\hat{c}^\dagger_{k,\nu}\hat{c}_{k,\nu'},\hat{c}^\dagger_{\tilde{k},\tilde{\nu}}\hat{c}_{\tilde{k},\tilde{\nu}'}\right]\left|\alpha\right\rangle \tag{6.89a}$$

$$= \frac{1}{\omega L}\sum_{\substack{k,\nu,\nu',\\ \tilde{k},\tilde{\nu},\tilde{\nu}'}}\tilde{\varepsilon}_{k,\nu,\nu'}\tilde{\varepsilon}_{\tilde{k},\tilde{\nu},\tilde{\nu}'}\left\langle\alpha\right|\left[\hat{c}^\dagger_{k,\nu}\hat{c}_{k,\nu'},\hat{c}^\dagger_{\tilde{k},\tilde{\nu}}\hat{c}_{\tilde{k},\tilde{\nu}'}\right]\left|\alpha\right\rangle\delta\big(\omega-\left(\varepsilon_{k,\nu}-\varepsilon_{k,\nu'}\right)\big), \tag{6.89b}$$

that is in this case the regular part of the optical conductivity measures the energy differences of the different bands.

Although all the considerations in this section are only mathematically correct in a very limited number of cases, that is for non-interacting time-independent systems and in case the state of reference is an eigenstate, the above stated principal result is also found in interacting setups as we will see in chapters 8 and 9.

6.2.3 Peierls Substitution

Light-matter interaction is a central concept in solid state physics and, as such, efficient methods to its modeling are required. While a full quantum treatment of a light pulse is quite cumbersome, often a semi classical treatment is sufficient. This approach is justified if the light's wavelength is orders of magnitude larger than the probe's lattice constant, which certainly holds in pump-probe experiments where solids are illuminated by lasers. Typical lattice constants are of the order of $a = 10^{-10}\,\mathrm{m}$ [17] and wavelengths of lasers are given by $\lambda > 10^{-7}\,\mathrm{m}$ [404] meeting the above assumption.

Hence, we aim at including a classical electromagnetic field into our formalism following reference [277]. The procedure to do so via minimal coupling [129], which corresponds to a situation with

large photon numbers or high intensities of the applied light, is referred as Peierls substitution [288]. We begin with general considerations (That is we shall briefly think in three dimensions.) and introduce an electric field $\vec{E}(\vec{r},t)$ and a magnetic field $\vec{B}(\vec{r},t)$. Assuming the fields to vanish for infinitely large distances we may express both quantities in Coulomb gauge by the vector potential $\vec{A}(\vec{r},t)$ via

$$\vec{E}(\vec{r},t) = -\frac{\partial}{\partial t}\vec{A}(\vec{r},t), \tag{6.90}$$

$$\vec{B}(\vec{r},t) = \vec{\nabla} \times \vec{A}(\vec{r},t). \tag{6.91}$$

We may, without loss of generality, further assume for the magnetic field to only point into z-direction, and, thus, the vector potential in only y-direction, such that equations (6.90) and (6.91) simplify to

$$E_{y}(\vec{r},t) = -\frac{\partial}{\partial t}A_{y}(\vec{r},t), \tag{6.92}$$

$$B_{z}(\vec{r},t) = \frac{\partial}{\partial x}A_{y}(\vec{r},t). \tag{6.93}$$

Following a redefinition of the Wannier functions, see, for instance, [277] for a derivation, the Peierls substitution manifests itself in two ways in second quantization. First, assuming a slow variance of $\vec{A}(\vec{r},t)$ the hopping term of the kinetic part of the model changes to

$$t_{\mathrm{hop},r,s} \to t_{\mathrm{hop},r,s}(t) \approx \exp\left(-\mathrm{i}\int_{\vec{R}_s}^{\vec{R}_r} \mathrm{d}\vec{r}\,'\,\vec{A}(\vec{r}\,',t)\right) t_{\mathrm{hop},r,s}, \tag{6.94}$$

where we have allowed the hopping to be site-dependent to cover a more general setup. Second, the system's overall energy is enhanced by an on-site term modeling the coupling of the electronic spin to the magnetic field

$$\hat{H}_{\mathrm{Zee}}(t) = g_{\mathrm{s}}\mu_{\mathrm{B}} \sum_{r} B_{z}(\vec{r}_{r},t)\,\hat{S}^{z}_{r}, \tag{6.95}$$

the so-called Zeeman term. Here we have introduced the Landé factor g_{s} and Bohr's magneton μ_{B}, as well as the spin operator $\hat{S}^{z}_{r}$. Note that often times $B_{z}(\vec{r},t)$ is orders of magnitude smaller than $E_{y}(\vec{r},t)$ and $A_{y}(\vec{r},t)$. In a concrete modeling this may easily be checked by means of equations (6.92) and (6.93). If so, the Zeeman term can be neglected, and bearing in mind that the spatial dependence of the vector potential only results in a finite magnetic field, c.f. equation (6.93), it may be chosen spatially independent in the first place. In this case equations (6.92) and (6.94) simplify to

$$E_{y}(t) = -\frac{\partial}{\partial t}A_{y}(t), \tag{6.96}$$

$$t_{\mathrm{hop},r,s} \to t_{\mathrm{hop},r,s}(t) \approx \exp\left(-\mathrm{i}A_{y}(t)\int_{\vec{R}_s}^{\vec{R}_r} \mathrm{d}\vec{r}\,'\right) t_{\mathrm{hop},r,s}, \tag{6.97}$$

respectively.

In case of only one-dimensional systems we take our model to point in x-direction and identify

$$E(r,t) = E_{y}(r,t), \tag{6.98}$$

$$A(r,t) = A_{y}(r,t), \tag{6.99}$$

$$B(r,t) = B_z(r,t). \tag{6.100}$$

Furthermore, equation (6.94) becomes exact and turns to

$$t_{\mathrm{hop},r} \to t_{\mathrm{hop},r}(t) = \exp\left(-\mathrm{i}\int_r^{r+1} \mathrm{d}r' A(r',t)\right) t_{\mathrm{hop},r} \tag{6.101a}$$

$$\approx \exp\left(-\frac{\mathrm{i}}{2}\left(A(r,t) + A(r+1,t)\right)\right) t_{\mathrm{hop},r}. \tag{6.101b}$$

For a spatially independent vector potential, the approximation in the above equation is again exact, such that the sole effect of the Peierls substitution is a change in the hopping amplitude as

$$t_{\mathrm{hop},r} \to t_{\mathrm{hop},r}(t) = \exp(-\mathrm{i}A(t))\, t_{\mathrm{hop},r}. \tag{6.102}$$

6.2.4 Numerical Computation

With MPSs, in principle it would be possible to compute the optical conductivity analogously to spectral functions by means of subsequent MPO applications, c.f. section 6.1.4. However, as is clear from its definition in section 6.2.1 the optical conductivity is a four point correlation function. Bearing in mind that both MPS time evolutions and applications of (global) operators lead to a quick growth of the MPS entanglement, it is understandable that this naive approach to computing the optical conductivity is rather cumbersome. Therefore, when it comes to the numerical we shall follow the experimentally motivated approach described in reference [336].

The main idea is to compute the optical conductivity through equation (6.74), which was strictly derived only for rather constrained cases, and extend this formalism to general setups. We wish to calculate the current with respect to a perturbation by an electric field $E(t)$. This electrical perturbation field is introduced to the procedure by means of a Peierls substitution. Thus, the current operator becomes

$$\hat{\jmath}(t',t) = -\mathrm{i}t_{\mathrm{hop}} \sum_r \left(\mathrm{e}^{\mathrm{i}A_{\mathrm{p}}(t',t)} \hat{c}^\dagger_{r+1}\hat{c}_r - \mathrm{e}^{-\mathrm{i}A_{\mathrm{p}}(t',t)} \hat{c}^\dagger_r \hat{c}_{r+1}\right), \tag{6.103}$$

while the kinetic part of the Hamiltonian changes to

$$\hat{H}_{\mathrm{kin}} \to \hat{H}_{\mathrm{kin,p}} = -t_{\mathrm{hop}} \sum_r \left(\mathrm{e}^{\mathrm{i}A_{\mathrm{p}}(t',t)} \hat{c}^\dagger_{r+1}\hat{c}_r + \mathrm{e}^{-\mathrm{i}A_{\mathrm{p}}(t',t)} \hat{c}^\dagger_r \hat{c}_{r+1}\right), \tag{6.104}$$

where we have introduced the vector potential $A_{\mathrm{p}}(t)$ which is related to the electric field via

$$E(t) = \frac{\partial}{\partial t} A_{\mathrm{p}}(t) \tag{6.105}$$

and already set the path for the use of relative coordinates, that is actually we have

$$A_{\mathrm{p}}(t',t) = A_{\mathrm{p}}(t'+t). \tag{6.106}$$

These prerequisites set, the time dependent probe current with respect to a general state $|\psi(t)\rangle$ at time t is then gained from evaluating

$$\begin{aligned} j_{\mathrm{p}}(t',t) = {} & \langle\psi(t)| U_{\mathrm{p}}(t,t'+t)\, \hat{\jmath}(t',t)\, U_{\mathrm{p}}(t'+t,t) |\psi(t)\rangle \\ & - \langle\psi(t)| U(t,t'+t)\, \hat{\jmath} U(t'+t,t) |\psi(t)\rangle, \end{aligned} \tag{6.107}$$

with $t' \geq 0$ and $\hat{\jmath}$ the time-independent current operator from equation (6.64). As $|\psi(t)\rangle$ could be any non-equilibrium state, we computed the expectation value of the current operator (6.103) twice in order to isolate the system's response onto the applied perturbation from the general non-equilibrium time evolution. First $\hat{\jmath}(t', t)$ is measured with respect to the time evolution of $|\psi(t)\rangle$ with the perturbative probe pulse switched on, that is $U_{\mathrm{p}}(t' + t, t)$ is the time evolution operator generated from the Hamiltonian of which the kinetic part is given by $\hat{H}_{\mathrm{kin,p}}$, c.f. equation (6.104). Second it is evaluated for the time evolution without the probe pulse, $U(t' + t, t)$ being derived from the original Hamiltonian $\hat{H}$. Then the latter current is subtracted from the former to isolate the effect of the probe pulse onto the current. We now compute a time-dependent optical conductivity in strict analogy to equation (6.74) via

$$\sigma(\omega, t) = \sigma_1(\omega, t) + \mathrm{i}\sigma_2(\omega, t) = \frac{j_{\mathrm{p}}(\omega, t)}{\mathrm{i}(\omega + \mathrm{i}\tilde{\eta})\, L A_{\mathrm{p}}(\omega, t)}, \tag{6.108}$$

where we have introduced the Fourier transformed current and vector potential

$$j_{\mathrm{p}}(\omega, t) = \int_{-\infty}^{\infty} \mathrm{d}t' \mathrm{e}^{-\mathrm{i}(\omega - \mathrm{i}\tilde{\eta})t'} j_{\mathrm{p}}(t', t), \tag{6.109}$$

$$A_{\mathrm{p}}(\omega, t) = \int_{-\infty}^{\infty} \mathrm{d}t' \mathrm{e}^{-\mathrm{i}(\omega - \mathrm{i}\tilde{\eta})t'} A_{\mathrm{p}}(t', t). \tag{6.110}$$

Here we have already incorporated the damping $\tilde{\eta}$ to enforce convergence. We stress that for these computations we explicitly do not assume time translational invariance as in equations (6.10) or (6.14). Note that for the optical conductivity we will only be interested in the part of $\omega > 0$ and therefore have adjusted the denominator of equation (6.108).

As for the probe pulse we choose it to be of Gaussian form

$$A_{\mathrm{p}}(t', t) = A_{0,\mathrm{p}} \mathrm{e}^{-\frac{(t + t' - \Delta t)^2}{2\tau^2}} \cos\big(\omega_{\mathrm{p}}(t + t' - \Delta t)\big), \tag{6.111}$$

which takes its maximum at $t + t' = \Delta t$. To ensure that this probe pulse captures the out-of-equilibrium situation at time t without having too much of an influence on the system's time evolution, the pulse's width τ has to be very small compared to any other time scales such as oscillation periods. Even a few time steps δ_t may suffice. The amplitude $A_{0,\mathrm{p}}$ may easily be several magnitudes smaller than the system's parameters and Δt is best to be chosen such that the peak is closest to time t as possible without $A_{\mathrm{p}}(t', t)$ becoming noticeably unsteady when approximating $A_{\mathrm{p}}(t', t) = 0$ for $t' < 0$. The probe frequency ω_{p} can than be chosen rather freely. We mention that in equation (6.111) we have used a rather simple form of the Peierls substitution as the site dependence was dropped to simplify the computations. Note that if the pumping of the system itself is modeled by a Peierls substitution, the probe process needs to be modeled through a second, superposing Peierls substitution. We conclude that in general the computation of the time-dependent probe current requires two time evolutions, one with and one without the probe pulse. In the easier case of a computation in equilibrium or if one knows that the pumping will have no effect on the expectation value of the current operator the subtrahend in equation (6.107) vanishes and requires no extra computation.

6.3 Classes of Out-of-equilibrium Problems and Approaches to Their Numerical Simulations for Excited Systems

As we have learned in section 6.1 in out-of-equilibrium setups the definition of the time-dependent spectral functions is far from being unique. Indeed, depending on what problem is to be theoretically described different definitions are applied.

Time-dependent spectral functions as we have defined them in section 6.1.2 have in the past been used to investigate mainly two kinds of problems. The first class is given by describing the post-quench behavior where excitations are modeled in a theoretically simple fashion by changing a parameter of the model system's Hamiltonian of which previously the ground state was computed. The procedure then consists of computing the time evolution of the initial ground state with respect to the quenched Hamiltonian such that in general a time-dependent spectral function will be obtained as the ground state of the initial Hamiltonian is no longer an eigenstate of the quenched one.

Other than this, Floquet systems where the Hamiltonian shows a periodicity in time have been investigated by means of these spectral functions. These systems seem to be particularly prone to such a treatment which does not come to too much surprise given that for Floquet systems an effective Hamiltonian can be derived [85] such that for long enough times the system should be considerable as quasi equilibrated. A variant of computing the spectral function consists of averaging over one time period, which of course looses the time dependence [382, 6]. Note that when it comes to the description of driven systems, we should distinguish between investigations that operate at longer times such that they are in a quasi steady state and, thus, an effective equilibrium, such that Floquet theory is applicable, and those where a driving has just turned on. In the latter case transient effects might occur which could lead to even unphysical artifacts in the spectral functions.

In recent years, a thorough theoretical description of pump-probe experiments has been aspired with particular focus on trARPES-like measurements. Here the ordinary time-dependent spectral functions we considered so far are not sufficient anymore. Instead, the probe pulse needs to be taken into account. A cumbersome derivation of Freericks et al. [104, 108, 103, 105, 106] and equally Braun et al. [43] culminated in a far more complex relation for time-dependent spectra, of which the essence is best summarized by the following formulation

$$\mathscr{A}(k,\omega,t) = \int_{-\infty}^{\infty}\int_{-\infty}^{\infty} \mathrm{d}t_1 \mathrm{d}t_2 \mathrm{e}^{-\mathrm{i}\omega(t_1-t_2)} s(t_1,t)\, s(t_2,t)\, \mathscr{G}^{<}(k,t_1,t_2) \tag{6.112}$$

with s being the probe pulse function. Note that the actual relation is even more complex. For a detailed analysis, we, thus, refer to the original work and its subsequent enhancements, and at this point shall only focus on the main differences to our previous approaches. We learn that here a full integration over both times of the two-time lesser Green's function is conducted and that the time dependence solely stems from the probe pulse function. The case of a continuous probe pulse is governed by setting $s \equiv 1$, which, however, is not guaranteed to converge anymore. Equation (6.112) will even diverge for equilibrium setups, meaning its application is also limited. However, we should mention that in the original formulation by Freericks et al. the spectral function did not loose its time dependence only from investigating a continuous probe pulse. We further note that there exist alternative expression for this relation as well, c.f. for instance [333], and that the interpretation regarding trARPES experiments is lengthly discussed in [109]. Albeit the rather complex structure of equation (6.112), its computation has already been pursued by means of full diagonalization [402],

DMFT [107], analytically [252], and also by means of MPSs [90]. As for the latter, another calculus by Zawadzki et al. [421] was conducted through a tunneling approach inspired by scanning tunneling spectroscopy [422]. The principal idea is to couple the sample under investigation to an ancilla probe system of which the sites themselves are uncoupled and to then measure the occupation of the probe chain over time for different coupling strengths. This approach has even been demonstrated to also recover results for equilibrium setups. However, it has nevertheless not been free of artifacts. Another ansatz, also proposed by Zawadzki et al. [423] is based on a recreation of a scattering effect [383].

We conclude that depending on the type of problem, a suitable theoretical definition of the spectral function must be chosen in advance to then design the simulation accordingly. At this point, there is again no general procedure.

7 Interacting and Non-interacting Models with Simple or Large Unit Cells and Their Band Structures

The main purpose of this chapter is introduce the principal model for our investigation, a one-dimensional Hubbard model with a magnetic superstructure, c.f. chapter 7.2.2. Beforehand, however, we begin with rather general considerations about models with trivial and non-trivial unit cells also introducing the tight binding model and the Hubbard model, which both are textbook standards. Of the many works we only give [229] as a reference at this point. Lastly, we will briefly discuss different mechanisms to model excitations thereby pushing the systems out of equilibrium.

7.1 Models with Trivial Unit Cells

We say a model has a trivial unit cell if (generally speaking only in the bulk) in real space its Hamiltonian is invariant against a translation by one lattice site.

In this case, the kinetic part is most often given by

$$\hat{H}_{\text{kin}} = -t_{\text{hop}} \sum_r \left(\hat{c}_r^\dagger \hat{c}_{r+1} + \hat{c}_{r+1}^\dagger \hat{c}_r \right), \tag{7.1}$$

where r takes again the role of a general index and t_{hop} is referred to as the hopping parameter. Furthermore, we take the system to be of L sites, i.e. $r \in \{0, \dots, L-1\}$ and set the lattice spacing to $a = 1$.

If we assume periodic boundary conditions, that is

$$r = L \equiv r = 0 \quad \Leftrightarrow \quad \hat{c}_L^{(\dagger)} = \hat{c}_0^{(\dagger)}, \tag{7.2}$$

equation (7.1) can easily be diagonalized by means of an ordinary (discrete) Fourier transform as introduced in sections 3.6.3 and A.1.1. Therefore, we define momentum space operators through

$$\hat{c}_k = \frac{1}{\sqrt{L}} \sum_r \mathrm{e}^{-\mathrm{i}kr} \hat{c}_r \quad \Leftrightarrow \quad \hat{c}_k^\dagger = \frac{1}{\sqrt{L}} \sum_r \mathrm{e}^{\mathrm{i}kr} \hat{c}_r^\dagger \tag{7.3a}$$

$$\Leftrightarrow \quad \hat{c}_r = \frac{1}{\sqrt{L}} \sum_k \mathrm{e}^{\mathrm{i}kr} \hat{c}_k \quad \Leftrightarrow \quad \hat{c}_r^\dagger = \frac{1}{\sqrt{L}} \sum_k \mathrm{e}^{-\mathrm{i}kr} \hat{c}_k^\dagger, \tag{7.3b}$$

with the discretized momenta k_μ given by

$$k_\mu = -\pi + \frac{2\pi\mu}{L}, \quad \mu \in \{0, \dots, L-1\} \quad \Rightarrow \quad k_\mu \in \left\{ 0, \dots, (L-1) \cdot \frac{2\pi}{L} \right\} \tag{7.4}$$

where we have exploited translational invariance to have the momenta run from $-\pi$ (inclusive) to $+\pi$ (exclusive). Inserting into equation (7.1), we find the kinetic part of the Hamiltonian to be determined by

$$\hat{H}_{\text{kin}} = -t_{\text{hop}} \frac{1}{L} \sum_{r,k,k'} \mathrm{e}^{-\mathrm{i}(k-k')r} \left(\mathrm{e}^{\mathrm{i}k'} + \mathrm{e}^{-\mathrm{i}k}\right) \hat{c}_k^\dagger \hat{c}_{k'} = -t_{\text{hop}} \sum_k 2\cos(k)\, \hat{c}_k^\dagger \hat{c}_k = \sum_k \varepsilon_k \hat{c}_k^\dagger \hat{c}_k, \quad (7.5)$$

where we have applied the Kronecker delta (3.57) expressed in the usual sloppy notation in the second equality. The quantity ε_k is called dispersion.

For open boundary conditions, which formally means

$$\hat{c}_L^{(\dagger)} = 0, \quad (7.6)$$

we can similarly diagonalize the Hamiltonian (7.1) by means of a sine transform, c.f. sections 3.7.2 and A.2, and also reference [29]. We define the following operators in momentum space

$$\hat{c}_k = \sqrt{\frac{2}{L+1}} \sum_r \sin(kr)\, \hat{c}_r \quad \Leftrightarrow \quad \hat{c}_k^\dagger = \sqrt{\frac{2}{L+1}} \sum_r \sin(kr)\, \hat{c}_r^\dagger \quad (7.7a)$$

$$\Leftrightarrow \quad \hat{c}_r = \sqrt{\frac{2}{L+1}} \sum_k \sin(kr)\, \hat{c}_k \quad \Leftrightarrow \quad \hat{c}_r^\dagger = \sqrt{\frac{2}{L+1}} \sum_k \sin(kr)\, \hat{c}_k^\dagger, \quad (7.7b)$$

for the discretized momenta

$$k_\mu = \frac{\pi\,(\mu+1)}{L+1}, \quad \mu \in \{0, \dots, L-1\} \quad \Rightarrow \quad k_\mu \in \left\{\frac{\pi}{L+1}, \dots, \frac{\pi}{L+1} \cdot L\right\}. \quad (7.8)$$

Inserting the above into equation (7.1) we obtain

$$\begin{aligned}
\hat{H}_{\text{kin}} &= -t_{\text{hop}} \frac{2}{L+1} \sum_{r,k,k'} \left(\sin(kr)\sin(k'(r+1))\, \hat{c}_k^\dagger \hat{c}_{k'} + \sin(k(r+1))\sin(k'r)\, \hat{c}_k^\dagger \hat{c}_{k'}\right) && (7.9a)\\
&= -t_{\text{hop}} \frac{2}{L+1} \sum_{r,k,k'} \left(\sin(kr)\sin(k'r)\cos(k')\, \hat{c}_k^\dagger \hat{c}_{k'} + \sin(kr)\cos(k'r)\sin(k')\, \hat{c}_k^\dagger \hat{c}_{k'}\right)\\
&\quad -t_{\text{hop}} \frac{2}{L+1} \sum_{r,k,k'} \left(\sin(kr)\sin(k'r)\cos(k)\, \hat{c}_k^\dagger \hat{c}_{k'} + \cos(kr)\sin(k'r)\sin(k)\, \hat{c}_k^\dagger \hat{c}_{k'}\right) && (7.9b)\\
&= -t_{\text{hop}} \sum_{k,k'} \left(\frac{2}{L+1} \sum_r \sin(kr)\sin(k'r)\cos(k')\, \hat{c}_k^\dagger \hat{c}_{k'}\right)\\
&\quad -t_{\text{hop}} \sum_{k,k'} \left(\frac{2}{L+1} \sum_r \sin(kr)\sin(k'r)\cos(k)\, \hat{c}_k^\dagger \hat{c}_{k'}\right)\\
&\quad -t_{\text{hop}} \sum_{k,k'} \left(\frac{2}{L+1} \sum_r \left(\sin(kr)\cos(k'r)\sin(k') + \cos(kr)\sin(k'r)\sin(k)\right) \hat{c}_k^\dagger \hat{c}_{k'}\right) && (7.9c)\\
&= -t_{\text{hop}} \sum_{k,k'} \left(\delta_{k,k'} \cos(k')\, \hat{c}_k^\dagger \hat{c}_{k'}\right) - t_{\text{hop}} \sum_{k,k'} \left(\delta_{k,k'} \cos(k)\, \hat{c}_k^\dagger \hat{c}_{k'}\right) && (7.9d)\\
&= -t_{\text{hop}} \sum_k 2\cos(k)\, \hat{c}_k^\dagger \hat{c}_k = \sum_k \varepsilon_k \hat{c}_k^\dagger \hat{c}_k. && (7.9e)
\end{aligned}$$

Here we have used the identity

$$\sin(x+y) = \sin(x)\cos(y) + \cos(x)\sin(y), \quad (7.10)$$

as well as the very important relations

$$\delta_{k,k'} = \frac{2}{L+1}\sum_r \sin(kr)\sin(k'r) \tag{7.11}$$

$$0 = \frac{2}{L+1}\sum_r \left(\sin(kr)\cos(k'l)\sin(k') + \cos(kr)\sin(k'r)\sin(k)\right) \quad \forall \quad k,k', \tag{7.12}$$

which we have again expressed in sloppy notation. Note that unfortunately

$$\frac{2}{L+1}\sum_r \sin(kr)\cos(k'r)\sin(k') \neq 0 \tag{7.13}$$

for arbitrary k and k'. This will significantly complicate matters for a non-trivial unit cell. Conveniently, we obtain the same dispersion relation ε_k for both cases of boundary conditions, the only difference being its sampling due to the different constraints of the discretized momenta.

The current operator, however, behaves entirely differently depending on the boundary conditions. For periodic boundary conditions we insert (7.3b) into equation (6.64) to find the similarly simple expression

$$\hat{\jmath} = -\mathrm{i}t_{\mathrm{hop}}\frac{1}{L}\sum_{r,k,k'} \mathrm{e}^{-\mathrm{i}(k-k')r}\left(\mathrm{e}^{\mathrm{i}k'} - \mathrm{e}^{-\mathrm{i}k}\right)\hat{c}_k^\dagger \hat{c}_{k'} = t_{\mathrm{hop}}\sum_k 2\sin(k)\,\hat{c}_k^\dagger \hat{c}_k = \sum_k \tilde{\varepsilon}_k \hat{c}_k^\dagger \hat{c}_k, \tag{7.14}$$

while for open boundaries using (7.7b) we obtain

$$\hat{\jmath} = +\mathrm{i}t_{\mathrm{hop}}\frac{2}{L+1}\sum_{r,k,k'}\left(\sin(kr)\sin(k'(r+1))\,\hat{c}_k^\dagger \hat{c}_{k'} - \sin(k(r+1))\sin(k'r)\,\hat{c}_k^\dagger \hat{c}_{k'}\right) \tag{7.15a}$$

$$\begin{aligned} = {} & +\mathrm{i}t_{\mathrm{hop}}\frac{2}{L+1}\sum_{r,k,k'}\left(\sin(kr)\sin(k'r)\cos(k')\,\hat{c}_k^\dagger \hat{c}_{k'} + \sin(kr)\cos(k'r)\sin(k')\,\hat{c}_k^\dagger \hat{c}_{k'}\right) \\ & -\mathrm{i}t_{\mathrm{hop}}\frac{2}{L+1}\sum_{r,k,k'}\left(\sin(kr)\sin(k'r)\cos(k)\,\hat{c}_k^\dagger \hat{c}_{k'} + \cos(kr)\sin(k'r)\sin(k)\,\hat{c}_k^\dagger \hat{c}_{k'}\right) \end{aligned} \tag{7.15b}$$

$$\begin{aligned} = {} & +\mathrm{i}t_{\mathrm{hop}}\sum_{k,k'}\left(\frac{2}{L+1}\sum_r \sin(kr)\sin(k'r)\cos(k')\,\hat{c}_k^\dagger \hat{c}_{k'}\right) \\ & -\mathrm{i}t_{\mathrm{hop}}\sum_{k,k'}\left(\frac{2}{L+1}\sum_r \sin(kr)\sin(k'r)\cos(k)\,\hat{c}_k^\dagger \hat{c}_{k'}\right) \\ & +\mathrm{i}t_{\mathrm{hop}}\sum_{k,k'}\left(\frac{2}{L+1}\sum_r \left(\sin(kr)\cos(k'r)\sin(k') - \cos(kr)\sin(k'r)\sin(k)\right)\hat{c}_k^\dagger \hat{c}_{k'}\right) \end{aligned} \tag{7.15c}$$

$$= +\mathrm{i}t_{\mathrm{hop}}\sum_{k,k'}\left(\frac{4}{L+1}\sum_r \left(\sin(kr)\cos(k'r)\sin(k')\right)\hat{c}_k^\dagger \hat{c}_{k'}\right) = \sum_{k,k'} \tilde{\varepsilon}_{k,k'}\hat{c}_k^\dagger \hat{c}_{k'}. \tag{7.15d}$$

Comparing equations (7.14) and (7.15) to one another, we note that the fundamental differences for both boundary conditions manifest in several ways. First, we note that for periodic boundaries, the current operator is purely real whilst it is purely imaginary for open boundaries. In either case, however, the operator is hermitian such that their expectation values are real. Second, for the former situation the operator is diagonal in momentum space, which does not hold true for the latter.

7.1.1 The Tight Binding Model and Its Extensions

Assuming free electrons, i.e. such that do not interact, the so-called tight binding model can be derived from the general solid state Hamiltonian, c.f. for instance [229]. We present it at this point for spinless fermions, that is

$$\hat{H}_{\mathrm{tb}} = -t_{\mathrm{hop}} \sum_{r} \left(\hat{f}_{r}^{\dagger} \hat{f}_{r+1} + \hat{f}_{r+1}^{\dagger} \hat{f}_{r} \right), \tag{7.16}$$

which is nothing but a specification of the kinetic Hamiltonian (7.1). Thus, its representation in momentum space is given by equation (7.5) or (7.9)

$$\hat{H}_{\mathrm{tb}} = -t_{\mathrm{hop}} \sum_{k} 2\cos(k)\, \hat{a}_{k}^{\dagger} \hat{a}_{k} = \sum_{k} \varepsilon_{k} \hat{a}_{k}^{\dagger} \hat{a}_{k}, \tag{7.17}$$

and for the current operator we have

$$\hat{\jmath}_{\mathrm{tb}} = t_{\mathrm{hop}} \sum_{k} 2\sin(k)\, \hat{a}_{k}^{\dagger} \hat{a}_{k}, \tag{7.18}$$

for periodic boundaries or

$$\hat{\jmath}_{\mathrm{tb}} = \mathrm{i}t_{\mathrm{hop}} \sum_{k,k'} \left(\frac{4}{L+1} \sum_{r} \left(\sin(kr) \cos(k'r) \sin(k') \right) \hat{a}_{k}^{\dagger} \hat{a}_{k'} \right) \tag{7.19}$$

for open boundaries, respectively, c.f. equation (7.14) or (7.15). The cosine-like dispersion relation ε_{k} is typical for free electrons. Here we have introduced the naming convention of indicating all creation and annihilation operators in momentum space for non-generic models by $\hat{a}_{k}^{\dagger}$ or $\hat{a}_{k}$, respectively.

The tight binding model can be extended by adding an interaction term as follows

$$\hat{H}_{tV} = \hat{H}_{t} + \hat{H}_{V} = -t_{\mathrm{hop}} \sum_{r} \left(\hat{f}_{r}^{\dagger} \hat{f}_{r+1} + \hat{f}_{r+1}^{\dagger} \hat{f}_{r} \right) + V \sum_{r} \hat{n}_{r} \hat{n}_{r+1}, \tag{7.20}$$

where we have obeyed the Pauli principle that two fermions cannot occupy the same site. This model is also referred to as the tV-chain. Note that the interaction term $\hat{H}_{V}$ is quadrilinear. Therefore, for finite interaction V the tV-chain cannot be diagonalized through the introduction of momentum space operators. Nevertheless, we can still express the model in terms of momentum space operators which yield equation (7.17) for $\hat{H}_{t} = \hat{H}_{\mathrm{tb}}$ as a diagonal part and

$$\hat{H}_{V} = V \sum_{k,k',k'',k'''} \Gamma_{k,k',k'',k'''} \hat{a}_{k}^{\dagger} \hat{a}_{k'} \hat{a}_{k''}^{\dagger} \hat{a}_{k'''}. \tag{7.21}$$

as an additional perturbation. Here we have introduced the transition tensor

$$\Gamma_{k,k',k'',k'''} = \sum_{r} S_{k,r}^{*} S_{k',r} S_{k'',r+1}^{*} S_{k''',r+1} \tag{7.22}$$

having exploited equation (6.35) with

$$S_{k,r} = \frac{1}{\sqrt{L}} \mathrm{e}^{-\mathrm{i}kr} \tag{7.23}$$

for periodic boundaries and

$$S_{k,r} = \sqrt{\frac{2}{L+1}} \sin(kr) \tag{7.24}$$

for open boundaries, respectively. Note that $\Gamma_{k,k',k'',k'''}$ can easily be evaluated numerically.

Regarding the interaction part there is an alternative of defining the tV-chain, that is

$$\hat{H}_V = V \sum_r \left(\hat{n}_r - \frac{1}{2}\right)\left(\hat{n}_{r+1} - \frac{1}{2}\right), \tag{7.25}$$

of which the advantage is that expressed this way the entire Hamiltonian is particle-hole symmetric, i.e. invariant under the transformation

$$\hat{f}_r^\dagger \to \hat{f}_r, \quad \Leftrightarrow \quad \hat{n}_r \to \left(1 - \hat{n}_r\right) \tag{7.26}$$

c.f. also [429] for further explanations. In this case, the entire Hamiltonian in momentum space reads

$$\hat{H}_{tV} = \hat{H}_t + \hat{H}_V \tag{7.27}$$

$$= \sum_k \left(-2t_{\text{hop}} \cos(k) - V\right) \hat{a}_k^\dagger \hat{a}_k + V \sum_{k,k',k'',k'''} \Gamma_{k,k',k'',k'''} \hat{a}_k^\dagger \hat{a}_{k'} \hat{a}_{k''}^\dagger \hat{a}_{k'''} + \frac{V}{4}, \tag{7.28}$$

i.e. the major changes are a shift in the dispersion and an additional constant.

7.1.2 The Hubbard Model

In attempt to explain electron correlations in narrow energy bands beginning in 1963 John Hubbard issued a series of publications [158, 159, 160, 161, 162, 163] where he proposed the following model

$$\hat{H}_{\text{Hub}} = \hat{H}_{\text{kin}} + \hat{H}_U = -t_{\text{hop}} \sum_{\sigma,r} \left(\hat{c}_{\sigma,r}^\dagger \hat{c}_{\sigma,r+1} + \hat{c}_{\sigma,r+1}^\dagger \hat{c}_{\sigma,r}\right) + U \sum_r \hat{n}_{\uparrow,r} \hat{n}_{\downarrow,r}. \tag{7.29}$$

Here we consider electrons with spin σ. The interaction is now on-site, meaning that two electrons of opposite spin occupying the same lattice site will cost an energy of U. The Hubbard model is of paramount importance in modern solid state physics as it is one of the easiest models of electronic systems to include interactions. Alongside with several modifications it has been studied extensively in the past [98] which amongst its original purpose led to a basic understanding of physical processes like for instance band magnetism, the Mott metal-insulator transition, high-T_c superconductivity, and, early on, ferromagnetism [133, 180]. To this day, no general solution to the Hubbard model is known. In one dimension, however, it can be solved exactly by means of a Bethe ansatz which leads to the introduction of the so-called Lieb-Wu equations [217, 218]. Note that the derivation is rather involved and not obtained in terms of second quantization. We will only present some very basic properties of the one-dimensional Hubbard model and refer to [97] for further reading.

Regarding its structure, the Hubbard model is quite similar to the tV-chain. For a non-interacting system, i.e. $U = 0$, we have nothing more than two independent tight-binding models, one for each spin direction. Hence, the kinetic part in momentum space reads

$$\hat{H}_{\text{kin}} = -t_{\text{hop}} \sum_{\sigma,k} 2\cos(k)\, \hat{a}_{\sigma,k}^\dagger \hat{a}_{\sigma,k} = \sum_{\sigma,k} \varepsilon_k \hat{a}_{\sigma,k}^\dagger \hat{a}_{\sigma,k}, \tag{7.30}$$

c.f. equation (7.5) or (7.9), the only difference to equation (7.17) being the summation over the spin. Note that while we present the spectral function only spin-resolved, the optical conductivity may either be shown totally or spin-resolved. We therefore define the total current operator as

$$\hat{\jmath}_{\mathrm{Hub}} = \sum_{\sigma} \hat{\jmath}_{\mathrm{Hub},\sigma}, \tag{7.31}$$

where with the help of equation (7.14) or (7.15) we have introduced the spin-resolved current operator

$$\hat{\jmath}_{\mathrm{Hub},\sigma} = t_{\mathrm{hop}} \sum_{k} 2\sin(k)\, \hat{a}^{\dagger}_{\sigma,k} \hat{a}_{\sigma,k}, \tag{7.32}$$

for periodic boundaries or

$$\hat{\jmath}_{\mathrm{Hub},\sigma} = \mathrm{i}t_{\mathrm{hop}} \sum_{k,k'} \left(\frac{4}{L+1} \sum_{r} \left(\sin(kr)\cos(k'r)\sin(k')\right) \hat{a}^{\dagger}_{\sigma,k} \hat{a}_{\sigma,k'} \right), \tag{7.33}$$

for open boundaries, again bearing strong similarities to equation (7.18) or (7.19), respectively. Similarly to the tV-chain, the interaction part in momentum space is given by

$$\hat{H}_U = U \sum_{k,k',k'',k'''} \Gamma_{k,k',k'',k'''} \hat{a}^{\dagger}_{\uparrow,k} \hat{a}_{\uparrow,k'} \hat{a}^{\dagger}_{\downarrow,k''} \hat{a}_{\downarrow,k'''} \tag{7.34}$$

with

$$\Gamma_{k,k',k'',k'''} = \sum_{r} S^{*}_{k,r} S_{k',r} S^{*}_{k'',r} S_{k''',r} \tag{7.35}$$

and the definitions from equations (7.23) and (7.24).

The Hubbard Hamiltonian can, just like the tV-chain, be expressed particle-hole symmetrically via

$$\hat{H}_U = U \sum_{r} \left(\hat{n}_{\uparrow,r} - \frac{1}{2} \right) \left(\hat{n}_{\downarrow,r+1} - \frac{1}{2} \right), \tag{7.36}$$

such that the entire Hamiltonian in momentum space becomes

$$\hat{H}_{\mathrm{Hub}} = \hat{H}_{\mathrm{kin}} + \hat{H}_U \tag{7.37}$$

$$= \sum_{\sigma,k} \left(-2t_{\mathrm{hop}}\cos(k) - U\right) \hat{a}^{\dagger}_{\sigma,k} \hat{a}_{\sigma,k} + U \sum_{k,k',k'',k'''} \Gamma_{k,k',k'',k'''} \hat{a}^{\dagger}_{\uparrow,k} \hat{a}_{\uparrow,k'} \hat{a}^{\dagger}_{\downarrow,k''} \hat{a}_{\downarrow,k'''} + \frac{U}{4}, \tag{7.38}$$

c.f. equation (7.25) and (7.27), respectively.

7.2 Models with Large Unit Cells

The Hamiltonian of a model with a unit cell of size X will only be translationally invariant with respect to shifts of X sites. In real space it is therefore useful to decompose the site index r into a cell index l and an intra cell index (or sub cell index) j, such that we have

$$r = Xl + j, \quad r \in \{0, \ldots, L-1\}, \quad l \in \{0, \ldots, N-1\}, \quad N = \frac{L}{X}, \quad j \in \{0, \ldots, X-1\}, \tag{7.39a}$$

$$\Rightarrow \hat{c}^{(\dagger)}_{r} = \hat{c}^{(\dagger)}_{l,j}, \tag{7.39b}$$

where the total system size L should be a multiple of the unit cell's size X.

For this case diagonalizing a bilinear Hamiltonian under periodic boundary conditions requires two steps. First we perform a (discrete) Fourier transform in the cell index l only, such that any non-interacting Hamiltonian will be given by

$$\hat{H}_0 = \sum_k \sum_{j,j'} C_{k,j,j'} \hat{c}^\dagger_{k,j} \hat{c}_{k,j'}, \tag{7.40}$$

where we have defined the Fourier transform via

$$\hat{c}_{k,j} = \frac{1}{\sqrt{N}} \sum_l \mathrm{e}^{-\mathrm{i}kl} \hat{c}_{l,j} \quad \Leftrightarrow \quad \hat{c}^\dagger_{k,j} = \frac{1}{\sqrt{N}} \sum_l \mathrm{e}^{\mathrm{i}kl} \hat{c}^\dagger_{l,j} \tag{7.41a}$$

$$\Leftrightarrow \quad \hat{c}_{l,j} = \frac{1}{\sqrt{N}} \sum_k \mathrm{e}^{\mathrm{i}kl} \hat{c}_{k,j} \quad \Leftrightarrow \quad \hat{c}^\dagger_{l,j} = \frac{1}{\sqrt{N}} \sum_k \mathrm{e}^{-\mathrm{i}kl} \hat{c}^\dagger_{k,j}. \tag{7.41b}$$

Here we have again used the usual sloppy notation. We clarify that here in real space the sampling is

$$l_n = Xn, \quad n \in \{0, \dots, N-1\}, \tag{7.42}$$

which yields in momentum space

$$k_\mu = -\frac{\pi}{X} + \frac{2\pi\mu}{XN}, \quad \mu \in \{0, \dots, N-1\} \quad \Rightarrow \quad k_\mu \in \left\{-\frac{\pi}{X}, \dots, (N-1) \cdot \frac{2\pi}{XN}\right\}. \tag{7.43}$$

From these considerations we already see that for a system with a non-trivial unit cell the Brillouin zone shrinks to the range $[-\pi/X, \pi/X[$ instead of $[-\pi, \dots, \pi[$ known from models with a one-site unit cell. The tensor C in equation (7.40) can be interpreted as a k-dependent matrix of size $X \times X$. As the whole Hamiltonian is hermitian the same needs to hold for C_k. Therefore we are able to introduce unitary matrices T_k to diagonalize this matrix, i.e.

$$C_k = T_k D_k T_k^\dagger \quad \Leftrightarrow \quad C_{k,j,j'} = \sum_\nu T_{k,j,\nu} D_{k,\nu,\nu} T^*_{k,j',\nu}, \tag{7.44}$$

D_k being a diagonal matrix. Hence, defining the full momentum space operators

$$\hat{c}_{k,\nu} = \sum_j T^*_{k,j,\nu} \hat{c}_{k,j} \qquad = \frac{1}{\sqrt{N}} \sum_{l,j} \mathrm{e}^{-\mathrm{i}kl} T^*_{k,j,\nu} \hat{c}_{l,j}, \tag{7.45a}$$

$$\Leftrightarrow \quad \hat{c}^\dagger_{k,\nu} = \sum_j T_{k,j,\nu} \hat{c}^\dagger_{k,j} \qquad = \frac{1}{\sqrt{N}} \sum_{l,j} \mathrm{e}^{\mathrm{i}kl} T_{k,j,\nu} \hat{c}^\dagger_{l,j}, \tag{7.45b}$$

$$\Leftrightarrow \quad \hat{c}_{l,j} = \frac{1}{\sqrt{N}} \sum_k \mathrm{e}^{\mathrm{i}kl} \hat{c}_{k,j} \quad = \frac{1}{\sqrt{N}} \sum_{k,\nu} \mathrm{e}^{\mathrm{i}kl} T_{k,j,\nu} \hat{c}_{k,\nu}, \tag{7.45c}$$

$$\Leftrightarrow \quad \hat{c}^\dagger_{l,j} = \frac{1}{\sqrt{N}} \sum_k \mathrm{e}^{-\mathrm{i}kl} \hat{c}^\dagger_{k,j} = \frac{1}{\sqrt{N}} \sum_{k,\nu} \mathrm{e}^{-\mathrm{i}kl} T^*_{k,j,\nu} \hat{c}^\dagger_{k,\nu}, \tag{7.45d}$$

we may diagonalize equation (7.40) completely, such that we obtain

$$\hat{H}_0 = \sum_{k,\nu} \varepsilon_{k,\nu} \hat{c}^\dagger_{k,\nu} \hat{c}_{k,\nu} \tag{7.46}$$

with the dispersion

$$\varepsilon_{k,\nu} \coloneqq D_{k,\nu,\nu}. \tag{7.47}$$

Mathematically speaking, the dispersion at momentum k is thus given by the eigenvalues of C_k, while the matrices T_k hold their corresponding eigenvectors. In this fully diagonalized notation the index ν is interpreted as labeling the band. Note that to comply with oral conventions, we will count the band index differently

$$\nu \in \{1, \dots, X\}. \tag{7.48}$$

We have thus shown that a non-trivial unit cell results in a multi band structure. Note that a rigorous application of the schemes derived in section 6.1 will result in the spectral functions depending on both, the momentum and the band (index), i.e.

$$\mathscr{A}_\nu^{<,>}(k,\omega,t) = \mathscr{A}^{<,>}(k,\nu,\omega,t). \tag{7.49}$$

We shall call this quantity the spectral component of band (index) ν, or the ν-component for short, to the total spectral function

$$\mathscr{A}^{<,>}(k,\omega,t) = \sum_\nu \mathscr{A}_\nu^{<,>}(k,\omega,t). \tag{7.50}$$

In principle this procedure can be extended to arbitrary quantum numbers. In all other cases however, namely the spin σ, we will evaluate all the channels of the respective quantum number individually.

Note that the Lehmann representations of the band components of the greater and lesser spectral function computed with respect to an eigenstate $|\alpha\rangle$, compare equations (6.25) and (6.26), are given in strict analogy to equation (7.49) as

$$\mathscr{A}_\nu^{<}(k,\omega) = \sum_n \delta\big(\omega - \big(E_\alpha^M - E_n^{M-1}\big)\big) \left|\left\langle n^{M-1}\right| \hat{c}_{k,\nu} \left|\alpha^M\right\rangle\right|^2, \tag{7.51}$$

$$\mathscr{A}_\nu^{>}(k,\omega) = \sum_n \delta\big(\omega + \big(E_\alpha^M - E_n^{M+1}\big)\big) \left|\left\langle n^{M+1}\right| \hat{c}_{k,\nu}^\dagger \left|\alpha^M\right\rangle\right|^2. \tag{7.52}$$

Inspired by the procedure applied in reference [3] we consider the case of a system to consist of a single unit cell only. Then we have $l = 0$, i.e. there will also only be a single momentum $k = 0$, such that we have

$$\hat{c}_{k,j}^{(\dagger)} = \hat{c}_{l,j}^{(\dagger)} \tag{7.53}$$

and hence equations (7.51) and (7.52) equal their momentum-independent forms

$$\mathscr{A}^{<}(\omega) = \sum_{n,j} \delta\big(\omega - \big(E_\alpha^M - E_n^{M-1}\big)\big) \left|\left\langle n^{M-1}\right| \hat{c}_{l=0,j} \left|\alpha^M\right\rangle\right|^2 = \sum_k \mathscr{A}^{<}(k,\omega), \tag{7.54}$$

$$\mathscr{A}^{>}(\omega) = \sum_{n,j} \delta\big(\omega + \big(E_\alpha^M - E_n^{M+1}\big)\big) \left|\left\langle n^{M+1}\right| \hat{c}_{l=0,j}^\dagger \left|\alpha^M\right\rangle\right|^2 = \sum_k \mathscr{A}^{>}(k,\omega). \tag{7.55}$$

For the current operator there is no general closed expression. The Fourier transform in the cell index can be easily applied yielding

$$\hat{j} = \sum_{k,\nu,\nu'} \tilde{\varepsilon}_{k,\nu,\nu'} \hat{c}_{k,\nu}^\dagger \hat{c}_{k,\nu'}, \tag{7.56}$$

where the specific structure of the model determines $\tilde{\varepsilon}_{k,\nu,\nu'}$ which may become arbitrarily unpleasant.

Just like the matrices of eigenvectors T_k, $\tilde{\varepsilon}_{k,\nu,\nu'}$ will often need to be evaluated numerically. Whilst this procedure may be quite cumbersome, it still provides a well-founded algorithm. Unfortunately, the situation is even more complex for open boundaries. Therefore we devote a new section to this matter. We do mention, however, that, if the model under investigation has special properties, other methods may also be applied, c.f. for instance [337].

7.2.1 The General Sine Transform

For open boundary conditions care needs to be taken when diagonalizing even a bilinear Hamiltonian if the unit cell is non-trivial [238]. As pointed out in reference [77] additional effects, e.g. Zak phases, can add to an already complex problem [240]. Because it always relies on some form of periodicity, we cannot even partially apply a (discrete) Fourier transform as in the case of periodic boundaries, neither can we make use of a sine transform. The problem, again, is that equation (7.13) does not vanish in general. Hence, we will introduce a scheme that very much resembles the procedure from equation (7.44) onwards, which also relies on a matrix diagonalization. As we will see below, this method comes with severe limitations.

We begin by noting that any bilinear Hamiltonian can be expressed through

$$\hat{H}_0 = \sum_{r,r'} H_{r,r'} \hat{c}_r^\dagger \hat{c}_r \tag{7.57}$$

with the Hamiltonian matrix H. This we diagonalize via

$$H = PDP^\dagger \quad \Leftrightarrow \quad H_{r,r'} = \sum_k P_{r',k} D_{k,k} P^*_{r,k}. \tag{7.58}$$

introducing a diagonal matrix D and a hermitian matrix P. Defining

$$\hat{c}_k = \sum_r P^*_{r,k} \hat{c}_r \quad \Leftrightarrow \quad \hat{c}_k^\dagger = \sum_r P_{r,k} \hat{c}_r^\dagger \quad \Leftrightarrow \quad \hat{c}_r = \sum_k P_{r,k} \hat{c}_k \quad \Leftrightarrow \quad \hat{c}_r^\dagger = \sum_k P^*_{r,k} \hat{c}_k^\dagger, \tag{7.59}$$

and identifying

$$\varepsilon_k = D_{k,k} \tag{7.60}$$

we arrive at

$$\hat{H}_0 = \sum_k \varepsilon_k \hat{c}_k^\dagger \hat{c}_k, \tag{7.61}$$

which is the desired diagonalization.

The crucial observation at this point is that when we apply this technique to Hamiltonian (7.1), of which the unit cell is trivial, with open boundaries, we obtain the exact same values for the dispersion ε_k as with the ordinary sine transform, c.f. section 3.7. Therefore, we label the momenta by

$$k_\mu = \frac{\pi(\mu+1)}{L+1}, \quad \mu \in \{0, \dots, L-1\} \quad \Rightarrow \quad k_\mu \in \left\{ \frac{\pi}{L+1}, \dots, \frac{2\pi}{L+1} \cdot L \right\}. \tag{7.62}$$

that is the same as in equation (7.8). Note that we have not used any properties of the unit cell in the above derivation, so the application to systems with trivial unit cells is well defined. As the methods yield the same result in this special case, including only depicting half of the first Brillouin zone, we refer to the procedure in this section as the general sine transform. Note, however, that its application is severely limited.

The problem is that our newly defined method comes *without any order* of the eigenvalues, that is, a priori it is not clear what eigenvalue ε_k belongs to what momentum k. Only the knowledge that for $k \geq 0$ the dispersion relation of the Hamiltonian (7.1) is monotonously increasing saved us here, meaning that if we arrange the eigenvalues ε_k ascendingly, we can *identify* them as corresponding to the momenta calculated from (7.62). Hence, in order for this method to be applicable, we need to know in advance that the dispersion is monotonous for momenta $k \geq 0$ and that we will only obtain results for positive momenta. This is obviously a strong restriction. A great illustrative example is to apply this scheme to the same Hamiltonian (7.1) but with periodic boundary conditions, of which we also know the dispersion relation, the famous cosine shape, c.f. equation (7.17). As in the case of periodic boundary conditions, the momenta's range stretches from negative values to positive ones, the second constraint is violated. With the exception of the edge and the center momentum of the first Brillouin zone, we will obtain two times the same eigenvalues ε_k, corresponding to the momenta k and $-k$, respectively. While the values themselves are perfectly correct, we have no technique to arrange them in the right order, which makes the method obsolete at this point. Note further that the knowledge of the monotonous behavior of the dispersion relation is most often only clear for the case of periodic boundaries. We will then just transfer this property to the system with open boundaries only because we have no reason to assume that it would change. There will be no mathematically rigorous derivation. Note that, indeed, in general especially at the edges, the results for the dispersion ε_k will deviate from their counterparts for periodic boundaries. This, however, is a finite size effect, that can in principle be corrected with the treatment of larger systems.

If we despite these restrictions and uncertainties still apply the general sine transform it is obvious from equation (7.62) that for a non-trivial unit cell the dispersion relation will be presented in the extended zone scheme. We will still need to manually fold the results back to the first Brillouin zone where we will reintroduce the band index via

$$\hat{c}^{(\dagger)}_{k',\nu} = \begin{cases} \hat{c}^{(\dagger)}_{(\nu-1)X\pi/(L+1)+k'}, & \nu \mod 2 = 1 \\ \hat{c}^{(\dagger)}_{(\nu X+1)\pi/(L+1)-k'}, & \nu \mod 2 = 0 \end{cases}, \quad \nu \in \{1, \dots, X\}, \tag{7.63}$$

which we have expressed in the usual sloppy notation having defined

$$k'_\mu = \frac{\pi\,(\mu+1)}{L+1}, \quad \mu \in \{0, \dots, N-1\} \quad \Rightarrow \quad k'_\mu \in \left\{ \frac{\pi}{L+1}, \dots, \frac{2\pi}{L+1} \cdot N \right\}. \tag{7.64}$$

Note that to perform this step we need to know the number of bands X in advance, which is likewise most often obtained from a computation using periodic boundary conditions. We further mention that in case we are only considering a single unit cell, equations (7.54) and (7.54) hold true in this situation as well.

Finally, we obtain the current operator from inserting (7.59) into equation (6.64)

$$\hat{\jmath} = -\mathrm{i}t_{\mathrm{hop}} \sum_{r,k,k'} \left(P^*_{r,k} P_{r+1,k'} - P^*_{r+1,k} P_{r,k'} \right) \hat{c}^\dagger_k \hat{c}_{k'}. \tag{7.65}$$

7.2.2 The Hubbard Model with a Magnetic Superstructure

In this thesis we will mostly study a variant of the one-dimensional Hubbard model presented in section (7.1.2), which we obtain by the addition of a magnetic superstructure

$$\hat{H} = \hat{H}_0 + \hat{H}_U = \hat{H}_{\mathrm{kin}} + \hat{H}_\Delta + \hat{H}_U, \tag{7.66a}$$

$$\hat{H}_{\text{kin}} = -t_{\text{hop}} \sum_{\sigma,r} \left(\hat{c}^{\dagger}_{\sigma,r} \hat{c}_{\sigma,r+1} + \hat{c}^{\dagger}_{\sigma,r+1} \hat{c}_{\sigma,r} \right), \tag{7.66b}$$

$$\hat{H}_{U} = U \sum_{r} \hat{n}_{\uparrow,r} \hat{n}_{\downarrow,r}, \tag{7.66c}$$

$$\hat{H}_{\Delta} = \sum_{r} \Delta_r S^z_r \quad \text{with} \quad S^z_r = \frac{1}{2} \left(\hat{n}_{\uparrow,r} - \hat{n}_{\downarrow,r} \right). \tag{7.66d}$$

New to the hopping amplitude t_{hop} and the on-site Coulomb repulsion U, comes Δ_r which describes an on-site Zeeman term of strength Δ and for finite values will lead to structure with multiple bands. Clearly, for $\Delta = 0$ the original Hubbard model is obtained. We will consider cases of staggered magnetic fields allowing us to express the Hamiltonian in terms of cell and intra cell indices as follows

$$\begin{aligned} \hat{H}_{\text{kin}} = & -t_{\text{hop}} \sum_{\sigma,l} \Bigg(\sum_{j=0}^{X-2} \left(\hat{c}^{\dagger}_{\sigma,l,j} \hat{c}_{\sigma,l,j+1} + \hat{c}^{\dagger}_{\sigma,l,j+1} \hat{c}_{\sigma,l,j} \right) \\ & + \left(\hat{c}^{\dagger}_{\sigma,l,X-1} \hat{c}_{\sigma,l+1,0} + \hat{c}^{\dagger}_{\sigma,l+1,0} \hat{c}_{\sigma,l,X-1} \right) \Bigg), \end{aligned} \tag{7.67a}$$

$$\hat{H}_{U} = U \sum_{l,j} \hat{n}_{\uparrow,l,j} \hat{n}_{\downarrow,l,j}, \tag{7.67b}$$

$$\hat{H}_{\Delta} = \sum_{l,j} \frac{\Delta_j}{2} \left(\hat{n}_{\uparrow,l,j} - \hat{n}_{\downarrow,l,j} \right), \tag{7.67c}$$

with X again being the size of the unit cell. Originally this model was proposed in references [33, 197, 195] with an on-site potential Δ_j alternating every two sites $(\Delta, \Delta, -\Delta, -\Delta)$ of strength Δ and, thus, a four-site unit cell. Here, for the ground state of praseodymium calcium manganite ($Pr_{1-x}Ca_xMnO_3$, PCMO) t_{2g} electrons of the manganese atoms were identified to freeze out, such that the so-formed crystal of Zener polarons due to Hund's coupling provides a pairwise antiferromagnetically aligned background, a superlattice, for free e_g electrons to move through the system. Taking repulsion between electrons into account and neglecting interactions with the lattice the Hamiltonian takes the above Hubbard-like form is obtained. While derived to model the situation best at quarter filling we will also consider the case of half filling where the model can be simplified to just a site wise alternating Δ_j, i.e. $(\Delta, -\Delta)$, and, hence, a two-site unit cell. We will use the superscripts 4Δ and 2Δ to distinguish between these two superlattices. In the context of this thesis, we will refer to these variants as the four band and the two band model, respectively. Note that in references [149, 148, 285, 310] similar structures were also found in OSMP [134, 395] states, which are obtained in ladder systems like $BaFe_2Se_3$, although the coupling of the conduction electrons there is realized via a Heisenberg exchange term rather than a Zeeman term.

We further mention that for finite sizes L this model is *not* particle-hole symmetric as $\hat{H}_{\Delta}$ flips its sign under transformation (7.26). Only the bare Hubbard model can be transformed such, c.f. equation (7.37). Note, however, that at least for periodic boundary conditions the dispersion of neither $\hat{H}^{4\Delta}$ nor $\hat{H}^{2\Delta}$ changes since only Δ^2 contributes to equations (7.73) or (7.78), respectively. As for $\hat{H}^{4\Delta}$ there exists another interesting property for open boundaries. Defining the unit cell differently with Δ_j being $(\Delta, -\Delta, -\Delta, \Delta)$ or $(-\Delta, \Delta, \Delta, -\Delta)$ we find edge states in its spectrum. We will not investigate this model in the remainder of this text in order to avoid potential interference to our simulations from this effect and leave this analysis for future research.

Next, for both cases we shall discuss the dispersion of the non-interacting part for periodic boundary conditions. Proceeding analogously to equations (7.40) to (7.41b) in order to diagonalize $\hat{H}_0^{4\Delta}$, we define

$$\hat{b}_{\sigma,k,j} = \frac{1}{\sqrt{N}} \sum_l \mathrm{e}^{-\mathrm{i}kl} \hat{c}_{\sigma,l,j} \quad \Leftrightarrow \quad \hat{b}^\dagger_{\sigma,k,j} = \frac{1}{\sqrt{N}} \sum_l \mathrm{e}^{\mathrm{i}kl} \hat{c}^\dagger_{\sigma,l,j} \tag{7.68a}$$

$$\Leftrightarrow \quad \hat{c}_{\sigma,l,j} = \frac{1}{\sqrt{N}} \sum_k \mathrm{e}^{\mathrm{i}kl} \hat{b}_{\sigma,k,j} \quad \Leftrightarrow \quad \hat{c}^\dagger_{\sigma,l,j} = \frac{1}{\sqrt{N}} \sum_k \mathrm{e}^{-\mathrm{i}kl} \hat{b}^\dagger_{\sigma,k,j}, \tag{7.68b}$$

such that we have

$$\hat{H}_0^{4\Delta} = \sum_{\sigma,k} \sum_{j,j'} C^{4\Delta}_{\sigma,k,j,j'} \hat{b}^\dagger_{\sigma,k,j} \hat{b}_{\sigma,k,j'}, \tag{7.69}$$

with

$$C^{4\Delta}_{\sigma,k} = \begin{pmatrix} \sigma\Delta/2 & -t_{\mathrm{hop}} & 0 & -t_{\mathrm{hop}}\mathrm{e}^{\mathrm{i}4k} \\ -t_{\mathrm{hop}} & \sigma\Delta/2 & -t_{\mathrm{hop}} & 0 \\ 0 & -t_{\mathrm{hop}} & -\sigma\Delta/2 & -t_{\mathrm{hop}} \\ -t_{\mathrm{hop}}\mathrm{e}^{-\mathrm{i}4k} & 0 & -t_{\mathrm{hop}} & -\sigma\Delta/2 \end{pmatrix}, \tag{7.70}$$

where we identify $\sigma = \uparrow \equiv +1$ and $\sigma = \downarrow \equiv -1$. Diagonalizing $C^{4\Delta}$ as in equation (7.44) we obtain the full momentum space operators

$$\hat{a}_{\sigma,k,\nu} = \sum_j T^*_{\sigma,k,j,\nu} \hat{b}_{\sigma,k,j} \quad \Leftrightarrow \quad \hat{a}^\dagger_{\sigma,k,\nu} = \sum_j T_{\sigma,k,j,\nu} \hat{b}^\dagger_{\sigma,k,j} \tag{7.71a}$$

$$\Leftrightarrow \quad \hat{b}_{\sigma,k,j} = \sum_\nu T_{\sigma,k,j,\nu} \hat{a}_{\sigma,k,\nu} \quad \Leftrightarrow \quad \hat{b}^\dagger_{\sigma,k,j} = \sum_\nu T^*_{\sigma,k,j,\nu} \hat{a}^\dagger_{\sigma,k,\nu}, \tag{7.71b}$$

and thus, c.f. equation (7.46),

$$\hat{H}_0^{4\Delta} = \sum_{\sigma,k,\nu} \varepsilon^{4\Delta}_{k,\nu} \hat{a}^\dagger_{\sigma,k,\nu} \hat{a}_{\sigma,k,\nu} \tag{7.72}$$

with the dispersion

$$\varepsilon^{4\Delta}_{k,\nu} = s_{1,\nu} t_{\mathrm{hop}} \sqrt{2 + \frac{\Delta^2}{4t_{\mathrm{hop}}^2} + s_{2,\nu} 2 \sqrt{\cos^2(2k) + \frac{\Delta^2}{4t_{\mathrm{hop}}^2}}}, \quad s = \begin{pmatrix} -1 & -1 & +1 & +1 \\ +1 & -1 & -1 & +1 \end{pmatrix} \tag{7.73}$$

for the four bands $\nu = 1, 2, 3, 4$. The discretized momenta follow from (7.43) as

$$k_\mu = -\frac{\pi}{4} + \frac{2\pi\mu}{4N}, \quad \mu \in \{0, \dots, N-1\} \quad \Rightarrow \quad k_\mu \in \left\{ -\frac{\pi}{4}, \dots, -\frac{\pi}{4} + (N-1) \cdot \frac{\pi}{2N} \right\}, \tag{7.74}$$

N being again the number of unit cells, and the first Brillouin zone (BZ), clearly, extends as $[-\pi/4, \dots, \pi/4[$.

As for $H_0^{2\Delta}$ we, likewise, employ equation (7.68) yielding

$$\hat{H}_0^{2\Delta} = \sum_{\sigma,k} \sum_{j,j'} C^{2\Delta}_{\sigma,k,j,j'} \hat{b}^\dagger_{\sigma,k,j} \hat{b}_{\sigma,k,j'}. \tag{7.75}$$

Here, the corresponding matrix takes the simpler form

$$C^{2\Delta}_{\sigma,k} = \begin{pmatrix} \sigma\Delta/2 & -t_{\mathrm{hop}} \left(1 + \mathrm{e}^{\mathrm{i}2k}\right) \\ -t_{\mathrm{hop}} \left(1 + \mathrm{e}^{-\mathrm{i}2k}\right) & -\sigma\Delta/2 \end{pmatrix}, \tag{7.76}$$

which by means of equation (7.44) can be diagonalized to obtain full momentum space operators analogous to those in equation (7.71) with adjusted eigenvector matrices $T_{\sigma,k}$. Therefrom, we derive the diagonalization

$$\hat{H}_0^{2\Delta} = \sum_{\sigma,k,\nu} \varepsilon_{k,\nu}^{2\Delta} \hat{a}_{\sigma,k,\nu}^\dagger \hat{a}_{\sigma,k,\nu} \tag{7.77}$$

with the dispersion

$$\varepsilon_{k,\nu}^{2\Delta} = s_\nu t_{\text{hop}} \sqrt{\frac{\Delta^2}{4t_{\text{hop}}^2} + 2\left(\cos(2k) + 1\right)}, \quad s_\nu = (-1)^\nu \tag{7.78}$$

for two bands $\nu = 1, 2$. The discretized momenta are given by

$$k_\mu = -\frac{\pi}{2} + \frac{2\pi\mu}{2N}, \quad \mu \in \{0, \dots, N-1\} \quad \Rightarrow \quad k_\mu \in \left\{-\frac{\pi}{2}, \dots, -\frac{\pi}{2} + (N-1)\cdot\frac{\pi}{N}\right\}, \tag{7.79}$$

such that the first Brillouin zone increases to $[-\pi/2, \dots, \pi/2[$.

In figure 7.1 we show $\varepsilon_{k,\nu}^{4\Delta}$ and $\varepsilon_{k,\nu}^{2\Delta}$ for various values of Δ. We first note that with increasing Δ

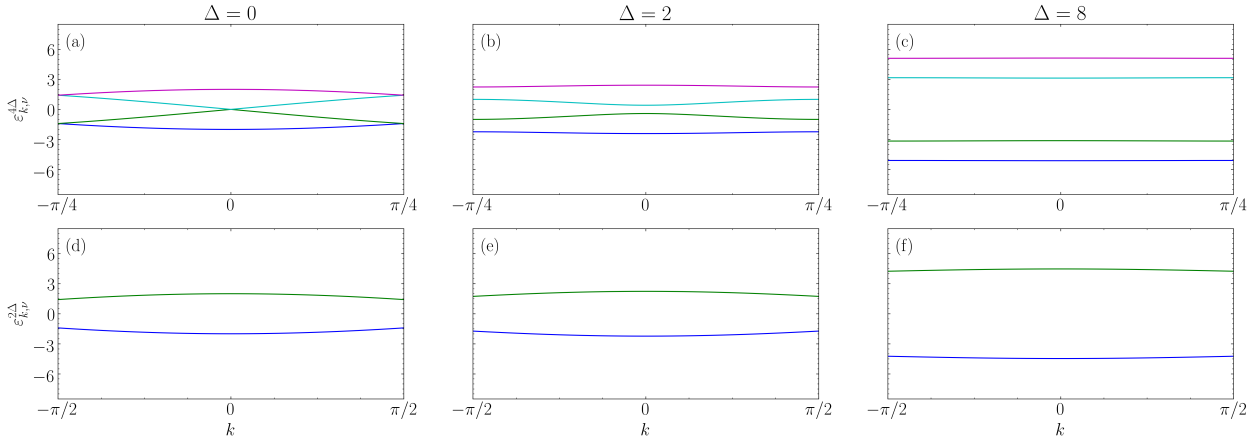

Figure 7.1: Dispersion relations of $\hat{H}_0^{4\Delta}$ and $\hat{H}_0^{2\Delta}$, $\varepsilon_{k,\nu}^{4\Delta}$ and $\varepsilon_{k,\nu}^{2\Delta}$, c.f. equations (7.73) and (7.78), for various values of Δ and PBCs. The contributions of $\nu = 1, 2, 3, 4$ are shown in blue, green, cyan, and magenta, respectively.

the bands flatten significantly, such that at $\Delta = 8$ they are nearly dispersionless. This feature is stronger for $\hat{H}_0^{4\Delta}$ than for $\hat{H}_0^{2\Delta}$, yet still the effect is clearly visible. We further observe that for $\hat{H}_0^{4\Delta}$ the system can be readily divided into two lower and two upper bands, their distance being for finite Δ always around a value of 2. The distance of the upper and lower band for $\hat{H}_0^{2\Delta}$, or the respective two for $\hat{H}_0^{4\Delta}$, roughly scales as $2\Delta/3$. Note that for $\Delta = 0$ in both cases we obtain nothing more than the cosine dispersion of the tight binding model but folded back to a quarter or half of the first Brillouin zone, respectively.

In the case of open boundaries, we apply the general sine transform as presented in section 7.2.1 to find the momentum space operators

$$\hat{a}_{\sigma,k',\nu}^{(\dagger)} = \begin{cases} \hat{a}_{\sigma,k'}^{(\dagger)}, & \nu = 1 \\ \hat{a}_{\sigma,(L/2+1)\pi/(L+1)-k'}^{(\dagger)}, & \nu = 2 \\ \hat{a}_{\sigma,(L/2)\pi/(L+1)+k'}^{(\dagger)}, & \nu = 3 \\ \hat{a}_{\sigma,\pi-k'}^{(\dagger)}, & \nu = 4 \end{cases} \tag{7.80}$$

with discretized momenta

$$k'_\mu = \frac{\pi\mu}{L+1}, \quad \mu \in \{1, \dots, L/4\} \quad \Rightarrow \quad k'_\mu \in \left\{ \frac{\pi}{L+1}, \dots, \frac{\pi}{L+1} \cdot \frac{L}{4} \right\} \tag{7.81}$$

for $\hat{H}_0^{4\Delta}$, while for $\hat{H}_0^{2\Delta}$ we obtain

$$\hat{a}^{(\dagger)}_{\sigma,k',\nu} = \begin{cases} \hat{a}^{(\dagger)}_{\sigma,k'}, & \nu = 1 \\ \hat{a}^{(\dagger)}_{\sigma,\pi-k'}, & \nu = 2 \end{cases} \tag{7.82}$$

alongside with

$$k'_\mu = \frac{\pi\mu}{L+1}, \quad \mu \in \{1, \dots, L/2\} \quad \Rightarrow \quad k'_\mu \in \left\{ \frac{\pi}{L+1}, \dots, \frac{\pi}{L+1} \cdot \frac{L}{2} \right\}. \tag{7.83}$$

As we already pointed out the bands follow the results for periodic boundaries well, however small deviations occur at the edges of the Brillouin zone for $\hat{H}_0^{4\Delta}$. We address this issue in figure 7.2 where we compare the results for both models at different system sizes L. We note that with increasing L the bulk is represented more and more accurately, while strictly at the edges the effect remains.

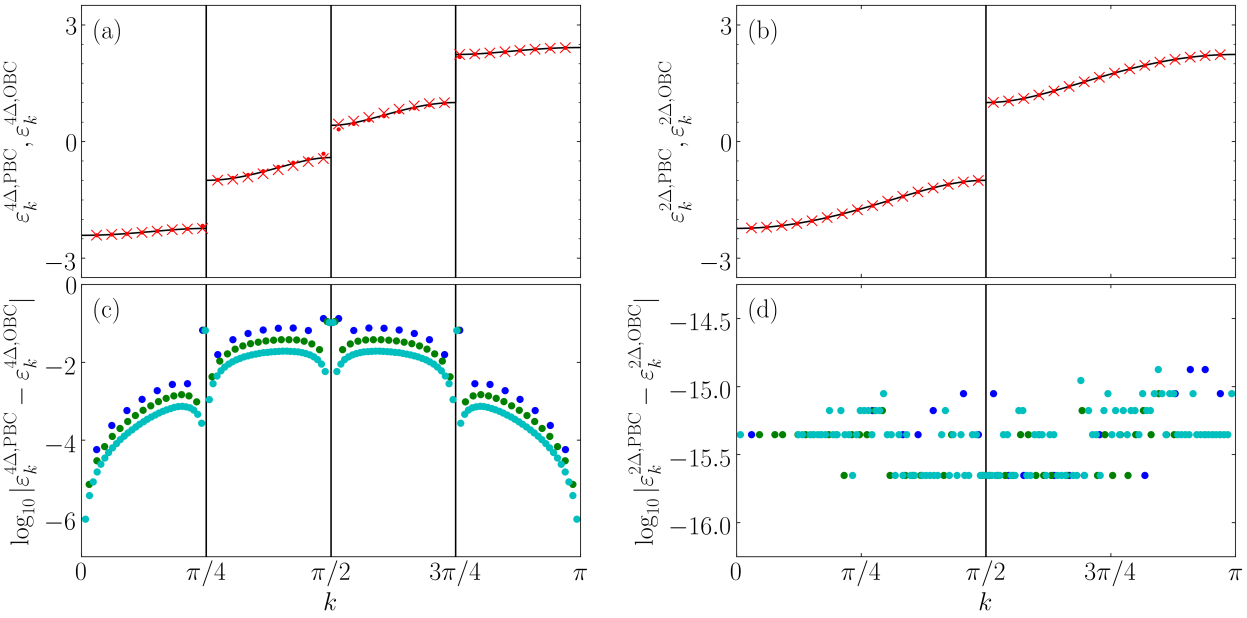

Figure 7.2: Comparison of the dispersion relations for OBCs and PBCs presented in the extended zone scheme. In the former case $\varepsilon_{k,\nu}^{4\Delta,\mathrm{OBC}}$ and $\varepsilon_{k,\nu}^{2\Delta,\mathrm{OBC}}$ are obtained from a general sine transform, c.f. section 7.2.1. For PBCs equations (7.73) and (7.78) are evaluated for the momenta gained from equation (7.81) or (7.83), respectively; for even ν the output is flipped; concatenating the so-obtained results of all bands we find $\varepsilon_{k,\nu}^{4\Delta,\mathrm{PBC}}$ and $\varepsilon_{k,\nu}^{2\Delta,\mathrm{PBC}}$ for $\hat{H}_0^{4\Delta}$ and $\hat{H}_0^{2\Delta}$. Black lines: Reference data according to equation (7.73) and (7.78), respectively. Top line: Comparison of (a) $\varepsilon_{k,\nu}^{4\Delta,\mathrm{OBC}}$ and $\varepsilon_{k,\nu}^{4\Delta,\mathrm{PBC}}$ or (b) $\varepsilon_{k,\nu}^{2\Delta,\mathrm{OBC}}$ and $\varepsilon_{k,\nu}^{2\Delta,\mathrm{PBC}}$ for $\Delta/t_{\mathrm{hop}} = 2$ and $L = 32$. Bottom line: Differences of these quantities for $L = 32$ (blue), $L = 64$ (green), and $L = 128$ (cyan). Vertical black lines: Edges of the unit cell.

Therefore, we take this to be a finite size effect and will primarily focus on the bulk behavior to neglect this feature. Evidently, for $L \to \infty$ and $k > 0$ the results for open boundaries will converge to their respective counterparts for periodic boundary conditions.

We close this discussion with a brief description of the current operator starting with the case of periodic boundary conditions. Expressing $\hat{\jmath}$ (6.64) in terms of cell and intra cell indices and subsequently inserting equations (7.68a) and (7.71a), we find for $\hat{H}^{4\Delta}$

$$\begin{aligned}
\hat{\jmath}^{4\Delta} =& -\mathrm{i}t_{\mathrm{hop}} \sum_{\sigma,l} \sum_{j=0}^{2} \left(\hat{c}^{\dagger}_{\sigma,l,j} \hat{c}_{\sigma,l,j+1} - \hat{c}^{\dagger}_{\sigma,l,j+1} \hat{c}_{\sigma,l,j} \right) \\
& -\mathrm{i}t_{\mathrm{hop}} \sum_{\sigma,l} \left(\hat{c}^{\dagger}_{\sigma,l,3} \hat{c}_{\sigma,l+1,0} - \hat{c}^{\dagger}_{\sigma,l+1,0} \hat{c}_{\sigma,l,3} \right) && (7.84a) \\
=& -\mathrm{i}t_{\mathrm{hop}} \frac{1}{N} \sum_{\sigma,l,k,k'} \mathrm{e}^{\mathrm{i}(k-k')l} \sum_{j=0}^{2} \left(\hat{b}^{\dagger}_{\sigma,k,j} \hat{b}_{\sigma,k',j+1} - \hat{b}^{\dagger}_{\sigma,k,j+1} \hat{b}_{\sigma,k',j} \right) \\
& -\mathrm{i}t_{\mathrm{hop}} \frac{1}{N} \sum_{\sigma,l,k,k'} \mathrm{e}^{\mathrm{i}(k-k')l} \left(\mathrm{e}^{\mathrm{i}4k'} \hat{b}^{\dagger}_{\sigma,k,3} \hat{b}_{\sigma,k',0} - \mathrm{e}^{-\mathrm{i}4k} \hat{b}^{\dagger}_{\sigma,k,0} \hat{b}_{\sigma,k',3} \right) && (7.84b) \\
=& -\mathrm{i}t_{\mathrm{hop}} \sum_{\sigma,k} \sum_{j=0}^{2} \left(\hat{b}^{\dagger}_{\sigma,k,j} \hat{b}_{\sigma,k,j+1} - \hat{b}^{\dagger}_{\sigma,k,j+1} \hat{b}_{\sigma,k,j} \right) \\
& -\mathrm{i}t_{\mathrm{hop}} \sum_{\sigma,k} \left(\mathrm{e}^{\mathrm{i}4k} \hat{b}^{\dagger}_{\sigma,k,3} \hat{b}_{\sigma,k,0} - \mathrm{e}^{-\mathrm{i}4k} \hat{b}^{\dagger}_{\sigma,k,0} \hat{b}_{\sigma,k,3} \right) && (7.84c) \\
=& -\mathrm{i}t_{\mathrm{hop}} \sum_{\sigma,k,\nu,\nu'} \left(\sum_{j=0}^{2} T^{*}_{\sigma,k,j,\nu} T_{\sigma,k,j+1,\nu'} - T^{*}_{\sigma,k,j+1,\nu} T_{\sigma,k,j,\nu'} \right) \hat{a}^{\dagger}_{\sigma,k,\nu} \hat{a}_{\sigma,k,\nu'} \\
& -\mathrm{i}t_{\mathrm{hop}} \sum_{\sigma,k,\nu,\nu'} \left(\mathrm{e}^{\mathrm{i}4k} T^{*}_{\sigma,k,3,\nu} T_{\sigma,k,0,\nu'} - \mathrm{e}^{-\mathrm{i}4k} T^{*}_{\sigma,k,0,\nu} T_{\sigma,k,3,\nu'} \right) \hat{a}^{\dagger}_{\sigma,k,\nu} \hat{a}_{\sigma,k,\nu'} && (7.84d) \\
=& \sum_{\sigma,k,\nu,\nu'} \tilde{\varepsilon}^{4\Delta}_{\sigma,k,\nu,\nu'} \hat{a}^{\dagger}_{\sigma,k,\nu} \hat{a}_{\sigma,k,\nu'}. && (7.84e)
\end{aligned}$$

Analogously, for $\hat{H}^{2\Delta}$ we obtain

$$\begin{aligned}
\hat{\jmath}^{2\Delta} =& -\mathrm{i}t_{\mathrm{hop}} \sum_{\sigma,l} \left(\hat{c}^{\dagger}_{\sigma,l,0} \hat{c}_{\sigma,l,1} - \hat{c}^{\dagger}_{\sigma,l,1} \hat{c}_{\sigma,l,0} + \hat{c}^{\dagger}_{\sigma,l,1} \hat{c}_{\sigma,l+1,0} - \hat{c}^{\dagger}_{\sigma,l+1,0} \hat{c}_{\sigma,l,1} \right) && (7.85a) \\
=& -\mathrm{i}t_{\mathrm{hop}} \frac{1}{N} \sum_{\sigma,l,k,k'} \mathrm{e}^{\mathrm{i}(k-k')l} \left(\hat{b}^{\dagger}_{\sigma,k,0} \hat{b}_{\sigma,k',1} - \hat{b}^{\dagger}_{\sigma,k,1} \hat{b}_{\sigma,k',0} \right) \\
& -\mathrm{i}t_{\mathrm{hop}} \frac{1}{N} \sum_{\sigma,l,k,k'} \mathrm{e}^{\mathrm{i}(k-k')l} \left(\mathrm{e}^{\mathrm{i}2k'} \hat{b}^{\dagger}_{\sigma,k,1} \hat{b}_{\sigma,k',0} - \mathrm{e}^{-\mathrm{i}2k} \hat{b}^{\dagger}_{\sigma,k,0} \hat{b}_{\sigma,k',1} \right) && (7.85b) \\
=& -\mathrm{i}t_{\mathrm{hop}} \sum_{\sigma,k} \left(\hat{b}^{\dagger}_{\sigma,k,0} \hat{b}_{\sigma,k,1} - \hat{b}^{\dagger}_{\sigma,k,1} \hat{b}_{\sigma,k,0} + \mathrm{e}^{\mathrm{i}2k} \hat{b}^{\dagger}_{\sigma,k,1} \hat{b}_{\sigma,k,0} - \mathrm{e}^{-\mathrm{i}2k} \hat{b}^{\dagger}_{\sigma,k,0} \hat{b}_{\sigma,k,1} \right) && (7.85c) \\
=& -\mathrm{i}t_{\mathrm{hop}} \sum_{\sigma,k,\nu,\nu'} \left(T^{*}_{\sigma,k,0,\nu} T_{\sigma,k,1,\nu'} - T^{*}_{\sigma,k,1,\nu} T_{\sigma,k,0,\nu'} \right) \hat{a}^{\dagger}_{\sigma,k,\nu} \hat{a}_{\sigma,k,\nu'} \\
& -\mathrm{i}t_{\mathrm{hop}} \sum_{\sigma,k,\nu,\nu'} \left(\mathrm{e}^{\mathrm{i}2k} T^{*}_{\sigma,k,1,\nu} T_{\sigma,k,0,\nu'} - \mathrm{e}^{-\mathrm{i}2k} T^{*}_{\sigma,k,0,\nu} T_{\sigma,k,1,\nu'} \right) \hat{a}^{\dagger}_{\sigma,k,\nu} \hat{a}_{\sigma,k,\nu'} && (7.85d) \\
=& \sum_{\sigma,k,\nu,\nu'} \tilde{\varepsilon}^{2\Delta}_{\sigma,k,\nu,\nu'} \hat{a}^{\dagger}_{\sigma,k,\nu} \hat{a}_{\sigma,k,\nu'}. && (7.85e)
\end{aligned}$$

For open boundary conditions equation (7.65) remains the most general expression demonstrating that the momentum space representation of $\hat{j}$ is in general cumbersome.

7.3 Floquet Driven Systems

If an explicitly time-dependent Hamiltonian is periodic in time, i.e.

$$\hat{H}(t) = \hat{H}(t+T), \tag{7.86}$$

where T is the period, it is referred to as a Floquet Hamiltonian named after French mathematician Gaston Floquet. Such models have some quite interesting properties, which is investigated in the field of Floquet theory, c.f. reference [138] for an introduction. From inserting into the time-dependent Schrödinger equation (2.20), formally a time-periodic time evolution operator

$$U_{\mathrm{F}}(t, t_0) = U_{\mathrm{F}}(t+T, t_0), \tag{7.87}$$

c.f. section 2.4, can be derived. Characteristic to Floquet theory is now that (with certain extensions to finite-dimensional systems on finite time scales) an effective Hamiltonian based on this time evolution operator can be derived as

$$\hat{H}_{\mathrm{F}} = U_{\mathrm{F}}^{\dagger}(t, t_0)\, \hat{H}(t)\, U_{\mathrm{F}}(t, t_0) - \mathrm{i} U_{\mathrm{F}}^{\dagger}(t, t_0)\, \frac{\mathrm{d}}{\mathrm{d}t} U_{\mathrm{F}}(t, t_0). \tag{7.88}$$

Crucially this effective Hamiltonian is time-independent, which, as described, e.g., in sections 6.1.3 and 6.2.2, significantly simplifies further computations. For more details on these and other properties of Floquet-driven systems see for instance [85]. In recent years, Floquet theory has become a topic of increased attention also in condensed matter theory, see for instance [179, 382], where its implications regarding spectral functions are discussed.

A very simple way to transform existing models into Floquet systems is the application of a Peierls substitution, which we discussed in section 6.2.3, c.f. for instance reference [241]. In this thesis we shall restrict ourselves to only investigating a simple particle-hole symmetric tV-chain, see equation (7.25), section 7.1.1, where we have transformed

$$t_{\mathrm{hop},r} \to t_{\mathrm{hop},r}(t) = \exp(-\mathrm{i}A(t))\, t_{\mathrm{hop},r}, \tag{7.89}$$

c.f. equation (6.102), with

$$A(t) = \sin(\omega_{\mathrm{F}} t). \tag{7.90}$$

7.4 Modeling of (Photo) Excitations

So far, we have discussed different models, their properties and applications. We shall now introduce mechanisms to the theoretical treatment of excitations pushing the system out of equilibrium. Here we discuss four such principal approaches.

Perhaps the most common way to model out-of equilibrium situations in theoretical or numerical solid state physics is the concept of a sudden quench. Here, a parameter of the Hamiltonian is

changed during the calculus or simulation process. This could involve a change at a certain point t_0 during a time evolution, i.e.

$$\hat{H}(t) = \begin{cases} \hat{H}_1(t), & \text{for} \quad t < t_0 \\ \hat{H}_2(t), & \text{for} \quad t \geq t_0 \end{cases}, \tag{7.91}$$

or conducting the time evolution with a different Hamiltonian the ground state was obtained with respect to corresponding to the special case $t_0 = 0$. The evident advantage of quench protocols is that they are easy to realize in theoretical computations or numerical simulations. However, judging in how far these changes mirror an experimental setup may be rather cumbersome.

A common approach in particular when it comes to the modeling of photo excitations is a semi-classical treatment by means of a Peierls substitution, c.f. section 6.2.3 or reference for [86] an application. The difficulty in this approach lies within the introduction of a time dependence to the Hamiltonian

$$\hat{H} \to \hat{H}_{\text{Peierls}}(t), \tag{7.92}$$

if the original model was chosen to be time-independent, since for instance, the evaluation of time-dependent expectation values is more complicated in general. Just like quenching the system a Peierls substitution usually changes the Hamiltonian globally. Therefore, both these ansatzes mainly correspond to rather strong excitations. For continuously driven systems the numerical treatment, at least by means of MPSs, is somewhat peculiar. When starting the simulation from a ground state, what is actually modeled is a system where the driving is suddenly switched on, which is contrary to the assumption of periodicity in time, c.f. equation (7.86). Thus, in this case only in the long-time limit the properties of this driven model can be safely expected to be understood from Floquet theory [85].

For more detailed analyses more parts of a model, like e.g. light fields, need to be described quantum mechanically. Clearly, a full quantum treatment with a principal system $\hat{H}_{\text{S}}$ that is to be excited and an exciting system $\hat{H}_{\text{E}}$ is also possible. In this case, the actual excitation is realized by some sort of coupling $\hat{C}\big(\hat{H}_{\text{S}}, \hat{H}_{\text{E}}\big)$ of the two respective systems, such that the total Hamiltonian reads

$$\hat{H} = \hat{H}_{\text{S}} + \hat{H}_{\text{E}} + \hat{C}\big(\hat{H}_{\text{S}}, \hat{H}_{\text{E}}\big). \tag{7.93}$$

This approach is by design the most exact one and, hence, in its rigorous execution the most complex.

Having quench protocols in mind, instead of changing the Hamiltonian another comparably simple approach is to change the quantum state of the system under consideration. When it comes to modeling a (photo) excitation this procedure corresponds to the application of an operator $\hat{\Lambda}$ to the ground state resulting in an out-of equilibrium state

$$|\psi\rangle = \hat{\Lambda}\,|\text{GS}\rangle. \tag{7.94}$$

The exact design of the operator then primarily defines the excitation. Again, there exist several approaches. If the system under consideration is given in spatial coordinates, the theoretically easiest realizable excitation would correspond to a shift in real space, i.e.

$$\hat{\Lambda} = \hat{c}_i^\dagger \hat{c}_j. \tag{7.95}$$

In principle any arbitrary operator may be chosen to push the syste out of equilibrium. The major task then is only to justify this choice. Due to the rapid change, this process is somewhat similar to

quenches. Unlike semi-classical or full quantum treatments these approaches can only model the effect of an excitation but not the actual process of the excitation itself. Nevertheless, if the primary goal is to understand the post excitation behavior both are fairly good approximations.

8 Spectral Quantities of the Hubbard Model with a Magnetic Superstructure in Equilibrium

Before we begin with the evaluation of full time-dependent spectral functions and optical conductivities, we first turn our attention to the conceptually easier task of computing these quantities in equilibrium, that is with respect to the ground state, such that we can tell effects in out-of-equilibrium setups apart from those that are intrinsic to the model. We study two variants of the Hubbard Hamiltonian wth a magnetic superstructure (7.66), namely the two-band and the four-band versions, $\hat{H}^{2\Delta}$ and $\hat{H}^{4\Delta}$, as introduced in section 7.2.2, restricting our analysis to the case of zero temperature, $T = 0$. The Hubbard and the tight binding model are then considered as special cases, setting $\Delta = 0$ or $\Delta = U = 0$, respectively. Note that we did not include phonons in any of our models. We expect this to be a valid analysis, as long as the coupling between phonons and itinerant electrons is weak. A simple model to incude such interactions is the Hubbard-Holstein model [367, 140] for which equilibrium spectral functions have been computed, for instance in [261].

The computations of both, the spectral functions, as well as the optical conductivities will be conducted applying MPSs following the procedures outlined in sections 6.1.4 and 6.2.4, respectively. We will consider systems of size $L = 32$, which for MPS computations is a rather small number. However, as we have learned in section 6.1.4 the computation of the spectral function scales with L which results in a considerable effort also for MPSs. In order to save on computational resources we shall work in the regime of open boundaries. Unless stated otherwise, all time evolutions are conducted using the TDVP in its two-site implementation with a maximum bond dimension of $\chi_{\max} = 500$. We will be working in units of the hopping amplitude t_{hop}, which equals setting $t_{\mathrm{hop}} = 1$. For the computation of the spectral functions, we use a time step of $\delta t' \cdot t_{\mathrm{hop}} = 0.05$ and choose a maximum time of $t'_{\max} \cdot t_{\mathrm{hop}} = 8.0$, at which the light cone associated to the Lieb-Robinson bounds hit the system's edges for an excitation in the center, c.f. section 6.1.4. In order to compute the discretized Fourier transforms we introduce the damping factor η, which we choose such that at the maximum time the input signal has dropped to a value of 0.05, i.e. $\eta = -\ln(0.05) \,/\, \left(t'_{\max} \cdot t_{\mathrm{hop}}\right)$. Furthermore, to artificially increase the resolution of our data, we apply zero padding such that the input signal of the Fourier transform increases to length $8 \cdot 2^{\lceil \log_2(t'_{\max}/\delta t + 1) \rceil}$. As for the optical conductivity, we choose the parameters of the probe pulse (6.111) as $\Delta t' \cdot t_{\mathrm{hop}} = 0.25$, $\tau \cdot t_{\mathrm{hop}} = 0.05$, $A_0 = 0.5$, and $\omega_{\mathrm{p}}/t_{\mathrm{hop}} = 2.38$. In this case we time evolve longer setting $t'_{\max} \cdot t_{\mathrm{hop}} = 25.0$ with a time step of $\delta t' \cdot t_{\mathrm{hop}} = 0.01$ and choose a damping factor of $\tilde{\eta}/t_{\mathrm{hop}} = 0.1$. We will present the optical conductivity in two ways, with and without zero padding to rule out misinterpretations due to possible artificial signals originating from this procedure. In the case of zero padding we enhance our data by 16 times its length with zeros.

In the remainder of this chapter we will discuss the case of $\Delta/t_{\mathrm{hop}} = 2$. Furthermore, only results for spin $\sigma =\uparrow$ will be shown as the dispersion relations are spin-independent, c.f. equations (7.73) and (7.78). Both, this and the succeeding chapter, are primarily based on the author's work [243]. However, we will present the results ins far greater detail here. The general concept will be to first discuss $\hat{H}^{4\Delta}$ and afterwards $\hat{H}^{2\Delta}$. We will find that the latter essentially captures the results of

the former model, whilst also being simpler. Nevertheless, we decided to first show $\hat{H}^{4\Delta}$ as it is closer to the original model describing manganites at quarter filling. As we will see, however, in this setup only minor effects occur in our treatment. Therefore we switched to half filling allowing the simplification to $\hat{H}^{2\Delta}$. In our analysis, we shall first discuss non-interacting setups, followed by two interacting ones with $U/t_{\mathrm{hop}} = 4$ and then $U/t_{\mathrm{hop}} = 16$ as a reference. Again, we will find essentially the same behavior for $U/t_{\mathrm{hop}} = 16$ as for $U/t_{\mathrm{hop}} = 4$. In either case we shall first present greater and lesser spectral functions followed by optical conductivities, which we will see to show signals at energies corresponding to the differences of those where the greater and lesser spectral function are non-zero. Since both quantities are relevant in experiments, we decided to discuss them both, also enabling us to compare to other work. We are well aware that this approach in general may at times feel quite repetitive. On the other hand, however, this way a complete overview is provided. Who has little time shall be advised that the key points of our findings will become clear from understanding the results for $\hat{H}^{4\Delta}$ with $U/t_{\mathrm{hop}} = 4$.

8.1 Properties of the Non-interacting System

As a first step to our analyses we compute the equilibrium spectral functions and optical conductivities for non-interacting systems, i.e. $U = 0$ which for finite values of Δ realize a band insulator. Clearly from a physical point of view these computations are unnecessary since for these setups analytical solutions exist as we have explained in detail in section 6.1.3 and 6.2.2, respectively. Numerics-wise however, the benefit is threefold: These computations provide an excellent benchmark to test the validity of our numerical approaches, from the results of these routines we learn about their general properties, and based on these insights we can better identify physical effects in subsequent more complex simulations for interacting systems where analytical solutions are not that easily obtained or even non-existent.

8.1.1 Four Band Model

We begin with an analysis of $\hat{H}^{4\Delta}$. In figure 8.1 we show the lesser and greater spectral functions for quarter and half filling in the first BZ alongside the analytical dispersion relations for periodic and open boundary conditions as obtained from equation (7.73) or (7.60), respectively. As expected, our numerical results perfectly follow the dispersion relation for OBCs. In the case of quarter filling only the first band of the lesser spectral function $\mathcal{A}_{\uparrow}^{<}(k,\omega)$ is occupied, while in the greater spectral function $\mathcal{A}_{\uparrow}^{>}(k,\omega)$ the weight is equally distributed amongst the top three bands. At half filling the results are equally satisfactory the bottom two bands being occupied for $\mathcal{A}_{\uparrow}^{<}(k,\omega)$ and the top two occupied for $\mathcal{A}_{\uparrow}^{>}(k,\omega)$. Comparing the dispersion relations for OBCs and PBCs we also note the deviation at the edges which we mentioned in section 7.2.1. We still depict the dispersion relation for PBCs to visualize these finite size effects from the OBCs. In addition to the main signals we also note weaker structures seemingly resembling the former.

In order to study the spectra in more detail, we turn to the examination of cross sections which we present in figure 8.2 taken at $k = 4\pi/33$, i.e. the center of half of the first BZ. Here we depict our results in even more detail showing not only the full spectral function, but also its components from each band. Just like theory predicts we find for each band only contributions from one band index in all cases investigated, confirming the quality of our MPS approach. We can now also comment on

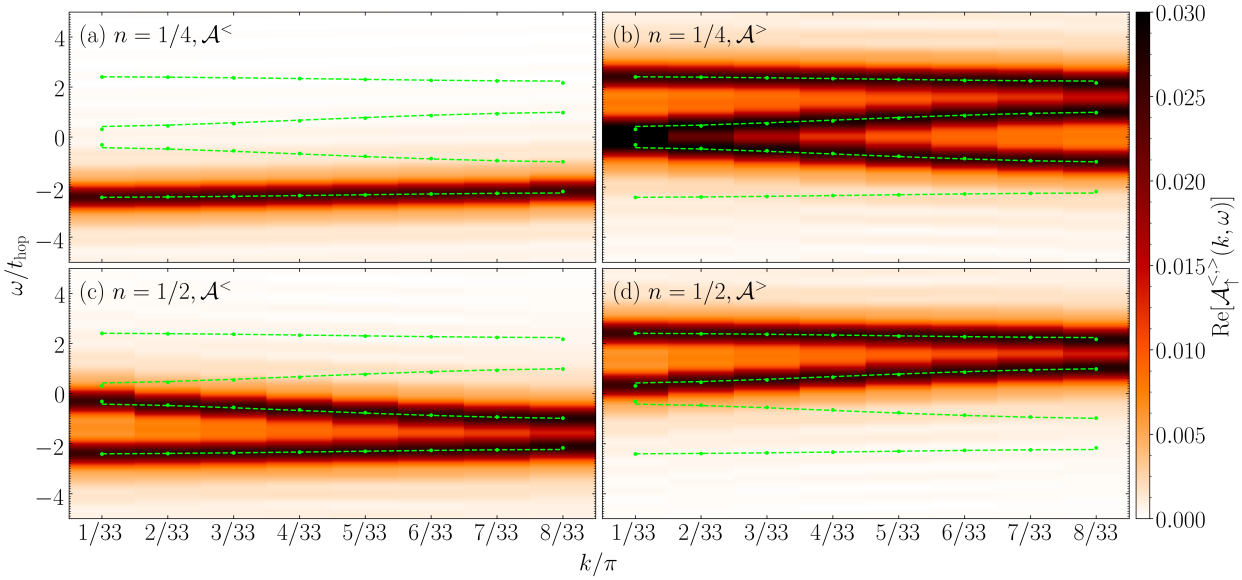

Figure 8.1: Single particle spectral functions $\mathcal{A}_\uparrow^<(k,\omega)$ and $\mathcal{A}_\uparrow^>(k,\omega)$ in equilibrium for $\hat{H}^{4\Delta}$ with $U/t_{\mathrm{hop}} = 0$ and $\Delta/t_{\mathrm{hop}} = 2$ for a system of $L = 32$ sites with OBCs in the first BZ at quarter, (a) and (b), and half ($\chi_{\mathrm{max}} = 1000$) filling, (c) and (d), respectively. The green dashed lines show the band structure of the non-interacting system calculated with PBCs, the green dots correspond to the calculation with OBCs.

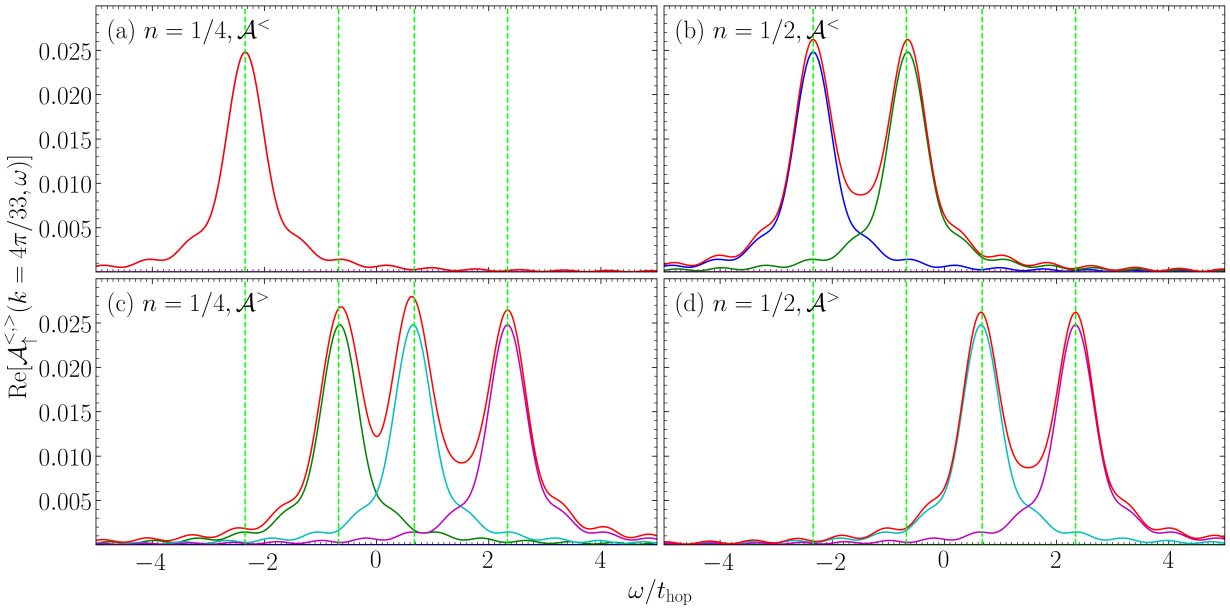

Figure 8.2: Cross section of the data shown in figure 8.1 at $k = 4\pi/33$ for quarter, (a) and (c), and half filling, (b) and (d). The total spectral function is shown in red, the contribution from the four band indices $\nu = 1, 2, 3, 4$ are given in blue, green, cyan, and magenta, respectively. Vertical dashed light green lines: ground state peak positions in the non-interacting case obtained for PBCs.

the resolution, where we find the peaks for each band to be rather broad. This is mainly due to the comparably short time t'_{max} we used to obtain the time evolved signal to apply the Fourier transform to. The broadening η then amplified this effect. We could reduce it by increasing the system size L which would allow for longer time evolutions. As we discussed above, however, the computational effort would be considerable especially when it comes to the time-dependent spectral functions to be computed. We further note that all peaks are accompanied by a certain ringing which we can trace back to originate from the discrete Fourier transform having observed the same feature in section A.1.7 as part of the discussion of different Fourier transforms. These wiggles are, thus, unphysical and should be regarded as to what accuracy we can safely interpret our numerical data. Still, this task is not as trivial as it might seem as can best be understood from figure 8.2(c), which shows that due to the large broadening of the individual band contributions the total spectral function shows quite strong in gap weights resulting from the superposition. From figures 8.2(b) and (d) we also learn that we cannot in general assume the ringing effects to cancel out in the total spectral function. By contrast, they might even add to each other. Another effect of the large broadening best to be observed in figure 8.2(c) is that the total spectral function might show different peak heights although the individual components are equally strong. We conclude that due to these numerical restrictions we should only interpret the spectral functions qualitatively. Nevertheless do our numerical results meet the analytical predictions. Upon close inspection, c.f. for instance the $\nu = 3$ contribution in figure 8.2(c), we also see that the peaks of the spectral functions do not exactly match their analytical positions. This, however, is only a minor effect and can again be explained by the use of OBCs in the MPS computations.

Lastly, we present the corresponding optical conductivity in figure 8.3. As discussed in section 6.2.2 we expect to find peaks at frequencies corresponding to energy differences of the different bands, however the hight of the respective peaks does not become clear from equation (6.89). We do find

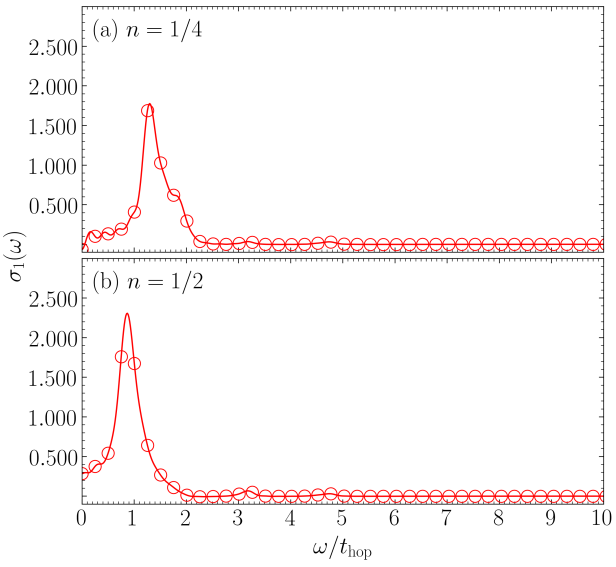

Figure 8.3: Real part of the optical conductivity $\sigma_1(\omega, t)$ in equilibrium for $\hat{H}^{4\Delta}$ with $U/t_{\mathrm{hop}} = 0$ and $\Delta/t_{\mathrm{hop}} = 2$ for a system of $L = 32$ sites with OBCs at quarter, (a), and half ($\chi_{\mathrm{max}} = 1000$) filling, (b), respectively. Data points: Obtained from Fourier transforming according to (6.109) and (6.110). Solid lines: Application of 16 times zero padding. This figure is adapted from the author's work [243].

massive differences between the heights of these peaks, yet still their positions indeed match the theoretical expectations.

8.1.2 Two Band Model

We now turn to the somewhat easier case of $\hat{H}^{2\Delta}$ starting with depicting the lesser and greater spectral function in figure 8.4. Here we only consider the situation of half filling. As before, we

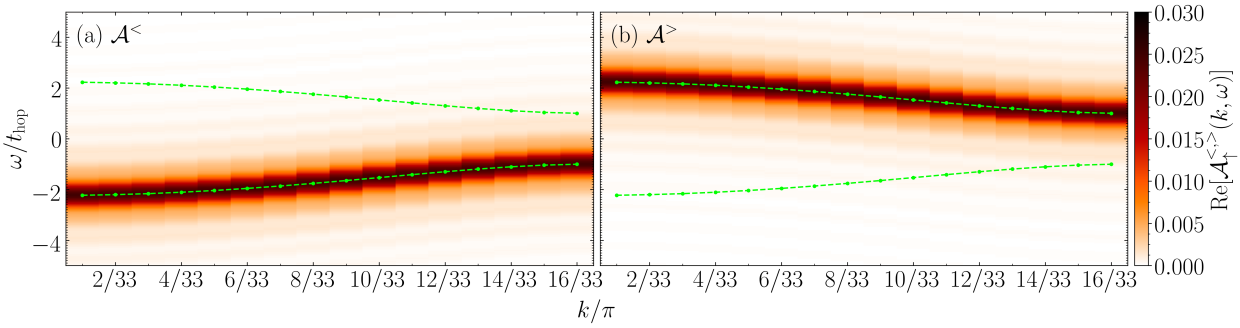

Figure 8.4: Single particle spectral functions $\mathcal{A}^<_\uparrow(k,\omega)$ and $\mathcal{A}^>_\uparrow(k,\omega)$ in equilibrium for $\hat{H}^{2\Delta}$ with $U/t_{\text{hop}} = 0$ and $\Delta/t_{\text{hop}} = 2$ for a system of $L = 32$ sites with OBCs in the first BZ at half filling. The green dashed lines show the band structure of the non-interacting system calculated with PBCs, the green dots correspond to the calculation with OBCs.

present our results in the first BZ and show the analytical dispersion relations for PBCs and OBCs as obtained from equation (7.78) or (7.60), respectively, as a reference. We find a near perfect agreement of the numerical data with these dispersions noting that here even in the analytical calculations the difference between the cases of PBCs and OBCs is almost imperceptible. With only two bands, at half filling clearly in $\mathcal{A}^<_\uparrow(k,\omega)$ and $\mathcal{A}^>_\uparrow(k,\omega)$ only the bottom or top one is occupied, respectively. As there is no interference of contributions from different bands in either spectral function we can also observe the ringing quite well.

The benefit of the two-band system also show in the analysis of the cross sections in figure 8.5. We again take the center of half of the first BZ as a reference, which in this case means $k = 8\pi/33$. Here we can clearly see that the total spectral function has only a contribution from one single band, the other one being zero for both the lesser, as well as the greater spectral function. This property is especially beneficial when it comes to interpreting the total spectral function since now no artificial weight from taking the sum over several bands may show up.

In figure 8.6 the optical conductivity for this setup is shown. From figure 8.5 we might expect a sole peak at $\omega/t_{\text{hop}} \approx 3.6$ which would be the difference of the peaks of the lesser and greater spectral function. Instead however, the peak is at $\omega/t_{\text{hop}} \approx 2.1$ and fades out until $\omega/t_{\text{hop}} \approx 4.5$ which is substantially longer than its behavior towards smaller frequencies. While at first sight these results do not seem to coincide, comparing to the full spectral functions in figure 8.4 provides an explanation. Here we find that at the edge of the BZ, i.e. at $k = 16\pi/33$ the distance of the lesser and greater spectral function is roughly $\omega/t_{\text{hop}} \approx 2$ which again matches the peak in the optical conductivity. The peak distance then steadily increases for smaller momenta until $\omega/t_{\text{hop}} \approx 4.5$ at $k = \pi/33$. As the optical conductivity is not a momentum-resolved quantity it will, hence, cover properties over the entire BZ. In the analysis of $\hat{H}^{4\Delta}$ in the preceding section these issues were not

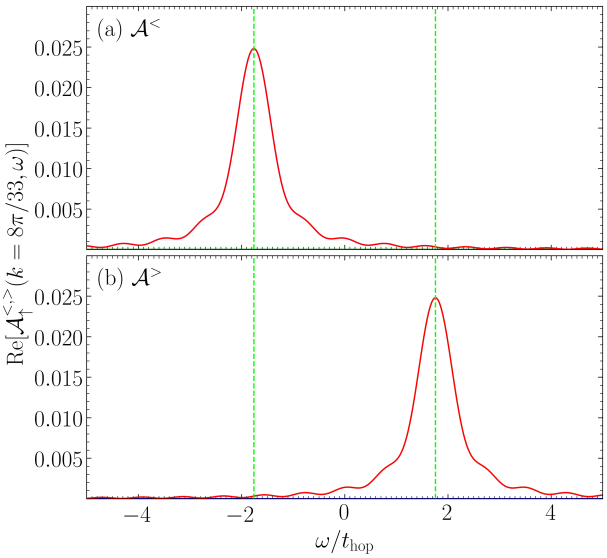

Figure 8.5: Cross section of the data shown in figure 8.4 at $k = 8\pi/33$. The total spectral function is shown in red, the contribution from the two band indices $\nu = 1, 2$ are given in blue and green, respectively. Vertical dashed light green lines: ground state peak positions in the non-interacting case obtained for PBCs.

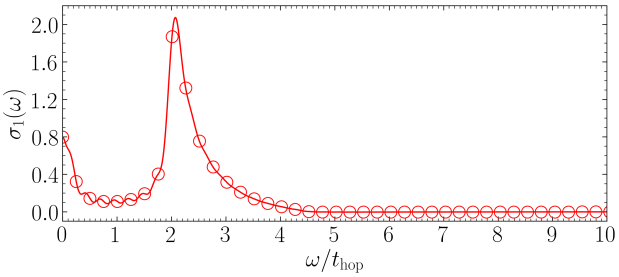

Figure 8.6: Real part of the optical conductivity $\sigma_1(\omega, t)$ in equilibrium for $\hat{H}^{2\Delta}$ with $U/t_{\mathrm{hop}} = 0$ and $\Delta/t_{\mathrm{hop}} = 2$ for a system of $L = 32$ sites with OBCs at half filling. Data points: Obtained from Fourier transforming according to (6.109) and (6.110). Solid lines: Application of 16 times zero padding. This figure is adapted from the author's work [243].

as obvious due to the less steep dispersion and the existence of multiple bands. This example nicely illustrates their interplay when it comes to the interpretation of these two quantities. Note that we also find a signal at $\omega = 0$. This, however, is an unphysical Drude peak which we obtain for finite systems as an artifact due to the discretization of the Fourier transform and, thus, ignore. Therefore, we shall only pay little attention to signals at small frequencies, c.f. [336].

8.2 Properties of the System with Interaction

We now analyze the introduction of a finite interaction U to the model in equilibrium to then judge the effects of a photo excitation. While in the non-interacting case, as we have discussed in section 6.1.3 and seen in the previous one, the spectral function will simply resemble the band

structure, for interacting systems the distribution of spectral weight cannot be associated to bands in a stricter sense anymore as their definition ceases to be valid due to the quadrilinear terms in equation (7.66c). Nevertheless, they still qualitatively describe the system under consideration and we will at times refer to contributions to the interacting spectral functions as belonging to a particular band corresponding to the non-interacting case (in the sense that in the limit $U \to 0$ the considered feature can be traced back to contribute to this band).

8.2.1 Four Band Model

We again begin with investigating $\hat{H}^{4\Delta}$ at half or quarter filling, the latter case corresponding to the toy-manganite system introduced in reference [197]. Due to the larger number of interacting particles, however, we expect stronger correlation effects at half filling at finite U leaving an extension of our study to also this situation, which goes beyond the aforementioned modeling, only logical.

In figures 8.7 and 8.8 we display the lesser and greater spectral functions in the periodic zone scheme, i.e. the first Brillouin zone (BZ), for $U/t_{\mathrm{hop}} = 4$ and $U/t_{\mathrm{hop}} = 16$, respectively. The former choice of the interaction approximately matches values obtained in reference [197] from ab-initio calculations, the latter one serves as a comparative study to strongly interacting systems. As a reference we also show the positions of the bands from the non-interacting system (7.73). We begin

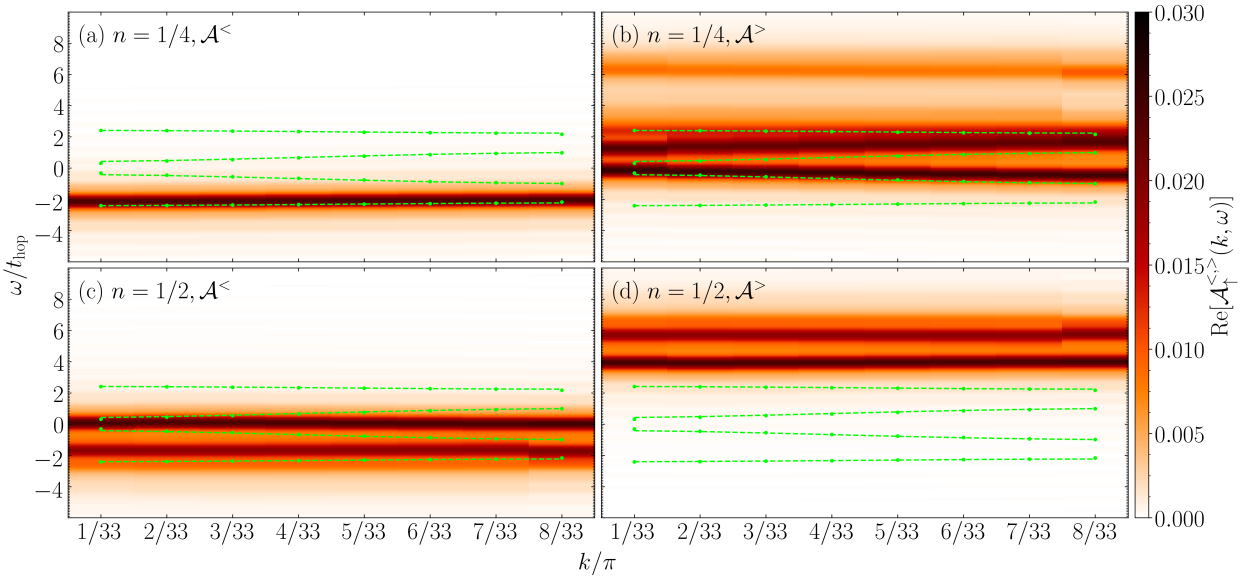

Figure 8.7: Single particle spectral functions $\mathscr{A}_\uparrow^<(k,\omega)$ and $\mathscr{A}_\uparrow^>(k,\omega)$ in equilibrium for $\hat{H}^{4\Delta}$ with $U/t_{\mathrm{hop}} = 4$ and $\Delta/t_{\mathrm{hop}} = 2$ for a system of $L = 32$ sites with OBCs in the first BZ at quarter, (a) and (b), and half filling, (c) and (d), respectively. The green dashed lines show the band structure of the non-interacting system calculated with PBCs, the green dots correspond to the calculation with OBCs. This figure is taken from the author's work [243].

by noting that there the discontinuity at the edges of the first BZ, which we already encountered in the non-interating case, c.f. figure 8.1, persists and is even featured more prominently as is best to be observed in figures 8.7(b) and 8.8(d).

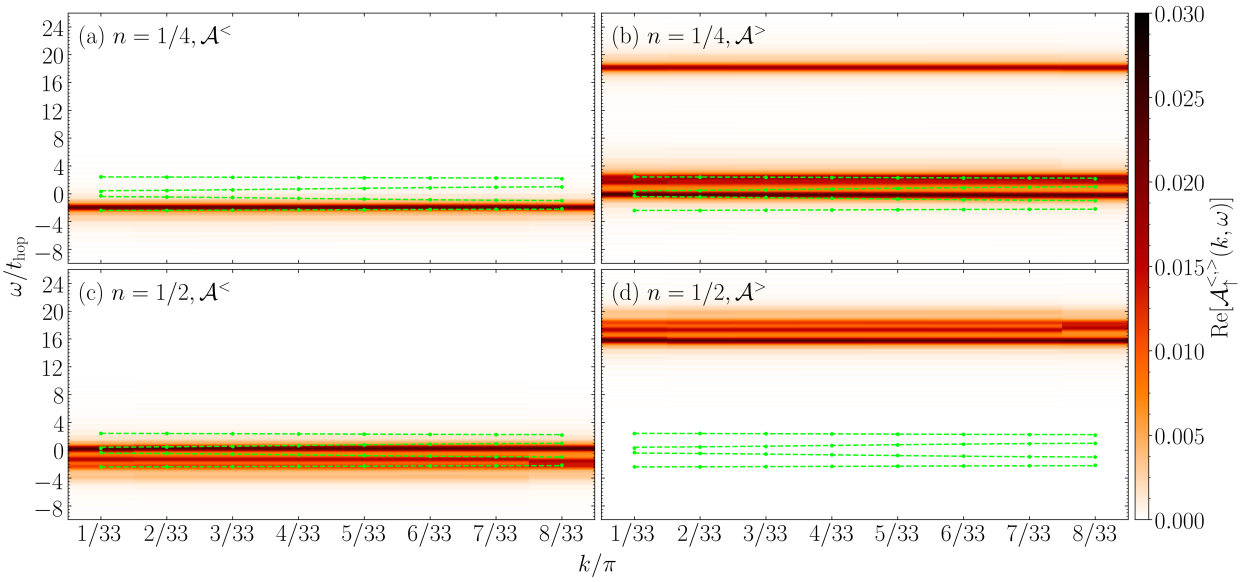

Figure 8.8: Single particle spectral functions $\mathcal{A}_\uparrow^<(k,\omega)$ and $\mathcal{A}_\uparrow^>(k,\omega)$ in equilibrium for $\hat{H}^{4\Delta}$ with $U/t_{\mathrm{hop}} = 16$ and $\Delta/t_{\mathrm{hop}} = 2$ for a system of $L = 32$ sites with OBCs in the first BZ at quarter, (a) and (b), and half filling, (c) and (d), respectively. The green dashed lines show the band structure of the non-interacting system calculated with PBCs, the green dots correspond to the calculation with OBCs.

At quarter filling, for $\mathcal{A}^<(k,\omega)$, c.f. figures 8.7(a) and 8.8(a), the result seems very similar to the non-interacting case, apart from a slight shift to higher frequencies and a weak flattening of the occupied band. Thus, U appears to only play a minor role and to cause merely a small renormalization of the band structure. This can be understood by the fact that a finite Δ suppresses double occupancies of a site with electrons of different spin directions, and that at low fillings hence the Coulomb interaction is not expected to show a strong effect on the occupied branch of the spectral function. By contrast, $\mathcal{A}^>(k,\omega)$ shown in figures 8.7(b) and 8.8(b) deviates strongly from the non-interacting band structure. While the second band is fairly closely reproduced by the accumulation of spectral weight, the shift of the third band is already considerable. In addition, a new feature at $\omega \approx 6$ or $\omega \approx 18$, respectively, is obtained, which is approximately at an energy of U/t_{hop} higher than the third band, where at $\omega \approx 2$ only a small signal can be observed. Thus, the fourth band in the non-interacting case appears to have split into two.

Contrary to the case of quarter filling, for a half-filled system the interaction has quite a significant impact on $\mathcal{A}^<(k,\omega)$ already as seen in figures 8.7(c) and 8.8(c), a splitting of the lowest band $\nu = 1$ compared to the non-interacting case being perhaps most prominent. Although the structure of four bands separated by a gap appears to remain, a significant shift to higher energies is visible, covering a larger region than the size of the band gap in the non-interacting systems. Accordingly, the unoccupied part of the spectral function, i.e. the greater spectral function $\mathcal{A}^>(k,\omega)$, also shows its weight at significantly higher energies. This is related to the large value of the Hubbard interaction, which at $\Delta = 0$ would lead to a separation of the upper and the lower Hubbard band $\sim U$ Since $\mathcal{A}^>(k,\omega)$ can be shown to reflect the behavior of $\mathcal{A}^<(k,\omega)$ mirrored at $U/2t_{\mathrm{hop}}$, as is evident from comparing figures 8.7(c) and 8.8(c) to 8.7(d) and 8.8(d), we interpret the system as possessing two Hubbard bands, a filled lower Hubbard band and an empty upper Hubbard band, separated by a gap, which, however, due to the finite value of Δ possess a further fine structure.

The corresponding Hubbard satellites appearing at energies $\omega/t_{\mathrm{hop}} \approx -2.5$ and $\omega/t_{\mathrm{hop}} \approx 6.5$ or $\omega/t_{\mathrm{hop}} \approx 18.5$, respectively, are visible at all values of k, although being less pronounced at $k = 8\pi/33 \approx \pi/4$, which, as we have already pointed out above, we attribute to our choice of OBCs. Hence, the interactions cause a splitting of the lowest band. This fine structure connects in part to the band-structure of the noninteracting system, as well as to correlation induced Hubbard satellites, c.f. for instance [375]. We, thus, interpret the system as a hybrid of a non-interacting band- and of a strongly correlated insulator, with a stronger reminiscence to Mott-Hubbard insulators. In the following we will therefore refer to our system as correlated band insulator. Irrespective of the filling or greater or lesser spectral function, we find all features to be rather flat, i.e. the dispersion depends only weakly on k, the effect increasing with growing interaction U.

To perform a more detailed analysis, we will focus on cross sections taken at fixed k. We again choose $k = 4\pi/33 \approx \pi/8$ as it is the center of half of the first BZ showing the results in figures 8.9 and 8.10. In addition to these cross sections, we also computed the excitation energies of the spectral

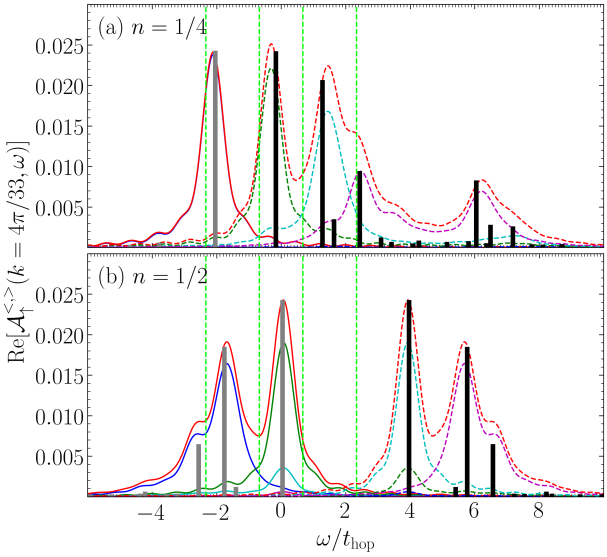

Figure 8.9: Cross section of the data shown in figure 8.7 at $k = 4\pi/33$ for quarter, (a) and (c), and half filling, (b) and (d). Solid lines: $\mathscr{A}_\uparrow^{<}(k = 4\pi/33, \omega)$; dashed lines: $\mathscr{A}_\uparrow^{>}(k = 4\pi/33, \omega)$. The total spectral function is shown in red, the contribution from the four band indices $\nu = 1, 2, 3, 4$ are given in blue, green, cyan, and magenta, respectively. Vertical dashed light green lines: ground state peak positions in the non-interacting case obtained for PBCs. Vertical gray (black) bars: excitation energies for $\mathscr{A}_\uparrow^{<}$ ($\mathscr{A}_\uparrow^{>}$) as obtained from equation (7.54) ((7.55)) for one unit cell, i.e. $L = 4$. The heights of the bars correspond to their respective weights. All bars have been scaled such that in each cross section the largest bar (irrespective of belonging to $\mathscr{A}_\uparrow^{<}$ or $\mathscr{A}_\uparrow^{>}$) takes a value of 0.8 times the plot's maximum range in y-direction. This figure is taken from the author's work [243].

functions of one unit cell, i.e. $L = 4$ for OBCs from the Lehmann representation of the Green's function, c.f. equations (7.54) and (7.55), by full diagonalization (FD). The motivation behind this approach is that, with the effective absence of a dispersion due to the interaction U, the particles are able to move almost freely within each band. Hence from this point of view the system size is not important anymore allowing the approximation by a single unit cell. We plot bars of heights corresponding to the weights at the so-obtained excitation energies having in addition scaled their sizes to match the scaling of the cross sections and, in general, we find a good agreement between

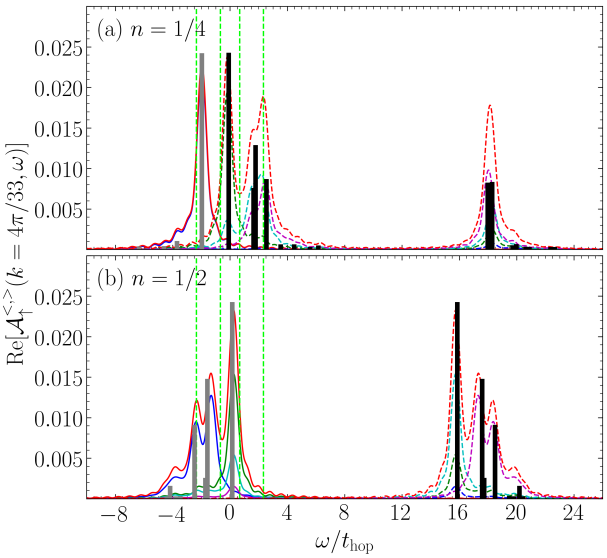

Figure 8.10: Cross section of the data shown in figure 8.8 at $k = 4\pi/33$ for quarter, (a) and (c), and half filling, (b) and (d). Solid lines: $\mathscr{A}_\uparrow^<(k = 4\pi/33, \omega)$; dashed lines: $\mathscr{A}_\uparrow^>(k = 4\pi/33, \omega)$. The total spectral function is shown in red, the contribution from the four band indices $\nu = 1, 2, 3, 4$ are given in blue, green, cyan, and magenta, respectively. Vertical dashed light green lines: ground state peak positions in the non-interacting case obtained for PBCs. Vertical gray (black) bars: excitation energies for $\mathscr{A}_\uparrow^<$ ($\mathscr{A}_\uparrow^>$) as obtained from equation (7.54) ((7.55)) for one unit cell, i.e. $L = 4$. The heights of the bars correspond to their respective weights. All bars have been scaled such that in each cross section the largest bar (irrespective of belonging to $\mathscr{A}_\uparrow^<$ or $\mathscr{A}_\uparrow^>$) takes a value of 0.8 times the plot's maximum range in y-direction.

our numerical data and the exact results for the small system. Note however, that due to the comparably large broadening η of the numerical data, we cannot reproduce small peaks neighboring larger ones, c.f. e.g. the components at $\omega/t_{\mathrm{hop}} \approx 1.6$ in figure 8.9(a) or $\omega/t_{\mathrm{hop}} \approx -1.7$ in figure 8.9(b) while for smaller peaks farther apart from a large one, their contribution is exaggeratedly represented in the total spectral function, as for instance at $\omega/t_{\mathrm{hop}} \approx 2.4$ in figure 8.9(a). Here, the FD results provide valuable additional information and help in identifying numerical artifacts. Nevertheless, in principle can we conclude that our numerical results match the FD ones fairly well, both with respect to peak positions, as well as their respective heights. We further find that the peaks in the total spectral functions are primarily determined by their corresponding bands in the non-interacting case.

Regarding the situation at quarter filling, which is depicted in figures 8.9(a) and 8.10(a) we, indeed, find the peak in $\mathscr{A}^<(k, \omega)$ to be primarily determined by its corresponding band in the non-interacting case. We can furthermore confirm our assumption that it was primarily the fourth band that split for $\mathscr{A}^>(k, \omega)$, while the other three unoccupied bands are largely unaffected at $U/t_{\mathrm{hop}} = 4$, c.f. figure 8.9(a). By contrast, for larger U all contributions of $\mathscr{A}^>(k, \omega)$ show this splitting as can be seen in figure 8.10. The distance of roughly $4 = U/t_{\mathrm{hop}}$ or $16 = U/t_{\mathrm{hop}}$ between the two subpeaks underpins our interpretation of the system as a hybrid of a non-interacting band insulator and of a strongly correlated insulator. At this point we emphasize again, that we need to refrain from the strict interpretation in terms of bands as in general for interacting systems not only one band index corresponds to a peak in the spectral weight. Note that actually in figure 8.9(a) already the

$\nu = 3$ contribution of $\mathscr{A}^{>}(k,\omega)$ in addition to a major signal close to the energy corresponding to the non-interacting system also has a contribution at $\omega/t_{\mathrm{hop}} \approx 7.4$, which is closer to the second peak of the spectral function corresponding to band index $\nu = 4$. Thus, if we wish to maintain the notion of bands in our discussion we need to water down its definition as a range of energies around a selected peak in the spectral function.

As for the case of half filling given in figures 8.9(b) and 8.10(b) we find the lesser and greater spectral function to be symmetric as expected. Regarding the structure of the spectral functions, the principal features remain to be the two peaks, which connect to the non-interacting band structure, but are shifted to higher energies. We read off the energy difference between the rightmost peak of $\mathscr{A}^{<}(k,\omega)$ and the leftmost peak of $\mathscr{A}^{>}(k,\omega)$ as $\Delta\omega/t_{\mathrm{hop}} \approx 3.9 \approx 4 = U/t_{\mathrm{hop}}$ and $\Delta\omega/t_{\mathrm{hop}} \approx 15.8 \approx 16 = U/t_{\mathrm{hop}}$, which further confirms our interpretation as a separation into an upper and a lower Hubbard band with a fine structure. In addition, we encounter a splitting of the leftmost peak of $\mathscr{A}^{<}(k,\omega)$, corresponding to the lowest band index $\nu = 1$ at $\omega/t_{\mathrm{hop}} \approx -2.5$ and accordingly the same feature for the rightmost peak of $\mathscr{A}^{>}(k,\omega)$, corresponding to the largest band index $\nu = 4$ at $\omega/t_{\mathrm{hop}} \approx 6.5$ or $\omega/t_{\mathrm{hop}} \approx 18.5$, respectively. We note that also in this case these features can all be well explained from the FD calculations.

In figures 8.11 and 8.12 we show the corresponding optical conductivities. Despite the rather noisy signal, we report that in either case the main peaks, to be found at energies $\omega \sim U$, both in number and in position match the energy distances of the energetically largest contribution of $\mathscr{A}^{<}(k,\omega)$ and the major contributions of $\mathscr{A}^{>}(k,\omega)$ which can be taken from the cross sections in figures 8.9 and 8.10, respectively. At quarter filling the first contribution is orders of magnitudes larger than all the remaining ones. To accurately display the latter ones, we have cut the figures at a maximum value. The dominance of this first signal comes to little surprise since the lowest unoccupied band

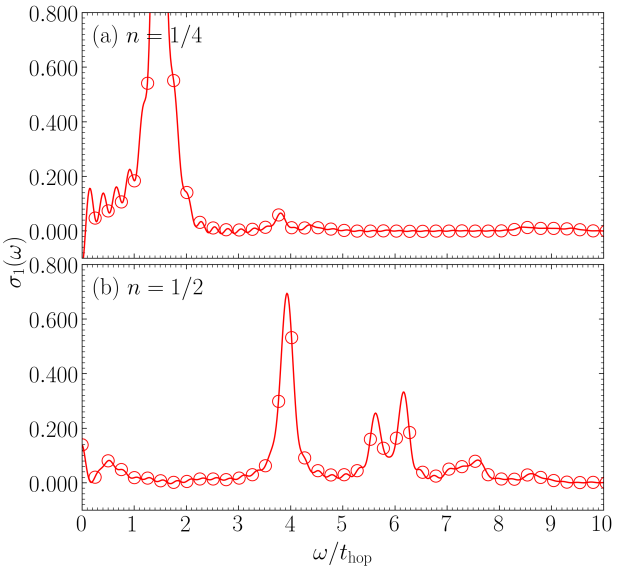

Figure 8.11: Real part of the optical conductivity $\sigma_1(\omega, t)$ in equilibrium for $\hat{H}^{4\Delta}$ with $U/t_{\mathrm{hop}} = 4$ and $\Delta/t_{\mathrm{hop}} = 2$ for a system of $L = 32$ sites with OBCs at quarter, (a), and half filling, (b), respectively. Data points: Obtained from Fourier transforming according to (6.109) and (6.110). Solid lines: Application of 16 times zero padding. This figure is adapted from the author's work [243].

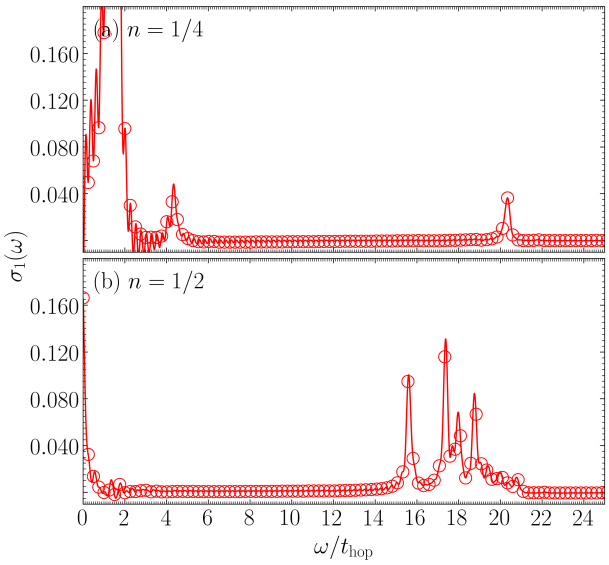

Figure 8.12: Real part of the optical conductivity $\sigma_1(\omega, t)$ in equilibrium for $\hat{H}^{4\Delta}$ with $U/t_{\mathrm{hop}} = 16$ and $\Delta/t_{\mathrm{hop}} = 2$ for a system of $L = 32$ sites with OBCs at quarter, (a), and half filling, (b), respectively. Data points: Obtained from Fourier transforming according to (6.109) and (6.110). Solid lines: Application of 16 times zero padding. This figure is adapted from the author's work [243].

of $\mathscr{A}^{>}(k, \omega)$ is energetically significantly closer to the highest occupied region of $\mathscr{A}^{<}(k, \omega)$ compared to the case of half filling. Hence, the peaks seen in the equilibrium optical conductivity mainly correspond to transferring a particle from the occupied to the unoccupied parts of the spectrum and, thus, mimic the band structure. There are also a number of further contributions occurring with lower weights which we attribute to distances to the multiple less dominant peaks in $\mathscr{A}^{<}(k, \omega)$ and $\mathscr{A}^{>}(k, \omega)$. Since many of these structures are energetically close to one another, our resolution is not strong enough to ensure an accurate display.

Let us briefly mention at this point that with increasing interaction strength U the lesser and greater spectral functions move farther apart from one another in energy and, thus, alongside do the signals in the optical conductivity shift to larger energies. We will also encounter this behavior in section 8.2.3. Note that this particular feature is just an effect of the absence of a chemical potential to our model (7.66) and has no further consequences regarding the physical effects we will find in the chapters to come.

8.2.2 Two Band Model

We now turn our attention to $\hat{H}^{2\Delta}$, where we only consider half filling, the primary aim being to find out, in how far this simplified model mirrors the features we encountered for $\hat{H}^{4\Delta}$ in this case. We present $\mathscr{A}^{<}(k, \omega)$ and $\mathscr{A}^{>}(k, \omega)$ in the first BZ for $U/t_{\mathrm{hop}} = 4$ and $U/t_{\mathrm{hop}} = 16$ in figures 8.13 and 8.14 analogously to the depiction in figures 8.7 and 8.8. Compared to $\hat{H}^{4\Delta}$ we find a significantly stronger dispersion at $U/t_{\mathrm{hop}} = 4$, which, however, also becomes less intense for larger interactions as evident from the depiction of the case of $U/t_{\mathrm{hop}} = 16$. Other than that, the behavior is quite similar, although, clearly, we now only encounter two major bands. A renormalization of

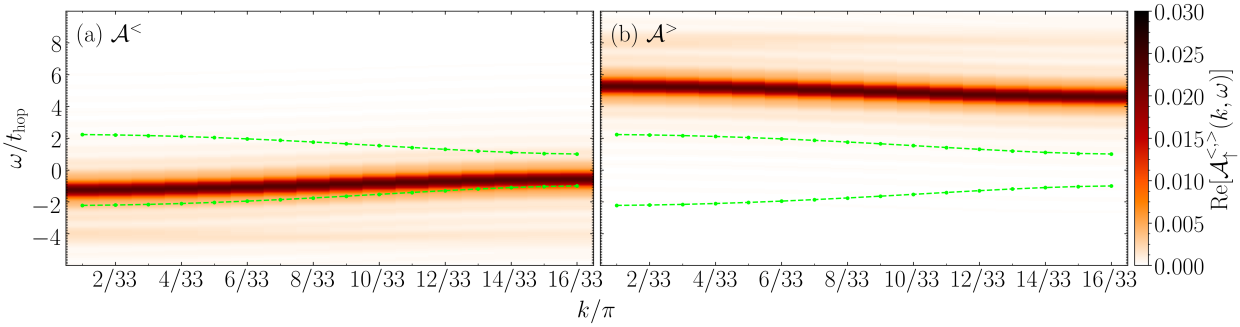

Figure 8.13: Single particle spectral functions $\mathcal{A}^<_\uparrow(k,\omega)$ and $\mathcal{A}^>_\uparrow(k,\omega)$ in equilibrium for $\hat{H}^{2\Delta}$ with $U/t_{\mathrm{hop}} = 4$ and $\Delta/t_{\mathrm{hop}} = 2$ for a system of $L = 32$ sites with OBCs in the first BZ at half filling. The green dashed lines show the band structure of the non-interacting system calculated with PBCs, the green dots correspond to the calculation with OBCs.

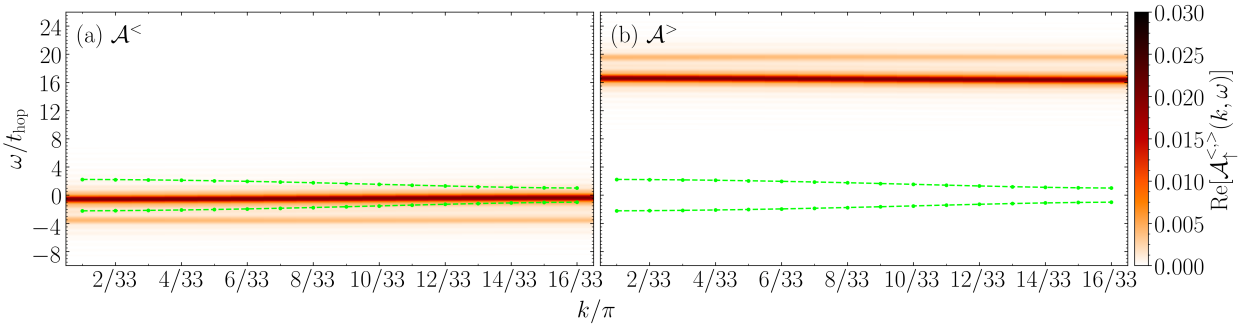

Figure 8.14: Single particle spectral functions $\mathcal{A}^<_\uparrow(k,\omega)$ and $\mathcal{A}^>_\uparrow(k,\omega)$ in equilibrium for $\hat{H}^{2\Delta}$ with $U/t_{\mathrm{hop}} = 16$ and $\Delta/t_{\mathrm{hop}} = 2$ for a system of $L = 32$ sites with OBCs in the first BZ at half filling. The green dashed lines show the band structure of the non-interacting system calculated with PBCs, the green dots correspond to the calculation with OBCs. This figure is taken from the author's work [243].

the band structure can be reported, as well as the formation of an additional signal below and above the dominant contribution for $\mathcal{A}^<(k,\omega)$ in figures 8.13(a) and 8.14(a) and $\mathcal{A}^>(k,\omega)$ in figures 8.13(b) and 8.14(b), respectively. We present the cross sections at $k = 4\pi/33 \approx \pi/8$ in figures 8.15 and 8.16 including FD results obtained for a single unit cell, i.e. $L = 2$, from the Lehmann representation, c.f. equations (7.54) and (7.55). We find $\mathcal{A}^<(k,\omega)$ to be almost entirely determined by contributions corresponding to first band index $\nu = 1$, while the same applies to $\mathcal{A}^>(k,\omega)$ for $\nu = 2$. For $U/t_{\mathrm{hop}} = 4$, due to the relatively strong dispersion the agreement between the MPS and the FD data is less good compared to $\hat{H}^{4\Delta}$. However, the FD results still qualitatively confirm the additional signal at $\omega/t_{\mathrm{hop}} \approx -3.8$ for $\mathcal{A}^<(k,\omega)$ and $\omega/t_{\mathrm{hop}} \approx 7.8$ for $\mathcal{A}^>(k,\omega)$, respectively. At larger U this discrepancy diminishes significantly, best to be observed in figure 8.16, where the additional Hubbard satellites at $\omega/t_{\mathrm{hop}} \approx -3.8$ and $\omega/t_{\mathrm{hop}} \approx 19.5$ for $\mathcal{A}^<(k,\omega)$ and $\mathcal{A}^>(k,\omega)$ almost perfectly match the FD data. Again, $\mathcal{A}^<(k,\omega)$ and $\mathcal{A}^>(k,\omega)$ are mirrored at $\omega = U/2t_{\mathrm{hop}}$. Thus, we can say that at half filling $\hat{H}^{2\Delta}$ preserves the key feature of a band splitting of the lowest band of $\mathcal{A}^<(k,\omega)$ and the highest band of $\mathcal{A}^>(k,\omega)$ with increasing U which we found for $\hat{H}^{4\Delta}$.

As for the optical conductivity, here the interpretation is once again much easier for $\hat{H}^{2\Delta}$ as compared to $\hat{H}^{4\Delta}$. We present our numerical results in figures 8.17 and 8.18 for $U/t_{\mathrm{hop}} = 4$ and

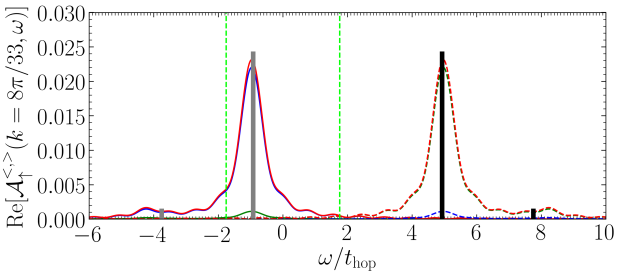

Figure 8.15: Cross section of the data shown in figure 8.13 at $k = 8\pi/33$. Solid lines: $\mathscr{A}_\uparrow^<(k = 8\pi/33, \omega)$; dashed lines: $\mathscr{A}_\uparrow^>(k = 8\pi/33, \omega)$. The total spectral function is shown in red, the contribution from the two band indices $\nu = 1, 2$ are given in blue and green, respectively. Vertical dashed light green lines: ground state peak positions in the non-interacting case obtained for PBCs. Vertical gray (black) bars: excitation energies for $\mathscr{A}_\uparrow^<$ ($\mathscr{A}_\uparrow^>$) as obtained from equation (7.54) ((7.55)) for one unit cell, i.e. $L = 2$. The heights of the bars correspond to their respective weights. All bars have been scaled such that in each cross section the largest bar (irrespective of belonging to $\mathscr{A}_\uparrow^<$ or $\mathscr{A}_\uparrow^>$) takes a value of 0.8 times the plot's maximum range in y-direction. This figure is taken from the author's work [243].

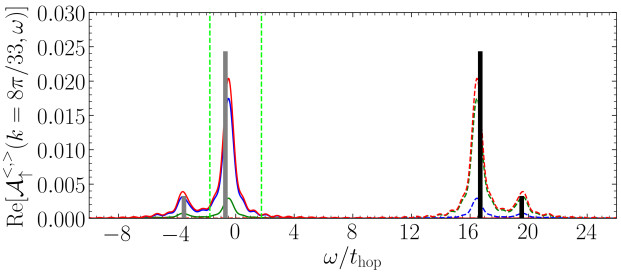

Figure 8.16: Cross section of the data shown in figure 8.14 at $k = 8\pi/33$. Solid lines: $\mathscr{A}_\uparrow^<(k = 8\pi/33, \omega)$; dashed lines: $\mathscr{A}_\uparrow^>(k = 8\pi/33, \omega)$. The total spectral function is shown in red, the contribution from the two band indices $\nu = 1, 2$ are given in blue and green, respectively. Vertical dashed light green lines: ground state peak positions in the non-interacting case obtained for PBCs. Vertical gray (black) bars: excitation energies for $\mathscr{A}_\uparrow^<$ ($\mathscr{A}_\uparrow^>$) as obtained from equation (7.54) ((7.55)) for one unit cell, i.e. $L = 2$. The heights of the bars correspond to their respective weights. All bars have been scaled such that in each cross section the largest bar (irrespective of belonging to $\mathscr{A}_\uparrow^<$ or $\mathscr{A}_\uparrow^>$) takes a value of 0.8 times the plot's maximum range in y-direction.

$U/t_{\mathrm{hop}} = 16$, respectively. For $U/t_{\mathrm{hop}} = 4$ we note that the dominant peaks at $\omega/t_{\mathrm{hop}} \approx 5.2$ and $\omega/t_{\mathrm{hop}} \approx 9.0$ roughly match the difference of the positions of the dominant peak in $\mathscr{A}^<(k, \omega)$ and the two peaks in $\mathscr{A}^>(k, \omega)$ as shown in figure 8.15. We again explain the discrepancies with the comparably large dispersion of this model. Our understanding is further supported by the situation of $U/t_{\mathrm{hop}} = 16$, the peaks at $\omega/t_{\mathrm{hop}} \approx 16.8$, $\omega/t_{\mathrm{hop}} \approx 20.2$, and $\omega/t_{\mathrm{hop}} \approx 22.5$ almost perfectly matching the differences of all the peak positions from $\mathscr{A}^<(k, \omega)$ and $\mathscr{A}^>(k, \omega)$ in figure 8.16. Further, we find a small contribution at $\omega/t_{\mathrm{hop}} \approx 1.6$ or $\omega/t_{\mathrm{hop}} \approx 3.3$, respectively, which corresponds to the differences of the two peak positions of either $\mathscr{A}^<(k, \omega)$ and $\mathscr{A}^>(k, \omega)$. We take that this contribution stems from the inaccurate description of interacting systems by means of bands and conclude that although not evident from equation (6.89) also in the interacting case the optical conductivity shows its peaks at energies corresponding to the energy differences of the

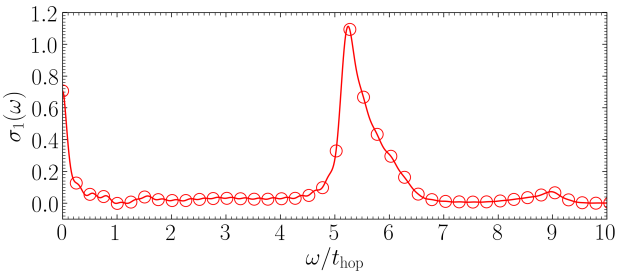

Figure 8.17: Real part of the optical conductivity $\sigma_1(\omega, t)$ in equilibrium for $\hat{H}^{2\Delta}$ with $U/t_{\mathrm{hop}} = 4$ and $\Delta/t_{\mathrm{hop}} = 2$ for a system of $L = 32$ sites with OBCs at half filling. Data points: Obtained from Fourier transforming according to (6.109) and (6.110). Solid lines: Application of 16 times zero padding. This figure is adapted from the author's work [243].

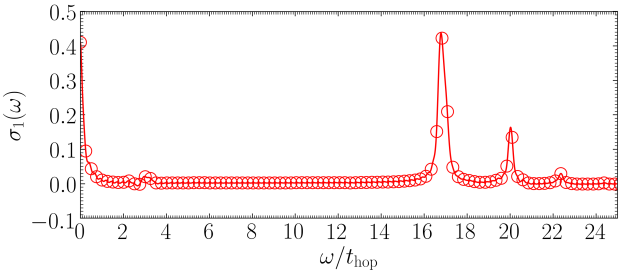

Figure 8.18: Real part of the optical conductivity $\sigma_1(\omega, t)$ in equilibrium for $\hat{H}^{2\Delta}$ with $U/t_{\mathrm{hop}} = 16$ and $\Delta/t_{\mathrm{hop}} = 2$ for a system of $L = 32$ sites with OBCs at half filling. Data points: Obtained from Fourier transforming according to (6.109) and (6.110). Solid lines: Application of 16 times zero padding. This figure is adapted from the author's work [243].

signals in the (greater and lesser) spectral functions.

8.2.3 Full Diagonalization Analysis of the Effect of the Interaction Strength

Driven by the observation that the approximative calculation of the spectral functions for large U with FD in a single unit cell provides rather clear insights, we further analyze the influence of U in figure 8.19. We begin our discussion with $\mathcal{A}^<(k, \omega)$ for $\hat{H}^{4\Delta}$ at half filling as given in figure 8.19(b). Starting from $U = 0$, we can directly follow how the non-interacting bands are renormalized regarding their positions and weights, and also, which new features are caused by U. For example, we find that a weak additional structure is formed at $\omega/t_{\mathrm{hop}} \approx -3$, which is not related to the non-interacting band structure. Also, we observe that both the first (around $\omega/t_{\mathrm{hop}} \approx -2$) and the second band (around $\omega/t_{\mathrm{hop}} \approx 0$) are subject to a renormalization with growing U. However, while the second band appears to saturate at a value of $\omega \approx 0$, a new structure due to U emerges in the vicinity of the first band, which for $U/t_{\mathrm{hop}} \gtrsim 10$ then becomes the dominant feature taking over the weight from the original first band. Starting at $U/t_{\mathrm{hop}} \approx 2$ we furthermore find the formation of a new signal beneath the original first band at $\omega/t_{\mathrm{hop}} \approx -2.5$ of which the weight grows further with increasing U. This explains the band splitting of the $\nu = 1$ band observed in figures 8.9(b) and 8.10(b). We also very vaguely encounter a small signal at $\omega/t_{\mathrm{hop}} \approx -4$ of which we found a trace in figure 8.9(b). Thus, for larger interactions $\mathcal{A}^<(k, \omega)$ predominantly possesses two renormalized bands, which stem from the non-interacting band structure, and two additional features, which

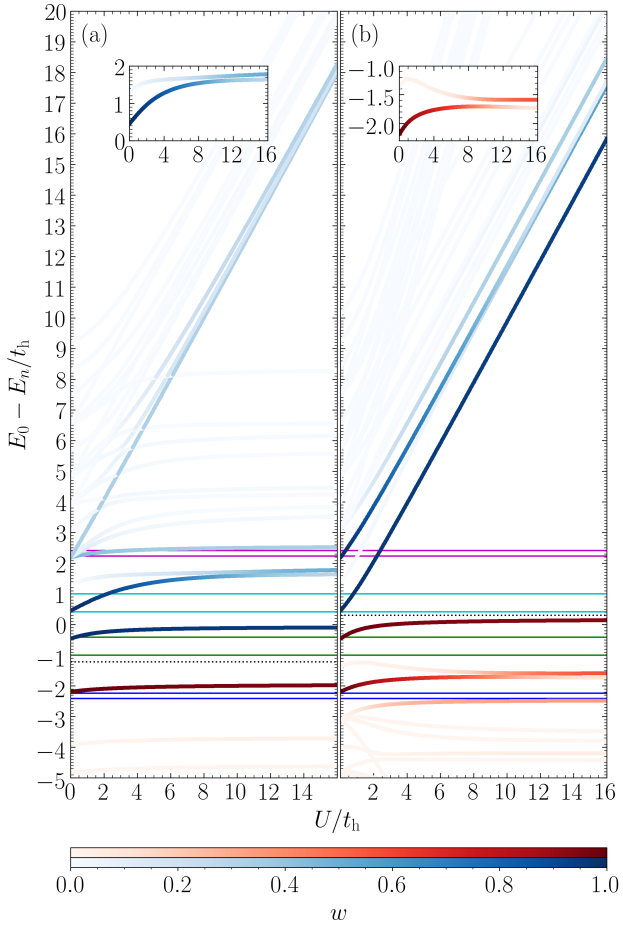

Figure 8.19: $\mathscr{A}_\uparrow^<(k,\omega)$ (red) and $\mathscr{A}_\uparrow^>(k,\omega)$ (blue) as a function of U obtained from FD of a single unit cell of $\hat{H}^{4\Delta}$ with OBCs according to equations (7.54) and (7.55) for the case of quarter (a) and half filling (b). The intensity of the line color indicates the weight w of the respective peaks, i.e. $w_n(U) = \sum_r \left|\langle n|\, \hat{c}_{\uparrow,r}\, |\mathrm{GS}\rangle(U)\right|^2$. The figure was cut at $E_0 - E_n = -5$ at the bottom and $E_0 - E_n = 20$ at the top when all peaks occur with $w \ll 0.2$. Insets: Zoom into the specified regions. Dashed lines: Separator of $\mathscr{A}_\uparrow^<(k,\omega)$ and $\mathscr{A}_\uparrow^>(k,\omega)$. Solid lines: Analytical results for the edges of bands $\nu = 1$ (blue), $\nu = 2$ (green), $\nu = 3$ (cyan), and $\nu = 4$ (magenta) for $U = 0$ and PBCs. Note that some lines with finite weights at $U = 0$ are not located in the respective bands which is due to their computation with OBCs. This figure is taken from the author's work [243].

are correlation induced. Figure 8.19(b) additionally depicts $\mathscr{A}_\uparrow^>(k,\omega)$, illustrating the symmetry of $\mathscr{A}_\uparrow^<(k,\omega)$ and $\mathscr{A}_\uparrow^>(k,\omega)$ at $U/2t_{\mathrm{hop}}$ as expected from analytical computations. This plot also suggests, that with increasing U the upper and lower Hubbard band we identified above will grow further apart matching the characteristics of a Mott insulator. The total spectral function, hence, is composed of two Hubbard bands with an additional peak structure, which partly is due to the non-interacting band structure, and partly due to interaction effects. Clearly, the weight takeover, which is highlighted in the inset also occurs for $\mathscr{A}_\uparrow^>(k,\omega)$, best to be seen at $U/t_{\mathrm{hop}} = 14$. From the inset, we find that at $U/t_{\mathrm{hop}} \approx 8$ the weights of the overtaking and overtaken line are roughly equal, while at $U/t_{\mathrm{hop}} = 16$ the process is more or less completed.

Interestingly, we find a similar behavior also at quarter filling as is shown in figure 8.19(a). Here, there is only little change to $\mathscr{A}_\uparrow^<(k,\omega)$ with growing U as expected due to the low particle density. While it comes only with a very small renormalization and three almost negligible side bands, $\mathscr{A}_\uparrow^>(k,\omega)$ exploits a much richer structure. In addition to a similar weight takeover to the third band as in the case of half filling, which is highlighted in the inset, the fourth band showcases another interesting phenomenon. At $U = 0$ one expects to find a sole signal of weight 1 analytically, but when looking into the numbers, we find in fact two signals of weight 0.5 each. Hence, two signals appear to have collapsed into one resulting in a degeneracy. This shows an actual band splitting for increasing U, unlike the weight take over, we discussed above. In the latter case, it is not clear from our computations, that it must be a contribution from the same band the weight from a fade out line is transferred to. The degeneracy, however, leaves no other explanation than an actual splitting. Note that only one of the two major branches from the split fourth band scales with U, the other one is only slightly renormalized around $\omega/t_{\mathrm{hop}} \approx 2.5$. Again, the former branch is subject to weight takeover for larger U.

For $\hat{H}^{2\Delta}$, due to the smaller unit cell of $L = 2$, the spectrum in the Lehmann representation is significantly less evolved than for $\hat{H}^{4\Delta}$ consisting only of two contributions as given in figure 8.20, a dominant band, which survives in the case $U = 0$, and a satellite band, which takes only some weight from the dominant one for large U. Both contributions are also subject to some renormalization. As $\mathscr{A}_\uparrow^>(k,\omega)$ will behave analogously apart from scaling with U we do not depict it for this setup. We may, as for the case of $\hat{H}^{4\Delta}$, interpret the system as being composed of two Hubbard bands with a fine structure.

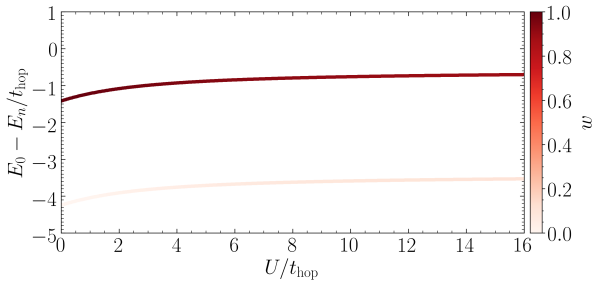

Figure 8.20: $\mathscr{A}_\uparrow^<(k,\omega)$ as a function of U obtained from FD of a single unit cell of $\hat{H}^{2\Delta}$ with OBC according to equation (7.54) for the case of half filling. The intensity of the line color indicates the weight w of the respective peaks $w_n(U) = \sum_r \left|\langle n|\, \hat{c}_{\uparrow,r}\, |\mathrm{GS}\rangle(U)\right|^2$. At $U = 0$ the non-interacting band structure is reproduced. This figure is taken from the author's work [243].

9 Spectral Quantities of the Hubbard Model with a Magnetic Superstructure Out of Equilibrium: Formation of Spatial Structures and Excitons

Now that we have gained a well-founded understanding of our model system in equilibrium, we turn to the analysis of out-of-equibrium setups. We will focus on simulations of photo excitations by, for example, sunlight which are characterized by carrying only a very small number of photons per unit of time. In the long run, we hope procedures of this type to be able to explain absorption processes in photoactive layers like solar cells. Regarding our model, the result of such a process corresponds to a transition of spectral weight in the ground state lesser spectral function to previously unoccupied regions, the simplest form being an excitation from the highest occupied band to the lowest unoccupied band. As already mentioned, in the strongly interacting system, the notion of bands is somewhat peculiar; what we mean in this case is an electron-hole excitation shifting an electron from a (k,ω)-value on the upper edge of the support of $\mathscr{A}^{<}(k,\omega)$ to the lower region of support of $\mathscr{A}^{>}(k,\omega)$ leaving a hole in the former. Furthermore do we focus on excitations of particles of a specific spin-direction (In this work we choose spin-$\uparrow$.) of which the purpose is twofold: (i) we are allowed to study the effect of interactions in greater detail by considering the dynamics in both spin directions separately; (ii) this procedure is reminiscent of spin-selective excitations, which can be realized, e.g., in spin-polarized ARPES experiments, typically by circularly polarized light.

As we have elaborated on in section 7.4 a suitable method to describe such setups is the manipulation of the ground state $|\mathrm{GS}\rangle$ by an operator $\hat{\Lambda}$, c.f. equation (7.94), since we are primarily interested in the time evolution of the system following the excitation rather than the excitation process itself. Here we choose

$$\hat{\Lambda} = \hat{a}^{\dagger}_{\uparrow,k',\mu}\hat{a}_{\uparrow,k,\nu}, \tag{9.1}$$

which for non-interacting systems corresponds to an exact shift of one particle of spin-$\uparrow$ at momentum k in band ν to momentum k' in band μ. We will restrict our discussion in this work to excitations that only change the band from the highest occupied to the lowest unoccupied one, but leave the momentum invariant, i.e. $\mu = \nu + 1$ and $k' = k$. Furthermore, we choose $k = 4\pi/33 \approx \pi/8$ for $\hat{H}^{4\Delta}$ and $k = 8\pi/33 \approx \pi/4$ for $\hat{H}^{2\Delta}$, i. e. the center of half of the first BZ, since in these cases finite size effects as on the edges of the first BZ, c.f. section 8.2, are expected to be negligible. Clearly, for $\hat{H}^{4\Delta}$ we have $\nu = 2$ and $\mu = 3$ at half and $\nu = 1$ and $\mu = 2$ at quarter filling, respectively, the latter pair of band indices also applying to the computations with $\hat{H}^{2\Delta}$ at half filling.

Note, that despite the operators $\hat{a}^{(\dagger)}_{\sigma,\nu,k}$ being obtained from the definition of a non-interacting system, we will still apply (9.1) as is for interacting systems as well. Hence, in these cases an approximative electron-hole excitation is modeled. Nevertheless, our findings justify this approach since in either case most of the respective structures corresponding to lower or upper bands in the non-interacting setup are affected as we will show below. Note further that the interpretation of exciting only one particle is quite naive when it comes to the interpretation of the spectral functions. We illustrate this by the following Gedanken experiment. Imagine applying the same procedure to

two (non-interacting) systems which only differ in size, the second one being twice as large as the first one. In this case due to the discretization, the signal in the post-excitation spectral function of the first system will appear to be twice as large as the signal in the second one. Therefore, we shall better think of this type of excitation as a shift of low electron densities rather than of actual particles.

9.1 Immediate Post-excitation Effects on Non-Interacting Systems

As we have already mentioned above, excitation (9.1) is exact for non-interacting systems. Computed in the same way as the ground state spectral functions we, hence, expect the exact same results with the exception of the momentum k and the band indices ν and $\nu+1$ the excitation was applied to. At k itself the contribution of ν should vanish entirely, while for $\nu+1$ it should look the same as the ν-contribution in the ground state the peak only being at $\omega = \varepsilon_{k,\nu+1}$ instead of $\omega = \varepsilon_{k,\nu}$. Hence, regarding the spectral function these computations provide a sanity check to the validity of equation (9.1).

9.1.1 Four Band Model

To confirm the above considerations we present the corresponding results for $\hat{H}^{4\Delta}$ in figure 9.1, where, indeed, we find the lesser spectral functions $\mathscr{A}^{<}_{\sigma}(k,\omega,t=0)$ to follow exactly their ground state counterparts, with the exception of $\mathscr{A}^{<}_{\uparrow}(k,\omega,t=0)$ at $k = 4\pi/33$ where in the case of quarter filling the entire weight from the first band has been shifted to the second one, c.f. figure 9.1(a), or from the second to the third band for a half filled system, c.f. figure 9.1(c), just as equation (9.1) demands. Note in particular, that in the spin-$\downarrow$ direction depicted in figures 9.1(b) and (d) no change in the spectral function is observed also meeting our expectations since in a non-interacting setup both spin channels are decoupled.

We further confirm these findings in figure 9.2, where we present the cross sections of the lesser spectral functions at $k = 4\pi/33$. As for the spin-$\downarrow$ direction shown in figures 9.2(c) and (d) we find that the lesser spectral function to exactly match the ground state case. Of more interest at this point is an analysis of the contributions of the bands to the total spectral function in the spin-$\uparrow$ direction. With figures 9.2(a) and (b) we further confirm that at quarter filling indeed the $\nu = 1$-contribution has vanished entirely the weight being solely transferred to the $\nu = 2$-contribution and analogously at half filling the $\nu = 2$-contribution has vanished while only the $\nu = 3$-contribution has taken over the spectral weight.

In addition to the spectral functions, we also present the corresponding optical conductivities in figure 9.3. Again, the spin-$\downarrow$ contributions do not differ from the ground state results, c.f. figures 9.3(e) and (f). We only find a new peak in the spin-$\uparrow$ contribution, which then affects the total optical conductivity. In the case of quarter filling this peak emerges at $\omega/t_{\mathrm{hop}} \approx 1.8$, see figures 9.3(a) and (c), which roughly equals the difference of the second and third band depicted in figure 9.2(a). At half filling the additional peak occurs at $\omega/t_{\mathrm{hop}} \approx 1.7$, c.f. figures 9.3(b) and (d), matching the energy difference of the third and fourth band as can be verified in figure 9.2(b). These findings further confirm our understanding of the optical conductivity showing peaks at the energy differences of occupied and unoccupied sectors of the total spectral function as predicted by equation (6.89).

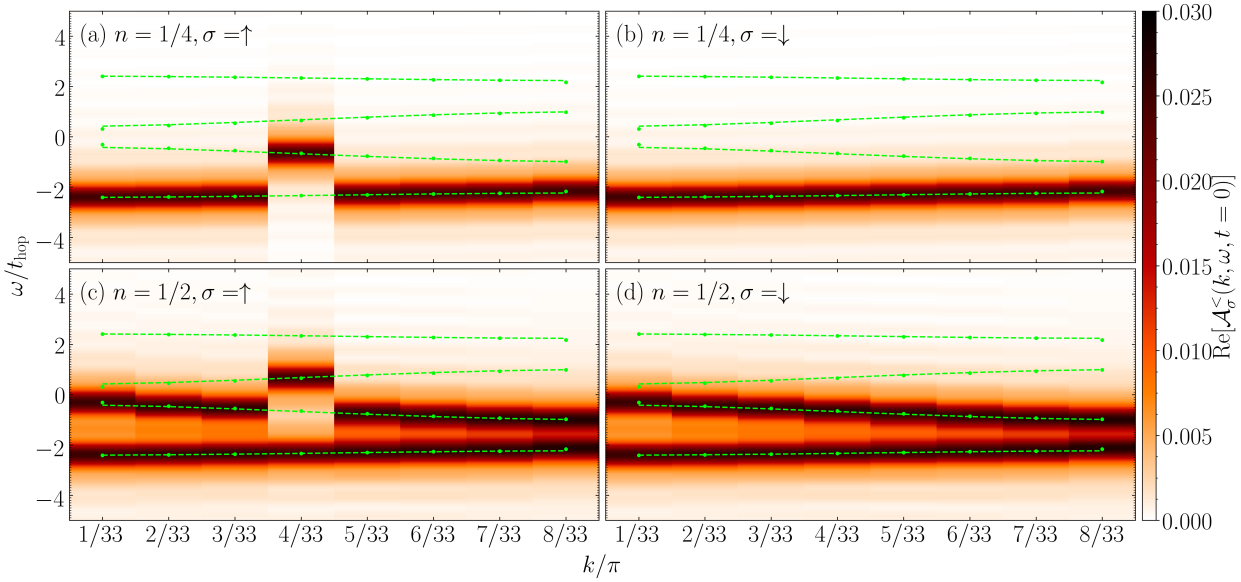

Figure 9.1: Lesser spectral function $\mathcal{A}_\sigma^<(k, \omega, t = 0)$ immediately after the electron-hole excitation (9.1) for $\hat{H}^{4\Delta}$ with $U/t_{\mathrm{hop}} = 0$ and $\Delta/t_{\mathrm{hop}} = 2$ for a system of $L = 32$ sites with OBCs in the first BZ at quarter, (a) and (b), and half filling, (c) and (d), respectively. (a) and (c) show the spin-↑ direction, (b) and (d) the spin-↓ direction. The green dashed lines show the band structure of the non-interacting system calculated with PBCs, the green dots correspond to the calculation with OBCs.

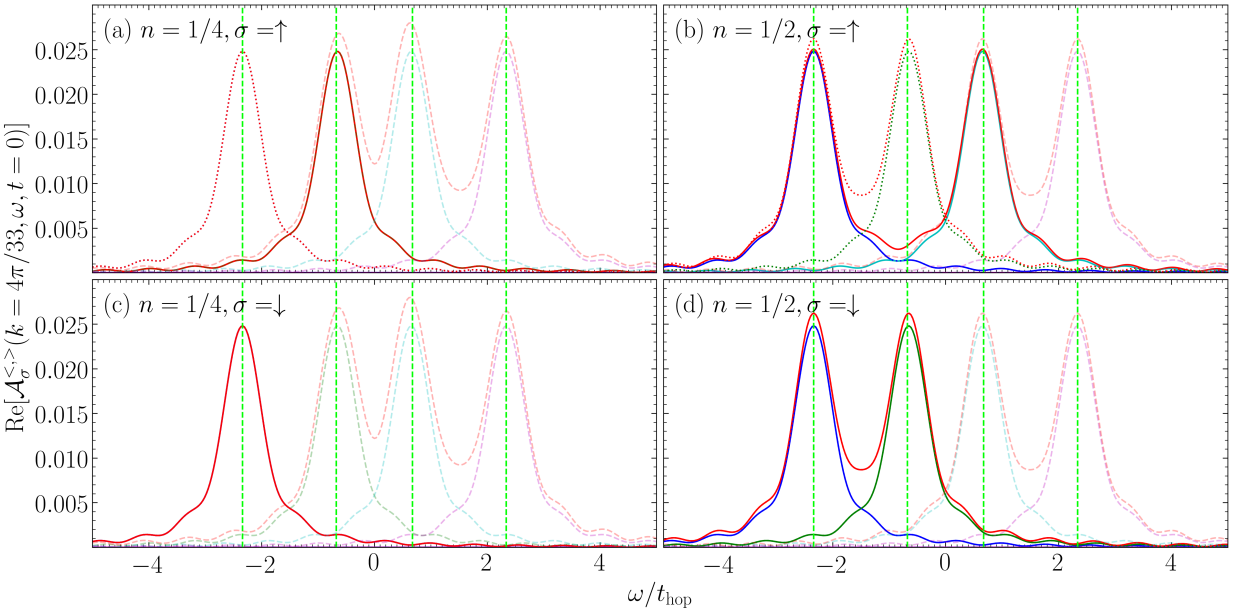

Figure 9.2: Cross section of the data shown in figure 9.1 at $k = 4\pi/33$ (solid lines) for quarter, (a) and (c) and half filling, (b) and (d). (a) and (b) show the spin-↑ direction, (c) and (d) the spin-↓ direction. The dotted (light dashed) lines show the ground state results of figure 8.2 for the lesser (greater) spectral functions. The total spectral function is shown in red, the contribution from the four band indices $\nu = 1, 2, 3, 4$ are given in blue, green, cyan, and magenta, respectively. Vertical dashed light green lines: ground state peak positions in the non-interacting case obtained for PBCs.

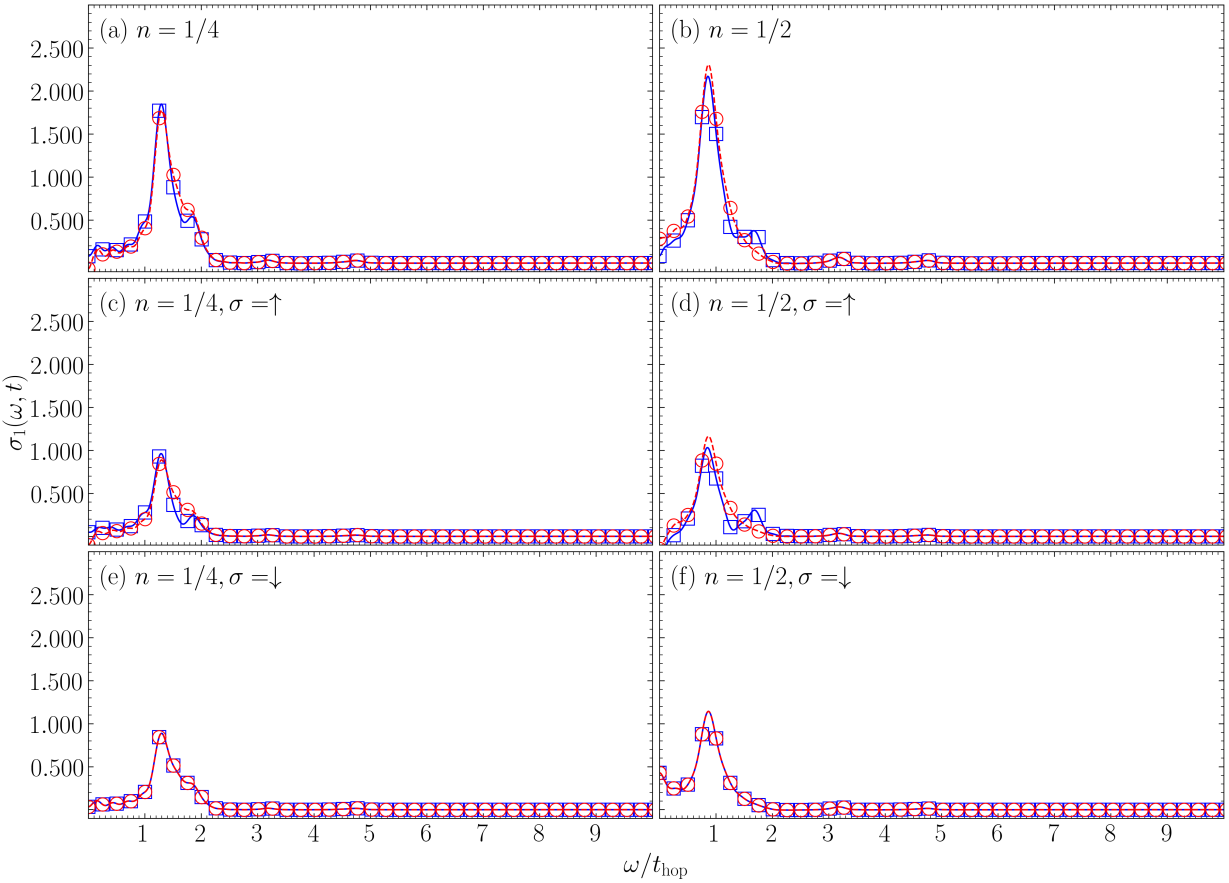

Figure 9.3: Real part of the optical conductivity $\sigma_1(\omega, t)$ immediately after the excitation, i.e. $t = 0$, (solid blue) for $\hat{H}^{4\Delta}$ with $U/t_{\mathrm{hop}} = 0$ and $\Delta/t_{\mathrm{hop}} = 2$ for a system of $L = 32$ sites with OBCs at quarter, (a), (c), and (e), and half filling, (b), (d), and (f), respectively. (a) and (b) show the total optical conductivity, (c) and (d) the spin-↑ direction, and (e) and (f) the spin-↓ direction. The dashed red lines show the equilibrium ground state results, i.e. $t = -\infty$. Data points: Obtained from Fourier transforming according to (6.109) and (6.110). Solid lines: Application of 16 times zero padding. This figure is adapted from the author's work [243].

9.1.2 Two Band Model

Qualitatively we obtain very much the same results for $\hat{H}^{2\Delta}$ as for $\hat{H}^{4\Delta}$. In figure 9.4 we again find the spin-↓ contribution of the lesser spectral function to be entirely unaffected by the excitation, while in the spin-↑ direction the only difference compared to the ground state lies at $k = 8\pi/33$ the weight from the first band being shifted to the second.

From the cross sections at $k = 8\pi/33$ as shown in figure 9.5 we confirm both these findings. Indeed, the weights in the spin-↓ direction overlap with the ground state values. In the spin-↑-direction the $\nu = 1$-contribution of the lesser spectral function has vanished the weight being taken by the $\nu = 2$-contribution. Note that for this easier setup with only two bands following excitation (9.1), if applied correctly, weight can only be transferred to the sole other empty band making the analysis less complicated.

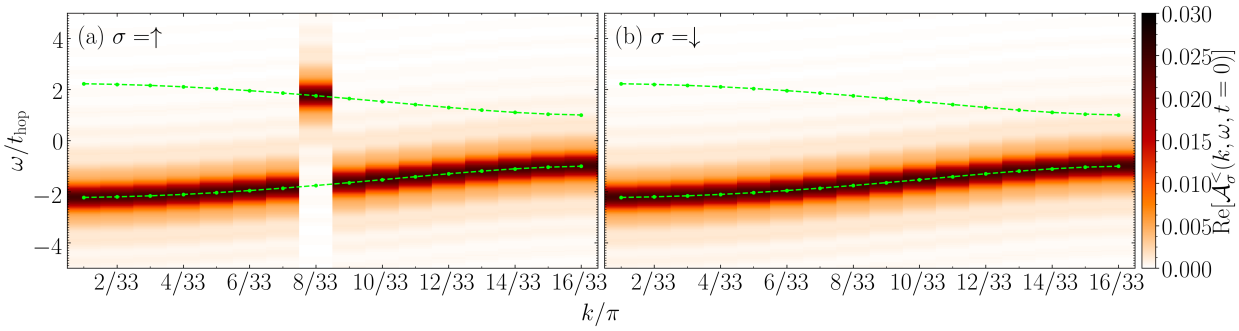

Figure 9.4: Single particle spectral functions $\mathcal{A}^{<}_{\sigma}(k, \omega, t = 0)$ immediately after the electron-hole excitation (9.1) for $\hat{H}^{2\Delta}$ with $U/t_{\text{hop}} = 0$ and $\Delta/t_{\text{hop}} = 2$ for a system of $L = 32$ sites with OBCs in the first BZ at half filling. (a) shows the spin-↑ direction, (b) the spin-↓ direction. The green dashed lines show the band structure of the non-interacting system calculated with PBCs, the green dots correspond to the calculation with OBCs.

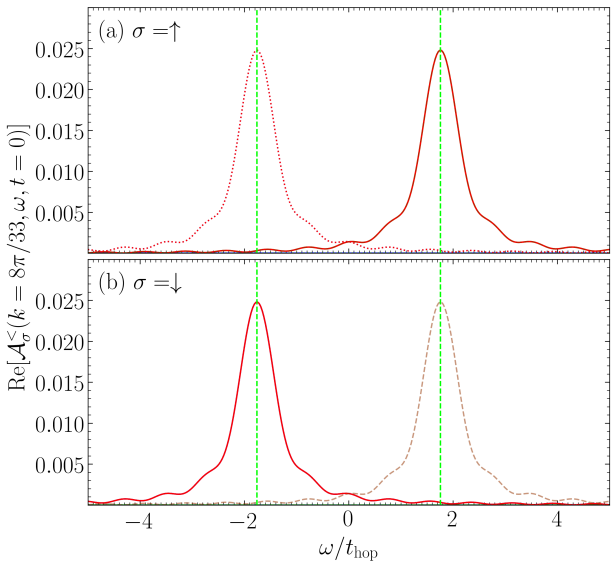

Figure 9.5: Cross section of the data shown in figure 9.4 at $k = 8\pi/33$ (solid lines) for half filling. (a) shows the spin-↑ direction, (b) the spin-↓ direction. The dotted (light dashed) lines show the ground state results of figure 8.5 for the lesser (greater) spectral functions. The total spectral function is shown in red, the contribution from the four band indices $\nu = 1, 2, 3, 4$ are given in blue, green, cyan, and magenta, respectively. Vertical dashed light green lines: ground state peak positions in the non-interacting case obtained for PBCs.

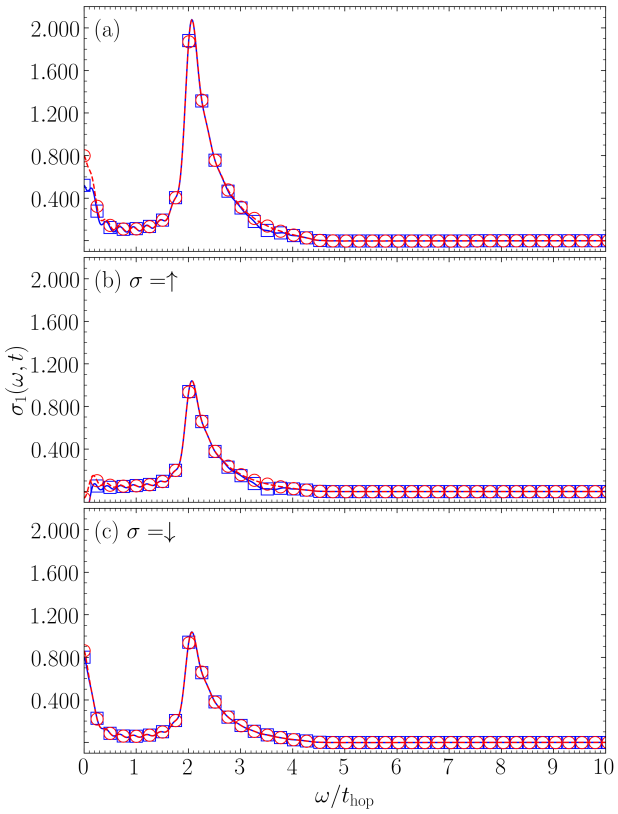

Figure 9.6: Real part of the optical conductivity $\sigma_1(\omega, t)$ immediately after the excitation, i.e. $t = 0$, (solid blue) for $\hat{H}^{2\Delta}$ with $U/t_{\text{hop}} = 0$ and $\Delta/t_{\text{hop}} = 2$ for a system of $L = 32$ sites with OBCs at half filling. (a) shows the total optical conductivity, (b) the spin-↑ direction, and (c) the spin-↓ direction. The dashed red lines show the equilibrium ground state results, i.e. $t = -\infty$. Data points: Obtained from Fourier transforming according to (6.109) and (6.110). Solid lines: Application of 16 times zero padding. This figure is adapted from the author's work [243].

We show the accompanying optical conductivity in figure 9.6. Here, the only difference to the ground state data, apart from a change in the Drude peak, stems from the spin-↑-direction, c.f. figures 9.6(a) and (b), where we find an additional contribution at $\omega/t_{\text{hop}} \approx 3.6$, which matches the difference of the first and second band, as can be seen in figure 9.5. Note that while this additional feature occurs at the correct frequency as predicted from equation (6.89) its behavior of decreasing the optical conductivity appears somewhat counterintuitive. However, the complex prefactors in equation (6.89) do not forbid such results which leads us to the conclusion that the optical conductivity is not necessarily easier to interpret than the spectral functions.

9.2 Immediate Post-excitation Effects on Interacting Systems

The non-interacting systems showing the expected behavior following the excitation (9.1) we now consider interacting systems applying, however, the same operator $\hat{\Lambda}$ as before. As we already mentioned above, some care needs to be taken since i) due to the scattering between the electrons, the weight corresponding to the quantum number ν is in general not restricted to one (k, ω)-point,

and ii) correlation effects will in general cause some weight to remain in the region it is supposed to be excited from. Nevertheless, we find that for the systems under investigation here, modeling the photo excitation in this way is justified as still the majority of weight is shifted.

9.2.1 Four Band Model

We begin our analysis with $\hat{H}^{4\Delta}$ for which in figure 9.7 we show the result of excitation (9.1) at $U/t_{\mathrm{hop}} = 4$ for both, half and quarter filling. In either case do we observe that in the spin-↑

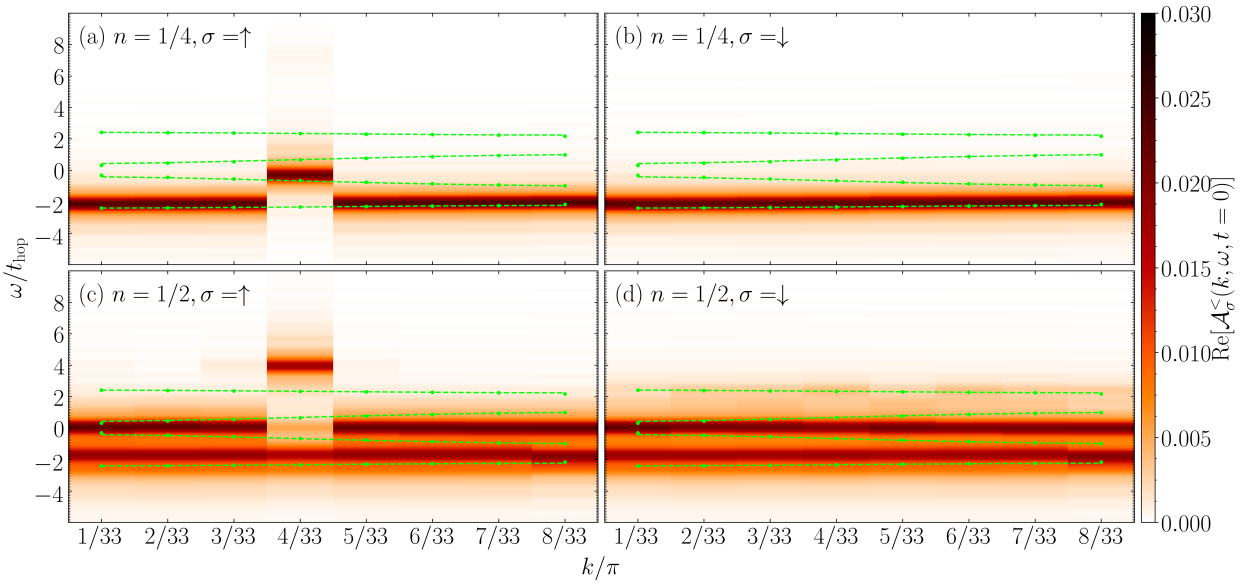

Figure 9.7: Single particle spectral functions $\mathcal{A}_\sigma^<(k,\omega,t=0)$ immediately after the electron-hole excitation (9.1) for $\hat{H}^{4\Delta}$ with $U/t_{\mathrm{hop}} = 4$ and $\Delta/t_{\mathrm{hop}} = 2$ for a system of $L = 32$ sites with OBCs in the first BZ at quarter, (a) and (b), and half filling, (c) and (d), respectively. (a) and (c) show the spin-↑ direction, (b) and (d) the spin-↓ direction. The green dashed lines show the band structure of the non-interacting system calculated with PBCs, the green dots correspond to the calculation with OBCs. This figure is taken from the author's work [243].

direction the upper occupied "band" gets emptied at $k = 4\pi/33$ as desired, and a restricted region at the same k-value but higher energies gets occupied corresponding to the support of the "lowest unoccupied band" in $\mathcal{A}_\uparrow^>(k,\omega)$, c.f. figures 9.7(a) and (c). From figures 9.7(a) and (b) we find that apart from the slight renormalization as already discussed in the previous section, at quarter filling the situation appears to resemble the non-interacting case even at finite U which further indicates that at this filling and value of the parameters interaction effects are not dominant. In the case of half filling as shown in figures 9.7(c) and (d), however, the behavior differs significantly from the non-interacting setup. First, in $\mathcal{A}_\uparrow^<(k = 4\pi/33, \omega, t = 0)$ a remnant of the electron remains at its ground state energy, and the population at higher energies in $\mathcal{A}_\uparrow^<(k,\omega,t=0)$ is smeared out a bit, that is also neighboring k-values to the one we chose take a certain although small amount of weight. At the same time, however, even though we did not apply an excitation there, we find the electrons in the spin-↓ to be affected as well for we observe a response *in between* the gap between the occupied and the unoccupied region of the spectral function at $\omega/t_{\mathrm{hop}} \approx 2.5$. This is a

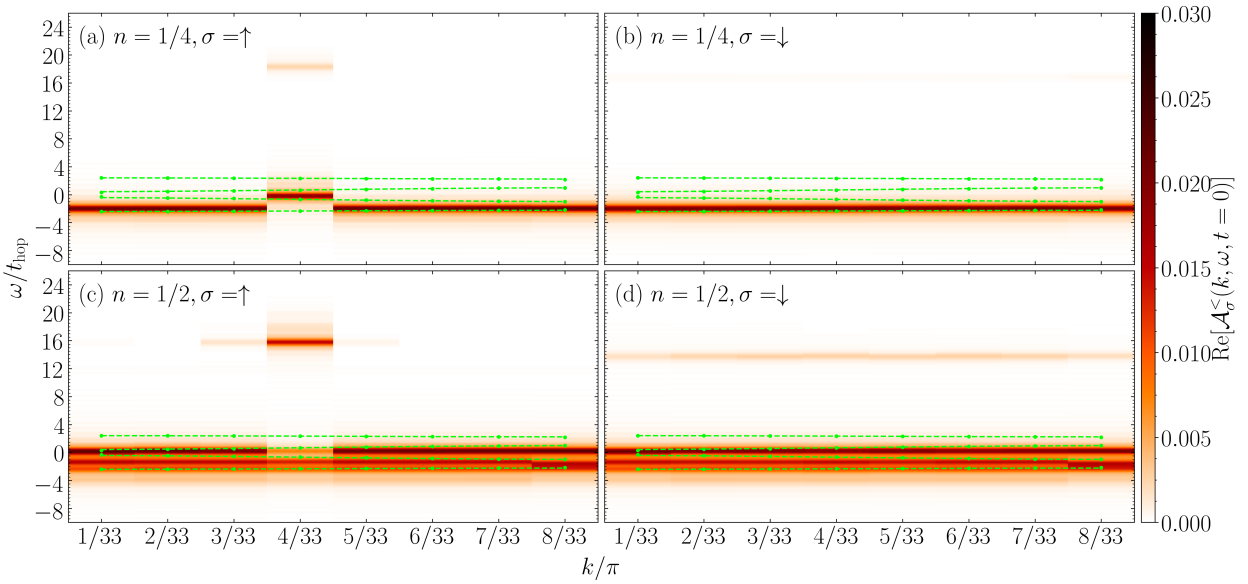

Figure 9.8: Single particle spectral functions $\mathcal{A}_\sigma^<(k, \omega, t = 0)$ immediately after the electron-hole excitation (9.1) for $\hat{H}^{4\Delta}$ with $U/t_{\mathrm{hop}} = 16$ and $\Delta/t_{\mathrm{hop}} = 2$ for a system of $L = 32$ sites with OBCs in the first BZ at quarter, (a) and (b), and half filling, (c) and (d), respectively. (a) and (c) show the spin-↑ direction, (b) and (d) the spin-↓ direction. The green dashed lines show the band structure of the non-interacting system calculated with PBCs, the green dots correspond to the calculation with OBCs.

remarkable finding, which we further analyze by changing the value of the interaction U. In figure 9.8 we show the spectral functions of figure 9.7 but this time for $U/t_{\mathrm{hop}} = 16$. Qualitatively, we find the same features. Two aspects, however, deserve some more attention. At quarter filling, c.f. figure 9.8(a), the excitation in the spin-↑ direction produces a somewhat twofold signal in $\mathcal{A}_\uparrow^<(k, \omega, t = 0)$ since we find considerable weight at $\omega/t_{\mathrm{hop}} \approx 18$ which corresponds more to the third than to the second band. For the half-filled system the additional signal in $\mathcal{A}_\downarrow^<(k, \omega, t = 0)$ shown in figure 9.8(d) occurs at $\omega/t_{\mathrm{hop}} \approx 13.8$ and is thus even more clearly separated from the lower edge of support of the greater spectral function.

In order to better quantify the features described above, we present cross sections at $k = 4\pi/33$ for all spectral functions given in figure 9.7 in figure 9.9 for the case of $U/t_{\mathrm{hop}} = 4$. Analogously, for $U/t_{\mathrm{hop}} = 16$ we show cross sections corresponding to figure 9.8 in figure 9.10. In addition, the figures also feature the ground state results from figures 8.9 and 8.10, respectively, allowing a direct comparison of the spectral function pre and post excitation. We begin with analyzing the situation for $U/t_{\mathrm{hop}} = 4$. At quarter filling as shown in figure 9.9(a) and (c), we indeed find the previously occupied lowest band at $\omega/t_{\mathrm{hop}} \approx -2$ to be completely emptied for the spin-↑ direction, c.f. figure 9.9(a). Instead $\mathcal{A}_\uparrow^<(k, \omega, t = 0)$ now takes the weight of the $\nu = 2$-contribution of the ground state greater spectral function $\mathcal{A}_\uparrow^>(k, \omega)$. Note that the respective lines overlap almost entirely, and other than this, there are no particular features noticeable in $\mathcal{A}_\uparrow^<(k, \omega, t = 0)$. The spin-↓ direction, c.f. figure 9.9(c), shows a similar expected behavior as $\mathcal{A}_\downarrow^<(k, \omega, t = 0)$ almost overlaps completely with the respective ground state spectral function $\mathcal{A}_\downarrow^<(k, \omega)$. We attribute the slight changes to the respective features of the ground state spectral function to scattering effects in between different k-values and conclude that at quarter filling, there is only a redistribution of

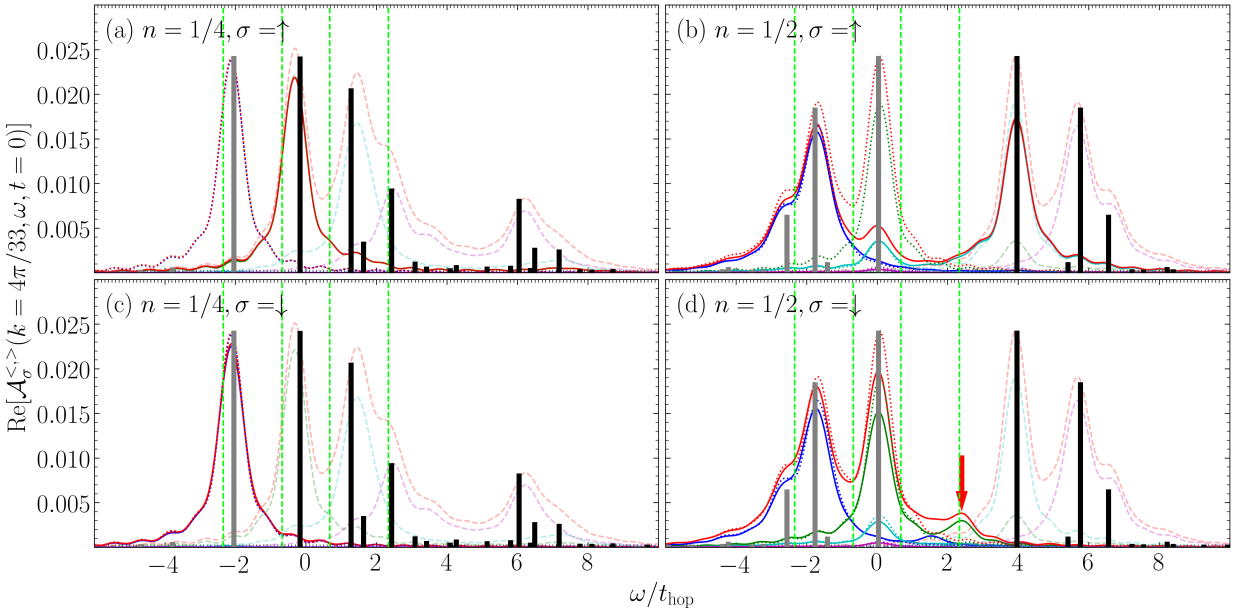

Figure 9.9: Cross section of the data shown in figure 9.7 at $k = 4\pi/33$ (solid lines) for quarter, (a) and (c) and half filling, (b) and (d). (a) and (b) show the spin-↑ direction, (c) and (d) the spin-↓ direction. The dotted (light dashed) lines show the ground state results of figure 8.9 for the lesser (greater) spectral functions. The total spectral function is shown in red, the contribution from the four band indices $\nu = 1, 2, 3, 4$ are given in blue, green, cyan, and magenta, respectively. Vertical dashed light green lines: ground state peak positions in the non-interacting case obtained for PBCs. Vertical gray (black) bars: excitation energies for $\mathcal{A}^{<}_\sigma$ ($\mathcal{A}^{>}_\sigma$) in the ground state as obtained from equation (9.1) for one unit cell, i.e. $L = 4$. The heights of the bars correspond to their respective weights. All bars have been scaled such that in each cross section the largest bar takes a value of 0.8 times the plot's maximum range in y-direction. The red arrow highlights the in-gap spectral weight in $\mathcal{A}^{<}_\downarrow(k, \omega, t = 0)$ (see text for further details). This figure is adapted from the author's work [243].

weight over the excitation energies known from the ground state calculus. Other effects appear to play only a negligible role. The spin-↑ direction at half filling depicted in figure 9.9(b) also behaves as expected, the dominant effect being that the spectral weight of the $\nu = 2$ contribution to $\mathcal{A}^{<}_\uparrow(k, \omega)$, which makes for most of the highest occupied band, has vanished. We find that it has been predominantly transferred mainly to energies of the $\nu = 3$ contribution of $\mathcal{A}^{>}_\uparrow(k, \omega)$, as both lines, again, almost overlap. The remnant of weight in the highest occupied band of $\mathcal{A}^{<}_\uparrow(k, \omega)$ can further be identified to stem from its $\nu = 3$ contribution, which is clearly unaffected in our modeled excitation (9.1) further illustrating its approximative character. Turning our attention to $\mathcal{A}^{<}_\downarrow(k, \omega, t = 0)$ in figure 9.9(d) we find that also in this case the $\nu = 2$ contribution of $\mathcal{A}^{<}_\downarrow(k, \omega)$ has dropped quite significantly. Unlike for the spin-↑ contribution, however, the removed weight does not appear at any frequency to be explained by the FD computation, but at $\omega \approx 2.5$, c.f. the red arrow in figure 9.9(d). Comparing to $\mathcal{A}^{>}_\downarrow(k, \omega)$ we can also surely conclude that this feature cannot be derived as an artifact of ground state properties, as the contribution of $\mathcal{A}^{<}_\downarrow(k, \omega, t = 0)$ at $\omega \approx 2.5$ is much higher than the left-hand edge of $\mathcal{A}^{>}_\downarrow(k, \omega)$. Thus, we take this feature to be a real mid-gap state. Bearing in mind that here all k-values are affected almost equally, c.f. figure 9.7, we will henceforth refer to this phenomenon as a mid-gap band. The cross sections for the case of $U/t_{\mathrm{hop}} = 16$ given in

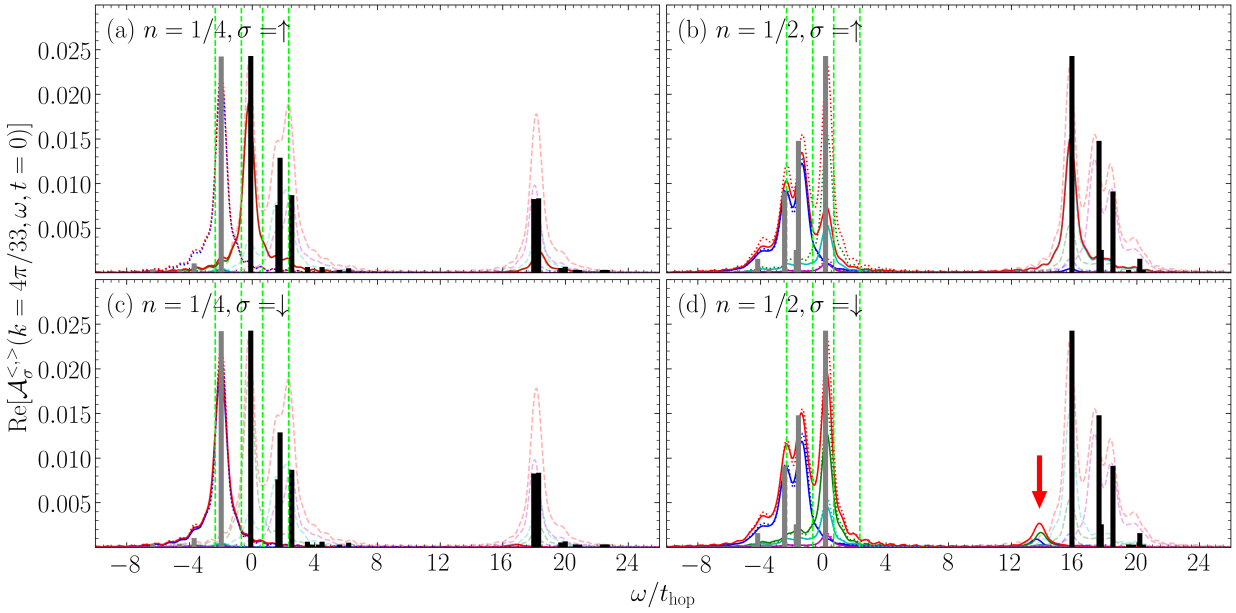

Figure 9.10: Cross section of the data shown in figure 9.8 at $k = 4\pi/33$ (solid lines) for quarter, (a) and (c) and half filling, (b) and (d). (a) and (b) show the spin-↑ direction, (c) and (d) the spin-↓ direction. The dotted (light dashed) lines show the ground state results of figure 8.10 for the lesser (greater) spectral functions. The total spectral function is shown in red, the contribution from the four band indices $\nu = 1, 2, 3, 4$ are given in blue, green, cyan, and magenta, respectively. Vertical dashed light green lines: ground state peak positions in the non-interacting case obtained for PBCs. Vertical gray (black) bars: excitation energies for $\mathcal{A}_\sigma^<$ ($\mathcal{A}_\sigma^>$) in the ground state as obtained from equation (9.1) for one unit cell, i.e. $L = 4$. The heights of the bars correspond to their respective weights. All bars have been scaled such that in each cross section the largest bar takes a value of 0.8 times the plot's maximum range in y-direction. The red arrow highlights the in-gap spectral weight in $\mathcal{A}_\downarrow^<(k, \omega, t = 0)$ (see text for further details). This figure is adapted from the author's work [243].

figure 9.10 further support these findings. We put particular emphasis on $\mathcal{A}_\uparrow^<(k, \omega, t = 0)$ at quarter filling shown in figure 9.10(a) where we find the split excitation we observed in figure 9.8(a) to be entirely explained by the FD data. Not only is the weight at $\omega/t_{\mathrm{hop}} \approx 18$ almost completely taken by the $\nu = 2$-contribution, as should be the case from the excitation, but also do the FD computations predict spectral weight at this energy. We can, hence, safely attribute this somewhat unintuitive appearance of $\mathcal{A}_\uparrow^<(k, \omega, t = 0)$ as an effect of the more complex spectrum due to the interaction. This is in stark contrast to the behavior of $\mathcal{A}_\downarrow^<(k, \omega, t = 0)$ as shown in figure 9.10(d). Again, the additional feature at $\omega/t_{\mathrm{hop}} \approx 13.8$ cannot be explained through features of the spectral function in equilibrium as neither the FD nor the MPS results predict a contribution there.

At half filling, the occurrence of these mid-gap bands also manifests itself in the optical conductivity $\sigma_1(\omega, t)$ which we show in figures 9.11 and 9.12 for $U/t_{\mathrm{hop}} = 4$ or $U/t_{\mathrm{hop}} = 16$, respectively. In addition we show the respective ground state data from figures 8.11 and 8.12 as a reference. For a more detailed analysis, we present the optical conductivity both in total as well as spin-resolved. At quarter filling only slight changes can be reported, where at $\omega/t_{\mathrm{hop}} \approx 3.8$ or $\omega/t_{\mathrm{hop}} \approx 4.3$ for $U/t_{\mathrm{hop}} = 4$ or $U/t_{\mathrm{hop}} = 16$, c.f. figures 8.11(a),(c),(e) or 8.12(a),(c),(e), respectively the weight

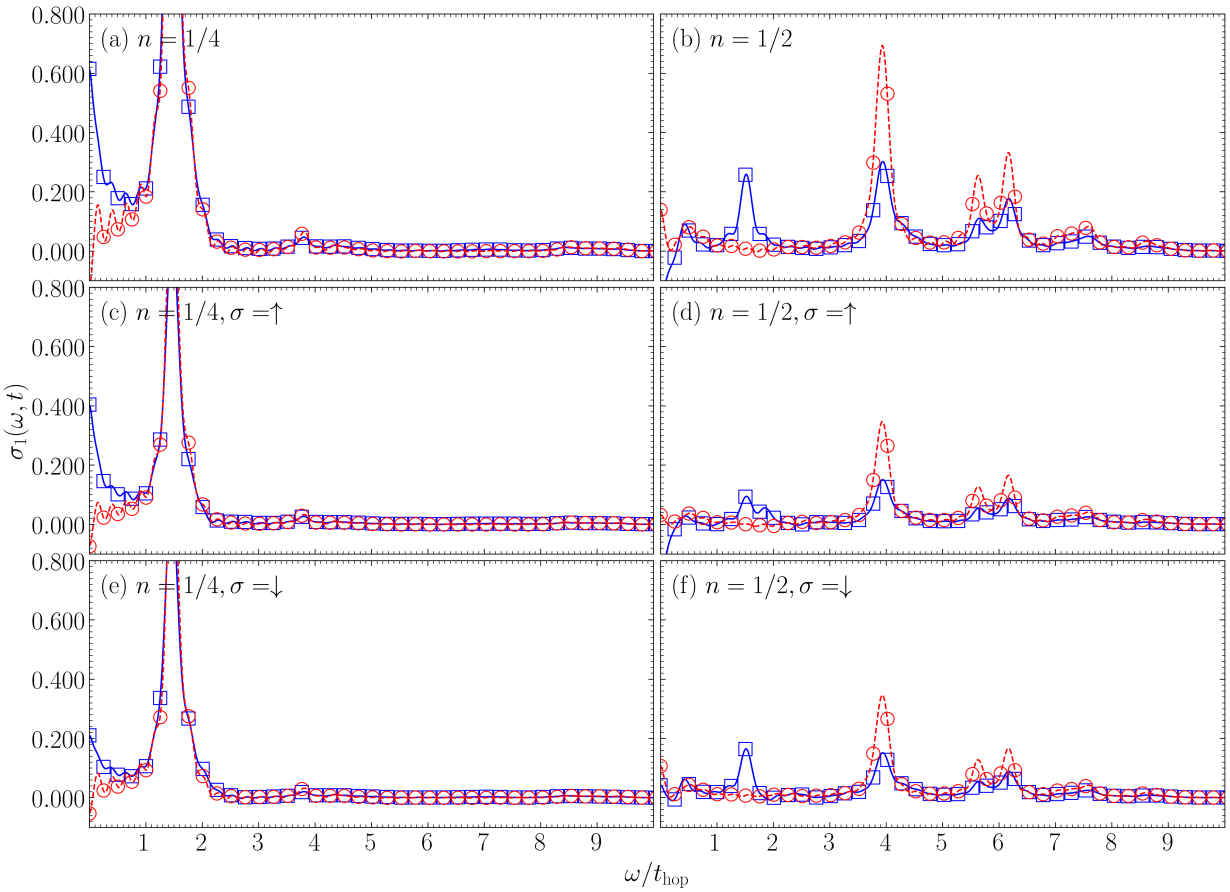

Figure 9.11: Real part of the optical conductivity $\sigma_1(\omega, t)$ immediately after the excitation, i.e. $t = 0$, (solid blue) for $\hat{H}^{4\Delta}$ with $U/t_{\mathrm{hop}} = 4$ and $\Delta/t_{\mathrm{hop}} = 2$ for a system of $L = 32$ sites with OBCs at quarter, (a), (c), and (e), and half filling, (b), (d), and (f), respectively. (a) and (b) show the total optical conductivity, (c) and (d) the spin-↑ direction, and (e) and (f) the spin-↓ direction. The dashed red lines show the equilibrium ground state results, i.e. $t = -\infty$. Data points: Obtained from Fourier transforming according to (6.109) and (6.110). Solid lines: Application of 16 times zero padding. This figure is adapted from the author's work [243].

increases at a very low rate. At half filling, however, as depicted in figures 8.11(b),(d),(f) or 8.12(b),(d),(f) the post excitation data match the ground state data with the exception of an additional peak at $\omega/t_{\mathrm{hop}} \approx 2$, which corresponds to the difference of the mid-gap band to the lowest occupied region of support of the equilibrium greater spectral function, c.f. figures 9.9(d) and 9.10(d). We conclude that in a general setup the notion of the optical conductivity exhibiting its peaks at those energies that need to be spent to transfer spectral weight from one band to another appears to be valid as well. Note that this particular behavior is not evident, since equation (6.89) has only been proven for the special case of a time-independent Hamiltonian and a computation of the optical conductivity with respect to an eigenstate. Other than that, the post excitation optical conductivities only differ from their ground state counterparts in the height of the remaining original peaks. The effect is quite intuitively understood when interpreting the peak heights as corresponding to a certain probability with which weight may be transferred. Following the excitation the spectral weight is distributed differently such that an adaption of their corresponding transfer options is only

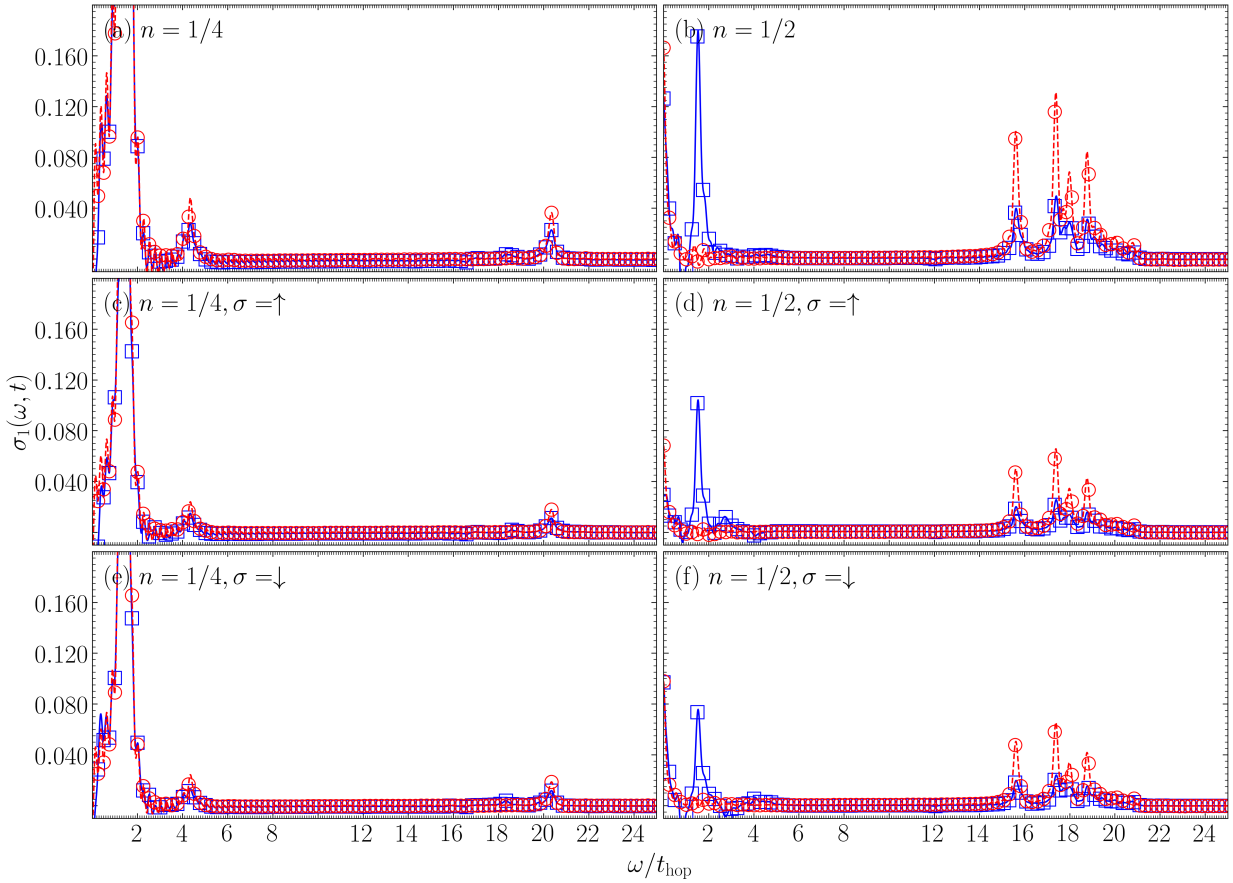

Figure 9.12: Real part of the optical conductivity $\sigma_1(\omega, t)$ immediately after the excitation, i.e. $t = 0$, (solid blue) for $\hat{H}^{4\Delta}$ with $U/t_{\mathrm{hop}} = 16$ and $\Delta/t_{\mathrm{hop}} = 2$ for a system of $L = 32$ sites with OBCs at quarter, (a), (c), and (e), and half filling, (b), (d), and (f), respectively. (a) and (b) show the total optical conductivity, (c) and (d) the spin-↑ direction, and (e) and (f) the spin-↓ direction. The dashed red lines show the equilibrium ground state results, i.e. $t = -\infty$. Data points: Obtained from Fourier transforming according to (6.109) and (6.110). Solid lines: Application of 16 times zero padding.

logical. At half filling, this effect is particularly strong, since the mid-gap band is closer to $\mathscr{A}^<(k, \omega)$, such that it is less costly and thus more likely to transfer weight from there to the energetically lowest lying contributions of the unoccupied part of the spectrum. This interpretation is in particular confirmed when comparing the two cases of $U/t_{\mathrm{hop}} = 4$ and $U/t_{\mathrm{hop}} = 16$, the additional peak being significantly larger for the latter, c.f. figure 9.11(b),(d),(f) and 9.12(b),(d),(f). Note further that, although in the spectral function there is no mid-gap band in the spin-↑ direction after the excitation, c.f. figures 9.7(c), 9.9(b), 9.8(c), and 9.10(b), the optical conductivity still exhibits the additional signal in both spin directions, and even more so does this effect also occur at quarter filling. As this behavior is not excluded by equation (6.89), we take it as a further consequence of the scattering effects due to interactions.

9.2.2 Two Band Model

We close these analyses with a discussion of the situation for $\hat{H}^{2\Delta}$ for which we give the full lesser spectral functions after the excitation $\mathscr{A}^{<}(k,\omega,t=0)$ in figures 9.13 and 9.14 for $U/t_{\mathrm{hop}}=4$ and $U/t_{\mathrm{hop}}=16$, respectively. When it comes to the effects of the excitation, in this simplified model,

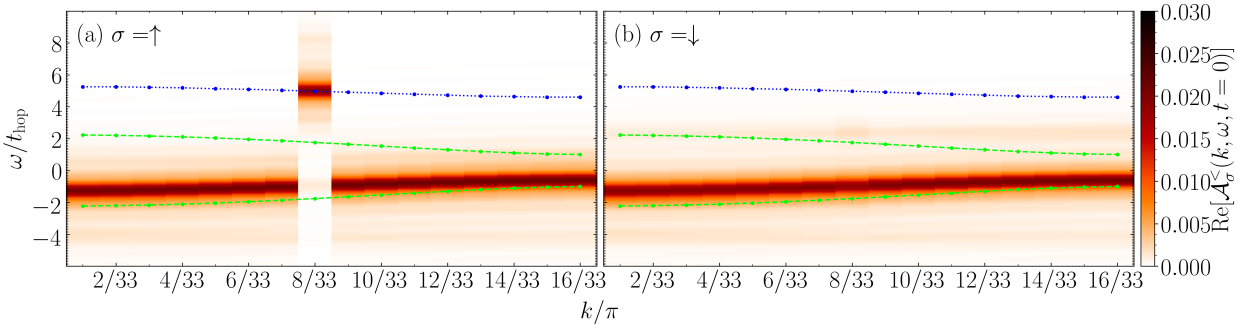

Figure 9.13: Single particle spectral functions $\mathscr{A}^{<}_{\sigma}(k,\omega,t=0)$ immediately after the electron-hole excitation (9.1) for $\hat{H}^{2\Delta}$ with $U/t_{\mathrm{hop}}=4$ and $\Delta/t_{\mathrm{hop}}=2$ for a system of $L=32$ sites with OBCs in the first BZ at half filling. (a) shows the spin-↑ direction, (b) the spin-↓ direction. The green dashed lines show the band structure of the non-interacting system calculated with PBCs, the green dots correspond to the calculation with OBCs. The blue dotted line depicts the maxima of $\mathscr{A}^{>}_{\sigma}(k,\omega)$ extracted from figure 8.13(b). This figure is taken from the author's work [243].

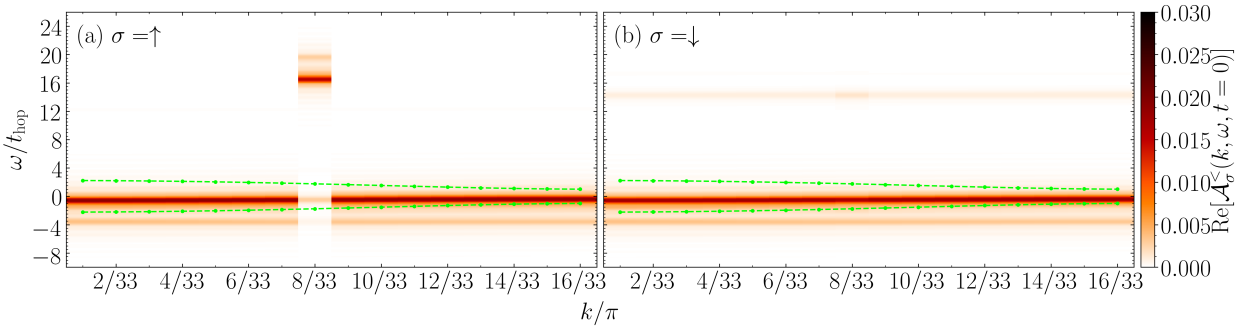

Figure 9.14: Single particle spectral functions $\mathscr{A}^{<}_{\sigma}(k,\omega,t=0)$ immediately after the electron-hole excitation (9.1) for $\hat{H}^{2\Delta}$ with $U/t_{\mathrm{hop}}=16$ and $\Delta/t_{\mathrm{hop}}=2$ for a system of $L=32$ sites with OBCs in the first BZ at half filling. (a) shows the spin-↑ direction, (b) the spin-↓ direction. The green dashed lines show the band structure of the non-interacting system calculated with PBCs, the green dots correspond to the calculation with OBCs.

we appear to have combined the advantageous features of the excitation of $\hat{H}^{4\Delta}$ at quarter and half filling. First, we note that in the spin-↑ direction in figures 9.13(a) and 9.14(a) the remaining weight in the lower band is significantly less than for the situation at half filling in $\hat{H}^{4\Delta}$, c.f. figures 8.13(c) and 8.14(c), respectively. Second, in addition we find a mid-gap band in the spin-↓ direction at $\omega/t_{\mathrm{hop}}\approx 2.4$ or $\omega/t_{\mathrm{hop}}\approx 16.8$, respectively, as seen in figures 9.13(b) and 9.14(b), the only difference being that in this case the weight in the mid-gap band is not as equally distributed as in figures 8.7(b) and 8.8(b). While for $U/t_{\mathrm{hop}}=4$ the weight is rather more accumulated at larger momenta in the case of $U/t_{\mathrm{hop}}=16$ it is a bit stronger in the center of the first BZ. In figure 9.13 we have

also sketched the first maximum of the greater spectral function as extracted from the data of figure 8.13(b) to further illustrate that in the spin-↑ direction after the excitation weight is actually shifted to energies corresponding to previously unoccupied regions of the spectrum and to clearly identify the additional feature in $\mathscr{A}_{\downarrow}^{<}(k,\omega,t=0)$ as a mid-gap band.

An analysis of the cross section at $k = 8\pi/33$ to be found in figures 9.15 and 9.16 confirms our findings. As expected, the dominant $\nu = 1$-contribution in $\mathscr{A}_{\uparrow}^{<}(k,\omega)$ has vanished entirely in

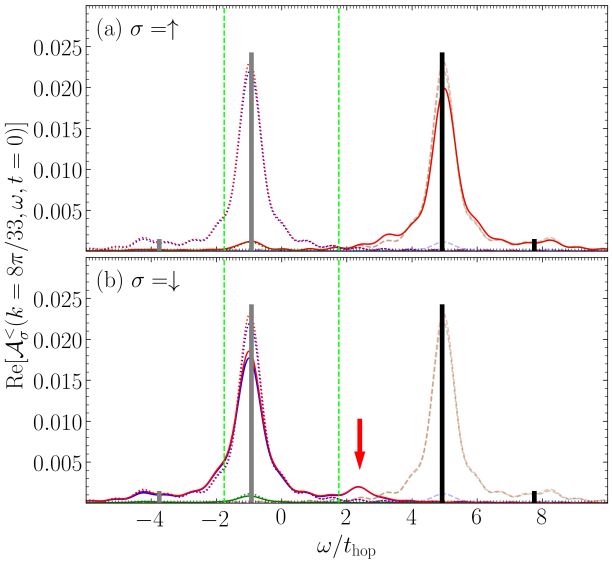

Figure 9.15: Cross section of the data shown in figure 9.13 at $k = 8\pi/33$ (solid lines) for half filling. (a) shows the spin-↑ direction, (b) the spin-↓ direction. The dotted (light dashed) lines show the ground state results of figure 8.15 for the lesser (greater) spectral functions. The total spectral function is shown in red, the contribution from the four band indices $\nu = 1, 2, 3, 4$ are given in blue, green, cyan, and magenta, respectively. Vertical dashed light green lines: ground state peak positions in the non-interacting case obtained for PBCs. Vertical gray (black) bars: excitation energies for $\mathscr{A}_{\sigma}^{<}$ ($\mathscr{A}_{\sigma}^{>}$) in the ground state as obtained from equation (9.1) for one unit cell, i.e. $L = 4$. The heights of the bars correspond to their respective weights. All bars have been scaled such that in each cross section the largest bar takes a value of 0.8 times the plot's maximum range in y-direction. The red arrow highlights the in-gap spectral weight in $\mathscr{A}_{\downarrow}^{<}(k,\omega,t=0)$ (see text for further details). This figure is adapted from the author's work [243].

$\mathscr{A}_{\uparrow}^{<}(k,\omega,t=0)$ and is to be found at the frequency corresponding to the $\nu = 2$ contribution of $\mathscr{A}_{\uparrow}^{>}(k,\omega)$, c.f. figures 9.15(a) and 9.16(a). Due to the significantly easier superstructure, there is only a slight remnant caused by the $\nu = 2$ contribution to $\mathscr{A}_{\uparrow}^{<}(k,\omega)$. As for the spin-↓ direction in figures 9.15(b) and 9.16(b), the mid-gap state can be shown not to correspond to any frequency of $\mathscr{A}_{\downarrow}^{>}(k,\omega)$ and for $U/t_{\mathrm{hop}} = 4$ is even further apart from its $\nu = 2$ contribution than in the case of $\hat{H}^{4\Delta}$, c.f. figure 9.9(d). Furthermore, figure 9.16(b) illustrates that the mid-gap band is more bound to the greater equilibrium spectral function than to the lesser. We attribute the other deviations between the spectral functions before and after excitation again to scattering processes in the k-values and conclude, that the formation of mid-gap bands appears to be general effect of a magnetic superstructure.

In figures 9.17 and 9.18 we again show the optical conductivities before and after the excitation

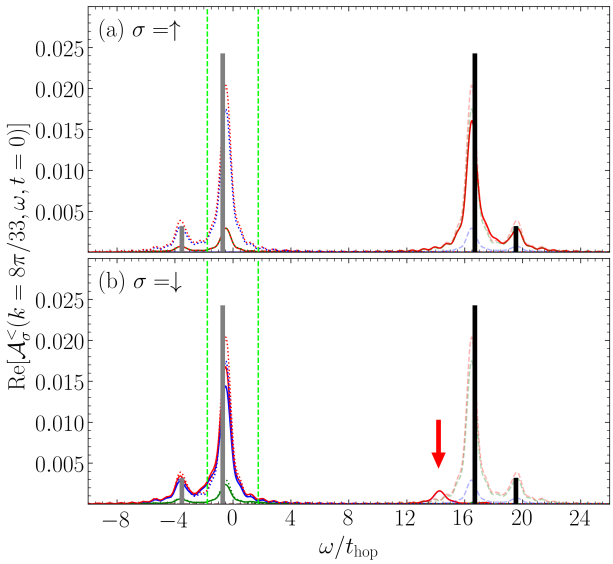

Figure 9.16: Cross section of the data shown in figure 9.14 at $k = 8\pi/33$ (solid lines) for half filling. (a) shows the spin-↑ direction, (b) the spin-↓ direction. The dotted (light dashed) lines show the ground state results of figure 8.16 for the lesser (greater) spectral functions. The total spectral function is shown in red, the contribution from the four band indices $\nu = 1, 2, 3, 4$ are given in blue, green, cyan, and magenta, respectively. Vertical dashed light green lines: ground state peak positions in the non-interacting case obtained for PBCs. Vertical gray (black) bars: excitation energies for $\mathscr{A}^<_\sigma$ ($\mathscr{A}^>_\sigma$) in the ground state as obtained from equation (9.1) for one unit cell, i.e. $L = 4$. The heights of the bars correspond to their respective weights. All bars have been scaled such that in each cross section the largest bar takes a value of 0.8 times the plot's maximum range in y-direction. The red arrow highlights the in-gap spectral weight in $\mathscr{A}^<_\downarrow(k, \omega, t = 0)$ (see text for further details).

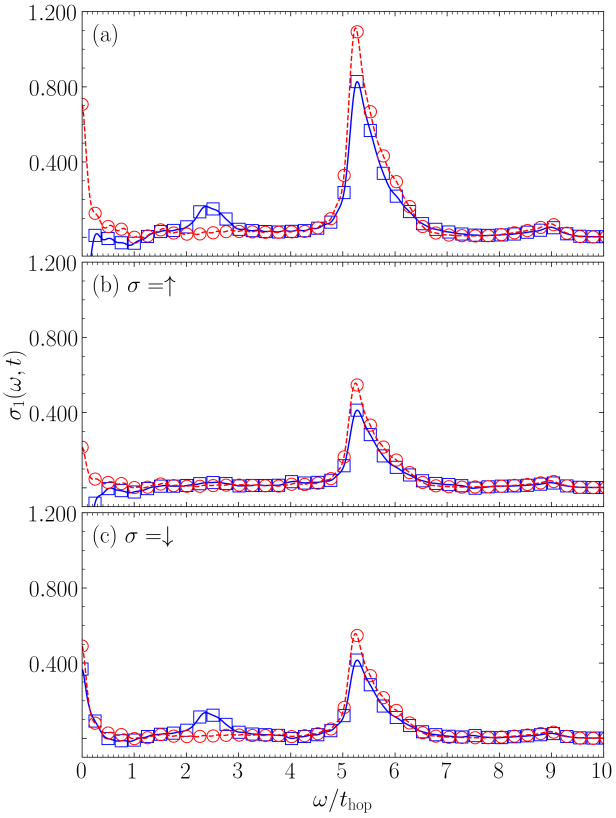

Figure 9.17: Real part of the optical conductivity $\sigma_1(\omega, t)$ immediately after the excitation, i.e. $t = 0$, (solid blue) for $\hat{H}^{2\Delta}$ with $U/t_{\text{hop}} = 4$ and $\Delta/t_{\text{hop}} = 2$ for a system of $L = 32$ sites with OBCs at half filling. (a) shows the total optical conductivity, (b) the spin-↑ direction, and (c) the spin-↓ direction. The dashed red lines show the equilibrium ground state results, i.e. $t = -\infty$. Data points: Obtained from Fourier transforming according to (6.109) and (6.110). Solid lines: Application of 16 times zero padding. This figure is adapted from the author's work [243].

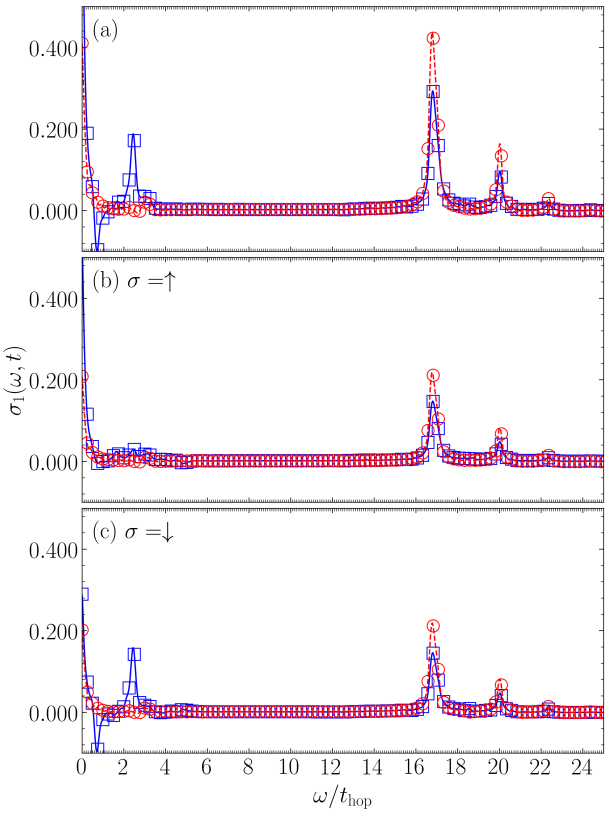

Figure 9.18: Real part of the optical conductivity $\sigma_1(\omega, t)$ immediately after the excitation, i.e. $t = 0$, (solid blue) for $\hat{H}^{2\Delta}$ with $U/t_{\text{hop}} = 16$ and $\Delta/t_{\text{hop}} = 2$ for a system of $L = 32$ sites with OBCs at half filling. (a) shows the total optical conductivity, (b) the spin-↑ direction, and (c) the spin-↓ direction. The dashed red lines show the equilibrium ground state results, i.e. $t = -\infty$. Data points: Obtained from Fourier transforming according to (6.109) and (6.110). Solid lines: Application of 16 times zero padding.

to find essentially the same features as in figures 9.11 and 9.12 for $\hat{H}^{4\Delta}$. After the excitation the optical conductivity shows an additional feature at $\omega/t_{\text{hop}} \approx 2$ corresponding to the energy difference of the mid-gap band and the equilibrium greater spectral function, as is evident from inspecting figures 9.15(b) and 9.16(b) and the contributions at the other energies are are less pronounced. The major difference to the situation at $\hat{H}^{4\Delta}$ is that in this case the additional peak in the optical conductivity is almost exclusively due to the spin-↓ contribution which makes the interpretation somewhat easier. We also refer to the simpler band structure of $\hat{H}^{2\Delta}$ as an explanation of this circumstance.

9.2.3 Formation of Excitons

In attempt to explain the mid-gap feature we identified in the preceding sections, we start with a simple calculation in the atomic limit, i.e. $t_{\text{hop}} \to 0$, allowing us to conduct the calculus in real space. In this case, the spectrum will consist of two Hubbard bands that are separated by the interaction strength U through a Mott gap.

We begin with considering a single unit cell for $\hat{H}^{4\Delta}$. In this case, the ground state and the corresponding ground state energy are straight forwardly obtained as

$$|\mathrm{GS}\rangle = |\downarrow\downarrow\uparrow\uparrow\rangle \qquad \equiv \qquad E_0 = -2\Delta. \tag{9.2}$$

An excitation in the spin-$\uparrow$ direction can now be approximated by shifting one particle such that a resulting state and its energy would be given by

$$|\psi_1\rangle = |\downarrow\updownarrow 0\uparrow\rangle \qquad \equiv \qquad E_{\psi_1} = U - \Delta. \tag{9.3}$$

We shall call the doubly occupied site a doublon, and the empty site a hole. As we are interested in the effect on the spin-$\downarrow$ direction, we remove a particle, where we have in principle two options

$$\hat{c}_\downarrow |\psi_1\rangle = \begin{cases} |0\updownarrow 0\uparrow\rangle & \equiv \quad E_{n=1} = U - \frac{\Delta}{2} \\ |\downarrow\uparrow 0\uparrow\rangle & \equiv \quad E_{n=2} = -\frac{\Delta}{2} \end{cases}, \tag{9.4}$$

such that the energy differences in equation (9.1) are given by

$$E_{\psi_1} - E_n = \begin{cases} -\frac{\Delta}{2}, & n = 1 \\ U - \frac{\Delta}{2}, & n = 2 \end{cases}. \tag{9.5}$$

Indeed, one of this rather primitive computations predicts a signal in the gap region U of $\mathscr{A}^<(k,\omega)$ and $\mathscr{A}^>(k,\omega)$. For this setup, we also consider a second order process which would correspond to shifting two spin-$\uparrow$ particles, i.e.

$$|\psi_2\rangle = |\updownarrow\updownarrow 00\rangle \qquad \equiv \qquad E_{\psi_2} = 2U, \tag{9.6}$$

based on which the effect of the spin-$\downarrow$ direction yields

$$\hat{c}_\downarrow |\psi_2\rangle = \begin{cases} |\uparrow\updownarrow 00\rangle & \equiv \quad E_{n=1} = U + \frac{\Delta}{2} \\ |\updownarrow\uparrow 00\rangle & \equiv \quad E_{n=2} = U + \frac{\Delta}{2} \end{cases}. \tag{9.7}$$

Since in this case the energies are identical, we find only a sole signal at energy

$$E_{\psi_2} - E_{n=1,2} = U - \frac{\Delta}{2}, \tag{9.8}$$

which is also in the gap region. For $\hat{H}^{2\Delta}$ the calculus is again easier since the unit cell consists of only two sites. The ground state and its energy are given by

$$|\mathrm{GS}\rangle = |\downarrow\uparrow\rangle \qquad \equiv \qquad E_0 = -\Delta, \tag{9.9}$$

which for the excited state yields

$$|\psi\rangle = |\updownarrow 0\rangle \qquad \equiv \qquad E_\psi = U. \tag{9.10}$$

Therefrom we obtain the state

$$\hat{c}_\downarrow |\psi\rangle = |\uparrow 0\rangle \qquad \equiv \qquad E_{n=1} = +\frac{\Delta}{2}, \tag{9.11}$$

which is needed in equation (9.1) to compute the peak positions in the spectral function as

$$E_\psi - E_{n=1} = U - \frac{\Delta}{2}. \tag{9.12}$$

As for $\hat{H}^{4\Delta}$ a mid-gap feature is predicted.

We now try to explain the physical origin of these mid-gap signals. As discussed in, e.g., reference [96] at equilibrium peaks in the optical conductivity below the Mott gap indicate the formation of excitons in interacting electron systems. Hence, the question arises if this interpretation also applies to the post excitation setup we investigate in this work; in case of exciton formation, we expect additional signals in both the optical conductivity and the spectral function. The latter is expected to show a feature at an energy, which corresponds to the conduction band (upper Hubbard band) minus the binding energy E_b of the exciton [61, 293]. In a Mott insulator the relation between the binding energy E_b, the Mott gap E_M and the peak position of an exciton in the optical conductivity ω_{exc} is given by [96, 172, 30] $E_b = E_M - \omega_{\text{exc}}$. The Mott gap can be read off directly from the spectral function, so that we do not need further computations and we can directly check for this expectation.

We find that we need to differentiate between $\hat{H}^{4\Delta}$ and $\hat{H}^{2\Delta}$. For the former we find an additional peak at $\omega/t_{\text{hop}} \approx 2$ in the optical conductivity independent of the interaction strength U, see figures 9.3, 9.11, and 9.12. Since at $U = 0$ the spin-↑ and spin-↓ electrons are not coupled, there is no additional signal in the spectral function, c.f. figure 9.1 and, hence, can its origin in general not be traced back to the formation of excitons. Thus, we conclude that additional peaks in the optical conductivity after a photo excitation do not necessarily indicate the formation of excitons. For $\hat{H}^{2\Delta}$ the situation is clearer due to the simpler band structure. We again find peaks at $\omega/t_{\text{hop}} \approx 2$ after the excitation, but this time it depends on U, c.f. figures 9.6, 9.17, and 9.18. Note that for $U = 0$ also the ground state optical conductivity shows a peak at $\omega \approx 2$ contrary to the cases of finite U. Hence, these signals cannot be of the same origin. We conclude that for $\hat{H}^{4\Delta}$ two effects are superimposed. We indeed take the additional signals at $\omega/t_{\text{hop}} \approx 2$ in either model at finite interaction U to be related to the formulation of spin-↓ excitons as they correspond to additional features in $\mathcal{A}_\downarrow^<(k, \omega, t = 0)$, the mid-gap states occurring at energies $\omega/t_{\text{hop}} \approx 2$ below the upper Hubbard band, c.f. figures 9.9(d), 9.10(d), 9.15(d), and 9.16(d). Note, that these are not the expected energies $E_M - E_b$ above the lower Hubbard band but rather $E_M - \omega_{\text{exc}}$, contrary to the situation investigated in [61].Therefrom we deduce that in the spectral function the excitonic mid-gap band is found below the upper Hubbard band, but shifted downwards by the excitonic energy ω_{exc} rather than the binding energy E_b. The additional peak for the case of $\hat{H}^{4\Delta}$ is also due to its particular band structure: In this case the upper and lower Hubbard bands show two internal structures, which are separated by $\omega/t_{\text{hop}} \approx 2$ for large Δ, which follows from equation (7.73). When a spin-↑ electron is in the third band, it takes $\omega/t_{\text{hop}} \approx 2$ to shift it to the fourth band, explaining the peak in figure 9.3 at $U = 0$ in the spin-↑ direction. Indeed, in the non-interacting case, there is no such peak in the spin-↓ direction, and also at finite U the major contribution is only in the spin-↑ direction, see figures 9.11 and 9.12. As there are only two bands for $\hat{H}^{2\Delta}$ at $U = 0$ following the excitation, the difference in energy between occupied and unoccupied parts of the spectrum will stay the same, namely $\omega/t_{\text{hop}} \approx 2$, so that in this case the peak in the optical conductivity is again due to the band structure.

Having the simplified picture of the atomic limit in mind, our findings are explained by the alternating magnetic background potential and the resulting preferred arrangement for the spin-↑ and spin-↓ electrons in the ground state. This particular superstructure hinders the motion of the hole and

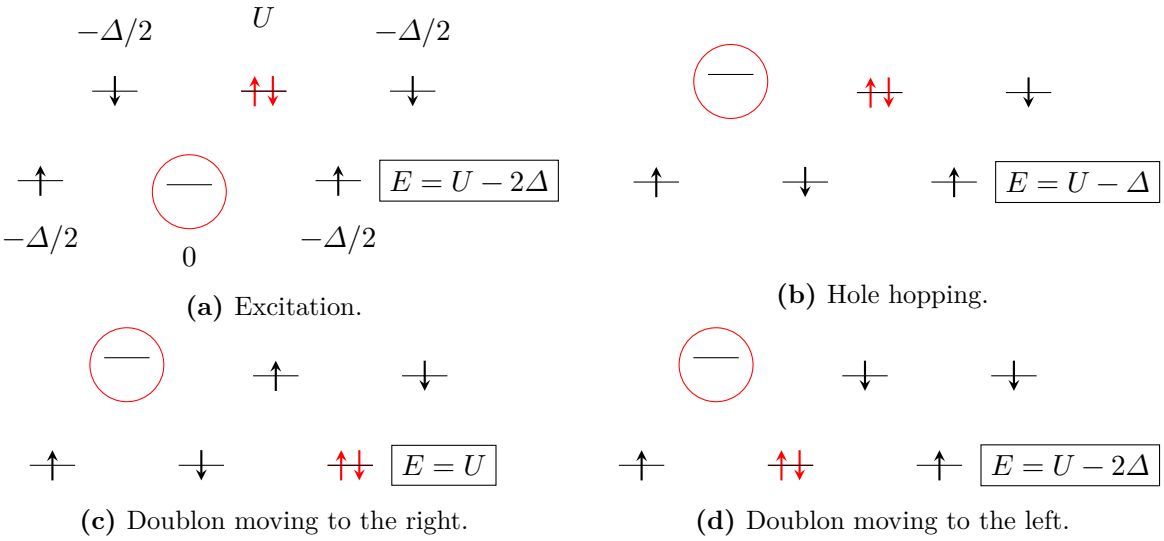

(a) Excitation.

(b) Hole hopping.

(c) Doublon moving to the right.

(d) Doublon moving to the left.

Figure 9.19: Illustration of the effect of spin-selective excitations, in which only the spin-up electrons are affected. In these simple illustrations, we assume the excitation induces a local current moving the spin-up electrons by one lattice site. (a) Situation immediately after the excitation. The numbers at each position give the energy cost in the atomic limit which sum up to the total energy E. (b) The hole has hopped to the right resulting in an increased total energy. (c) Situation in case the doublon moves away from the hole: The total energy increases further. (d) Situation in case the doublon moves with the hole: E decreases again. We conclude that it is most beneficial for the hole and doublon to move as a pair realizing an excitonic binding. This figure is adapted from the author's work [243].

of the doublon after the excitation, as illustrated in figure 9.19 for a single localized excitation in $\hat{H}^{2\Delta}$: At finite U, after the excitation the spin-$\downarrow$ electrons are on the one hand repelled by the excited spin-$\uparrow$ electron and would favor to move away, on the other hand they are hindered by the staggered potential in their motion, so that an effective binding to the original place is realized. Furthermore, at half filling the energy of the system grows with the separation d of the hole and the doublon as $d \cdot \Delta$. This leads to a confinement of doublon and hole, since the energy is lowest if both are neighboring each other, and hence to the formation of an exciton. Note that the exciton is able to move through the system, since the energy of the system remains the same as long as doublon and hole occupy neighboring sites. The spin-$\uparrow$ electron can furthermore not directly move back to the original place, as it has no channel to distribute the energy gained after the excitation. Such a recombination process is only possible when scattering to further particles takes place and will be studied in section 9.4.

In reference [35] midgap states in the spectral function of correlated insulators were associated to excitons in two-dimensional extended Hubbard systems with nearest neighbor (n.n.) interaction V, which is the cause for the binding between hole and doublon as it induces an attraction between a doubly occupied and an empty site. The resulting binding then incures the formation of an exciton, which can be seen in photoemission spectra. In comparison, the exciton observed here has some unusal properties: i) in contrast to references [96, 172] the excitonic signature in $\sigma_1(\omega, t)$ appears only *after* the photoexcitation; ii) the exciton is formed without a V-term in the Hubbard Hamiltonian, i.e. even at very strong screening; iii) the features differ for both spin directions and, hence, we shall like to label this exciton spinful; iv) it appears at a different energy.

The study of exciton signatures in ARPES is an ongoing topic [331, 304, 173, 293, 399, 81, 346, 228]. In these experiments, an electron is emitted, and hence only the breaking of an exciton can be observed, i.e. the system needs to be subject to a photo excitation first, like in pump-probe setups, to create the exciton. Due to the finite binding energy of the electron-hole pair, an in-gap signature is expected to appear at frequencies below the conduction or upper Hubbard band, respectively, for band or Mott insulators. The energy difference of this exciton signature and the conduction or upper Hubbard band is the binding energy [61, 293]. As mentioned above, here the new feature in the spectral function appears at an energy E_b *above* the lower Hubbard band. This is the case, since the upper Hubbard band in the spin-$\downarrow$ direction remains empty even after the excitation. Hence, removing a spin-$\downarrow$ electron in the photoemission process will cost the energy given by the band structure plus the binding energy of the exciton, leading to the feature at the observed energy in the spectral function. This would also be true if the excitation existed not only in one spin direction, so that the spectral function would also show such a feature at $E_M - \omega_{\text{exc}}$. As a consequence we find that in correlated band insulators like the ones considered here, trARPES measurements in pump-probe setups obtain an additional feature not at the energy expected for bright excitons, i.e. the energy of the upper Hubbard band minus the binding energy, but at the energy given by the lower Hubbard band plus the binding energy.

We come to conclude that an on-site Hubbard interaction U in the presence of a magnetic superstructure can generically lead to the formation of a spinful exciton in the spin direction opposite to the excited one. This interpretation is further supported by the similarity of our findings for the two different models $\hat{H}^{4\Delta}$ and $\hat{H}^{2\Delta}$ as well as the results of Lenarčič et al. which also involved excitons in systems with a magnetic background [211, 210]. In these works the presence of short range antiferromagnetic spin correlations in ground states was essential, as well as spin excitations which also connect to the approach we outlined above.

9.3 Excursus: Transient Behavior in Real Space – Formation of Spatial Patterns

We now investigate the transient behavior of our system. Before we turn back to the spectra, however, we first analyze the effect of the excitation (9.1) onto local observables and discuss their time evolutions as done by the author and his collaborators in reference [198]. This section will predominantly include those parts of the work, to which we refer the interested reader for further information, the author himself was most dedicated to. We will consider the local particle density $\langle \hat{n}_j \rangle(t)$, as well as the local magnetization $\langle \hat{S}^z_j \rangle(t)$. For these computations, we slightly change the model's parameters to $L = 40$ and $k = \pi/11$. We will furthermore only discuss $\hat{H}^{4\Delta}$ at quarter filling. Our results are shown in figure 9.20, where by means of equation (9.1) we perform the weakest spin-selective excitation possible. In the top row of figure 9.20 we first show results for the non-interacting system in the absence of a magnetic field, i.e. $U = \Delta = 0$. We find that Friedel-like oscillations [117, 28] in the local particle densities $\langle \hat{n}_j \rangle$ we encounter in the ground state are preserved after the excitation, however being slightly more pronounced. This behavior can be explained with the observation that now, through the excitation, the system has absorbed a little amount of energy which does not decay with time t. Most importantly, however, we do not encounter the formation of a new pattern in the local particle densities $\langle \hat{n}_j \rangle(t)$ following the excitation. By contrast, for the local spin densities $\langle \hat{S}^z_j \rangle(t)$, we do find a very vague pattern following the excitation, which we attribute to the energy absorption. If Δ takes a finite value as

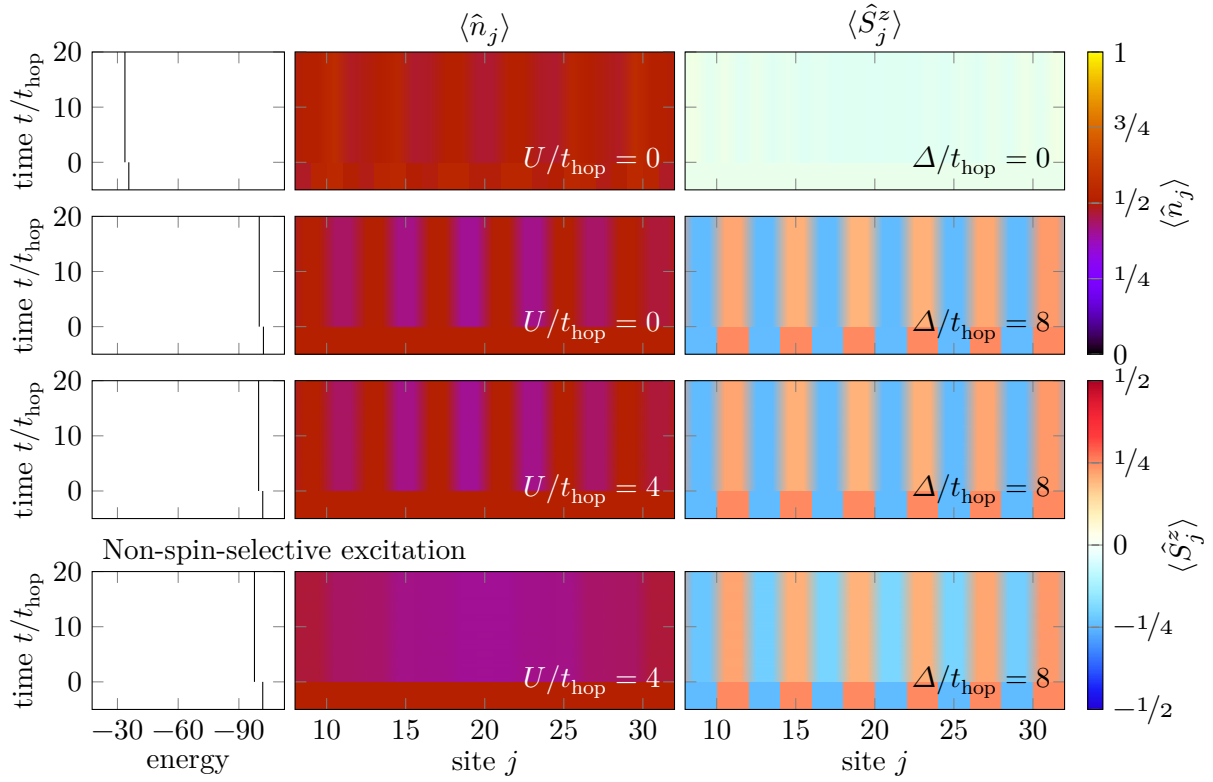

Figure 9.20: Time evolution of system (7.66) with $L = 40$ sites from tDMRG at quarter filling following the operator-based spin-selective excitation (7.94) at time $t = 0$. First column: total energy of the system. Second column: particle density $\langle \hat{n}_j \rangle(t)$ in the bulk (sites 8-32). Third column: local magnetizations $\langle \hat{S}^z_j \rangle(t)$, also in the bulk. The color bars on the right indicate the values for $\langle \hat{n}_j \rangle(t)$ and $\langle \hat{S}^z_j \rangle(t')$, respectively. The top row shows results for an excitation acting only on spin-↑ particles in the absence of a magnetic structure, $\Delta = 0$, and without interaction, $U = 0$. The second row shows results for the same excitation, but with $\Delta/t_{\mathrm{hop}} = 8$ (and, thus, for adjusted operators) and $U = 0$. In contrast, the third row shows results for the same excitation and also $\Delta/t_{\mathrm{hop}} = 8$ but $U = 4$. The bottom row shows results for an excitation acting on both spin directions for $\Delta/t_{\mathrm{hop}} = 8$ and $U/t_{\mathrm{hop}} = 4$. The time evolutions are obtained employing the TDVP in its two-site implementation with a time step $\delta t = 0.05$, a maximum bond dimension $\chi = 1000$, and a discarded weight of $\epsilon < 10^{-12}$. Note that for times $t < 0$ no time evolution was calculated explicitly as for this case analytics require the system to stay invariant. Instead the corresponding data of the ground states was plotted repeatedly to better illustrate the effect of the excitation. This figure is adapted from the author's work [198].

in the second row of figure 9.20, the periodic pattern in the local spin densities $\langle \hat{S}^z_j \rangle(t)$, which follows the magnetic microstructure, is weakened after the excitation and a stable CDW-like pattern in the charge density $\langle \hat{n}_j \rangle(t)$ is induced following the periodicity of the Zeeman term in equation (7.66) as is also shown in reference [326]. Furthermore, we find from the third panel of figure 9.20 that the introduction of an interaction U to the system yields the same observations. Finally, the bottom panel depicts the time evolution for a photoexcitation coupling to both spin directions, i.e. equation (9.1) has to be expanded by spin-↓ operators. Again, the periodic pattern in the local spin densities $\langle \hat{S}^z_j \rangle(t)$, is weakened after the excitation, however the energy absorption does not result

in a pattern in the charge density $\langle \hat{n}_j \rangle(t)$, where we just encounter an increased spread across the whole bulk.

In reference [198] we find qualitatively the same behavior for the case of a spin-selective Peierls substitution. Due to the weaker nature of the excitation performed here, the emerging structures are less pronounced, nevertheless does this show that the observed features are generic to spin-selective photoexcitations. In either case we find the induced charge and spin patterns to have a much longer lifetime than the time scales amenable to an MPS treatment. We explain this behavior generically, i.e. independent of the model's dimension. The excitation leads to a redistribution of k-modes, which in this model are conserved quantities. Hence, without further effects no decay mechanism could lead to a destruction of the spatial patterns. To better estimate the lifetime of the patterns, further effects, like phonons, would need to be included, which we leave for future research at this point.

Note that in the case of low photon densities details of the charge density pattern depend on peculiarities of the excitation, e.g., whether it is at the edge of the Brillouin-zone or close to the center. Employing the scheme outlined above applying more creation and annihilation operators, the effects of going to higher energy densities (i.e., allowing for a larger number of electrons to be excited) may also be investigated. We then expect to see a stronger charge density pattern, but also leave this problem for future research.

9.4 Transient Behavior of Spectral Quantities

Now we analyze the time evolution of the excited system in greater detail putting particular focus on the lifetimes of the mid-gap bands, we identified in section 9.2. For $\hat{H}^{4\Delta}$ at quarter filling following the electron-hole excitation (9.1), we only identify a rather quick but not entire decay back into the ground state on the same time scales we will investigate in this section. Therefore, we only consider the case of half filling at this point.

9.4.1 Four Band Model

We begin with a benchmark computation for $U/t_{\mathrm{hop}} = 0$. In figure 9.21 we show shots of $\mathscr{A}_\sigma^<(k,\omega,t)$ at selected times t, starting from $t \cdot t_{\mathrm{hop}} = 1$ corresponding to figures 9.1(c) and (d). From section 6.1.3 we know the spectral function of non-interacting systems to be independent of time t, if the Hamiltonian itself is time-independent, and, therefore, expect not to find any changes in the numerical data. This is indeed the case, which we take as proof for our approach to be valid. Analogously, in figures 9.22 and 9.23 we present shots of $\mathscr{A}_\sigma^<(k,\omega,t)$ in a similar way at selected times t, including $t = 0$ corresponding to figures 9.7(c) and (d) and 9.8(c) and (d), respectively. Comparing figures 9.22(a) and (i) or 9.23(a) and (i), in the spin-$\uparrow$ direction we indeed find a decay of weight back into the ground state configuration at $k = 4\pi/33$, where the particle was taken from, that is the main effect appears to be a recombination of the particle-hole pair. In addition there is a clear accumulation of weight at frequencies corresponding to the lowest lying band of $\mathscr{A}_\uparrow^>(k,\omega)$, c.f. figures 8.7(d) and 8.8(d). Furthermore, weight is also transferred to neighboring momenta. Strikingly, in the $\downarrow$-direction, we cannot report a major decay of the mid-gap band.

In order to further quantify these findings, we compute the total weight of $\mathscr{A}_\sigma^<(k,\omega,t)$ for certain frequency regions we associate with particular bands as a function of time presenting the results

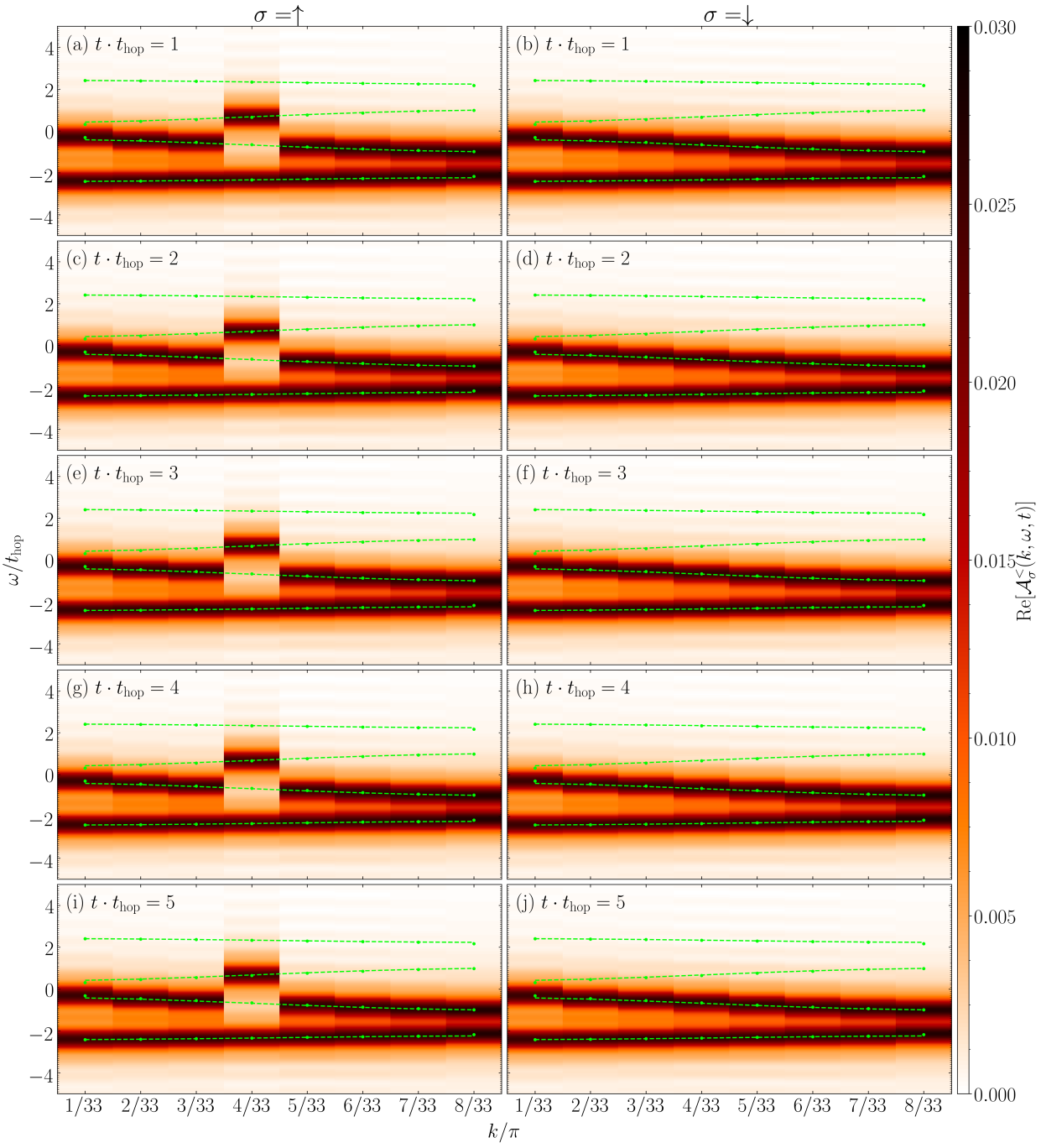

Figure 9.21: Single particle spectral function $\mathcal{A}^{<}_{\sigma}(k, \omega, t)$ at different times, $t = 0$ being directly after the electron-hole excitation in the spin-↑ direction at $k = 8\pi/33$, for $\hat{H}^{4\Delta}$ with $U/t_{\text{hop}} = 0$ and $\Delta/t_{\text{hop}} = 2$ for a system of $L = 32$ sites with OBCs in the first BZ at half filling, c.f. figures 9.1(c) and (d). The left column shows results for the spin-↑ direction, the right results for the spin-↓ direction. The light green dashed lines show the band structure of the non-interacting system calculated with PBCs, the green dots correspond to the calculation with OBCs.

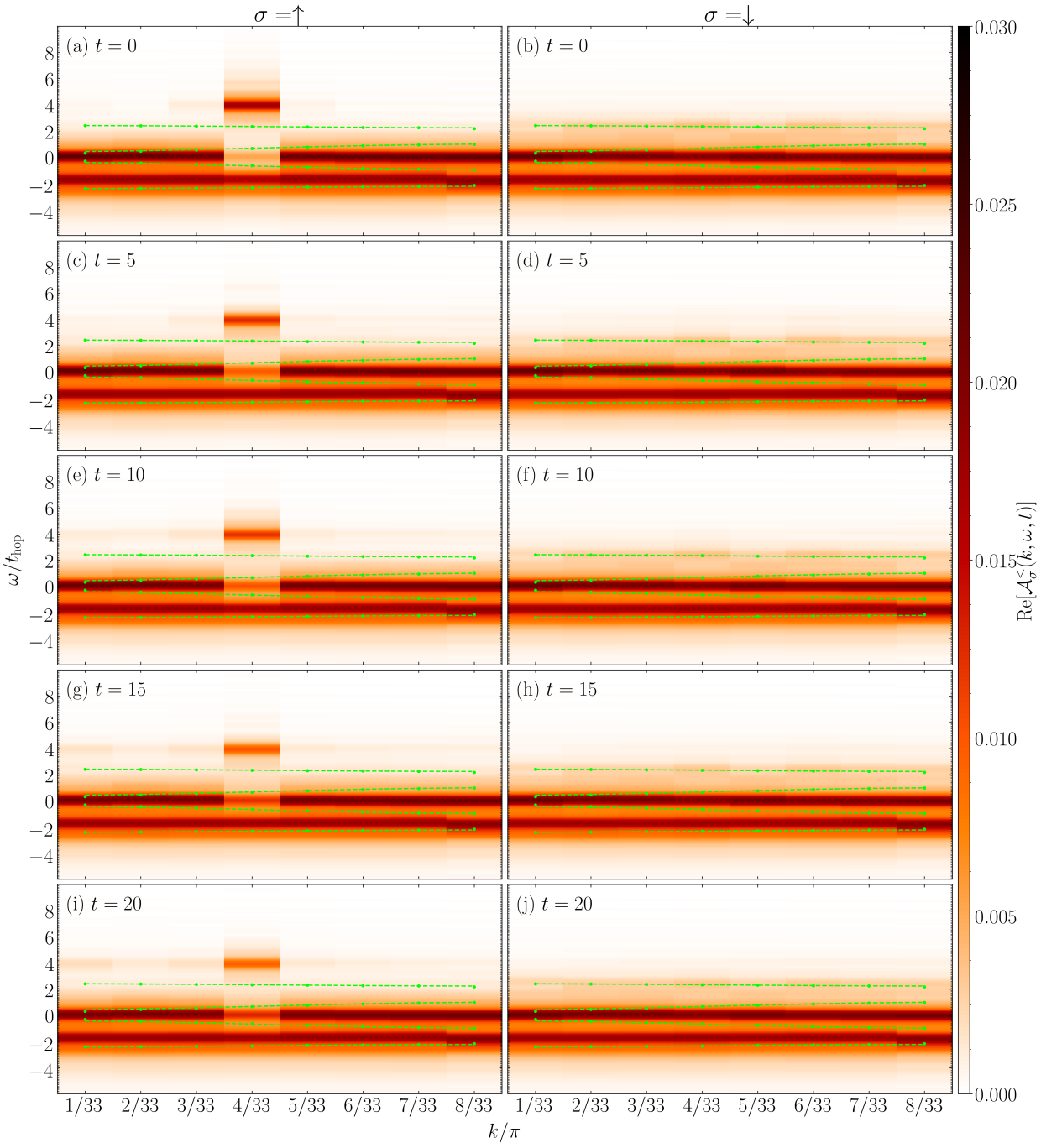

Figure 9.22: Single particle spectral function $\mathcal{A}_\sigma^<(k,\omega,t)$ at different times, $t = 0$ being directly after the electron-hole excitation in the spin-↑ direction at $k = 8\pi/33$, for $\hat{H}^{4\Delta}$ with $U/t_{\text{hop}} = 4$ and $\Delta/t_{\text{hop}} = 2$ for a system of $L = 32$ sites with OBCs in the first BZ at half filling, c.f. figures 9.7(c) and (d). The left column shows results for the spin-↑ direction, the right results for the spin-↓ direction. The light green dashed lines show the band structure of the non-interacting system calculated with PBCs, the green dots correspond to the calculation with OBCs.

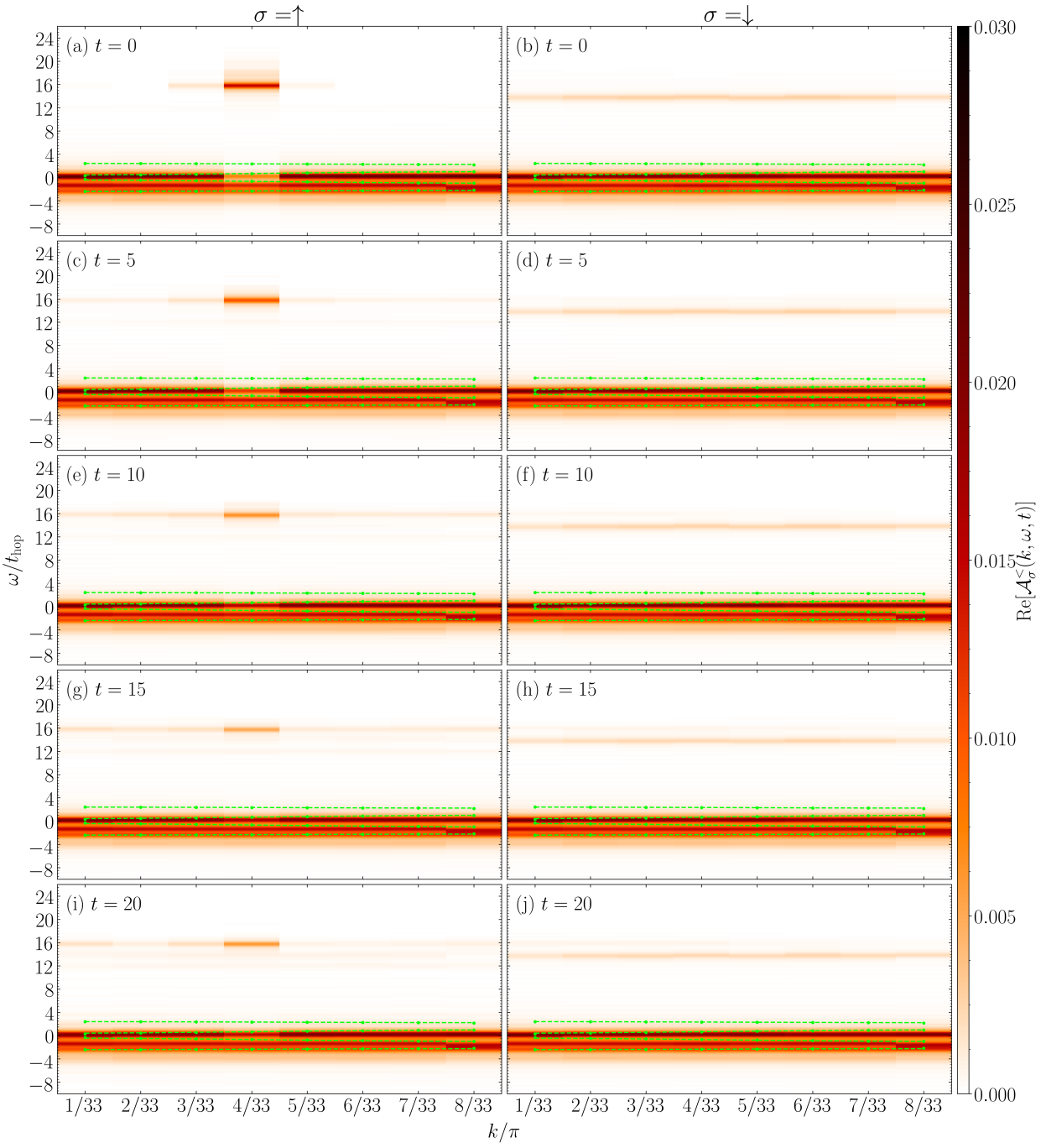

Figure 9.23: Single particle spectral function $\mathcal{A}^{<}_{\sigma}(k,\omega,t)$ at different times, $t = 0$ being directly after the electron-hole excitation in the spin-↑ direction at $k = 8\pi/33$, for $\hat{H}^{4\Delta}$ with $U/t_{\text{hop}} = 16$ and $\Delta/t_{\text{hop}} = 2$ for a system of $L = 32$ sites with OBCs in the first BZ at half filling, c.f. figures 9.8(c) and (d). The left column shows results for the spin-↑ direction, the right results for the spin-↓ direction. The light green dashed lines show the band structure of the non-interacting system calculated with PBCs, the green dots correspond to the calculation with OBCs.

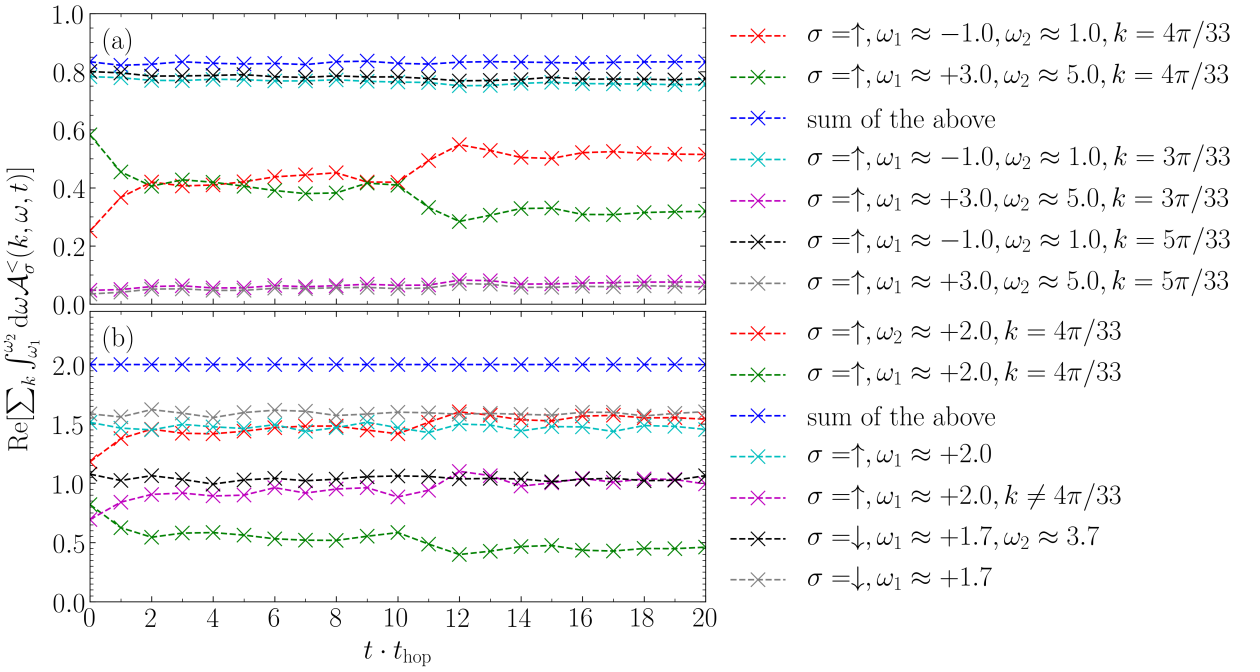

Figure 9.24: Total spectral weight of $\mathscr{A}_\sigma^<(k,\omega,t)$ in between frequencies ω_1 and ω_2 summed over certain momenta k for $\hat{H}^{4\Delta}$ at half filling after the electron-hole excitation as specified in figure 9.22. In case ω_1 or ω_2 is not given, the range was extended until ω_{min} or ω_{max}, respectively.

in figures 9.24 and 9.25. We define those regions of interest (ROIs) in two different ways. A first approach is to limit these regions by an upper and a lower frequency, ω_1 and ω_2, respectively. Numerically, however in doing so we may only report tendencies in the behavior of the system. In particular, the total weight will in general not sum up to a natural number, which would correspond to a particle number the reason being that due to the discrete Fourier transforms also the numerous side peaks we observed in appendix A.1.1 will contribute to the total particle weight even though they are displaced to arbitrarily large frequencies. As a consequence only summing over all frequencies ω and momenta k without restrictions yields the total number of particles of spin σ in the system, i.e. 16. Hence, a second approach is to exploit symmetries of the system and define the ROIs in only setting the lower or upper frequency, ω_1 or ω_2, the remaining one then being the numerically maximum or minimum resolvable frequency, ω_{max} or ω_{min}, respectively. The green and red lines in figures 9.24(a) and 9.25(a) show the population in the ROI at momentum $k = 4\pi/33$ to which the particle was excited to or from which it was taken from. The blue line shows the sum of both. We find that the populations in these ROIs are ~ 0.25 or ~ 0.6, respectively, at time $t = 0$. The interactions then induce a recombination of this electron-hole pair, and we find that by $t \cdot t_{\mathrm{hop}} = 2$ already the weight of both regions has become equal. The recombination process continuous, but apparently takes much longer than the time scales we are able to investigate. The sum of both weights is approximately constant in time, but shows small fluctuations. In figures 9.24(b) and 9.25(b) we have defined the ROIs exploiting the system's symmetry at $\omega = U/2$ at half filling, which we then took as the separating frequency. Here, the sum indeed yield 2 at all times corresponding to the half filling meaning that at all times each momentum must take a total of 2 particles. The disadvantage for this particular system is that with this definition the bottom band that was not primarily affected by the excitation is incorporated in the analysis, such that we cannot identify a

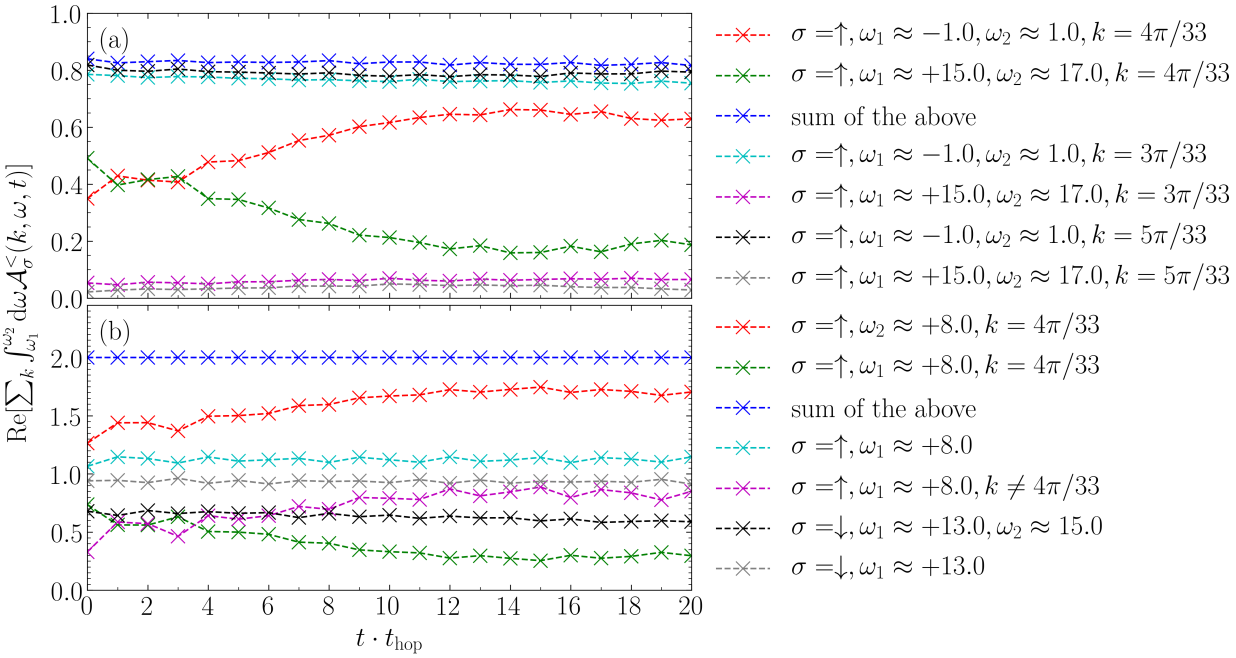

Figure 9.25: Total spectral weight of $\mathcal{A}_\sigma^<(k,\omega,t)$ in between frequencies ω_1 and ω_2 summed over certain momenta k for $\hat{H}^{4\Delta}$ at half filling after the electron-hole excitation as specified in figure 9.23. In case ω_1 or ω_2 is not given, the range was extended until ω_{min} or ω_{max}, respectively.

time scale at which the recombination process has led to an equal occupation of the emptied an filled region immediately after the excitation. Going back to the restricted ROIs in figures 9.24(a) and 9.25(a) we conclude that, since the sum of both contributions is approximately constant, scattering from or to other momenta seems to play a minor role. Therefore, we show the time evolution in the same ROIs at neighboring momenta, where we find that interband scattering leads to a slight redistribution of weights from the lower to the upper Hubbard band in the course of time, the change in population being linear. For all momenta further away the populations within our estimated accuracy do not change noticeably in time. In order to quantify in how far the weight in the upper band increases over time, we show the weight over all momenta k, as well as the difference to the contribution from $k = 4\pi/33$ in figures 9.24(b) and 9.25(b), where we have again divided the system into an upper and a lower half at $\omega = U/2$. While the weight at $k = 4\pi/33$ drops as expected with increasing time, the total weight in the upper band stays again nearly constant with only some slight oscillations, such that the difference only makes up for the losses at $k = 4\pi/33$. We attribute this effect to intra-band scattering as the dominant feature. As the contribution to the total weight in the upper band is only little, we come to the conclusion that we are not to expect effects like carrier multiplication or impact ionization in these setups. For the spin-$\downarrow$ direction we show the behavior in two ROIs, with and without restrictions. As is clearly visible over time there are only slight oscillations to this particular weight which leads us to the conclusion that at least for the time scales treatable by our methods, this mid-gap band is a stable persisting feature, its actual lifetime being substantially longer.

We complement this discussion by analyzing the time dependence of the optical conductivity shown in figures 9.26 and 9.27 putting particular focus on the features induced by the excitation. We

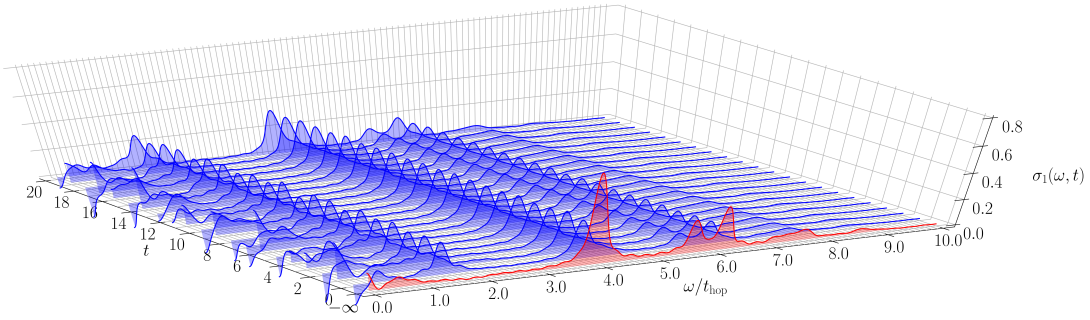

Figure 9.26: Real part of the time-dependent optical conductivity $\sigma_1(\omega, t)$ for $\hat{H}^{4\Delta}$ with $\Delta/t_{\mathrm{hop}} = 2$ and $U/t_{\mathrm{hop}} = 4$ for a system of $L = 32$ sites with OBCs at half filling before (ground state, $t = -\infty$, red; c.f. figure 9.11(b)) and after ($t \geq 0$, blue) the excitation (9.1). 16 times zero padding was applied.

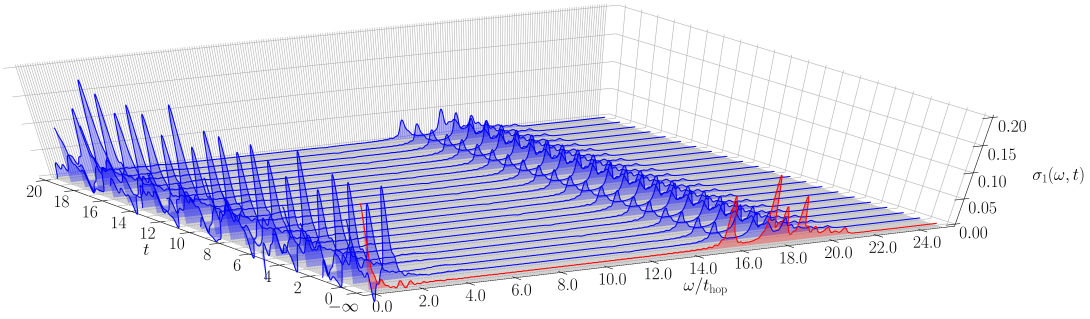

Figure 9.27: Real part of the time-dependent optical conductivity $\sigma_1(\omega, t)$ for $\hat{H}^{4\Delta}$ with $\Delta/t_{\mathrm{hop}} = 2$ and $U/t_{\mathrm{hop}} = 16$ for a system of $L = 32$ sites with OBCs at half filling before (ground state, $t = -\infty$, red; c.f. figure 9.12(b)) and after ($t \geq 0$, blue) the excitation (9.1). 16 times zero padding was applied.

find that the additional peak at $\omega/t_{\mathrm{hop}} \approx 2$ to be stable and to essentially not change with time, an observation which further supports that the lifetime of the excitonic state is substantially longer than the time scales amenable to an MPS treatment. We further see that the other features at frequencies $\omega/t_{\mathrm{hop}} \gtrsim 2$ also do not change in time, and that no other features appear. At low frequencies, we observe a time dependent oscillation at $\omega \to 0$, which rather than a physical effect is merely a consequence of the numerical computation of the optical conductivity as elaborated on in section 6.2.4.

Lenarčič et al. [211, 210] for their antiferromagnetic system report a recombination of excitons through magnon emission. To what extend this behavior relates to our setups needs to be investigated.

9.4.2 Two Band Model

We find essentially the same behavior, that is a redistribution of weight in the upper band for the spin-↑ direction and in the mid-gap band in the spin-↓ direction also for the easier model $\hat{H}^{2\Delta}$ at half filling. As in section 9.4.1 we first benchmark our computations for $U/t_{\mathrm{hop}} = 0$ to be found in figure 9.28, compare also figure 9.4. The benchmark again meets our expectations.

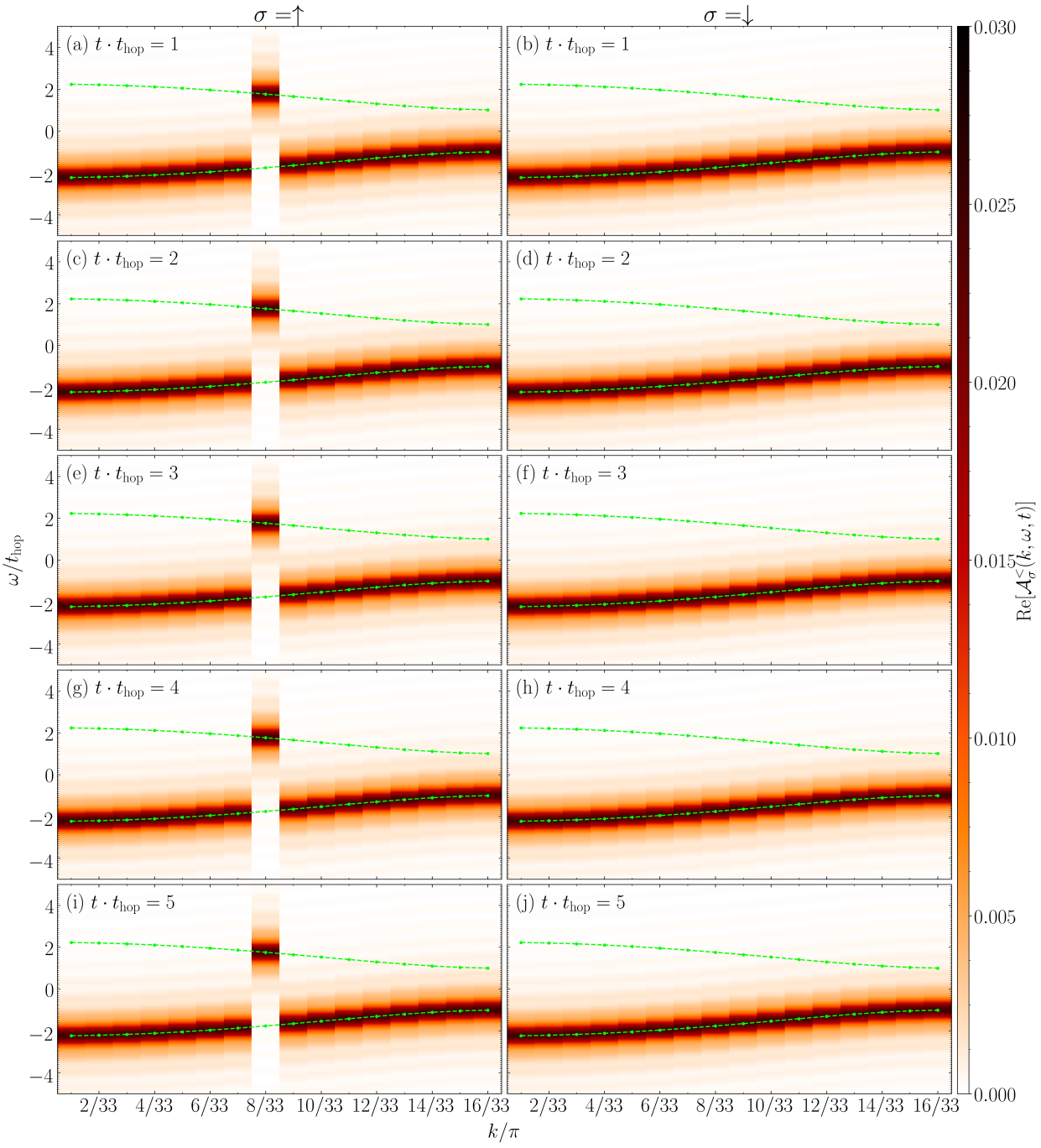

Figure 9.28: Single particle spectral function $\mathcal{A}^{<}_{\sigma}(k,\omega,t)$ at different times, $t = 0$ being directly after the electron-hole excitation in the spin-↑ direction at $k = 8\pi/33$, for $\hat{H}^{2\Delta}$ with $U/t_{\mathrm{hop}} = 0$ and $\Delta/t_{\mathrm{hop}} = 2$ for a system of $L = 32$ sites with OBCs in the first BZ at half filling, c.f. figure 9.4. The left column shows results for the spin-↑ direction, the right results for the spin-↓ direction. The light green dashed lines show the band structure of the non-interacting system calculated with PBCs, the green dots correspond to the calculation with OBCs.

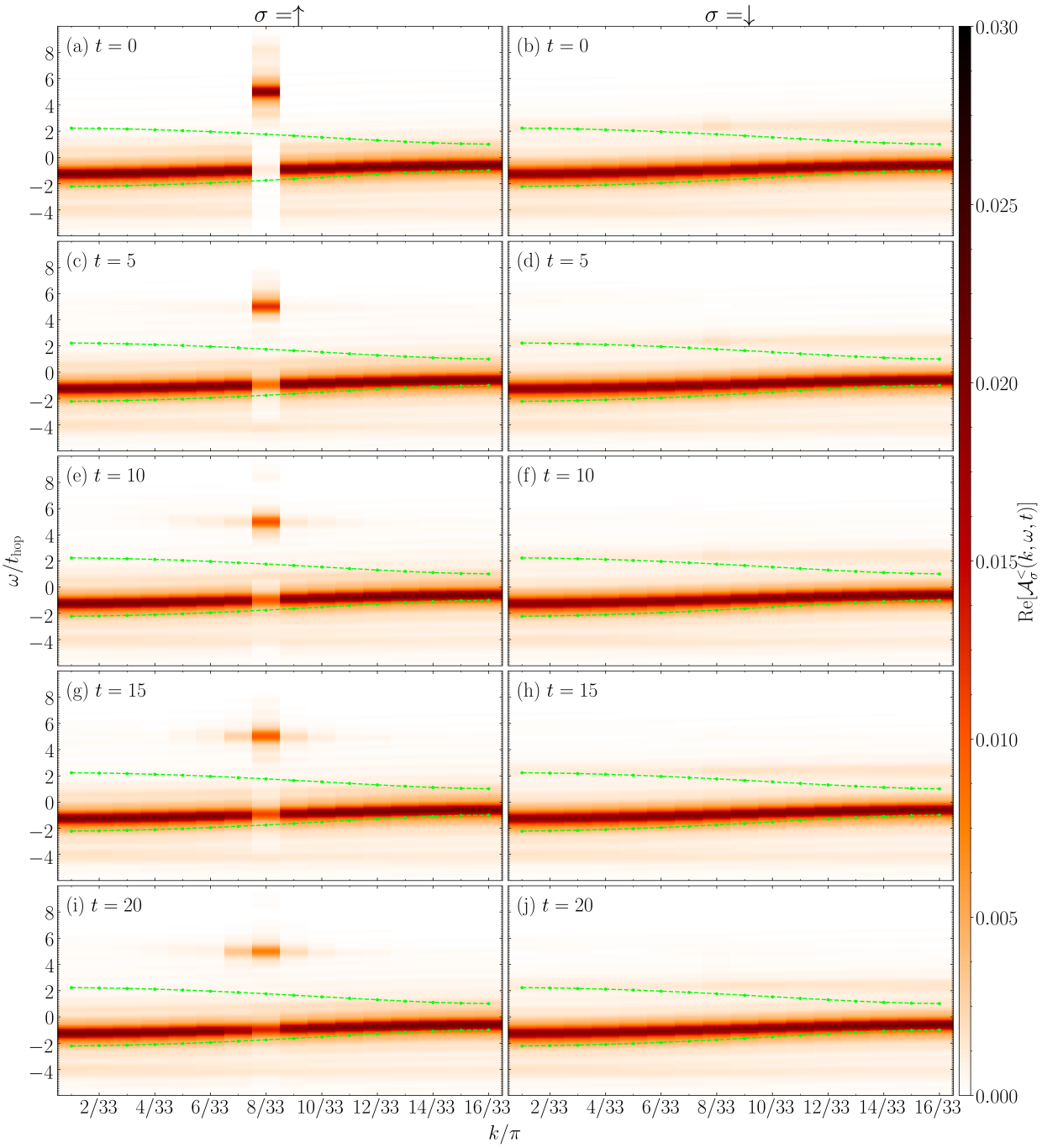

Figure 9.29: Single particle spectral function $\mathscr{A}^{<}_{\sigma}(k,\omega,t)$ at different times, $t = 0$ being directly after the electron-hole excitation in the spin-↑ direction at $k = 8\pi/33$, for $\hat{H}^{2\Delta}$ with $U/t_{\text{hop}} = 4$ and $\Delta/t_{\text{hop}} = 2$ for a system of $L = 32$ sites with OBCs in the first BZ at half filling, c.f. figure 9.13. The left column shows results for the spin-↑ direction, the right results for the spin-↓ direction. The light green dashed lines show the band structure of the non-interacting system calculated with PBCs, the green dots correspond to the calculation with OBCs. This figure is adapted from the author's work [243].

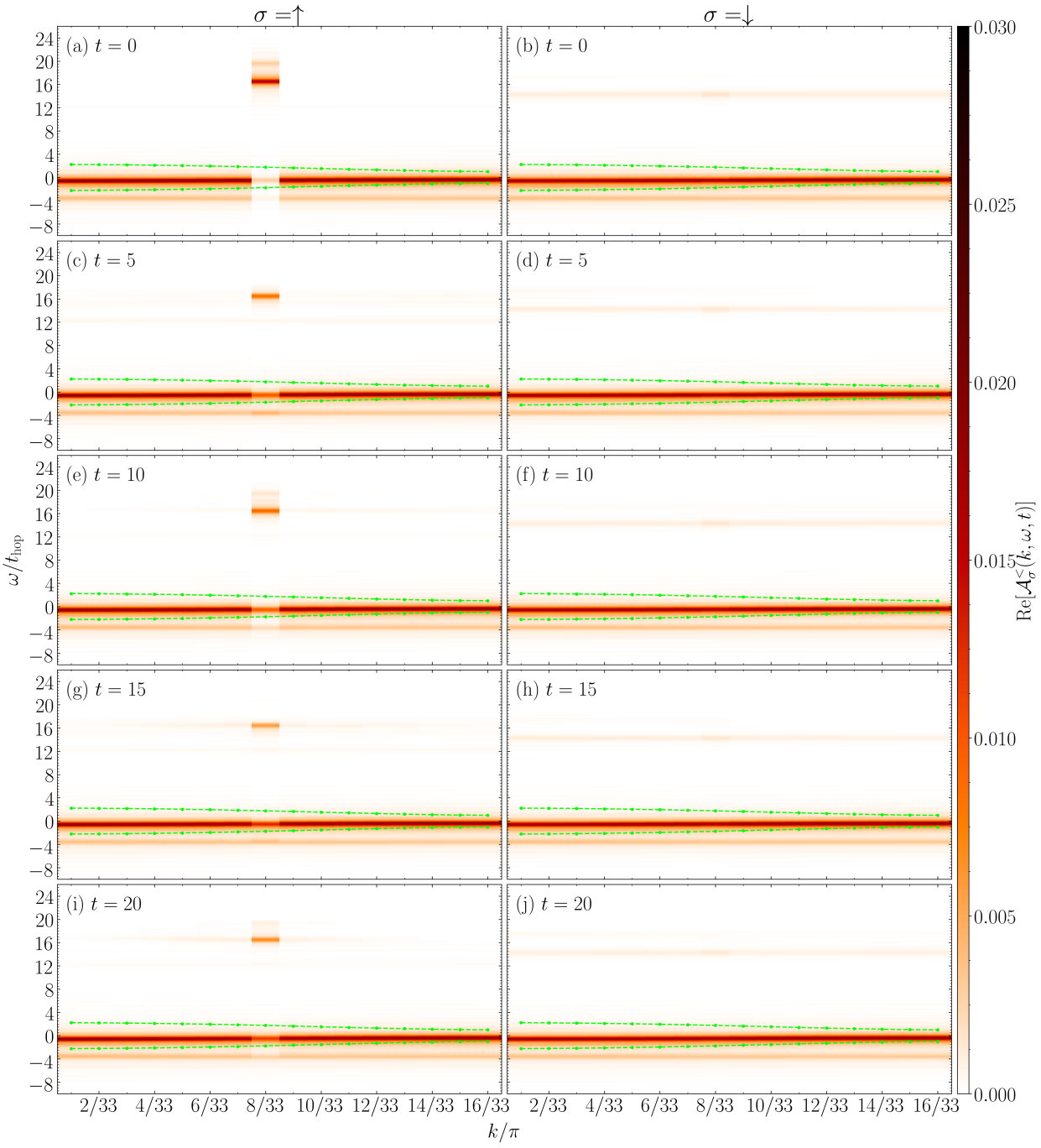

Figure 9.30: Single particle spectral function $\mathscr{A}^{<}_{\sigma}(k,\omega,t)$ at different times, $t = 0$ being directly after the electron-hole excitation in the spin-↑ direction at $k = 8\pi/33$, for $\hat{H}^{2\Delta}$ with $U/t_{\text{hop}} = 16$ and $\Delta/t_{\text{hop}} = 2$ for a system of $L = 32$ sites with OBCs in the first BZ at half filling, c.f. figure 9.14. The left column shows results for the spin-↑ direction, the right results for the spin-↓ direction. The light green dashed lines show the band structure of the non-interacting system calculated with PBCs, the green dots correspond to the calculation with OBCs.

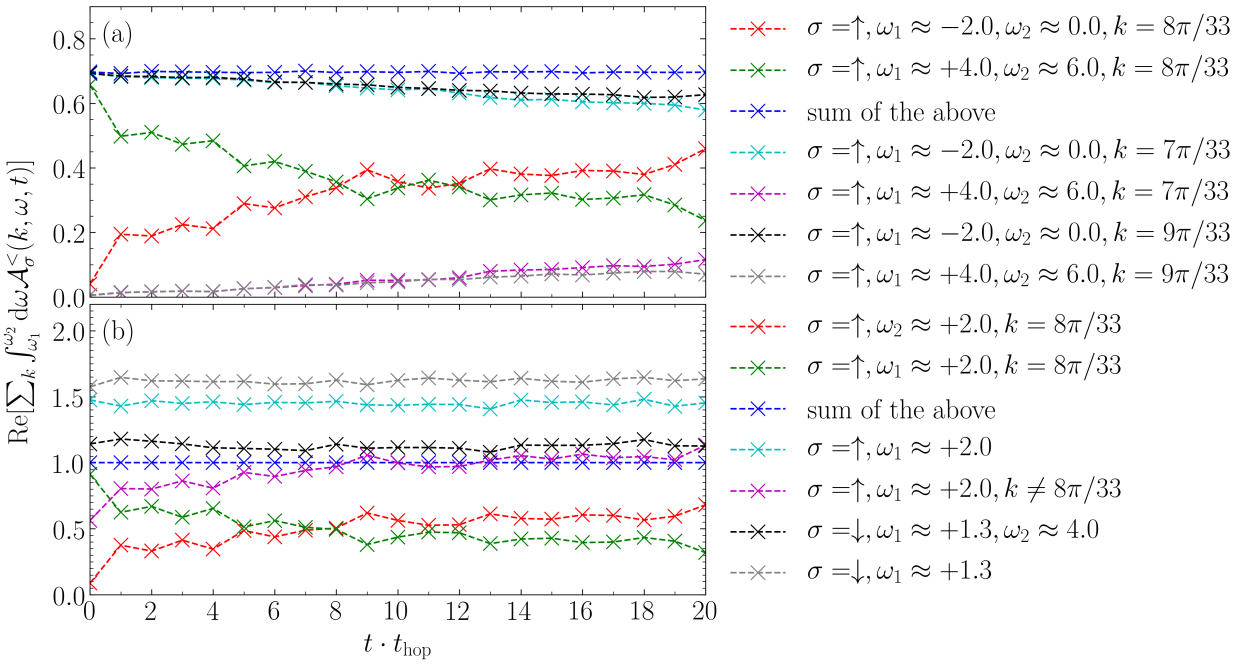

Figure 9.31: Total spectral weight of $\mathcal{A}_\sigma^<(k,\omega,t)$ in between frequencies ω_1 and ω_2 summed over certain momenta k for $\hat{H}^{2\Delta}$ at half filling after the electron-hole excitation as specified in figure 9.29. In case ω_1 or ω_2 is not given, the range was extended until ω_{min} or ω_{max}, respectively. This figure is adapted from the author's work [243].

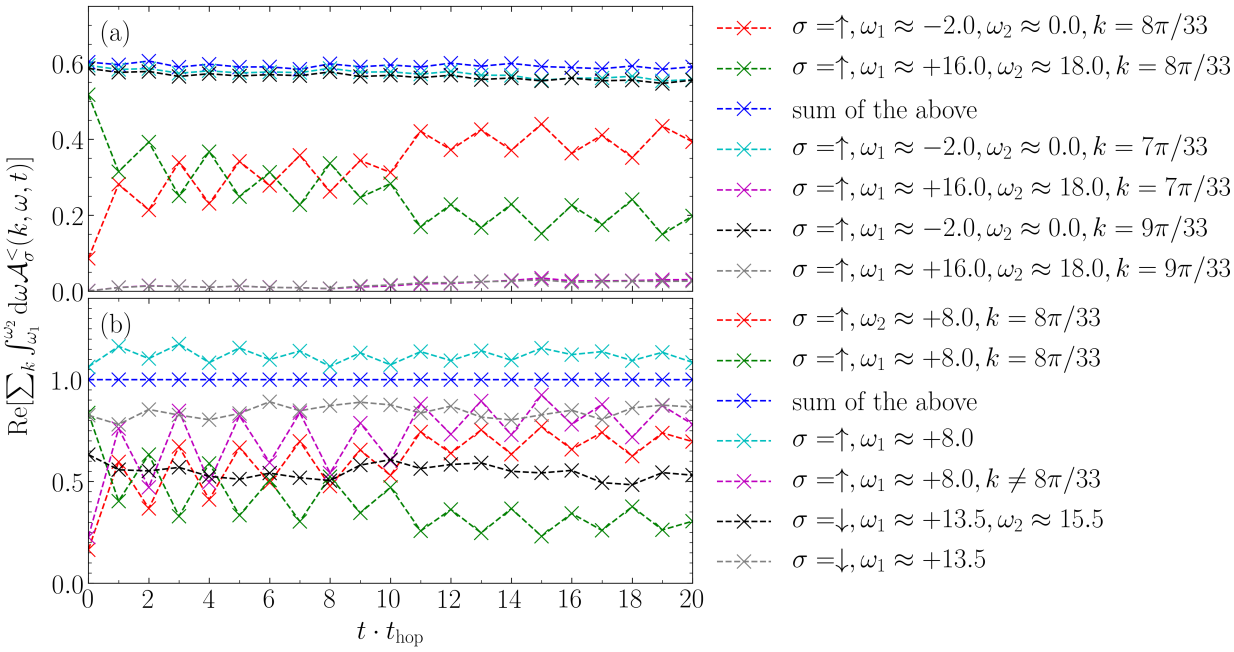

Figure 9.32: Total spectral weight of $\mathcal{A}_\sigma^<(k,\omega,t)$ in between frequencies ω_1 and ω_2 summed over certain momenta k for $\hat{H}^{2\Delta}$ at half filling after the electron-hole excitation as specified in figure 9.30. In case ω_1 or ω_2 is not given, the range was extended until ω_{min} or ω_{max}, respectively.

From figures 9.29 and 9.30 we, however, learn that here the redistribution of weight is more localized than for $\hat{H}^{4\Delta}$. In the spin-↑ direction the weight is only transferred to momenta neighboring $k = 8\pi/33$ and in the spin-↓ direction the mid-gap band is more pronounced at larger momenta. We attribute this behavior to the comparably strong dispersion of $\hat{H}^{2\Delta}$ compared to $\hat{H}^{4\Delta}$.

Nevertheless, following an analogous treatment as conducted before, we can confirm the stability over time of both effects in figures 9.31 and 9.32. The major difference to $\hat{H}^{4\Delta}$ here is that the recombination in the spin-↑ direction takes longer as to be seen in figures 9.31(a) and 9.32(a), the weights at $k = 8\pi/33$ becoming roughly equal only at $t \cdot t_{\text{hop}} = 8$.

This feature, however, has no major effect on the time evolution of the optical conductivity, which we present in figures 9.33 and 9.34. The additional peak at $\omega/t_{\text{hop}} \approx 2$ stays stable over time as do the original features from the ground state.

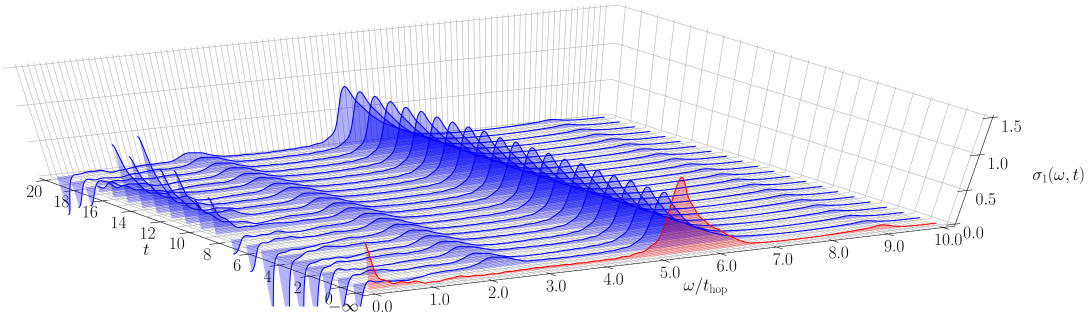

Figure 9.33: Real part of the time-dependent optical conductivity $\sigma_1(\omega, t)$ for $\hat{H}^{2\Delta}$ with $\Delta/t_{\text{hop}} = 2$ and $U/t_{\text{hop}} = 4$ for a system of $L = 32$ sites with OBCs at half filling before (ground state, $t = -\infty$, red; c.f. figure 9.17(a)) and after ($t \geq 0$, blue) the excitation (9.1). 16 times zero padding was applied. This figure is adapted from the author's work [243].

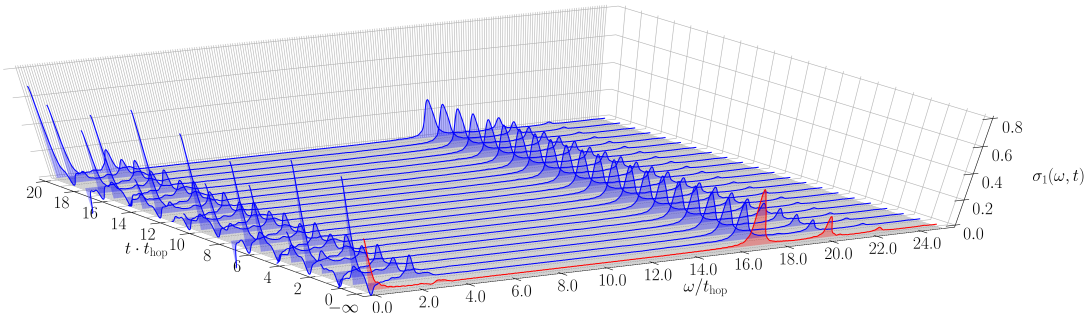

Figure 9.34: Real part of the time-dependent optical conductivity $\sigma_1(\omega, t)$ for $\hat{H}^{2\Delta}$ with $\Delta/t_{\text{hop}} = 2$ and $U/t_{\text{hop}} = 16$ for a system of $L = 32$ sites with OBCs at half filling before (ground state, $t = -\infty$, red; c.f. figure 9.18(a)) and after ($t \geq 0$, blue) the excitation (9.1). 16 times zero padding was applied.

10 In-gap Band Formation in a Periodically Driven Charge Density Wave Insulator

We extend our studies of non-equilibrium spectral functions to Floquet-driven correlated setups. This chapter is part of the author's publication [278]. Contrary to our analysis so far, our system is now subject to a time-dependent continuous driving rather than a quench-like excitation. As already pointed out in section 7.4, this procedure allows us to also study the excitation process itself contrary to the situations investigated so far. Here, we conduct our simulations on the simpler model of a tV-chain of spinless fermions as introduced in section 7.1.1 where we have set $V/t_{\mathrm{hop}} = 5$ in order to focus on effects of the driving. Since the spinless fermions are numerically less costly to evaluate, we increased the system size to $L = 64$. Compared to our previous analysis, we make some more changes. Whilst we shall still make use of relative coordinates, we shall obey equation (6.13), such that equation (6.14) does not hold anymore. As a consequence we will perform the Fourier transforms only by applying a damping, c.f. equation (6.15), and zero padding of eight times the input signal's length. Hence, we cannot expect the spectral function to be strictly positive anymore. As is also explained in appendix C we will present the real and imaginary part, as well as the absolute value of our results in this chapter, where for the interpretation we mainly focus on the real part and the absolute value. That way, we are enabled to rule out possible leaking effects in the imaginary part due to the discretization of the Fourier transform. We shall, furthermore, apart from the lesser spectral function (6.11) also investigate the total spectrum (6.16). As a benchmark for the MPS-generated data of the time evolution of the non-equilibrium Green's functions, reference results were provided by Alexander Osterkorn. In that, for non-interacting systems the corresponding equations of motion of the Green's functions were set up using the Heisenberg equation of motion (2.43) and subsequently integrated numerically. Here, a good agreement was found. Note that in our numerical calculus, we clearly cannot start our time-evolutions from an infinitely evolved initial state. Instead at $t \cdot t_{\mathrm{hop}} = 0$ we take the system to be in the ground state. Hence, our simulation is more reminiscent of a sudden switching on of the driving.

Inspired by the work of Kennes et al. [185] we investigate two situations. The tV-chain, a Bethe ansatz integrable model, is known to exhibit a quantum phase transition from a metallic phase, also called a Luttinger liquid, c.f. reference [321] for an introduction, into a CDW Mott insulator phase at $V/t_{\mathrm{hop}} = 2$. Hence, at $V/t_{\mathrm{hop}} = 5$ we are deep in the CDW Mott insulating phase. In this case the spectrum will consist of an upper and a lower Mott band, which are separated by a gap $G/t_{\mathrm{hop}} \approx 1.58$. In the so-called Magnus case, that is when the system is driven at a frequency well above the band gap G, an effective time-independent Hamiltonian can be derived by means of a zeroth order approximation [241, 63] with a renormalized hopping parameter

$$t_{\mathrm{hop}}^{\mathrm{eff}} = J_0(1)\, t_{\mathrm{hop}} \approx 0.7652 t_{\mathrm{hop}}, \tag{10.1}$$

where J_0 is the zeroth Bessel function.

We present the spectra for this Magnus case in figures 10.1, 10.2, and 10.3 for the real part, imaginary part, and absolute value, respectively. In figure 10.1(a) and 10.3(a) we first show the equilibrium

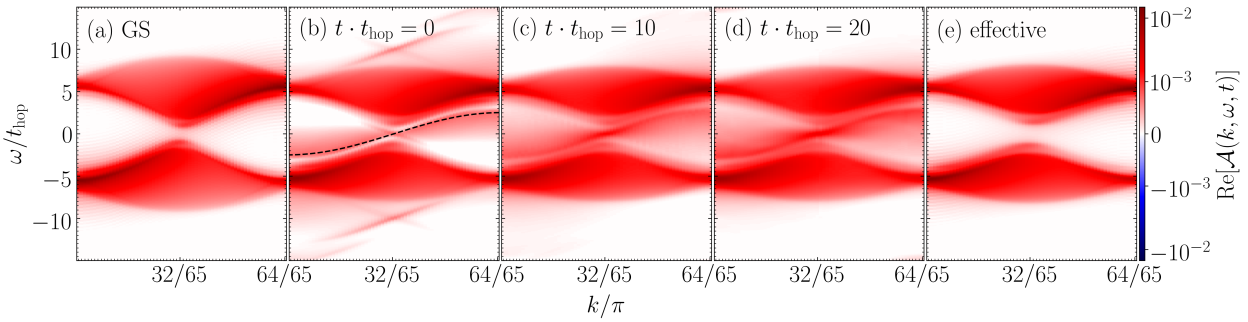

Figure 10.1: Real part of the spectra $\mathcal{A}(k, \omega, t)$ of the (periodically driven, $\omega_{\mathrm{F}}/t_{\mathrm{hop}} = 10$) tV-chain at $V/t_{\mathrm{hop}} = 5$. Panel (a) shows the spectrum of the undriven system in equilibrium, whereas panel (e) depicts the equilibrium spectrum of the model with renormalized hopping, c.f. equation (10.1). The remaining panels show the spectra of the driven system at different times. In the gap of the system we find spectral weight appearing that is well approximated by equation (10.2) (dashed line). All data is obtained for a system with $L = 64$ sites and open boundary conditions.

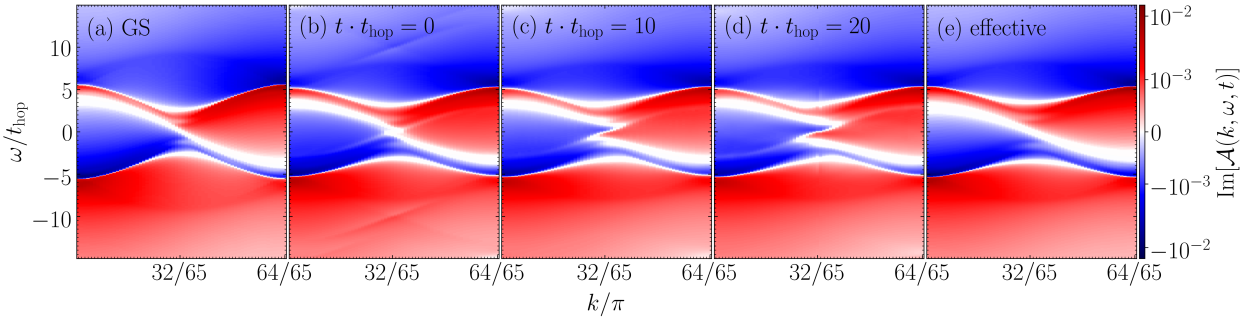

Figure 10.2: Imaginary part of the spectra $\mathcal{A}(k, \omega, t)$ of the (periodically driven, $\omega_{\mathrm{F}}/t_{\mathrm{hop}} = 10$) tV-chain at $V/t_{\mathrm{hop}} = 5$. Panel (a) shows the spectrum of the undriven system in equilibrium, whereas panel (e) depicts the equilibrium spectrum of the model with renormalized hopping, c.f. equation (10.1). The remaining panels show the spectra of the driven system at different times. All data is obtained for a system with $L = 64$ sites and open boundary conditions.

spectrum, that is in the case of $A(t) = 0$ as a reference. Next, in figures 10.1(b), (c), and (d), and 10.3(b), (c), and (d) we show the non-equilibrium spectra at times $t \cdot t_{\mathrm{hop}} = 0, 10$, and 20, respectively. Finally, a reference equilibrium spectrum with the effective hopping according to equation (10.1) is shown in figures 10.1(e) and 10.3(e). From figures 10.1(a) and 10.3(a) we find the holon continuum [291] at equilibrium to be separated by a gap around $\omega/t_{\mathrm{hop}} = 0$ of which the minimum size at $k = 32\pi/65 \approx \pi/2$ is given by $G/t_{\mathrm{hop}} \approx 2$ which matches the Bethe ansatz result. We then choose $\omega_{\mathrm{F}}/t_{\mathrm{hop}}$ as the driving frequency. The non-equilibrium spectrum at $t \cdot t_{\mathrm{hop}} = 0$ is very similar to the equilibrium result. Still, it possesses some additional features, already, these being the appearance of a new in-gap band and a slight change of the holon continuum in size and form. In addition, around frequencies $\omega/t_{\mathrm{hop}} \approx \pm 10$, weak signals appear, which seem to echo the in-gap feature. These are reminiscent of Floquet side bands, which are expected for this periodically driven system, since Floquet theory predicts a periodic repetition of band structures in frequency space [334], and have already been observed in experiment [99]. However, it is noteworthy that one

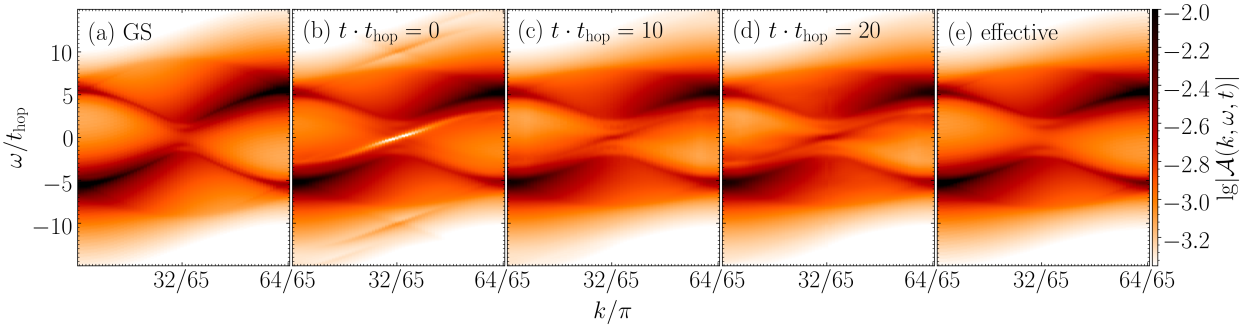

Figure 10.3: Absolute value of the spectra $\mathcal{A}(k, \omega, t)$ of the (periodically driven, $\omega_{\mathrm{F}}/t_{\mathrm{hop}} = 10$) tV-chain at $V/t_{\mathrm{hop}} = 5$. Panel (a) shows the spectrum of the undriven system in equilibrium, whereas panel (e) depicts the equilibrium spectrum of the model with renormalized hopping, c.f. equation (10.1). The remaining panels show the spectra of the driven system at different times. All data is obtained for a system with $L = 64$ sites and open boundary conditions.

seems to obtain such echoes only of the in-gap signal, but not of the other features. A reason for this might be that at the chosen intensity of the driving the strength of further Floquet echoes is smaller than our numerical resolution. At later times $t \cdot t_{\mathrm{hop}} = 10$ and $t \cdot t_{\mathrm{hop}} = 20$, the shape of the holon continuum does not further change, but the in-gap signal becomes more pronounced. Interestingly, the Floquet-like bands for our choice of parameters do not appear at the instances of time depicted. However, at other times they indeed do weakly occur again, which suggests that they oscillate in time. An explanation for this particular behavior could be that the simulation corresponds to a sudden switching on of the driving. We observed similar effects also in our benchmark calculations for non-interacting setups.

In addition, we find the in-gap signal to be reminiscent of a cosine band as we illustrate by showing the function

$$\varepsilon_k = -2.5 t_{\mathrm{hop}} \cos(k) \tag{10.2}$$

in figure 10.1(b). Indeed, this reproduces the structure fairly well. The change in size of the holon continuum, on the other hand, is to be expected according to the renormalization of the hopping strength in the effective Floquet-Hamiltonian, see again reference [185]. In figures 10.1(e) and 10.3(e) a good comparison of the corresponding features of the driven system is obtained.

Our findings are further confirmed by figure 10.4, which shows cross sections at $k = 32\pi/65 \approx \pi/2$ of the real part of the spectrum at times $t \cdot t_{\mathrm{hop}} = 0$, 10 and 20. In all cases, we identify two main bands and smaller peaks. We focus in the following on the behavior of the main bands and of the largest peak at $\omega/t_{\mathrm{hop}} = 0$. At time $t \cdot t_{\mathrm{hop}} = 0$, the Mott bands show a small difference between the non-equilibrium result and the result of the effective Hamiltonian, which decreases further at later times. It is noteworthy that the similarity is already obtained at waiting time $t \cdot t_{\mathrm{hop}} = 0$, although Floquet theory is expected to be most predictive in the long time limit. On the time scale treated by us, the peak at $\omega/t_{\mathrm{hop}} = 0$ becomes more pronounced with time and is a stable new feature. Furthermore, when increasing the system size it appears to sharpen. Note that for this kind of simulations, the real part of the spectral function is not necessarily guaranteed to be positive. Hence, the analysis as a representation of the density of states is comparably complicated. Here, however, our results seem to be entirely positive. If occurring at all, negative weights turned out to be negligibly small. Still, we find that the time-dependent signal is not at all times symmetric

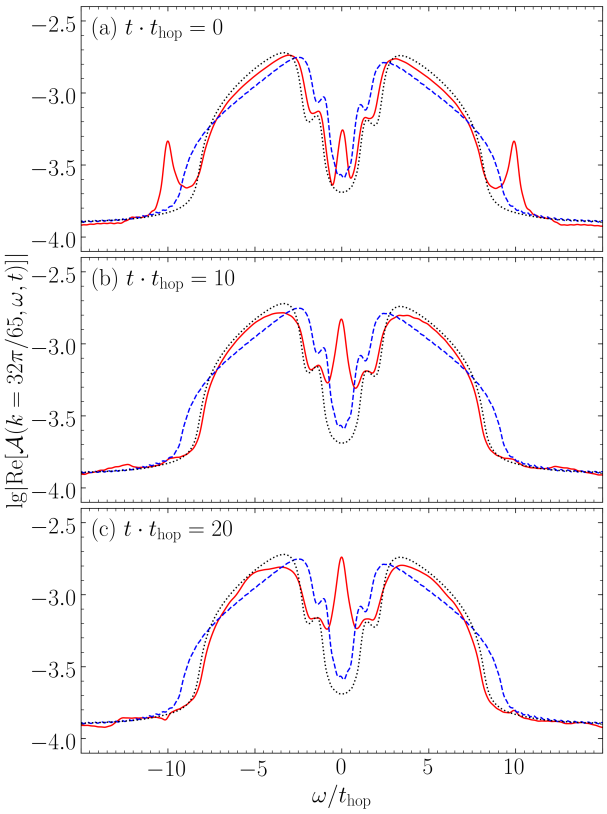

Figure 10.4: Cross section of the data shown in figure 10.1 at $k = 32\pi/65 \approx \pi/2$ (solid red lines) at times $t \cdot t_{\mathrm{hop}} = 0$, 10 and 20, (a), (b), and (c), respectively. The dashed blue (dotted black) lines show the equilibrium results as in figure 10.1(a) (the equilibrium results of the effective model as in figure 10.1(e)) as a reference.

, c.f. in particular figure 10.4(c). To account for the redistribution of weight as a consequence of the mid-gap signal we show normalized data for figure 10.4 in figure 10.5. Here we further confirm the good approximation of the effective Floquet Hamiltonian with the exception of the additional signal.

To better understand these findings, we study in figures 10.6, 10.7, and 10.8 the second setup, where the same system is driven with frequency $\omega_{\mathrm{F}}/t_{\mathrm{hop}} \approx 4.2$ (corresponding to laser light with wavelength 500 nm, c.f. reference [198]) for comparison. This setup is not resonant, since $\omega_{\mathrm{F}} > G$, however, neither are we in the Magnus case anymore. We shall refer to this configuration as close-to-resonance in subsequent discussions. Note that for this simulation we only consider the lesser spectral function. In this case, the additional feature in the gap region is even stronger pronounced and it goes hand in hand with a significant reduction of the original spectral features of the Mott insulator, indicating a rather complete melting of the CDW crystal state after a waiting time of $t \cdot t_{\mathrm{hop}} \sim 10$.

We further find that the formation of the in-gap signal is, indeed, accompanied by a melting of the CDW structure this model exhibits in its ground state. We study the time evolution of the CDW order parameter

$$\mathcal{O}_{\mathrm{CDW}}(t) = \frac{1}{L} \sum_{l \in \mathscr{C}} \left(\langle \hat{n}_{l+1}(t) \rangle - \langle \hat{n}_l(t) \rangle \right) \tag{10.3}$$

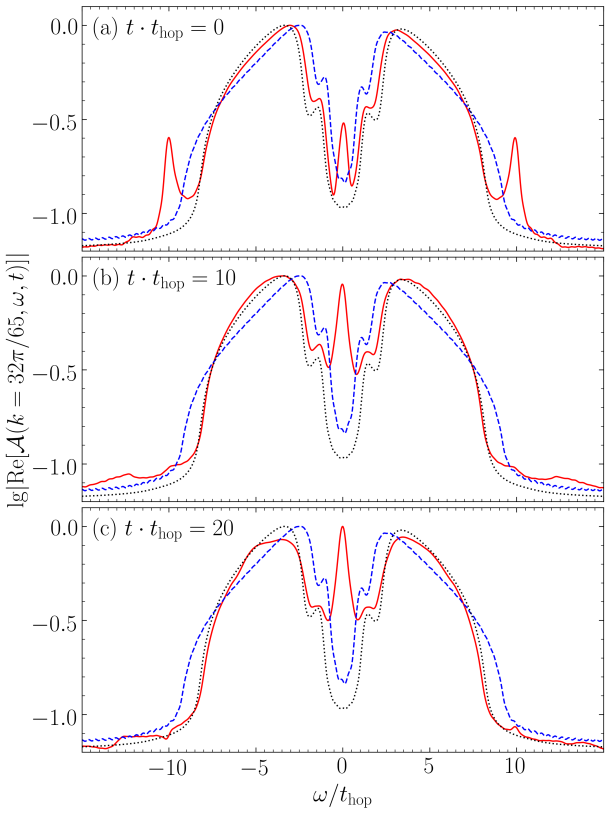

Figure 10.5: Cross section of the data shown in figure 10.1 at $k = 32\pi/65 \approx \pi/2$ (solid red lines) at times $t \cdot t_{\mathrm{hop}} = 0$, 10 and 20, (a), (b), and (c), respectively. The dashed blue (dotted black) lines show the equilibrium results as in figure 10.1(a) (the equilibrium results of the effective model as in figure 10.1(e)) as a reference. This figure shows the same data as figure 10.4 but normalized.

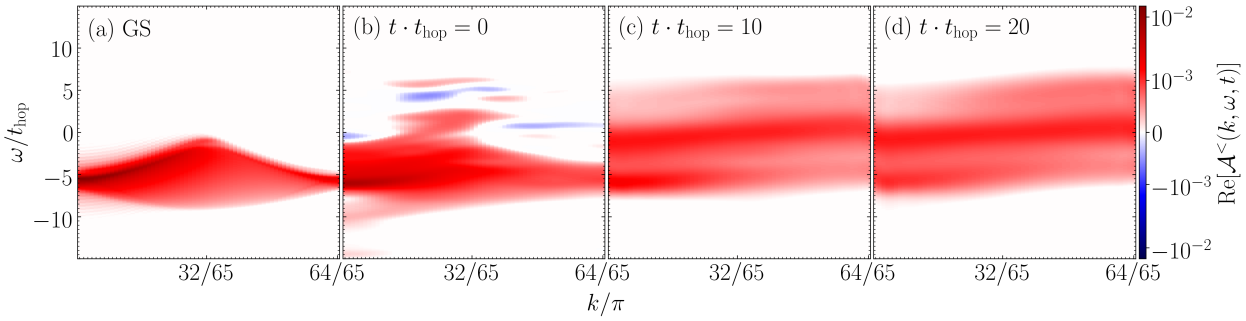

Figure 10.6: Real part of the spectra $\mathcal{A}(k, \omega, t)$ of the (periodically driven, $\omega_{\mathrm{F}}/t_{\mathrm{hop}} \approx 4.2$) tV-chain at $V/t_{\mathrm{hop}} = 5$. Panel (a) shows the spectrum of the undriven system in equilibrium. The remaining panels show the spectra of the driven system at different times. All data is obtained for a system with $L = 64$ sites and open boundary conditions.

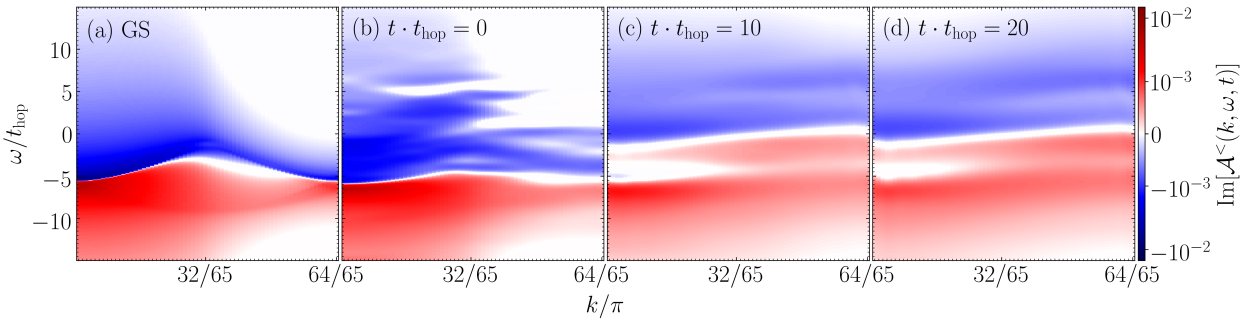

Figure 10.7: Imaginary part of the spectra $\mathcal{A}(k, \omega, t)$ of the (periodically driven, $\omega_{\mathrm{F}}/t_{\mathrm{hop}} \approx 4.2$) tV-chain at $V/t_{\mathrm{hop}} = 5$. Panel (a) shows the spectrum of the undriven system in equilibrium. The remaining panels show the spectra of the driven system at different times. All data is obtained for a system with $L = 64$ sites and open boundary conditions.

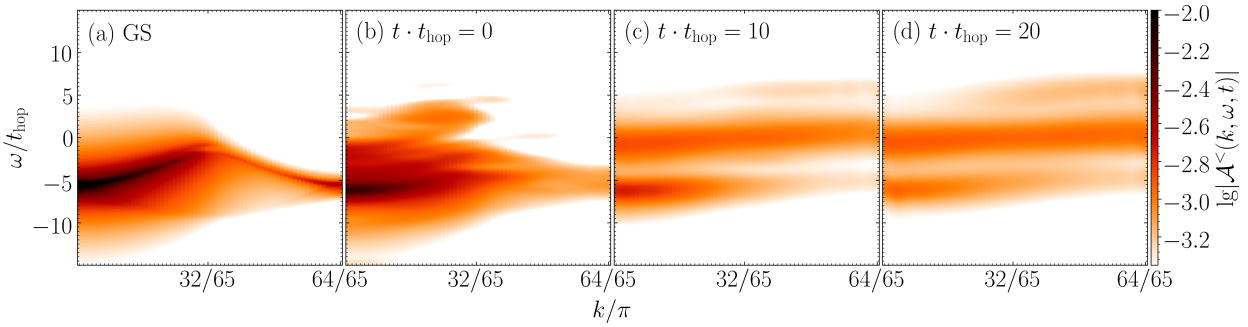

Figure 10.8: Absolute value of the spectra $\mathcal{A}(k, \omega, t)$ of the (periodically driven, $\omega_{\mathrm{F}}/t_{\mathrm{hop}} \approx 4.2$) tV-chain at $V/t_{\mathrm{hop}} = 5$. Panel (a) shows the spectrum of the undriven system in equilibrium. The remaining panels show the spectra of the driven system at different times. All data is obtained for a system with $L = 64$ sites and open boundary conditions.

where $\mathscr{C}$ includes the four even center sites of the system Since the CDW phase of this model is characterized by an exact superposition of two symmetry-broken ground states, for a finite system the order parameter vanishes in a completely symmetric setup. Thus, to be able to track the dynamics of the CDW order parameter, we apply a "pinning field" at the edge of the system, which selects one of the ground states. In addition, we keep track of the time evolution of the energy, $E(t) = \left\langle \hat{H}(t) \right\rangle$, which serves as a measure for the heating of the system. As can be seen in figure 10.9(a), closer to resonance, i.e. $\omega_{\mathrm{F}}/t_{\mathrm{hop}} \approx 4.2$, $\mathcal{O}_{\mathrm{CDW}}(t)$ vanishes completely on a time scale $t \cdot t_{\mathrm{hop}} \sim 10$, which is in agreement with the time scale on which the holon continuum disappears in the spectral function. At $\omega_{\mathrm{F}}/t_{\mathrm{hop}} = 10$ the situation is more complicated, but also in this case we report a partial melting of the CDW state, which seems to continue to longer times than the ones amenable to our methods. Furthermore, an oscillatory behavior is observed, which we leave for future investigations. Since the parameters of the effective Hamiltonian are deeper in the CDW phase, at equilibrium one would expect a larger CDW order parameter. However, here in this out-of-equilibrium setup we, instead, find a weakening of the order. Non-integrable Floquet systems in the long time limit are assumed to realize an infinite temperature state, c.f. [85]. We monitor the energy in figure 10.9(b) finding it to increase as a function of time, which indicates that on the

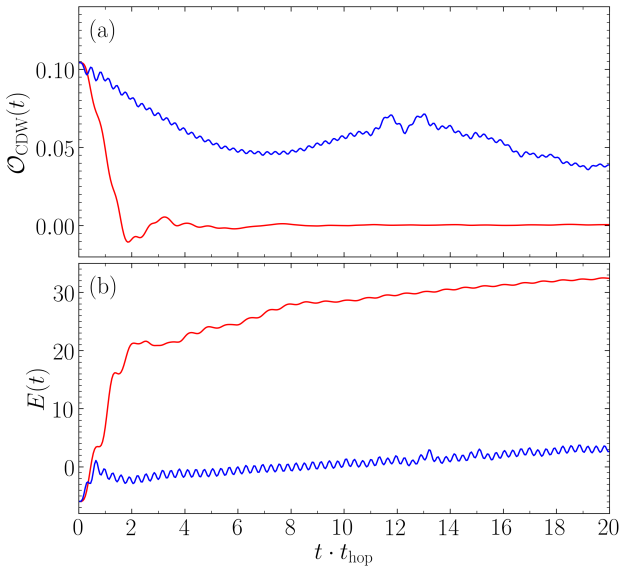

Figure 10.9: Dynamics of the order parameter $\mathcal{O}_{\mathrm{CDW}}(t)$ (a) and the total energy $E(t)$ (b) after the sudden switch on of the driving field at $t \cdot t_{\mathrm{hop}} = 0$. The data for the Magnus case, i.e. $\omega_{\mathrm{F}}/t_{\mathrm{hop}} = 10$, (close-to-resonance case, i.e. $\omega_{\mathrm{F}}/t_{\mathrm{hop}} \approx 4.2$) is shown in blue (red). For this simulation we have $L = 32$ and keep $V/t_{\mathrm{hop}} = 5$.

transient time scales inspected the infinite temperature state is not yet achieved.

Our analysis indeed shows some intriguing results. Yet still open questions remain. In particular, the exact reasons behind the formation of the in-gap band is curious. Here, a Bethe ansatz-based calculus could lead to further insights. Moreover does the possibility of negative weights pose difficulties regarding the interpretation of any data of this kind of simulations. So far, a conclusive general scheme has not been found. This very basic problem is most likely to spark further research. A starting point could be to investigate the behavior of differently defined spectral functions, compare, e.g., section 6.1.2 and references [179] and [382].

11 Summary and Outlook

In this thesis we discussed numerical methods to predict or explain results from spectroscopy experiments in out-of-equilibrium setups. Based on the works by Freericks et al. [104, 108, 103, 105] or equally Braun et al. [43] we therefore first introduced a possible extension of the definition of spectral functions to a time-dependent quantity, where, following the findings by Kalthoff et al. [179], we also discussed different approaches. With our so-obtained routines we aim at providing an explanation for measurements of time-resolved ARPES-like experiments. In addition, we also simulated the time-dependent optical conductivity as proposed by Shao et al. [336] and Lenarčič et al. [212].

Our numerical methods of choice were MPS-based algorithms, in particular the MPS implementation of the DMRG for ground state searches, the TDVP to compute time evolutions, and MPS alterations by a variational MPO application. After a rather extensive introduction to these numerical concepts and their associated algorithms we presented routines to compute the above mentioned observables in great detail.

With these tools in our hand, we investigated the behavior of two variants of a one-dimensional Hubbard model with a magnetic superstructure as introduced in [197, 195, 33] following a spin selective (photo)excitation. First, however, we needed to properly understand the model in equilibrium. Therefore, in a first step, we considered the ground state spectral function of two variants of the system, where we identified at finite interactions U an upper and a lower Hubbard band, which each possess an additional fine structure caused by the super structure. We confirmed these results by means of an FD calculation for a system consisting of only a single unit cell and found that the peaks of the optical conductivity can be identified with band transitions in the spectral function.

As is further elaborated on in reference [198] this spin-selective photoexcitation together with the microstructure leads to the formation of periodic spin- or charge patterns on femtosecond time scales, a scenario which connects to the recently introduced OISTR effect [78, 92]. In this case theory predicts ultrafast spin transfer using ab-initio methods, which was experimentally confirmed in Heusler- and magnetic materials [366, 348, 150]. While in the OISTR setup, the site-dependent difference of the local density of states of the minority and majority spins in equilibrium is found to be the reason for ultrafast transfer of magnetic moments, in reference [198] the excitation was first modeled by high intensity light pulses of duration ~ 10fs by a generalized Peierls substitution ansatz, which then led to the formation of patterns during the application of the pulse. For this thesis we altered the way the excitation is modeled to a more microscopic variant, which involved the subsequent approximations of a creation and annihilation operator in momentum space. The principal idea here was for the interaction to be of so low intensity that it could simply be understood as a single-photon excitation, in which at fixed momentum one particle is excited over a band-gap. We chose the excitation to involve only spin-$\uparrow$ operators and did, indeed, find qualitatively the same effects as for the Peierls substitution.

For this setup we then evaluated the time evolution and computed the time-dependent spectral functions and optical conductivities. In the former we observed recombination of the excited

electron and the hole and found the populations to have become equally strong at $t \cdot t_{\mathrm{hop}} \sim 10$. In addition, at neighboring momenta inter band scattering led to a population growth in the upper Hubbard band in the spin-↑ direction. While for systems without interaction our results matched our expectations from analytical calculations, we found for $U/t_{\mathrm{hop}} > 0$ in all cases an in-gap signal in the spin-↓ direction even though it was not touched by our excitation. These new features were also accompanied by additional peaks in the optical conductivity. Inspired by similar work by Bittner et al. [35] we found a confinement of doublons and holes to nearest neighbors, which similar to their explanation allowed us to interpret the new mid-gap band as a manifestation of the formation of excitons. This understanding was further supported by works of Lenarčič et al. who report the existence of excitons in systems with a magnetic background [211, 210]. Since in our case the excitons only appeared after the photoexcitation and only in the opposite spin direction we labeled them spinful. Another special property of this exciton is given by the fact that the additional in-gap signal in the spectral function of these excitons occurs at an energy of the edge of the lower Hubbard band plus the binding energy contrary to the findings in reference [61]. We find the new features to be nearly time-independent in both the spectral function and the optical conductivity on the time scales investigated.

In experiment it would be interesting to investigate for these peculiar spinful excitons using materials which show magnetic super structures. Such materials are indeed known to exist, examples being CE-structures in manganites [155], or orbital-selective Mott phases in iron-based ladder compounds such as $BaFe_2Se_3$ [148, 285, 149, 310]. Alternatively, this can also be studied in ultracold gases on optical lattices, where there is a great amount of expertise regarding their creation [36, 38], as well as their control [37]. The realization of a magnetic background on such lattices has also already been demonstrated by Aidelsburger et al. [12, 11], the knowledge on how to set up systems with superlattices being even older [289, 328] with research in this field also incorporating quantum computing [14], charge pumps [223], or superexchange [379]. Note also that the successful implementation of spin-dependent optical superlattices [413] or such systems that are based on varying spin degrees of freedom [327] has been reported. Models with an ionic, c.f. reference [242], instead of a magnetic pattern may also be investigated. The spin-selective photoexcitation might be implemented by means of modulation spectroscopy [199, 128], an approach that has also been applied to investigate decay times of doublons [358, 332]. In materials, spin-selective excitations may furthermore be realized via circularly polarized monochromatic light [46]. As for optical lattices, dynamics can be investigated using quantum-gas microscopes which, since they allow for a single-site resolution [22, 287, 59, 269, 40], are also relevant in the field of quantum computing [132, 131]. Finally, spectral functions have also already been measured, e.g. by Stewart el al. [350]. In the long run it would be interesting to extend the studies to systems with more than only two species of particles, e.g., SU(N) systems like the ones proposed in reference [126] based on alkaline-earth atoms. Furthermore, since in reference [198] compounds with locally alternating chemical potentials are shown to behave similarly as those with a magnetic microstructure regarding the formation of CDWs, it seems promising to analyze them as well. For theoretical studies the Fermi-Hubbard-Harper model, c.f. for instance [349], or the so-called ionic Hubbard model [164] appear suitable [73]. Its phase diagram is already known in one dimension [233] and CDWs have been observed [242]. Candidate materials are charge transfer salts [181]. Also, since we never relied on the dimensions of our models in our reasoning, we expect our scenario to be valid for generic systems with a microstructure.

One might be tempted to believe that it would now be up to experimental physics to deliver the final piece to obtain a complete picture of these phenomena. This, however, is a clear misjudgment

as there are numerous theoretical issues to also be addressed, which becomes most apparent in the analysis of a simple Floquet-driven tV-chain. While we did find the general shape of the non-equilibrium spectral function to be predicted correctly by an effective Floquet Hamiltonian, computing only several variants of the spectral functions, we also found Floquet side bands as they are predicted by Floquet theory not to occur at all times under the driving. Further, we observed another in-gap feature for interacting systems which seems to be connected to the melting of a CDW. Since both quantities, the time-dependent spectral functions, as well as the time-dependent optical conductivity are not uniquely defined, it would be desirable to compare the results for different definitions as mentioned above, similarly to the procedure in references [257] and [254]. Regarding Floquet Hamiltonians also analyzing the time-averaged spectral functions as proposed by Uhrig et al. [382] should also be considered. Moreover, in reference [335] an analysis applying the procedure introduced by Freericks et al. as explained in section 6.3 led to convincing results for a driven system. For this model it would also be nice to compare to an analytical solution obtained from a Bethe ansatz.

Setting up the Hubbard model with the magnetic superstructure for open boundaries has also shed light on an entirely different field of physics. If the unit cell is chosen such that for open boundaries it shows dangling bonds at the edges, this property could be a starting point for an analysis on the topological properties, which is another field of intense research activity [204], also in the context of ARPES-type experiments, c.f. for instance [191].

Regarding the findings associated to the excitonic mid-gap signal, this work could pave the way to setting up protocols for the creation and control of excitonic features in solids. Similarly to what is known as Floquet engineering, in future works it might be possible to create compounds with excitons of arbitrary properties, that is to do an exciton engineering.

A Additional Information on the Discrete Fourier and the Discrete Sine Transform

We shed light on further aspects regarding the discrete Fourier and the discrete sine transform. This appendix can be seen as a direct continuation of sections 3.6 and 3.7, respectively.

A.1 The Discrete Fourier Transform

A.1.1 One-dimensional Discrete Fourier Transform from Real to Reciprocal Space

The physical problem at hand is to transform a quantity given at a position r_m into another quantity given for a momentum k_μ. Thus, we identify $x = r$ and $y = k$ in comparison to section 3.6.3. Inspired by the name of the output space, for this type of transform the reciprocal space is often times referred to as momentum or k-space.

In one dimension we consider a chain of L sites, i.e. the position is given by

$$r_m = a \cdot m, \quad m \in \{0, \dots, L-1\} \quad \Rightarrow \quad r_m \in \{0, \dots, (L-1) \cdot a\}, \tag{A.1}$$

where $a = \delta_r$ is the step size we use to sample over the chain, a convenient choice being the lattice constant. As we investigate crystals, naturally the signal $\vec{c}_r$ is periodic in real space, i.e. (3.65) holds true, provided of course we cover a signal over a multiple of the unit cell, which we will always assume. This constraint then yields the corresponding physical values for the momenta

$$k_\mu = \frac{2\pi\mu}{aL}, \quad \mu \in \{0, \dots, L-1\} \quad \Rightarrow \quad k_\mu \in \left\{0, \dots, (L-1) \cdot \frac{2\pi}{aL}\right\}. \tag{A.2}$$

Note that technically we would have to multiply by $\hbar$ which is set to $\hbar = 1$ for these notes.

The step size for the momenta k_μ is thus given by

$$\delta_k = \frac{2\pi}{aL}. \tag{A.3}$$

In order to obtain a higher resolution in reciprocal space, this step size has to be decreased, which obviously means either increasing the length L of the signal or the real space step size a. As the latter quantity is intrinsic to the system, only the former option is physically meaningful. Hence, the range of the reciprocal space is determined by a.

We close this section with the remark that one often encounters the sloppy notation

$$c_m \coloneqq c_{r_m}, \tag{A.4}$$

$$c_k \coloneqq c_{k_\mu}. \tag{A.5}$$

in literature, especially if $a = 1$ is set for numerical convenience.

A.1.2 One-dimensional Discrete Fourier from Time to Frequency Space

As before we use the results from section 3.6.3, with the input signal given in the time domain, i.e. $x = t$, and the output signal living in frequency space, i.e. $y = \omega$. From a physical point of view the major difference to the Fourier transform from real to reciprocal space is that the Fourier transform from time to frequency space is by definition one-dimensional as there is only one dimension of time. In terms of Fourier's original idea, we want to decompose the input signal into a superposition of periodic sine or cosine signals with frequencies ω allowing us to reconstruct the input signal from these components. Clearly, the assumption here is that the input signal is just one period of an infinitely periodic system. In general, however, especially when dealing with the time evolution of a complex many-body system this cannot be true, making (3.65) an intrinsic source of errors to this procedure.

We consider a signal of L time steps δ_t. Thus, the current time is given by

$$t_m = \delta_t \cdot m, \quad m \in \{0, \dots, L-1\} \quad \Rightarrow \quad t_m \in \{0, \dots, (L-1) \cdot \delta_t\}, \tag{A.6}$$

and we find for the frequencies

$$\omega_\mu = \frac{2\pi\mu}{\delta_t L}, \quad \mu \in \{0, \dots, L-1\} \quad \Rightarrow \quad \omega_\mu \in \left\{0, \dots, (L-1) \cdot \frac{2\pi}{\delta_t L}\right\} \tag{A.7}$$

of which the step size is, hence, given by

$$\delta_\omega = \frac{2\pi}{\delta_t L}. \tag{A.8}$$

A higher resolution in frequency space is obtained by either increasing the length L of the signal or the time step δ_t. For one usually aims at a well-resolved signal in the time domain as well resulting in a rather small time step δ_t, the maximum time and, thus, the length L of the input signal need to be chosen comparably large.

We further note that the ω_μ physically define an angular frequency, rather than an ordinary frequency ν_μ, both quantities being related by

$$\omega_{(\mu)} = 2\pi\nu_{(\mu)}. \tag{A.9}$$

The ordinary frequency is, thus, given by

$$\nu_\mu = \frac{\omega_\mu}{2\pi} = \frac{\mu}{\delta_t L}, \tag{A.10}$$

which is, however, rarely used in applications.

A.1.3 Shifts

As mentioned in section 3.6.3 the range of the output signal goes from $y_{\mu=0} = 0$ to $y_{\mu=L-1} = (L-1)\,\frac{2\pi}{\delta_x L}$, which is also the way most implementations store the data. However, in most applications in physics we prefer an ordering from $y_{\mu=-\lfloor L/2 \rfloor} = -\left\lfloor \frac{L}{2} \right\rfloor \frac{2\pi}{\delta_x L} = -\frac{\pi}{\delta_x}$ to $y_{\mu=\lfloor L/2 \rfloor - 1} =$

$\left(\left\lfloor \frac{L}{2} \right\rfloor - 1\right) \frac{2\pi}{\delta_x L}$. Exploiting the symmetry from equation (3.69), our problem can be sketched as follows:

given order	aspired order
$y_{\mu=0}$	$y_{\mu=-\lfloor L/2 \rfloor}$
$\vdots$	$\vdots$
$y_{\mu=\lfloor L/2 \rfloor - 1}$	$y_{\mu=-1}$
$y_{\mu=\lfloor L/2 \rfloor} = y_{\mu=-\lfloor L/2 \rfloor}$	$y_{\mu=0}$
$\vdots$	$\vdots$
$y_{\mu=L-1} = y_{\mu=-1}$	$y_{\mu=\lfloor L/2 \rfloor - 1}$

The aspired order may, hence, be obtained by taking the last $\lceil L/2 \rceil$ values of the output signal and shifting them to its beginning.

This step can be circumvented by introducing

$$y_{\mu'} = y_{\mu - \lfloor L/2 \rfloor}, \tag{A.11}$$

which yields

$$c_{y_{\mu'}} = \sum_{x_m} \mathrm{e}^{-\mathrm{i} x_m y_{\mu'}} c_{x_m} = \sum_{x_m} \mathrm{e}^{-\mathrm{i} x_m y_\mu} c_{x_m} \mathrm{e}^{-\mathrm{i} x_m \frac{2\pi}{\delta_x L}\left(-\frac{L}{2}\right)} = \sum_{x_m} \mathrm{e}^{-\mathrm{i} x_m y_\mu} c_{x_m} \mathrm{e}^{-\mathrm{i}\delta_x m \frac{2\pi}{\delta_x L}\left(-\frac{L}{2}\right)} \tag{A.12a}$$

$$= \sum_{x_m} \mathrm{e}^{-\mathrm{i} x_m y_\mu} c_{x_m} \mathrm{e}^{\mathrm{i}\pi m} = \sum_{x_m} \mathrm{e}^{-\mathrm{i} x_m y_\mu} c_{x_m} (-1)^m =: \sum_{x_m} \mathrm{e}^{-\mathrm{i} x_m y_\mu} c'_{x_m}. \tag{A.12b}$$

Thus, by multiplying the input signal c_{x_μ} alternately by ± 1 the output signal $c_{y_{\mu'}}$ will be shifted by half the range L, just as desired. Note that for this procedure to work, the length of the signal L must be an even number.

A.1.4 Back Transform

Let us assume that we have only a one-way implementation of the discrete Fourier transform, e.g. (3.60). Then, we have to generate (3.61) from our only implementation. Applying the forward discrete Fourier transform twice, we obtain exploiting (3.65):

input	transform	second transform
$c_{x_{m=0}}$	$c_{y_{\mu=0}}$	$L \cdot c_{x_{m=-0}} = L \cdot c_{x_{m=0}}$
$c_{x_{m=1}}$	$c_{y_{\mu=1}}$	$L \cdot c_{x_{m=-1}} = L \cdot c_{x_{m=L-1}}$
$\vdots$	$\vdots$	$\vdots$
$c_{x_{m=L-1}}$	$c_{y_{\mu=L-1}}$	$L \cdot c_{x_{m=-(L-1)}} = L \cdot c_{x_{m=1}}$

Two problems are evident: First, the final result after the second transform is now multiplied by the size L of the signal. This error can be corrected easily by just dividing by L. Second and more importantly, the order is incorrect. We would have needed to rearrange (and stretch) the signal such that

input	transform	rearrange	second transform

$$
\begin{array}{cc}
c_{x_{m=0}} & c_{y_{\mu=0}} \\
c_{x_{m=1}} & c_{y_{\mu=1}} \\
\vdots & \vdots \\
c_{x_{m=L-1}} & c_{y_{\mu=L-1}}
\end{array}
\qquad
\begin{array}{cc}
\frac{1}{L}c_{y_{\mu=-0}} = \frac{1}{L}c_{y_{\mu=0}} & \frac{L}{L}\cdot c_{x_{m=-0}} = c_{x_{m=0}} \\
\frac{1}{L}c_{y_{\mu=-1}} = \frac{1}{L}c_{y_{\mu=L-1}} & \frac{L}{L}\cdot c_{x_{m=-(L-1)}} = c_{x_{m=1}} \\
\vdots & \vdots \\
\frac{1}{L}c_{y_{\mu=-(L-1)}} = \frac{1}{L}c_{y_{\mu=1}} & \frac{L}{L}\cdot c_{x_{m=-1}} = c_{x_{m=L-1}}
\end{array}
$$

Unfortunately this correction cannot be achieved by a phase shift. One has to rearrange by hand. However, one is free to either first apply the discrete Fourier transform first and then rearrange or do it the other way around. Note that this problem cannot be fixed by just reversing the order of the coefficients after the first transform, as this procedure would yield:

$$
\begin{array}{cc}
\text{input} & \text{transform} \\
c_{x_{m=0}} & c_{y_{\mu=0}} \\
c_{x_{m=1}} & c_{y_{\mu=1}} \\
\vdots & \vdots \\
c_{x_{m=L-1}} & c_{y_{\mu=L-1}}
\end{array}
\qquad
\begin{array}{cc}
\text{reverse} & \text{second transform} \\
c_{y_{\mu=L-1}} & L\cdot c_{x_{m=-(L-1)}} = L\cdot c_{x_{m=1}} \\
\vdots & \vdots \\
c_{y_{\mu=1}} & L\cdot c_{x_{m=-1}} = L\cdot c_{x_{m=L-1}} \\
c_{y_{\mu=0}} & L\cdot c_{x_{m=-0}} = L\cdot c_{x_{m=0}}
\end{array}
$$

Here, still the coefficient for $m = 0$ is misplaced. Therefore, if provided it is highly recommendable to use a math library's explicit implementation of the back transform.

A.1.5 Normalization

Computing the sum over the entire output signal as obtained from equation (3.60), we find

$$
\sum_{y_\mu} c_{y_\mu} = \sum_{x_m, y_\mu} \mathrm{e}^{-\mathrm{i}x_m y_\mu} c_{x_m} = \sum_{x_m} \left(\sum_{y_\mu} \mathrm{e}^{-\mathrm{i}\delta_x m \frac{2\pi\mu}{\delta_x L}} \right) c_{x_m} = \sum_{x_m} \left(\frac{L}{L} \sum_{y_\mu} \mathrm{e}^{-\mathrm{i}2\pi \frac{m\mu}{L}} \right) c_{x_m} \tag{A.13a}
$$

$$
= L \sum_{x_m} \delta_{m,0} c_{x_m} = L c_{x_0}. \tag{A.13b}
$$

The total of the output signal is, hence, determined by the first component of the input signal stretched by a factor of the length of the signal. In physical applications, this additional factor proves to be impractical when it comes to the interpretation of the output signal, especially when c_{x_0} is known to have a particular meaning. Furthermore does it introduce problems in the comparison of data sets. Take for instance the case, where we have the exact same input signal over the exact same range twice but sampled with a different step size. Both data sets then differ only in length, but should contain the same information. When computing (A.13), however, different results are obtained.

For these two reasons it is desirable to modify the definitions of the discrete Fourier transform from (3.60) and (3.61) to

$$
c_{y_\mu} = \frac{1}{L} \sum_{x_m} \mathrm{e}^{-\mathrm{i}x_m y_\mu} c_{x_m}, \tag{A.14}
$$

$$c_{x_m} = \sum_{y_\mu} \mathrm{e}^{\mathrm{i} y_\mu x_m} c_{y_\mu}, \tag{A.15}$$

respectively, such that

$$\sum_{y_\mu} c_{y_\mu} = c_{x_0}. \tag{A.16}$$

Unless stated otherwise, we will always make use of this convention in the remainder of this work using (A.16) as a sanity check. We emphasize that definition (A.14) now resembles the discretization of (3.46), making it the more appropriate convention. Unfortunately, the common convention does not have it that way. One may have alternatively exchanged the use of forward and backward Fourier transform the interpretation being that the given input signal is more naturally represented in Fourier space.

A.1.6 Spectral Leaking

So far, we have investigated properties of the discrete Fourier transform regarding its various definitions and conventions. Now, we will take a closer look at how the input signal may influence the output signal. This Fourier analysis is a central aspect of signal processing. In addition to the textbooks mentioned so far concerning this topic we give [270, 363, 296] as the primary sources for this section. Reference [298] provides an overview form an engineering perspective.

We will illustrate our findings with the help of the example function

$$f(x) = 1 + \sin(\omega_0 \cdot x - \varphi), \quad \varphi = 0, \quad \omega_0 = 2\pi \cdot \frac{4}{5} \approx 5.03, \tag{A.17}$$

of which we from (3.38) and (3.44) know the Fourier transform to be given by

$$\frac{\mathscr{F}[f(x)](y)}{2\pi} = \delta(y) + \frac{\mathrm{i}}{2}\left(\delta(y+\omega_0) - \delta(y-\omega_0)\right). \tag{A.18}$$

Note that we have chosen a real function for illustrative purposes only. All considerations presented in the following could likewise be performed for complex functions as well. In figure A.1 we show the discrete Fourier transform of (A.17) as obtained from (A.14), where we have taken an input signal of length 1000 and step size $\delta_x = 0.005$ as specified by (3.53) yielding in one dimension

$$c_{x_m} = f(x_m). \tag{A.19}$$

A few remarks are in order. Comparing the center and the bottom line holdings the zoomed images of figure A.1 we note that while the spectrum covers a broad range, the spectral resolution in the area of interest is quite poor, illustrating the considerations regarding equation (3.68). Contrary to the analytically computed Fourier transform, the discrete Fourier transform does not show delta distributions but rather peaks of finite length, of which the size corresponds to their prefactors in equation (A.18). The peaks in the discrete Fourier transform can, nevertheless, be identified to occur exactly at the predicted points for both the real and the imaginary part of the output signal.

The above observations, however, only apply to a very special case of the discrete Fourier transform, that is, when the input signal precisely covers a multiple of its period. We change the length of the input signal to $L = 800$ and present the discrete Fourier transform calculated in the same way

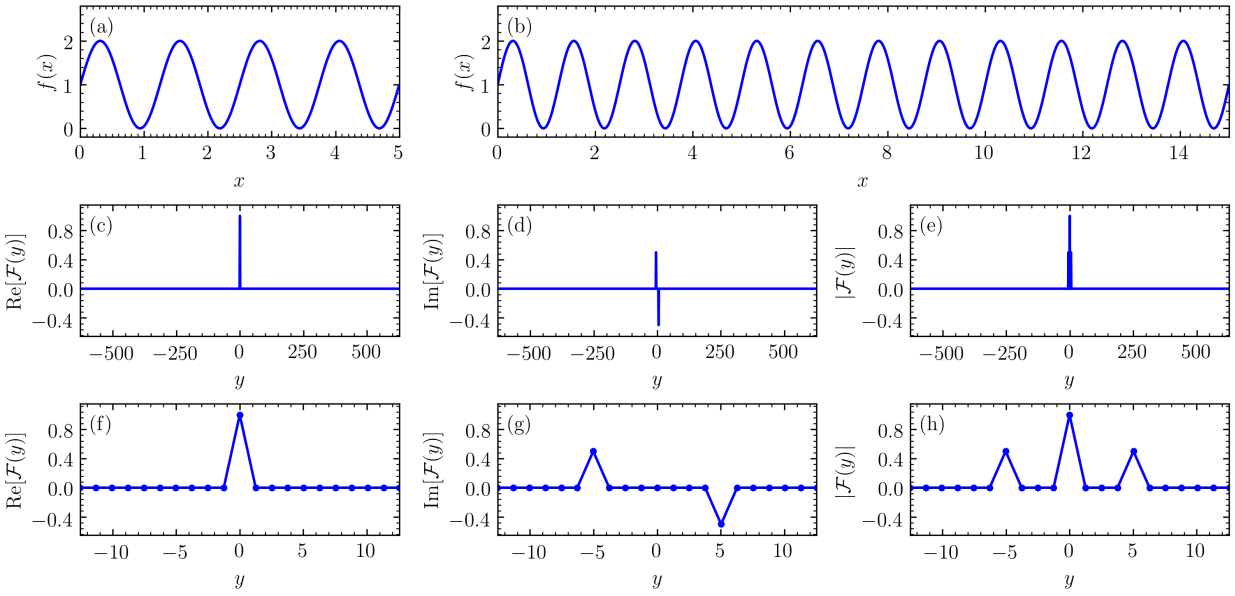

Figure A.1: Discrete Fourier transform of (A.17) for $L = 1000$ and $\delta_x = 0.005$. Input signal (a) and its assumed continuation by the algorithm (b). Real part (c), imaginary part (d), and absolute value (e) of the discrete Fourier transform and respective zomms into the center of the spectrum (f), (g), and (h). In this example, the input signal covers a multiple of the input function's period.

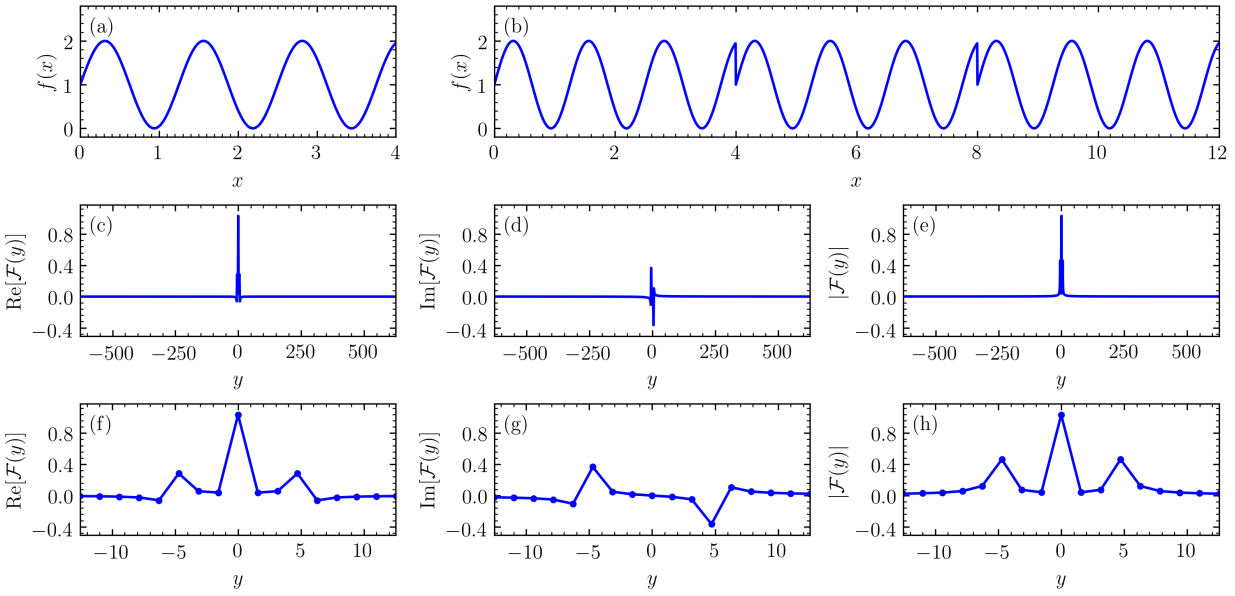

Figure A.2: Discrete Fourier transform of (A.17) for $L = 800$ and $\delta_x = 0.005$. Input signal (a) and its assumed continuation by the algorithm (b). Real part (c), imaginary part (d), and absolute value (e) of the discrete Fourier transform and respective zomms into the center of the spectrum (f), (g), and (h). In this example, the input signal covers a multiple of the input function's period.

as before in figure A.2. The input signal is now of incomplete period, which is also the default case for most applications in practice where one does not know the function modeling the input signal in advance. As the plot of the periodic continuation in figure A.2(b) shows, the input signal now has discontinuities resulting in contributions from the previously only imaginary part of the output signal to be also found in the real part. This effect is known as spectral leaking. Additionally an over or undershooting of the output signal close to the original peak positions is encountered. If there are many contributions close to one another in the output signal, these effects are particularly problematic fostering misinterpretations. Note, however, that the absolute value remains qualitatively the same, which is why, when interpreting discrete Fourier transforms one often sticks to describing properties of its absolute value. However, the peak positions, which are often most important, are now not hit precisely anymore due to an insufficient sampling. Another evident disadvantage is that any information concerning the sign is lost with this procedure. In summary, although both sampling describe the same function and, thus, are analytically described by the same Fourier transform, we obtain substantially different outcomes for the discrete Fourier transform.

Tackling the aforementioned problems of the discrete Fourier transform is the principal objective of Fourier analysis in signal processing. The idea is to modify the input signal in such a way that its spectral properties are enhanced in the discrete Fourier transform, while the so-introduced error stay negligibly small. One approach is to make the input signal *as periodic as possible*. This feature can be achieved through the multiplication by window functions, i.e.

$$c_{x_m} \mapsto c_{x_m} \cdot w(x_m) \tag{A.20}$$

There exist quite a bunch of such functions, each with certain properties, see e.g. [297, 49, 253] for an overview. In what follows we shall restrict ourselves to discussing only two representatives. We begin with the so-called von-Hann window which is defined via

$$w_{\mathrm{vH}}(x_m) = \frac{1}{2}\left(1 - \cos\left(\frac{2\pi m}{L-1}\right)\right). \tag{A.21}$$

The results for the discrete Fourier transform of the adjusted input signal are given in figure A.3. With the von-Hann window vanishing at its beginning and end, the input signal can obviously be periodically continued. Note that this feature may become problematic, if the input signal does not show any periodicity and takes particularly large values at the beginning. Moreover will the sanity check (A.16) not function anymore. Regarding our example function, however, the procedure works reasonably well. In comparison to the bare signal depicted in figure A.2 we find the absolute value of the ouput signal to be less broadened. Still, however, the agreement to the exact transform is only of qualitative nature. One finds the ringing effects in the real and imaginary part in figures A.3(f) and A.3(g) to be enhanced as compared to their respective counterparts in figure A.2. As an alternative to the von-Hann window we present the Hamming function

$$w_{\mathrm{H}}(x_m) = \frac{25}{46} - \frac{21}{46} \cdot \cos\left(\frac{2\pi m}{L-1}\right). \tag{A.22}$$

showing the corresponding results in figure A.4. With $w_{\mathrm{H}}(x_0) = {}^{4}\!/_{46} \neq 0$ (A.16) may now be applied again, multiplying the result by ${}^{46}\!/_{4}$. Other than that the results hardly differ from the modification with the von-Hann window, the only apparent difference being that the input signal again exhibits discontinuities.

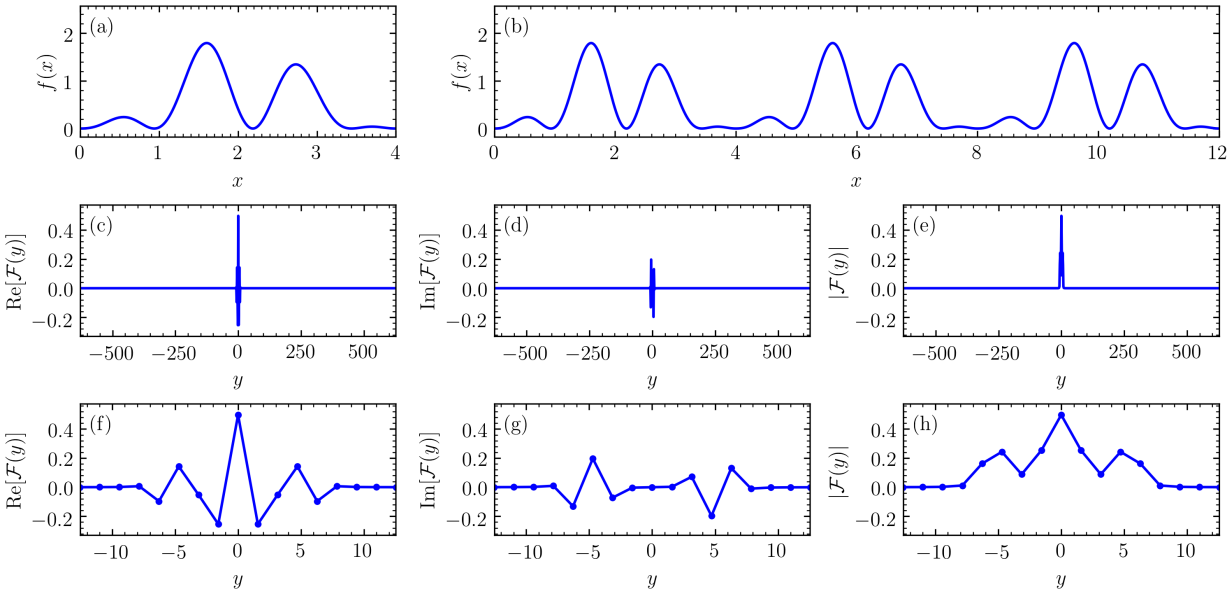

Figure A.3: Discrete Fourier transform of (A.17) adjusted with a von-Hann window for $L = 800$ and $\delta_x = 0.005$. Input signal (a) and its assumed continuation by the algorithm (b). Real part (c), imaginary part (d), and absolute value (e) of the discrete Fourier transform and respective zomms into the center of the spectrum (f), (g), and (h). In this example, the input signal covers a multiple of the input function's period.

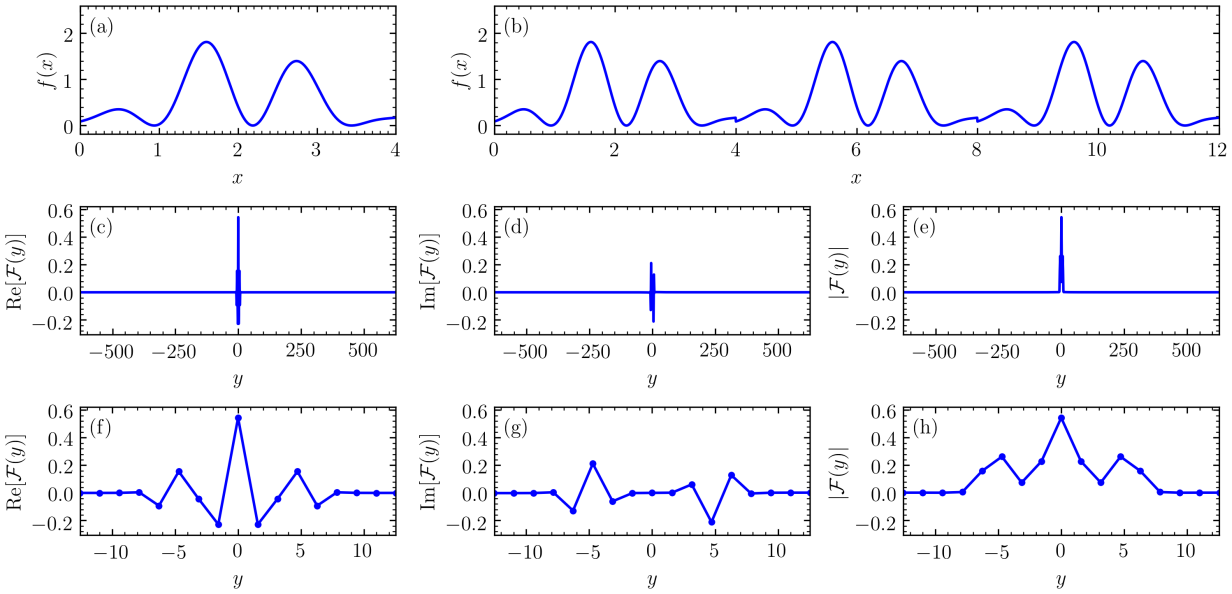

Figure A.4: Discrete Fourier transform of (A.17) adjusted with a Hamming window for $L = 800$ and $\delta_x = 0.005$. Input signal (a) and its assumed continuation by the algorithm (b). Real part (c), imaginary part (d), and absolute value (e) of the discrete Fourier transform and respective zomms into the center of the spectrum (f), (g), and (h). In this example, the input signal covers a multiple of the input function's period.

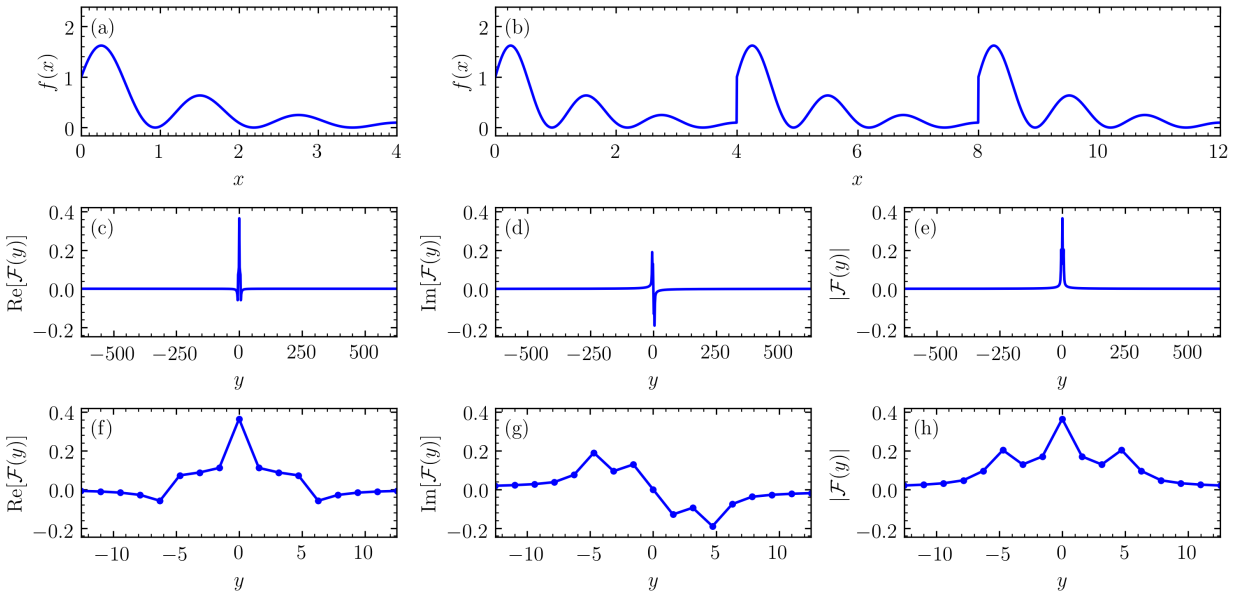

Figure A.5: Discrete Fourier transform of (A.17) modulated by a damping with $\eta = 0.75$ for $L = 800$ and $\delta_x = 0.005$. Input signal (a) and its assumed continuation by the algorithm (b). Real part (c), imaginary part (d), and absolute value (e) of the discrete Fourier transform and respective zomms into the center of the spectrum (f), (g), and (h). In this example, the input signal covers a multiple of the input function's period.

Another important modification of the input signal is the introduction of a damping

$$c_{x_m} \mapsto c_{x_m} \cdot \mathrm{e}^{-\eta \cdot x_m} \tag{A.23}$$

with the damping constant $\eta > 0$. We present the results for this procedure in figure A.5 finding them to be qualitatively the same as the application window functions in figures A.3 and A.4. Again, only the absolute value provides a proper basis for interpretations. Note that due to the damping the signal at earlier instances is preferred and, thus, is particularly useful for signals where the beginning differs considerably from the center and end. Modulating the input signal with a damping is, however, not only done by means of correcting the output signal removing unwanted side effects. Its primary aim is often also to apply a converging factor to the input signal, a property that is particularly useful when the input signal is known to contain degeneracies or increase towards its end. The actual choice of the value for the damping η is nevertheless a rather delicate affair. Chosen too large, it may suppress features at later signals of the input signal entirely, while when it takes an insufficiently large value numerical noise may turn out to be improperly removed. The choice is, thus, rather problem specific requiring some experience and often times several tries.

We have already mentioned that while the spectrum of the output signal, i.e. the range of the quantity y is rather large, the particular region is only poorly resolved. In section 3.6.3 we found that the resolution can be increased for a larger value of L. In practice one often has a signal of given length, of which the continuation is not known. The aim is now to continue the signal artificially without changing its content. There exists several techniques, e.g. linear prediction [270] where subsequent coefficients of the input signal are computed from fitting the given data. An easier approach is the so-called zero padding, where the size of the input signal is increased form

$$L \to L' \tag{A.24}$$

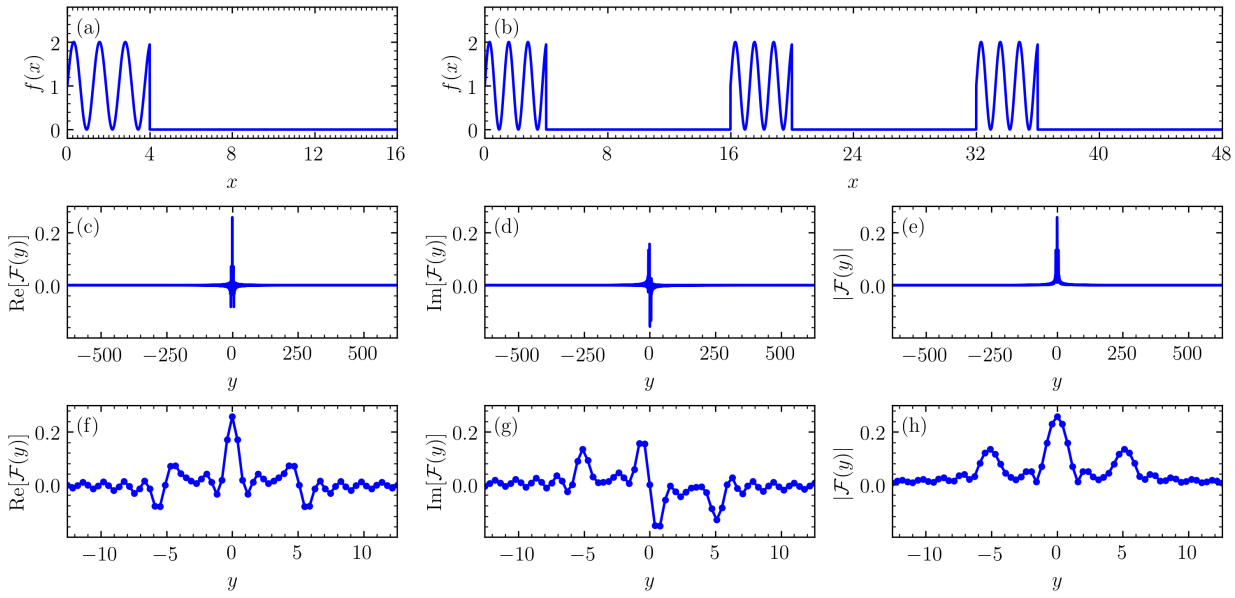

Figure A.6: Discrete Fourier transform of (A.17) with additional zero padding of $3L$ for $L = 800$ and $\delta_x = 0.005$. Input signal (a) and its assumed continuation by the algorithm (b). Real part (c), imaginary part (d), and absolute value (e) of the discrete Fourier transform and respective zomms into the center of the spectrum (f), (g), and (h). In this example, the input signal covers a multiple of the input function's period.

with L' being usually a multiple of L and setting all new coefficients to zero

$$c_{x_L} = \cdots = c_{x_{L'-1}} = 0. \tag{A.25}$$

Note that conversely, zero padding may also be understood in terms of the application of a rectangular window function, which of a given input signal will remove all entries for later instances. We present the effects of this procedure in figure A.6 where we have extended the length of the signal to four times its original size. From A.6(b) we find the obvious discontinuous nature of the so-defined input signal. One usually aims at choosing L' so large that the period of the discontinuity is too small to be resolved by the discrete spectrum. Comparing the results with the previous figures we find qualitatively the same behavior. However, the output signal now exhibits an enormous ringing, i.e. in addition to the expected peaks, there exist multiple smaller subpeaks. This is a particularly unwanted side effect of zero padding. When the output signal is unknown this feature may introduce significant errors to the output, especially when there are contributions to the spectrum of similar weight.

Zero padding is, thus, rarely used alone to modify the input signal, but rather in combination with one of the above methods. In figure A.7 we show the Fourier transforms combining the three measures introduced above with a zero padding of eight times the original length of the signal. In comparison to the analytical result and the previous figures we find only the absolute value to yield a proper interpretation. Bearing in mind, however that actually at the respective points one expects a delta peak the broadening of the output signal due to these measures becomes evident, a feature that is particularly problematic if the spectrum consists of components close to one another. We further note that there are still slight remnants of the ringing introduced by the zero padding in the output signal, which are, however, small compared to the signal's actual peaks.

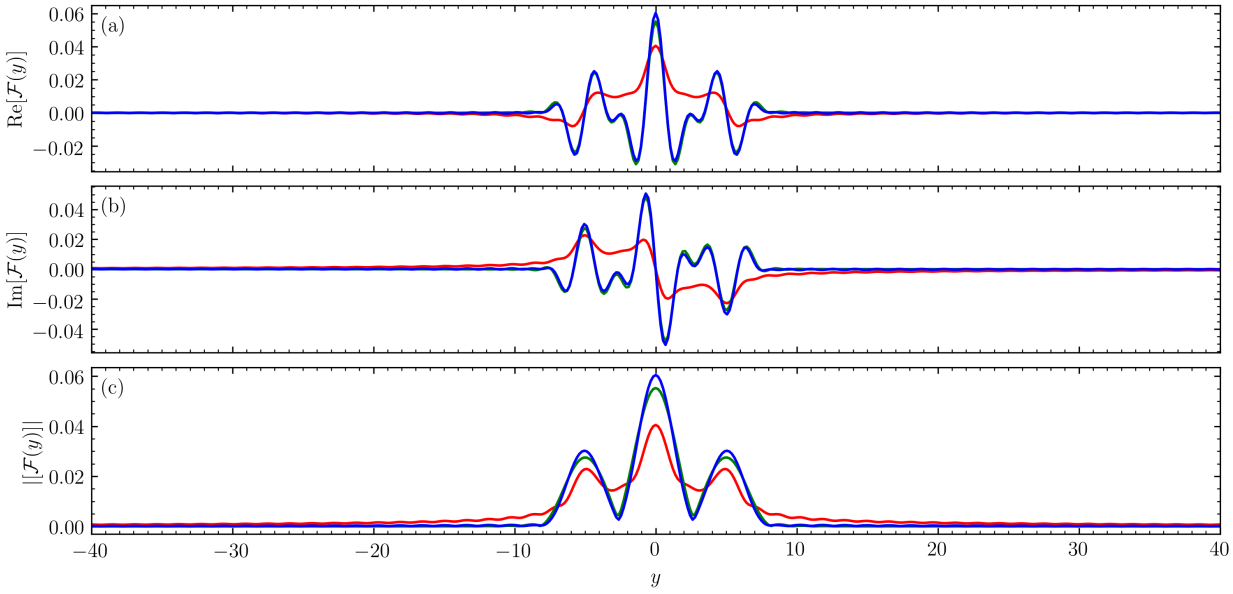

Figure A.7: Discrete Fourier transform of (A.17) with additional zero padding of $8L$ for $L = 800$ and $\delta_x = 0.005$ and a modification of the original data with a von-Hann window (green), a Hamming window (blue), and a damping of $\eta = 0.75$ (red): (a) real part, (b) imaginary part, (c) absolute value.

We conclude that the discrete Fourier transform in general yields results of only qualitative nature. Furthermore is in general only the absolute value to be interpreted, or should at least be considered predominantly, due to spectral leaking. Often times the input signal is on an excerpt, that is it does not start at the beginning of its period but is rather shifted by a phase, in our example (A.17) this could mean $\varphi \neq 0$. The absolute value is in particular useful when one is only interested in where spectral weight occurs, as it can be shown to be independent of this very phase. Window functions, damping and zero padding may smoothen the output signal, however they also introduce errors to the output signal, broaden actual peaks and may suppress properties of the input signal. We emphasize again that there is no generic procedure to obtain the best output signal from a discrete Fourier transform as the choice of the appropriate technique depends largely on properties of the input signal. It is, hence, advisable to vary procedures in advance before choosing a final scheme. Moreover, when it comes to comparing different data sets and their discrete Fourier transforms, it is highly recommendable to use the same technique to have the same artifacts to be expected.

A.1.7 Transforming Non-periodic Signals Exploiting Symmetries

In the previous section we found that discrete Fourier transforms most often only yield qualitative results, only the absolute value being of importance when it comes to interpreting the output signal. If, however, an additional symmetry is known to exists to the data, its inclusion into the discrete Fourier transform results in a considerably better understanding of the output signal.

An important symmetry in the context of physics is given by

$$c_{x_{-m}} = c^*_{x_m}. \tag{A.26}$$

Suppose now, we have an input signal of length L and know that (A.26) holds true. We extend the input signal to be of length $L' = 2L - 1$ adding coefficients

$$c_{x_{2L-m}} = c^*_{x_m} \quad \forall \quad m \in \{1, \dots, L-1\}\,. \tag{A.27}$$

We have, thus, added the preceding values of the input signal accoring to (A.26) to its end making use of equation (3.65). As a result, we obtain

$$\begin{aligned}
c_{y_\mu} &= \frac{1}{L}\sum_{x_m} \mathrm{e}^{-\mathrm{i}x_m y_\mu} c_{x_m} = \frac{1}{L}\mathrm{e}^{-\mathrm{i}x_0 y_\mu} c_{x_0} + \frac{1}{L}\sum_{m=1}^{2L-1} \mathrm{e}^{-\mathrm{i}x_m y_\mu} c_{x_m} && \text{(A.28a)}\\
&= \frac{1}{L} c_{x_0} + \frac{1}{L}\sum_{m=1}^{L-1} \left(\mathrm{e}^{-\mathrm{i}x_m y_\mu} c_{x_m} + \mathrm{e}^{-\mathrm{i}x_{2L-m} y_\mu} c_{x_{2L-m}}\right) && \text{(A.28b)}\\
&= \frac{1}{L} c_{x_0} + \frac{1}{L}\sum_{m=1}^{L-1} \left(\mathrm{e}^{-\mathrm{i}x_m y_\mu} c_{x_m} + \mathrm{e}^{-\mathrm{i}x_{-m} y_\mu} c^*_{x_m}\right) && \text{(A.28c)}\\
&= \frac{1}{L} c_{x_0} + \frac{1}{L}\sum_{m=1}^{L-1} \left(\mathrm{e}^{-\mathrm{i}x_m y_\mu} c_{x_m} + \mathrm{e}^{\mathrm{i}x_m y_\mu} c^*_{x_m}\right) && \text{(A.28d)}\\
&= \frac{\mathrm{i}}{L}\mathrm{Im}\left[c_{x_0}\right] + \frac{1}{L}\mathrm{Re}\left[c_{x_0}\right] + \frac{2}{L}\sum_{m=1}^{L-1} \mathrm{Re}\left[\mathrm{e}^{-\mathrm{i}x_m y_\mu} c_{x_m}\right] && \text{(A.28e)}
\end{aligned}$$

again using (3.65). Note that in order to obtain a smooth output signal, we could have additionally first damped the input signal and then applied zeros to its end as described in the preceding section.

We find the output signal to be entirely real apart from an imaginary contribution of the input signal's first entry. If this term also vanishes we are not restricted to interpreting only the absolute value anymore. In fact, even if the imaginary part does not vanish do we know it to only occur at one instance of the output signal, which we may regard separately. Hence, using the symmetry (A.26) we managed to keep the sign information of the discrete Fourier transform. This feature is highly useful when it comes to interpreting data, in particular if other constraints apply, e.g. the requirement for all values to be positive.

In figure A.8 we illustrate this procedure for the example function

$$f(x) = \cos(\omega_0 \cdot x) - \cos(\omega_1 \cdot x)\,, \quad \omega_0 = 2\pi \cdot \frac{4}{5} \approx 5.03, \quad \omega_1 = 2\pi \cdot \frac{7}{5} \approx 8.8, \tag{A.29}$$

for which (A.26) clearly holds true with (A.19), having also damped the input signal and applied zero padding as mentioned before. The Fourier transform given by, c.f. (3.38) and (3.44),

$$\frac{\mathscr{F}[f(x)](y)}{2\pi} = \frac{1}{2}\left(\delta(y+\omega_0) + \delta(y-\omega_0) - \delta(y+\omega_1) - \delta(y-\omega_1)\right). \tag{A.30}$$

we show the numerical results for different dampings η. We find that all output signals resemble the analytical result quite well having in mind our findings from the previous section. Despite a broadening due to zero padding and damping the peaks including their orientation match their expected position. We also briefly discuss the effects of a damping at this example. For $\eta = 0.5$ the input signal is clearly underdamped with considerable ringing amplitudes being clearly visible. On the other hand, for $\eta = 3.0$ the signal is overdamped, the exact peak positions being hardly distinguishable. For the intermediate dampings $\eta = 0.75, 1.0, 1.5$ the informational gain in equal the

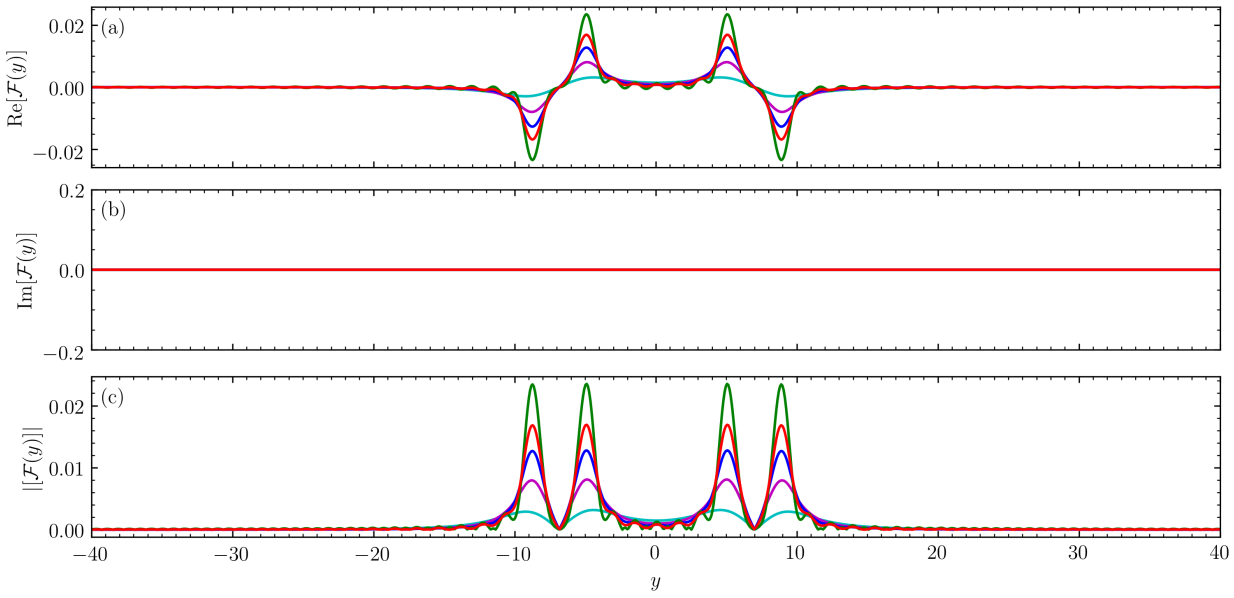

Figure A.8: Discrete Fourier transform of (A.29) exploiting (A.26) with additional zero padding of $8L$ for a given signal of $L = 800$ with $\delta_x = 0.005$ and a damping of $\eta = 3.0$ (cyan), $\eta = 1.5$ (magenta), $\eta = 1.0$ (blue), $\eta = 0.75$ (red), and $\eta = 0.5$ (green): (a) real part, (b) imaginary part, (c) absolute value.

peaks broadening more and more with increasing damping. An appropriate choice for η is thus a value at which ringing effects are vaguely visible allowing to classify them as an numerical artefact thereby depicting the maximally resolvable peak sizes. We close this section with the remark that in this procedure the damping must not be substituted by the application of a von-Hann or Hamming window, (A.21) or (A.22), respectively, as these procedures will yield very wrong results further illustrating the challenge of finding the proper scheme to apply a discrete Fourier transform.

A.2 The Discrete Sine Transform

We discuss the one-dimensional discrete sine transform from real to reciprocal space. In strict analogy to the problem outlined in section A.1.1 we wish to transform a quantity given at a position r_m into another quantity given for a momentum k_μ thereby identifying $x = r$ and $y = k$.

With L as the length of the system the (quasi) position, i.e. after the implicit inclusion of the original input signal, is given by

$$r_m = a \cdot m, \quad m \in \{1, \dots, L\}, \quad \Rightarrow \quad r_m \in \{a, \dots, La\}, \tag{A.31}$$

with the lattice constant $a = \delta_r$. The discrete sine transform is best suited for physical problems with open boundaries. With the inclusion of two extra data points of zero in (3.88) and (3.89) the underlying idea for the quantum mechanical wave function to vanish at the edges of a system with open boundaries is implemented. The extension according to (3.90) is then purely mathematical and has no further physical interpretation. Thus, for the (quasi) momenta we obtain

$$k_\mu = \frac{\pi}{(L+1)\,a} \cdot \mu, \quad \mu \in \{1, \dots, L\}, \quad \Rightarrow \quad k_\mu \in \left\{ \frac{\pi}{(L+1)\,a}, \dots, \frac{\pi}{(L+1)\,a} \cdot L \right\}, \tag{A.32}$$

where, again, we have set $\hbar = 1$, and their step size is given by

$$\delta_k = \frac{\pi}{(L+1)\,a}. \tag{A.33}$$

Clearly, the quasi momenta cover only half of the Brillouin zone, which is a direct consequence of the quasi positions technically covering only half of the input signal after its enhancement. Likewise, there is no physical meaning to the transformed data for negative quasi momenta. Hence, for both the positions and momenta, only positive values are considered and the prefix "quasi" is dropped in general discussions.

B Simple Illustrations for MPSs

We consider the maximum dimensions the individual matrices need to take in order for an MPS to exactly represent its associated quantum state. As already explained in section 4.2, in general an exact representation requires $2\sum_{i=1}^{\lfloor L/2 \rfloor} d^{2i} + (L \mod 2)\, d^{2\lfloor L/2 \rfloor + 1}$ matrix elements. The approach to reduce this number is then to introduce a maximum dimension of $(\chi_{\max} \times \chi_{\max})$ to the matrices. For large enough system sizes L this then leads to a dramatic decrease in the number of elements to be operated with and, hence, an enormous speed-up in runtime, as well as a significant decrease in computational resources. An example illustrating these considerations is presented in figure B.1.

We close this introduction to matrix product states with a few examples, similar to the presentation in [4], thereby motivating the subsequent sections. Let us consider a one-dimensional system of length $L = 4$ with a local Hilbert space dimension of $d = 2$, e.g. a spin-$1/2$ system with $\sigma_i \in \{\uparrow, \downarrow\}\ \forall i$. First, we want to encode the state $|\psi^1\rangle = |\uparrow\uparrow\downarrow\uparrow\rangle$ as a product of matrices. This is possible using the matrices given in figure B.2. The state $|\psi^1\rangle$ is obviously a product state consisting of just one basis state. Hence, the matrices M^{σ_i} need to be chosen in such a way that only one combination of multiplications of one representative per site i yields a value of 1 whilst all the other products vanish such that they will not contribute to the superposition in equation (4.3). The bottom two lines in figure B.2 show a choice of a set of matrices M^{σ_i} obeying the dimensions given above. However, as can be seen in lines three and four there exists another (by far more convenient) choice of a set of matrices M^{σ_i} with significantly less dimensions. On a large scale such a simplification may dramatically increase the performance of an MPS-based code. Hence, the numbers for the matrix dimensions given above only serve as an upper bound for the number of matrix elements to be operated with. Next, we decompose the state $|\psi^2\rangle = 1/\sqrt{2}\,|\uparrow\downarrow\downarrow\uparrow\rangle + 1/\sqrt{2}\,|\uparrow\uparrow\downarrow\uparrow\rangle$, which also is a product state, into a product of matrices. The result is depicted in figure B.3 As can be seen immediately the matrix decomposition of this state can also be chosen in such a way that only matrices of trivial dimensions (1×1) need to be applied. These observation lead to the claim that the matrix dimensions will have to decrease if the state to be compressed is entangled. Indeed this is the case which we will demonstrate by attempting to express $|\psi^3\rangle = 1/\sqrt{3}\,|\uparrow\uparrow\uparrow\uparrow\rangle + 1/\sqrt{3}\,|\downarrow\downarrow\downarrow\downarrow\rangle + 1/\sqrt{3}\,|\uparrow\downarrow\downarrow\uparrow\rangle$ in terms of MPSs as can be obtained from figure B.4. For this state there is no decomposition making use of only (1×1) matrices. Instead, the maximum number of matrix dimensions possible needs to be exploited to represent only the desired basis states in the sum according to equation (4.3). Note that this is still a rather simple case and that here all three basis states contribute equally to the total state $|\psi^3\rangle$ – which rarely occurs in many-body problems. Despite its simplicity, however, this example illustrates the effects of truncation very well. Suppose that we will only allow a maximum matrix dimension of $\chi_{\max} = 3$. Hence, the second and third matrix need to be truncated to matrices of dimension (2×3) and (3×2) respectively. This procedure will obviously introduce an error to the MPS representation of the state $|\psi^3\rangle$. A first and very naive way to perform this truncation might be to just omit the fourth column for matrices M^{σ_2} and the fourth row for matrices M^{σ_3}. This procedure will naturally reduce the matrices to the maximum allowed dimensions, however it comes with the severe drawback that the obtained MPS representation will now encode the state $|\tilde{\psi}^3\rangle = 1/\sqrt{3}\,|\uparrow\uparrow\uparrow\uparrow\rangle + 1/\sqrt{3}\,|\uparrow\downarrow\downarrow\uparrow\rangle$ which is in no way close to the original state $|\psi^3\rangle$ also loosing its normalization.

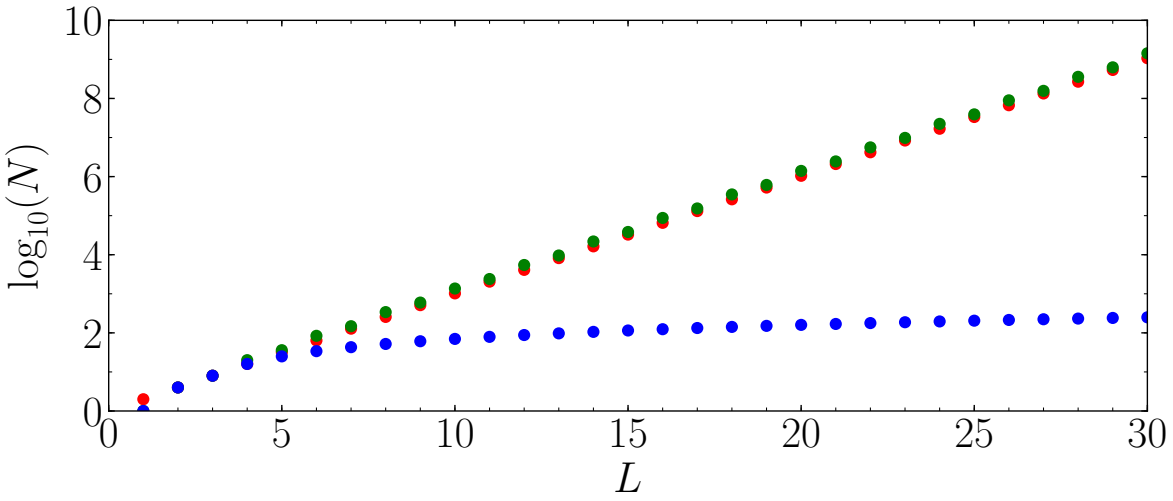

Figure B.1: Comparison of the number N of coefficients $c_{\sigma_1,\sigma_2,\ldots,\sigma_{L-1},\sigma_L}$ (red) versus the number N of matrix elements of an MPS representation of state $|\psi\rangle$ with (blue) and without (green) truncation $\chi_{\max} = 3$ for different system sizes L with a local Hilbert space dimension of $d = 2$. Note that the number of coefficients grows exponentially in L and is surpassed by the number of matrix elements if no truncation is employed. With truncation, however, the number of matrix elements only grows polynomially leading to a massive increase in performance.

$$
\begin{array}{rcccccc}
|\psi^1\rangle & = & | & \uparrow & \uparrow & \downarrow & \uparrow & \rangle \\
i & = & & 1 & 2 & 3 & 4 & \\
M_i^{\uparrow} & = & & (1) & (1) & (0) & (1) & \\
M_i^{\downarrow} & = & & (0) & (0) & (1) & (0) & \\
M_i^{\uparrow} & = & & \begin{pmatrix} 1 & 0 \end{pmatrix} & \begin{pmatrix} 1 & 0 & 0 & 0 \\ 0 & 0 & 0 & 0 \end{pmatrix} & \begin{pmatrix} 0 & 0 \\ 0 & 0 \\ 0 & 0 \\ 0 & 0 \end{pmatrix} & \begin{pmatrix} 1 \\ 0 \end{pmatrix} & \\
M_i^{\downarrow} & = & & \begin{pmatrix} 0 & 0 \end{pmatrix} & \begin{pmatrix} 0 & 0 & 0 & 0 \\ 0 & 0 & 0 & 0 \end{pmatrix} & \begin{pmatrix} 1 & 0 \\ 0 & 0 \\ 0 & 0 \\ 0 & 0 \end{pmatrix} & \begin{pmatrix} 0 \\ 0 \end{pmatrix} &
\end{array}
$$

Figure B.2: Representation of the state $|\psi^1\rangle = |\uparrow\uparrow\downarrow\uparrow\rangle$ in terms of matrix products.

$$
\begin{array}{rcll}
|\psi^2\rangle & = & \frac{1}{\sqrt{2}} \; | & \uparrow \quad \downarrow \quad \downarrow \quad \uparrow \quad \rangle \\
 & & +\frac{1}{\sqrt{2}} \; | & \uparrow \quad \uparrow \quad \downarrow \quad \uparrow \quad \rangle \\
i & = & & 1 \qquad 2 \qquad 3 \qquad 4 \\
M_i^{\uparrow} & = & & \left(\frac{1}{\sqrt{2}}\right) \quad (1) \quad (0) \quad (1) \\
M_i^{\downarrow} & = & & (0) \quad (1) \quad (1) \quad (0) \\
M_i^{\uparrow} & = & & \begin{pmatrix} \frac{1}{\sqrt{2}} & 0 \end{pmatrix} \quad \begin{pmatrix} 1 & 0 & 0 & 0 \\ 0 & 0 & 0 & 0 \end{pmatrix} \quad \begin{pmatrix} 0 & 0 \\ 0 & 0 \\ 0 & 0 \\ 0 & 0 \end{pmatrix} \quad \begin{pmatrix} 1 \\ 0 \end{pmatrix} \\
M_i^{\downarrow} & = & & \begin{pmatrix} 0 & 0 \end{pmatrix} \quad \begin{pmatrix} 1 & 0 & 0 & 0 \\ 0 & 0 & 0 & 0 \end{pmatrix} \quad \begin{pmatrix} 1 & 0 \\ 0 & 0 \\ 0 & 0 \\ 0 & 0 \end{pmatrix} \quad \begin{pmatrix} 0 \\ 0 \end{pmatrix}
\end{array}
$$

Figure B.3: Representation of the state $|\psi^2\rangle = {}^1/\sqrt{2}\,|\uparrow\downarrow\downarrow\uparrow\rangle + {}^1/\sqrt{2}\,|\uparrow\uparrow\downarrow\uparrow\rangle$ in terms of matrix products.

$$
\begin{array}{rcll}
|\psi^3\rangle & = & \frac{1}{\sqrt{3}} \; | & \uparrow \quad \uparrow \quad \uparrow \quad \uparrow \quad \rangle \\
 & & +\frac{1}{\sqrt{3}} \; | & \downarrow \quad \downarrow \quad \downarrow \quad \downarrow \quad \rangle \\
 & & +\frac{1}{\sqrt{3}} \; | & \uparrow \quad \downarrow \quad \downarrow \quad \uparrow \quad \rangle \\
i & = & & 1 \qquad 2 \qquad 3 \qquad 4 \\
M_i^{\uparrow} & = & & (1 \quad 1) \quad \begin{pmatrix} 1 & 0 & 0 & 0 \\ 0 & 0 & 0 & 0 \end{pmatrix} \quad \begin{pmatrix} 1 & 0 \\ 0 & 0 \\ 0 & 0 \\ 0 & 0 \end{pmatrix} \quad \begin{pmatrix} \frac{1}{\sqrt{3}} \\ 0 \end{pmatrix} \\
M_i^{\downarrow} & = & & (0 \quad 1) \quad \begin{pmatrix} 0 & 0 & 1 & -1 \\ 0 & 0 & 0 & 1 \end{pmatrix} \quad \begin{pmatrix} 0 & 0 \\ 0 & 0 \\ 1 & 0 \\ 0 & 1 \end{pmatrix} \quad \begin{pmatrix} 0 \\ \frac{1}{\sqrt{3}} \end{pmatrix}
\end{array}
$$

Figure B.4: Representation of the state $|\psi^3\rangle = {}^1/\sqrt{3}\,|\uparrow\uparrow\uparrow\uparrow\rangle + {}^1/\sqrt{3}\,|\downarrow\downarrow\downarrow\downarrow\rangle + {}^1/\sqrt{3}\,|\uparrow\downarrow\downarrow\uparrow\rangle$ in terms of matrix products. Red: Elements to be omitted when naively truncating the matrices to be of no larger dimension $\chi_{\max} = 3$. This truncation will neither represent the original state $|\psi^3\rangle$ but rather $|\tilde{\psi}^3\rangle = {}^1/\sqrt{3}\,|\uparrow\uparrow\uparrow\uparrow\rangle + {}^1/\sqrt{3}\,|\uparrow\downarrow\downarrow\uparrow\rangle$ nor will it preserve the normalization.

C Comparison of Variants of the Discrete Fourier Transform and Their Effect on the Spectral Function

We discuss how different approaches to tackle spectral leaking as introduced in appendix A.1.6 affect spectral functions which we defined in section 6.1.2. Here we consider the example of $\mathscr{A}^{<}_{\sigma}(k,\omega,t=0)$ immediately after the electron-hole excitation (9.1) for $\hat{H}^{4\Delta}$ with $U/t_{\mathrm{hop}}=0$ and $\Delta/t_{\mathrm{hop}}=2$ at half filling only, c.f. figures 9.1(c) and (d), section 9.1.1. Note that since this is a non-interacting problem it may be solved analytically, as contrary to equation (6.13) Hermitian symmetry in t' actually holds true, c.f. section 6.1.3. We nevertheless chose an exactly solvable model at this point to illustrate the effects of the different approaches and their deviation form the exact results. This particular choice has the additional advantage that since both spin sectors in this model are entirely decoupled, with the excitation only in the spin-↑ direction, the spin-↓ direction will resemble the ground state, such that we are allowed to study the post-excitation behavior as well with just a single evaluation of the data.

Before we begin, however, we first show that using relative coordinates, both the lesser, as well as the greater spectral function are positive real quantities for a time-independent Hamiltonian regardless of whether the system is interacting or not. Therefore, we again make use of the Lehmann representation we encountered multiple times in chapter 6 and exploit that in this case the time evolution operator is given by

$$U(t_2,t_1)\left|\psi\right\rangle = \mathrm{e}^{-\mathrm{i}\hat{H}(t_2-t_1)}\left|\psi\right\rangle, \tag{C.1}$$

c.f. also equation (6.17). Thus, for the lesser spectral function we find

$$\begin{aligned}
\mathscr{A}^{<}(k,\omega,t) &= \int_{-\infty}^{\infty}\mathrm{d}t'\mathrm{e}^{-\mathrm{i}\omega t'}\left\langle\psi(t)\right|\hat{c}_k^{\dagger}(t')\,\hat{c}_k\left|\psi(t)\right\rangle && \text{(C.2a)}\\
&= \sum_{n,m,p}\int_{-\infty}^{\infty}\mathrm{d}t'\mathrm{e}^{-\mathrm{i}\omega t'}\left\langle\psi(t)\middle|m^M\right\rangle\left\langle m^M\right|\mathrm{e}^{\mathrm{i}\hat{H}t'}\hat{c}_k^{\dagger}\mathrm{e}^{-\mathrm{i}\hat{H}t'}\left|n^{M-1}\right\rangle\\
&\quad \left\langle n^{M-1}\right|\hat{c}_k\left|p^M\right\rangle\left\langle p^M\middle|\psi(t)\right\rangle && \text{(C.2b)}\\
&= \sum_{n,m,p}\int_{-\infty}^{\infty}\mathrm{d}t'\mathrm{e}^{-\mathrm{i}(\omega-(E_m^M-E_n^{M-1}))t'}\left\langle\psi(t)\middle|m^M\right\rangle\left\langle m^M\right|\hat{c}_k^{\dagger}\left|n^{M-1}\right\rangle\\
&\quad \left\langle n^{M-1}\right|\hat{c}_k\left|p^M\right\rangle\left\langle p^M\middle|\psi(t)\right\rangle && \text{(C.2c)}\\
&= \sum_{n}\int_{-\infty}^{\infty}\mathrm{d}t'\mathrm{e}^{-\mathrm{i}\left(\omega-\left(E_{(n+1)}^M-E_n^{M-1}\right)\right)t'}\left\langle\psi(t)\middle|(n+1)^M\right\rangle\left\langle(n+1)^M\right|\hat{c}_k^{\dagger}\left|n^{M-1}\right\rangle\\
&\quad \left\langle n^{M-1}\right|\hat{c}_k\left|(n+1)^M\right\rangle\left\langle(n+1)^M\middle|\psi(t)\right\rangle && \text{(C.2d)}\\
&= \sum_{n}\delta\left(\omega-\left(E_{(n+1)}^M-E_n^{M-1}\right)\right)\left|\left\langle(n+1)^M\right|\hat{c}_k^{\dagger}\left|n^{M-1}\right\rangle\right|^2\left|\left\langle(n+1)^M\middle|\psi(t)\right\rangle\right|^2. && \text{(C.2e)}
\end{aligned}$$

The greater spectral function is given analogously via

$$\mathscr{A}^{>}(k,\omega,t) = \int_{-\infty}^{\infty}\mathrm{d}t'\mathrm{e}^{-\mathrm{i}\omega t'}\left\langle\psi(t)\right|\hat{c}_k\hat{c}_k^{\dagger}(t')\left|\psi(t)\right\rangle \tag{C.3a}$$

$$= \sum_{n,m,p} \int_{-\infty}^{\infty} \mathrm{d}t' \mathrm{e}^{-\mathrm{i}\omega t'} \langle \psi(t) | m^M \rangle \langle m^M | \hat{c}_k | n^{M+1} \rangle \langle n^{M+1} | \mathrm{e}^{\mathrm{i}\hat{H}t'} \hat{c}_k^\dagger \mathrm{e}^{-\mathrm{i}\hat{H}t'} | p^M \rangle \langle p^M | \psi(t) \rangle \tag{C.3b}$$

$$= \sum_{n,m,p} \int_{-\infty}^{\infty} \mathrm{d}t' \mathrm{e}^{-\mathrm{i}(\omega + (E_p^M - E_n^{M+1}))t'} \langle \psi(t) | m^M \rangle \langle m^M | \hat{c}_k | n^{M+1} \rangle \langle n^{M+1} | \hat{c}_k^\dagger | p^M \rangle \langle p^M | \psi(t) \rangle \tag{C.3c}$$

$$= \sum_{n} \int_{-\infty}^{\infty} \mathrm{d}t' \mathrm{e}^{-\mathrm{i}\left(\omega + \left(E_{(n-1)}^M - E_n^{M+1}\right)\right)t'} \langle \psi(t) | (n-1)^M \rangle \langle (n-1)^M | \hat{c}_k | n^{M+1} \rangle \langle n^{M+1} | \hat{c}_k^\dagger | (n-1)^M \rangle \langle (n-1)^M | \psi(t) \rangle \tag{C.3d}$$

$$= \sum_{n} \delta\left(\omega + \left(E_{(n-1)}^M - E_n^{M+1}\right)\right) \left| \langle (n-1)^M | \hat{c}_k | n^{M+1} \rangle \right|^2 \left| \langle (n-1)^M | \psi(t) \rangle \right|^2. \tag{C.3e}$$

Note that, unfortunately, these equations do not hold when Wigner coordinates are employed, since the state $|\psi\rangle$ also depends on t' and, hence, the Fourier transform cannot be guaranteed to be positive. Note further that in practice in the above calculations we have $t' \geq 0$ which, however, leads to similar results for the real part of the Fourier transform.

Even so, however, also when using relative coordinates, not assuming Hermitian symmetry in t' and not mirroring the input signal as explained in appendix A.1.7 has some unpleasant side effects. First, it may lead to unphysical negative spectral weights, and second the imaginary part of the output signal is not guaranteed to vanish, c.f. also section 6.1.2. Therefore we shall now examine the real and imaginary part, as well as the absolute value of the spectral function to gain a complete overview of the situation. To better illustrate negative weights we have changed the color code for the two former observables.

We begin by adjusting the input signal of the Fourier transform from time to frequency space with a von-Hann window and applying zero padding of eight times the signal's length. The resulting spectral function is then presented in figures C.1, C.2, and C.3 showing its real, imaginary part, and absolute value, respectively. For the former two, we find major overshootings in the output

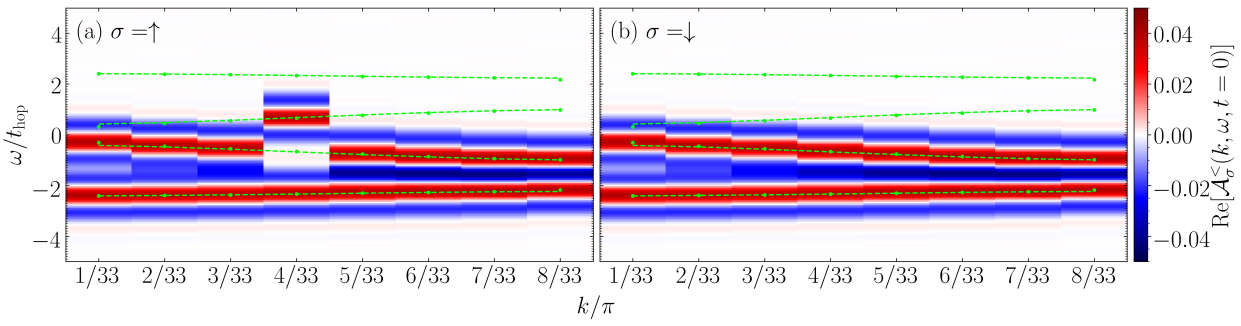

Figure C.1: Real part of the single particle spectral functions $\mathscr{A}_\sigma^<(k, \omega, t = 0)$ immediately after the electron-hole excitation (9.1) for $\hat{H}^{4\Delta}$ with $U/t_{\mathrm{hop}} = 0$ and $\Delta/t_{\mathrm{hop}} = 2$ for a system of $L = 32$ sites with OBCs in the first BZ at half filling. (a) shows the spin-↑ direction, (b) the spin-↓ direction. The green dashed lines show the band structure of the non-interacting system calculated with PBCs, the green dots correspond to the calculation with OBCs. For these computations the signal was adjusted with a von-Hann window and enhanced with a string of zeros eight times its length.

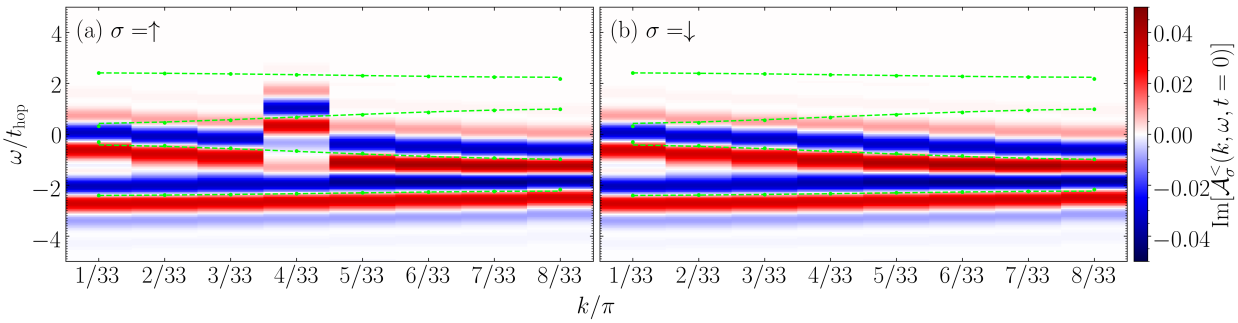

Figure C.2: Imaginary part of the single particle spectral functions $\mathcal{A}_\sigma^<(k,\omega,t=0)$ immediately after the electron-hole excitation (9.1) for $\hat{H}^{4\Delta}$ with $U/t_{\mathrm{hop}}=0$ and $\Delta/t_{\mathrm{hop}}=2$ for a system of $L=32$ sites with OBCs in the first BZ at half filling. (a) shows the spin-↑ direction, (b) the spin-↓ direction. The green dashed lines show the band structure of the non-interacting system calculated with PBCs, the green dots correspond to the calculation with OBCs. For these computations the signal was adjusted with a von-Hann window and enhanced with a string of zeros eight times its length.

signal making a reasonable analysis impossible. We conclude that in this case, only the absolute value should be interpreted. Here, the results match the analytical results. Comparing to figures 9.1(c) and (d) we find significantly less oscillations close to the actual bands. However, the entire spectrum is less sharply reproduced.

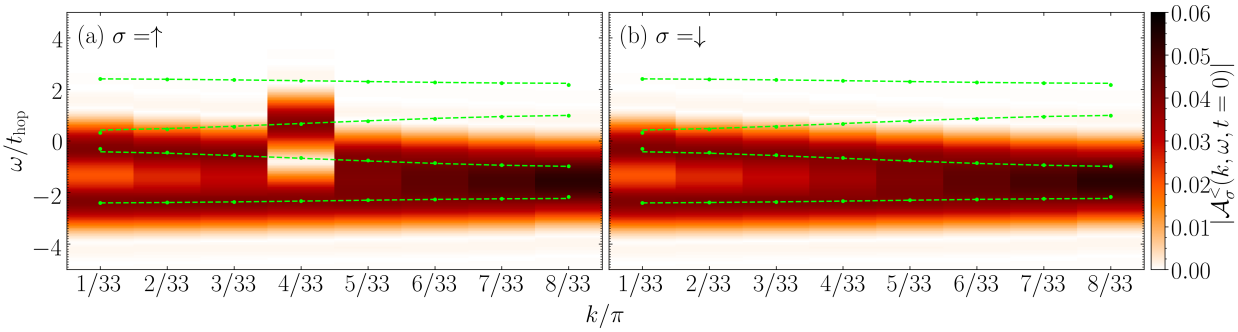

Figure C.3: Absolute value of the single particle spectral functions $\mathcal{A}_\sigma^<(k,\omega,t=0)$ immediately after the electron-hole excitation (9.1) for $\hat{H}^{4\Delta}$ with $U/t_{\mathrm{hop}}=0$ and $\Delta/t_{\mathrm{hop}}=2$ for a system of $L=32$ sites with OBCs in the first BZ at half filling. (a) shows the spin-↑ direction, (b) the spin-↓ direction. The green dashed lines show the band structure of the non-interacting system calculated with PBCs, the green dots correspond to the calculation with OBCs. For these computations the signal was adjusted with a von-Hann window and enhanced with a string of zeros eight times its length.

As can be seen in figures C.4, C.5, and C.6 we find essentially the same behavior when substituting the von-Hann window by a Hamming window.

Lastly, we investigate the procedure of applying a damping and eight times zero padding without assuming Hermitian symmetry in t'. The real part shown in figure C.7 resembles the reference results in figures 9.1(c) and (d) quite well. Interestingly, for this example, there are no negative weights, which, however must not be understood as a general statement. However, the imaginary part now takes non-zero values contrary to the analytical result, c.f. figure C.8. Hence, in general it

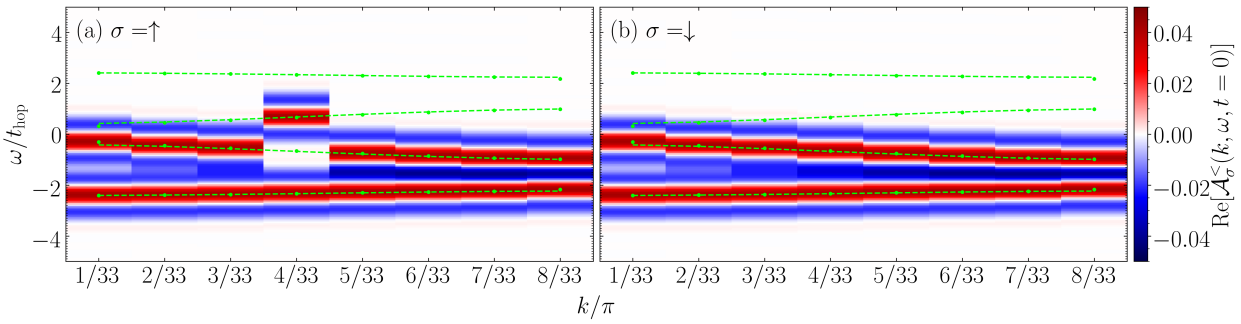

Figure C.4: Real part of the single particle spectral functions $\mathcal{A}^{<}_{\sigma}(k,\omega,t=0)$ immediately after the electron-hole excitation (9.1) for $\hat{H}^{4\Delta}$ with $U/t_{\mathrm{hop}}=0$ and $\Delta/t_{\mathrm{hop}}=2$ for a system of $L=32$ sites with OBCs in the first BZ at half filling. (a) shows the spin-↑ direction, (b) the spin-↓ direction. The green dashed lines show the band structure of the non-interacting system calculated with PBCs, the green dots correspond to the calculation with OBCs. For these computations the signal was adjusted with a Hamming window and enhanced with a string of zeros eight times its length.

appears to be advantageous to, again, interpret the absolute value as shown in figure C.9. Here, the results match the reference data in figures 9.1(c) and (d) well again, however, with a significantly stronger background. As a positive side effect, on the other hand, the oscillations in the reference data are now suppressed.

We conclude that for the numerical computations of spectral functions it is best to make use of Hermitian symmetry in t' when its application is physically reasonable. In other cases damping and zero padding the input signal may already lead to satisfactory results for the real part, while the absolute value should always be considered as interpretable in order to be able to rule out effects originating from spectral leaking.

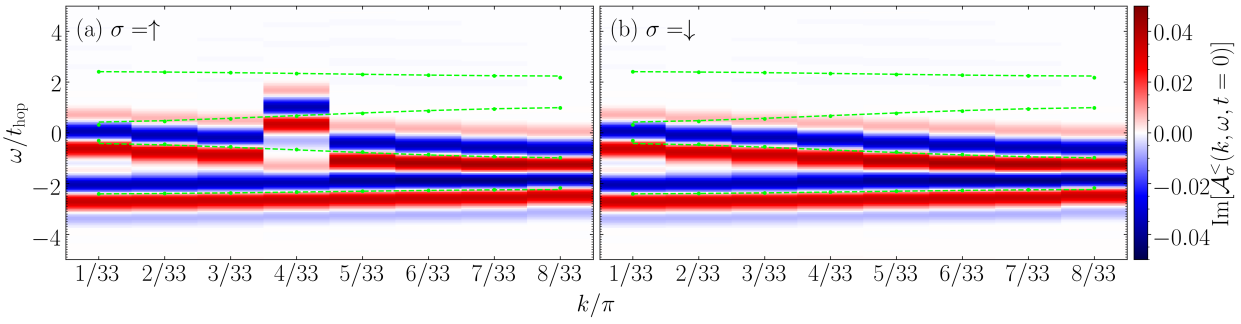

Figure C.5: Imaginary part of the single particle spectral functions $\mathcal{A}^{<}_{\sigma}(k,\omega,t=0)$ immediately after the electron-hole excitation (9.1) for $\hat{H}^{4\Delta}$ with $U/t_{\mathrm{hop}}=0$ and $\Delta/t_{\mathrm{hop}}=2$ for a system of $L=32$ sites with OBCs in the first BZ at half filling. (a) shows the spin-↑ direction, (b) the spin-↓ direction. The green dashed lines show the band structure of the non-interacting system calculated with PBCs, the green dots correspond to the calculation with OBCs. For these computations the signal was adjusted with a Hamming window and enhanced with a string of zeros eight times its length.

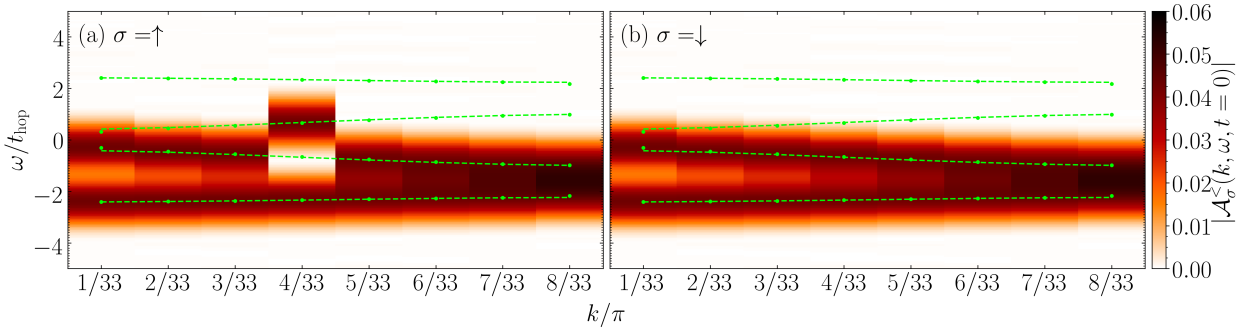

Figure C.6: Absolute value of the single particle spectral functions $\mathcal{A}_\sigma^<(k,\omega,t=0)$ immediately after the electron-hole excitation (9.1) for $\hat{H}^{4\Delta}$ with $U/t_{\mathrm{hop}}=0$ and $\Delta/t_{\mathrm{hop}}=2$ for a system of $L=32$ sites with OBCs in the first BZ at half filling. (a) shows the spin-↑ direction, (b) the spin-↓ direction. The green dashed lines show the band structure of the non-interacting system calculated with PBCs, the green dots correspond to the calculation with OBCs. For these computations the signal was adjusted with a Hamming window and enhanced with a string of zeros eight times its length.

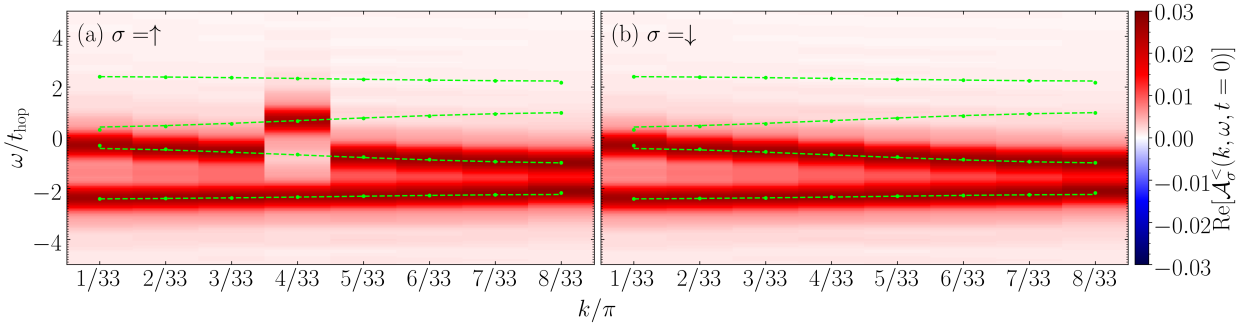

Figure C.7: Real part of the single particle spectral functions $\mathcal{A}_\sigma^<(k,\omega,t=0)$ immediately after the electron-hole excitation (9.1) for $\hat{H}^{4\Delta}$ with $U/t_{\mathrm{hop}}=0$ and $\Delta/t_{\mathrm{hop}}=2$ for a system of $L=32$ sites with OBCs in the first BZ at half filling. (a) shows the spin-↑ direction, (b) the spin-↓ direction. The green dashed lines show the band structure of the non-interacting system calculated with PBCs, the green dots correspond to the calculation with OBCs. For these computations the signal was only damped with an exponential function and enhanced with a string of zeros eight times its length.

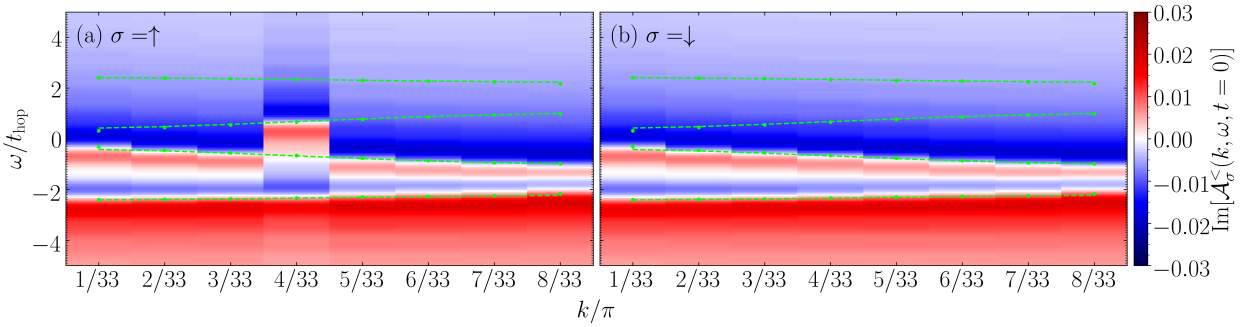

Figure C.8: Imaginary part of the single particle spectral functions $\mathcal{A}_\sigma^<(k,\omega,t=0)$ immediately after the electron-hole excitation (9.1) for $\widehat{H}^{4\Delta}$ with $U/t_{\mathrm{hop}}=0$ and $\Delta/t_{\mathrm{hop}}=2$ for a system of $L=32$ sites with OBCs in the first BZ at half filling. (a) shows the spin-↑ direction, (b) the spin-↓ direction. The green dashed lines show the band structure of the non-interacting system calculated with PBCs, the green dots correspond to the calculation with OBCs. For these computations the signal was only damped with an exponential function and enhanced with a string of zeros eight times its length.

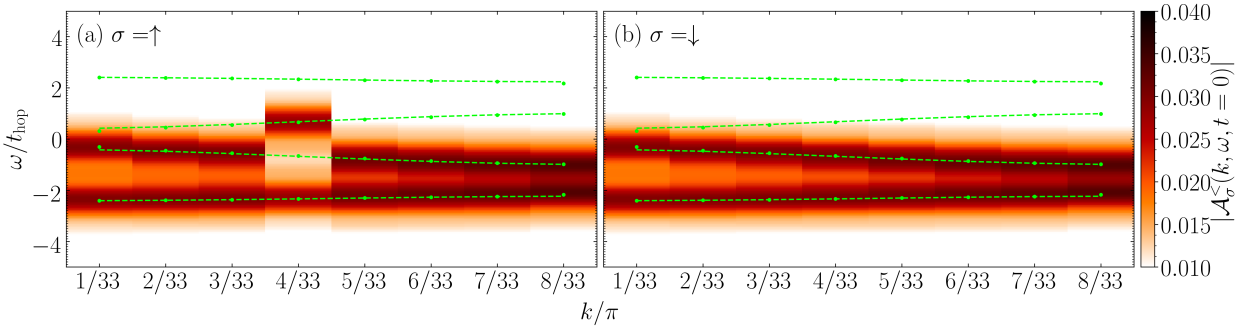

Figure C.9: Absolute value of the single particle spectral functions $\mathcal{A}_\sigma^<(k,\omega,t=0)$ immediately after the electron-hole excitation (9.1) for $\widehat{H}^{4\Delta}$ with $U/t_{\mathrm{hop}}=0$ and $\Delta/t_{\mathrm{hop}}=2$ for a system of $L=32$ sites with OBCs in the first BZ at half filling. (a) shows the spin-↑ direction, (b) the spin-↓ direction. The green dashed lines show the band structure of the non-interacting system calculated with PBCs, the green dots correspond to the calculation with OBCs. For these computations the signal was only damped with an exponential function and enhanced with a string of zeros eight times its length.

Research Data Management Statement

The data that is associated to the author's publications has been copied to these git repositories:

[198] `https://gitlab.gwdg.de/meyer349/paper_cdw.git`

Thomas Köhler, Sebastian Paeckel, Salvatore R. Manmana, and Constantin Meyer have access.

[243] `https://gitlab.gwdg.de/meyer349/paper_excitons.git`

Salvatore R. Manmana and Constantin Meyer have access.

[278] `https://gitlab.gwdg.de/meyer349/paper_floquet.git`

Alexander Osterkorn, Salvatore R. Manmana, and Constantin Meyer have access.

This entire thesis including its data is available in the following git repository:

`https://gitlab.gwdg.de/meyer349/dissertation_cm.git`

So far, only Constantin Meyer has access. When this work is published, Salvatore R. Manmana will also be granted access.

Moreover, before leaving the institute, all important data will be stored on tape in the 10-Years-Archive provided by the IT-service of the Institut für Theoretische Physik, Georg-August-Universität Göttingen.

Danksagung

Nach bald vier Jahren Promotion in Göttingen, in denen wieder so Vieles anders gekommen ist, als ich es erwartet hätte – und damit meine ich nicht nur die Pandemie, möchte ich diese Gelegenheit nutzen, mich bei all den Leuten zu bedanken, die mich auf diesem Weg begleitet haben.

Zunächst danke ich meinem Betreuer Salvatore R. Manmana dafür, dass er mich in seine Arbeitsgruppe aufgenommen und mir damit die Möglichkeit zur Promotion gegeben hat. Ich möchte an dieser Stelle auch seine Bemühungen in sozialen Fragen ausdrücklich würdigen. Es war ihm immer ein Anliegen, seine Leute in Lohn und Brot zu halten und dafür zu sorgen, dass Neuankömmlinge gut in Göttingen integriert werden. Dafür gebührt ihm mein höchster Respekt.

Stefan Kehrein bin ich für die Übernahme des Zweitgutachtens zu dieser Arbeit ebenfalls zu großem Dank verpflichtet. Bei Fabian Heidrich-Meisner und Martin Wenderoth bedanke ich mich dafür, dass sie sich als Zweit- beziehungsweise Drittbetreuer zur Verfügung gestellt haben. Letzterem von beiden und ebenso Michael Seibt, Peter Blöchl, sowie Matthias Krüger möchte ich meinen Dank dafür aussprechen, dass sie Teil meiner Prüfungskommission sind.

Mein wahrscheinlich größter Dank gilt Thomas Köhler und Sebastian Paeckel, meinen beiden akademischen Papas, ohne die diese Arbeit so mit Sicherheit nicht existieren würde. Beide haben nicht nur den Code, auf dessen Basis ich nahezu alle numerischen Simulationen durchgeführt habe, implementiert und mich in dessen Bedienung eingewiesen, sie standen auch zu den noch so unorthoxesten Uhrzeiten für Fragen jedweder Art und seelisch moralischen Beistand zur Verfügung. Ich werde die Koch- und Bowlingabende, wie auch die angenehme gemeinsame Zeit im Büro in guter Erinnerung behalten. Danke euch beiden, danke für Alles!

Auch bei den Studenten, die sich im Laufe der Zeit mehr oder weniger offiziell, mehr oder weniger zufällig unter meine Fittiche begeben haben, möchte ich mich herzlich bedanken. Das sind im Besonderen Leander Thiessen, Svenja Marten und Steffen Bollmann. Ich habe es sehr genossen, mit ihnen zu arbeiten und sie bei ihren Problemen zu unterstützen. Zu sehen, wie sie das, was ich ihnen beigebracht hatte, umgesetzt haben, wie sie dies dann weiter entwickelt haben und wie sie letztendich als Wissenschaftler und als Menschen an ihren Herausforderungen gewachsen sind war mir das größte Geschenk. Ich wünsche ihnen allen dreien das beste für ihre weiteren Lebenswege. Bei Svenja Marten möchte ich mich auch noch dafür bedanken, dass sie mich etwas aus dem Institut heraus gelockt hat. Sie war nicht nur meine zuverlässigste Hutbaugehilfin, sondern auch meine begabteste, motivierteste und vor allem geduldigste Jonglierlehrerin. Mittlerweile bekomme ich das wirklich alleine hin, auch wenn es echt lange gedauert hat. Vielen Dank an dieser Stelle auch an die ganze Truppe vom Hochschulsport. Das hat Spaß mit euch gemacht.

Das, was ein Institut letztendlich ausmacht, sind die Leute, die dort arbeiten. Danke an Veronica Chappa für Extrastunden in Spanisch und an Laura Endter für Klavier- und Gesangsunterricht. Vielen Dank an Kurt Schönhammer, Florian Sohn, Kristof Harms, Simon Luca Villani, Karun Gadge, Arturo Perez Romero, Jan Stolpp, Jonas Breustedt, Jan Louw, Nils Abeling, Michael ten Brink, Manuel Kreye, Lukas Rump, Trisha Nath, Kai Stroh, Alexander Osterkorn, Niklas Bölter, Lorenzo Cevolani, Tridev Mishra, Andrew Hayward, Miroslav Hopjan, Suman Mondal, Colin Koch,

Louis Pigard, Christian Gaß, Yuliya Smirnova, Jelger Risselada, Enrico Bothmann und alle Anderen, die ich jetzt noch vergessen habe, für die vielen gemeinsamen Kaffee- und Mensapausen, Film- und Grillabende, Barbesuche und die damit verbundenen mehr oder weniger sinnvollen Diskussionen zu Physik und dem Sinn des Lebens. Ein herzlicher Dank gilt auch meinen beiden Quasibürokollegen David Jansen und Eric Bertok, sowie den Granden des zweiten Stockes Eva Paprotzki, Stefan Gräber, Jakob Lötfering, Vibhu Mishra und Karl Royen.

Natürlich möchte ich mich auch bei allen Verantwortlichen des Sonderforschungsbereiches 1073 bedanken. Neben der finanziellen Sicherheit wurden uns Doktoranden auch viele weitere Möglichkeiten zum Lernen, Forschen und Spaß haben geboten. Vielen Dank in diesem Zusammenhang an Jörg Hoffmann, Carmen Kaspar und Regina Vinnen. Der Gruppe um Stefan Mathias möchte ich in diesem Zusamenhang für die vielen Diskussionen in unserem gemeinsamen Journal Club danken. Für Unterstützung in administrativen Fragen, Kümmern und dafür, dass sie das Institut am Laufen halten, ein herzlicher Dank an Katrin Glormann, Gabriele Schubert und Kati Oldenburg.

Für IT-Beratung in allen Lebenslagen danke ich Jürgen Holm. Außerdem möchte ich noch meinen Haus- und Hofadmins bei der GWDG und am HLRN, Sebastian Krey, Markus Boden und Azat Khuziyakhmetov bedanken für das Lesen meiner ewig langen Problemberichte, für Notfallvideokonferenzen und Verbesserungsvorschläge meiner Skripte. Ich wollte das Cluster nie bewusst in die Knie zwingen. Vielen Dank auch an Robert Schade und Axel Ehrich für die Unterstützung am Clausthaler Cluster.

Bei Birgit Neuroth-Hartmann, Akram Bishr, Jana Newiger, Amparo Marco Gomez, Sara Spanghero, Robert Wolf, Pasqualina Sorrentino, Valentina Reggio, Marianne Broermann, Murielle Férez, Holger Wiedenstried, Dirk Koschewa und Hiromi Yoshida möchte ich mich dafür bedanken, dass sie versucht haben, mir noch mehr Sprachen beizubringen, mal mit mehr, mal mit weniger Erfolg.

Neben vielen bereits Genannten danke ich auch Isabel Köhler für das Korrekturlesen von Teilen dieser Arbeit. Außerdem danke ich Ivana Hildebrandt dafür, dass sie mir das Gefühl gibt, Optimist zu sein, sowie Lucia Baldauf, Cornelius Wittig, Ilona Wedel, Pascal Farin, Simon Demming, Philipp Weinert und Catrin Burgardt für viele aufbauende Worte. Grüße an dieser Stelle auch an Thea und an Giulia.

Schlussendlich möchte ich mich noch bei meinen Eltern und meinem Bruder für die kontinuierliche Unterstützung in den letzten vier Jahren und insbesondere den letzten Monaten bedanken. Sie alle haben mir immer den Rücken gestärkt, wenn es mir mal nicht gut ging, und stehen seit meinem Studienbeginn fest an meiner Seite. Danke dafür. Ich glaube, ich sage es viel zu selten: Ich hab' euch lieb.

Bibliography

[1] Ulrich Schollwöck. "DMRG: Ground States, Time Evolution, and Spectral Functions". In: *Emergent Phenomena in Correlated Matter*. Ed. by Eva Pavarini, Erik Koch, and Ulrich Schollwöck. Vol. 3. Schriften des Forschungszentrums Jülich. Reihe modeling and simulation. Autumn School on Correlated Electrons, Jülich (Germany), 23 Sep 2013 - 27 Sep 2013. Jülich: Forschungszentrum Jülich GmbH Zentralbibliothek, Verlag, Sept. 23, 2013. Chap. 16, pp. 16.1–16.34. ISBN: 978-3-89336-884-6. URL: https://hdl.handle.net/2128/5389.

[2] Erik Koch. "The Lanczos Method". In: *The LDA+DMFT approach to strongly correlated materials*. Ed. by Eva Pavarini et al. Vol. 1. Schriften des Forschungszentrums Jülich. Reihe modeling and simulation. Record converted from VDB: 12.11.2012. Autumn School on Correlated Electrons, Jülich (Germany), 04 Oct 2011 - 07 Oct 2011. Jülich: Forschungszentrum Jülich GmbH Zentralbibliothek, Verlag, 2011. Chap. 8, pp. 8.1–8.30. ISBN: 978-3-89336-734-4. URL: http://hdl.handle.net/2128/7348.

[3] Robert Eder. "Introduction to the Hubbard Model". In: *The Physics of Correlated Insulators, Metals, and Superconductors*. Ed. by Eva Pavarini et al. Vol. 7. Schriften des Forschungszentrums Jülich. Reihe Modeling and Simulation. Autumn School on Correlated Electrons, Jülich (Germany), 25 Sep 2017 - 29 Sep 2017. Jülich: Forschungszentrum Jülich GmbH Zentralbibliothek, Verlag, Sept. 25, 2017. Chap. 6, pp. 6.1–6.30. ISBN: 978-3-95806-224-5. URL: http://hdl.handle.net/2128/15283.

[4] Hans Gerd Evertz. "DMRG for Multiband Impurity Solvers". In: *DMFT: From Infinite Dimensions to Real Materials*. Ed. by Eva Pavarini et al. Vol. 8. Schriften des Forschungszentrums Jülich. Reihe modeling and simulation. Autumn School on Correlated Electrons, Jülich (Germany), 17 Sep 2018 - 21 Sep 2018. Jülich: Forschungszentrum Jülich GmbH Zentralbibliothek, Verlag, Sept. 17, 2018. Chap. 9, pp. 9.1–9.31. ISBN: 978-3-95806-313-6. URL: https://hdl.handle.net/2128/19720.

[5] James K. Freericks. "Introduction to Many-Body Green Functions In and Out Of Equilibrium". In: *Many-Body Methods for Real Materials*. Ed. by Eva Pavarini, Erik Koch, and Schiwei Zhang. Vol. 9. Schriften des Forschungszentrums Jülich. Modeling and Simulation. Autumn School on Correlated Electrons, Jülich (Germany), 16 Sep 2019 - 20 Sep 2019. Jülich: Forschungszentrum Jülich GmbH Zentralbibliothek, Verlag, Sept. 16, 2019. Chap. 13, pp. 13.1–13.26. ISBN: 978-3-95806-400-3. URL: http://hdl.handle.net/2128/22740.

[6] Matteo Acciai et al. "Spectral properties of interacting helical channels driven by Lorentzian pulses". In: *New Journal of Physics* 21.10 (Oct. 2019), p. 103031. DOI: 10.1088/1367-2630/ab494b. URL: https://doi.org/10.1088/1367-2630/ab494b.

[7] A. J. Achkar et al. "Distinct Charge Orders in the Planes and Chains of Ortho-III-Ordered $YBa_2Cu_3\mathbf{O}_{6+\delta}$ Superconductors Identified by Resonant Elastic X-ray Scattering". In: *Phys. Rev. Lett.* 109 (16 Oct. 2012), p. 167001. DOI: 10.1103/PhysRevLett.109.167001. URL: https://link.aps.org/doi/10.1103/PhysRevLett.109.167001.

[8] Sven Aeschlimann. "Ultrafast Quasiparticle Dynamics in Graphene and 2D Heterostructures". PhD thesis. Universität Hamburg, 2018. URL: https://ediss.sub.uni-hamburg.de/handle/ediss/8126.

[9] Ian Affleck et al. "Rigorous results on valence-bond ground states in antiferromagnets". In: *Phys. Rev. Lett.* 59 (7 Aug. 1987), pp. 799–802. DOI: 10.1103/PhysRevLett.59.799. URL: https://link.aps.org/doi/10.1103/PhysRevLett.59.799.

[10] Ian Affleck et al. "Valence bond ground states in isotropic quantum antiferromagnets". In: *Communications in Mathematical Physics* 115.3 (Sept. 1988), pp. 477–528. ISSN: 1432-0916. DOI: 10.1007/BF01218021. URL: https://doi.org/10.1007/BF01218021.

[11] M. Aidelsburger et al. "Experimental Realization of Strong Effective Magnetic Fields in an Optical Lattice". In: *Phys. Rev. Lett.* 107 (25 Dec. 2011), p. 255301. DOI: 10.1103/PhysRevLett.107.255301. URL: https://link.aps.org/doi/10.1103/PhysRevLett.107.255301.

[12] M. Aidelsburger et al. "Experimental realization of strong effective magnetic fields in optical superlattice potentials". In: *Applied Physics B* 113.1 (Oct. 2013), pp. 1–11. ISSN: 1432-0649. DOI: 10.1007/s00340-013-5418-1. URL: https://doi.org/10.1007/s00340-013-5418-1.

[13] Jessica Alfonsi, Guglielmo Lanzani, and Moreno Meneghetti. "Exact diagonalization of Hubbard models for the optical properties of single-wall carbon nanotubes". In: *New Journal of Physics* 12.8 (Aug. 2010), p. 083009. DOI: 10.1088/1367-2630/12/8/083009. URL: https://doi.org/10.1088/1367-2630/12/8/083009.

[14] Marco Anderlini et al. "Controlled exchange interaction between pairs of neutral atoms in an optical lattice". In: *Nature* 448.7152 (July 2007), pp. 452–456. ISSN: 1476-4687. DOI: 10.1038/nature06011. URL: https://doi.org/10.1038/nature06011.

[15] Hideo Aoki et al. "Nonequilibrium dynamical mean-field theory and its applications". In: *Rev. Mod. Phys.* 86 (2 June 2014), pp. 779–837. DOI: 10.1103/RevModPhys.86.779. URL: https://link.aps.org/doi/10.1103/RevModPhys.86.779.

[16] W. E. Arnoldi. "The principle of minimized iterations in the solution of the matrix eigenvalue problem". In: *Quarterly of Applied Mathematics* 9.1 (1951), pp. 17–29. ISSN: 0033569X, 15524485. DOI: 10.1090/qam/42792. URL: https://www.ams.org/journals/qam/1951-09-01/S0033-569X-1951-42792-9/.

[17] Neil W. Ashcroft and N. David Mermin. *Solid State Physics*. International Edition. Philadelphia: Saunders College, 1976. ISBN: 0-03-049346-3.

[18] I Avigo et al. "Doping dependence and electron–boson coupling in the ultrafast relaxation of hot electron populations in Ba(Fe1–xCox)2As2". In: *New Journal of Physics* 18.9 (Sept. 2016), p. 093028. DOI: 10.1088/1367-2630/18/9/093028. URL: https://doi.org/10.1088/1367-2630/18/9/093028.

[19] V M Axt and T Kuhn. "Femtosecond spectroscopy in semiconductors: a key to coherences, correlations and quantum kinetics". In: *Reports on Progress in Physics* 67.4 (Mar. 2004), pp. 433–512. DOI: 10.1088/0034-4885/67/4/r01. URL: https://doi.org/10.1088/0034-4885/67/4/r01.

[20] G. H. Bach and F. Marsiglio. "Optical conductivity for a dimer in the dynamic Hubbard model". In: *Phys. Rev. B* 85 (15 Apr. 2012), p. 155134. DOI: 10.1103/PhysRevB.85.155134. URL: https://link.aps.org/doi/10.1103/PhysRevB.85.155134.

[21] Zhaojun Bai et al., eds. *Templates for the Solution of Algebraic Eigenvalue Problems: A Practical Guide*. 1st ed. Software, Environments, and Tools. Philadelphia: Society for Industrial and Applied Mathematics, 2000. ISBN: 978-0-89871-471-5. DOI: 10.1137/1.9780898719581. eprint: https://epubs.siam.org/doi/pdf/10.1137/1.9780898719581. URL: https://epubs.siam.org/doi/abs/10.1137/1.9780898719581.

[22] Waseem S. Bakr et al. "A quantum gas microscope for detecting single atoms in a Hubbard-regime optical lattice". In: *Nature* 462.7269 (Nov. 2009), pp. 74–77. ISSN: 1476-4687. DOI: 10.1038/nature08482. URL: https://doi.org/10.1038/nature08482.

[23] William Barford. "Excitons in the strong coupling limit of the one-dimensional extended Hubbard model". In: *Phys. Rev. B* 65 (20 May 2002), p. 205118. DOI: 10.1103/PhysRevB.65.205118. URL: https://link.aps.org/doi/10.1103/PhysRevB.65.205118.

[24] Daniel Bauernfeind et al. "Fork Tensor-Product States: Efficient Multiorbital Real-Time DMFT Solver". In: *Phys. Rev. X* 7 (3 July 2017), p. 031013. DOI: 10.1103/PhysRevX.7.031013. URL: https://link.aps.org/doi/10.1103/PhysRevX.7.031013.

[25] Peter Baum, Ding-Shyue Yang, and Ahmed H. Zewail. "4D Visualization of Transitional Structures in Phase Transformations by Electron Diffraction". In: *Science* 318.5851 (2007), pp. 788–792. DOI: 10.1126/science.1147724. eprint: https://www.science.org/doi/pdf/10.1126/science.1147724. URL: https://www.science.org/doi/abs/10.1126/science.1147724.

[26] R. J. Baxter. "Dimers on a Rectangular Lattice". In: *Journal of Mathematical Physics* 9.4 (1968), pp. 650–654. DOI: 10.1063/1.1664623. eprint: https://doi.org/10.1063/1.1664623. URL: https://doi.org/10.1063/1.1664623.

[27] J. Becker et al. "Finite-temperature dynamics and thermal intraband magnon scattering in Haldane spin-one chains". In: *Phys. Rev. B* 96 (6 Aug. 2017), p. 060403. DOI: 10.1103/PhysRevB.96.060403. URL: https://link.aps.org/doi/10.1103/PhysRevB.96.060403.

[28] G. Bedürftig et al. "Friedel oscillations in the open Hubbard chain". In: *Phys. Rev. B* 58 (16 Oct. 1998), pp. 10225–10235. DOI: 10.1103/PhysRevB.58.10225. URL: https://link.aps.org/doi/10.1103/PhysRevB.58.10225.

[29] H. Benthien, F. Gebhard, and E. Jeckelmann. "Spectral Function of the One-Dimensional Hubbard Model away from Half Filling". In: *Phys. Rev. Lett.* 92 (25 June 2004), p. 256401. DOI: 10.1103/PhysRevLett.92.256401. URL: https://link.aps.org/doi/10.1103/PhysRevLett.92.256401.

[30] H. Benthien and E. Jeckelmann. "Optical conductivity of the one-dimensional dimerized Hubbard model at quarter filling". In: *The European Physical Journal B - Condensed Matter and Complex Systems* 44.3 (Apr. 2005), pp. 287–297. ISSN: 1434-6036. DOI: 10.1140/epjb/e2005-00128-1. URL: https://doi.org/10.1140/epjb/e2005-00128-1.

[31] József Zsolt Bernád. "Optical conductivity of single-layer graphene induced by temporal mass-gap fluctuations". In: *Physica B: Condensed Matter* 407.22 (2012), pp. 4446–4452. ISSN: 0921-4526. DOI: https://doi.org/10.1016/j.physb.2012.07.040. URL: https://www.sciencedirect.com/science/article/pii/S092145261200751X.

[32] R. Bertoni et al. "Generation and Evolution of Spin-, Valley-, and Layer-Polarized Excited Carriers in Inversion-Symmetric WSe_2". In: *Phys. Rev. Lett.* 117 (27 Dec. 2016), p. 277201. DOI: 10.1103/PhysRevLett.117.277201. URL: https://link.aps.org/doi/10.1103/PhysRevLett.117.277201.

[33] Fabian Ralf Anton Biebl. "Thermalization in one-dimensional quantum-many-body systems". PhD thesis. Georg-August-Universität Göttingen, Jan. 2017. URL: http://hdl.handle.net/11858/00-1735-0000-002B-7D11-6.

[34] Nikolaj Bittner et al. "Effects of frustration on the nonequilibrium dynamics of photoexcited lattice systems". In: *Phys. Rev. B* 102 (23 Dec. 2020), p. 235169. DOI: 10.1103/PhysRevB.102.235169. URL: https://link.aps.org/doi/10.1103/PhysRevB.102.235169.

[35] Nikolaj Bittner et al. "Photoenhanced excitonic correlations in a Mott insulator with nonlocal interactions". In: *Phys. Rev. B* 101 (8 Feb. 2020), p. 085127. DOI: 10.1103/PhysRevB.101.085127. URL: https://link.aps.org/doi/10.1103/PhysRevB.101.085127.

[36] Immanuel Bloch. "Ultracold quantum gases in optical lattices". In: *Nature Physics* 1.1 (Oct. 2005), pp. 23–30. ISSN: 1745-2481. DOI: 10.1038/nphys138. URL: https://doi.org/10.1038/nphys138.

[37] Immanuel Bloch, Jean Dalibard, and Sylvain Nascimbène. "Quantum simulations with ultracold quantum gases". In: *Nature Physics* 8.4 (Apr. 2012), pp. 267–276. ISSN: 1745-2481. DOI: 10.1038/nphys2259. URL: https://doi.org/10.1038/nphys2259.

[38] Immanuel Bloch, Jean Dalibard, and Wilhelm Zwerger. "Many-body physics with ultracold gases". In: *Rev. Mod. Phys.* 80 (3 July 2008), pp. 885–964. DOI: 10.1103/RevModPhys.80.885. URL: https://link.aps.org/doi/10.1103/RevModPhys.80.885.

[39] M.L. Boas. *Mathematical Methods in the Physical Sciences*. 3rd ed. Wiley-VCH, 2005. ISBN: 978-0-471-19826-0.

[40] Martin Boll et al. "Spin- and density-resolved microscopy of antiferromagnetic correlations in Fermi-Hubbard chains". In: *Science* 353.6305 (2016), pp. 1257–1260. DOI: 10.1126/science.aag1635. eprint: https://www.science.org/doi/pdf/10.1126/science.aag1635. URL: https://www.science.org/doi/abs/10.1126/science.aag1635.

[41] J. Bonča. "Spectral function of an electron coupled to hard-core bosons". In: *Phys. Rev. B* 102 (3 July 2020), p. 035135. DOI: 10.1103/PhysRevB.102.035135. URL: https://link.aps.org/doi/10.1103/PhysRevB.102.035135.

[42] J. Bonča, S. A. Trugman, and M. Berciu. "Spectral function of the Holstein polaron at finite temperature". In: *Phys. Rev. B* 100 (9 Sept. 2019), p. 094307. DOI: 10.1103/PhysRevB.100.094307. URL: https://link.aps.org/doi/10.1103/PhysRevB.100.094307.

[43] J. Braun et al. "One-step theory of pump-probe photoemission". In: *Phys. Rev. B* 91 (3 Jan. 2015), p. 035119. DOI: 10.1103/PhysRevB.91.035119. URL: https://link.aps.org/doi/10.1103/PhysRevB.91.035119.

[44] J. van den Brink, R Eder, and G. A Sawatzky. "Charged excitons in doped extended Hubbard model systems". In: *Europhysics Letters (EPL)* 37.7 (Mar. 1997), pp. 471–476. DOI: 10.1209/epl/i1997-00174-3. URL: https://doi.org/10.1209/epl/i1997-00174-3.

[45] V. Britanak, P.C. Yip, and K.R. Rao. *Discrete Cosine and Sine Transforms: General Properties, Fast Algorithms and Integer Approximations*. Oxford: Academic Press, 2007. ISBN: 978-0-12-373624-6. DOI: 10.1016/B978-0-12-373624-6.X5000-0.

[46] P. Bruno, Y. Suzuki, and C. Chappert. "Magneto-optical Kerr effect in a paramagnetic overlayer on a ferromagnetic substrate: A spin-polarized quantum size effect". In: *Phys. Rev. B* 53 (14 Apr. 1996), pp. 9214–9220. DOI: 10.1103/PhysRevB.53.9214. URL: https://link.aps.org/doi/10.1103/PhysRevB.53.9214.

[47] Dagmar Bruß. "Characterizing entanglement". In: *Journal of Mathematical Physics* 43.9 (2002), pp. 4237–4251. DOI: 10.1063/1.1494474. eprint: https://doi.org/10.1063/1.1494474. URL: https://doi.org/10.1063/1.1494474.

[48] H. Bruus and K. Flensberg. *Many-Body Quantum Theory in Condensed Matter Physics: An Introduction*. Oxford Graduate Texts. Oxford: Oxford University Press, 2004. ISBN: 0-19-856633-6.

[49] Tilman Butz. *Fouriertransformation für Fußgänger*. 7th ed. Wiesbaden: Vieweg+Teubner Verlag, 2012. ISBN: 978-3-8348-0946-9. DOI: 10.1007/978-3-8348-8295-0.

[50] Pasquale Calabrese and John Cardy. "Entanglement entropy and quantum field theory". In: *Journal of Statistical Mechanics: Theory and Experiment* 2004.06 (June 2004), P06002. DOI: 10.1088/1742-5468/2004/06/p06002. URL: https://doi.org/10.1088/1742-5468/2004/06/p06002.

[51] Alessio Calzona et al. "Quench-induced entanglement and relaxation dynamics in Luttinger liquids". In: *Phys. Rev. B* 96 (8 Aug. 2017), p. 085423. DOI: 10.1103/PhysRevB.96.085423. URL: https://link.aps.org/doi/10.1103/PhysRevB.96.085423.

[52] Gaetano Campi et al. "X-Rays Writing/Reading of Charge Density Waves in the CuO2 Plane of a Simple Cuprate Superconductor". In: *Condensed Matter* 2.3 (2017). ISSN: 2410-3896. DOI: 10.3390/condmat2030026. URL: https://www.mdpi.com/2410-3896/2/3/26.

[53] Fabio Caruso, Dino Novko, and Claudia Draxl. "Photoemission signatures of nonequilibrium carrier dynamics from first principles". In: *Phys. Rev. B* 101 (3 Jan. 2020), p. 035128. DOI: 10.1103/PhysRevB.101.035128. URL: https://link.aps.org/doi/10.1103/PhysRevB.101.035128.

[54] Jean-Sébastien Caux and Jean Michel Maillet. "Computation of Dynamical Correlation Functions of Heisenberg Chains in a Magnetic Field". In: *Phys. Rev. Lett.* 95 (7 Aug. 2005), p. 077201. DOI: 10.1103/PhysRevLett.95.077201. URL: https://link.aps.org/doi/10.1103/PhysRevLett.95.077201.

[55] J. Chang et al. "Direct observation of competition between superconductivity and charge density wave order in YBa2Cu3O6.67". In: *Nature Physics* 8.12 (Dec. 2012), pp. 871–876. ISSN: 1745-2481. DOI: 10.1038/nphys2456. URL: https://doi.org/10.1038/nphys2456.

[56] R. Y. Chen et al. "Revealing Extremely Low Energy Amplitude Modes in the Charge-Density-Wave Compound $LaAgSb_2$". In: *Phys. Rev. Lett.* 118 (10 Mar. 2017), p. 107402. DOI: 10.1103/PhysRevLett.118.107402. URL: https://link.aps.org/doi/10.1103/PhysRevLett.118.107402.

[57] Yuan Chen et al. "Observing photo-induced chiral edge states of graphene nanoribbons in pump-probe spectroscopies". In: *npj Quantum Materials* 5.1 (Nov. 2020), p. 84. ISSN: 2397-4648. DOI: 10.1038/s41535-020-00283-5. URL: https://doi.org/10.1038/s41535-020-00283-5.

[58] Alexey Chernikov et al. "Population inversion and giant bandgap renormalization in atomically thin WS2 layers". In: *Nature Photonics* 9.7 (July 2015), pp. 466–470. ISSN: 1749-4893. DOI: 10.1038/nphoton.2015.104. URL: https://doi.org/10.1038/nphoton.2015.104.

[59] Lawrence W. Cheuk et al. "Quantum-Gas Microscope for Fermionic Atoms". In: *Phys. Rev. Lett.* 114 (19 May 2015), p. 193001. DOI: 10.1103/PhysRevLett.114.193001. URL: https://link.aps.org/doi/10.1103/PhysRevLett.114.193001.

[60] Soonwon Choi et al. "Observation of discrete time-crystalline order in a disordered dipolar many-body system". In: *Nature* 543.7644 (Mar. 2017), pp. 221–225. ISSN: 1476-4687. DOI: 10.1038/nature21426. URL: https://doi.org/10.1038/nature21426.

[61] Dominik Christiansen et al. "Theory of exciton dynamics in time-resolved ARPES: Intra- and intervalley scattering in two-dimensional semiconductors". In: *Phys. Rev. B* 100 (20 Nov. 2019), p. 205401. DOI: 10.1103/PhysRevB.100.205401. URL: https://link.aps.org/doi/10.1103/PhysRevB.100.205401.

[62] Eleanor Chu. *Discrete and Continuous Fourier Transforms: Analysis, Applications and Fast Algorithms*. 1st ed. Boca Raton, FL: Chapman and Hall/CRC, 2008. ISBN: 1-4200-6363-4. DOI: 10.1201/9781420063646.

[63] Martin Claassen et al. "Dynamical time-reversal symmetry breaking and photo-induced chiral spin liquids in frustrated Mott insulators". In: *Nature Communications* 8.1 (Oct. 2017), p. 1192. ISSN: 2041-1723. DOI: 10.1038/s41467-017-00876-y. URL: https://doi.org/10.1038/s41467-017-00876-y.

[64] Claude Cohen-Tannoudji, Bernard Diu, and Franck Laloë. *Quantum Mechanics*. 1st ed. Vol. 1. Wiley-VCH, 1977. ISBN: 0471164333.

[65] Claude Cohen-Tannoudji, Bernard Diu, and Franck Laloë. *Quantum Mechanics*. 1st ed. Vol. 2. Wiley-VCH, 1977. ISBN: 0471164357.

[66] Eric Collet et al. "Laser-Induced Ferroelectric Structural Order in an Organic Charge-Transfer Crystal". In: *Science* 300.5619 (2003), pp. 612–615. DOI: 10.1126/science.1082001. eprint: https://www.science.org/doi/pdf/10.1126/science.1082001. URL: https://www.science.org/doi/abs/10.1126/science.1082001.

[67] Gregory M. Crosswhite and Dave Bacon. "Finite automata for caching in matrix product algorithms". In: *Phys. Rev. A* 78 (1 July 2008), p. 012356. DOI: 10.1103/PhysRevA.78.012356. URL: https://link.aps.org/doi/10.1103/PhysRevA.78.012356.

[68] Gregory M. Crosswhite, A. C. Doherty, and Guifré Vidal. "Applying matrix product operators to model systems with long-range interactions". In: *Phys. Rev. B* 78 (3 July 2008), p. 035116. DOI: 10.1103/PhysRevB.78.035116. URL: https://link.aps.org/doi/10.1103/PhysRevB.78.035116.

[69] E. Dagotto et al. "Optical conductivity of the two-dimensional Hubbard model". In: *Phys. Rev. B* 45 (17 May 1992), pp. 10107–10110. DOI: 10.1103/PhysRevB.45.10107. URL: https://link.aps.org/doi/10.1103/PhysRevB.45.10107.

[70] A J Daley et al. "Time-dependent density-matrix renormalization-group using adaptive effective Hilbert spaces". In: *Journal of Statistical Mechanics: Theory and Experiment* 2004.04 (Apr. 2004), P04005. DOI: 10.1088/1742-5468/2004/04/p04005. URL: https://doi.org/10.1088/1742-5468/2004/04/p04005.

[71] Andrea Damascelli, Zahid Hussain, and Zhi-Xun Shen. "Angle-resolved photoemission studies of the cuprate superconductors". In: *Rev. Mod. Phys.* 75 (2 Apr. 2003), pp. 473–541. DOI: 10.1103/RevModPhys.75.473. URL: https://link.aps.org/doi/10.1103/RevModPhys.75.473.

[72] P. E. Dargel et al. "Lanczos algorithm with matrix product states for dynamical correlation functions". In: *Phys. Rev. B* 85 (20 May 2012), p. 205119. DOI: 10.1103/PhysRevB.85.205119. URL: https://link.aps.org/doi/10.1103/PhysRevB.85.205119.

[73] Nagamalleswararao Dasari and Martin Eckstein. "Photoexcited states in correlated band insulators". In: *Phys. Rev. B* 98 (3 July 2018), p. 035113. DOI: 10.1103/PhysRevB.98.035113. URL: https://link.aps.org/doi/10.1103/PhysRevB.98.035113.

[74] Nagamalleswararao Dasari et al. "Photoinduced strange metal with electron and hole quasiparticles". In: *Phys. Rev. B* 103 (20 May 2021), p. L201116. DOI: 10.1103/PhysRevB.103.L201116. URL: https://link.aps.org/doi/10.1103/PhysRevB.103.L201116.

[75] Stéphane Daul and Michael Dzierzawa. "Second order self-energy of the two-dimensional Hubbard model". In: *Zeitschrift für Physik B Condensed Matter* 103.1 (Mar. 1997), pp. 41–44. ISSN: 1431-584X. DOI: 10.1007/s002570050332. URL: https://doi.org/10.1007/s002570050332.

[76] Ernest R. Davidson and William J. Thompson. "Monster Matrices: Their Eigenvalues and Eigenvectors". In: *Computers in Physics* 7.5 (1993), pp. 519–522. DOI: 10.1063/1.4823212. eprint: https://aip.scitation.org/doi/pdf/10.1063/1.4823212. URL: https://aip.scitation.org/doi/abs/10.1063/1.4823212.

[77] P. Delplace, D. Ullmo, and G. Montambaux. "Zak phase and the existence of edge states in graphene". In: *Phys. Rev. B* 84 (19 Nov. 2011), p. 195452. DOI: 10.1103/PhysRevB.84.195452. URL: https://link.aps.org/doi/10.1103/PhysRevB.84.195452.

[78] John Kay Dewhurst et al. "Laser-Induced Intersite Spin Transfer". In: *Nano Letters* 18.3 (2018). PMID: 29424230, pp. 1842–1848. DOI: 10.1021/acs.nanolett.7b05118. eprint: https://doi.org/10.1021/acs.nanolett.7b05118. URL: https://doi.org/10.1021/acs.nanolett.7b05118.

[79] P. A. M. Dirac. "A new notation for quantum mechanics". In: *Mathematical Proceedings of the Cambridge Philosophical Society* 35.3 (1939), pp. 416–418. DOI: 10.1017/S0305004100021162.

[80] Shuo Dong et al. "Direct measurement of key exciton properties: Energy, dynamics, and spatial distribution of the wave function". In: *Natural Sciences* 1.1 (2021), e10010. DOI: https://doi.org/10.1002/ntls.10010. eprint: https://onlinelibrary.wiley.com/doi/pdf/10.1002/ntls.10010. URL: https://onlinelibrary.wiley.com/doi/abs/10.1002/ntls.10010.

[81] Shuo Dong et al. "Direct measurement of key exciton properties: Energy, dynamics, and spatial distribution of the wave function". In: *Natural Sciences* 1.1 (2021), e10010. DOI: https://doi.org/10.1002/ntls.10010. eprint: https://onlinelibrary.wiley.com/doi/pdf/10.1002/ntls.10010. URL: https://onlinelibrary.wiley.com/doi/abs/10.1002/ntls.10010.

[82] F. Dorfner et al. "Real-time decay of a highly excited charge carrier in the one-dimensional Holstein model". In: *Phys. Rev. B* 91 (10 Mar. 2015), p. 104302. DOI: 10.1103/PhysRevB.91.104302. URL: https://link.aps.org/doi/10.1103/PhysRevB.91.104302.

[83] Reiner M. Dreizler and Eberhard K.U. Gross. *Density Functional Theory: An Approach to the Quantum Many-Body Problem*. 1st ed. Berlin, Heidelberg: Springer, 1990. ISBN: 978-3-540-51993-5. DOI: 10.1007/978-3-642-86105-5.

[84] Dukelsky, J. et al. "Equivalence of the variational matrix product method and the density matrix renormalization group applied to spin chains". In: *Europhys. Lett.* 43.4 (1998), pp. 457–462. DOI: 10.1209/epl/i1998-00381-x. URL: https://doi.org/10.1209/epl/i1998-00381-x.

[85] André Eckardt. "Colloquium: Atomic quantum gases in periodically driven optical lattices". In: *Rev. Mod. Phys.* 89 (1 Mar. 2017), p. 011004. DOI: 10.1103/RevModPhys.89.011004. URL: https://link.aps.org/doi/10.1103/RevModPhys.89.011004.

[86] Martin Eckstein and Philipp Werner. "Nonequilibrium dynamical mean-field simulation of inhomogeneous systems". In: *Phys. Rev. B* 88 (7 Aug. 2013), p. 075135. DOI: 10.1103/PhysRevB.88.075135. URL: https://link.aps.org/doi/10.1103/PhysRevB.88.075135.

[87] Martin Eckstein and Philipp Werner. "Ultra-fast photo-carrier relaxation in Mott insulators with short-range spin correlations". In: *Scientific Reports* 6.1 (Feb. 2016), p. 21235. ISSN: 2045-2322. DOI: 10.1038/srep21235. URL: https://doi.org/10.1038/srep21235.

[88] S. D. Edkins et al. "Magnetic field-induced pair density wave state in the cuprate vortex halo". In: *Science* 364.6444 (2019), pp. 976–980. DOI: 10.1126/science.aat1773. eprint: https://www.science.org/doi/pdf/10.1126/science.aat1773. URL: https://www.science.org/doi/abs/10.1126/science.aat1773.

[89] Tim Eggebrecht et al. "Light-Induced Metastable Magnetic Texture Uncovered by in situ Lorentz Microscopy". In: *Phys. Rev. Lett.* 118 (9 Mar. 2017), p. 097203. DOI: 10.1103/PhysRevLett.118.097203. URL: https://link.aps.org/doi/10.1103/PhysRevLett.118.097203.

[90] S. Ejima, F. Lange, and H. Fehske. "Nonequilibrium dynamics in pumped Mott insulators". In: *Phys. Rev. Research* 4 (1 Feb. 2022), p. L012012. DOI: 10.1103/PhysRevResearch.4.L012012. URL: https://link.aps.org/doi/10.1103/PhysRevResearch.4.L012012.

[91] Satoshi Ejima et al. "Photoinduced η-pairing at finite temperatures". In: *Phys. Rev. Research* 2 (3 July 2020), p. 032008. DOI: 10.1103/PhysRevResearch.2.032008. URL: https://link.aps.org/doi/10.1103/PhysRevResearch.2.032008.

[92] P. Elliott et al. "Ultrafast laser induced local magnetization dynamics in Heusler compounds". In: *Scientific Reports* 6.1 (Dec. 2016), p. 38911. ISSN: 2045-2322. DOI: 10.1038/srep38911. URL: https://doi.org/10.1038/srep38911.

[93] Dominic V. Else, Bela Bauer, and Chetan Nayak. "Floquet Time Crystals". In: *Phys. Rev. Lett.* 117 (9 Aug. 2016), p. 090402. DOI: 10.1103/PhysRevLett.117.090402. URL: https://link.aps.org/doi/10.1103/PhysRevLett.117.090402.

[94] Dominic V. Else, Bela Bauer, and Chetan Nayak. "Prethermal Phases of Matter Protected by Time-Translation Symmetry". In: *Phys. Rev. X* 7 (1 Mar. 2017), p. 011026. DOI: 10.1103/PhysRevX.7.011026. URL: https://link.aps.org/doi/10.1103/PhysRevX.7.011026.

[95] D. Erben et al. "Excitation-induced transition to indirect band gaps in atomically thin transition-metal dichalcogenide semiconductors". In: *Phys. Rev. B* 98 (3 July 2018), p. 035434. DOI: 10.1103/PhysRevB.98.035434. URL: https://link.aps.org/doi/10.1103/PhysRevB.98.035434.

[96] F. H. L. Essler, F. Gebhard, and E. Jeckelmann. "Excitons in one-dimensional Mott insulators". In: *Phys. Rev. B* 64 (12 Sept. 2001), p. 125119. DOI: 10.1103/PhysRevB.64.125119. URL: https://link.aps.org/doi/10.1103/PhysRevB.64.125119.

[97] Fabian H. L. Essler et al. *The One-Dimensional Hubbard Model*. Cambridge University Press, 2005. DOI: 10.1017/CBO9780511534843.

[98] Tilman Esslinger. "Fermi-Hubbard Physics with Atoms in an Optical Lattice". In: *Annual Review of Condensed Matter Physics* 1.1 (2010), pp. 129–152. DOI: 10.1146/annurev-conmatphys-070909-104059. eprint: https://doi.org/10.1146/annurev-conmatphys-070909-104059. URL: https://doi.org/10.1146/annurev-conmatphys-070909-104059.

[99] Aaron Farrell, A. Arsenault, and T. Pereg-Barnea. "Dirac cones, Floquet side bands, and theory of time-resolved angle-resolved photoemission". In: *Phys. Rev. B* 94 (15 Oct. 2016), p. 155304. DOI: 10.1103/PhysRevB.94.155304. URL: https://link.aps.org/doi/10.1103/PhysRevB.94.155304.

[100] D. Fausti et al. "Light-Induced Superconductivity in a Stripe-Ordered Cuprate". In: *Science* 331.6014 (2011), pp. 189–191. DOI: 10.1126/science.1197294. eprint: https://www.science.org/doi/pdf/10.1126/science.1197294. URL: https://www.science.org/doi/abs/10.1126/science.1197294.

[101] Holger Fehske, Ralf Schneider, and Alexander Weiße, eds. *Computational Many-Particle Physics*. 1st ed. Lecture Notes in Physics. Berlin, Heidelberg: Springer, 2008. ISBN: 978-3-540-74685-0. DOI: 10.1007/978-3-540-74686-7.

[102] Adrian E. Feiguin and Steven R. White. "Time-step targeting methods for real-time dynamics using the density matrix renormalization group". In: *Phys. Rev. B* 72 (2 July 2005), p. 020404. DOI: 10.1103/PhysRevB.72.020404. URL: https://link.aps.org/doi/10.1103/PhysRevB.72.020404.

[103] J. K. Freericks, H. R. Krishnamurthy, and Th. Pruschke. "Erratum: Theoretical Description of time-Resolved Photoemission Spectroscopy: Application to Pump-Probe Experiments [Phys. Rev. Lett. 102, 136401 (2009)]". In: *Phys. Rev. Lett.* 119 (18 Nov. 2017), p. 189903. DOI: 10.1103/PhysRevLett.119.189903. URL: https://link.aps.org/doi/10.1103/PhysRevLett.119.189903.

[104] J. K. Freericks, H. R. Krishnamurthy, and Th. Pruschke. "Theoretical Description of Time-Resolved Photoemission Spectroscopy: Application to Pump-Probe Experiments". In: *Phys. Rev. Lett.* 102 (13 Mar. 2009), p. 136401. DOI: 10.1103/PhysRevLett.102.136401. URL: https://link.aps.org/doi/10.1103/PhysRevLett.102.136401.

[105] J K Freericks et al. "Gauge invariance in the theoretical description of time-resolved angle-resolved pump/probe photoemission spectroscopy". In: *Physica Scripta* T165 (Oct. 2015), p. 014012. DOI: 10.1088/0031-8949/2015/t165/014012. URL: https://doi.org/10.1088/0031-8949/2015/t165/014012.

[106] J K Freericks et al. "Theoretical description of pump/probe experiments in electron-mediated charge-density-wave insulators". In: *Physica Scripta* 92.3 (Feb. 2017), p. 034007. DOI: 10.1088/1402-4896/aa5b6c. URL: https://doi.org/10.1088/1402-4896/aa5b6c.

[107] J. K. Freericks et al. "Theoretical description of time-resolved pump/probe photoemission in TaS2: a single-band DFT+DMFT(NRG) study within the quasiequilibrium approximation". In: *physica status solidi (b)* 246.5 (2009), pp. 948–954. DOI: https://doi.org/10.1002/pssb.200881555. eprint: https://onlinelibrary.wiley.com/doi/pdf/10.1002/pssb.200881555. URL: https://onlinelibrary.wiley.com/doi/abs/10.1002/pssb.200881555.

[108] James K. Freericks and H. R. Krishnamurthy. "Constant Matrix Element Approximation to Time-Resolved Angle-Resolved Photoemission Spectroscopy". In: *Photonics* 3.4 (2016). ISSN: 2304-6732. DOI: 10.3390/photonics3040058. URL: https://www.mdpi.com/2304-6732/3/4/58.

[109] J.K. Freericks and Alexander F. Kemper. "What do the two times in two-time correlation functions mean for interpreting tr-ARPES?" In: *Journal of Electron Spectroscopy and Related Phenomena* 251 (2021), p. 147104. ISSN: 0368-2048. DOI: https://doi.org/10.1016/j.elspec.2021.147104. URL: https://www.sciencedirect.com/science/article/pii/S036820482100058X.

[110] M. Frigo and S.G. Johnson. "The Design and Implementation of FFTW3". In: *Proceedings of the IEEE* 93.2 (2005), pp. 216–231. DOI: 10.1109/JPROC.2004.840301.

[111] Juan José García-Ripoll. "Time evolution of Matrix Product States". In: *New Journal of Physics* 8.12 (Dec. 2006), pp. 305–305. DOI: 10.1088/1367-2630/8/12/305. URL: https://doi.org/10.1088/1367-2630/8/12/305.

[112] Florian Gebhard. *The Mott Metal-Insulator Transition: Models and Methods*. 1st ed. Vol. 137a. Springer Tracts in Modern Physics. Berlin, Heidelberg: Springer, 1997. ISBN: 3-540-61481-8. DOI: 10.1007/3-540-14858-2.

[113] F. Gebhard et al. "Fourth-order perturbation theory for the half-filled Hubbard model in infinite dimensions". In: *The European Physical Journal B - Condensed Matter and Complex Systems* 36.4 (Dec. 2003), pp. 491–509. ISSN: 1434-6036. DOI: 10.1140/epjb/e2004-00005-5. URL: https://doi.org/10.1140/epjb/e2004-00005-5.

[114] Antoine Georges et al. "Dynamical mean-field theory of strongly correlated fermion systems and the limit of infinite dimensions". In: *Rev. Mod. Phys.* 68 (1 Jan. 1996), pp. 13–125. DOI: 10.1103/RevModPhys.68.13. URL: https://link.aps.org/doi/10.1103/RevModPhys.68.13.

[115] S. Gerber et al. "Three-dimensional charge density wave order in $YBa_2Cu_3O_{6.67}$ at high magnetic fields". In: *Science* 350.6263 (2015), pp. 949–952. DOI: 10.1126/science.aac6257. eprint: https://www.science.org/doi/pdf/10.1126/science.aac6257. URL: https://www.science.org/doi/abs/10.1126/science.aac6257.

[116] Giacomo Ghiringhelli et al. "Long-Range Incommensurate Charge Fluctuations in (Y,Nd) $Ba_2Cu_3O_{6+x}$". In: *Science* 337.6096 (2012), pp. 821–825. DOI: 10.1126/science.1223532. eprint: https://www.science.org/doi/pdf/10.1126/science.1223532. URL: https://www.science.org/doi/abs/10.1126/science.1223532.

[117] Thierry Giamarchi. *Quantum Physics in One Dimension*. International Series of Monographs on Physics. Oxford: Oxford University Press, 2003.

[118] A. Gill. *Introduction to the Theory of Finite-state Machines*. Electronic science series. McGraw-Hill, 1962. ISBN: 9780070232433.

[119] Konrad Gillmeister et al. "Ultrafast coupled charge and spin dynamics in strongly correlated NiO". In: *Nature Communications* 11.1 (Aug. 2020), p. 4095. ISSN: 2041-1723. DOI: 10.1038/s41467-020-17925-8. URL: https://doi.org/10.1038/s41467-020-17925-8.

[120] Dimitri Gioev and Israel Klich. "Entanglement Entropy of Fermions in Any Dimension and the Widom Conjecture". In: *Phys. Rev. Lett.* 96 (10 Mar. 2006), p. 100503. DOI: 10.1103/PhysRevLett.96.100503. URL: https://link.aps.org/doi/10.1103/PhysRevLett.96.100503.

[121] Denis Golež, Philipp Werner, and Martin Eckstein. "Photoinduced gap closure in an excitonic insulator". In: *Phys. Rev. B* 94 (3 July 2016), p. 035121. DOI: 10.1103/PhysRevB.94.035121. URL: https://link.aps.org/doi/10.1103/PhysRevB.94.035121.

[122] Denis Golež et al. "Dynamics of photodoped charge transfer insulators". In: *Phys. Rev. B* 100 (4 July 2019), p. 041111. DOI: 10.1103/PhysRevB.100.041111. URL: https://link.aps.org/doi/10.1103/PhysRevB.100.041111.

[123] G. H. Golub and C. Reinsch. "Singular value decomposition and least squares solutions". In: *Numerische Mathematik* 14.5 (Apr. 1970), pp. 403–420. ISSN: 0945-3245. DOI: 10.1007/BF02163027. URL: https://doi.org/10.1007/BF02163027.

[124] G. Golub and W. Kahan. "Calculating the Singular Values and Pseudo-Inverse of a Matrix". In: *Journal of the Society for Industrial and Applied Mathematics: Series B, Numerical Analysis* 2.2 (1965), pp. 205–224. ISSN: 0887459X. DOI: 10.1137/0702016. URL: https://epubs.siam.org/doi/10.1137/0702016.

[125] Gene H. Golub and Charles F. Van Loan. *Matrix Computations, Third Edition*. 3rd ed. Johns Hopkins Studies in the Mathematical Sciences. Baltimore, MD: The Johns Hopkins University Press, 1996. ISBN: 0801854148.

[126] A. V. Gorshkov et al. "Two-orbital S U(N) magnetism with ultracold alkaline-earth atoms". In: *Nature Physics* 6.4 (Apr. 2010), pp. 289–295. ISSN: 1745-2481. DOI: 10.1038/nphys1535. URL: https://doi.org/10.1038/nphys1535.

[127] Shimpei Goto and Ippei Danshita. "Performance of the time-dependent variational principle for matrix product states in the long-time evolution of a pure state". In: *Phys. Rev. B* 99 (5 Feb. 2019), p. 054307. DOI: 10.1103/PhysRevB.99.054307. URL: https://link.aps.org/doi/10.1103/PhysRevB.99.054307.

[128] Daniel Greif et al. "Probing Nearest-Neighbor Correlations of Ultracold Fermions in an Optical Lattice". In: *Phys. Rev. Lett.* 106 (14 Apr. 2011), p. 145302. DOI: 10.1103/PhysRevLett.106.145302. URL: https://link.aps.org/doi/10.1103/PhysRevLett.106.145302.

[129] Walter Greiner. *Relativistic Quantum Mechanics. Wave Equations*. 2nd ed. Berlin, Heidelberg: Springer, 2000. ISBN: 3-540-61621-7. DOI: 10.1007/978-3-662-04275-5.

[130] David J Griffiths. *Introduction to Elementary Particles – Second, Revised Edition*. 2nd ed. Weinheim: Wiley-VCH, 2010. ISBN: 9783527406012.

[131] Christian Gross and Immanuel Bloch. "Erratum for the Review "Quantum simulations with ultracold atoms in optical lattices" by C. Gross and I. Bloch". In: *Science* 357.6357 (2017), eaap9526. DOI: 10.1126/science.aap9526. eprint: https://www.science.org/doi/pdf/10.1126/science.aap9526. URL: https://www.science.org/doi/abs/10.1126/science.aap9526.

[132] Christian Gross and Immanuel Bloch. "Quantum simulations with ultracold atoms in optical lattices". In: *Science* 357.6355 (2017), pp. 995–1001. DOI: 10.1126/science.aal3837. eprint: https://www.science.org/doi/pdf/10.1126/science.aal3837. URL: https://www.science.org/doi/abs/10.1126/science.aal3837.

[133] Martin C. Gutzwiller. "Effect of Correlation on the Ferromagnetism of Transition Metals". In: *Phys. Rev. Lett.* 10 (5 Mar. 1963), pp. 159–162. DOI: 10.1103/PhysRevLett.10.159. URL: https://link.aps.org/doi/10.1103/PhysRevLett.10.159.

[134] Andreas Hackl and Matthias Vojta. "Pressure-induced magnetic transition and volume collapse in FeAs superconductors: an orbital-selective Mott scenario". In: *New Journal of Physics* 11.5 (May 2009), p. 055064. DOI: 10.1088/1367-2630/11/5/055064. URL: https://doi.org/10.1088/1367-2630/11/5/055064.

[135] Jutho Haegeman et al. "Time-Dependent Variational Principle for Quantum Lattices". In: *Phys. Rev. Lett.* 107 (7 Aug. 2011), p. 070601. DOI: 10.1103/PhysRevLett.107.070601. URL: https://link.aps.org/doi/10.1103/PhysRevLett.107.070601.

[136] Jutho Haegeman et al. "Unifying time evolution and optimization with matrix product states". In: *Phys. Rev. B* 94 (16 Oct. 2016), p. 165116. DOI: 10.1103/PhysRevB.94.165116. URL: https://link.aps.org/doi/10.1103/PhysRevB.94.165116.

[137] M. H. Hamidian et al. *Magnetic-field Induced Interconversion of Cooper Pairs and Density Wave States within Cuprate Composite Order*. 2018. arXiv: 1508.00620 [cond-mat.supr-con].

[138] Peter Hänggi. "Driven Quantum Systems". In: *Quantum Transport and Dissipation*. Weinheim: Wiley-VCH, 1998. Chap. 5, pp. 249–286. ISBN: 3-527-29261-6.

[139] M. Hanke-Bourgeois. *Grundlagen der Numerischen Mathematik und des Wissenschaftlichen Rechnens*. 1st ed. Mathematische Leitfäden. Wiesbaden: Vieweg+Teubner Verlag, 2002. ISBN: 978-3-519-00356-4. DOI: 10.1007/978-3-322-94877-9.

[140] R. P. Hardikar and R. T. Clay. "Phase diagram of the one-dimensional Hubbard-Holstein model at half and quarter filling". In: *Phys. Rev. B* 75 (24 June 2007), p. 245103. DOI: 10.1103/PhysRevB.75.245103. URL: https://link.aps.org/doi/10.1103/PhysRevB.75.245103.

[141] Charles R. Harris et al. "Array programming with NumPy". In: *Nature* 585.7825 (Sept. 2020), pp. 357–362. DOI: 10.1038/s41586-020-2649-2. URL: https://doi.org/10.1038/s41586-020-2649-2.

[142] Hiroshi Hashimoto and Sumio Ishihara. "Photoinduced charge-order melting dynamics in a one-dimensional interacting Holstein model". In: *Phys. Rev. B* 96 (3 July 2017), p. 035154. DOI: 10.1103/PhysRevB.96.035154. URL: https://link.aps.org/doi/10.1103/PhysRevB.96.035154.

[143] K. A. Al-Hassanieh et al. "Excitons in the One-Dimensional Hubbard Model: A Real-Time Study". In: *Phys. Rev. Lett.* 100 (16 Apr. 2008), p. 166403. DOI: 10.1103/PhysRevLett.100.166403. URL: https://link.aps.org/doi/10.1103/PhysRevLett.100.166403.

[144] M B Hastings. "An area law for one-dimensional quantum systems". In: *Journal of Statistical Mechanics: Theory and Experiment* 2007.08 (Aug. 2007), P08024–P08024. DOI: 10.1088/1742-5468/2007/08/p08024. URL: https://doi.org/10.1088/1742-5468/2007/08/p08024.

[145] Hartmut Haug and Stephan W Koch. *Quantum Theory of the Optical and Electronic Properties of Semiconductors*. 2nd. Singapore, New Jersey, London, Hong Kong: World Scientific, 1993. ISBN: 981-02-1341-7. DOI: 10.1142/1977. eprint: https://www.worldscientific.com/doi/pdf/10.1142/1977. URL: https://www.worldscientific.com/doi/abs/10.1142/1977.

[146] Fabian Heidrich-Meisner. "Transport properties of low-dimensional quantum spin systems". PhD thesis. Technische Universität Carolo-Wilhelmina zu Braunschweig, Mar. 2005. DOI: 10.24355/dbbs.084-200511080100-331. URL: http://www.digibib.tu-bs.de/?docid=00001712.

[147] S. Hellmann et al. "Time-domain classification of charge-density-wave insulators". In: *Nature Communications* 3.1 (Sept. 2012), p. 1069. ISSN: 2041-1723. DOI: 10.1038/ncomms2078. URL: https://doi.org/10.1038/ncomms2078.

[148] J. Herbrych et al. "Block orbital-selective Mott insulators: A spin excitation analysis". In: *Phys. Rev. B* 102 (11 Sept. 2020), p. 115134. DOI: 10.1103/PhysRevB.102.115134. URL: https://link.aps.org/doi/10.1103/PhysRevB.102.115134.

[149] J. Herbrych et al. "Novel Magnetic Block States in Low-Dimensional Iron-Based Superconductors". In: *Phys. Rev. Lett.* 123 (2 July 2019), p. 027203. DOI: 10.1103/PhysRevLett.123.027203. URL: https://link.aps.org/doi/10.1103/PhysRevLett.123.027203.

[150] M. Hofherr et al. "Ultrafast optically induced spin transfer in ferromagnetic alloys". In: *Science Advances* 6.3 (2020), eaay8717. DOI: 10.1126/sciadv.aay8717. eprint: https://www.science.org/doi/pdf/10.1126/sciadv.aay8717. URL: https://www.science.org/doi/abs/10.1126/sciadv.aay8717.

[151] Sebastian Holtz, Thorsten Rohwedder, and Reinhold Schneider. "On manifolds of tensors of fixed TT-rank". In: *Numerische Mathematik* 120.4 (Apr. 2012), pp. 701–731. ISSN: 0945-3245. DOI: 10.1007/s00211-011-0419-7. URL: https://doi.org/10.1007/s00211-011-0419-7.

[152] Andreas Holzner et al. "Chebyshev matrix product state approach for spectral functions". In: *Phys. Rev. B* 83 (19 May 2011), p. 195115. DOI: 10.1103/PhysRevB.83.195115. URL: https://link.aps.org/doi/10.1103/PhysRevB.83.195115.

[153] J. E. Hopcroft, R. Motwani, and J. D. Ullman. *Introduction to Automata Theory, Languages, and Computation*. 3rd ed. Addison-Wesley, 2006. ISBN: 0-321-45536-3. URL: http://www-db.stanford.edu/~ullman/ialc.html.

[154] J. E. Hopcroft and J. D. Ullman. *Introduction to Automata Theory, Languages, and Computation*. 1st ed. Addison-Wesley, 1979. ISBN: 0-201-02988-X. URL: http://www-db.stanford.edu/~ullman/ialc.html.

[155] Takashi Hotta and Elbio Dagotto. "Theory of Manganites". In: *Colossal Magnetoresistive Manganites*. Ed. by Tapan Chatterji. 1st ed. Dordrecht: Kluwer Academic Publishers, 2004, pp. 207–262. ISBN: 1-4020-1844-4. DOI: 10.1007/978-94-015-1244-2_5.

[156] D. Hsieh et al. "Observation of a metal-to-insulator transition with both Mott-Hubbard and Slater characteristics in Sr_2IrO_4 from time-resolved photocarrier dynamics". In: *Phys. Rev. B* 86 (3 July 2012), p. 035128. DOI: 10.1103/PhysRevB.86.035128. URL: https://link.aps.org/doi/10.1103/PhysRevB.86.035128.

[157] W. Hu et al. "Optically enhanced coherent transport in YBa2Cu3O6.5 by ultrafast redistribution of interlayer coupling". In: *Nature Materials* 13.7 (July 2014), pp. 705–711. ISSN: 1476-4660. DOI: 10.1038/nmat3963. URL: https://doi.org/10.1038/nmat3963.

[158] J. Hubbard and Brian Hilton Flowers. "Electron correlations in narrow energy bands". In: *Proceedings of the Royal Society of London. Series A. Mathematical and Physical Sciences* 276.1365 (1963), pp. 238–257. DOI: 10.1098/rspa.1963.0204. eprint: https://royalsocietypublishing.org/doi/pdf/10.1098/rspa.1963.0204. URL: https://royalsocietypublishing.org/doi/abs/10.1098/rspa.1963.0204.

[159] J. Hubbard and Brian Hilton Flowers. "Electron correlations in narrow energy bands. II. The degenerate band case". In: *Proceedings of the Royal Society of London. Series A. Mathematical and Physical Sciences* 277.1369 (1964), pp. 237–259. DOI: 10.1098/rspa.1964.0019. eprint: https://royalsocietypublishing.org/doi/pdf/10.1098/rspa.1964.0019. URL: https://royalsocietypublishing.org/doi/abs/10.1098/rspa.1964.0019.

[160] J. Hubbard and Brian Hilton Flowers. "Electron correlations in narrow energy bands III. An improved solution". In: *Proceedings of the Royal Society of London. Series A. Mathematical and Physical Sciences* 281.1386 (1964), pp. 401–419. DOI: 10.1098/rspa.1964.0190. eprint: https://royalsocietypublishing.org/doi/pdf/10.1098/rspa.1964.0190. URL: https://royalsocietypublishing.org/doi/abs/10.1098/rspa.1964.0190.

[161] J. Hubbard and Brian Hilton Flowers. "Electron correlations in narrow energy bands - IV. The atomic representation". In: *Proceedings of the Royal Society of London. Series A. Mathematical and Physical Sciences* 285.1403 (1965), pp. 542–560. DOI: 10.1098/rspa.1965.0124. eprint: https://royalsocietypublishing.org/doi/pdf/10.1098/rspa.1965.0124. URL: https://royalsocietypublishing.org/doi/abs/10.1098/rspa.1965.0124.

[162] J. Hubbard and Brian Hilton Flowers. "Electron correlations in narrow energy bands V. A perturbation expansion about the atomic limit". In: *Proceedings of the Royal Society of London. Series A. Mathematical and Physical Sciences* 296.1444 (1967), pp. 82–99. DOI: 10.1098/rspa.1967.0007. eprint: https://royalsocietypublishing.org/doi/pdf/10.1098/rspa.1967.0007. URL: https://royalsocietypublishing.org/doi/abs/10.1098/rspa.1967.0007.

[163] J. Hubbard and Brian Hilton Flowers. "Electron correlations in narrow energy bands VI. The connexion with many-body perturbation theory". In: *Proceedings of the Royal Society of London. Series A. Mathematical and Physical Sciences* 296.1444 (1967), pp. 100–112. DOI: 10.1098/rspa.1967.0008. eprint: https://royalsocietypublishing.org/doi/pdf/10.1098/rspa.1967.0008. URL: https://royalsocietypublishing.org/doi/abs/10.1098/rspa.1967.0008.

[164] J. Hubbard and J. B. Torrance. "Model of the Neutral-Ionic Phase Transformation". In: *Phys. Rev. Lett.* 47 (24 Dec. 1981), pp. 1750–1754. DOI: 10.1103/PhysRevLett.47.1750. URL: https://link.aps.org/doi/10.1103/PhysRevLett.47.1750.

[165] Claudius Hubig. "Symmetry-Protected Tensor Networks". PhD thesis. Ludwig-Maximilians-Universität München, 2017. DOI: 10.5282/edoc.21348.

[166] M. Hücker et al. "Competing charge, spin, and superconducting orders in underdoped $YBa_2Cu_3O_y$". In: *Phys. Rev. B* 90 (5 Aug. 2014), p. 054514. DOI: 10.1103/PhysRevB.90.054514. URL: https://link.aps.org/doi/10.1103/PhysRevB.90.054514.

[167] Michael Innerberger et al. "Electron-light interaction in nonequilibrium: exact diagonalization for time-dependent Hubbard Hamiltonians". In: *The European Physical Journal Plus* 135.11 (Nov. 2020), p. 922. ISSN: 2190-5444. DOI: 10.1140/epjp/s13360-020-00919-2. URL: https://doi.org/10.1140/epjp/s13360-020-00919-2.

[168] Sumio Ishihara. "Photoinduced Ultrafast Phenomena in Correlated Electron Magnets". In: *Journal of the Physical Society of Japan* 88.7 (2019), p. 072001. DOI: 10.7566/JPSJ.88.072001. eprint: https://doi.org/10.7566/JPSJ.88.072001. URL: https://doi.org/10.7566/JPSJ.88.072001.

[169] David Jansen, Janez Bonča, and Fabian Heidrich-Meisner. "Finite-temperature density-matrix renormalization group method for electron-phonon systems: Thermodynamics and Holstein-polaron spectral functions". In: *Phys. Rev. B* 102 (16 Oct. 2020), p. 165155. DOI: 10.1103/PhysRevB.102.165155. URL: https://link.aps.org/doi/10.1103/PhysRevB.102.165155.

[170] E. Jeckelmann, F. Gebhard, and F. H. L. Essler. "Optical Conductivity of the Half-Filled Hubbard Chain". In: *Phys. Rev. Lett.* 85 (18 Oct. 2000), pp. 3910–3913. DOI: 10.1103/PhysRevLett.85.3910. URL: https://link.aps.org/doi/10.1103/PhysRevLett.85.3910.

[171] Eric Jeckelmann. "Dynamical density-matrix renormalization-group method". In: *Phys. Rev. B* 66 (4 July 2002), p. 045114. DOI: 10.1103/PhysRevB.66.045114. URL: https://link.aps.org/doi/10.1103/PhysRevB.66.045114.

[172] Eric Jeckelmann. "Optical excitations in a one-dimensional Mott insulator". In: *Phys. Rev. B* 67 (7 Feb. 2003), p. 075106. DOI: 10.1103/PhysRevB.67.075106. URL: https://link.aps.org/doi/10.1103/PhysRevB.67.075106.

[173] Xiang Jiang et al. "Real-time *GW*-BSE investigations on spin-valley exciton dynamics in monolayer transition metal dichalcogenide". In: *Science Advances* 7.10 (2021), eabf3759. DOI: 10.1126/sciadv.abf3759. eprint: https://www.science.org/doi/pdf/10.1126/sciadv.abf3759. URL: https://www.science.org/doi/abs/10.1126/sciadv.abf3759.

[174] Chenhao Jin et al. "Observation of moiré excitons in WSe2/WS2 heterostructure superlattices". In: *Nature* 567.7746 (Mar. 2019), pp. 76–80. ISSN: 1476-4687. DOI: 10.1038/s41586-019-0976-y. URL: https://doi.org/10.1038/s41586-019-0976-y.

[175] Chenhao Jin et al. "Ultrafast dynamics in van der Waals heterostructures". In: *Nature Nanotechnology* 13.11 (Nov. 2018), pp. 994–1003. ISSN: 1748-3395. DOI: 10.1038/s41565-018-0298-5. URL: https://doi.org/10.1038/s41565-018-0298-5.

[176] Peter D Johnson. "Spin-polarized photoemission". In: *Reports on Progress in Physics* 60.11 (Nov. 1997), pp. 1217–1304. DOI: 10.1088/0034-4885/60/11/002. URL: https://doi.org/10.1088/0034-4885/60/11/002.

[177] Peter David Johnson and Gernot Güntherodt. "Spin-polarized Photoelectron Spectroscopy as a Probe of Magnetic Systems". In: *Handbook of Magnetism and Advanced Magnetic Materials*. John Wiley & Sons, Ltd, 2007. ISBN: 9780470022184. DOI: https://doi.org/10.1002/9780470022184.hmm315. eprint: https://onlinelibrary.wiley.com/doi/pdf/10.1002/9780470022184.hmm315. URL: https://onlinelibrary.wiley.com/doi/abs/10.1002/9780470022184.hmm315.

[178] Leo P. Kadanoff and Gordon Baym. *Quantum Statistical Mechanics: Green's Function Methods in Equilibrium and Nonequilibrium Problems*. Frontiers in Physics: A Lecture Note and Reprint Series. New York, NY: W. A. Benjamin, Inc., 1962. DOI: 10.1201/9780429493218.

[179] Mona H. Kalthoff, Götz S. Uhrig, and J. K. Freericks. "Emergence of Floquet behavior for lattice fermions driven by light pulses". In: *Phys. Rev. B* 98 (3 July 2018), p. 035138. DOI: 10.1103/PhysRevB.98.035138. URL: https://link.aps.org/doi/10.1103/PhysRevB.98.035138.

[180] Junjiro Kanamori. "Electron Correlation and Ferromagnetism of Transition Metals". In: *Progress of Theoretical Physics* 30.3 (Sept. 1963), pp. 275–289. ISSN: 0033-068X. DOI: 10.1143/PTP.30.275. eprint: https://academic.oup.com/ptp/article-pdf/30/3/275/5278869/30-3-275.pdf. URL: https://doi.org/10.1143/PTP.30.275.

[181] Ryui Kaneko et al. "Charge orders in organic charge-transfer salts". In: *New Journal of Physics* 19.10 (Oct. 2017), p. 103033. DOI: 10.1088/1367-2630/aa887b. URL: https://doi.org/10.1088/1367-2630/aa887b.

[182] C. Karrasch, D. M. Kennes, and J. E. Moore. "Transport properties of the one-dimensional Hubbard model at finite temperature". In: *Phys. Rev. B* 90 (15 Oct. 2014), p. 155104. DOI: 10.1103/PhysRevB.90.155104. URL: https://link.aps.org/doi/10.1103/PhysRevB.90.155104.

[183] Frederik Keim. "Effective one-dimensional models including two-particle interaction from matrix product states". PhD thesis. Technische Universität Dortmund, 2018. DOI: 10.17877/DE290R-18860. URL: http://hdl.handle.net/2003/36860.

[184] A. F. Kemper et al. "Review of the Theoretical Description of Time-Resolved Angle-Resolved Photoemission Spectroscopy in Electron-Phonon Mediated Superconductors". In: *Annalen der Physik* 529.9 (2017), p. 1600235. DOI: https://doi.org/10.1002/andp.201600235. eprint: https://onlinelibrary.wiley.com/doi/pdf/10.1002/andp.201600235. URL: https://onlinelibrary.wiley.com/doi/abs/10.1002/andp.201600235.

[185] D. M. Kennes et al. "Floquet Engineering in Quantum Chains". In: *Phys. Rev. Lett.* 120 (12 Mar. 2018), p. 127601. DOI: 10.1103/PhysRevLett.120.127601. URL: https://link.aps.org/doi/10.1103/PhysRevLett.120.127601.

[186] Marius Keunecke. "Ultrafast electron dynamics measured with a novel time-resolved high-repetition rate momentum microscopy setup". PhD thesis. Georg-August-Universität Göttingen, Mar. 2021. URL: http://hdl.handle.net/21.11130/00-1735-0000-0008-57CC-1.

[187] Marius Keunecke et al. *Direct Access to Auger recombination in Graphene*. 2020. arXiv: 2012.01256 [cond-mat.other].

[188] Marius Keunecke et al. "Electromagnetic dressing of the electron energy spectrum of Au(111) at high momenta". In: *Phys. Rev. B* 102 (16 Oct. 2020), p. 161403. DOI: 10.1103/PhysRevB.102.161403. URL: https://link.aps.org/doi/10.1103/PhysRevB.102.161403.

[189] C. W. von Keyserlingk, Vedika Khemani, and S. L. Sondhi. "Absolute stability and spatiotemporal long-range order in Floquet systems". In: *Phys. Rev. B* 94 (8 Aug. 2016), p. 085112. DOI: 10.1103/PhysRevB.94.085112. URL: https://link.aps.org/doi/10.1103/PhysRevB.94.085112.

[190] Vedika Khemani et al. "Phase Structure of Driven Quantum Systems". In: *Phys. Rev. Lett.* 116 (25 June 2016), p. 250401. DOI: 10.1103/PhysRevLett.116.250401. URL: https://link.aps.org/doi/10.1103/PhysRevLett.116.250401.

[191] Jimin Kim et al. "Two-Dimensional Dirac Fermions Protected by Space-Time Inversion Symmetry in Black Phosphorus". In: *Phys. Rev. Lett.* 119 (22 Nov. 2017), p. 226801. DOI: 10.1103/PhysRevLett.119.226801. URL: https://link.aps.org/doi/10.1103/PhysRevLett.119.226801.

[192] M. Kira and S.W. Koch. "Many-body correlations and excitonic effects in semiconductor spectroscopy". In: *Progress in Quantum Electronics* 30.5 (2006), pp. 155–296. ISSN: 0079-6727. DOI: https://doi.org/10.1016/j.pquantelec.2006.12.002. URL: https://www.sciencedirect.com/science/article/pii/S0079672706000280.

[193] Mackillo Kira and Stephan W. Koch. *Semiconductor Quantum Optics*. 1st ed. Cambridge: Cambridge University Press, 2011. ISBN: 978-0-521-87509-7. DOI: 10.1017/CBO9781139016926.

[194] J. Kirschner. *Polarized Electrons at Surfaces*. 1st ed. Vol. 106. Springer Tracts in Modern Physics. Berlin, Heidelberg, New York, Tokyo: Springer-Verlag, 1985. ISBN: 3-540-15003-X. DOI: 10.1007/BFb0108668.

[195] Thomas Köhler. "Photoexcitations of Model Manganite Systems using Matrix-Product States". PhD thesis. Georg-August-Universität Göttingen, Jan. 2019. URL: http://hdl.handle.net/11858/00-1735-0000-002E-E579-B.

[196] Thomas Köhler, Jan Stolpp, and Sebastian Paeckel. "Efficient and Flexible Approach to Simulate Low-Dimensional Quantum Lattice Models with Large Local Hilbert Spaces". In: *SciPost Phys.* 10 (3 2021), p. 58. DOI: 10.21468/SciPostPhys.10.3.058. URL: https://scipost.org/10.21468/SciPostPhys.10.3.058.

[197] Thomas Köhler et al. "Relaxation of photoexcitations in polaron-induced magnetic microstructures". In: *Phys. Rev. B* 97 (23 June 2018), p. 235120. DOI: 10.1103/PhysRevB.97.235120. URL: https://link.aps.org/doi/10.1103/PhysRevB.97.235120.

[198] T. Köhler et al. "Formation of spatial patterns by spin-selective excitations of interacting fermions". In: *Phys. Rev. B* 102 (23 Dec. 2020), p. 235166. DOI: 10.1103/PhysRevB.102.235166. URL: https://link.aps.org/doi/10.1103/PhysRevB.102.235166.

[199] C. Kollath et al. "Modulation spectroscopy with ultracold fermions in an optical lattice". In: *Phys. Rev. A* 74 (4 Oct. 2006), p. 041604. DOI: 10.1103/PhysRevA.74.041604. URL: https://link.aps.org/doi/10.1103/PhysRevA.74.041604.

[200] P. E Kornilovitch. "Photoemission spectroscopy and sum rules in dilute electron-phonon systems". In: *Europhysics Letters (EPL)* 59.5 (Sept. 2002), pp. 735–741. DOI: 10.1209/epl/i2002-00187-x. URL: https://doi.org/10.1209/epl/i2002-00187-x.

[201] Ronnie Kosloff. "Time-dependent quantum-mechanical methods for molecular dynamics". In: *The Journal of Physical Chemistry* 92.8 (Apr. 1988), pp. 2087–2100. ISSN: 0022-3654. DOI: 10.1021/j100319a003. URL: https://doi.org/10.1021/j100319a003.

[202] Ferenc Krausz and Misha Ivanov. "Attosecond physics". In: *Rev. Mod. Phys.* 81 (1 Feb. 2009), pp. 163–234. DOI: 10.1103/RevModPhys.81.163. URL: https://link.aps.org/doi/10.1103/RevModPhys.81.163.

[203] Tobias Küchel. "Dynamics of one-dimensional electron systems". PhD thesis. Karlsruher Institut für Technologie, 2009. DOI: 10.5445/IR/1000013836. URL: https://publikationen.bibliothek.kit.edu/1000013836.

[204] Flore K. Kunst, Guido van Miert, and Emil J. Bergholtz. "Extended Bloch theorem for topological lattice models with open boundaries". In: *Phys. Rev. B* 99 (8 Feb. 2019), p. 085427. DOI: 10.1103/PhysRevB.99.085427. URL: https://link.aps.org/doi/10.1103/PhysRevB.99.085427.

[205] Jens Kunstmann et al. "Momentum-space indirect interlayer excitons in transition-metal dichalcogenide van der Waals heterostructures". In: *Nature Physics* 14.8 (Aug. 2018), pp. 801–805. ISSN: 1745-2481. DOI: 10.1038/s41567-018-0123-y. URL: https://doi.org/10.1038/s41567-018-0123-y.

[206] Tomotaka Kuwahara and Keiji Saito. "Lieb-Robinson Bound and Almost-Linear Light Cone in Interacting Boson Systems". In: *Phys. Rev. Lett.* 127 (7 Aug. 2021), p. 070403. DOI: 10.1103/PhysRevLett.127.070403. URL: https://link.aps.org/doi/10.1103/PhysRevLett.127.070403.

[207] Cornelius Lanczos. "An Iteration Method for the Solution of the Eigenvalue Problem of Linear Differential and Integral Operators". In: *Journal of Research of the National Bureau of Standards* 45.4 (Oct. 1950), pp. 255–282. DOI: 10.6028/jres.045.026. URL: https://nvlpubs.nist.gov/nistpubs/jres/045/jresv45n4p255_A1b.pdf.

[208] C. Laulhé et al. "Ultrafast Formation of a Charge Density Wave State in $1T-TaS_2$: Observation at Nanometer Scales Using Time-Resolved X-Ray Diffraction". In: *Phys. Rev. Lett.* 118 (24 June 2017), p. 247401. DOI: 10.1103/PhysRevLett.118.247401. URL: https://link.aps.org/doi/10.1103/PhysRevLett.118.247401.

[209] Xu Lei and Zhang Jun. "Drude Weight, Optical Conductivity of Two-Dimensional Hubbard Model at Half Filling". In: *Communications in Theoretical Physics* 50.01, 237 (2008), p. 237. URL: https://ctp.itp.ac.cn/EN/abstract/article_11324.shtml.

[210] Zala Lenarčič and Peter Prelovšek. "Charge recombination in undoped cuprates". In: *Phys. Rev. B* 90 (23 Dec. 2014), p. 235136. DOI: 10.1103/PhysRevB.90.235136. URL: https://link.aps.org/doi/10.1103/PhysRevB.90.235136.

[211] Zala Lenarčič and Peter Prelovšek. "Ultrafast Charge Recombination in a Photoexcited Mott-Hubbard Insulator". In: *Phys. Rev. Lett.* 111 (1 July 2013), p. 016401. DOI: 10.1103/PhysRevLett.111.016401. URL: https://link.aps.org/doi/10.1103/PhysRevLett.111.016401.

[212] Zala Lenarčič et al. "Optical response of highly excited particles in a strongly correlated system". In: *Phys. Rev. B* 89 (12 Mar. 2014), p. 125123. DOI: 10.1103/PhysRevB.89.125123. URL: https://link.aps.org/doi/10.1103/PhysRevB.89.125123.

[213] Benjamin Lenz. "Unconventional Phases in Two-Dimensional Hubbard and Kondo-Lattice Models by Variational Cluster Approaches". PhD thesis. Georg-August-Universität Göttingen, Mar. 2017. URL: http://hdl.handle.net/11858/00-1735-0000-0023-3DFC-1.

[214] Jiajun Li and Martin Eckstein. "Nonequilibrium steady-state theory of photodoped Mott insulators". In: *Phys. Rev. B* 103 (4 Jan. 2021), p. 045133. DOI: 10.1103/PhysRevB.103.045133. URL: https://link.aps.org/doi/10.1103/PhysRevB.103.045133.

[215] Tianqi Li et al. "Femtosecond switching of magnetism via strongly correlated spin–charge quantum excitations". In: *Nature* 496.7443 (Apr. 2013), pp. 69–73. ISSN: 1476-4687. DOI: 10.1038/nature11934. URL: https://doi.org/10.1038/nature11934.

[216] Elliott H. Lieb and Derek W. Robinson. "The finite group velocity of quantum spin systems". In: *Communications in Mathematical Physics* 28.3 (Sept. 1972), pp. 251–257. ISSN: 1432-0916. DOI: 10.1007/BF01645779. URL: https://doi.org/10.1007/BF01645779.

[217] Elliott H. Lieb and F. Y. Wu. "Absence of Mott Transition in an Exact Solution of the Short-Range, One-Band Model in One Dimension". In: *Phys. Rev. Lett.* 20 (25 June 1968), pp. 1445–1448. DOI: 10.1103/PhysRevLett.20.1445. URL: https://link.aps.org/doi/10.1103/PhysRevLett.20.1445.

[218] Elliott H. Lieb and F. Y. Wu. "Absence of Mott Transition in an Exact Solution of the Short-Range, One-Band Model in One Dimension". In: *Phys. Rev. Lett.* 21 (3 July 1968), pp. 192–192. DOI: 10.1103/PhysRevLett.21.192.2. URL: https://link.aps.org/doi/10.1103/PhysRevLett.21.192.2.

[219] M. Ligges et al. "Erratum: Ultrafast Doublon Dynamics in Photoexcited $1T-TaS_2$ [Phys. Rev. Lett. 120, 166401 (2018)]". In: *Phys. Rev. Lett.* 122 (15 Apr. 2019), p. 159901. DOI: 10.1103/PhysRevLett.122.159901. URL: https://link.aps.org/doi/10.1103/PhysRevLett.122.159901.

[220] M. Ligges et al. "Ultrafast Doublon Dynamics in Photoexcited $1T$-TaS_2". In: *Phys. Rev. Lett.* 120 (16 Apr. 2018), p. 166401. DOI: 10.1103/PhysRevLett.120.166401. URL: https://link.aps.org/doi/10.1103/PhysRevLett.120.166401.

[221] Erfu Liu et al. "Signatures of moiré trions in WSe2/MoSe2 heterobilayers". In: *Nature* 594.7861 (June 2021), pp. 46–50. ISSN: 1476-4687. DOI: 10.1038/s41586-021-03541-z. URL: https://doi.org/10.1038/s41586-021-03541-z.

[222] Fang Liu et al. "Direct Determination of Band-Gap Renormalization in the Photoexcited Monolayer MoS_2". In: *Phys. Rev. Lett.* 122 (24 June 2019), p. 246803. DOI: 10.1103/PhysRevLett.122.246803. URL: https://link.aps.org/doi/10.1103/PhysRevLett.122.246803.

[223] M. Lohse et al. "A Thouless quantum pump with ultracold bosonic atoms in an optical superlattice". In: *Nature Physics* 12.4 (Apr. 2016), pp. 350–354. ISSN: 1745-2481. DOI: 10.1038/nphys3584. URL: https://doi.org/10.1038/nphys3584.

[224] Hantao Lu et al. "Enhanced Charge Order in a Photoexcited One-Dimensional Strongly Correlated System". In: *Phys. Rev. Lett.* 109 (19 Nov. 2012), p. 197401. DOI: 10.1103/PhysRevLett.109.197401. URL: https://link.aps.org/doi/10.1103/PhysRevLett.109.197401.

[225] Hantao Lu et al. "Photoinduced in-gap excitations in the one-dimensional extended Hubbard model". In: *Phys. Rev. B* 91 (24 June 2015), p. 245117. DOI: 10.1103/PhysRevB.91.245117. URL: https://link.aps.org/doi/10.1103/PhysRevB.91.245117.

[226] Christian Lubich, Ivan V. Oseledets, and Bart Vandereycken. "Time Integration of Tensor Trains". In: *SIAM Journal on Numerical Analysis* 53.2 (2015), pp. 917–941. DOI: 10.1137/140976546. eprint: https://doi.org/10.1137/140976546. URL: https://doi.org/10.1137/140976546.

[227] Ma Luo. "Floquet states of valley-polarized metal with one-way spin or charge transport in zigzag nanoribbons". In: *Phys. Rev. B* 99 (7 Feb. 2019), p. 075406. DOI: 10.1103/PhysRevB.99.075406. URL: https://link.aps.org/doi/10.1103/PhysRevB.99.075406.

[228] Julien Madéo et al. "Directly visualizing the momentum-forbidden dark excitons and their dynamics in atomically thin semiconductors". In: *Science* 370.6521 (2020), pp. 1199–1204. DOI: 10.1126/science.aba1029. eprint: https://www.science.org/doi/pdf/10.1126/science.aba1029. URL: https://www.science.org/doi/abs/10.1126/science.aba1029.

[229] Gerald D. Mahan. *Many-Particle Physics*. 3rd ed. Physics of Solids and Liquids. Boston, MA: Springer, 2000. ISBN: 978-0-306-46338-9. DOI: 10.1007/978-1-4757-5714-9.

[230] Sandra Ju-Sil Mahlert. "Störungstheorie in vierter Ordnungfür das halbgefüllte Hubbard-Modellim Limes hoher Dimensionen". PhD thesis. Philipps-Universität Marburg, 2003. DOI: https://doi.org/10.17192/z2003.0122.

[231] Ermin Malic et al. "Dark excitons in transition metal dichalcogenides". In: *Phys. Rev. Materials* 2 (1 Jan. 2018), p. 014002. DOI: 10.1103/PhysRevMaterials.2.014002. URL: https://link.aps.org/doi/10.1103/PhysRevMaterials.2.014002.

[232] R. Mankowsky et al. "Dynamical Stability Limit for the Charge Density Wave in $K_{0.3}MoO_3$". In: *Phys. Rev. Lett.* 118 (11 Mar. 2017), p. 116402. DOI: 10.1103/PhysRevLett.118.116402. URL: https://link.aps.org/doi/10.1103/PhysRevLett.118.116402.

[233] S. R. Manmana et al. "Quantum critical behavior of the one-dimensional ionic Hubbard model". In: *Phys. Rev. B* 70 (15 Oct. 2004), p. 155115. DOI: 10.1103/PhysRevB.70.155115. URL: https://link.aps.org/doi/10.1103/PhysRevB.70.155115.

[234] S. R. Manmana et al. "Strongly Correlated Fermions after a Quantum Quench". In: *Phys. Rev. Lett.* 98 (21 May 2007), p. 210405. DOI: 10.1103/PhysRevLett.98.210405. URL: https://link.aps.org/doi/10.1103/PhysRevLett.98.210405.

[235] Salvatore R. Manmana, Alejandro Muramatsu, and Reinhard M. Noack. "Time evolution of one-dimensional Quantum Many Body Systems". In: *AIP Conference Proceedings* 789.1 (2005), pp. 269–278. DOI: 10.1063/1.2080353. eprint: https://aip.scitation.org/doi/pdf/10.1063/1.2080353. URL: https://aip.scitation.org/doi/abs/10.1063/1.2080353.

[236] Efstratios Manousakis. "Optimizing the role of impact ionization in conventional insulators". In: *Scientific Reports* 9.1 (Dec. 2019), p. 20395. ISSN: 2045-2322. DOI: 10.1038/s41598-019-56974-y. URL: https://doi.org/10.1038/s41598-019-56974-y.

[237] Efstratios Manousakis. "Photovoltaic effect for narrow-gap Mott insulators". In: *Phys. Rev. B* 82 (12 Sept. 2010), p. 125109. DOI: 10.1103/PhysRevB.82.125109. URL: https://link.aps.org/doi/10.1103/PhysRevB.82.125109.

[238] A M Marques and R G Dias. "Analytical solution of open crystalline linear 1D tight-binding models". In: *Journal of Physics A: Mathematical and Theoretical* 53.7 (Jan. 2020), p. 075303. DOI: 10.1088/1751-8121/ab6a6e. URL: https://doi.org/10.1088/1751-8121/ab6a6e.

[239] S. Mathias et al. "Self-amplified photo-induced gap quenching in a correlated electron material". In: *Nature Communications* 7.1 (Oct. 2016), p. 12902. ISSN: 2041-1723. DOI: 10.1038/ncomms12902. URL: https://doi.org/10.1038/ncomms12902.

[240] A. Matulis and F. M. Peeters. "Analogy between one-dimensional chain models and graphene". In: *American Journal of Physics* 77.7 (2009), pp. 595–601. DOI: 10.1119/1.3127143. eprint: https://doi.org/10.1119/1.3127143. URL: https://doi.org/10.1119/1.3127143.

[241] J. H. Mentink, K. Balzer, and M. Eckstein. "Ultrafast and reversible control of the exchange interaction in Mott insulators". In: *Nature Communications* 6.1 (Mar. 2015), p. 6708. ISSN: 2041-1723. DOI: 10.1038/ncomms7708. URL: https://doi.org/10.1038/ncomms7708.

[242] Michael Messer et al. "Exploring Competing Density Order in the Ionic Hubbard Model with Ultracold Fermions". In: *Phys. Rev. Lett.* 115 (11 Sept. 2015), p. 115303. DOI: 10.1103/PhysRevLett.115.115303. URL: https://link.aps.org/doi/10.1103/PhysRevLett.115.115303.

[243] Constantin Meyer and Salvatore R. Manmana. *Formation of spinful dark excitons in Hubbard systems with magnetic superstructures*. 2021. arXiv: 2109.07037 [cond-mat.str-el].

[244] M. Mitrano et al. "Possible light-induced superconductivity in K3C60 at high temperature". In: *Nature* 530.7591 (Feb. 2016), pp. 461–464. ISSN: 1476-4687. DOI: 10.1038/nature16522. URL: https://doi.org/10.1038/nature16522.

[245] M. Mitrano et al. "Pressure-Dependent Relaxation in the Photoexcited Mott Insulator ET$--$$F_2$TCNQ: Influence of Hopping and Correlations on Quasiparticle Recombination Rates". In: *Phys. Rev. Lett.* 112 (11 Mar. 2014), p. 117801. DOI: 10.1103/PhysRevLett.112.117801. URL: https://link.aps.org/doi/10.1103/PhysRevLett.112.117801.

[246] T. Miyamoto et al. "Biexciton in one-dimensional Mott insulators". In: *Communications Physics* 2.1 (Oct. 2019), p. 131. ISSN: 2399-3650. DOI: 10.1038/s42005-019-0223-8. URL: https://doi.org/10.1038/s42005-019-0223-8.

[247] R. Moessner and S. L. Sondhi. "Equilibration and order in quantum Floquet matter". In: *Nature Physics* 13.5 (May 2017), pp. 424–428. ISSN: 1745-2481. DOI: 10.1038/nphys4106. URL: https://doi.org/10.1038/nphys4106.

[248] Nevill Mott. *Metal-Insulator Transitions*. 1st ed. London: Taylor & Francis, 1974. ISBN: 0850660793. DOI: 10.1201/b12795.

[249] Yuta Murakami et al. "Photoinduced Enhancement of Excitonic Order". In: *Phys. Rev. Lett.* 119 (24 Dec. 2017), p. 247601. DOI: 10.1103/PhysRevLett.119.247601. URL: https://link.aps.org/doi/10.1103/PhysRevLett.119.247601.

[250] M. X. Na et al. "Direct determination of mode-projected electron-phonon coupling in the time domain". In: *Science* 366.6470 (2019), pp. 1231–1236. DOI: 10.1126/science.aaw1662. eprint: https://www.science.org/doi/pdf/10.1126/science.aaw1662. URL: https://www.science.org/doi/abs/10.1126/science.aaw1662.

[251] Bruno Nachtergaele, Robert Sims, and Amanda Young. "Quasi-locality bounds for quantum lattice systems. I. Lieb-Robinson bounds, quasi-local maps, and spectral flow automorphisms". In: *Journal of Mathematical Physics* 60.6 (2019), p. 061101. DOI: 10.1063/1.5095769. eprint: https://doi.org/10.1063/1.5095769. URL: https://doi.org/10.1063/1.5095769.

[252] R. D. Nesselrodt and J. K. Freericks. "Exact solution of two simple non-equilibrium electron-phonon and electron-electron coupled systems: The atomic limit of the Holstein-Hubbard model and the generalized Hatsugai-Komoto model". In: *Phys. Rev. B* 104 (15 Oct. 2021), p. 155104. DOI: 10.1103/PhysRevB.104.155104. URL: https://link.aps.org/doi/10.1103/PhysRevB.104.155104.

[253] André Neubauer. *DFT – Diskrete Fourier-Transformation: Elementare Einführung*. 1st ed. Wiesbaden: Vieweg+Teubner Verlag, 2012. ISBN: 978-3-8348-1996-3. DOI: 10.1007/978-3-8348-1997-0.

[254] H. T. M. Nghiem and T. A. Costi. "Self-energy method for time-dependent spectral functions of the Anderson impurity model within the time-dependent numerical renormalization group approach". In: *Phys. Rev. B* 104 (20 Nov. 2021), p. 205113. DOI: 10.1103/PhysRevB.104.205113. URL: https://link.aps.org/doi/10.1103/PhysRevB.104.205113.

[255] H. T. M. Nghiem and T. A. Costi. "Time Evolution of the Kondo Resonance in Response to a Quench". In: *Phys. Rev. Lett.* 119 (15 Oct. 2017), p. 156601. DOI: 10.1103/PhysRevLett.119.156601. URL: https://link.aps.org/doi/10.1103/PhysRevLett.119.156601.

[256] H. T. M. Nghiem and T. A. Costi. "Time-dependent numerical renormalization group method for multiple quenches: Towards exact results for the long-time limit of thermodynamic observables and spectral functions". In: *Phys. Rev. B* 98 (15 Oct. 2018), p. 155107. DOI: 10.1103/PhysRevB.98.155107. URL: https://link.aps.org/doi/10.1103/PhysRevB.98.155107.

[257] H. T. M. Nghiem, H. T. Dang, and T. A. Costi. "Time-dependent spectral functions of the Anderson impurity model in response to a quench with application to time-resolved photoemission spectroscopy". In: *Phys. Rev. B* 101 (11 Mar. 2020), p. 115117. DOI: 10.1103/PhysRevB.101.115117. URL: https://link.aps.org/doi/10.1103/PhysRevB.101.115117.

[258] M.P. Nightingale and Cyrus J. Umrigar, eds. *Quantum Monte Carlo Methods in Physics and Chemistry*. 1st ed. Nato Science Series C. Dordrecht: Springer Netherlands, 1999. ISBN: 978-0-7923-5551-9.

[259] Reinhard M. Noack and Salvatore R. Manmana. "Diagonalization- and Numerical Renormalization-Group-Based Methods for Interacting Quantum Systems". In: *AIP Conference Proceedings* 789.1 (2005), pp. 93–163. DOI: 10.1063/1.2080349. eprint: https://aip.scitation.org/doi/pdf/10.1063/1.2080349. URL: https://aip.scitation.org/doi/abs/10.1063/1.2080349.

[260] Alberto Nocera, Fabian H. L. Essler, and Adrian E. Feiguin. "Finite-temperature dynamics of the Mott insulating Hubbard chain". In: *Phys. Rev. B* 97 (4 Jan. 2018), p. 045146. DOI: 10.1103/PhysRevB.97.045146. URL: https://link.aps.org/doi/10.1103/PhysRevB.97.045146.

[261] A. Nocera et al. "Interplay of charge, spin, and lattice degrees of freedom in the spectral properties of the one-dimensional Hubbard-Holstein model". In: *Phys. Rev. B* 90 (19 Nov. 2014), p. 195134. DOI: 10.1103/PhysRevB.90.195134. URL: https://link.aps.org/doi/10.1103/PhysRevB.90.195134.

[262] W. Nolting. "Methode der Spektralmomente für das Hubbard-Modell eines schmalenS-Bandes". In: *Zeitschrift für Physik A Hadrons and nuclei* 255.1 (Feb. 1972), pp. 25–39. ISSN: 0939-7922. DOI: 10.1007/BF01391669. URL: https://doi.org/10.1007/BF01391669.

[263] Fabio Novelli et al. "Witnessing the formation and relaxation of dressed quasi-particles in a strongly correlated electron system". In: *Nature Communications* 5.1 (Oct. 2014), p. 5112. ISSN: 2041-1723. DOI: 10.1038/ncomms6112. URL: https://doi.org/10.1038/ncomms6112.

[264] H. P. Ojeda Collado et al. "Nonlinear dynamics of driven superconductors with dissipation". In: *Phys. Rev. B* 101 (5 Feb. 2020), p. 054502. DOI: 10.1103/PhysRevB.101.054502. URL: https://link.aps.org/doi/10.1103/PhysRevB.101.054502.

[265] H. Okamoto et al. "Photoinduced transition from Mott insulator to metal in the undoped cuprates Nd_2CuO_4 and La_2CuO_4". In: *Phys. Rev. B* 83 (12 Mar. 2011), p. 125102. DOI: 10.1103/PhysRevB.83.125102. URL: https://link.aps.org/doi/10.1103/PhysRevB.83.125102.

[266] Junichi Okamoto. "Time-dependent spectral properties of a photoexcited one-dimensional ionic Hubbard model: an exact diagonalization study". In: *New Journal of Physics* 21.12 (Dec. 2019), p. 123040. DOI: 10.1088/1367-2630/ab5c54. URL: https://doi.org/10.1088/1367-2630/ab5c54.

[267] Junichi Okamoto and Sajad Mirmohammadi. *Photoinduced intra-domain dynamics and nonthermal switching of metastable states in the one-dimensional extended Peierls-Hubbard model*. 2021. arXiv: 2201.00056 [cond-mat.str-el].

[268] Taichi Okuda. "Recent trends in spin-resolved photoelectron spectroscopy". In: *Journal of Physics: Condensed Matter* 29.48 (Nov. 2017), p. 483001. DOI: 10.1088/1361-648x/aa8f28. URL: https://doi.org/10.1088/1361-648x/aa8f28.

[269] Ahmed Omran et al. "Microscopic Observation of Pauli Blocking in Degenerate Fermionic Lattice Gases". In: *Phys. Rev. Lett.* 115 (26 Dec. 2015), p. 263001. DOI: 10.1103/PhysRevLett.115.263001. URL: https://link.aps.org/doi/10.1103/PhysRevLett.115.263001.

[270] Alan V. Oppenheim and Ronald W. Schafer. *Discrete-Time Signal Processing*. 3rd ed. USA: Prentice Hall Press, 2009. ISBN: 0131988425.

[271] J. M. Ortega and W. C. Rheinboldt. *Iterative Solution of Nonlinear Equations in Several Variables*. Society for Industrial and Applied Mathematics, 2000. DOI: 10.1137/1.9780898719468. eprint: https://epubs.siam.org/doi/pdf/10.1137/1.9780898719468. URL: https://epubs.siam.org/doi/abs/10.1137/1.9780898719468.

[272] Román Orús. "A practical introduction to tensor networks: Matrix product states and projected entangled pair states". In: *Annals of Physics* 349 (2014), pp. 117–158. ISSN: 0003-4916. DOI: https://doi.org/10.1016/j.aop.2014.06.013. URL: https://www.sciencedirect.com/science/article/pii/S0003491614001596.

[273] I. V. Oseledets. "A new tensor decomposition". In: *Doklady Mathematics* 80.1 (Aug. 2009), pp. 495–496. ISSN: 1531-8362. DOI: 10.1134/S1064562409040115. URL: https://doi.org/10.1134/S1064562409040115.

[274] I. V. Oseledets. "Tensor-Train Decomposition". In: *SIAM Journal on Scientific Computing* 33.5 (2011), pp. 2295–2317. DOI: 10.1137/090752286. eprint: https://doi.org/10.1137/090752286. URL: https://doi.org/10.1137/090752286.

[275] Juan Osorio Iregui, Matthias Troyer, and Philippe Corboz. "Infinite matrix product states versus infinite projected entangled-pair states on the cylinder: A comparative study". In: *Phys. Rev. B* 96 (11 Sept. 2017), p. 115113. DOI: 10.1103/PhysRevB.96.115113. URL: https://link.aps.org/doi/10.1103/PhysRevB.96.115113.

[276] Alexander Osterkorn. private communication.

[277] Alexander Osterkorn. "Light-induced dynamics of correlations in t-J chains using matrix product states". MA thesis. Georg-August-Universität Göttingen, Aug. 2018.

[278] Alexander Osterkorn, Constantin Meyer, and Salvatore R. Manmana. *In-Gap Band Formation in a Periodically Driven Charge Density Wave Insulator*. 2022. arXiv: 2205.09557 [cond-mat.str-el].

[279] Stellan Östlund and Stefan Rommer. "Thermodynamic Limit of Density Matrix Renormalization". In: *Phys. Rev. Lett.* 75 (19 Nov. 1995), pp. 3537–3540. DOI: 10.1103/PhysRevLett.75.3537. URL: https://link.aps.org/doi/10.1103/PhysRevLett.75.3537.

[280] Sebastian Paeckel. "Topological and non-equilibrium superconductivity in low-dimensional strongly correlated quantum systems". PhD thesis. Georg-August-Universität Göttingen, May 2020. URL: http://hdl.handle.net/21.11130/00-1735-0000-0005-1395-D.

[281] Sebastian Paeckel and Thomas Köhler. *SymMPS*. https://www.symmps.eu. Accessed: 2020-09-23. URL: https://www.symmps.eu.

[282] Sebastian Paeckel, Thomas Köhler, and Salvatore R. Manmana. "Automated construction of $U(1)$-invariant matrix-product operators from graph representations". In: *SciPost Phys.* 3 (5 2017), p. 035. DOI: 10.21468/SciPostPhys.3.5.035. URL: https://scipost.org/10.21468/SciPostPhys.3.5.035.

[283] Sebastian Paeckel et al. "Time-evolution methods for matrix-product states". In: *Annals of Physics* 411 (2019), p. 167998. ISSN: 0003-4916. DOI: https://doi.org/10.1016/j.aop.2019.167998. URL: https://www.sciencedirect.com/science/article/pii/S0003491619302532.

[284] S. Paeckel et al. "Detecting superconductivity out of equilibrium". In: *Phys. Rev. B* 101 (18 May 2020), p. 180507. DOI: 10.1103/PhysRevB.101.180507. URL: https://link.aps.org/doi/10.1103/PhysRevB.101.180507.

[285] Bradraj Pandey et al. "Prediction of exotic magnetic states in the alkali-metal quasi-one-dimensional iron selenide compound Na_2FeSe_2". In: *Phys. Rev. B* 102 (3 July 2020), p. 035149. DOI: 10.1103/PhysRevB.102.035149. URL: https://link.aps.org/doi/10.1103/PhysRevB.102.035149.

[286] Tae Jun Park and J. C. Light. "Unitary quantum time evolution by iterative Lanczos reduction". In: *The Journal of Chemical Physics* 85.10 (1986), pp. 5870–5876. DOI: 10.1063/1.451548. eprint: https://doi.org/10.1063/1.451548. URL: https://doi.org/10.1063/1.451548.

[287] Maxwell F. Parsons et al. "Site-Resolved Imaging of Fermionic ^{6}Li in an Optical Lattice". In: *Phys. Rev. Lett.* 114 (21 May 2015), p. 213002. DOI: 10.1103/PhysRevLett.114.213002. URL: https://link.aps.org/doi/10.1103/PhysRevLett.114.213002.

[288] R. Peierls. "Zur Theorie des Diamagnetismus von Leitungselektronen". In: *Zeitschrift für Physik* 80.11 (Nov. 1933), pp. 763–791. ISSN: 0044-3328. DOI: 10.1007/BF01342591. URL: https://doi.org/10.1007/BF01342591.

[289] S. Peil et al. "Patterned loading of a Bose-Einstein condensate into an optical lattice". In: *Phys. Rev. A* 67 (5 May 2003), p. 051603. DOI: 10.1103/PhysRevA.67.051603. URL: https://link.aps.org/doi/10.1103/PhysRevA.67.051603.

[290] Roger Penrose. "Applications of negative dimensional tensors". In: *Combinatorial Mathematics and Its Applications: Proceedings of a Conference Held at the Mathematical Institute, Oxford, from 7-10 July, 1969*. Ed. by D.J.A. Welsh. Conference series / Institute of Mathematics and its Applications. London: Academic Press, 1971, pp. 221–244. ISBN: 0127433503.

[291] Rodrigo G. Pereira, Steven R. White, and Ian Affleck. "Spectral function of spinless fermions on a one-dimensional lattice". In: *Phys. Rev. B* 79 (16 Apr. 2009), p. 165113. DOI: 10.1103/PhysRevB.79.165113. URL: https://link.aps.org/doi/10.1103/PhysRevB.79.165113.

[292] E. Perfetto and G. Stefanucci. "Ultrafast creation and melting of nonequilibrium excitonic condensates in bulk WSe_2". In: *Phys. Rev. B* 103 (24 June 2021), p. L241404. DOI: 10.1103/PhysRevB.103.L241404. URL: https://link.aps.org/doi/10.1103/PhysRevB.103.L241404.

[293] E. Perfetto and G. Stefanucci. "Ultrafast creation and melting of nonequilibrium excitonic condensates in bulk WSe_2". In: *Phys. Rev. B* 103 (24 June 2021), p. L241404. DOI: 10.1103/PhysRevB.103.L241404. URL: https://link.aps.org/doi/10.1103/PhysRevB.103.L241404.

[294] Francesco Petocchi et al. "Hund excitations and the efficiency of Mott solar cells". In: *Phys. Rev. B* 100 (7 Aug. 2019), p. 075147. DOI: 10.1103/PhysRevB.100.075147. URL: https://link.aps.org/doi/10.1103/PhysRevB.100.075147.

[295] Marko M. Petrić et al. "Tuning the Optical Properties of a MoSe2 Monolayer Using Nanoscale Plasmonic Antennas". In: *Nano Letters* 22.2 (Jan. 2022), pp. 561–569. ISSN: 1530-6984. DOI: 10.1021/acs.nanolett.1c02676. URL: https://doi.org/10.1021/acs.nanolett.1c02676.

[296] Paolo Prandoni and Martin Vetterli. *Signal Processing for Communications*. 1st ed. Communication Sciences. EPFL Press English Imprint, June 17, 2008. ISBN: 1420070460. URL: https://www.sp4comm.org/.

[297] William H. Press et al. *Numerical Recipes: The Art of Scientific Computing, Third Edition*. 3rd ed. New York, NY: Cambridge University Press, 2007. ISBN: 9780521880688. URL: http://numerical.recipes/.

[298] L.R. Rabiner and B. Gold. *Theory and Application of Digital Signal Processing*. 1st ed. Englewood Cliffs, NJ: Prentice-Hall, Inc., 1975. ISBN: 0-13-914101-4.

[299] L. Rettig et al. "Persistent order due to transiently enhanced nesting in an electronically excited charge density wave". In: *Nature Communications* 7.1 (Jan. 2016), p. 10459. ISSN: 2041-1723. DOI: 10.1038/ncomms10459. URL: https://doi.org/10.1038/ncomms10459.

[300] Julián Rincón, Elbio Dagotto, and Adrian E. Feiguin. "Photoinduced Hund excitons in the breakdown of a two-orbital Mott insulator". In: *Phys. Rev. B* 97 (23 June 2018), p. 235104. DOI: 10.1103/PhysRevB.97.235104. URL: https://link.aps.org/doi/10.1103/PhysRevB.97.235104.

[301] Julián Rincón and Adrian E. Feiguin. "Nonequilibrium optical response of a one-dimensional Mott insulator". In: *Phys. Rev. B* 104 (8 Aug. 2021), p. 085122. DOI: 10.1103/PhysRevB.104.085122. URL: https://link.aps.org/doi/10.1103/PhysRevB.104.085122.

[302] Matteo Rini et al. "Control of the electronic phase of a manganite by mode-selective vibrational excitation". In: *Nature* 449.7158 (Sept. 2007), pp. 72–74. ISSN: 1476-4687. DOI: 10.1038/nature06119. URL: https://doi.org/10.1038/nature06119.

[303] Jörg Rissler et al. "Excited states of ladder-type poly-*p*-phenylene oligomers". In: *Phys. Rev. B* 64 (4 July 2001), p. 045122. DOI: 10.1103/PhysRevB.64.045122. URL: https://link.aps.org/doi/10.1103/PhysRevB.64.045122.

[304] C. Robert et al. "Measurement of the spin-forbidden dark excitons in MoS2 and MoSe2 monolayers". In: *Nature Communications* 11.1 (Aug. 2020), p. 4037. ISSN: 2041-1723. DOI: 10.1038/s41467-020-17608-4. URL: https://doi.org/10.1038/s41467-020-17608-4.

[305] K Rodriguez et al. "Coherent matter waves emerging from Mott-insulators". In: *New Journal of Physics* 8.8 (Aug. 2006), pp. 169–169. DOI: 10.1088/1367-2630/8/8/169. URL: https://doi.org/10.1088/1367-2630/8/8/169.

[306] Timm Rohwer et al. "Collapse of long-range charge order tracked by time-resolved photoemission at high momenta". In: *Nature* 471.7339 (Mar. 2011), pp. 490–493. ISSN: 1476-4687. DOI: 10.1038/nature09829. URL: https://doi.org/10.1038/nature09829.

[307] Enrico Ronca et al. "Time-Step Targeting Time-Dependent and Dynamical Density Matrix Renormalization Group Algorithms with ab Initio Hamiltonians". In: *Journal of Chemical Theory and Computation* 13.11 (Nov. 2017), pp. 5560–5571. ISSN: 1549-9618. DOI: 10.1021/acs.jctc.7b00682. URL: https://doi.org/10.1021/acs.jctc.7b00682.

[308] Andrea Ronchi et al. "Ultrafast orbital manipulation and Mott physics in multi-band correlated materials". In: *Ultrafast Phenomena and Nanophotonics XXII*. Ed. by Markus Betz and Abdulhakem Y. Elezzabi. Vol. 10530. International Society for Optics and Photonics. SPIE, 2018, pp. 77–93. DOI: 10.1117/12.2284783. URL: https://doi.org/10.1117/12.2284783.

[309] Roberto Rosati et al. "Dark exciton anti-funneling in atomically thin semiconductors". In: *Nature Communications* 12.1 (Dec. 2021), p. 7221. ISSN: 2041-1723. DOI: 10.1038/s41467-021-27425-y. URL: https://doi.org/10.1038/s41467-021-27425-y.

[310] Maksymilian Środa, Elbio Dagotto, and Jacek Herbrych. "Quantum magnetism of iron-based ladders: Blocks, spirals, and spin flux". In: *Phys. Rev. B* 104 (4 July 2021), p. 045128. DOI: 10.1103/PhysRevB.104.045128. URL: https://link.aps.org/doi/10.1103/PhysRevB.104.045128.

[311] Yousef Saad. *Iterative Methods for Sparse Linear Systems*. Second. Society for Industrial and Applied Mathematics, 2003. DOI: 10.1137/1.9780898718003. eprint: https://epubs.siam.org/doi/pdf/10.1137/1.9780898718003. URL: https://epubs.siam.org/doi/abs/10.1137/1.9780898718003.

[312] Krzysztof Sacha and Jakub Zakrzewski. "Time crystals: a review". In: *Reports on Progress in Physics* 81.1 (Nov. 2017), p. 016401. DOI: 10.1088/1361-6633/aa8b38. URL: https://doi.org/10.1088/1361-6633/aa8b38.

[313] Derek G. Sahota et al. "Many-body recombination in photoexcited insulating cuprates". In: *Phys. Rev. Research* 1 (3 Dec. 2019), p. 033214. DOI: 10.1103/PhysRevResearch.1.033214. URL: https://link.aps.org/doi/10.1103/PhysRevResearch.1.033214.

[314] Jun John Sakurai and Jim Napolitano. *Modern Quantum Mechanics – International Edition*. 2nd ed. San Francisco, CA: Addison-Wesley, 2011. ISBN: 0-321-50336-8.

[315] H. Schaefer, V. V. Kabanov, and J. Demsar. "Collective modes in quasi-one-dimensional charge-density wave systems probed by femtosecond time-resolved optical studies". In: *Phys. Rev. B* 89 (4 Jan. 2014), p. 045106. DOI: 10.1103/PhysRevB.89.045106. URL: https://link.aps.org/doi/10.1103/PhysRevB.89.045106.

[316] Markus Scheb. "Variational Optimization of finite Projected Entangled Pair States". PhD thesis. Philipps-Universität Marburg, 2021. DOI: https://doi.org/10.17192/z2021.0111.

[317] F. Schmitt et al. "Transient Electronic Structure and Melting of a Charge Density Wave in $TbTe_3$". In: *Science* 321.5896 (2008), pp. 1649–1652. DOI: 10.1126/science.1160778. eprint: https://www.science.org/doi/pdf/10.1126/science.1160778. URL: https://www.science.org/doi/abs/10.1126/science.1160778.

[318] L. Schneebeli, M. Kira, and S. W. Koch. "Characterization of Strong Light-Matter Coupling in Semiconductor Quantum-Dot Microcavities via Photon-Statistics Spectroscopy". In: *Phys. Rev. Lett.* 101 (9 Aug. 2008), p. 097401. DOI: 10.1103/PhysRevLett.101.097401. URL: https://link.aps.org/doi/10.1103/PhysRevLett.101.097401.

[319] U. Schollwöck. "The density-matrix renormalization group". In: *Rev. Mod. Phys.* 77 (1 Apr. 2005), pp. 259–315. DOI: 10.1103/RevModPhys.77.259. URL: https://link.aps.org/doi/10.1103/RevModPhys.77.259.

[320] Ulrich Schollwöck. "The density-matrix renormalization group in the age of matrix product states". In: *Annals of Physics* 326.1 (2011). January 2011 Special Issue, pp. 96–192. ISSN: 0003-4916. DOI: https://doi.org/10.1016/j.aop.2010.09.012. URL: https://www.sciencedirect.com/science/article/pii/S0003491610001752.

[321] Kurt Schönhammer. "Luttinger Liquids: The Basic Concepts". In: *Strong Interactions in Low Dimensions*. Ed. by D. Baeriswyl and L. Degiorgi. Physics and Chemistry of Materials with Low-Dimens. Dordrecht: Kluwer Academic Publishers, 2004. Chap. 4, pp. 93–136. ISBN: 1-4020-1798-7. DOI: https://doi.org/10.1007/978-1-4020-3463-3_4.

[322] E. Schrödinger. "Quantisierung als Eigenwertproblem". In: *Annalen der Physik* 384.4 (1926), pp. 361–376. DOI: https://doi.org/10.1002/andp.19263840404. eprint: https://onlinelibrary.wiley.com/doi/pdf/10.1002/andp.19263840404. URL: https://onlinelibrary.wiley.com/doi/abs/10.1002/andp.19263840404.

[323] E. Schrödinger. "Quantisierung als Eigenwertproblem". In: *Annalen der Physik* 384.6 (1926), pp. 489–527. DOI: https://doi.org/10.1002/andp.19263840602. eprint: https://onlinelibrary.wiley.com/doi/pdf/10.1002/andp.19263840602. URL: https://onlinelibrary.wiley.com/doi/abs/10.1002/andp.19263840602.

[324] E. Schrödinger. "Quantisierung als Eigenwertproblem". In: *Annalen der Physik* 385.13 (1926), pp. 437–490. DOI: https://doi.org/10.1002/andp.19263851302. eprint: https://onlinelibrary.wiley.com/doi/pdf/10.1002/andp.19263851302. URL: https://onlinelibrary.wiley.com/doi/abs/10.1002/andp.19263851302.

[325] E. Schrödinger. "Quantisierung als Eigenwertproblem". In: *Annalen der Physik* 386.18 (1926), pp. 109–139. DOI: https://doi.org/10.1002/andp.19263861802. eprint: https://onlinelibrary.wiley.com/doi/pdf/10.1002/andp.19263861802. URL: https://onlinelibrary.wiley.com/doi/abs/10.1002/andp.19263861802.

[326] Ole Schumann. "Model Study of Light Absorption in a Manganite". MA thesis. Georg-August-Universität Göttingen, Nov. 2016.

[327] C. Schweizer et al. "Spin Pumping and Measurement of Spin Currents in Optical Superlattices". In: *Phys. Rev. Lett.* 117 (17 Oct. 2016), p. 170405. DOI: 10.1103/PhysRevLett.117.170405. URL: https://link.aps.org/doi/10.1103/PhysRevLett.117.170405.

[328] J. Sebby-Strabley et al. "Lattice of double wells for manipulating pairs of cold atoms". In: *Phys. Rev. A* 73 (3 Mar. 2006), p. 033605. DOI: 10.1103/PhysRevA.73.033605. URL: https://link.aps.org/doi/10.1103/PhysRevA.73.033605.

[329] Nicholas Sedlmayr et al. "Closed and Open System Dynamics in a Fermionic Chain with a Microscopically Specified Bath: Relaxation and Thermalization". In: *Phys. Rev. Lett.* 110 (10 Mar. 2013), p. 100406. DOI: 10.1103/PhysRevLett.110.100406. URL: https://link.aps.org/doi/10.1103/PhysRevLett.110.100406.

[330] Malte Selig et al. "Dark and bright exciton formation, thermalization, and photoluminescence in monolayer transition metal dichalcogenides". In: *2D Materials* 5.3 (May 2018), p. 035017. DOI: 10.1088/2053-1583/aabea3. URL: https://doi.org/10.1088/2053-1583/aabea3.

[331] Malte Selig et al. "Dark and bright exciton formation, thermalization, and photoluminescence in monolayer transition metal dichalcogenides". In: *2D Materials* 5.3 (May 2018), p. 035017. DOI: 10.1088/2053-1583/aabea3. URL: https://doi.org/10.1088/2053-1583/aabea3.

[332] Rajdeep Sensarma et al. "Lifetime of double occupancies in the Fermi-Hubbard model". In: *Phys. Rev. B* 82 (22 Dec. 2010), p. 224302. DOI: 10.1103/PhysRevB.82.224302. URL: https://link.aps.org/doi/10.1103/PhysRevB.82.224302.

[333] M. A. Sentef. "Light-enhanced electron-phonon coupling from nonlinear electron-phonon coupling". In: *Phys. Rev. B* 95 (20 May 2017), p. 205111. DOI: 10.1103/PhysRevB.95.205111. URL: https://link.aps.org/doi/10.1103/PhysRevB.95.205111.

[334] M. A. Sentef et al. "Theory of Floquet band formation and local pseudospin textures in pump-probe photoemission of graphene". In: *Nature Communications* 6.1 (May 2015), p. 7047. ISSN: 2041-1723. DOI: 10.1038/ncomms8047. URL: https://doi.org/10.1038/ncomms8047.

[335] Can Shao et al. "Analysis of time-resolved single-particle spectrum on the one-dimensional extended Hubbard model". In: *Phys. Rev. B* 101 (4 Jan. 2020), p. 045128. DOI: 10.1103/PhysRevB.101.045128. URL: https://link.aps.org/doi/10.1103/PhysRevB.101.045128.

[336] Can Shao et al. "Numerical method to compute optical conductivity based on pump-probe simulations". In: *Phys. Rev. B* 93 (19 May 2016), p. 195144. DOI: 10.1103/PhysRevB.93.195144. URL: https://link.aps.org/doi/10.1103/PhysRevB.93.195144.

[337] W. Shen, T. P. Devereaux, and J. K. Freericks. "Exact solution for Bloch oscillations of a simple charge-density-wave insulator". In: *Phys. Rev. B* 89 (23 June 2014), p. 235129. DOI: 10.1103/PhysRevB.89.235129. URL: https://link.aps.org/doi/10.1103/PhysRevB.89.235129.

[338] Wen Shen et al. "Nonequilibrium "Melting" of a Charge Density Wave Insulator via an Ultrafast Laser Pulse". In: *Phys. Rev. Lett.* 112 (17 May 2014), p. 176404. DOI: 10.1103/PhysRevLett.112.176404. URL: https://link.aps.org/doi/10.1103/PhysRevLett.112.176404.

[339] Y.-Y. Shi, L.-M. Duan, and G. Vidal. "Classical simulation of quantum many-body systems with a tree tensor network". In: *Phys. Rev. A* 74 (2 Aug. 2006), p. 022320. DOI: 10.1103/PhysRevA.74.022320. URL: https://link.aps.org/doi/10.1103/PhysRevA.74.022320.

[340] C. W. Siders et al. "Detection of Nonthermal Melting by Ultrafast X-ray Diffraction". In: *Science* 286.5443 (1999), pp. 1340–1342. DOI: 10.1126/science.286.5443.1340. eprint: https://www.science.org/doi/pdf/10.1126/science.286.5443.1340. URL: https://www.science.org/doi/abs/10.1126/science.286.5443.1340.

[341] Eduardo H. da Silva Neto et al. "Ubiquitous Interplay Between Charge Ordering and High-Temperature Superconductivity in Cuprates". In: *Science* 343.6169 (2014), pp. 393–396. DOI: 10.1126/science.1243479. eprint: https://www.science.org/doi/pdf/10.1126/science.1243479. URL: https://www.science.org/doi/abs/10.1126/science.1243479.

[342] A. Singer et al. "Photoinduced Enhancement of the Charge Density Wave Amplitude". In: *Phys. Rev. Lett.* 117 (5 July 2016), p. 056401. DOI: 10.1103/PhysRevLett.117.056401. URL: https://link.aps.org/doi/10.1103/PhysRevLett.117.056401.

[343] Gerard L. G. Sleijpen and Henk A. Van der Vorst. "A Jacobi–Davidson Iteration Method for Linear Eigenvalue Problems". In: *SIAM Review* 42.2 (2000), pp. 267–293. DOI: 10.1137/S0036144599363084. eprint: https://doi.org/10.1137/S0036144599363084. URL: https://doi.org/10.1137/S0036144599363084.

[344] C. Sohrt et al. "How fast can a Peierls–Mott insulator be melted?" In: *Faraday Discuss.* 171 (2014), pp. 243–257. DOI: 10.1039/C4FD00042K. URL: http://dx.doi.org/10.1039/C4FD00042K.

[345] G. Stefanucci and E. Perfetto. "From carriers and virtual excitons to exciton populations: Insights into time-resolved ARPES spectra from an exactly solvable model". In: *Phys. Rev. B* 103 (24 June 2021), p. 245103. DOI: 10.1103/PhysRevB.103.245103. URL: https://link.aps.org/doi/10.1103/PhysRevB.103.245103.

[346] G. Stefanucci and E. Perfetto. "From carriers and virtual excitons to exciton populations: Insights into time-resolved ARPES spectra from an exactly solvable model". In: *Phys. Rev. B* 103 (24 June 2021), p. 245103. DOI: 10.1103/PhysRevB.103.245103. URL: https://link.aps.org/doi/10.1103/PhysRevB.103.245103.

[347] Gianluca Stefanucci and Robert van Leeuwen. *Nonequilibrium Many-Body Theory of Quantum Systems: A Modern Introduction*. Cambridge University Press, 2013. DOI: 10.1017/CBO9781139023979.

[348] Daniel Steil et al. "Efficiency of ultrafast optically induced spin transfer in Heusler compounds". In: *Phys. Rev. Research* 2 (2 May 2020), p. 023199. DOI: 10.1103/PhysRevResearch.2.023199. URL: https://link.aps.org/doi/10.1103/PhysRevResearch.2.023199.

[349] L. Stenzel et al. "Quantum phases and topological properties of interacting fermions in one-dimensional superlattices". In: *Phys. Rev. A* 99 (5 May 2019), p. 053614. DOI: 10.1103/PhysRevA.99.053614. URL: https://link.aps.org/doi/10.1103/PhysRevA.99.053614.

[350] J. T. Stewart, J. P. Gaebler, and D. S. Jin. "Using photoemission spectroscopy to probe a strongly interacting Fermi gas". In: *Nature* 454.7205 (Aug. 2008), pp. 744–747. ISSN: 1476-4687. DOI: 10.1038/nature07172. URL: https://doi.org/10.1038/nature07172.

[351] L. Stojchevska et al. "Mechanisms of nonthermal destruction of the superconducting state and melting of the charge-density-wave state by femtosecond laser pulses". In: *Phys. Rev. B* 84 (18 Nov. 2011), p. 180507. DOI: 10.1103/PhysRevB.84.180507. URL: https://link.aps.org/doi/10.1103/PhysRevB.84.180507.

[352] L. Stojchevska et al. "Ultrafast Switching to a Stable Hidden Quantum State in an Electronic Crystal". In: *Science* 344.6180 (2014), pp. 177–180. DOI: 10.1126/science.1241591. eprint: https://www.science.org/doi/pdf/10.1126/science.1241591. URL: https://www.science.org/doi/abs/10.1126/science.1241591.

[353] Jan Felix Stolpp. "Transport and nonequilibrium dynamics in 1d many-body systems with bosonic degrees of freedom". PhD thesis. Georg-August-Universität Göttingen, Dec. 2021. URL: http://hdl.handle.net/21.11130/00-1735-0000-0008-59B5-8.

[354] Jan Stolpp et al. "Charge-density-wave melting in the one-dimensional Holstein model". In: *Phys. Rev. B* 101 (3 Jan. 2020), p. 035134. DOI: 10.1103/PhysRevB.101.035134. URL: https://link.aps.org/doi/10.1103/PhysRevB.101.035134.

[355] Jan Stolpp et al. "Comparative study of state-of-the-art matrix-product-state methods for lattice models with large local Hilbert spaces without U(1) symmetry". In: *Computer Physics Communications* 269 (2021), p. 108106. ISSN: 0010-4655. DOI: https://doi.org/10.1016/j.cpc.2021.108106. URL: https://www.sciencedirect.com/science/article/pii/S0010465521002186.

[356] E M Stoudenmire and Steven R White. "Minimally entangled typical thermal state algorithms". In: *New Journal of Physics* 12.5 (May 2010), p. 055026. DOI: 10.1088/1367-2630/12/5/055026. URL: https://doi.org/10.1088/1367-2630/12/5/055026.

[357] Thomas Strohm. "Electronic Raman scattering in high-temperature superconductors". PhD thesis. Universität Stuttgart, 1999.

[358] Niels Strohmaier et al. "Observation of Elastic Doublon Decay in the Fermi-Hubbard Model". In: *Phys. Rev. Lett.* 104 (8 Feb. 2010), p. 080401. DOI: 10.1103/PhysRevLett.104.080401. URL: https://link.aps.org/doi/10.1103/PhysRevLett.104.080401.

[359] K. Sturm. "Dynamic Structure Factor: An Introduction". In: *Zeitschrift für Naturforschung A* 48.1-2 (1993), pp. 233–242. DOI: doi:10.1515/zna-1993-1-244. URL: https://doi.org/10.1515/zna-1993-1-244.

[360] Masuo Suzuki. "Fractal decomposition of exponential operators with applications to many-body theories and Monte Carlo simulations". In: *Physics Letters A* 146.6 (1990), pp. 319–323. ISSN: 0375-9601. DOI: https://doi.org/10.1016/0375-9601(90)90962-N. URL: https://www.sciencedirect.com/science/article/pii/037596019090962N.

[361] Masuo Suzuki. "General theory of fractal path integrals with applications to many-body theories and statistical physics". In: *Journal of Mathematical Physics* 32.2 (1991), pp. 400–407. DOI: 10.1063/1.529425. eprint: https://doi.org/10.1063/1.529425. URL: https://doi.org/10.1063/1.529425.

[362] Masuo Suzuki. "Relationship between d-Dimensional Quantal Spin Systems and (d+1)-Dimensional Ising Systems: Equivalence, Critical Exponents and Systematic Approximants of the Partition Function and Spin Correlations". In: *Progress of Theoretical Physics* 56.5 (Nov. 1976), pp. 1454–1469. ISSN: 0033-068X. DOI: 10.1143/PTP.56.1454. eprint: https://academic.oup.com/ptp/article-pdf/56/5/1454/5264429/56-5-1454.pdf. URL: https://doi.org/10.1143/PTP.56.1454.

[363] Li Tan and Jean Jiang. *Digital Signal Processing: Fundamentals and Applications*. 2nd ed. Boston: Academic Press, 2013. ISBN: 978-0-12-415893-1. DOI: 10.1016/C2011-0-05250-X.

[364] Yasuhiro Tanaka and Kenji Yonemitsu. "Photoinduced dynamics of excitonic order and Rabi oscillations in the two-orbital Hubbard model". In: *Phys. Rev. B* 102 (7 Aug. 2020), p. 075118. DOI: 10.1103/PhysRevB.102.075118. URL: https://link.aps.org/doi/10.1103/PhysRevB.102.075118.

[365] Zhensheng Tao et al. "Direct time-domain observation of attosecond final-state lifetimes in photoemission from solids". In: *Science* 353.6294 (2016), pp. 62–67. DOI: 10.1126/science.aaf6793. eprint: https://www.science.org/doi/pdf/10.1126/science.aaf6793. URL: https://www.science.org/doi/abs/10.1126/science.aaf6793.

[366] Phoebe Tengdin et al. "Direct light-induced spin transfer between different elements in a spintronic Heusler material via femtosecond laser excitation". In: *Science Advances* 6.3 (2020), eaaz1100. DOI: 10.1126/sciadv.aaz1100. eprint: https://www.science.org/doi/pdf/10.1126/sciadv.aaz1100. URL: https://www.science.org/doi/abs/10.1126/sciadv.aaz1100.

[367] Masaki Tezuka, Ryotaro Arita, and Hideo Aoki. "Phase diagram for the one-dimensional Hubbard-Holstein model: A density-matrix renormalization group study". In: *Phys. Rev. B* 76 (15 Oct. 2007), p. 155114. DOI: 10.1103/PhysRevB.76.155114. URL: https://link.aps.org/doi/10.1103/PhysRevB.76.155114.

[368] Yifan Tian and Steven R. White. "Matrix product state recursion methods for computing spectral functions of strongly correlated quantum systems". In: *Phys. Rev. B* 103 (12 Mar. 2021), p. 125142. DOI: 10.1103/PhysRevB.103.125142. URL: https://link.aps.org/doi/10.1103/PhysRevB.103.125142.

[369] Alexander Clemens Tiegel. "Finite-temperature dynamics of low-dimensional quantum systems with DMRG methods". PhD thesis. Georg-August-Universität Göttingen, Aug. 2016. URL: http://hdl.handle.net/11858/00-1735-0000-0028-8801-A.

[370] Alexander C. Tiegel et al. "Erratum: Matrix product state formulation of frequency-space dynamics at finite temperatures [Phys. Rev. B 90, 060406(R) (2014)]". In: *Phys. Rev. B* 94 (17 Nov. 2016), p. 179908. DOI: 10.1103/PhysRevB.94.179908. URL: https://link.aps.org/doi/10.1103/PhysRevB.94.179908.

[371] Alexander C. Tiegel et al. "Matrix product state formulation of frequency-space dynamics at finite temperatures". In: *Phys. Rev. B* 90 (6 Aug. 2014), p. 060406. DOI: 10.1103/PhysRevB.90.060406. URL: https://link.aps.org/doi/10.1103/PhysRevB.90.060406.

[372] Alexander C. Tiegel et al. "Optical conductivity of the Hubbard chain away from half filling". In: *Phys. Rev. B* 93 (12 Mar. 2016), p. 125108. DOI: 10.1103/PhysRevB.93.125108. URL: https://link.aps.org/doi/10.1103/PhysRevB.93.125108.

[373] T. Tohyama. "Nonequilibrium photo dynamics of low-dimensional strongly correlated electron systems". In: *The European Physical Journal Special Topics* 222.5 (July 2013), pp. 1065–1075. ISSN: 1951-6401. DOI: 10.1140/epjst/e2013-01907-y. URL: https://doi.org/10.1140/epjst/e2013-01907-y.

[374] T. Tohyama. "Symmetry of Photoexcited States and Large-Shift Raman Scattering in Two-Dimensional Mott Insulators". In: *Journal of the Physical Society of Japan* 75.3 (2006), p. 034713. DOI: 10.1143/JPSJ.75.034713. eprint: https://doi.org/10.1143/JPSJ.75.034713. URL: https://doi.org/10.1143/JPSJ.75.034713.

[375] Jan Martin Tomczak. "Propriétés spectrales et optiques des Matériaux corrélés." Theses. Ecole Polytechnique X, Sept. 2007. URL: https://pastel.archives-ouvertes.fr/pastel-00003163.

[376] A. Tomeljak et al. "Dynamics of Photoinduced Charge-Density-Wave to Metal Phase Transition in $\mathbf{K}_{0.3}MoO_3$". In: *Phys. Rev. Lett.* 102 (6 Feb. 2009), p. 066404. DOI: 10.1103/PhysRevLett.102.066404. URL: https://link.aps.org/doi/10.1103/PhysRevLett.102.066404.

[377] Kha Tran et al. "Evidence for moiré excitons in van der Waals heterostructures". In: *Nature* 567.7746 (Mar. 2019), pp. 71–75. ISSN: 1476-4687. DOI: 10.1038/s41586-019-0975-z. URL: https://doi.org/10.1038/s41586-019-0975-z.

[378] Lloyd N. Trefethen and David Bau. *Numerical Linear Algebra*. Philadelphia: SIAM, 1997. ISBN: 0898713617.

[379] S. Trotzky et al. "Time-Resolved Observation and Control of Superexchange Interactions with Ultracold Atoms in Optical Lattices". In: *Science* 319.5861 (2008), pp. 295–299. DOI: 10.1126/science.1150841. eprint: https://www.science.org/doi/pdf/10.1126/science.1150841. URL: https://www.science.org/doi/abs/10.1126/science.1150841.

[380] Naoto Tsuji and Philipp Werner. "Nonequilibrium dynamical mean-field theory based on weak-coupling perturbation expansions: Application to dynamical symmetry breaking in the Hubbard model". In: *Phys. Rev. B* 88 (16 Oct. 2013), p. 165115. DOI: 10.1103/PhysRevB.88.165115. URL: https://link.aps.org/doi/10.1103/PhysRevB.88.165115.

[381] A. M. Turing. "On Computable Numbers, with an Application to the Entscheidungsproblem". In: *Proceedings of the London Mathematical Society* s2-42.1 (1937), pp. 230–265. DOI: 10.1112/plms/s2-42.1.230. eprint: https://londmathsoc.onlinelibrary.wiley.com/doi/pdf/10.1112/plms/s2-42.1.230. URL: https://londmathsoc.onlinelibrary.wiley.com/doi/abs/10.1112/plms/s2-42.1.230.

[382] Götz S. Uhrig, Mona H. Kalthoff, and James K. Freericks. "Positivity of the Spectral Densities of Retarded Floquet Green Functions". In: *Phys. Rev. Lett.* 122 (13 Apr. 2019), p. 130604. DOI: 10.1103/PhysRevLett.122.130604. URL: https://link.aps.org/doi/10.1103/PhysRevLett.122.130604.

[383] Léon Van Hove. "Correlations in Space and Time and Born Approximation Scattering in Systems of Interacting Particles". In: *Phys. Rev.* 95 (1 July 1954), pp. 249–262. DOI: 10.1103/PhysRev.95.249. URL: https://link.aps.org/doi/10.1103/PhysRev.95.249.

[384] F. Verstraete and J. I. Cirac. "Matrix product states represent ground states faithfully". In: *Phys. Rev. B* 73 (9 Mar. 2006), p. 094423. DOI: 10.1103/PhysRevB.73.094423. URL: https://link.aps.org/doi/10.1103/PhysRevB.73.094423.

[385] F. Verstraete and J. I. Cirac. *Renormalization algorithms for Quantum-Many Body Systems in two and higher dimensions*. 2004. arXiv: cond-mat/0407066 [cond-mat.str-el].

[386] F. Verstraete, J. J. García-Ripoll, and J. I. Cirac. "Matrix Product Density Operators: Simulation of Finite-Temperature and Dissipative Systems". In: *Phys. Rev. Lett.* 93 (20 Nov. 2004), p. 207204. DOI: 10.1103/PhysRevLett.93.207204. URL: https://link.aps.org/doi/10.1103/PhysRevLett.93.207204.

[387] F. Verstraete, D. Porras, and J. I. Cirac. "Density Matrix Renormalization Group and Periodic Boundary Conditions: A Quantum Information Perspective". In: *Phys. Rev. Lett.* 93 (22 Nov. 2004), p. 227205. DOI: 10.1103/PhysRevLett.93.227205. URL: https://link.aps.org/doi/10.1103/PhysRevLett.93.227205.

[388] F. Verstraete et al. "Criticality, the Area Law, and the Computational Power of Projected Entangled Pair States". In: *Phys. Rev. Lett.* 96 (22 June 2006), p. 220601. DOI: 10.1103/PhysRevLett.96.220601. URL: https://link.aps.org/doi/10.1103/PhysRevLett.96.220601.

[389] G. Vidal. "Class of Quantum Many-Body States That Can Be Efficiently Simulated". In: *Phys. Rev. Lett.* 101 (11 Sept. 2008), p. 110501. DOI: 10.1103/PhysRevLett.101.110501. URL: https://link.aps.org/doi/10.1103/PhysRevLett.101.110501.

[390] G. Vidal. "Classical Simulation of Infinite-Size Quantum Lattice Systems in One Spatial Dimension". In: *Phys. Rev. Lett.* 98 (7 Feb. 2007), p. 070201. DOI: 10.1103/PhysRevLett.98.070201. URL: https://link.aps.org/doi/10.1103/PhysRevLett.98.070201.

[391] Guifré Vidal. "Efficient Classical Simulation of Slightly Entangled Quantum Computations". In: *Phys. Rev. Lett.* 91 (14 Oct. 2003), p. 147902. DOI: 10.1103/PhysRevLett.91.147902. URL: https://link.aps.org/doi/10.1103/PhysRevLett.91.147902.

[392] Guifré Vidal. "Efficient Simulation of One-Dimensional Quantum Many-Body Systems". In: *Phys. Rev. Lett.* 93 (4 July 2004), p. 040502. DOI: 10.1103/PhysRevLett.93.040502. URL: https://link.aps.org/doi/10.1103/PhysRevLett.93.040502.

[393] Pauli Virtanen et al. "SciPy 1.0: Fundamental Algorithms for Scientific Computing in Python". In: *Nature Methods* 17 (2020), pp. 261–272. DOI: 10.1038/s41592-019-0686-2.

[394] S. Vogelgesang et al. "Phase ordering of charge density waves traced by ultrafast low-energy electron diffraction". In: *Nature Physics* 14.2 (Feb. 2018), pp. 184–190. ISSN: 1745-2481. DOI: 10.1038/nphys4309. URL: https://doi.org/10.1038/nphys4309.

[395] Matthias Vojta. "Orbital-Selective Mott Transitions: Heavy Fermions and Beyond". In: *Journal of Low Temperature Physics* 161.1 (Oct. 2010), pp. 203–232. ISSN: 1573-7357. DOI: 10.1007/s10909-010-0206-3. URL: https://doi.org/10.1007/s10909-010-0206-3.

[396] M L Wall and Lincoln D Carr. "Out-of-equilibrium dynamics with matrix product states". In: *New Journal of Physics* 14.12 (Dec. 2012), p. 125015. DOI: 10.1088/1367-2630/14/12/125015. URL: https://doi.org/10.1088/1367-2630/14/12/125015.

[397] S. Wall et al. "Quantum interference between charge excitation paths in a solid-state Mott insulator". In: *Nature Physics* 7.2 (Feb. 2011), pp. 114–118. ISSN: 1745-2481. DOI: 10.1038/nphys1831. URL: https://doi.org/10.1038/nphys1831.

[398] Robert Wallauer et al. "Momentum-Resolved Observation of Exciton Formation Dynamics in Monolayer WS2". In: *Nano Letters* 21.13 (July 2021), pp. 5867–5873. ISSN: 1530-6984. DOI: 10.1021/acs.nanolett.1c01839. URL: https://doi.org/10.1021/acs.nanolett.1c01839.

[399] Robert Wallauer et al. "Momentum-Resolved Observation of Exciton Formation Dynamics in Monolayer WS2". In: *Nano Letters* 21.13 (2021). PMID: 34165994, pp. 5867–5873. DOI: 10.1021/acs.nanolett.1c01839. eprint: https://doi.org/10.1021/acs.nanolett.1c01839. URL: https://doi.org/10.1021/acs.nanolett.1c01839.

[400] Yao Wang et al. "Emergence of quasiparticles in a doped Mott insulator". In: *Communications Physics* 3.1 (Nov. 2020), p. 210. ISSN: 2399-3650. DOI: 10.1038/s42005-020-00480-5. URL: https://doi.org/10.1038/s42005-020-00480-5.

[401] Yao Wang et al. "Light-Enhanced Spin Fluctuations and d-Wave Superconductivity at a Phase Boundary". In: *Phys. Rev. Lett.* 120 (24 June 2018), p. 246402. DOI: 10.1103/PhysRevLett.120.246402. URL: https://link.aps.org/doi/10.1103/PhysRevLett.120.246402.

[402] Yao Wang et al. "Producing coherent excitations in pumped Mott antiferromagnetic insulators". In: *Phys. Rev. B* 96 (23 Dec. 2017), p. 235142. DOI: 10.1103/PhysRevB.96.235142. URL: https://link.aps.org/doi/10.1103/PhysRevB.96.235142.

[403] Y. Wang et al. "Using Nonequilibrium Dynamics to Probe Competing Orders in a Mott-Peierls System". In: *Phys. Rev. Lett.* 116 (8 Feb. 2016), p. 086401. DOI: 10.1103/PhysRevLett.116.086401. URL: https://link.aps.org/doi/10.1103/PhysRevLett.116.086401.

[404] Marvin J. Weber, ed. *Handbook of Laser Wavelengths*. 1st ed. Boca Raton, FL: CRC Press, 1998. ISBN: 0-8493-3508-6. DOI: 10.1201/9781315219639.

[405] Alexander Weiße et al. "The kernel polynomial method". In: *Rev. Mod. Phys.* 78 (1 Mar. 2006), pp. 275–306. DOI: 10.1103/RevModPhys.78.275. URL: https://link.aps.org/doi/10.1103/RevModPhys.78.275.

[406] Steven R. White. "Density matrix formulation for quantum renormalization groups". In: *Phys. Rev. Lett.* 69 (19 Nov. 1992), pp. 2863–2866. DOI: 10.1103/PhysRevLett.69.2863. URL: https://link.aps.org/doi/10.1103/PhysRevLett.69.2863.

[407] Steven R. White. "Density-matrix algorithms for quantum renormalization groups". In: *Phys. Rev. B* 48 (14 Oct. 1993), pp. 10345–10356. DOI: 10.1103/PhysRevB.48.10345. URL: https://link.aps.org/doi/10.1103/PhysRevB.48.10345.

[408] Steven R. White and Adrian E. Feiguin. "Real-Time Evolution Using the Density Matrix Renormalization Group". In: *Phys. Rev. Lett.* 93 (7 Aug. 2004), p. 076401. DOI: 10.1103/PhysRevLett.93.076401. URL: https://link.aps.org/doi/10.1103/PhysRevLett.93.076401.

[409] Kenneth G. Wilson. "The renormalization group: Critical phenomena and the Kondo problem". In: *Rev. Mod. Phys.* 47 (4 Oct. 1975), pp. 773–840. DOI: 10.1103/RevModPhys.47.773. URL: https://link.aps.org/doi/10.1103/RevModPhys.47.773.

[410] Michael M. Wolf. "Violation of the Entropic Area Law for Fermions". In: *Phys. Rev. Lett.* 96 (1 Jan. 2006), p. 010404. DOI: 10.1103/PhysRevLett.96.010404. URL: https://link.aps.org/doi/10.1103/PhysRevLett.96.010404.

[411] Tao Wu et al. "Magnetic-field-induced charge-stripe order in the high-temperature superconductor YBa2Cu3Oy". In: *Nature* 477.7363 (Sept. 2011), pp. 191–194. ISSN: 1476-4687. DOI: 10.1038/nature10345. URL: https://doi.org/10.1038/nature10345.

[412] T. Yamaguchi et al. "Excitonic optical spectra and energy structures in a one-dimensional Mott insulator demonstrated by applying a many-body Wannier functions method to a charge model". In: *Phys. Rev. B* 103 (4 Jan. 2021), p. 045124. DOI: 10.1103/PhysRevB.103.045124. URL: https://link.aps.org/doi/10.1103/PhysRevB.103.045124.

[413] Bing Yang et al. "Spin-dependent optical superlattice". In: *Phys. Rev. A* 96 (1 July 2017), p. 011602. DOI: 10.1103/PhysRevA.96.011602. URL: https://link.aps.org/doi/10.1103/PhysRevA.96.011602.

[414] Chun Yang and Adrian E. Feiguin. "Spectral function of Mott-insulating Hubbard ladders: From fractionalized excitations to coherent quasiparticles". In: *Phys. Rev. B* 99 (23 June 2019), p. 235117. DOI: 10.1103/PhysRevB.99.235117. URL: https://link.aps.org/doi/10.1103/PhysRevB.99.235117.

[415] N. Y. Yao et al. "Discrete Time Crystals: Rigidity, Criticality, and Realizations". In: *Phys. Rev. Lett.* 118 (3 Jan. 2017), p. 030401. DOI: 10.1103/PhysRevLett.118.030401. URL: https://link.aps.org/doi/10.1103/PhysRevLett.118.030401.

[416] N. Y. Yao et al. "Erratum: Discrete Time Crystals: Rigidity, Criticality, and Realizations [Phys. Rev. Lett. 118, 030401 (2017)]". In: *Phys. Rev. Lett.* 118 (26 June 2017), p. 269901. DOI: 10.1103/PhysRevLett.118.269901. URL: https://link.aps.org/doi/10.1103/PhysRevLett.118.269901.

[417] M. Yarmohammadi et al. "Dynamical properties of a driven dissipative dimerized $S = \frac{1}{2}$ chain". In: *Phys. Rev. B* 103 (4 Jan. 2021), p. 045132. DOI: 10.1103/PhysRevB.103.045132. URL: https://link.aps.org/doi/10.1103/PhysRevB.103.045132.

[418] Kenji Yonemitsu. "Photoinduced Enhancement of Anisotropic Charge Correlations on Triangular Lattices with Trimers". In: *Journal of the Physical Society of Japan* 86.2 (2017), p. 024711. DOI: 10.7566/JPSJ.86.024711. eprint: https://doi.org/10.7566/JPSJ.86.024711. URL: https://doi.org/10.7566/JPSJ.86.024711.

[419] Long Yuan et al. "Twist-angle-dependent interlayer exciton diffusion in WS2–WSe2 heterobilayers". In: *Nature Materials* 19.6 (June 2020), pp. 617–623. ISSN: 1476-4660. DOI: 10.1038/s41563-020-0670-3. URL: https://doi.org/10.1038/s41563-020-0670-3.

[420] Michael P. Zaletel et al. "Time-evolving a matrix product state with long-ranged interactions". In: *Phys. Rev. B* 91 (16 Apr. 2015), p. 165112. DOI: 10.1103/PhysRevB.91.165112. URL: https://link.aps.org/doi/10.1103/PhysRevB.91.165112.

[421] Krissia Zawadzki and Adrian E. Feiguin. "Time- and momentum-resolved tunneling spectroscopy of pump-driven nonthermal excitations in Mott insulators". In: *Phys. Rev. B* 100 (19 Nov. 2019), p. 195124. DOI: 10.1103/PhysRevB.100.195124. URL: https://link.aps.org/doi/10.1103/PhysRevB.100.195124.

[422] Krissia Zawadzki, Alberto Nocera, and Adrian E. Feiguin. *A time-dependent scattering approach to core-level spectroscopies*. 2020. arXiv: 2002.04142 [cond-mat.str-el].

[423] Krissia Zawadzki, Luhang Yang, and Adrian E. Feiguin. "Time-dependent approach to inelastic scattering spectroscopies in and away from equilibrium: Beyond perturbation theory". In: *Phys. Rev. B* 102 (23 Dec. 2020), p. 235141. DOI: 10.1103/PhysRevB.102.235141. URL: https://link.aps.org/doi/10.1103/PhysRevB.102.235141.

[424] Peymon Zereshki, Pavel Valencia-Acuna, and Hui Zhao. "All-optical control of charge transfer and interlayer excitons in transition metal dichalcogenide heterostructures". In: *Phys. Rev. B* 103 (16 Apr. 2021), p. 165416. DOI: 10.1103/PhysRevB.103.165416. URL: https://link.aps.org/doi/10.1103/PhysRevB.103.165416.

[425] J. Zhang et al. "Observation of a discrete time crystal". In: *Nature* 543.7644 (Mar. 2017), pp. 217–220. ISSN: 1476-4687. DOI: 10.1038/nature21413. URL: https://doi.org/10.1038/nature21413.

[426] Haiming Zhu et al. "Interfacial Charge Transfer Circumventing Momentum Mismatch at Two-Dimensional van der Waals Heterojunctions". In: *Nano Letters* 17.6 (June 2017), pp. 3591–3598. ISSN: 1530-6984. DOI: 10.1021/acs.nanolett.7b00748. URL: https://doi.org/10.1021/acs.nanolett.7b00748.

[427] Z.-H. Zhu et al. "Photoelectron Spin-Polarization Control in the Topological Insulator Bi_2Se_3". In: *Phys. Rev. Lett.* 112 (7 Feb. 2014), p. 076802. DOI: 10.1103/PhysRevLett.112.076802. URL: https://link.aps.org/doi/10.1103/PhysRevLett.112.076802.

[428] J. E. Zimmermann et al. *Ultrafast charge-transfer dynamics in twisted MoS_2/WSe_2 heterostructures*. 2021. arXiv: 2105.05812 [cond-mat.mtrl-sci].

[429] Martin R. Zirnbauer. "Particle–hole symmetries in condensed matter". In: *Journal of Mathematical Physics* 62.2 (2021), p. 021101. DOI: 10.1063/5.0035358. eprint: https://doi.org/10.1063/5.0035358. URL: https://doi.org/10.1063/5.0035358.

[430] V. Zlati et al. "Some remarks on second-order perturbation theory for the Hubbard model". In: *Philosophical Magazine B* 65.6 (1992), pp. 1255–1266. DOI: 10.1080/13642819208215091. eprint: https://doi.org/10.1080/13642819208215091. URL: https://doi.org/10.1080/13642819208215091.

[431] X. Zotos and P. Prelovšek. "Transport in One Dimensional Quantum Systems". In: *Strong Interactions in Low Dimensions*. Ed. by D. Baeriswyl and L. Degiorgi. Physics and Chemistry of Materials with Low-Dimens. Dordrecht: Kluwer Academic Publishers, 2004. Chap. 11, pp. 347–382. ISBN: 1-4020-1798-7. DOI: https://doi.org/10.1007/978-1-4020-3463-3_11.

[432] Michael Zwolak and Guifré Vidal. "Mixed-State Dynamics in One-Dimensional Quantum Lattice Systems: A Time-Dependent Superoperator Renormalization Algorithm". In: *Phys. Rev. Lett.* 93 (20 Nov. 2004), p. 207205. DOI: 10.1103/PhysRevLett.93.207205. URL: https://link.aps.org/doi/10.1103/PhysRevLett.93.207205.